CMS physics technical design report, volume II: Physics performance

CMS Physics Technical Design Report, Volume II: Physics Performance

2007 J. Phys. G: Nucl. Part. Phys. 34 995

(http://iopscience.iop.org/0954-3899/34/6/S01)

IOP PUBLISHING JOURNAL OF PHYSICS G: NUCLEAR AND PARTICLE PHYSICS

J. Phys. G: Nucl. Part. Phys. **34** (2007) 995–1579 doi:10.1088/0954-3899/34/6/S01

CMS Physics Technical Design Report, Volume II: Physics Performance

The CMS Collaboration

Received 3 January 2007
Published 20 April 2007
Online at stacks.iop.org/JPhysG/34/995

Abstract

CMS is a general purpose experiment, designed to study the physics of pp collisions at 14 TeV at the Large Hadron Collider (LHC). It currently involves more than 2000 physicists from more than 150 institutes and 37 countries. The LHC will provide extraordinary opportunities for particle physics based on its unprecedented collision energy and luminosity when it begins operation in 2007.

The principal aim of this report is to present the strategy of CMS to explore the rich physics programme offered by the LHC. This volume demonstrates the physics capability of the CMS experiment. The prime goals of CMS are to explore physics at the TeV scale and to study the mechanism of electroweak symmetry breaking—through the discovery of the Higgs particle or otherwise. To carry out this task, CMS must be prepared to search for new particles, such as the Higgs boson or supersymmetric partners of the Standard Model particles, from the start-up of the LHC since new physics at the TeV scale may manifest itself with modest data samples of the order of a few fb^{-1} or less.

The analysis tools that have been developed are applied to study in great detail and with all the methodology of performing an analysis on CMS data specific benchmark processes upon which to gauge the performance of CMS. These processes cover several Higgs boson decay channels, the production and decay of new particles such as Z' and supersymmetric particles, B_s production and processes in heavy ion collisions. The simulation of these benchmark processes includes subtle effects such as possible detector miscalibration and misalignment. Besides these benchmark processes, the physics reach of CMS is studied for a large number of signatures arising in the Standard Model and also in theories beyond the Standard Model for integrated luminosities ranging from $1\,\mathrm{fb}^{-1}$ to $30\,\mathrm{fb}^{-1}$. The Standard Model processes include QCD, B-physics, diffraction, detailed studies of the top quark properties, and electroweak physics topics such as the W and Z^0 boson properties. The production and decay of the Higgs particle is studied for many observable decays, and the precision with which the Higgs boson properties can be derived is determined. About ten different supersymmetry benchmark points are analysed using full simulation. The CMS discovery reach is evaluated in the SUSY parameter space covering a large variety of decay signatures.

Furthermore, the discovery reach for a plethora of alternative models for new physics is explored, notably extra dimensions, new vector boson high mass states, little Higgs models, technicolour and others. Methods to discriminate between models have been investigated.

This report is organized as follows. Chapter 1, the Introduction, describes the context of this document. Chapters 2–6 describe examples of full analyses, with photons, electrons, muons, jets, missing E_{T}, B-mesons and τ's, and for quarkonia in heavy ion collisions. Chapters 7–15 describe the physics reach for Standard Model processes, Higgs discovery and searches for new physics beyond the Standard Model.

Acknowledgments

This report is the result of several years of work on the preparation for physics analysis at the LHC with CMS. Subprojects in all areas were involved (Detector, PRS, Software, and Computing) in order to produce the large Monte Carlo simulation samples needed, to develop the software to analyse those samples, to perform the studies reported in this Report, and to write and review our findings.

We wish to thank, for the many useful discussions, our theory and phenomenology colleagues, in particular J Campbell, D Dominici, A Djouadi, S Heinemeyer, W Hollik, V Khoze, T Plehn, M Raidal, M Spira and G Weiglein for their contributions to this Report.

For their constructive comments and guidance, we would like to thank the CPT internal reviewers: J Alexander, J Branson, Y Karyotakis, M Kasemann and R Tenchini.

We would like to thank L Malgeri and R Tenchini for their efficient organisation of the CMS Notes.

For their patience in meeting sometimes impossible demands, we wish to thank the CMS Secretariat: K Aspola, M Azeglio, N Bogolioubova, D Denise, D Hudson, G Martin, and M C Pelloux.

We also would like to thank G Alverson and L Taylor for their invaluable technical assistance in the preparation of this manuscript.

Finally, we wish to thank the CMS management for their strong support and encouragement.

The CMS Collaboration

The CMS Collaboration

Yerevan Physics Institute, Yerevan, ARMENIA
G L Bayatian, S Chatrchyan, G Hmayakyan, A M Sirunyan

Institut für Hochenergiephysik der OeAW, Wien, AUSTRIA
W Adam, T Bergauer, M Dragicevic, J Erö, M Friedl, R Fruehwirth, V Ghete, P Glaser, J Hrubec, M Jeitler, M Krammer, I Magrans, I Mikulec, W Mitaroff, T Noebauer, M Pernicka, P Porth, H Rohringer, J Strauss, A Taurok, W Waltenberger, G Walzel, E Widl, C-E Wulz

Research Institute for Nuclear Problems, Minsk, BELARUS
A Fedorov, M Korzhik, O Missevitch, R Zuyeuski

National Centre for Particle and High Energy Physics, Minsk, BELARUS
V Chekhovsky, O Dvornikov, I Emeliantchik, A Litomin, V Mossolov, N Shumeiko, A Solin, R Stefanovitch, J Suarez Gonzalez, A Tikhonov

Byelorussian State University, Minsk, BELARUS
V Petrov

Vrije Universiteit Brussel, Brussel, BELGIUM
J D'Hondt, S De Weirdt, R Goorens, J Heyninck, S Lowette, S Tavernier, W Van Doninck[1], L Van Lancker

Université Libre de Bruxelles, Bruxelles, BELGIUM
O Bouhali, B Clerbaux, G De Lentdecker, J P Dewulf, T Mahmoud, P E Marage, L Neukermans, V Sundararajan, C Vander Velde, P Vanlaer, J Wickens

Université Catholique de Louvain, Louvain-la-Neuve, BELGIUM
S Assouak, J L Bonnet, G Bruno, J Caudron, B De Callatay, J De Favereau De Jeneret, S De Visscher, C Delaere, P Demin, D Favart, E Feltrin, E Forton, G Grégoire, S Kalinin, D Kcira, T Keutgen, G Leibenguth, V Lemaitre, Y Liu, D Michotte, O Militaru, A Ninane, S Ovyn, T Pierzchala, K Piotrzkowski, V Roberfroid, X Rouby, D Teyssier, O Van der Aa, M Vander Donckt

Université de Mons-Hainaut, Mons, BELGIUM
E Daubie, P Herquet, A Mollet, A Romeyer

Universiteit Antwerpen, Wilrijk, BELGIUM
W Beaumont, M Cardaci, E De Langhe, E A De Wolf, L Rurua

Centro Brasileiro de Pesquisas Fisicas, Rio de Janeiro, RJ, BRAZIL
M H G Souza

Universidade do Estado do Rio de Janeiro, Rio de Janeiro, RJ, BRAZIL
V Oguri, A Santoro, A Sznajder

Instituto de Fisica, Universidade Federal do Rio de Janeiro, Rio de Janeiro, RJ, BRAZIL
M Vaz

Instituto de Fisica Teorica, Universidade Estadual Paulista, Sao Paulo, SP, BRAZIL
E M Gregores, S F Novaes

[1] Also at CERN, European Organization for Nuclear Research, Geneva, Switzerland.

Institute for Nuclear Research and Nuclear Energy, Sofia, BULGARIA
T Anguelov, G Antchev, I Atanasov, J Damgov, N Darmenov[1], L Dimitrov, V Genchev[1], P Iaydjiev, B Panev, S Piperov, S Stoykova, G Sultanov, I Vankov

University of Sofia, Sofia, BULGARIA
A Dimitrov, V Kozhuharov, L Litov, M Makariev, A Marinov, E Marinova, S Markov, M Mateev, B Pavlov, P Petkov, C Sabev, S Stoynev, Z Toteva[1], V Verguilov

Institute of High Energy Physics, Beijing, CHINA
G M Chen, H S Chen, K L He, C H Jiang, W G Li, H M Liu, X Meng, X Y Shen, H S Sun, M Yang, W R Zhao, H L Zhuang

Peking University, Beijing, CHINA
Y Ban, J Cai, S Liu, S J Qian, Z C Yang, Y L Ye, J Ying

University for Science and Technology of China, Hefei, Anhui, CHINA
J Wu, Z P Zhang

Technical University of Split, Split, CROATIA
N Godinovic, I Puljak, I Soric

University of Split, Split, CROATIA
Z Antunovic, M Dzelalija, K Marasovic

Institute Rudjer Boskovic, Zagreb, CROATIA
V Brigljevic, D Ferencek, K Kadija, S Morovic, M Planinic[2]

University of Cyprus, Nicosia, CYPRUS
C Nicolaou, A Papadakis, P A Razis, D Tsiakkouri

National Institute of Chemical Physics and Biophysics, Tallinn, ESTONIA
A Hektor, M Kadastik, K Kannike, E Lippmaa, M Müntel, M Raidal

Laboratory of Advanced Energy Systems, Helsinki University of Technology, Espoo, FINLAND
P A Aarnio

Helsinki Institute of Physics, Helsinki, FINLAND
S Czellar, E Haeggstroem, A Heikkinen, J Härkönen, V Karimäki, R Kinnunen, T Lampén, K Lassila-Perini, S Lehti, T Lindén, P R Luukka, S Michal[1], T Mäenpää, J Nysten, M Stettler[1], E Tuominen, J Tuominiemi, L Wendland

Lappeenranta University of Technology, Lappeenranta, FINLAND
T Tuuva

Laboratoire d'Annecy-le-Vieux de Physique des Particules, IN2P3-CNRS, Annecy-le-Vieux, FRANCE
J P Guillaud, P Nedelec, D Sillou

DSM/DAPNIA, CEA/Saclay, Gif-sur-Yvette, FRANCE
M Anfreville, S Beauceron, E Bougamont, P Bredy, R Chipaux, M Dejardin, D Denegri, J Descamps, B Fabbro, J L Faure, S Ganjour, F X Gentit, A Givernaud, P Gras, G Hamel de Monchenault, P Jarry, F Kircher, M C Lemaire[3], B Levesy[1], E Locci, J P Lottin,

[2] Also at University of Zagreb, Zagreb, Croatia.
[3] Also at California Institute of Technology, Pasadena, USA.

I Mandjavidze, M Mur, E Pasquetto, A Payn, J Rander, J M Reymond, F Rondeaux, A Rosowsky, Z H Sun, P Verrecchia

Laboratoire Leprince-Ringuet, Ecole Polytechnique, IN2P3-CNRS, Palaiseau, FRANCE
S Baffioni, F Beaudette, M Bercher, U Berthon, S Bimbot, J Bourotte, P Busson, M Cerutti, D Chamont, C Charlot, C Collard, D Decotigny, E Delmeire, L Dobrzynski, A M Gaillac, Y Geerebaert, J Gilly, M Haguenauer, A Karar, A Mathieu, G Milleret, P Miné, P Paganini, T Romanteau, I Semeniouk, Y Sirois

Institut Pluridisciplinaire Hubert Curien, IN2P3-CNRS, ULP, UHA Mulhouse, Strasbourg, FRANCE
J D Berst, J M Brom, F Didierjean, F Drouhin[1], J C Fontaine[4], U Goerlach[5], P Graehling, L Gross, L Houchu, P Juillot, A Lounis[5], C Maazouzi, D Mangeol, C Olivetto, T Todorov [1], P Van Hove, D Vintache

Institut de Physique Nucléaire, IN2P3-CNRS, Université Claude Bernard Lyon 1, Villeurbanne, FRANCE
M Ageron, J L Agram, G Baulieu, M Bedjidian, J Blaha, A Bonnevaux, G Boudoul[1], E Chabanat, C Combaret, D Contardo[1], R Della Negra, P Depasse, T Dupasquier, H El Mamouni, N Estre, J Fay, S Gascon, N Giraud, C Girerd, R Haroutunian, J C Ianigro, B Ille, M Lethuillier, N Lumb[1], H Mathez, G Maurelli, L Mirabito[1], S Perries, O Ravat

Institute of High Energy Physics and Informatization, Tbilisi State University, Tbilisi, GEORGIA
R Kvatadze

Institute of Physics Academy of Science, Tbilisi, GEORGIA
V Roinishvili

RWTH, I. Physikalisches Institut, Aachen, GERMANY
R Adolphi, R Brauer, W Braunschweig, H Esser, L Feld, A Heister, W Karpinski, K Klein, C Kukulies, J Olzem, A Ostapchuk, D Pandoulas, G Pierschel, F Raupach, S Schael, G Schwering, M Thomas, M Weber, B Wittmer, M Wlochal

RWTH, III. Physikalisches Institut A, Aachen, GERMANY
A Adolf, P Biallass, M Bontenackels, M Erdmann, H Fesefeldt, T Hebbeker, S Hermann, G Hilgers, K Hoepfner[1], C Hof, S Kappler, M Kirsch, D Lanske, B Philipps, H Reithler, T Rommerskirchen, M Sowa, H Szczesny, M Tonutti, O Tsigenov

RWTH, III. Physikalisches Institut B, Aachen, GERMANY
F Beissel, M Davids, M Duda, G Flügge, T Franke, M Giffels, T Hermanns, D Heydhausen, S Kasselmann, G Kaussen, T Kress, A Linn, A Nowack, M Poettgens, O Pooth, A Stahl, D Tornier, M Weber

Deutsches Elektronen-Synchrotron, Hamburg, GERMANY
A Flossdorf, B Hegner, J Mnich, C Rosemann

University of Hamburg, Hamburg, GERMANY
G Flucke, U Holm, R Klanner, U Pein, N Schirm, P Schleper, G Steinbrück, M Stoye, R Van Staa, K Wick

[4] Also at Université de Haute-Alsace, Mulhouse, France.
[5] Also at Université Louis Pasteur, Strasbourg, France.

Institut für Experimentelle Kernphysik, Karlsruhe, GERMANY
P Blüm, V Buege, W De Boer, G Dirkes[1], M Fahrer, M Feindt, U Felzmann, J Fernandez Menendez[6], M Frey, A Furgeri, F Hartmann[1], S Heier, C Jung, B Ledermann, Th. Müller, M Niegel, A Oehler, T Ortega Gomez, C Piasecki, G Quast, K Rabbertz, C Saout, A Scheurer, D Schieferdecker, A Schmidt, H J Simonis, A Theel, A Vest, T Weiler, C Weiser, J Weng [1], V Zhukov[7]

University of Athens, Athens, GREECE
G Karapostoli[1], P Katsas, P Kreuzer, A Panagiotou, C Papadimitropoulos

Institute of Nuclear Physics "Demokritos", Attiki, GREECE
G Anagnostou, M Barone, T Geralis, C Kalfas, A Koimas, A Kyriakis, S Kyriazopoulou, D Loukas, A Markou, C Markou, C Mavrommatis, K Theofilatos, G Vermisoglou, A Zachariadou

University of Ioánnina, Ioánnina, GREECE
X Aslanoglou, I Evangelou, P Kokkas, N Manthos, I Papadopoulos, G Sidiropoulos, F A Triantis

KFKI Research Institute for Particle and Nuclear Physics, Budapest, HUNGARY
G Bencze[1], L Boldizsar, C Hajdu[1], D Horvath[8], A Laszlo, G Odor, F Sikler, N Toth, G Vesztergombi, P Zalan

Institute of Nuclear Research ATOMKI, Debrecen, HUNGARY
J Molnar

University of Debrecen, Debrecen, HUNGARY
N Beni, A Kapusi, G Marian, P Raics, Z Szabo, Z Szillasi, G Zilizi

Panjab University, Chandigarh, INDIA
H S Bawa, S B Beri, V Bhandari, V Bhatnagar, M Kaur, R Kaur, J M Kohli, A Kumar, J B Singh

University of Delhi, Delhi, INDIA
A Bhardwaj, S Bhattacharya[9], S Chatterji, S Chauhan, B C Choudhary, P Gupta, M Jha, K Ranjan, R K Shivpuri, A K Srivastava

Bhabha Atomic Research Centre, Mumbai, INDIA
S Borkar, M Dixit, M Ghodgaonkar, S K Kataria, S K Lalwani, V Mishra, A K Mohanty, A Topkar

Tata Institute of Fundamental Research - EHEP, Mumbai, INDIA
T Aziz, S Banerjee, S Bose, N Cheere, S Chendvankar, P V Deshpande, M Guchait[10], A Gurtu, M Maity[11], G Majumder, K Mazumdar, A Nayak, M R Patil, S Sharma, K Sudhakar, S C Tonwar

[6] Now at Instituto de Física de Cantabria (IFCA), CSIC-Universidad de Cantabria, Santander, Spain.
[7] Also at Moscow State University, Moscow, Russia.
[8] Also at Institute of Nuclear Research ATOMKI, Debrecen, Hungary.
[9] Also at University of California, San Diego, La Jolla, USA.
[10] Also at Tata Institute of Fundamental Research - HECR, Mumbai, India.
[11] Also at University of Visva-Bharati, Santiniketan, India.

Tata Institute of Fundamental Research - HECR, Mumbai, INDIA
B S Acharya, S Banerjee, S Bheesette, S Dugad, S D Kalmani, V R Lakkireddi, N K Mondal, N Panyam, P Verma

Institute for Studies in Theoretical Physics & Mathematics (IPM), Tehran, IRAN
M Arabgol, H Arfaei, M Hashemi, M Mohammadi, M Mohammadi Najafabadi, A Moshaii, S Paktinat Mehdiabadi

University College Dublin, Dublin, IRELAND
M Grunewald

Università di Bari, Politecnico di Bari e Sezione dell' INFN, Bari, ITALY
M Abbrescia, L Barbone, A Colaleo[1], D Creanza, N De Filippis, M De Palma, G Donvito, L Fiore, D Giordano, G Iaselli, F Loddo, G Maggi, M Maggi, N Manna, B Marangelli, M S Mennea, S My, S Natali, S Nuzzo, G Pugliese, V Radicci, A Ranieri, F Romano, G Selvaggi, L Silvestris, P Tempesta, R Trentadue, G Zito

Università di Bologna e Sezione dell' INFN, Bologna, ITALY
G Abbiendi, W Bacchi, A Benvenuti, D Bonacorsi, S Braibant-Giacomelli, P Capiluppi, F R Cavallo, C Ciocca, G Codispoti, I D'Antone, G M Dallavalle, F Fabbri, A Fanfani, P Giacomelli[12], C Grandi, M Guerzoni, L Guiducci, S Marcellini, G Masetti, A Montanari, F Navarria, F Odorici, A Perrotta, A Rossi, T Rovelli, G Siroli, R Travaglini

Università di Catania e Sezione dell' INFN, Catania, ITALY
S Albergo, M Chiorboli, S Costa, M Galanti, G Gatto Rotondo, F Noto, R Potenza, G Russo, A Tricomi, C Tuve

Università di Firenze e Sezione dell' INFN, Firenze, ITALY
A Bocci, G Ciraolo, V Ciulli, C Civinini, R D'Alessandro, E Focardi, C Genta, P Lenzi, A Macchiolo, N Magini, F Manolescu, C Marchettini, L Masetti, S Mersi, M Meschini, S Paoletti, G Parrini, R Ranieri, M Sani

Università di Genova e Sezione dell' INFN, Genova, ITALY
P Fabbricatore, S Farinon, M Greco

Istituto Nazionale di Fisica Nucleare e Universita Degli Studi Milano-Bicocca, Milano, ITALY
G Cattaneo, A De Min, M Dominoni, F M Farina, F Ferri, A Ghezzi, P Govoni, R Leporini, S Magni, M Malberti, S Malvezzi, S Marelli, D Menasce, L Moroni, P Negri, M Paganoni, D Pedrini, A Pullia, S Ragazzi, N Redaelli, C Rovelli, M Rovere, L Sala, S Sala, R Salerno, T Tabarelli de Fatis, S Vigano'

Istituto Nazionale di Fisica Nucleare de Napoli (INFN), Napoli, ITALY
G Comunale, F Fabozzi, D Lomidze, S Mele, P Paolucci, D Piccolo, G Polese, C Sciacca

Università di Padova e Sezione dell' INFN, Padova, ITALY
P Azzi, N Bacchetta[1], M Bellato, M Benettoni, D Bisello, E Borsato, A Candelori, P Checchia, E Conti, M De Mattia, T Dorigo, V Drollinger, F Fanzago, F Gasparini, U Gasparini, M Giarin, P Giubilato, F Gonella, A Kaminskiy, S Karaevskii, V Khomenkov, S Lacaprara, I Lippi, M Loreti, O Lytovchenko, M Mazzucato, A T Meneguzzo, M Michelotto, F Montecassiano[1], M Nigro, M Passaseo, M Pegoraro, G Rampazzo, P Ronchese, E Torassa, S Ventura, M Zanetti, P Zotto, G Zumerle

[12] Also at University of California, Riverside, Riverside, USA.

Università di Pavia e Sezione dell' INFN, Pavia, ITALY
G Belli, U Berzano, C De Vecchi, R Guida, M M Necchi, S P Ratti, C Riccardi, G Sani, P Torre, P Vitulo

Università di Perugia e Sezione dell' INFN, Perugia, ITALY
F Ambroglini, E Babucci, D Benedetti, M Biasini, G M Bilei[1], B Caponeri, B Checcucci, L Fanò, P Lariccia, G Mantovani, D Passeri, M Pioppi, P Placidi, V Postolache, D Ricci[1], A Santocchia, L Servoli, D Spiga

Università di Pisa, Scuola Normale Superiore e Sezione dell' INFN, Pisa, ITALY
P Azzurri, G Bagliesi, A Basti, L Benucci, J Bernardini, T Boccali, L Borrello, F Bosi, F Calzolari, R Castaldi, C Cerri, A S Cucoanes, M D'Alfonso, R Dell'Orso, S Dutta, L Foà, S Gennai[13], A Giammanco, A Giassi, D Kartashov, F Ligabue, S Linari, T Lomtadze, G A Lungu, B Mangano, G Martinelli, M Massa, A Messineo, A Moggi, F Palla, F Palmonari, G Petrucciani, F Raffaelli, A Rizzi, G Sanguinetti, G Segneri, D Sentenac, A T Serban, G Sguazzoni, A Slav, P Spagnolo, R Tenchini, G Tonelli, A Venturi, P G Verdini, M Vos

Università di Roma I e Sezione dell' INFN, Roma, ITALY
S Baccaro[14], L Barone, A Bartoloni, F Cavallari, S Costantini, I Dafinei, D Del Re[9], M Diemoz, C Gargiulo, E Longo, P Meridiani, G Organtini, S Rahatlou

Università di Torino e Sezione dell' INFN, Torino, ITALY
E Accomando, M Arneodo[15], A Ballestrero, R Bellan, C Biino, S Bolognesi, N Cartiglia, G Cerminara, M Cordero, M Costa, G Dellacasa, N Demaria, E Maina, C Mariotti, S Maselli, P Mereu, E Migliore, V Monaco, M Nervo, M M Obertino, N Pastrone, G Petrillo, A Romero, M Ruspa[15], R Sacchi, A Staiano, P P Trapani

Università di Trieste e Sezione dell' INFN, Trieste, ITALY
S Belforte, F Cossutti, G Della Ricca, A Penzo

Kyungpook National University, Daegu, KOREA
K Cho, S W Ham, D Han, D H Kim, G N Kim, J C Kim, W Y Kim, M W Lee, S K Oh, W H Park, S R Ro, D C Son, J S Suh

Chonnam National University, Kwangju, KOREA
J Y Kim

Konkuk University, Seoul, KOREA
S Y Jung, J T Rhee

Korea University, Seoul, KOREA
B S Hong, S J Hong, K S Lee, I Park, S K Park, K S Sim, E Won

Seoul National University, Seoul, KOREA
S B Kim

Universidad Iberoamericana, Mexico City, MEXICO
S Carrillo Moreno

Centro de Investigacion y de Estudios Avanzados del IPN, Mexico City, MEXICO
H Castilla Valdez, A Sanchez Hernandez

[13] Also at Centro Studi Enrico Fermi, Roma, Italy.
[14] Also at ENEA - Casaccia Research Center, S. Maria di Galeria, Italy.
[15] Now at Università del Piemonte Orientale, Novara, Italy.

Benemerita Universidad Autonoma de Puebla, Puebla, MEXICO
H A Salazar Ibarguen

Universidad Autonoma de San Luis Potosi, San Luis Potosi, MEXICO
A Morelos Pineda

University of Auckland, Auckland, NEW ZEALAND
R N C Gray, D Krofcheck

University of Canterbury, Christchurch, NEW ZEALAND
N Bernardino Rodrigues, P H Butler, J C Williams

National Centre for Physics, Quaid-I-Azam University, Islamabad, PAKISTAN
Z Aftab, M Ahmad, U Ahmad, I Ahmed, J Alam Jan, M I Asghar, S Asghar, M Hafeez, H R Hoorani, M Ibrahim, M Iftikhar, M S Khan, N Qaiser, I Rehman, T Solaija, S Toor

Institute of Nuclear Physics, Polish Academy of Sciences, Cracow, POLAND
J Blocki, A Cyz, E Gladysz-Dziadus, S Mikocki, J Turnau, Z Wlodarczyk[16], P Zychowski

Institute of Experimental Physics, Warsaw, POLAND
K Bunkowski, H Czyrkowski, R Dabrowski, W Dominik, K Doroba, A Kalinowski, M Konecki, J Krolikowski, I M Kudla, M Pietrusinski, K Pozniak[17], W Zabolotny[17], P Zych

Soltan Institute for Nuclear Studies, Warsaw, POLAND
M Bluj, R Gokieli, L Goscilo, M Górski, K Nawrocki, P Traczyk, G Wrochna, P Zalewski

Laboratório de Instrumentaçoãe Física Experimental de Partículas, Lisboa, PORTUGAL
R Alemany-Fernandez, C Almeida, N Almeida, A Araujo Trindade, P Bordalo, P Da Silva Rodrigues, M Husejko, A Jain, M Kazana, P Musella, S Ramos, J Rasteiro Da Silva, P Q Ribeiro, M Santos, J Semiao, P Silva, I Teixeira, J P Teixeira, J Varela[1]

Joint Institute for Nuclear Research, Dubna, RUSSIA
S Afanasiev, K Babich, I Belotelov, V Elsha, Y Ershov, I Filozova, A Golunov, I Golutvin, N Gorbounov, I Gramenitski, V Kalagin, A Kamenev, V Karjavin, S Khabarov, V Khabarov, Y Kiryushin, V Konoplyanikov, V Korenkov, G Kozlov, A Kurenkov, A Lanev, V Lysiakov, A Malakhov, I Melnitchenko, V V Mitsyn, K Moisenz, P Moisenz, S Movchan, E Nikonov, D Oleynik, V Palichik, V Perelygin, A Petrosyan, E Rogalev, V Samsonov, M Savina, R Semenov, S Shmatov, S Shulha, V Smirnov, D Smolin, A Tcheremoukhine, O Teryaev, E Tikhonenko, S Vassiliev, A Vishnevskiy, A Volodko, N Zamiatin, A Zarubin, P Zarubin, E Zubarev

Petersburg Nuclear Physics Institute, Gatchina (St Petersburg), RUSSIA
N Bondar, V Golovtsov, A Golyash, Y Ivanov, V Kim, V Kozlov, V Lebedev, G Makarenkov, E Orishchin, A Shevel, V Sknar, I Smirnov, V Sulimov, V Tarakanov, L Uvarov, G Velichko, S Volkov, A Vorobyev

Institute for Nuclear Research, Moscow, RUSSIA
Yu Andreev, A Anisimov, S Gninenko, N Golubev, D Gorbunov, M Kirsanov, A Kovzelev, N Krasnikov, V Matveev, A Pashenkov, V E Postoev, A Sadovski, A Solovey, A Solovey, D Soloviev, L Stepanova, A Toropin

[16] Also at Institute of Physics, Swietokrzyska Academy, Kielce, Poland.
[17] Also at Warsaw University of Technology, Institute of Electronic Systems, Warsaw, Poland.

Institute for Theoretical and Experimental Physics, Moscow, RUSSIA
V Gavrilov, N Ilina, V Kaftanov[1], I Kiselevich, V Kolosov, M Kossov[1], A Krokhotin, S Kuleshov, A Oulianov, G Safronov, S Semenov, V Stolin, E Vlasov[1], V Zaytsev

P N Lebedev Physical Institute, Moscow, RUSSIA
A M Fomenko, N Konovalova, V Kozlov, A I Lebedev, N Lvova, S V Rusakov, A Terkulov

Moscow State University, Moscow, RUSSIA
E Boos, M Dubinin[3], L Dudko, A Ershov, A Gribushin, V Ilyin, V Klyukhin[1], O Kodolova, I Lokhtin, S Petrushanko, L Sarycheva, V Savrin, A Sherstnev, A Snigirev, K Teplov, I Vardanyan

State Research Center of Russian Federation - Institute for High Energy Physics, Protvino, RUSSIA
V Abramov, I Azhguirei, S Bitioukov, K Datsko, A Filine, P Goncharov, V Grishin, A Inyakin, V Kachanov, A Khmelnikov, D Konstantinov, A Korablev, V Krychkine, A Levine, I Lobov, V Petrov, V Pikalov, R Ryutin, S Slabospitsky, A Sourkov[1], A Sytine, L Tourtchanovitch, S Troshin, N Tyurin, A Uzunian, A Volkov, S Zelepoukine[18]

Vinca Institute of Nuclear Sciences, Belgrade, SERBIA
P Adzic, D Krpic[19], D Maletic, P Milenovic, J Puzovic[19], N Smiljkovic[1], M Zupan

Centro de Investigaciones Energeticas Medioambientales y Tecnologicas, Madrid, SPAIN
M Aguilar-Benitez, J Alberdi, J Alcaraz Maestre, M Aldaya Martin, P Arce[1], J M Barcala, C Burgos Lazaro, J Caballero Bejar, E Calvo, M Cardenas Montes, M Cerrada, M Chamizo Llatas, N Colino, M Daniel, B De La Cruz, C Fernandez Bedoya, A Ferrando, M C Fouz, P Garcia-Abia, J M Hernandez, M I Josa, J M Luque, J Marin, G Merino, A Molinero, J J Navarrete, J C Oller, E Perez Calle, L Romero, J Salicio, C Villanueva Munoz, C Willmott, C Yuste

Universidad Autónoma de Madrid, Madrid, SPAIN
C Albajar, J F de Trocóniz, M Fernandez, I Jimenez, R F Teixeira

Universidad de Oviedo, Oviedo, SPAIN
J Cuevas, J M Lopez, H Naves Sordo, J M Vizan Garcia

Instituto de Física de Cantabria (IFCA), CSIC-Universidad de Cantabria, Santander, SPAIN
A Calderon, D Cano Fernandez, I Diaz Merino, L A Garcia Moral, G Gomezo, I Gonzalez Cabellero, J Gonzalez Sanchez, A Lopez Virto, J Marco, R Marco, C Martinez Rivero, P Martinez Ruiz del Arbol, F Matorras, A Patino Revuelta[1], T Rodrigo, D Rodriguez Gonzalez, A Ruiz Jimeno, M Sobron Sanudo, I Vila, R Vilar Cortabitarte

CERN, European Organization for Nuclear Research, Geneva, SWITZERLAND
D Abbaneo, S M Abbas, L Agostino, I Ahmed, S Akhtar, N Amapane, B Araujo Meleiro, S Argiro[20], S Ashby, P Aspell, E Auffray, M Axer, A Ball, N Bangert, D Barney, C Bernet, W Bialas, C Bloch, P Bloch, S Bonacini, M Bosteels, V Boyer, A Branson, A M Brett,

[18] Also at Institute for Particle Physics, ETH Zurich, Zurich, Switzerland.
[19] Also at Faculty of Physics of University of Belgrade, Belgrade, Serbia.
[20] Also at INFN-CNAF, Bologna, Italy.

H Breuker, R Bruneliere, O Buchmuller, D Campi, T Camporesi, E Cano, E Carrone, A Cattai, R Chierici, T Christiansen, S Cittolin, E Corrin, M Corvo, S Cucciarelli, B Curé, A De Roeck, D Delikaris, M Della Negra, D D'Enterria, A Dierlamm, A Elliott-Peisert, M Eppard, H Foeth, R Folch, S Fratianni, W Funk, A Gaddi, M Gastal, J C Gayde, H Gerwig, K Gill, A S Giolo-Nicollerat, F Glege, R Gomez-Reino Garrido, R Goudard, J Gutleber, M Hansen, J Hartert, A Hervé, H F Hoffmann, A Honma, M Huhtinen, G Iles, V Innocente, W Jank, P Janot, K Kloukinas, C Lasseur, M Lebeau, P Lecoq, C Leonidopoulos, M Letheren, C Ljuslin, R Loos, G Magazzu, L Malgeri, M Mannelli, A Marchioro, F Meijers, E Meschi, R Moser, M Mulders, J Nash, R A Ofierzynski, A Oh, P Olbrechts, A Onnela, L Orsini, I Pal, G Papotti, R Paramatti, G Passardi, B Perea Solano, G Perinic, P Petagna, A Petrilli, A Pfeiffer, M Pimiä, R Pintus, H Postema, R Principe, J Puerta Pelayo, A Racz, J Rehn, S Reynaud, M Risoldi, P Rodrigues Simoes Moreira, G Rolandi, P Rosinsky, P Rumerio, H Sakulin, D Samyn, F P Schilling, C Schwick, C Schäfer, I Segoni, A Sharma, P Siegrist, N Sinanis, P Sphicas[21], M Spiropulu, F Szoncsó, O Teller, D Treille, J Troska, E Tsesmelis, D Tsirigkas, A Tsirou, D Ungaro, F Vasey, M Vazquez Acosta, L Veillet, P Vichoudis, P Wertelaers, A Wijnant, M Wilhelmsson, I M Willers

Paul Scherrer Institut, Villigen, SWITZERLAND
W Bertl, K Deiters, W Erdmann, K Gabathuler, S Heising, R Horisberger, Q Ingram, H C Kaestli, D Kotlinski, S König, D Renker, T Rohe, M Spira

Institute for Particle Physics, ETH Zurich, Zurich, SWITZERLAND
B Betev, G Davatz, G Dissertori, M Dittmar, L Djambazov, J Ehlers, R Eichler, G Faber, K Freudenreich, J F Fuchs[1], C Grab, A Holzner, P Ingenito, U Langenegger, P Lecomte, G Leshev, A Lister[22], P D Luckey, W Lustermann, J D Maillefaud[1], F Moortgat, A Nardulli, F Nessi-Tedaldi, L Pape, F Pauss, H Rykaczewski[23], U Röser, D Schinzel, A Starodumov[24], F Stöckli, H Suter, L Tauscher, P Trüb[25], H P von Gunten, M Wensveen[1]

Universität Zürich, Zürich, SWITZERLAND
E Alagoz, C Amsler, V Chiochia, C Hoermann, K Prokofiev, C Regenfus, P Robmann, T Speer, S Steiner, L Wilke

National Central University, Chung-Li, TAIWAN
S Blyth, Y H Chang, E A Chen, A Go, C C Hung, C M Kuo, W Lin

National Taiwan University (NTU), Taipei, TAIWAN
P Chang, Y Chao, K F Chen, Z Gao[1], Y Hsiung, Y J Lei, J Schümann, J G Shiu, K Ueno, Y Velikzhanin, P Yeh

Cukurova University, Adana, TURKEY
S Aydin, M N Bakirci, S Cerci, I Dumanoglu, S Erturk, S Esen, E Eskut, A Kayis Topaksu, P Kurt, H Ozkurt, A Polatöz, K Sogut, H Topakli, M Vergili, T Yetkin, G Önengüt

[21] Also at University of Athens, Athens, Greece.
[22] Now at University of California, Davis, Davis, USA.
[23] Now at ESO, Munich-Garching, Germany.
[24] Also at Institute for Theoretical and Experimental Physics, Moscow, Russia.
[25] Also at Paul Scherrer Institut, Villigen, Switzerland.

Middle East Technical University, Physics Department, Ankara, TURKEY
H Gamsizkan, C Ozkan, S Sekmen, M Serin-Zeyrek, R Sever, E Yazgan, M Zeyrek

Bogaziçi University, Department of Physics, Istanbul, TURKEY
A Cakir[26], K Cankocak[27], M Deliomeroglu, D Demir[26], K Dindar, E Gülmez, E Isiksal[28], M Kaya[29], O Kaya, S Ozkorucuklu[30], N Sonmez[31]

Institute of Single Crystals of National Academy of Science, Kharkov, UKRAINE
B Grinev, V Lyubynskiy, V Senchyshyn

National Scientific Center, Kharkov Institute of Physics and Technology, Kharkov, UKRAINE
L Levchuk, P Sorokin

University of Bristol, Bristol, UNITED KINGDOM
D S Bailey, T Barrass, J J Brooke, R Croft, D Cussans, D Evans, R Frazier, N Grant, M Hansen, G P Heath, H F Heath, B Huckvale, C Lynch, C K Mackay, S Metson, D M Newbold[32], V J Smith, R J Tapper

Rutherford Appleton Laboratory, Didcot, UNITED KINGDOM
S A Baird, K W Bell, R M Brown, D J A Cockerill, J A Coughlan, P S Flower, V B Francis, M French, J Greenhalgh, R Halsall, J Hill, L Jones, B W Kennedy, L Lintern, A B Lodge, J Maddox, Q Morrissey, P Murray, M Pearson, S Quinton, J Salisbury, A Shah, C Shepherd-Themistocleous, B Smith, M Sproston, R Stephenson, S Taghavirad, I R Tomalin, J H Williams

Imperial College, University of London, London, UNITED KINGDOM
F Arteche[1], R Bainbridge, G Barber, P Barrillon, R Beuselinck, F Blekman, D Britton, D Colling, G Daskalakis, G Dewhirst, S Dris[1], C Foudas, J Fulcher, S Greder, G Hall, J Jones, J Leaver, B C MacEvoy, O Maroney, A Nikitenko[24], A Papageorgiou, D M Raymond, M J Ryan, C Seez, P Sharp[1], M Takahashi, C Timlin, T Virdee[1], S Wakefield, M Wingham, A Zabi, Y Zhang, O Zorba

Brunel University, Uxbridge, UNITED KINGDOM
C Da Via, I Goitom, P R Hobson, P Kyberd, C Munro, J Nebrensky, I Reid, O Sharif, R Taylor, L Teodorescu, S J Watts, I Yaselli

Boston University, Boston, Massachusetts, USA
E Hazen, A H Heering, D Lazic, E Machado, D Osborne, J Rohlf, L Sulak, F Varela Rodriguez, S Wu

Brown University, Providence, Rhode Island, USA
D Cutts, R Hooper, G Landsberg, R Partridge, S Vanini[33]

[26] Also at Izmir Institute of Technology (IYTE), Izmir, Turkey.
[27] Also at Mugla University, Mugla, Turkey.
[28] Also at Marmara University, Istanbul, Turkey.
[29] Also at Kafkas University, Kars, Turkey.
[30] Also at Suleyman Demirel University, Isparta, Turkey.
[31] Also at Ege University, Izmir, Turkey.
[32] Also at Rutherford Appleton Laboratory, Didcot, United Kingdom.
[33] Also at Università di Padova e Sezione dell' INFN, Padova, Italy.

University of California, Davis, Davis, California, USA
R Breedon, M Case, M Chertok, J Conway, P T Cox, R Erbacher, J Gunion, B Holbrook, W Ko, R Lander, D Pellett, J Smith, A Soha, M Tripathi, R Vogt

University of California, Los Angeles, Los Angeles, California, USA
V Andreev, K Arisaka, D Cline, R Cousins, S Erhan[1], M Felcini[1], J Hauser, M Ignatenko, B Lisowski, D Matlock, C Matthey, B Mohr, J Mumford, S Otwinowski, G Rakness, P Schlein, Y Shi, J Tucker, V Valuev, R Wallny, H G Wang, X Yang, Y Zheng

University of California, Riverside, Riverside, California, USA
R Clare, D Fortin, D Futyan[1], J W Gary, M Giunta[1], G Hanson, G Y Jeng, S C Kao, H Liu, G Pasztor[34], A Satpathy, B C Shen, R Stringer, V Sytnik, R Wilken, D Zer-Zion

University of California, San Diego, La Jolla, California, USA
J G Branson, E Dusinberre, J Letts, T Martin, M Mojaver, H P Paar, H Pi, M Pieri, A Rana, V Sharma, A White, F Würthwein

University of California, Santa Barbara, Santa Barbara, California, USA
A Affolder, C Campagnari, C Hill, J Incandela, S Kyre, J Lamb, J Richman, D Stuart, D White

California Institute of Technology, Pasadena, California, USA
J Albert, A Bornheim, J Bunn, J Chen, G Denis, P Galvez, M Gataullin, I Legrand, V Litvine, Y Ma, D Nae, H B Newman, S Ravot, S Shevchenko, S Singh, C Steenberg, X Su, M Thomas, V Timciuc, F van Lingen, J Veverka, B R Voicu[1], A Weinstein, R Wilkinson, X Yang, Y Yang, L Y Zhang, K Zhu, R Y Zhu

Carnegie Mellon University, Pittsburgh, Pennsylvania, USA
T Ferguson, M Paulini, J Russ, N Terentyev, H Vogel, I Vorobiev

University of Colorado at Boulder, Boulder, Colorado, USA
J P Cumalat, W T Ford, D Johnson, U Nauenberg, K Stenson, S R Wagner

Cornell University, Ithaca, NY, USA
J Alexander, D Cassel, K Ecklund, B Heltsley, C D Jones, V Kuznetsov, J R Patterson, A Ryd, J Thom, P Wittich

Fairfield University, Fairfield, Connecticut, USA
C P Beetz, G Cirino, V Podrasky, C Sanzeni, D Winn

Fermi National Accelerator Laboratory, Batavia, Illinois, USA
S Abdullin[24], M A Afaq[1], M Albrow, J Amundson, G Apollinari, M Atac, W Badgett, J A Bakken, B Baldin, L A T Bauerdick, A Baumbaugh, U Baur, P C Bhat, F Borcherding, K Burkett, J N Butler, H Cheung, I Churin, S Cihangir, M Demarteau, D P Eartly, J E Elias, V D Elvira, D Evans, I Fisk, J Freeman, P Gartung, F J M Geurts, D A Glenzinski, E Gottschalk, G Graham, D Green, G M Guglielmo, Y Guo, O Gutsche, A Hahn, J Hanlon, S Hansen, R M Harris, T Hesselroth, S L Holm, B Holzman, S Iqbal, E James, M Johnson, U Joshi, B Klima, J Kowalkowski, T Kramer, S Kwan, E La Vallie, M Larwill, S Los, L Lueking, G Lukhanin, S Lusin[1], K Maeshima, P McBride, S J Murray, V O'Dell, M Paterno, J Patrick, D Petravick, R Pordes, O Prokofyev, V Rasmislovich, N Ratnikova, A Ronzhin, V Sekhri, E Sexton-Kennedy, T Shaw, D Skow, R P Smith, W J Spalding, L Spiegel, M Stavrianakou, G Stiehr, I Suzuki, P Tan, W Tanenbaum, S Tkaczyk, S Veseli, R Vidal, H Wenzel, J Whitmore, W J Womersley, W M Wu, Y Wu, A Yagil, J Yarba, J C Yun

[34] Also at KFKI Research Institute for Particle and Nuclear Physics, Budapest, Hungary.

University of Florida, Gainesville, Florida, USA
D Acosta, P Avery, V Barashko, P Bartalini, D Bourilkov, R Cavanaugh, A Drozdetskiy, R D Field, Y Fu, L Gray, D Holmes, B J Kim, S Klimenko, J Konigsberg, A Korytov, K Kotov, P Levchenko, A Madorsky, K Matchev, G Mitselmakher, Y Pakhotin, C Prescott, P Ramond, J L Rodriguez, M Schmitt, B Scurlock, H Stoeck, J Yelton

Florida International University, Miami, Florida, USA
W Boeglin, V Gaultney, L Kramer, S Linn, P Markowitz, G Martinez, B Raue, J Reinhold

Florida State University, Tallahassee, Florida, USA
A Askew, M Bertoldi, W G D Dharmaratna, Y Gershtein, S Hagopian, V Hagopian, M Jenkins, K F Johnson, H Prosper, H Wahl

Florida Institute of Technology, Melbourne, Florida, USA
M Baarmand, L Baksay[35], S Guragain, M Hohlmann, H Mermerkaya, R Ralich, I Vodopiyanov

University of Illinois at Chicago (UIC), Chicago, Illinois, USA
M R Adams, R R Betts, C E Gerber, E Shabalina, C Smith, T Ten

The University of Iowa, Iowa City, Iowa, USA
U Akgun, A S Ayan, A Cooper, P Debbins, F Duru, M Fountain, N George, E McCliment, J P Merlo, A Mestvirishvili, M J Miller, C R Newsom, E Norbeck, Y Onel, I Schmidt, S Wang

Iowa State University, Ames, Iowa, USA
E W Anderson, O Atramentov, J M Hauptman, J Lamsa

Johns Hopkins University, Baltimore, Maryland, USA
B A Barnett, B Blumenfeld, C Y Chien, D W Kim, P Maksimovic, S Spangler, M Swartz

The University of Kansas, Lawrence, Kansas, USA
P Baringer, A Bean, D Coppage, O Grachov, E J Kim, M Murray

Kansas State University, Manhattan, Kansas, USA
D Bandurin, T Bolton, A Khanov[24], Y Maravin, D Onoprienko, F Rizatdinova, R Sidwell, N Stanton, E Von Toerne

University of Maryland, College Park, Maryland, USA
D Baden, R Bard, S C Eno, T Grassi, N J Hadley, R G Kellogg, S Kunori, F Ratnikov, A Skuja

Massachusetts Institute of Technology, Cambridge, Massachusetts, USA
R Arcidiacono, M Ballintijn, G Bauer, P Harris, I Kravchenko, C Loizides, S Nahn, C Paus, S Pavlon, C Roland, G Roland, K Sumorok, S Vaurynovich, G Veres, B Wyslouch

University of Minnesota, Minneapolis, Minnesota, USA
D Bailleux, S Corum, P Cushman, A De Benedetti, A Dolgopolov, R Egeland, G Franzoni, W J Gilbert, J Grahl, J Haupt, Y Kubota, J Mans, N Pearson, R Rusack, A Singovsky

University of Mississippi, University, Mississippi, USA
L M Cremaldi, R Godang, R Kroeger, D A Sanders, D Summers

University of Nebraska-Lincoln, Lincoln, Nebraska, USA
K Bloom, D R Claes, A Dominguez, M Eads, C Lundstedt, S Malik, G R Snow, A Sobol

[35] Also at University of Debrecen, Debrecen, Hungary.

State University of New York at Buffalo, Buffalo, New York, USA
I Iashvili, A Kharchilava

Northeastern University, Boston, Massachusetts, USA
G Alverson, E Barberis, O Boeriu, G Eulisse, Y Musienko[36], S Muzaffar, I Osborne, S Reucroft, J Swain, L Taylor, L Tuura, D Wood

Northwestern University, Evanston, Illinois, USA
B Gobbi, M Kubantsev, H Schellman, M Schmitt, E Spencer, M Velasco

University of Notre Dame, Notre Dame, Indiana, USA
B Baumbaugh, N M Cason, M Hildreth, D J Karmgard, N Marinelli[21], R Ruchti, J Warchol, M Wayne

The Ohio State University, Columbus, Ohio, USA
B Bylsma, L S Durkin, J Gilmore, J Gu, D Herman, P Killewald, K Knobbe, T Y Ling

Princeton University, Princeton, New Jersey, USA
P Elmer, D Marlow, P Piroué, D Stickland, C Tully, T Wildish, S Wynhoff, Z Xie

Purdue University, West Lafayette, Indiana, USA
A Apresyan, K Arndt, K Banicz, V E Barnes, G Bolla, D Bortoletto, A Bujak, A F Garfinkel, O Gonzalez Lopez, L Gutay, N Ippolito, Y Kozhevnikov[1], A T Laasanen, C Liu, V Maroussov, P Merkel, D H Miller, J Miyamoto, N Neumeister, C Rott, A Roy, A Sedov, I Shipsey

Purdue University Calumet, Hammond, Indiana, USA
N Parashar

Rice University, Houston, Texas, USA
G Eppley, S J Lee, J Liu, M Matveev, T Nussbaum, B P Padley, J Roberts, A Tumanov, P Yepes

University of Rochester, Rochester, New York, USA
A Bodek, H Budd, Y S Chung, P De Barbaro[1], R Demina, R Eusebi, G Ginther, Y Gotra, A Hocker, U Husemann, S Korjenevski, W Sakumoto, P Slattery, P Tipton, M Zielinski

Rutgers, the State University of New Jersey, Piscataway, New Jersey, USA
E Bartz, J Doroshenko, E Halkiadakis, P F Jacques, M S Kalelkar, D Khits, A Lath, A Macpherson[1], L Perera, R Plano, K Rose, S Schnetzer, S Somalwar, R Stone, G Thomson, T L Watts

Texas Tech University, Lubbock, Texas, USA
N Akchurin, K W Carrell, K Gumus, C Jeong, H Kim, V Papadimitriou, A Sill, M Spezziga, E Washington, R Wigmans, L Zhang

Vanderbilt University, Nashville, Tennessee, USA
T Bapty, D Engh, W Johns, T Keskinpala, E Luiggi Lopez, S Neema, S Nordstrom, S Pathak, P Sheldon, E W Vaandering, M Webster

[36] Also at Institute for Nuclear Research, Moscow, Russia.

University of Virginia, Charlottesville, Virginia, USA
M W Arenton, S Conetti, B Cox, R Hirosky, R Imlay, A Ledovskoy, D Phillips II, H Powell, M Ronquest, D Smith

University of Wisconsin, Madison, Wisconsin, USA
Y W Baek, J N Bellinger, D Bradley, D Carlsmith, I Crotty[1], S Dasu, F Feyzi, T Gorski, M Grothe[37], W Hogg, M Jaworski, P Klabbers, A Lanaro, R Loveless, M Magrans de Abril, D Reeder, W H Smith, D Wenman

Yale University, New Haven, Connecticut, USA
G S Atoyan[36], S Dhawan, V Issakov, H Neal, A Poblaguev, M E Zeller

Institute of Nuclear Physics of the Uzbekistan Academy of Sciences, Ulugbek, Tashkent, UZBEKISTAN
B S Yuldashev

[37] Also at Università di Torino e Sezione dell' INFN, Torino, Italy.

Contents

Chapter 1. Introduction

The Large Hadron Collider (LHC) [1], at the CERN Laboratory, the European Laboratory for Particle Physics, outside Geneva, Switzerland, will be completed in 2007. The LHC will be a unique tool for fundamental physics research and will be the highest energy accelerator in the world for many years following its completion. The LHC will provide two proton beams, circulating in opposite directions, at an energy of 7 TeV each (centre-of-mass $\sqrt{s} = 14$ TeV). The CMS experiment [2, 3] is a general purpose detector at the LHC to explore physics at an unprecedented physics energy scale, namely that at the TeV scale [4–6]. It is expected that the data produced at the LHC will elucidate the electroweak symmetry breaking mechanism (EWSB) and provide evidence of physics beyond the Standard Model. CMS will also be an instrument to perform precision measurements, e.g., of parameters of the Standard Model, mainly as a result of the very high event rates, as demonstrated for a few processes in Table 1.1 for a luminosity of $\mathcal{L} = 2 \times 10^{33}\,\mathrm{cm}^{-2}\,\mathrm{s}^{-1}$. The LHC will be a Z factory, a W factory, a b quark factory, a top quark factory and even a Higgs or SUSY particle factory if these new particles have TeV scale masses.

The Physics Technical Design Report (PTDR) reports on detailed studies that have been performed with the CMS detector software and analysis tools. The CMS detector and its performance are described in detail in Volume 1 of the PTDR [7], while in the present Volume (Volume 2) the physics reach with the CMS detector is explored.

The CMS detector, shown in Fig. 1.1, measures roughly 22 metres in length, 15 metres in diameter, and 12,500 metric tons in weight. Its central feature is a huge, high field (4 tesla) solenoid, 13 metres in length, and 6 metres in diameter. Its "compact" design is large enough to contain the electromagnetic and hadron calorimetry surrounding a tracking system, and allows a superb muon detection system. All subsystems of CMS are bound by means of the data acquisition and trigger system.

In the CMS coordinate system the origin coincides with the nominal collision point at the geometrical center of the detector. The z direction is given by the beam axis. The rest frame of the hard collision is generally boosted relative to the lab frame along the beam direction, θ is the polar angle with respect to the z axis and ϕ the azimuthal angle with respect to the LHC plane. The detector solid angle segmentation is designed to be invariant under boosts along the z direction. The *pseudorapidity* η, is related to the polar angle θ and defined as $\eta \equiv -\ln(\tan(\theta/2))$. The transverse momentum component z-axis is given by $p_\mathrm{T} = p\sin\theta$ and similarly $E_\mathrm{T} = E\sin\theta$ is the transverse energy of a physics object.

The experiment comprises a tracker, a central calorimeter barrel part for $|\eta| \leqslant 1.5$, and endcaps on both sides, and muon detectors. The tracking system is made of several layers of silicon pixel and silicon strip detectors and covers the region $|\eta| < 2.5$. The electromagnetic calorimeter consists of lead tungstate ($PbWO_4$) crystals covering $|\eta| < 3$ (with trigger coverage $|\eta| < 2.6$). Its resolution at the initial luminosity ($\mathcal{L} = 2 \times 10^{33}\,\mathrm{cm}^{-2}\,\mathrm{s}^{-1}$) is $\Delta E/E = 3\%/\sqrt{E} \oplus 0.5\%$. The surrounding hadronic calorimeter uses brass/scintillator tiles in the barrel and endcaps. Its resolution for jets, when combined with the electromagnetic calorimeter, is $\Delta E/E = 100\%/\sqrt{E} \oplus 5\%$. The region $3 < |\eta| < 5$ is covered by forward calorimeters with a resolution of $\Delta E/E = 180\%/\sqrt{E} \oplus 10\%$. Muons are measured in gas chambers in the iron return yoke. The muon momentum measurement using the muon chambers and the central tracker covers the range $|\eta| < 2.4$ with a resolution of $\Delta p_\mathrm{T}/p_\mathrm{T} = 5\%$ at $p_\mathrm{T} = 1$ TeV and $\Delta p_\mathrm{T}/p_\mathrm{T} = 1\%$ at $p_\mathrm{T} = 100$ GeV. The muon trigger extends over the pseudorapidity range $|\eta| < 2.1$.

In total CMS has $\sim 10^8$ data channels that are checked each bunch crossing. The design data-size per event is about 1 MB. At start-up it is essential to allow for a larger event size,

Table 1.1. Approximate event rates of some physics processes at the LHC for a luminosity of $\mathcal{L} = 2 \times 10^{33}\,\mathrm{cm}^{-2}\,\mathrm{s}^{-1}$. For this table, one year is equivalent to $20\,\mathrm{fb}^{-1}$.

Process	Events/s	Events/year
$W \to e\nu$	40	4×10^8
$Z \to ee$	4	4×10^7
$t\bar{t}$	1.6	1.6×10^7
$b\bar{b}$	10^6	10^{13}
$\tilde{g}\tilde{g}$ ($m = 1\,\mathrm{TeV}$)	0.002	2×10^4
Higgs ($m = 120\,\mathrm{GeV}$)	0.08	8×10^5
Higgs ($m = 120\,\mathrm{GeV}$)	0.08	8×10^5
Higgs ($m = 800\,\mathrm{GeV}$)	0.001	10^4
QCD jets $p_\mathrm{T} > 200\,\mathrm{GeV}$	10^2	10^9

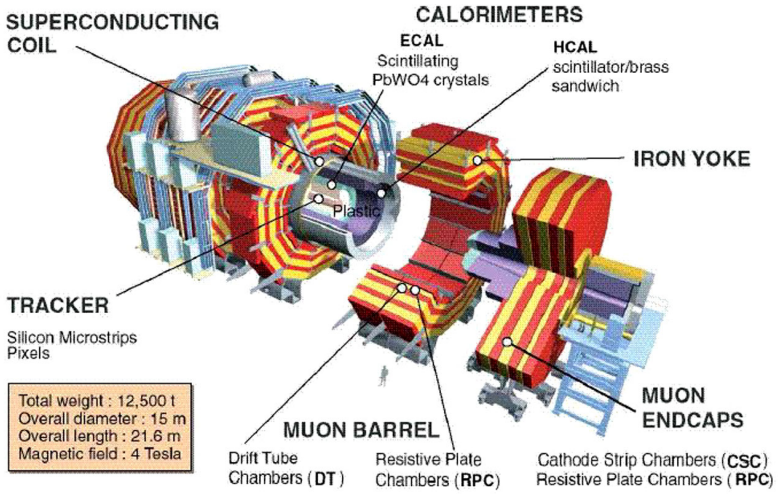

Figure 1.1. Three dimensional view of the CMS detector, and its detector components.

up to 1.5 MB per event, in order to be able to thoroughly study and understand the detector performance.

This Volume is organised in two parts. In the first part a number of physics channels challenging for the detector are studied in detail. Each of these channels is associated with certain physics objects, such as electrons, photons, muons, jets, missing E_T and so on. The analyses are performed in a fully realistic environment as the one expected for real data. Methods on determining the backgrounds from the data as well as on evaluating the experimental systematic effects, e.g., due to miscalibration and misalignment, resolution and signal significance are developed. In short these analyses are performed imitating real data analyses to the maximum possible extent.

In the second part the physics reach is studied for a large number of physics processes, for data samples mostly with luminosities in the range of 1 to $30\,\mathrm{fb}^{-1}$, expected to be collected during the first years of operation at the LHC. Standard model measurements of, e.g., W and top quark mass determinations are studied; many production and decay mechanisms for the SM and MSSM Higgs are studied, and several models beyond the Standard Model are explored.

1.1. The full analyses

In total 11 analyses were studied in full detail. All the studies were performed with detailed Geant4 based simulation of the CMS detector and reconstruction of the data, including event pile-up, and a detailed analysis of the systematics.

The $H \to \gamma\gamma$ analysis covers one of the most promising channels for a low mass Higgs discovery and for precision Higgs mass measurement at the LHC. This channel has been an important motivation for the design of the electromagnetic calorimeter (ECAL) of CMS. It is used here as a benchmark channel for identifying photons with high purity and efficiency, and as a driver for optimising the ECAL energy resolution and calibration of the analyses. Furthermore, new statistical techniques that make use of event kinematics and neural network event selection algorithms have been used to enhance the sensitivity in this channel.

The analysis $H \to ZZ \to 4$ electrons covers electron identification and selection optimisation. In particular, the classification of electron candidates according to quality criteria which depends on their passage through the material of the tracker was studied, and the impact on the Higgs search quantified.

The same process has been studied in the muon decay channel $H \to ZZ \to 4\mu$. This process is an important benchmark for optimising the muon analysis tools. It is one of the cleanest discovery channels for a Standard Model Higgs with a mass up to $600\,\mathrm{GeV/c^2}$. Methods to minimise the systematics errors have been developed.

The channel $H \to WW \to 2\mu 2\nu$ is of particular importance if the mass of the Higgs is around $165\,\mathrm{GeV/c^2}$, and is again an interesting muon benchmark channel. The challenge is to establish with confidence a dimuon excess, since this channel does not allow reconstruction of the Higgs mass on an event by event basis. The event statistics after reconstruction and selection is large enough for an early discovery, even with about $1\,\mathrm{fb}^{-1}$ of integrated luminosity, provided the systematic uncertainty on the background can be kept well under control.

The production of a new gauge boson with a mass in the TeV range is one of the possible early discoveries at the LHC. The clean final state for the decays into two high p_T leptons leads to a clearly detectable signal in CMS. The channel $Z' \to \mu\mu$ was selected as a benchmark to study muons with p_T in the TeV/c range. Dedicated reconstruction techniques were developed for TeV muons and the experimental systematics e.g. due to misalignment effects were studied in detail.

Jets will be omnipresent in the LHC collisions. The analysis of dijets events and the dijet invariant mass has been studied in detail. A pre-scaling strategy of the jet threshold for the trigger, in order to allow a dijet mass measurement starting from approximately $300\,\mathrm{GeV/c^2}$ has been developed. Calibration procedures, and experimental and theoretical systematics on the dijet mass distribution have been evaluated in detail. The results were interpreted as sensitivities to new physics scenarios.

The determination of the missing transverse momentum in collisions at a hadron collider is in general a difficult measurement, since it is very susceptible to detector inefficiencies, mis-measurements, backgrounds such a halo muons or cosmic muons, and instrumental backgrounds. On the other hand, it is probably the most striking signature for new physics with escaping weakly interacting particles, such as the neutralinos in supersymmetry. A low mass mSUGRA SUSY benchmark point was selected to exercise a full analysis, including techniques to suppress spurious backgrounds as well as QCD residual contribution due to mis-measurements. Techniques to calibrate the $E_\mathrm{T}^\mathrm{miss}$ with known Standard Model processes have been also developed. Such a low mass SUSY scenario could already be detected with $0.1\,\mathrm{fb}^{-1}$ of data with a well understood detector and well controlled background.

The decay $B_s \to J/\psi\phi$ is chosen as a benchmark channel since it is representative of exclusive B-physics studies. It allows to study the capability of CMS to identify, select and reconstruct a fully reconstructed decay of the B_s, which presents a significant challenge due to its relatively low momentum and high background. In addition, the measurement is performed of the width difference $\Delta\Gamma$ on a sample of untagged $B_s \to J/\psi\phi \to \mu^+\mu^- K^+K^-$ candidates using a maximum likelihood fit of the time dependent angular distribution.

The detection of the τ particle will be very important at the LHC since, a clear excess of τ production is also a sign of new physics. The τ selection and analysis tools have been used to search for and measure the A/H heavy Higgs bosons in the MSSM. Various decay channels of the τ have been considered, and τ tagging tools have been deployed and refined. A τ-trigger is very challenging but necessary for these physics studies, and has been studied in detail.

The process of associated production of a Higgs particle with top quarks, and with the Higgs decaying into b-quarks, is no doubt one of the most challenging channels studied in this part of the TDR. The physics interest is high since, this channel gives access to a measurement of the $H \to bb$ decay and thus, to the Yukawa coupling of the Higgs to the b quark. The inclusive $H \to bb$ production channel cannot be used due to a too large QCD $b\bar{b}$ background. This analysis uses techniques to tag b quarks and calibration methods to reconstruct top quarks from multi-jet decays. Furthermore, the backgrounds such as $t\bar{t}$ jet-jet have been carefully examined. The results demonstrate that this will be a very challenging measurement even with the highest luminosity in the first phase of the LHC operation.

Finally, a benchmark channel for heavy ions collisions was studied. Quarkonia (J/ψ, Υ) were reconstructed and measured via the two muon decay modes. The particular challenge is an efficient track reconstruction in an environment of 2000 to perhaps even 5000 tracks produced per unit of rapidity. The analysis shows that the detection of the quarkonia is possible with reasonable efficiencies and leads to a good event statistics for detailed studies of the "melting" of these resonances in a hot dense region.

In general, these detailed studies in this first part of the PTDR have demonstrated that the CMS experiment is up and ready to meet the challenge, and can deliver measurements with the quality and precision as anticipated from its detector design.

1.2. The physics reach

The physics reach of the Report contains three main parts: Standard Model processes, Higgs searches and measurements and searches beyond the Standard Model.

The Standard Model sections contain a study of the strong interactions, top quark physics and electroweak physics. Jet production is revisited but this time to measure inclusive single jet p_{T} spectra, with emphasis placed on the experimental uncertainties related to such a measurement. The underlying event is still enigmatic, and procedures are outlined to get better insight with the first LHC data. B-hadrons will be copiously produced at the LHC and inclusive B production and B_c production have been studied. At the LHC about one top quark pair is produced per second. Such a huge sample of top quarks allows for detailed measurements of the top quark properties such as cross sections and mass, spin properties, single top production, and searches for new physics in top decays. A detailed study on the mass measurement precision, limited by the systematics errors, is reported. In the electroweak part of this chapter, the production of W and Z bosons is discussed, as well as multi-boson production, and a precise measurement of the Drell–Yan process. The precision with which the mass of the W boson can be determined is analysed.

One of the main missions of the LHC is the discovery of the origin of the electroweak symmetry breaking mechanism. Therefore, the search for the Higgs particle is a major task

for the experiments. The Higgs particle search is studied for the SM and MSSM Higgs(es) in the full mass range starting from the LEP exclusion limits. Detailed systematic studies were included in the estimates for the integrated luminosity needed for a 5σ discovery. The methods used to calculate the 5σ discovery limit are detailed in Appendix A. Over a large range of Higgs boson masses, a discovery is possible with a few fb^{-1}, but for the interesting mass region below $130\,\mathrm{GeV/c^2}$, $10\,\mathrm{fb}^{-1}$ will be needed. MSSM Higgs discoveries are studied both for neutral and charged Higgs particles, and discovery regions are presented. Finally, the Higgs chapter also contains studies of other scalar particles such as the radion that emerges in models with warped extra dimensions, and a double charged Higgs that may be produced in Little Higgs scenarios.

The LHC will probe the TeV energy scale and is expected to break new ground. An important part of the CMS program will be to search for new physics. If low mass supersymmetry exists it will be within the reach of the LHC. The studies in this Report are mainly signature based, to test the discovery potential in as many channels as possible, using a number of chosen benchmark points covering a large part of different signatures. The discovery reach for scenarios with extra dimensions, and new vector bosons high mass states are analysed using several different experimental signals. The methods used to calculate the 5σ discovery limit are detailed in Appendix A. Finally alternative signatures for new physics such as technicolour, contact interactions, heavy Majorana neutrinos, heavy top in Little Higgs models, and same sign top quarks have been analysed.

While many signals and processes have been studied, it was not the goal of this PTDR to study and to include all possible channels to give a full physics review. Besides, what is contained here in this Report, there are other ongoing analyses nearing completion on topics such as GMSB SUSY, UED extra dimensions, split SUSY scenarios, invisible Higgs production, TGC sensitivity of dibosons, strongly interacting vector boson scattering, and others. The channels included in this Report have however, been very instrumental to test and deploy the tools and techniques for performing physics studies with CMS at the LHC.

1.3. Tools used in the studies for the PTDR

1.3.1. Detector simulation and reconstruction

For the studies presented in this TDR, the CMS detector response was simulated using the package OSCAR [8]. It is an application of the Geant4 [9] toolkit for detector description and simulation. OSCAR is used to describe the detector geometry and materials. It also includes and uses information about the magnetic field. OSCAR reads the individual generated events and simulates the effects of energy loss, multiple scattering and showering in the detector materials with Geant4. The digitisation (simulation of the electronic response), the emulation of the Level-1 and High-Level Triggers (HLT), and the offline reconstruction of physics objects were performed with the CMS full-reconstruction ORCA package [10].

A number of analyses for the physics reach studies were performed with the fast parameterised simulation FAMOS [11]. FAMOS has been tuned to the detailed simulation and reconstruction and is roughly about a factor 1000 faster. FAMOS allows to perform, e.g., accurate sensitivity scans in a large parameter space of a model for new physics.

1.3.2. Pile-up treatment

The total inelastic cross section at the LHC is assumed to be $\sigma_{\mathrm{T}} \sim 80\,\mathrm{mb}$. The LHC will operate at a bunch crossing rate of 40 MHz. Only 80 % of the bunches will be filled , resulting in an effective bunch crossing rate of 32 MHz. The instantaneous luminosity in the first

two years after start-up is expected to be $\mathcal{L} = 2 \times 10^{33}\,\mathrm{cm}^{-2}\,\mathrm{s}^{-1}$ and subsequently upgraded to $\mathcal{L} = 10^{34}\,\mathrm{cm}^{-2}\,\mathrm{s}^{-1}$ in a second phase. The average number of inelastic non-diffractive interactions per bunch crossing μ is $\mu = 25$ at high and $\mu = 5$ at low luminosity.

Both the detailed simulation and reconstruction chain OSCAR/ORCA and FAMOS allow the overlay of pile-up events, according to a Poisson distribution with average μ, on top of real signal events, exactly as for real data. These events were sampled from a data base of 600K minimum bias events, generated with parameters discussed in Appendix C.

All the studies reported in this TDR include the effects of pile-up on the signal. For all studies with luminosities up to 60 fb^{-1} $\mu = 5$ was used. Several techniques have been developed to minimise the effect of pile-up, and have been used in the studies reported in this TDR. Both in-time and out-of-time pile-up has been included.

1.3.3. Systematic effects on measurements

The results of the PTDR Volume 1 were used to form the baseline for all systematic studies in this Volume. Systematic effects include energy scale uncertainties for the calorimeters, effects of misalignment, uncertainties in the background estimation either from theory or from techniques to estimate these backgrounds from data. Misalignments of the tracker and of the muon system expected at the initial and at the well-advanced stages of the data taking have been taken into account by using two misalignment scenarios developed in the framework of the CMS reconstruction.

A comprehensive review on the experimental and theoretical systematics used in this PTDR is presented in Appendix B.

1.3.4. Event generators

The studies for this physics TDR have been performed with a variety of event generators, suitably chosen for each processes studied. The main work-horse was PYTHIA, the general multi-purpose generator, and in some case checks have been performed with HERWIG. More specialised generators which include a more complete description of the relevant matrix elements, have been used for a number processes, as detailed in the analysis reports. A list of generators used in this TDR is given in Appendix C.

An important aspect for the LHC, is the QCD multi-jet production in various physics channels, and a correct and thorough understanding of Standard Model processes such as W + jets, Z + jets and $t\bar{t}$ + jet production will be paramount before discoveries can be claimed in channels such as jets + $E_{\mathrm{T}}^{\mathrm{miss}}$ and jets + leptons. CMS will measure these Standard Model processes in an early phase of the experiment, to reduce the impact of inherent uncertainties in the Monte Carlo models on searches and discoveries, using methods demonstrated in this TDR. These will allow estimation of the expected backgrounds directly or will allow to tune the generators in order to use these with increased confidence in regions of phase space not directly accessible with measurements from the data.

Generators with multi-parton final states are available at Leading Order (LO) for most Standard Model processes. Recently, Next to Leading Order (NLO) generators have become available as well, be it for a more restricted number of processes. Sophisticated algorithms that match the hard jets generated by the matrix elements, with the softer parton jets, have become available. An example is the ALPGEN generator, which has been used for some studies and comparisons in this Report. For some of the detailed analyses, such as the $E_{\mathrm{T}}^{\mathrm{miss}}$ low mass SUSY search, it was shown that the effect of using ALPGEN instead of PYTHIA did not lead to different result, while for other analyses, such as background to ttH production, the difference was important.

Another difficulty in the estimation of the background to processes is the rate of QCD multi-jet events. Typically, samples of events of more than 10^8 or 10^9 events would be needed to cover possible tails. Detailed simulation of such background samples cannot be easily done, and therefore, other approaches were taken in this TDR. These include pre-selections at the generator level, fast simulation of large samples and factorising the efficiencies of independent selections cuts.

Hence, one has to keep in mind that the exact results presented in this TDR could depend on the generators. They should therefore, be taken as an indication albeit a good indication of what can be expected at the LHC.

1.3.5. Parton distributions and higher order corrections

One of the key differences between a hadron and an e^+e^- collider is that for hadrons the partons collide with a strongly varying incident energy, given by the distribution of the longitudinal momentum fraction x of the parton in the proton. These parton densities are determined from data, in particular from deep inelastic scattering data and other measurements of hard scattering processes. Several groups have fitted parton distribution functions (PDFs) to these data, e.g., the CTEQ [12] and MRST [13] groups.

For the studies in this report, the simulated event samples were generated with CTEQ5L but CTEQ6 was used to normalise cross sections and to study the PDF uncertainties. CTEQ 6.1 has 40 different error PDFs, 20 PDFs at positive error, and 20 PDFs at negative error. We use the CTEQ6.1M eigenvector PDF sets [12] and the "master" equations as detailed in Appendix B to evaluate the uncertainties characterising current knowledge of the parton distributions.

The precise knowledge of the parton distributions will remain an extremely important subject for the physics at the LHC. Currently, a study group in the framework of the HERA-LHC workshop is tackling this topic in order to get as good knowledge as possible of the PDFs [14] and their uncertainties at the time of the startup of the LHC. Once the LHC starts data collection, several QCD process can be used to help to constrain the PDFs, as has been shown, e.g., using W production with studies at the HERA-LHC workshop.

1.4. Outlook

The work detailed in this Volume of the PTDR constitutes the pedestal for the physics studies that the experiment will pursue both at the start-up and the longer term running. In the process of carrying out these studies CMS has gained valuable experience in all aspects, both technical and strategic, in executing a high performance physics program. Of great value is also the identification of shortcomings and challenges that emerged in the context of completing these analyses.

As a follow-up of this work, CMS is planning an elaborate program for the start-up studies and physics commissioning from the combined magnet test effort (MTCC) as well as the experience of the upcoming computing, software and analysis challenge (CSA06) that incorporates the full calibration and alignment framework in combination with the full-trigger path exercise. The whole edifice for data collecting and analysis is expected to be complete and tested by the turn-on of the LHC in 2007.

Part I. Complete Analyses

Chapter 2. Physics Studies with Photons and Electrons

2.1. Benchmark Channel: $H \rightarrow \gamma\gamma$

The $H \rightarrow \gamma\gamma$ channel has been studied since the initial planning of the LHC and SSC as an important channel for the discovery of Higgs particles at masses beyond the upper reach of LEP and below about 150 GeV [3, 15, 16]. The signature sought in the inclusive analysis is two high E_T isolated photons. The challenge for discovery of a Higgs in this mode is the small branching fraction of about 0.002, since in this mass range the dominant decay mode of the Higgs is $b\bar{b}$. The $\gamma\gamma$ decay mode can be well identified experimentally but the signal rate is small compared to the backgrounds coming both from two prompt photons (irreducible), and from those in which one or more of the photons are due to decay products or mis-identified particles in jets (reducible). It has long been understood that $H \rightarrow \gamma\gamma$ can be detected as a narrow mass peak above a large background. The background magnitude can be determined from the region outside the peak. After event selection, for an integrated luminosity of 20 fb^{-1} and for a Higgs boson mass of 120 GeV/c^2, we expect approximately 350 signal events in a mass window of 2 GeV/c^2 over 7000 background events. An example of a $pp \rightarrow H + X$ event with Higgs particle decay $H \rightarrow \gamma\gamma$ is shown in colour plate CP1.

In this study we present two complementary inclusive analyses for the $H \rightarrow \gamma\gamma$ channel: a standard cut based analysis and a high performance, discovery-oriented analysis, based on the method described in [17, 18]. Both are carried out with our present knowledge of the expected background, estimated with full detector simulation. Further details can be found in [19]. The study concentrates on the first years of LHC operation and uses simulated events with pileup corresponding to a luminosity of 2×10^{33} cm^{-2} s^{-1}.

The idea of measuring the rate of background by using the mass regions adjoining the Higgs peak is extended to also measure the characteristics of the background, and using this information to help separate background from signal. The $H \rightarrow \gamma\gamma$ channel is particularly well suited to this technique because the signal is relatively small and can be confined to a narrow mass region thanks to the excellent photon energy and position resolution of the CMS detector [7].

By using photon isolation and photon kinematic information, significant additional discrimination between signal and background can be achieved. The optimised analysis uses this information to discriminate between signal and background by comparing data in mass side-bands with signal Monte Carlo. Use is made of a neural network, but likelihood variables or other techniques may prove to be better in the future. The expected purity in terms of signal/background, corresponding to each event, can be estimated based on this information and each event then can be used optimally to evaluate the likelihood of a signal plus background hypothesis compared to a background-only hypothesis.

In the optimised analysis the expected signal to background ratio is calculated for each event. By dividing the cut-based analysis in various categories with different s/b ratios results improve toward those that are obtained with the optimised analysis. If the maximum s/b ratio in the optimised analysis is limited to the best category used in the cut-based analysis, the performances of the two analyses are nearly identical.

The optimised, discovery-oriented analysis is particularly appropriate to the $H \rightarrow \gamma\gamma$ channel because the Higgs signal appears in a narrow mass peak allowing analysis of the large background in the mass side-bands. The analysis will not be limited by the poor simulation of the background once data will be available.

Table 2.1. NLO cross sections for the different Higgs boson production processes and branching ratios.

M_H	115 GeV/c^2	120 GeV/c^2	130 GeV/c^2	140 GeV/c^2	150 GeV/c^2
σ (gg fusion)	39.2 pb	36.4 pb	31.6 pb	27.7 pb	24.5 pb
σ (WVB fusion)	4.7 pb	4.5 pb	4.1 pb	3.8 pb	3.6 pb
σ (WH, ZH, $t\bar{t}$ H)	3.8 pb	3.3 pb	2.6 pb	2.1 pb	1.7 pb
Total σ	47.6 pb	44.2 pb	38.3 pb	33.6 pb	29.7 pb
$H \to \gamma\gamma$ Branching ratio	0.00208	0.00220	0.00224	0.00195	0.00140
Inclusive $\sigma \times B.R.$	99.3 fb	97.5 fb	86.0 fb	65.5 fb	41.5 fb

The study described requires a comprehensive understanding and simulation of the CMS detector. The electromagnetic calorimeter is used to make the primary measurements of photon energy and position. The tracker is used to measure the position of the interaction vertex. The tracker, ECAL and HCAL are used to determine, if the photon candidate is well isolated. While background characteristics will be measured from data, the signal must be well simulated to perform the analysis described below. This requires a detailed understanding of the detector performance as well as its calibration.

2.1.1. Higgs boson production and decay

For this inclusive study the Higgs boson production mechanisms with the largest cross-sections in the Standard Model have been simulated: gluon fusion, qqH production through Weak Vector Boson Fusion (WBF), associated Higgs production with W or Z bosons, and Higgs production associated with a $t\bar{t}$ pair. The cross sections for the different production processes [20] and the $H \to \gamma\gamma$ branching ratios [21] are summarised in Table 2.1. The analysis described in this chapter has been limited to careful measurement of the inclusive diphoton channel, to address the main detector issues, and no use has been made of tagging leptons or jets. In the future, channel identification, based on additional leptons and jets. will improve the sensitivity. For the moment these 'tagged' channels are investigated individually in other studies [22, 23]. Figure 2.1 shows an event display of a $H \to \gamma\gamma$ event with $M_H = 120\,\text{GeV/c}^2$.

2.1.2. Backgrounds

Backgrounds with two real prompt high E_T photons are called "irreducible", although they can be somewhat reduced due to kinematic differences from signal processes in which high mass particles are produced. Two photons can be produced from two gluons in the initial state through a "box diagram" or from initial quark and anti-quark annihilation.

Backgrounds in which at least one final state jet is interpreted as a photon are called "reducible" and are much harder to simulate since, jets are copiously produced at the LHC and Monte Carlo samples that correspond to 10 fb^{-1} are much too large to fully simulate. Selections at generator level have been devised in order to be able to select multi-jet and γ plus jets events that contribute to the background of the $H \to \gamma\gamma$ channel and reject events that have negligible chance of producing background to the final analysis.

The γ + jet sample can be viewed, from the selection point of view, as coming from two different sources: one where another photon is radiated during the fragmentation of the jet (two prompt photons), the other where there is only one prompt photon in the final state and the other photon candidate corresponds to a mis-identified jet or isolated π^0 (one prompt plus one fake photon). These two processes have been separated using generator level information, and are listed separately in the tables below. Also, different K-factors are applied.

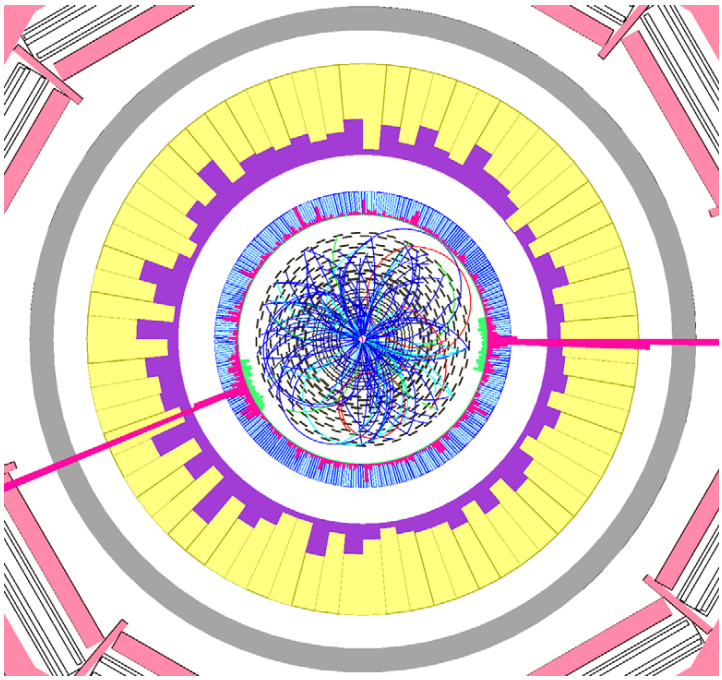

Figure 2.1. $H \to \gamma\gamma$ event produced in gluon fusion with $M_H = 120\,\text{GeV}$ observed in the CMS detector.

The generator level pre-selection of γ + jet events that contribute to the $H \to \gamma\gamma$ background is straightforward. For $pp \to$ jets, a much tighter set of cuts at the particle generator level was carefully developed and studied. Groups of particles, protocandidates, which might form a photon candidate after event simulation are identified. Cuts are applied on the transverse energy of two protocandidates and on their invariant mass, and this involves an estimate on the lower and upper limits to the energy of the photon candidates that might be reconstructed from the protocandidates after the simulation. An estimate is also made on likely level of isolation of the resulting photon candidate.

With such selection a rejection of a factor of about 41000 can be obtained, with an estimated inefficiency of 14% for $pp \to$ jets events generated with PYTHIA with $\hat{p}_\perp > 30\,\text{GeV}$ (transverse momentum of the products of the hard interaction). The inefficiency after the final analysis selection was estimated by using a looser pre-selection similar to that used for the $pp \to \gamma$ + jet simulation. Further details can be found in [19]. Events rejected by the pre-selection have rather low E_T photons and are not very important for the final analysis.

The Monte Carlo samples used are summarised in Table 2.2. All events were generated with PYTHIA [24], simulated with the GEANT-based [9] CMSIM [25] or OSCAR [8], and reconstructed with ORCA version 8.7.3 [10]. Pile-up events from minimum bias interactions were added to the hard interaction, assuming a luminosity of $\mathcal{L} = 2 \times 10^{33}\,\text{cm}^{-2}\,\text{s}^{-1}$.

K-factors are applied to take into account the expected differences between the lowest order cross sections given by PYTHIA and the NLO cross sections of the different background processes [26–30]. The K-factors used for each background are summarised in Table 2.3 and are estimated to have an uncertainty of 20–30%.

Table 2.2. Monte Carlo samples used in the $H \to \gamma\gamma$ analysis with LO cross section from PYTHIA and total corresponding integrated luminosities of the analysed samples.

Process	$\hat{p}_\perp$ (GeV/c)	M_H (GeV/c^2)	σ(pb)	Pre-sel. σ(pb)	Events Analysed	Int Lum. (fb^{-1})
$H \to \gamma\gamma$ (gg fusion)	-	120	-	-	181 K	-
$H \to \gamma\gamma$ (WB fusion)	-	120	-	-	193 K	-
$H \to \gamma\gamma$ (gg fusion)	-	115–150	-	-	20 K	-
$H \to \gamma\gamma$ (WB fusion)	-	115–150	-	-	20 K	-
$H \to \gamma\gamma$ (WH,ZH,ttH)	-	115–150	-	-	20 K	-
$pp \to \gamma\gamma$ (born)	>25	-	82	44	920 K	30
$pp \to \gamma\gamma$ (box)	>25	-	82	31	668 K	20
$pp \to \gamma$ + jet	>30	-	5×10^4	2.5×10^3	5.5 M	2.2
$pp \to$ jets	>50	-	2.8×10^7	4.7×10^3	4.5 M	1.0
Drell–Yan ee	-	-	4×10^3	4×10^3	460 K	0.1

Table 2.3. Background K-factors applied to PYTHIA cross sections.

$pp \to \gamma\gamma$ (Born)	1.5
$pp \to \gamma\gamma$ (Box)	1.2
$pp \to \gamma$ + jet (2 prompt)	1.72
$pp \to \gamma$ + jet (1 prompt + 1 fake)	1
$pp \to$ jets	1

2.1.3. Reconstruction, selection, and signal significance calculation

2.1.3.1. Trigger. $H \to \gamma\gamma$ events are selected with extremely high efficiency both by the Level-1 and High Level triggers that are described in details in Ref. [31]. Since in the analysis selection tighter E_T and isolation cuts are applied, the inefficiency due to the trigger is negligible.

2.1.3.2. Photon reconstruction. Photons are reconstructed with the standard ECAL algorithms [7, 32]. At this level the photon reconstruction efficiency is over 99.5% for photons in the region covered by the ECAL.

The energy resolution of reconstructed photons is excellent for photons that do not convert or that convert late in the tracker. Energy resolution deteriorates somewhat for photons that convert early in the tracker. Nevertheless, the photon energy resolution is substantially less affected by tracker material than is electron energy resolution and the Higgs reconstruction in the calorimeter is quite reliable even for converted photons.

For signal events, where this effect is relevant, the energy response of the individual crystals of the ECAL has been smeared using a miscalibration file randomly generated to correspond to the intercalibration precision expected after calibration with $W \to e\nu$ events obtained with an integrated luminosity of 10 fb^{-1}, as described in [7]. The precision is 0.3% in the central part on the barrel, growing up to 1.0% at the edge of the barrel and in the endcaps.

The tools that have been developed to identify and reconstruct photon conversions in the tracker [33], and π^0 rejection tools developed for the endcap silicon preshower detector and the barrel crystals, have not yet been included in the analysis.

2.1.3.3. Primary vertex identification. The bunch length at LHC has an rms width of 75 mm resulting in a longitudinal spread of interaction vertices of 53 mm. If the mean longitudinal

position is used (nominal vertex), the invariant mass of a two-photon state, such as the $H \to \gamma\gamma$, is smeared by about $1.5\,\mathrm{GeV/c^2}$, due to the mis-measurement of the angle between the two photons related to the uncertainty of the photon directions.

The two high E_T photons coming from the Higgs boson decay are produced in association with other tracks that may come from the underlying event and initial state gluon radiation or from the other particles produced with the Higgs boson in the case of WBF fusion, WH or ZH production and $t\bar{t}H$ production.

The charged tracks associated to the Higgs production vertex are typically harder than those coming from minimum bias interactions. Therefore, the vertex can be identified by reconstructing the primary vertices in the event and selecting the one that most likely corresponds to the Higgs boson production, based on charged tracks.

At low luminosity ($2 \times 10^{33}\mathrm{cm^{-2}\,s^{-1}}$) we are able to identify the correct vertex, defined as being within 5 mm of the actual vertex, in about 81% of the signal events passing the selection described in Section 2.1.4.1. Clearly, these results will be affected by any significant variation of the characteristics of the pileup events from what is simulated in our pileup samples.

2.1.3.4. Photon isolation. Detailed studies have been made of photon isolation and its optimisation [34, 35]. Fake photon signals due to jets can be rejected by looking for additional energetic particles accompanying the photon candidate. Charged pions and kaons can be detected in the tracker or in the calorimeters. Neutral pions and other particles decaying to photons can be detected in the ECAL. The hadron calorimeter may be important for detecting charged particles not efficiently reconstructed in the tracker, particularly at high η, or other particles like neutrons or K^0_{long}.

2.1.3.5. Separation into categories based on lateral shower shape and pseudorapidity. The shower shape variable R_9, defined as the fraction of the super-cluster energy found inside the 3×3 array of crystals centred around the highest energy crystal, is effective in distinguishing photon conversions in the material of the tracker. Photon candidates with large values of R_9 either did not convert or converted late in the tracker and have good energy resolution. Photons converting early have lower values of R_9 and worse energy resolution.

The variable R_9 has been shown to be very useful also in discriminating between photons and jets. This occurs both because of the conversion discrimination – either of the photons from a π^0 can convert – and because, looking in a small 3×3 crystal area inside the super-cluster, the R_9 variable can provide very local isolation information about narrow jets.

In the multi-category analysis, the events are separated into categories based on R_9 so as to take advantage of better mass resolution where it is expected (the unconverted photons), and yet still use all the events (since the mass resolution varies by at most a factor of 2). This separation also tends to put background events involving jets into categories with lower R_9.

We also find that photons detected in the endcaps have worse energy resolution and higher background than photons detected in the barrel so that it is useful to separate events with one or more photons in the endcaps from those with both photons in the barrel.

2.1.3.6. Calculation of confidence levels. Confidence levels are computed by using the Log Likelihood Ratio frequentist method, as described in [36]. Given the expected signal and background distributions in the final variable (the mass distribution for the cut-based analysis), we simulate many possible outcomes of the experiment by means of Monte Carlo. This is done both in the hypothesis that the signal exists and that it does not exist. To compute a confidence level, we order our trials according to an estimator. This is a single number

that is useful to order random trials from most background-only-like to most signal-plus-background-like. The simplest and probably best estimator is the Log Likelihood Ratio (LLR) which compares the likelihood of the data to come from a background-only distribution to the likelihood to come from a signal-plus-background distribution. Each likelihood is the product of probabilities from all the bins. The median confidence level is computed both for discovery and for exclusion.

2.1.3.7. Effect of systematic errors. To include systematic errors the background and signal expectation are randomised by the systematic error during the generation of the random trials, while keeping their expectations at the nominal value. If necessary, the correlations between the errors on the different analysis bins is included. It is observed that the signal systematic error has no effect on the median LLR of signal-plus-background experiments, nor on that of background-only experiments. Of course, the distribution corresponding to the signal-plus-background experiments is enlarged by the systematic error on the signal and this makes exclusion more difficult. On the other hand the effect of the systematic error on the background is very large, because of the small signal over background ratio. The mean of the distributions is still unchanged but the widths are enlarged both for background-only experiments and for signal-plus-background experiments. This decreases both the discovery and exclusion sensitivities.

2.1.4. Cut-based analysis

2.1.4.1. Selection. Two photon candidates are required with pseudo-rapidity $|\eta| < 2.5$, with transverse energies larger than 40 GeV and 35 GeV respectively, and satisfying the following isolation requirements:

- No tracks with p_T larger than 1.5 GeV/c must be present inside a cone with $\Delta R < 0.3$ around the photon candidate. We only consider tracks with hits in at least two layers of the silicon pixel detector, therefore converted photons are likely to be rejected only if they convert before the second pixel layer.
- The total E_T of all ECAL island basic clusters with $0.06 < \Delta R < 0.35$ around the direction of the photon candidate, regardless of whether they belong to the super-cluster or not must be less than 6 GeV in the barrel and 3 GeV in the endcaps.
- The total transverse energies of HCAL towers within $\Delta R < 0.3$ around the photon candidate must be less than 6 GeV in the barrel and 5 GeV in the endcaps.

In order to further reduce the background that is higher when at least one of the photons is detected in the electromagnetic calorimeter endcaps and to increase the performance of the analysis in the forward region additional isolation requirements are applied for events where one, or more, of the candidates has $|\eta| > 1.4442$. For these events, the candidate in the barrel is required to satisfy the tighter isolation selection that is applied to photons in the endcaps: ECAL isolation less than 3 GeV and HCAL isolation less than 5 GeV.

Figure 2.2 shows the mass distribution after the selection. The efficiency for a 120 GeV/c^2 Higgs boson is 30% and the total expected background is 178 fb/GeV. The number of expected background events for the different types of background is shown in Table 2.4 while the Higgs efficiency in different mass windows is shown in Table 2.5. The efficiency is computed using all generated signal events. The signal contribution to the total number of events is very small, particularly outside the mass region under study. The background can be estimated by a fit to the data mass distribution.

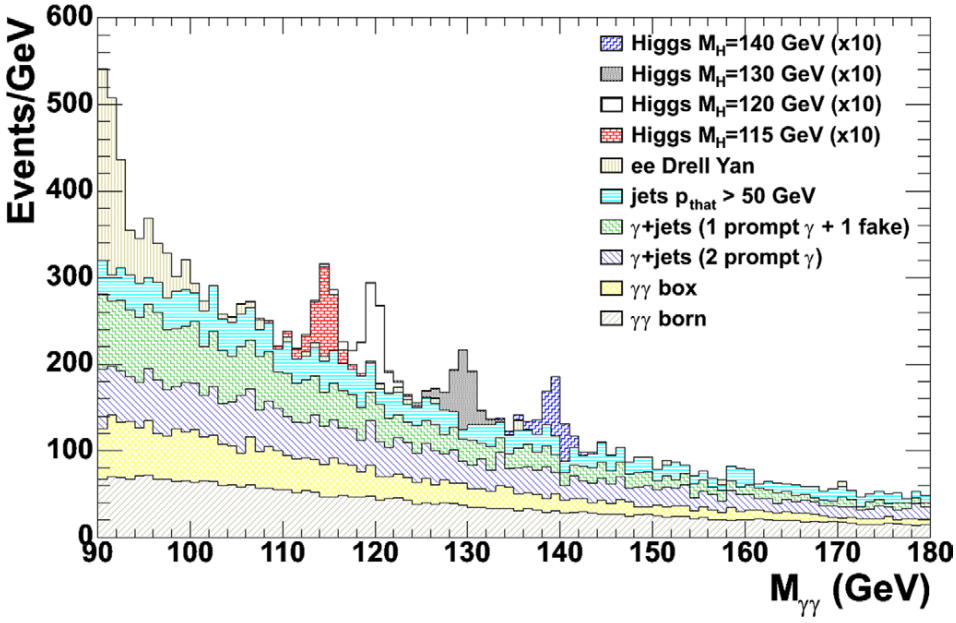

Figure 2.2. Diphoton invariant mass spectrum after the selection for the cut-based analysis. Events are normalised to an integrated luminosity of 1 fb^{-1} and the Higgs signal, shown for different masses, is scaled by a factor 10.

Table 2.4. Expected background after the selection for Higgs boson masses between 115 and 150 GeV/c^2, expressed in fb/GeV.

Process	115 GeV/c^2	120 GeV/c^2	130 GeV/c^2	140 GeV/c^2	150 GeV/c^2
$pp \to \gamma\gamma$ (Born)	48	44	36	29	24
$pp \to \gamma\gamma$ (Box)	36	31	23	16	12
$pp \to \gamma$ + jet (2 prompt)	43	40	32	26	22
$pp \to \gamma$ + jet (prompt + fake)	40	34	22	19	14
$pp \to$ jets	29	27	20	18	14
Drell–Yan ee	2	2	1	1	1
Total background	203	178	134	109	86

Table 2.5. Selection efficiency for the Higgs signal in different mass windows.

M_H (GeV/c^2)	Window ±1 GeV/c^2	Window ±1.5 GeV/c^2	Window ±2.5 GeV/c^2	Window ±5 GeV/c^2	Window Total
115	17%	21%	25%	28%	29%
120	18%	22%	26%	29%	30%
130	18%	22%	27%	31%	32%
140	18%	23%	28%	32%	34%
150	28%	24%	29%	33%	36%

The error on the background estimation comes from two sources:

- the statistical precision which decreases with the size of the mass range that is used to perform the fit;
- the systematic error related to the shape of the function that is used to fit the distribution.

It is not possible to know the exact functional form of the background shape and the error must be estimated by assuming a function, simulating a distribution and then using a different function to fit the data. Clearly, this error grows with the size of the mass range used. For a reasonable mass range of $\pm 10 - 20\,\mathrm{GeV/c^2}$ excluding +3 and $-5\,\mathrm{GeV/c^2}$ from the Higgs boson mass under study and for an integrated luminosity of $20\,\mathrm{fb}^{-1}$ the statistical and systematic errors are estimated to be 0.4% and 0.5% respectively. The statistical error decreases with the integrated luminosity while the systematic error is constant.

2.1.4.2. Splitting into categories. Changing the cuts or adding new discriminating variables to this analysis does not give large improvements in the sensitivity. This can be seen, for example, from the fact that it is not possible to use the very powerful variable, R_9, to reject events without loosing performance. This is because, the increase in s/b ratio does not compensate the loss in efficiency.

The way to improve the sensitivity of the analysis is to keep all selected events but to split the sample into categories with different s/b ratios.

The following 3 possibilities are considered:

- 1 single category;
- 4 categories from 2 R_9^{min} ranges (R_9^{min} larger or smaller than 0.93) times 2 pseudo-rapidity regions $|\eta|^{\mathrm{max}}$ in barrel or endcaps;
- 12 categories from 3 R_9^{min} ranges ($R_9^{\mathrm{min}} > 0.948, 0.9 < R_9^{\mathrm{min}} < 0.948$ and $R_9^{\mathrm{min}} < 0.9$) times 4 pseudo-rapidity regions ($|\eta|^{\mathrm{max}} < 0.9$, $0.9 < |\eta|^{\mathrm{max}} < 1.4442$, $1.4442 < |\eta|^{\mathrm{max}} < 2.1$ and $|\eta|^{\mathrm{max}} > 2.1$).

Figure 2.3 shows the mass spectrum after splitting into four categories. The signal over background ratio is much larger in the best category and the composition of the background varies between the different samples: irreducible backgrounds dominate for large R_9 and reducible backgrounds are larger for small R_9.

Table 2.6 shows, for the 12 category analysis, the fraction of events along with the maximum s/b ratio in each category.

2.1.4.3. Systematic errors. The total error on the background is approximately 0.65% and is due to the uncertainty of the function fit to the side-bands of the mass distribution, estimated to be 0.5%, plus the statistical error on the fit that is approximately 0.4% for an integrated luminosity of $20\,\mathrm{fb}^{-1}$.

An error of 0.65% has a very large effect on the discovery CL when only one category is used. The reason is that a large fraction of signal events corresponds to a very low s/b, of the order of a percent. The effect can be reduced by applying a cut on the signal over background s/b. This corresponds to using events in a mass window around the analysed mass, until s/b becomes smaller than the chosen cut. The optimal cut for this analysis is 0.02.

When the events are split into categories the number of background events in each category is reduced on average by $1/N_{\mathrm{cat}}$ and this increases the statistical error on the background estimation by approximately a factor $\sqrt{N_{\mathrm{cat}}}$, but this error is completely uncorrelated between the different categories. The error related to the uncertainty of the fit function remains constant and it is also uncorrelated between the different categories because, due to the different cuts the background shapes are different and described by different

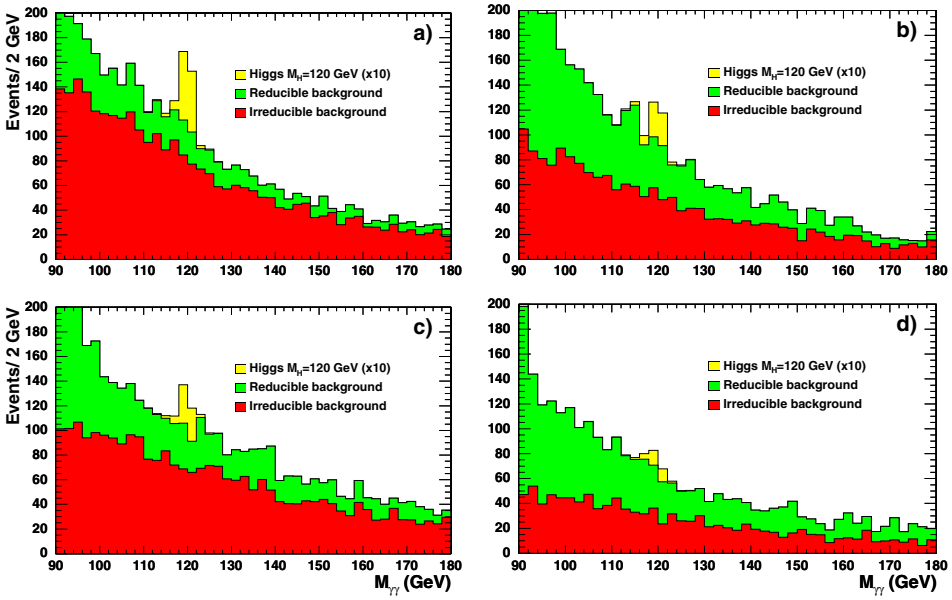

Figure 2.3. Invariant mass spectrum after the selection relative to the cut-based analysis with four categories defined in the text: barrel with large R_9 (a), barrel with small R_9 (b), endcaps with large R_9 (c) and endcaps with small R_9 (d), Events are normalised to an integrated luminosity of 1 fb^{-1} and the Higgs signal, shown for different masses, is scaled by a factor 10.

Table 2.6. Fractions of events in each of the 12 categories and maximum s/b in the mass region of 120 GeV/c^2.

	$\lvert\eta\rvert^{max} < 0.9$		$0.9 < \lvert\eta\rvert^{max} < 1.4442$		$1.4442 < \lvert\eta\rvert^{max} < 2.1$		$\lvert\eta\rvert^{max} > 2.1$	
	frac.	s/b	frac.	s/b	frac.	s/b	frac.	s/b
$R_9^{min} > 0.948$	15.5%	14.7%	13.1%	9.0%	10.8%	6.1%	8.5%	4.5%
$0.9 < R_9^{min} < 0.948$	9.4%	12.2%	6.8%	6.8%	6.7%	4.8%	2.7%	2.8%
$R_9^{min} < 0.9$	8.3%	7.6%	11.1%	4.3%	5.4%	3.2%	1.7%	2.2%

functions. The total error is then less than the total error reduced by $1/\sqrt{N_{cat}}$. This reduces the effect of the systematic error on the discovery.

The effect of the systematic error on the background estimation is also related to the signal over background of the analysis. A more sensitive analysis, for which a larger part of the signal has a higher s/b ratio, is less affected by the same relative uncertainty on the background.

Clearly the current understanding of the background is affected by larger uncertainties such as: cross section, diphoton kinematic distributions and efficiency of the selection (mainly affected by jet fragmentation, pile-up and by the structure of the underlying events).

The systematic error on the signal, that as has been mentioned has no effect on the discovery CL, has contributions from the theoretical uncertainty of the cross section (+15–12% from the scale variation and +4–5%), from the measurement of the integrated luminosity (∼5%), from the trigger (∼1%), from the analysis selection (that will be measured for example with $Z \to \mu\mu\gamma$) and from the uncertainties on the photon energy resolution.

Table 2.7. Integrated luminosity needed to discover or exclude the Higgs boson with mass 120 GeV/c^2 with or without taking into account the systematic errors (fb^{-1}).

Analysis	5σ discovery no syst	5σ discovery syst	3σ evidence no syst	3σ evidence syst	95% exclusion no syst	95% exclusion syst
counting exp.	27.4	48.7	10.0	13.2	4.5	6.5
1 category	24.5	39.5	8.9	11.5	4.1	5.8
4 categories	21.3	26.0	7.5	9.1	3.5	4.8
12 categories	19.3	22.8	7.0	8.1	3.2	4.4

Other effects that could modify the ability to discover the Higgs boson are: uncertainties on the structure of the underlying events, that could change the efficiency of the primary vertex determination and the amount of material in the tracker before the electromagnetic calorimeter.

The effect on the performances of the analysis of an increase of 20% of the tracker material has been evaluated. The main effects on such change on the analysis would be:

- increase of the inefficiency of the track isolation requirements for early photon conversions, before or inside the second layer of the pixel detector.
- increase of the inefficiency of ECAL isolation cut;
- decrease of the value of R_9 for all photons that would cause a migration of events from more sensitive categories to less sensitive categories.

It was estimated that such change would increase the luminosity needed to achieve a given discovery CL of approximately 6%. Given that the amount of tracker material will be known with a precision of $\sim 2\%$ the related systematic error is less than 1%.

In what follows a conservative 20% systematic error on the signal is assumed. It affects exclusion of a signal, not discovery, since the signal rate is directly measured from data in case of discovery.

2.1.4.4. Results of the cut-based analysis. Table 2.7 shows the integrated luminosity needed to obtain 5σ discovery or 95% CL exclusion for a 120 GeV/c^2 mass Higgs boson with the different splittings. The effect of the systematic errors is also shown. We can observe how the performance increases and the effect of the error on the background estimation decreases with the number of categories. In the three cases (1, 4 and 12 categories) the event selection is the same and that the differences in performance come from the splitting of the total sample in different sub-samples with different sensitivities (s/b). In the split category analyses the computation of the log-likelihood ratio estimator is made separately for each 1 GeV/c^2 bin in mass, whereas in the "counting experiment" only a single (optimum) mass window is evaluated.

The integrated luminosity needed for discovery and exclusion, using the 12-category analysis, for the mass range studied between 115 and 150 GeV/c^2 are shown in the plots at the end of the section (Fig. 2.10). The Higgs boson can be discovered with mass between 115 and 140 GeV/c^2 with less than 30 fb^{-1} and excluded in the same mass range, at 95% CL, with less than 5 fb^{-1}.

As mentioned before, all these results have been obtained assuming an intercalibration of the ECAL, after having collected an integrated luminosity of 10 fb^{-1}. With the whole ECAL intercalibrated to a precision better than 0.5% over all the solid angle, the results improve such that approximately 10% less integrated luminosity is needed for discovery.

2.1.5. Optimised analysis estimating s/b for each event

In the optimised analysis 6 categories are used, 3 in which both photons are in the barrel and 3 in which at least 1 photon is in an endcap. The 3 categories are defined, as for the cut-based analysis, to have the lowest R_9 photon candidate with $R_9 > 0.948$, $0.948 > R_9 > 0.90$ and $R_9 < 0.90$ respectively. The categories are labelled with numbers from 0 to 5: first, the 3 barrel categories with decreasing values of R_9 then the 3 endcap categories again with decreasing values of R_9.

2.1.5.1. Mass distributions in categories. The diphoton mass distributions enable the separation of signal from background. Signal peaks sharply at the Higgs mass while the backgrounds are quite smooth. This allows good estimation of the magnitude of the background under the peak.

The best mass resolution and the best s/b ratio in the peak is found in category 0, with high R_9 in the barrel.

2.1.5.2. Loose selection of events for optimised analysis. Isolation requirements are applied to photon candidates prior to the computation of the neural network isolation variables NN_{isol}:

- the transverse E_T of the photon candidates must be larger than 40 GeV and the absolute value of their pseudo-rapidity less than 2.5;
- no tracks with p_T larger than 1.5 GeV/c must be present inside a cone with $\Delta R < 0.1$ around the photon candidate;
- the total E_T of all ECAL island basic clusters with $\Delta R < 0.3$ around the photon candidate, excluding those belonging to the super-cluster itself must be less than 5 GeV;
- the total transverse energies of HCAL towers within $\Delta R < 0.35$ around the photon candidate must be less than 35 GeV;
- the sum of the transverse momenta of charged tracks within $\Delta R < 0.2$ around the photon candidate must be less than 100 GeV/c.

Before optimising the final analysis, some additional cuts are applied. These both simplify the neural network training and slightly improve the performance. It is required that:

- the events pass the double photon High Level Trigger;
- the isolation neural net output is greater than 0.25 for both photons.

2.1.5.3. Optimised use of kinematic variables to separate signal and background. In addition to the mass, there are kinematic differences between signal and background. In particular the signal has a harder photon E_T distribution than the background – the background can have a high mass by having a large η difference between the photon candidates. Weak Boson Fusion and associated production of a Higgs with other massive particles enhance these differences between signal and background. The large, reducible backgrounds often have photon candidates that are not well isolated.

As with the Higgs searches performed at LEP, higher performance can be achieved if the expected signal over background, s/b, is estimated for each event. This is particularly effective if, the s/b varies significantly from event to event. This is the case here due to wide variations in photon isolation and photon E_T. There is also significant dependence of the s/b on photon conversion and on location in the detector.

One photon isolation variable NN_{isol} for each photon, is combined with kinematic variables to help separate signal and background. A neural net is trained to distinguish background events, taken from the mass side-bands, from signal Monte Carlo events. There is

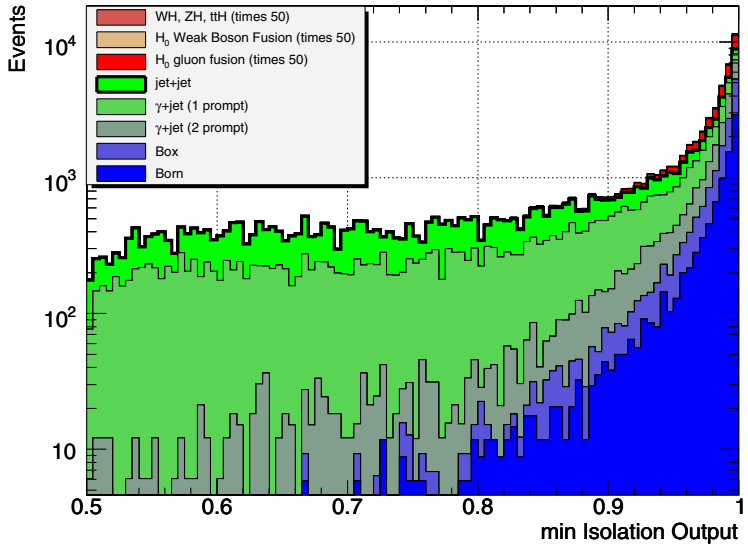

Figure 2.4. Distribution of the minimum value of the NN_{isol} variables of the two photon candidates. Events are normalised to an integrated luminosity of 7.7 fb^{-1} and the signal ($M_H = 120\,GeV/c^2$) is scaled by a factor 50.

no danger of over-training since background events from the signal mass region are not used and independent samples are used for the signal Monte Carlo. The input variables are devised to be insensitive to the diphoton mass so that the background rejection due to the kinematics and isolation is independent of the background rejection from the mass distribution.

Six variables are used as inputs to a neural net. They are the isolation NN outputs NN_{isol} for the 2 photons, the transverse energies of the 2 photons, normalised to the diphoton mass, the absolute value of the rapidity difference between the 2 photons, and the longitudinal momentum of the photon pair.

The distributions of the input variables are shown for signal and background in Figs. 2.4 and 2.5. Kinematic information that are likely to be highly sensitive to higher order corrections to the background simulation has not been used. Such information, like the E_T of the Higgs boson candidate, the E_T transverse to the photon direction, and information about additional jets will ultimately be useful but may not be reliable until better simulations or actual data are available to train on.

The neural net is trained in each of the 6 categories independently. The net has 6 input nodes, 12 intermediate nodes in a single layer, and 1 output node. The error function has been modified from the standard to improve training toward a high signal over background region. A minimum neural net output cut is applied that eliminates 1% of the signal in each category and a function is fit to the distribution above that cut. These functions are used to bin the data and to smooth the background in a limited region.

It is useful to examine the neural net output distribution for events from different sources (Fig. 2.6). Low NN outputs are dominated by photon candidates from jets which are not well isolated. The large peak at 0.85 represents both signal and background where the photon is relatively well isolated and the photon E_T is $M_H/2$, corresponding to events with a large value of NN_{isol}. Higher photon E_T events are found in the peak near 1. There is an enhancement of the signal, particularly for the WBF and associated production processes. The background there is dominated by events with at least one jet interpreted as a photon.

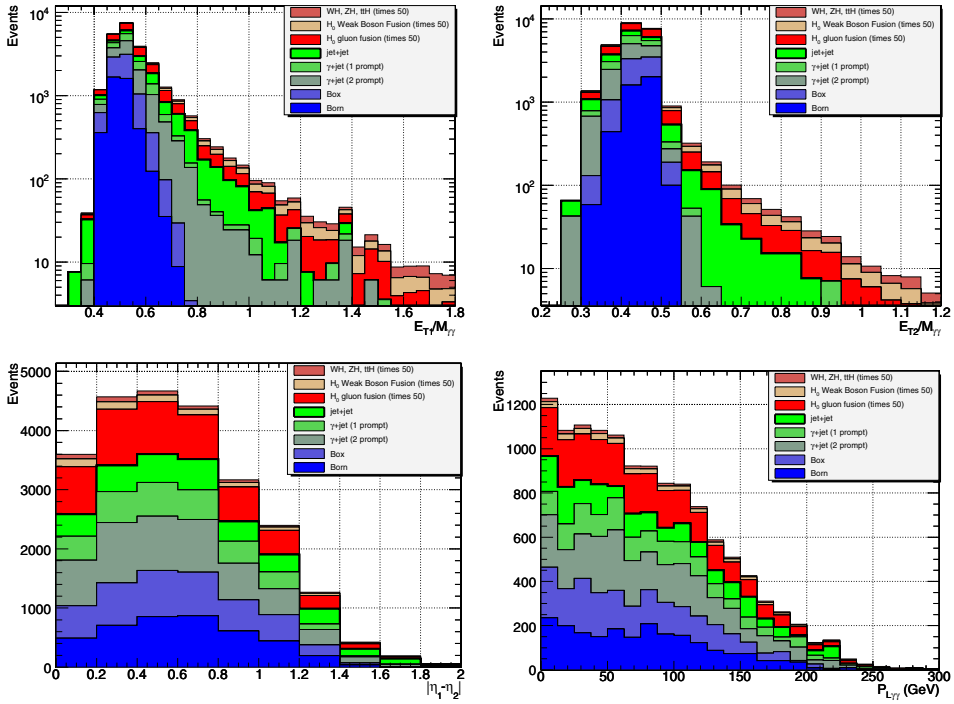

Figure 2.5. Distribution of the kinematic inputs to the neural network for signal and background sources. A value of the neural net output is required to be greater than 0.85. Events are normalised to an integrated luminosity of 7.7 fb^{-1} and the signal ($\mathrm{M_H} = 120\,\mathrm{GeV/c^2}$) is scaled by a factor 50.

2.1.5.4. Estimation of signal to background ratio for each event. In order to get the most information out of each event, the signal over background is estimated for each event. In the simplest analyses, cuts are applied to select only high signal over background events and those are counted. Such a simple analysis looses information because, some of the events that are cut could contribute to the measurement and because, some of the events that are accepted are not used optimally.

Events in the mass peak for the Higgs mass hypothesis under consideration have high signal over background expectation while events outside the peak have lower expected s/b. Similarly, events at high $\mathrm{NN_{kin}}$ output have higher s/b expectation. The kinematics and isolation information in $\mathrm{NN_{kin}}$ has been made independent of mass information so the two s/b ratios can be multiplied to get a good estimate of the s/b expectation for the event:

$$\left(\frac{s}{b}\right)_{\mathrm{est}} = \left(\frac{s}{b}\right)_{\mathrm{mass}} \times \left(\frac{s}{b}\right)_{\mathrm{kin}} .$$

This is an estimate that is to bin signal and background events. If the estimate is bad, the performance of the analysis suffers because good s/b events are not well separated from bad ones. It is not possible for a bad estimate to make the analysis appear to perform too well. The s/b estimate need not be normalised correctly, since it is a relative number used to bin events.

The events are binned according to the s/b estimate. Histograms are made in each of the six categories. The actual signal to background ratio is computed for the binned events and

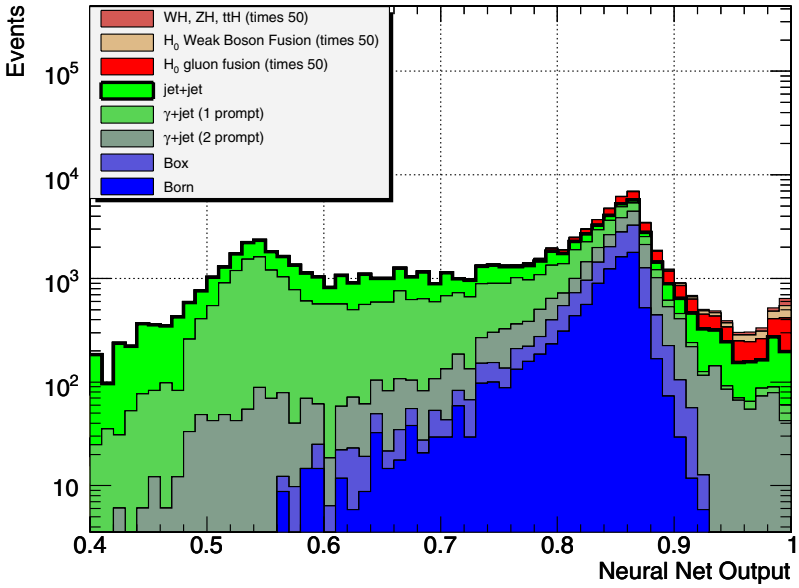

Figure 2.6. The neural net output for events in the barrel for each signal ($M_H = 120\,GeV/c^2$) and background source. Events are normalised to an integrated luminosity of $7.7\,fb^{-1}$ and the Higgs signal is scaled by a factor 50.

used to calculate confidence levels that data are consistent with a background-only hypothesis or with a signal-plus-background hypothesis.

2.1.5.5. Smoothing the background. The $H \to \gamma\gamma$ channel has the good feature that the mass is essentially independent of isolation and suitably chosen kinematic variables. With this factorisation assumption, background can be smoothed well even in regions with low statistics.

The background expectation in a bin must be reliably estimated in order to correctly calculate confidence levels. Downward fluctuations in the background estimation can have a significant impact on the CL. The number of simulated events for the irreducible (jet) backgrounds is about one seventh of the number that will be available in the data at the time it would be expected to discover the Higgs. Therefore, problems with background estimation are even more difficult now than they will be when we have data.

The background distributions are very smooth in the mass variable, so the distribution in mass can be reliably smoothed. This is done by spreading each event over a $\pm 5\,GeV/c^2$ region according to the functions fit to the mass distribution. A wider mass region could be used but this would interfere with the training of the analysis on an independent sample in the mass side-bands.

The background distribution in the neural net output is also smoothed over a region of ± 0.05 using the fit functions. It is therefore, quite important that the background fit functions accurately represent the neural net distribution. In the smoothing process, the normalisation of the background is carefully maintained to high accuracy.

With this two-dimensional smoothing accurate background expectations are obtained except in the regions with extremely small amounts of background. In such regions, bins must be combined until sufficient background events are available. If a s/b bin has too few MC

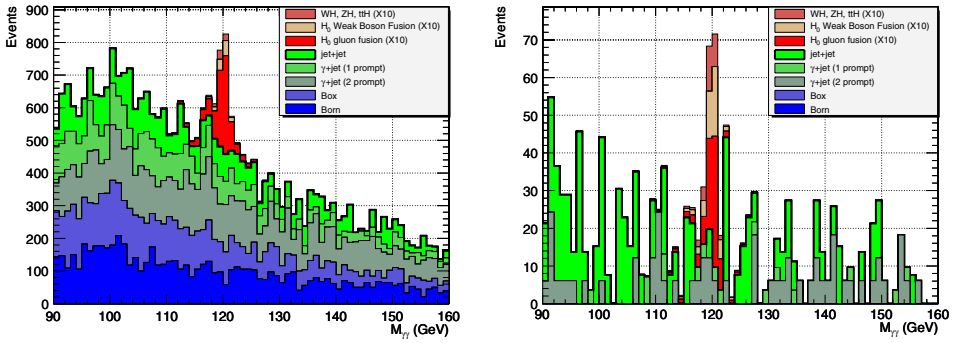

Figure 2.7. The diphoton mass distribution for each source for barrel events with kinematic neural net output greater than 0.85 (left) and 0.97 (right). Events are normalised to an integrated luminosity of 7.7 fb^{-1} and the Higgs signal ($\mathrm{M_H} = 120\,\mathrm{GeV/c^2}$) is scaled by a factor 10.

background events contributing to it, it is combined with the nearest (lower s/b) bin. This is continued until there are sufficient events. This combination clearly reduces the sensitivity of the analysis but cannot be avoided without a more detailed understanding of the background, which is a goal for the future. At present, at least 20 Monte Carlo background events are required in a bin. Since the current MC samples contain about seven times less events than expected in the data, significant improvements are possible, allowing higher s/b bins to be used, resulting in better performance.

Figure 2.7 shows the mass distributions for barrel events with two different cuts on the neural net output. The looser cut simply excludes most of the obviously non-isolated candidates. It can be seen that all of the backgrounds are important at this level. The tighter cut highly enhances the s/b ratio and emphasises the importance of smoothing, which has not been applied to the background in this distribution.

Figure 2.8 shows the mass distribution for neural net output greater than 0.97 in category 0. Again it is clear that smoothing in two dimensions is needed to get a reasonable estimate of the background. It is useful to note that even in this very high s/b region, the largest contribution to the signal is from gluon fusion, although the relative contributions of the other production processes has increased.

2.1.5.6. Combination of categories into final s/b distribution. At this point the signal and background is binned in s/b in six categories. These could be used to calculate the confidence level, however, it seems most useful, in the light of future plans to analyse separate channels, to combine the categories into one s/b plot in a similar way as may be used to re-combine channels. The six histograms are combined into one which can be used calculate confidence levels. The combination is based on the actual signal to background in each bin. In principle, this is the same as combining results from different channels or even from different experiments in a way that makes optimal use of all channels and does not pollute high quality channels with data of lesser purity.

The final binning of data into s/b bins is shown in Fig. 2.9. The plot extends from very low signal to background to a small number of events with $s/b > 1$.

The relative contribution of barrel and endcap categories can be estimated from the total LLR computed and LLRs computed excluding each category. The six categories have rather widely varying contributions to the Log Likelihood Ratio and hence to the performance of the analysis. Table 2.8 shows the fraction of signal and the fraction of the LLR for each category.

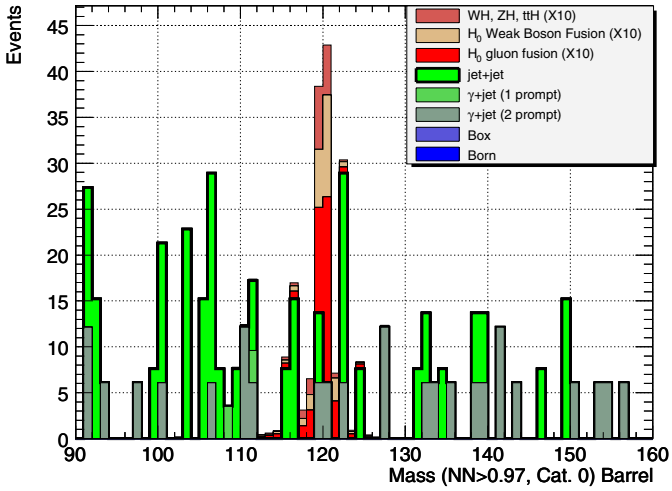

Figure 2.8. The diphoton mass distribution for each source for barrel events with kinematic neural net output greater than 0.97 and $R_9 > 0.948$. Events are normalised to an integrated luminosity of $7.7\,\mathrm{fb}^{-1}$ and the Higgs signal ($M_H = 120\,\mathrm{GeV/c^2}$) is scaled by a factor 10.

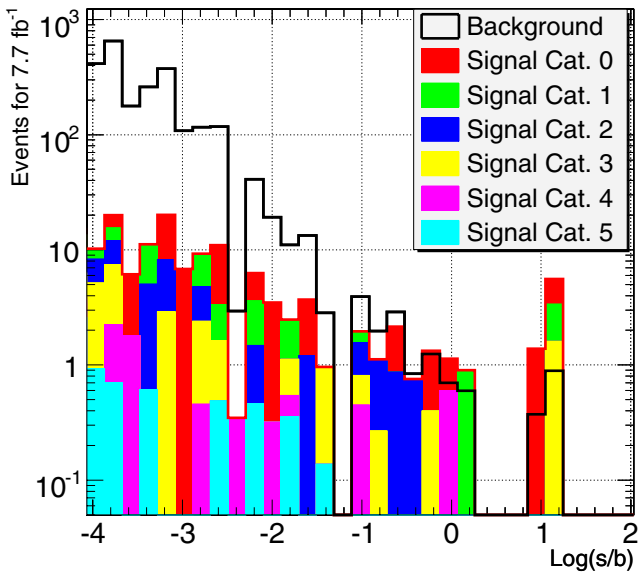

Figure 2.9. The final distribution of binned signal ($M_H = 120\,\mathrm{GeV/c^2}$) and background in $\log(s/b)$ for an integrated luminosity of $7.7\,\mathrm{fb}^{-1}$. Here the Higgs signal is normalised to the integrated luminosity and the statistics benefits of the smoothing of the background. Signal and background events are added independently.

Some of the categories have a fairly small effect on the final result. This remains true after the application of systematic normalisation uncertainties described below. It is clear that photon conversions result in a significant deterioration of the performance. It is hoped to mitigate this somewhat by using the conversion track reconstruction in the future, but the poorer mass resolution cannot be recovered and a big effect is not expected.

Table 2.8. Performance in the six categories for $M_H = 120\,GeV/c^2$.

Category	Signal%	LLR %
0	27.8	48.0
1	16.1	24.8
2	21.7	11.9
3	16.6	9.7
4	9.0	4.1
5	8.8	1.5

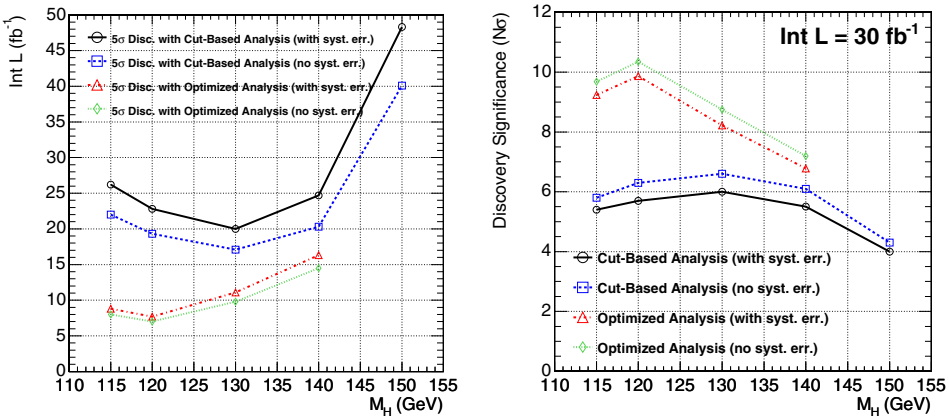

Figure 2.10. Integrated luminosity needed for a 5σ discovery (left) and discovery sensitivity with an integrated luminosity of $30\,fb^{-1}$ (right) with the optimised analysis. The results from the cut-based analysis in 12 categories are also shown for comparison.

2.1.5.7. Results of the optimised analysis. The same estimates of systematic error are used to obtain the results in the optimised analysis as are used in the cut-based analysis. Most of the development and studies have been made for a Higgs mass of $120\,GeV/c^2$. For this mass, a 5σ discovery can be made with about $7\,fb^{-1}$ luminosity. A 1% background normalisation uncertainty corresponds to an increase of the luminosity needed for a 5σ discovery from $7\,fb^{-1}$ to $7.7\,fb^{-1}$.

There is a great deal of uncertainty in this benchmark estimate of luminosity due to our poor understanding of the backgrounds we will contend with when the LHC starts running, however, this is not considered here as a systematic error on a discovery since, it is proposed to measure the background from the data. Figure 2.10 shows the luminosity needed for a 5σ discovery and the discovery sensitivity with an integrated luminosity of $30\,fb^{-1}$ for several Higgs masses, both for the fully optimised analysis and for the cut-based analysis using 12 categories described in Section 2.1.4.4. It seems possible to discover, or at least have strong evidence for a low mass Higgs in the first good year of running.

2.1.6. Measurement of the Higgs boson mass

If the Higgs boson will be discovered in the $H \to \gamma\gamma$ channel then we will be able to measure its mass. We have studied the mass measurements with the cut based analysis with two different methods:

Table 2.9. Expected statistical errors on the Higgs boson mass measurement for 30 fb^{-1}.

M_H	115 $\mathrm{GeV/c^2}$	120 $\mathrm{GeV/c^2}$	130 $\mathrm{GeV/c^2}$	140 $\mathrm{GeV/c^2}$	150 $\mathrm{GeV/c^2}$
All events	184 $\mathrm{MeV/c^2}$ 0.16%	184 $\mathrm{MeV/c^2}$ 0.15%	201 $\mathrm{MeV/c^2}$ 0.15%	222 $\mathrm{MeV/c^2}$ 0.16%	298 $\mathrm{MeV/c^2}$ 0.20%
12 categories	127 $\mathrm{MeV/c^2}$ 0.11%	139 $\mathrm{MeV/c^2}$ 0.12%	129 $\mathrm{MeV/c^2}$ 0.10%	156 $\mathrm{MeV/c^2}$ 0.11%	204 $\mathrm{MeV/c^2}$ 0.14%

- measurement from the Δ Log(likelihood) using all events;
- measurement from the Δ Log(likelihood) using the cut-based analysis split in 12 categories.

The expected statistical errors are shown in Table 2.9 for an integrated luminosity of 30 fb^{-1}. The statistical errors simply scale with $1/\sqrt{\mathrm{Int\,L}}$. The errors are slightly asymmetric, due to the tail of the reconstructed Higgs mass distribution at lower masses, the positive error being approximately 10% smaller than the negative. The table shows the average between the two.

As we can see the statistical error will be 0.1 to 0.2% already with 30 fb^{-1}, when the significance of the discovery would be 5 to 6 σ with the cut based analysis. Of course, this measurement will be affected by the uncertainty of the absolute scale of the photon energy measurement that will be derived for example by the measurement of the Z mass in the radiative Z decays $\mathrm{Z} \to \mu\mu\gamma$.

2.1.7. Summary

A standard cut-based analysis can discover the Higgs boson with 5σ significance between the LEP lower limit and 140 $\mathrm{GeV/c^2}$ with less than 30 fb^{-1} of integrated luminosity. Approximately 5 fb^{-1} are needed to exclude its existence in the same mass range.

It has been shown that the $\mathrm{H} \to \gamma\gamma$ channel can be used to discover a low mass Higgs with an integrated luminosity not too different from that needed for higher mass Higgs, 7.7 fb^{-1} at 120 $\mathrm{GeV/c^2}$ with an analysis using an event by event estimation of the s/b ratio. Because of the excellent mass resolution expected in the diphoton channel, the background rate and characteristics from the data can be determined from diphoton events at masses away from the Higgs mass hypothesis.

An inclusive analysis has been presented. In future the various signal channels will be identified by looking for additional jets, leptons, or missing energy. This will clearly improve the sensitivity of the analysis.

2.2. Benchmark Channel: $H \to ZZ^{(*)} \to 4$ electrons

One of the most promising road towards a discovery at the LHC of the Higgs boson postulated in the SM is via single production followed by a cascade decay into charged leptons, $\mathrm{H} \to \mathrm{ZZ}^{(*)} \to l^+l^-l^+l^-$.

The single Higgs boson production benefits from a high cross-section, with values of about 40×10^3 fb at $m_\mathrm{H} = 130\,\mathrm{GeV/c^2}$ and decreasing monotonically to about 10×10^3 fb around $m_\mathrm{H} = 300\,\mathrm{GeV/c^2}$. The production cross-section is dominated ($\gtrsim 80\%$) over this mass range by gluon-gluon fusion processes via triangular loops involving heavy quark (mostly the top quark) flavours. The branching ratio for the $\mathrm{H} \to \mathrm{ZZ}^{(*)}$ decay in the SM is sizeable for any m_H value above 130 $\mathrm{GeV/c^2}$. It remains above 2% for $m_\mathrm{H} \leqslant 2 \times M_W$ with a peak above 8% around $m_\mathrm{H} \simeq 150\,\mathrm{GeV/c^2}$, and rises to values of 20 to 30% for $m_\mathrm{H} \geqslant 2 \times m_\mathrm{Z}$. The

Z bosons have a 10% probability to yield a pair of charged leptons. Thus, the decay chain $H \to ZZ^{(*)} \to l^+l^-l^+l^-$ (in short $H \to 4l$) offers a possibly significant and very clean and simple multi-lepton final state signature for the SM Higgs boson at the LHC. An example of an event candidate in the CMS detector for the Higgs boson decay channel $H \to ZZ^* \to 4e$ is shown in colour plate CP2.

Ultimately, the channel can provide a precision determination of the Higgs boson mass and production cross-section. The anti-correlation of the Z spin projections in the $H \to ZZ$ decay and the polarisation of each Z boson can be used to constrain, and eventually determine, the spin and CP quantum numbers of the Higgs resonance. Furthermore, the $ZZ^{(*)}$ and $WW^{(*)}$ decay modes are related via $SU(2)$ and the combination of channels could allow for cancellation of some systematic uncertainties in a determination of the Higgs coupling. But first and foremost is the necessity to be best prepared for a discovery at the LHC.

In this section, the discovery potential of the CMS experiment for the SM Higgs boson is discussed in the mass range of $120 \leqslant m_H \leqslant 300\,\mathrm{GeV/c^2}$, focusing on the $4e$ channel. The analysis [37] relies on a detailed simulation of the detector response in the experimental conditions of the first years of low luminosity LHC running. The signal and background Monte Carlo datasets used for this prospective are described in Section 2.2.1. The detailed High Level Trigger (HLT) and reconstruction algorithms used at each step of this analysis have been presented in [7]. Basic, and in part compulsory, triggering and pre-selection steps for data reduction are described in Section 2.2.2. Simple observables from the electron reconstruction are used to characterise the event signature for this pre-selection step. The final event selection relies on more involved requirements for primary electrons coupled with basic event kinematics and is presented in Section 2.2.3. The selection is optimised to preserve a best signal detection efficiency and highest significance for a discovery. Emphasis is put on realistic strategies for the control of experimental errors and the estimation of systematic uncertainties on physics background rates. These are described in Section 2.2.4. Results on the expected discovery reach of the SM Higgs boson in CMS in the $H \to 4e$ channel and for the measurement of its mass, width and cross-section are finally presented in Section 2.2.5.

2.2.1. Datasets for signal and background processes

Monte Carlo data samples for the signal from single SM Higgs boson production as well as for SM background from $ZZ^{(*)}$ pair production, $t\bar{t}$ pair production and $Zb\bar{b}$ associated production are used. The signal and background processes are generated for pp collisions at the LHC at a centre-of-mass energy $\sqrt{pp} = 14\,\mathrm{TeV}$, with pile-up conditions from multiple collisions as expected in a collider machine configuration providing an instantaneous luminosity of $2 \times 10^{33}\,\mathrm{cm^{-2}s^{-1}}$ (of $\mathcal{O}(10)\,\mathrm{fb^{-1}/year}$). All cross-sections are normalised within acceptance to Next to Leading Order (NLO) calculations. The event generators are interfaced with PHOTOS [38, 39] for the simulation of QED final state radiations. The non-perturbative parton density functions (PDFs) in the proton are taken to be the CTEQ6 distributions [12].

The Higgs boson is produced via either gluon fusion and weak boson fusion processes. The $4e$ signal samples are generated at various m_H with PYTHIA [24]. The Higgs boson is forced to decay into a Z boson pair. The Z bosons are subsequently forced to undergo a decay in electron-positron pair. The signal is normalised to the value of total cross-section at NLO calculated including all Higgs boson production processes via HIGLU [40], with branching ratios $BR(H \to ZZ^{(*)})$ calculated via HDECAY [41].

In the $4e$ channel (and similarly for the 4μ channel), an additional enhancement of the signal is considered which is due to the constructive final state interference between like-sign electrons originating from different $Z^{(*)}$ bosons [42]. This enhancement has been

Table 2.10. Total cross-sections at NLO (pb), cross-section in the $4e$ channel within acceptance (fb), and number of accepted events in data samples available for analysis.

m_{H} (GeV/c^2)	σ_{NLO} (pb)	$\sigma_{NLO} \times BR \times Acc.$ (fb)	$N_{simul.}$
115	47.73	0.27	10000
120	44.30	0.48	10000
130	38.44	1.11	10000
140	33.69	1.78	10000
150	29.81	1.94	10000
160	26.56	0.92	10000
170	23.89	0.43	10000
180	21.59	0.98	10000
190	19.67	3.58	10000
200	17.96	3.94	10000
250	12.37	3.07	10000
300	9.58	2.60	10000
$ZZ^{(*)}$	29.0	20.2	150 000
$Zb\bar{b}$	276.3	120.4	87 000
$t\bar{t}$	840	194.0	500 000

re-evaluated with CompHEP [43] and amounts to a factor 1.130 ± 0.006 at $m_{\mathrm{H}} = 115\,\mathrm{GeV/c^2}$, slowly decreasing to a negligible value when approaching $m_{\mathrm{H}} \approx 2m_{\mathrm{Z}}$.

The $ZZ^{(*)}$ SM background continuum is generated using PYTHIA [24]. This includes only the t-channel contribution with $q\bar{q}$ in the initial state. The missing s-channel might contribute up to 10% for low Higgs boson masses and can be neglected for higher masses. The differential cross-section is re-weighted using m_{4e} dependent NLO K-factors obtained with MCFM 4.1, with an average K-factor of $\langle K_{NLO} \rangle = 1.35$. Both Z bosons are constrained within the mass range 5–150 GeV/c^2 and are forced to decay into charged lepton pairs, with the τ leptons subsequently forced to undergo leptonic decays via $\tau \to \mu\nu$ or $\tau \to e\nu$. The missing gg contribution is estimated to be of order 20% at LO [42], with $\pm 8\%$ uncertainties and with unknown NLO K-factors. Recent calculations with TopReX [44] of the gluon fusion production process of two real Z confirm the above assumptions, and this contribution has been shown to remain stable after kinematic cuts for a $\mathrm{H} \to 4l$ analysis. The cross-section here is simply increased by the mean expected contribution.

The $t\bar{t}$ background sample is also generated with PYTHIA [24], with W bosons and τ leptons forced to leptonic decays, but with b quarks left to decay freely. Both gluon fusion and quark annihilation initial states are simulated and the cross-section is normalised to the NLO value of $840 \pm 5\%(\mathrm{scale}) \pm 3\%(\mathrm{PDF})$ pb [45].

The $Zb\bar{b}$ background is generated using all lowest order $gg \to e^+e^-b\bar{b}$ and $qq' \to e^+e^-b\bar{b}$ diagrams (excluding diagrams involving the SM Higgs boson) calculated with CompHEP [43] and interfaced with PYTHIA [24] for showering and hadronisation. All possible combinations of quarks are considered in the initial state. The total LO cross-section for $m_{ee} > 5\,\mathrm{GeV/c^2}$ is 115 pb of which about 89% originates from gg processes, 7.7% involve u-like quarks and 3.2% involve d-like quarks in the initial state. The hadronisation and decay of the b quarks are left free. A NLO K-factor of 2.4 ± 0.3 is applied. Signal and background events are filtered at generator level for further analysis if satisfying the following acceptance requirements: $\geqslant 2e^+$ and $\geqslant 2e^-$ with $p_{\mathrm{T}}^e > 5\,\mathrm{GeV/c}$ in $|\eta| < 2.7$. In addition for the $Zb\bar{b}$ background, at least two e^+e^- pairs with invariant mass in the range 5–400 GeV/c^2 are required. In Table 2.10 cross-sections at NLO and after pre-selection, as well as number of events in data samples available for analysis after pre-selection are given.

Detailed simulation of the CMS detector is performed using the official CMS simulation OSCAR. Reconstruction of physics objects is performed in ORCA.

2.2.2. Data reduction

The events of interest for the Higgs boson search in the $H \to 4e$ channel must satisfy a minimal set of requirements.

A first and compulsory condition for the events is to satisfy the CMS Level 1 (hardware) trigger conditions and the filtering of the (software) HLT. This triggering step is described in Section 2.2.2.1. The basic electron triggers are expected to be saturated by SM processes such as the single Z and W production. Further filtering is obtained with a minimal set of additional electron requirements as described in Section 2.2.2.2.

The pre-selection must preserve the signal acceptance, and especially the electron reconstruction efficiency, until later stages where the analysis can best profit from more involved algorithms applied to reduced event samples.

2.2.2.1. Triggering. The events must have satisfied the *single e*, *double e* or *double relaxed e* requirements at L1/HLT level. The *single e* trigger requires one isolated (charged) "electromagnetic" object with a threshold set at a reconstructed transverse energy in the electromagnetic calorimeter (ECAL) of $E_T = 26\,\text{GeV}$. The *double e* trigger requires two isolated (charged) "electromagnetic" objects, each above a threshold of $E_T = 14.5\,\text{GeV}$. In contrast, the *double relaxed e* trigger does not imposed isolation for the (charged) "electromagnetic" objects and the increased rate is compensated by a higher threshold of $E_T = 21.8\,\text{GeV}$.

The trigger efficiency for the Higgs boson signal, normalised to the cross-section within acceptance as defined in Section 2.2.1, is above 95% for masses $m_H > 130\,\text{GeV/c}^2$.

2.2.2.2. Pre-selection of four electron candidates. Following the Level-1 and HLT filtering steps, the event candidates must further satisfy basic electron pre-selection requirements. These requirements are designed to reduce possible background sources involving "fake" electron contamination from QCD jets.

For Higgs bosons with a mass m_H below $300\,\text{GeV/c}^2$, the $4e$ final state always involves at least one (or few) low p_T^e electron(s). In the range of m_H values below the Z pair production threshold, where the Z and Z* bosons themselves receive in general only small transverse momentum, the mean p_T^e of the softest electron falls in a range where a full combination of tracking and calorimetry information becomes important. The p_T^e spectra for signal events at $m_H = 150\,\text{GeV/c}^2$ is shown in Fig. 2.11a. The softest electron, which generally couples to the off-shell $Z^{(*)}$, has a most probable p_T^e value below $10\,\text{GeV/c}$ for masses $m_H \lesssim 140\,\text{GeV/c}^2$. Hence, an excellent electron reconstruction is essential down to very low p_T^e values, well below the range of $p_T^e \simeq 40$–$45\,\text{GeV/c}$ for which the reconstruction will be best constrained in CMS via measurements with SM single Z and single W production. The control of systematic uncertainties from experimental data is a major issue for such low p_T^e electrons and this will be discussed in detail in Section 2.2.4.

This analysis makes use of the elaborate reconstruction procedures which have been introduced very recently in CMS and have been described in detail in Ref. [46]. The electron identification and momentum measurements are somewhat distorted by the amount of tracker material which is distributed in front of the ECAL, and by the presence of a strong magnetic field aligned with the collider beam z axis. The procedures introduced in Ref. [46] provide new useful observables that allow to better deal with these detector effects, combining information from the pixel detector, the silicon strip tracker and the ECAL.

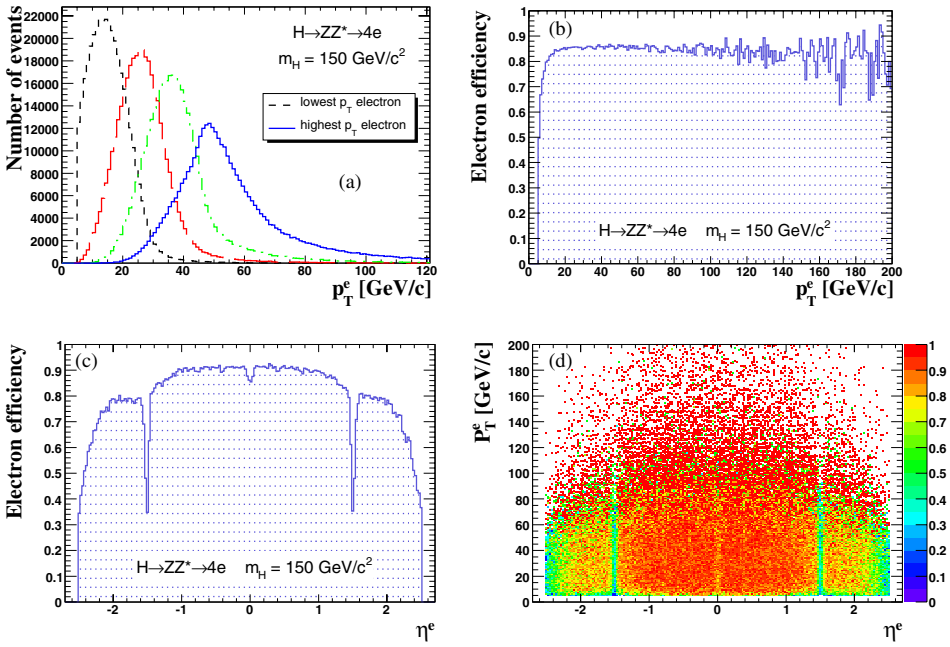

Figure 2.11. Electrons in SM Higgs boson $4e$ decay channel for $m_{\mathrm{H}} = 150\,\mathrm{GeV/c^2}$: (a) transverse momentum of each of the four final state electrons; (b) efficiency at pre-selection as a function of p_{T}^{e}; (c) efficiency at pre-selection as a function of η_e; (d) efficiency in the p_{T}^{e} versus η_e plane.

The pre-selection of the signal event candidates relies on the presence of at least 2 e^+ and 2 e^- candidates within the acceptance $|\eta| < 2.5$ and each with $p_{\mathrm{T}} > 5\,\mathrm{GeV/c}$, verifying the following characteristics:

- $E_{\mathrm{sc}}/p_{\mathrm{in}} < 3$, where E_{sc} is the supercluster energy and p_{in} the track momentum at the interaction vertex;
- $|\Delta\phi_{\mathrm{in}}| = |\phi_{\mathrm{sc}} - \phi_{\mathrm{in}}^{\mathrm{extrap}}| < 0.1$, where ϕ_{sc} is the energy weighted ϕ position of the supercluster and $\phi_{\mathrm{in}}^{\mathrm{extrap}}$ is the ϕ of the track at vertex, extrapolated to the ECAL assuming a perfect helix;
- $|\Delta\eta_{\mathrm{in}}| = |\eta_{\mathrm{sc}} - \eta_{\mathrm{in}}^{\mathrm{extrap}}| < 0.02$, with notations as above;
- $H/E < 0.2$, where H is the energy deposited in the HCAL tower just behind the electromagnetic seed cluster and E the energy of the electromagnetic seed cluster;
- $\sum_{cone} p_{\mathrm{T}}^{\mathrm{tracks}}/p_{\mathrm{T}}^{e} < 0.5$, a loose track isolation requirement, whose calculation will be described in Section 2.2.3.1.

The electron pre-selection efficiency is shown in Fig. 2.11b and Fig. 2.11c as a function of p_{T}^{e} and η^{e} for the electrons from Higgs boson events at $m_{\mathrm{H}} = 150\,\mathrm{GeV/c^2}$. The efficiency steeply rises and reaches a plateau around 86% for $p_{\mathrm{T}}^{e} \gtrsim 20\,\mathrm{GeV/c}$. The efficiency is above 90% for $|\eta| \lesssim 1.1$ and decreases towards the edge of the tracker acceptance when approaching $|\eta| \simeq 2.5$. The pre-selection efficiency for electrons from the same sample is represented in Fig. 2.11d as a two-dimensional map in the p_{T} versus η plane.

The absolute efficiencies for the Higgs boson signal at different m_{H} values and for the backgrounds are shown in Fig. 2.12a after triggering and the multi-electron pre-selection step. The acceptance for the Higgs boson signal is maintained above 50% in the full relevant mass range.

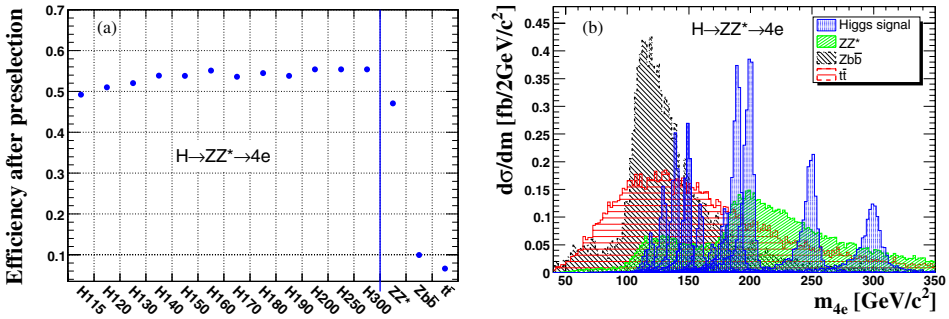

Figure 2.12. Higgs boson signal and dominant background sources after pre-selection step: (a) overall pre-selection efficiency for m_{H} in the range from 115 to 300 GeV/c^2 and the background from ZZ$^{(*)}$ continuum, from Zb$\bar{\mathrm{b}}$ and t$\bar{\mathrm{t}}$; (b) separate signal and background contributions to the spectrum of reconstructed invariant mass m_{4e}.

The signal and background events fulfilling the triggering and pre-selection steps are represented in the reconstructed invariant mass m_{4e} spectrum in Fig. 2.12b. The Higgs boson signal is seen to emerge above the background for masses around 150 GeV/c^2 and above $\simeq 2m_{\mathrm{Z}}$. More background suppression is required elsewhere.

2.2.3. Event selection and kinematic reconstruction

The further steps of the event selection rely on a more detailed characterisation of the electron candidates and simple kinematic expectations. The electrons from the Higgs boson, in contrast to at least one e^+e^- pair from the t$\bar{\mathrm{t}}$ and Zb$\bar{\mathrm{b}}$ backgrounds, are isolated and originate from a common primary vertex. The corresponding analysis requirements are discussed in Section 2.2.3.1. Profiting from the expectation of a narrow resonance in the m_{4e} spectrum, and of the likely presence of a real Z boson in the final state, the kinematics and its simple evolution with m_{H} can be further exploited. The electrons of the e^+e^- pair at lowest m_{ee} have on average a much harder p_{T}^e spectrum for the Higgs boson signal than for the $t\bar{t}$ and $t\bar{t}$ backgrounds. Moreover, the combination of the Z and Z$^{(*)}$ mass spectra distinguishes the Higgs boson signal from the ZZ$^{(*)}$ SM background continuum. These kinematic requirements are discussed in Section 2.2.3.2.

2.2.3.1. Isolated primary electrons. A loose vertex constraint is first imposed on the longitudinal impact parameter for the four electron candidates in each event. All electrons should verify $IP_L/\sigma_L < 13$, where σ_L is the error on the longitudinal impact parameter IP_L. The main vertex constraint is imposed on the transverse impact parameter of the electrons to suppress secondary vertices. Secondary electrons appear for instance in semi-leptonic decays in the hadronisation of the b quark jets in $Zb\bar{b}$ and $t\bar{t}$ background events. The sum of the transverse impact parameter significance ($IP_{\mathrm{T}}/\sigma_{\mathrm{T}}$), i.e. the ratio of the transverse impact parameter IP_{T} over its error σ_{T}, is shown in Fig. 2.13a (Fig. 2.13b) for the e^+e^- pair with invariant mass m_{ee} closest (next-to-closest) to the nominal Z boson mass m_{Z}. For both of these background sources, the displaced vertices are most likely to appear in the softest pair of reconstructed electrons. A best rejection power is obtained by imposing $\sum IP_{\mathrm{T}}/\sigma_{\mathrm{T}} < 30$ for the pair with $m_{ee} \simeq m_{\mathrm{Z}}$ and a more stringent cut of $\sum IP_{\mathrm{T}}/\sigma_{\mathrm{T}} < 15$ for the other pair.

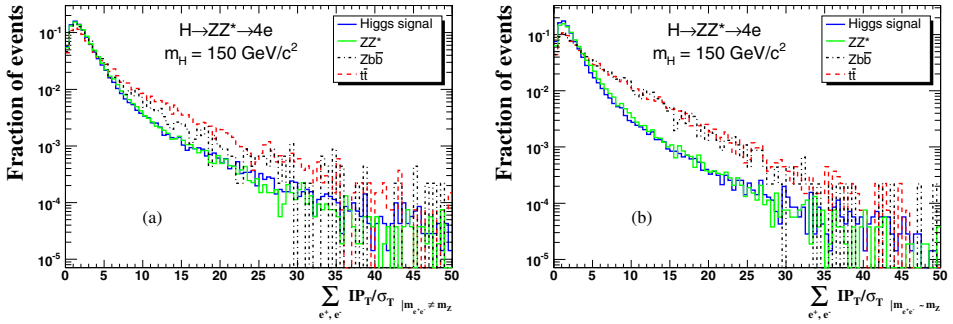

Figure 2.13. Sum of the transverse impact parameter significance (IP_T/σ_T) of e^+e^- pairs for a Higgs boson at $m_H = 150\,\mathrm{GeV/c^2}$, for the $ZZ^{(*)}$ continuum, and for Zbb and $t\bar{t}$: (a) $\sum IP_T/\sigma_T$ from the electrons of the e^+e^- pair with a reconstructed mass m_{ee} best matching the Z boson mass; (b) $\sum IP_T/\sigma_T$ from the second e^+e^- pair.

Another powerful discriminant against secondary electrons in b jets or in general against fake electrons in QCD jets, is provided by isolation requirements. The electrons coupled to the Z or $Z^{(*)}$ in the $H \to 4e$ channel are expected to be on average well isolated from hadronic activity. Hadronic activity in single Higgs boson production appears in NLO processes, in the recoil against the Higgs boson. The Higgs boson itself generally receives a significant longitudinal boost in the laboratory reference frame but, as a scalar, decays uniformly in its centre-of-mass reference frame. In contrast, the electrons in the b jets from $t\bar{t}$ or $Zb\bar{b}$ are accompanied by significant hadronic activity.

Two partly complementary observables can be best used for the isolation of low p_T^e electrons. These rely either on measurements of primary tracks or on the energy flow in the hadronic calorimeter (HCAL). Both observables are insensitive to the eventual electron-induced electromagnetic showering in the tracker material. For the "track isolation", an isolation cone of size $\Delta R = \sqrt{\Delta\eta^2 + \Delta\phi^2} = 0.2$ is defined around the electron direction, and tracks with $p_T > 1.5\,\mathrm{GeV/c}$ originating from the same primary vertex within $|\Delta IP_L| < 0.1$ cm are considered. To avoid suppressing signal events, tracks attached to an electron candidate of opposite charge, and giving $m_{e^+e^-} > 10\,\mathrm{GeV/c^2}$, are discarded. All the 4 electrons from the Higgs boson candidate events must satisfy $\sum_{cone} p_T^{\mathrm{tracks}}/p_T^e < 0.1$. Distributions of this track isolation observable are shown in Fig. 2.14a. For the "hadronic isolation", all HCAL towers in an isolation cone size as above, and contributing with $E_T > 0.5\,\mathrm{GeV}$ are considered in the ratio $\sum_{cone} E_T^{HCAL}/p_T^e$. This ratio is required to be below 0.05 for at least three electrons. The cut is relaxed to 0.2 for the fourth electron. Distributions of this hadronic isolation observable are shown in Fig. 2.14b.

Further electron identification requirements must be imposed to suppress the possible background, involving "fake" electrons, from Drell–Yan processes at NLO where a $Z^{(*)}$ recoils against jet(s). Different electron identification cuts are used depending on the distinct classes of track-supercluster electron patterns [46] in order to preserve the electron detection efficiency at all η^e. More details can be found in Ref. [37]. This tightening of the electron identification entails an absolute efficiency loss for the Higgs boson signal below 5%.

2.2.3.2. Kinematics. The cascade $H \to ZZ^{(*)} \to 4e$ for a Higgs boson, mostly produced at small transverse momentum, leads to very distinctly ordered p_T^e spectra for the four final state electrons. Moreover, the p_T^e spectra of the softest electrons for the Higgs boson signal is on average harder than the one expected from secondary electrons from the $Zb\bar{b}$ or $t\bar{t}$ backgrounds. Thus, it is advantageous to profit from the knowledge of the expected p_T^e

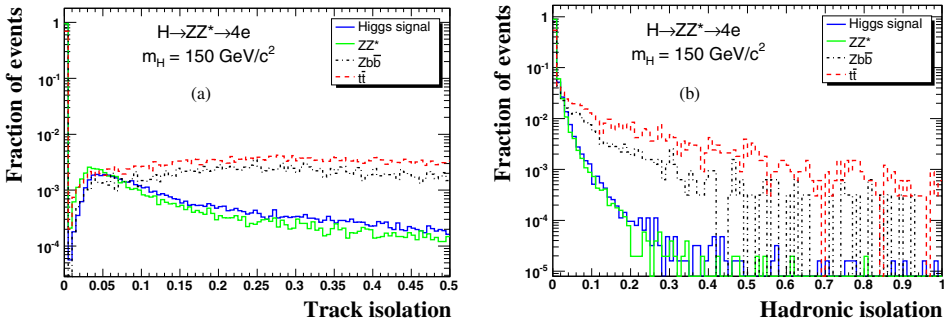

Figure 2.14. Electron isolation observables for the signal at $m_{\mathrm{H}} = 150\,\mathrm{GeV/c^2}$ and the SM backgrounds: (a) track isolation, $\sum_{cone} p_{\mathrm{T}}^{\mathrm{tracks}}/p_{\mathrm{T}}^{e}$; (b) hadronic isolation, $\sum_{cone} E_{\mathrm{T}}^{HCAL}/p_{\mathrm{T}}^{e}$, for the second least isolated electrons.

Table 2.11. Electron p_{T} cuts, from the lowest to the highest p_{T} electron and reconstructed Z_1 and Z_2 invariant mass cuts.

m_{H} ($\mathrm{GeV/c^2}$)	p_{T}^{1}	p_{T}^{2}	p_{T}^{3}	p_{T}^{4}	$m_{\mathrm{Z}_1}^{min}$	$m_{\mathrm{Z}_1}^{max}$	$m_{\mathrm{Z}_2}^{min}$	$m_{\mathrm{Z}_2}^{max}$
	($\mathrm{GeV/c}$)				($\mathrm{GeV/c^2}$)			
115	7	10	10	15	51	101	10	50
120	7	12	15	15	51	101	10	50
130	7	12	15	15	61	101	10	60
140	7	12	15	15	71	101	10	65
150	7	12	15	15	71	101	15	65
160	7	15	15	15	71	101	15	70
170	7	15	15	20	81	101	20	80
180	7	15	15	20	81	101	30	90
190	7	15	20	30	81	101	40	100
200	7	15	25	30	81	101	40	110
250	7	20	40	50	51	131	20	200
300	7	30	40	60	51	131	15	300

distributions for the Higgs boson signal. A best set of p_{T}^{e} cuts as a function of m_{H} is given in Table 2.11.

The cut on the softest electron is maintained to a lowest value for simplicity and to preserve the signal efficiency at low m_{H}. Otherwise the p_{T}^{e} cuts are seen to slowly evolve for as long as $m_{\mathrm{H}} < 2m_{\mathrm{Z}}$ and then rise faster above the Z pair production threshold. The p_{T}^{e} cuts lead for example [37] to a reduction by a factor of 5 to 10 of the $\mathrm{Zb\bar{b}}$ background, and a factor of 3 to 5 of the $\mathrm{t\bar{t}}$ background for $m_{4e} < 2m_{\mathrm{Z}}$. Both backgrounds are also heavily suppressed above $2m_{\mathrm{Z}}$.

Labelling Z_1 the boson reconstructed with an m_{ee} closest to the nominal Z mass and Z_2 the one reconstructed from the second e^+e^- pair, one expects for $m_{4e} < 2m_{\mathrm{Z}}$ in the case of the Higgs boson signal that $m_{4e} \simeq m_{\mathrm{Z}_1} + m_{\mathrm{Z}_2}$ with most often the presence of a Z boson on its mass shell, $m_{\mathrm{Z}_1} \simeq m_{\mathrm{Z}}$. The Z boson masses saturate the phase space and are dominantly produced with small velocity in the Higgs boson rest frame. The requirement of one real Z boson suppresses further the $\mathrm{t\bar{t}}$ backgrounds for low m_{4e}. The cut on Z_2 is powerful against the $\mathrm{ZZ}^{(*)}$ continuum and further suppresses the $\mathrm{Zb\bar{b}}$ and $\mathrm{t\bar{t}}$ backgrounds. A set of optimal Z_1 and Z_2 cuts is given in Table 2.11 as a function of m_{H}. The cuts lead for example [37]

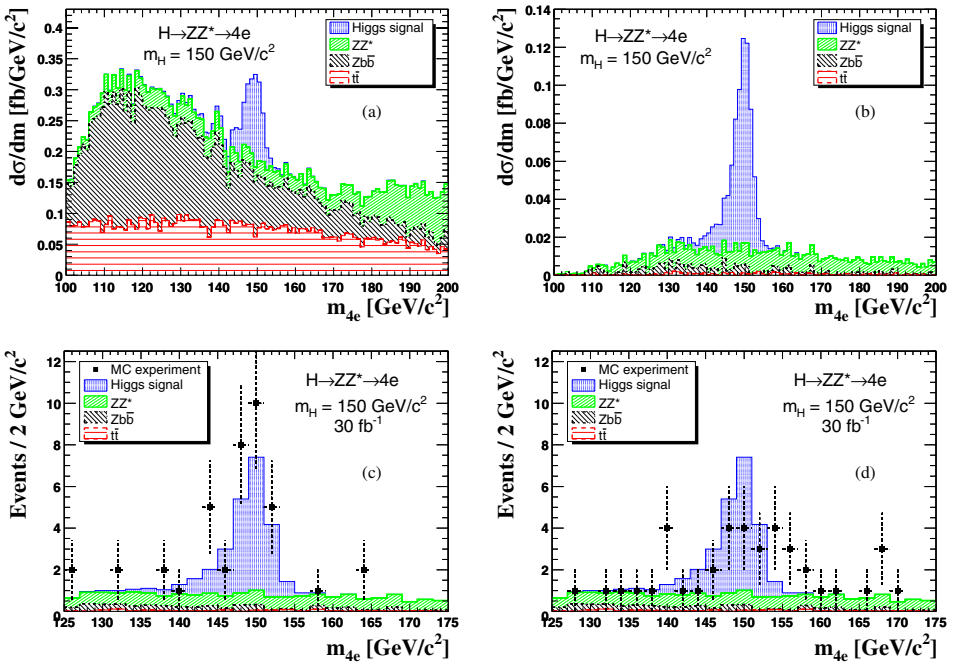

Figure 2.15. Distributions of the reconstructed invariant mass m_{4e} for the SM Higgs bosons signal at $m_{\mathrm{H}} = 150\,\mathrm{GeV/c^2}$ and for the SM backgrounds after (a) pre-selection step and (b) after all cuts. The number of events are normalised in cross-section. Single Monte Carlo experiments corresponding to an integrated luminosity of $30\,\mathrm{fb}^{-1}$ for (c) a favourable case and (d) a less favourable case.

for $m_{4e} \simeq 150\,\mathrm{GeV/c^2}$ to a reduction of the $\mathrm{ZZ}^{(*)}$ continuum by a factor of about 6.5 and a reduction of the $\mathrm{t\bar{t}}$ background by a factor of about 2.5.

Figure 2.15a shows as an illustration the expected m_{4e} invariant mass distributions for the signal at $m_{\mathrm{H}} = 150\,\mathrm{GeV/c^2}$ and for backgrounds after triggering and pre-selection. The further background suppression from the isolated primary electron requirement, the p_{T}^{e} and Z mass cuts is seen by comparison in Fig. 2.15b. The global selection efficiency (normalised to the acceptance defined at the generation level) is given in Table 2.12 for the signal and backgrounds. Figures 2.15c and 2.15d show for illustration the possible outcome of two random Monte Carlo experiments corresponding to favourable and less favourable fluctuations of the Higgs boson signal for an integrated luminosity of $30\,\mathrm{fb}^{-1}$. The Poissonian probability to have equal or more favourable (respectively equal or less favourable) fluctuations is of about 5% for the example cases shown.

2.2.4. Systematics

In this section the systematic errors are discussed in the context of a discovery via a simple event counting method. The "theoretical" and "experimental" sources of errors are distinguished. The theoretical uncertainties concern the estimation of the background rates within the cuts defining the acceptance of the Higgs boson signal and are discussed in Section 2.2.4.1. The experimental uncertainties take into account the limited knowledge of

Table 2.12. Summary of selection efficiencies normalised to the generation pre-selection efficiency.

m_H	115	120	130	140	150	160	170	180	190	200	250	300
						(GeV/c^2)						
Signal	24.3	26.0	31.2	35.2	36.0	37.4	38.0	39.9	40.9	42.5	41.2	38.6
$ZZ^{(*)}$	5.24	4.94	5.68	5.95	5.14	5.23	6.87	17.8	25.1	26.2	22.3	13.9
$Zb\bar{b}$	0.22	0.16	0.17	0.17	0.16	0.10	0.097	0.068	0.037	0.031	0.013	0.001
$t\bar{t}$	0.054	0.044	0.043	0.033	0.032	0.022	0.021	0.011	0.008	0.008	0.013	0.006

the detector responses and efficiencies, and of the corresponding Monte Carlo modelling. These are discussed in Section 2.2.4.2. A comparison of different methods for the control of background systematics is presented in Section 2.2.4.3.

2.2.4.1. Theoretical errors. The theoretical uncertainty on the number of background events in the signal region from PDFs and QCD scales variations has been estimated by the MCFM program [47]. CTEQ6M PDF are used and 20 eigenvector parameters have been varied by $\pm 1\sigma$. Both QCD normalisation and factorisation scales have been varied independently up and down for a factor two from their nominal values of $2m_Z$. The resulting uncertainties from PDF and QCD scale are of the order of 6% for direct estimation of ZZ background, from 2 to 8% for normalisation to single $Z \to 2e$, and from 0.5 to 4% for the normalisation to sidebands (discussed further in Section 2.2.4.3). The gluon fusion cross-section uncertainties in the ZZ background of 8% is also considered as a part of theoretical uncertainties.

The uncertainty on the normalisation of the measurements to the pp luminosity of the LHC collider is estimated to be of the order of 3% for an integrated luminosity above 10 fb^{-1}.

2.2.4.2. Experimental errors. The main remaining sources of experimental systematics expected in the CMS experiment after having collected of $\mathcal{O}(10)$ fb^{-1}, and relevant for the $H \to 4e$ channel, originate from uncertainties on knowledge of the amount of tracker material in front of the ECAL, from the precision of the (pattern dependent) energy calibration of electron objects, and from the control of electron efficiencies. The strategy adopted consists of relying on experimental data, and in particular on single Z and W production, to minimise these systematic errors. The electrons from $W \to e\nu$ and $Z \to ee$ decays are used to control the energy measurements and reconstruction efficiencies.

A change of the integral amount of tracker material traversed by electrons before reaching the ECAL is susceptible of affecting the electron selection and identification efficiencies, as well as energy measurement scales and resolution. The uncertainty on the material budget will limit the precision of the acceptance calculations, when using the Monte Carlo model to extrapolate away from the kinematic domain best constrained via single Z and W measurements.

There are many observables that are directly or indirectly sensitive to the amount of tracker material, and that have been used in collider experiments. Examples are the distribution of converted photon vertices, or the shape of the E/p comparing tracker momentum measurement p to the energy E measured in the calorimeter in finite cluster volume, or a comparison of data and Monte Carlo for the Z mass resolution, etc. A new technique is used which is based on the electron GSF tracking introduced recently in Ref. [46]. The difference between the momentum magnitude at vertex and at the last hit, $p_{in} - p_{out}$, is a measure of the integral amount of bremsstrahlung. The mean fraction f_{brem} of the energy radiated along the complete trajectory is roughly proportional to the integral amount

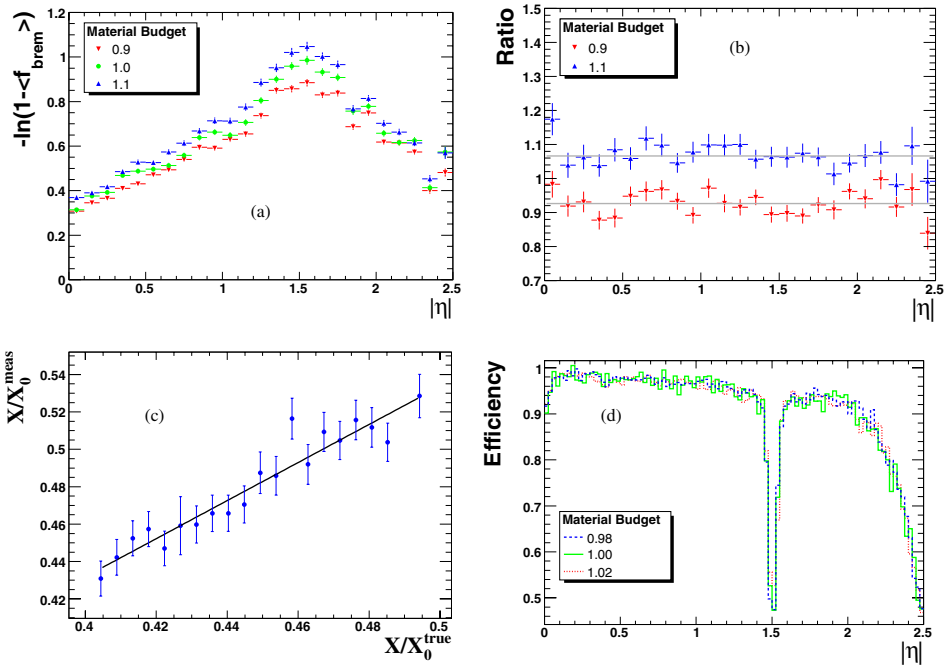

Figure 2.16. Sensitivity to variations of the tracker material budget from electron measurements based on GSF tracks: (a) measured amount of material as a function of $|\eta|$ for the nominal tracker configuration and for an integral material budget changed by $\pm 10\%$; (b) ratio of the measured mount of material as a function of $|\eta|$; (c) measured versus true thickness in X_0 of the tracker material; (d) effect of a change of 2% of the material budget on the electron reconstruction efficiency.

of material traversed. Hence, one can relate f_{brem} to the material thickness X/X_0 where X_0 is the characteristic radiation length via the formula $\langle X \rangle / X_0 \simeq -\ln(1 - f_{\text{brem}})$, where $f_{\text{brem}} = (p_{\text{in}} - p_{\text{out}})/p_{\text{in}}$.

The amount of tracker material measured in this way for single electron data is shown in Fig. 2.16a. The results obtained in the configuration corresponding to the nominal tracker material coincide very well with the known material distribution as given in Ref. [7]. Figure 2.16b shows the ratio of the measured material thickness obtained in configurations where the amount of material was changed by $\pm 10\%$, normalised to the measurement results in the nominal case. The ratio is found to be remarkably stable as a function of η, despite the fact that the integral amount of material has a strong η dependence. Thus, single electrons can be used in CMS to tune the Monte Carlo model of the tracker material per η slice. Figure 2.16c shows that in a given η slice the measured material thickness is linearly correlated to a change (at least within a range of $\pm 10\%$) of the true material thickness. Similar results are obtained when considering various restricted range of p_{T}^e within a sample of uniformly distributed electrons in the p_{T}^e range from 5 to 100 GeV/c. With the electron statistics expected from single Z production for an integrated LHC luminosity of $\mathcal{O}(10)$ fb^{-1}, it should be possible to determine the tracker material thickness to a precision better than 2% over the full acceptance in η. Figure 2.16d shows that such a 2% uncertainty on the material budget will have almost no effect on electron reconstruction efficiency.

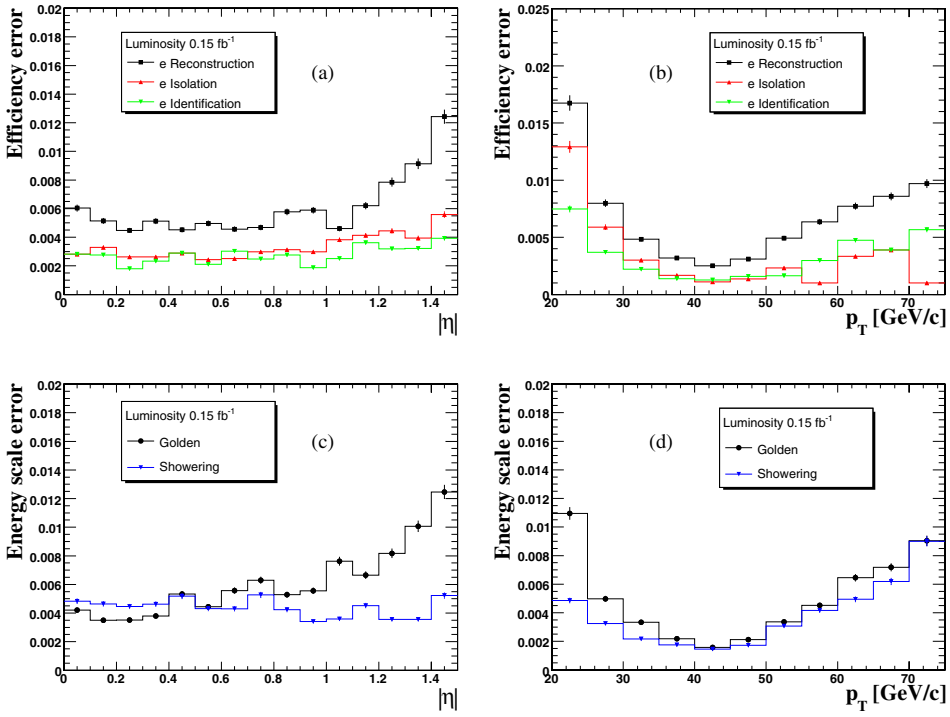

Figure 2.17. Control of experimental uncertainties using SM data; uncertainties on measurements of electron reconstruction, isolation and identification as a function of (a) η and (b) p_{T}; uncertainties on measuring the energy scale for golden and showering electrons as a function of (c) η and (d) p_{T}.

Electron reconstruction efficiencies and energy scales will be controlled by electrons from $\mathrm{W} \to e\nu$ and $\mathrm{Z} \to ee$ decay. Huge cross-sections of these two processes will allow for a significant reduction of reconstruction uncertainties already after few fb^{-1}. Electrons from $\mathrm{Z} \to ee$ are produced centrally with a characteristic Jacobian p_{T} distributions around $45\,\mathrm{GeV/c}$. It is therefore, expected that the best control of experimental systematics is obtained in the central part of the detector and for electrons around the Jacobian peak.

Electron reconstruction uncertainties as a function of η and p_{T} are given in Fig. 2.17a and Fig. 2.17b respectively, for an integrated luminosity of $0.15\,\mathrm{fb}^{-1}$. The expected behaviour of increased uncertainties when moving away from the Jacobian peak or from the central η region can be clearly seen. From the expected reconstruction errors evolution with the luminosity, all reconstruction efficiency uncertainties can be safely absorbed in a single factor of 1% per electron, for integrated luminosities larger than $10\,\mathrm{fb}^{-1}$.

The second important systematic effect is the uncertainty on the energy scale determination. Using single Z production, it has been shown in Ref. [48] that the absolute energy scale for electrons can in principle be controlled with great precision with average uncertainties reaching values below 0.1%. The systematic uncertainty has to be studied as a function of p_{T}^{e} and η^{e} given the different electron spectrum in $\mathrm{H} \to \mathrm{ZZ}^{(*)} \to 4e$ and $\mathrm{Z} \to ee$ decays. The reachable precision depends on the amount of integrated LHC luminosity. In this analysis, the second leg of a Z boson decay, tagged as an electron by imposing stringent

electron identification requirements on the first leg combined with a kinematic constraint to the Z boson mass, is used as a probe to estimate systematics on the energy scale.

Uncertainties versus η and p_T for golden and showering electrons are shown in Fig. 2.17c and Fig. 2.17d, for the integrated luminosity of $0.15\,\text{fb}^{-1}$. With expected evolution of these uncertainties with the luminosity, it is found that an uncertainty in energy scale of 0.5% in the barrel region, and 1% in the endcaps, for integrated luminosities larger than $10\,\text{fb}^{-1}$, can be safely considered.

2.2.4.3. Control of background rates. Following the primary and isolated electron selection and the application of basic kinematic requirements, only the $ZZ^{(*)}$ continuum remains as the dominant or sole background over the full mass range in consideration for the SM Higgs boson search. Thus, the determination of the mean expected number of SM $ZZ^{(*)}$ background events in the signal region, defined e.g. by a simple sliding window in the m_{4e} spectrum, remains as a key issue.

The three main methods for the estimation of $ZZ^{(*)}$ continuum contribution to the background in the signal region are:

- direct simulation of the $ZZ^{(*)} \to 4e$ process,
- normalisation to the $Z \to 2e$ data,
- normalisation to the sidebands.

The first method entirely relies on existing SM constraints and the theoretical knowledge, with uncertainties coming from the PDFs used to describe the colliding protons and from QCD scale variations. It furthermore is reliant on the LHC luminosity uncertainties, and on the Monte Carlo modelling of the acceptance and detector response for the uncertainties arising from electron reconstruction and selection. Otherwise, the method potentially benefits from the fact that the statistical precision on the mean background expectation is only limited by the Monte Carlo statistics, and can therefore be assumed negligible in the context of a prospective for an analysis to be performed in a future CMS experiment.

The second method aims at profiting from the fact that the SM single Z production cross-sections is measured with great precision in an experiment which will have integrated a luminosity of $\mathcal{O}(10)\,\text{fb}^{-1}$ at the LHC. Using the ratio of $ZZ \to 4e$ to $Z \to 2e$ rates allows to profit from a full cancellation of pp luminosity uncertainties, while providing a partial cancellation of PDF and QCD scale variations uncertainties (due to their correlations in a part of the initial state phase space) and a partial cancellation of experimental uncertainties.

In the method of the normalisation from sidebands, the number of background events *inside* the acceptance of the signal region is determined from the number of background events measured *outside* the signal region, by multiplying the latter with the ratio α_{MC} between *inside* and *outside* expectations as determined using Monte Carlo simulation. Using the sidebands one also expects to fully cancel luminosity uncertainties, to reduce PDF and QCD scale variation uncertainties and substantially reduce experimental uncertainties too. Statistical errors with sidebands normalisation come from the statistics of the background rate outside the signal region and can be a limiting factor for the method. By relaxing some of late analysis cuts, such as invariant Z mass, the background events rate outside the signal region increases, reducing therefore statistical errors for this method. The price to pay is an increased background rate in the signal region too and, therefore, some balancing is needed.

Using results from previous sections, both theoretical and experimental uncertainties are evaluated for two methods: normalisation to the $Z \to 2e$ measurements and normalisation to the sidebands. For the normalisation to single $Z \to 2e$ measurements results are shown in Fig. 2.18a. The overall systematic uncertainty with this method is of about 5%. Experimental

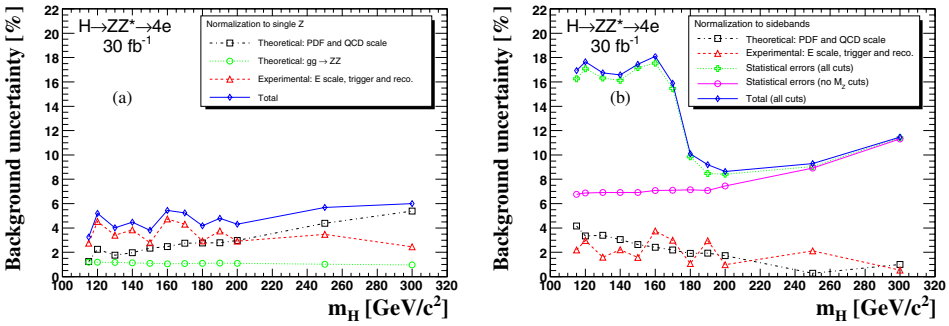

Figure 2.18. Theoretical and experimental uncertainty estimations for both methods for evaluation of background from data: (a) normalisation to the single $Z \to 2e$ measurements and (b) normalisation to the sidebands. Expected statistical errors for sidebands are also shown, for integrated luminosity of 30 fb^{-1}.

Table 2.13. Expected number of Higgs boson signal (N_S) and SM background (N_B) events for an integrated luminosity of 30 fb^{-1}, in the optimised window for the reconstructed invariant mass m_{4e}. The uncertainties (δN_B) are given for systematics from experimental (exp.) and theoretical (theo.) sources, for an analysis where the ZZ$^{(*)}$ continuum has been normalised to the measurement of single Z production.

m_H	115	120	130	140	150	160	170	180	190	200	250	300
						(GeV/c^2)						
N_S	1.52	2.97	8.18	15.80	17.19	8.38	3.76	9.95	34.05	38.20	27.68	21.69
N_B	2.26	1.94	3.71	4.31	3.68	3.10	3.37	6.42	14.62	17.29	13.40	7.63
δN_B												
exp.	0.063	0.089	0.126	0.167	0.105	0.148	0.145	0.187	0.551	0.505	0.466	0.187
theo.	0.039	0.049	0.079	0.098	0.095	0.084	0.100	0.191	0.440	0.549	0.602	0.417

uncertainties are seen to dominate for $m_H \simeq 2m_Z$ while theoretical errors take over above the pair production threshold. Uncertainties for the sidebands normalisation are shown in Fig. 2.18b. Statistical uncertainties scale as the square root of the number of background events outside the signal region and are shown for an integrated luminosity of 30 fb^{-1} and for two analysis scenarios: after all analysis cuts and without cuts on the mass of both Z bosons. A trade-off in the second method is in a somewhat lower nominal significance (for about 8%) while statistical errors decrease by a factor of about 2.5. Full significance calculations with and without systematics and statistical uncertainties are presented in the following section.

2.2.5. $H \to 4e$ Observability, mass and cross-section measurements

2.2.5.1. Discovery reach. A simple counting experiment is used here to quantify the sensitivity of the experiment to the presence of a Higgs boson signal. The expected number of signal (N_S) and background (N_B) events are evaluated in a sliding window whose central position m_{4e} varies between 100 and 320 GeV/c^2. The size of the optimal window increases progressively from 6 GeV/c^2 at $m_{4e} = 115$ GeV/c^2 to 24 GeV/c^2 at $m_{4e} = 300$ GeV/c^2. The Table 2.13 presents for each Higgs boson mass hypothesis the mean expected number of signal and background events, and associated uncertainties.

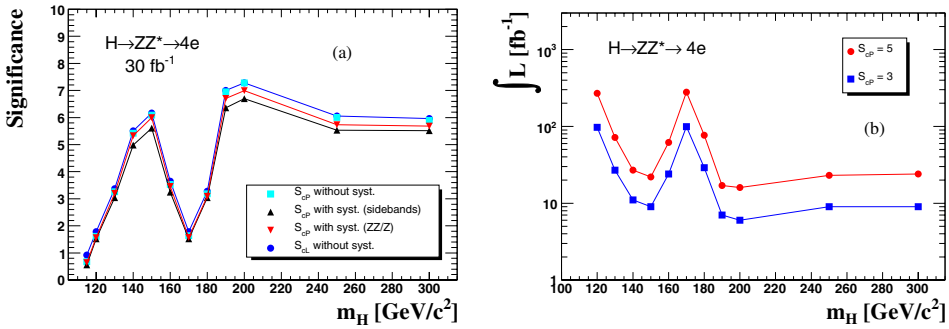

Figure 2.19. (a) Significance S_{cP} for an integrated luminosity of 30 fb^{-1} as a function of the Higgs boson mass without and with systematics included in both options of ZZ$^{(*)}$ normalisation to the measured sidebands or the measured single Z production cross-section. The significance S_{cL} is also shown. (b) Luminosity needed for a 3σ observation and 5σ discovery with the systematics included using ZZ$^{(*)}$ normalisation to the Z cross-section.

The significance of the H $\to$ 4e signal observation is shown as a function of m_{H} in Fig. 2.19a as expected for an integrated luminosity of 30 fb^{-1}. The results are given for both the S_{cP} and the S_{cL} significance estimators. The S_{cP} is defined as the probability for a Poisson distribution with mean N_B to observe a number of events equal or greater than $N_S + N_B$, converted in the equivalent number of standard deviations of a Gaussian distribution. The S_{cL} corresponds to the widely used log-likelihood ratio significance [49] and is given for comparison. The effect of including experimental and theoretical systematics, described in section 2.2.4 and listed in Table 2.13, on the significance S_{cP} [50] is also shown, for two different methods of controlling the background uncertainties. A signal observation with a significance above 3 standard deviations is expected in the H $\to$ 4e channel alone for m_{H} in the range from 130 to 160 GeV/c^2, and above 180 GeV/c^2. The integrated luminosity needed for a 5 standard deviations discovery of the SM Higgs boson in the H $\to$ 4e channel alone is also shown as a function of m_{H} in Fig. 2.19b. Systematic errors from normalisation to the Z cross-section have been included.

2.2.5.2. Mass, width and cross-section measurements. At an early stage of the Higgs boson search and discovery in the H $\to$ 4e channel, given very low statistics, a robust and simple estimation of m_{H} can be obtained by a simple mean (or weighted mean) of the m_{4e} values measured for individual events. The events falling in the pre-defined optimal mass window introduced in the above Section 2.2.5.1 and used to establish the signal significance, can be used for such purposes. For higher statistics, a fit of the m_{4e} mass distribution to a signal plus background shape can be used to extract simultaneously the mass and the cross-section $\times$ branching ratio of a Higgs boson signal. Detector effects dominate the Higgs boson mass resolution below the Z pair production threshold and a sensitivity to the Higgs boson intrinsic width is expected only for masses well above $2m_{\mathrm{Z}}$.

The precision on the parameter measurements for the Higgs boson depend on the quality of the reconstructed electrons and can, in general, be improved using event-by-event errors on the electron momentum estimation [46]. Example cases for two different sub-samples of Higgs boson events differing by the pattern of the four reconstructed electrons are presented in Fig. 2.20. Clearly, event candidates built from four *non-showering* electrons in the barrel part of the ECAL, a subset representing only about 1.76% of all signal events, allow for

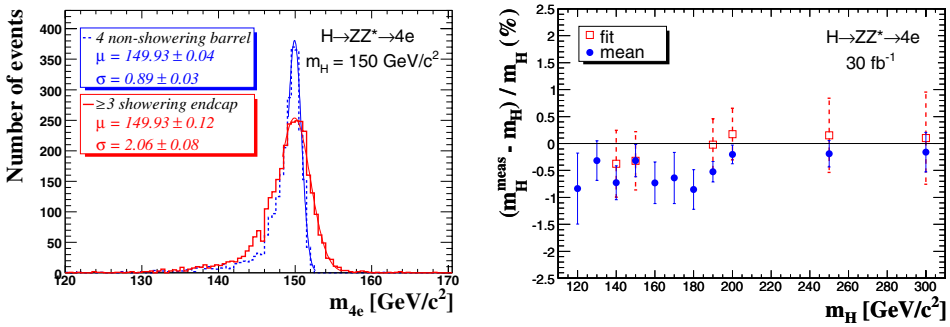

Figure 2.20. Mass measurements: (a) example case for two different event sub-samples differing by the pattern of the four reconstructed electrons; (b) relative errors as a function of the Higgs boson mass using the mean mass and the fitted mass as obtained for an integrated luminosity of 30 fb^{-1}.

a much better m_{H} measurement (smallest errors on average and least dispersion of the mass measurement errors) than candidates built mainly from e.g. *showering* electrons in the endcaps part of the ECAL. About 36.7% of the signal event candidates contain three or more *showering* electrons. A weighted mean of the events of the m_{4e} distribution falling in the signal window has been considered for the estimation of the Higgs boson mass in Ref. [37]. A simple mean can be also used for simplicity.

The reconstructed Higgs boson mass and its error obtained from the mean value for events falling in the expected signal window is presented in Fig. 2.20b. The error is obtained from the dispersion of the mean values obtained from large number of Monte Carlo experiments at an integrated luminosity of 30 fb^{-1}. The results are shown as a function of the Higgs boson mass. The systematic bias on the mass estimate for the low m_{H} cases for this simple mean approach is due to the asymmetric shape of the reconstructed signal and can be modelled. In the mass ranges where the Higgs boson signal significance exceeds 3 standard deviations, the uncertainty on the mass determination is found to be everywhere below 0.4%. It reaches values below 0.2% for $m_{\mathrm{H}} \simeq 200\,\mathrm{GeV/c^2}$. For comparison, results obtained by fitting the m_{4e} distribution are also shown. The fit method requires a significant number of events (typically $\gtrsim \mathcal{O}(10)$) to converge and provide reasonably stable results. The m_{4e} distribution is fitted by a signal plus background shape. The signal contribution is modelled with two Gaussians, describing respectively the core and the low m_{4e} tail of the signal distribution. The tail parameters (fraction, mean and dispersion) are fixed by fitting the "signal only" expectation. The background is modelled using a flat distribution up to about $m_{4e} \approx 2m_{\mathrm{Z}}$ and a linear function (non-zero slope) for higher Higgs boson masses. This has been found to provide a sufficiently good model of the observation in a restricted mass range around the signal region. A likelihood fit is then performed on each Monte Carlo experiments and the reconstructed mass and precision are extracted from the distribution of the fitted values of the peak of the Gaussian core. Where the fit can be performed, Fig. 2.20b shows that an unbiased estimation of m_{H} is obtained within errors.

The fitted number of signal events is used to estimate the production cross-section by correcting for the global acceptance efficiency. The statistical precision on this measurement is here also obtained from the width of the distribution of the fitted parameters in Monte Carlo experiments. An unbiased measurement of the cross-section is obtained over the full mass range considered here, with a precision of the cross-section measurement between

20 and 30%. With such a precision, the influence of the detector systematics (about 5%) and of the uncertainty on the luminosity measurement (less than 3% for 30 fb^{-1}) is marginal. For an integrated luminosity of 60 fb^{-1}, the precision on the cross-section measurement improves to about 15%.

A measurement of the width is possible only for Higgs boson masses above $\gtrsim 2m_Z$ where at the same time the Higgs natural width is becoming large and the detector resolution is improving. A Gaussian width with central values of about 2.3 GeV/c^2 for $m_H = 200\,GeV/c^2$ and 4.2 GeV/c^2 for $m_H = 300\,GeV/c^2$ is obtained from the fit, but with a rather large uncertainty of about 50%.

Chapter 3. Physics Studies with Muons

3.1. Benchmark Channel: $H \to ZZ^{(*)} \to 4$ muons

The $H \to ZZ^{(*)} \to 4\,\mu$ process is one of the cleanest channels for discovering the Standard Model Higgs boson at LHC. This section presents the CMS potential for discovering the Higgs boson in this decay mode and measuring its mass, width, and production cross section, in the range of Higgs boson masses from 115 GeV/c^2 to 600 GeV/c^2. Both signal and background event samples are generated at the Leading Order (LO) approximation, and Next to Leading Order (NLO) production cross sections, computed using different methods, are used for their normalisation. To simulate the detector response and reconstruct physics objects, the full CMS detector simulation and reconstruction software was used. A full treatment of the most important theoretical and instrumental systematic uncertainties are presented, together with their effect on the evaluation of the significance of the Higgs boson observation and on the measurement of its parameters. To minimise systematic uncertainties, new methods of reconstructing the most important corrections directly from data were developed.

3.1.1. Physics processes and their simulation

The Higgs boson event samples for 18 Higgs boson mass points and the three main background processes, $t\bar{t}$, $(Z^{(*)}/\gamma^*)b\bar{b}$ and $(Z^{(*)}/\gamma^*)(Z^{(*)}/\gamma^*)$ were simulated using the CMS simulation [8] and reconstruction [10] software. These three backgrounds will be hereafter referred to as $t\bar{t}$, $Zb\bar{b}$ and ZZ, respectively. Details on the generator-level simulation conditions, cross sections and K-factors can be found in [51]. Many other plausible background candidates, $b\bar{b}b\bar{b}$, $b\bar{b}c\bar{c}$, $c\bar{c}c\bar{c}$, single-top, $Zc\bar{c}$, $Wb\bar{b}$, $Wc\bar{c}$, fake and π/K decay muons in QCD, were considered and found to be negligible. An example of an $H \to ZZ \to 4\mu$ event is shown in colour plate CP3.

Only events with at least $2\mu^+$ and $2\mu^-$ in pseudorapidity range $|\eta| < 2.4$ and with $p_T > 3$ GeV/c were retained for further analysis. Muons outside these kinematic limits could not be reconstructed in the CMS detector. Additional cuts were applied on dimuon invariant masses for the Higgs boson samples ($m_Z > 5$ GeV/c^2) and for ZZ and $Zb\bar{b}$ samples ($m\mu^+\mu^- > 5$ GeV/c^2). The first $\mu^+\mu^-$ pair in the ZZ and $Zb\bar{b}$ samples was defined as the one with its invariant mass closest to m_Z, while the second $\mu^+\mu^-$ pair was made out of the two remaining highest p_T muons of opposite charge. These cuts do not bias the Monte Carlo samples since all the analysis cuts, described below, are tighter.

The Higgs boson samples were generated with PYTHIA 6.225 [24] (LO gluon and weak boson fusion, $gg \to H$ and $q\bar{q} \to q\bar{q}H$) interfaced via CMKIN [52]. Events were re-weighted to correspond to the total NLO cross section $\sigma(pp \to H) \cdot BR(H \to ZZ) \cdot BR(Z \to 2\ell)^2$ (Fig. 3.1). The cross section $\sigma(pp \to H)$ and the branching ratio $BR(H \to ZZ)$ were taken from [53]; $BR(Z \to 2\ell) = 0.101$ [54]. Interference of permutations of identical leptons originating from different Z bosons results in an enhancement to the cross section for $H \to ZZ^{(*)} \to 4\ell$) processes with identical leptons [51], which is about 15% for $m_H = 115$ GeV/c^2 and steadily goes to zero for $m_H = 180$ GeV/c^2. This correction was calculated with COMPHEP.

The $t\bar{t}$ sample was generated with PYTHIA 6.225 (LO $gg \to t\bar{t}$ and $q\bar{q} \to t\bar{t}$). Events were re-weighted to correspond to the total NLO cross section $\sigma(pp \to t\bar{t}) \cdot BR(W \to \ell\nu)^2$. The NLO cross section $\sigma(pp \to t\bar{t}) = 840$ pb was taken from [55] and the branching ratio $BR(W \to \ell\nu) = 0.320$ from [54].

The $Zb\bar{b} \to \mu^+\mu^- b\bar{b}$ sample was generated with the COMPHEP 4.2p1 [43] matrix element generator, interfaced to PYTHIA 6.225 for showering and hadronisation. Included

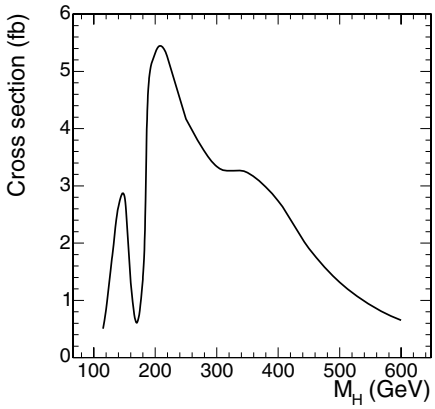

Figure 3.1. Standard Model NLO cross section for the process $(ZZ^{(*)} \to 4\,\mu vs$. Higgs boson mass.

sub-processes were $q\bar{q}/gg \to (Z/\gamma^*)b\bar{b} \to \mu^+\mu^- b\bar{b}$. The corresponding COMPHEP LO cross section was found to be 116 pb. To obtain the NLO cross section a NLO K-factor $K_{NLO} = 2.4 \pm 0.3$, computed with MCFM [56], was used.

The $q\bar{q} \to ZZ \to 4\mu$ and $q\bar{q} \to ZZ \to 2\mu 2\tau$ event samples were generated with COMPHEP, including both the t- and s-channel diagrams [57]. The COMPHEP events were further interfaced to PYTHIA 6.225 for showering and hadronisation. The COMPHEP LO cross sections for the two sub-processes were 113 fb and 157 fb. To account for contributions due to all the NLO diagrams and due to the NNLO gluon fusion ($gg \to ZZ$, known to contribute $\sim 20\%$ with respect to the LO [42] cross section), events are reweighted with the $m_{4\mu}$-dependent K-factor $K(m_{4\mu}) = K_{NLO}(m_{4\mu}) + 0.2$. The NLO K-factor $K_{NLO}(m_{4\mu})$ was obtained with MCFM. The details on the dynamic differences between NLO and LO are summarised elsewhere [58].

The $m_{4\mu}$ distributions for a Higgs boson signal of $m_H = 140\,\mathrm{GeV/c^2}$ and the main backgrounds are shown in Fig. 3.2 after the pre-selection cuts described above.

3.1.2. Event selection

3.1.2.1. Trigger and offline muon selection. CMS has been designed and optimised to detect and reconstruct muons. These particles provide a very clean signature and thus a very high trigger efficiency, with an average of 98% for the Level-1 Global Muon Trigger [7]. The inclusive muon triggers based on the selection of a single muon with $p_T > 19\,\mathrm{GeV/c}$ or dimuons with $p_T > 7\,\mathrm{GeV/c}$ assures an efficiency of practically 100% for collecting events with four high-p_T muons.

In order to minimise muon reconstruction systematic uncertainties, we select only those reconstructed muons that have transverse momentum $p_T > 7\,\mathrm{GeV/c}$, if they are in the central pseudo-rapidity region ($|\eta| < 1.1$), or with momentum $p > 13/$, GeV/c, if they are in the endcaps ($|\eta| > 1.1$) [59]. These cuts do not affect the number of accepted signal events significantly.

Also, we require that all four possible combinations of the reconstructed dimuon masses be above $12\,\mathrm{GeV/c^2}$, $m_{\mu^+\mu^-} > 12\,\mathrm{GeV/c^2}$. As in the previous case, this cut has a very little effect on the Higgs boson events and is primarily intended to suppress poorly simulated hadron background contributions originating from charmonium and bottomium dimuon decays.

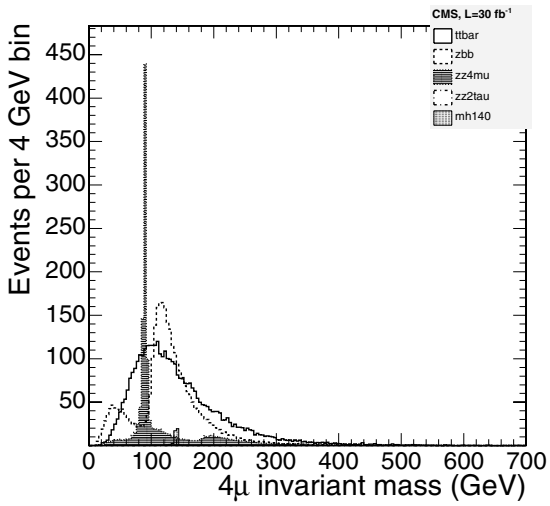

Figure 3.2. Distributions of $m_{4\mu}$ after pre-selection cuts for $t\bar{t}$, $Zb\bar{b}$, ZZ and a Higgs boson signal of $m_H = 140\,GeV/c^2$.

3.1.2.2. Discriminating variables. The $H \to ZZ^{(*)} \to 4\,\mu$ signal presents a characteristic topology, which consists of two opposite charge muon-pairs in the final state. All four muons are isolated, have a high transverse momentum and point to the same Z-boson mass, depending on the restrictions in the phase space introduced by the Higgs boson mass itself. The four-muon invariant mass peaks at the Higgs boson mass, within the detector resolution. The width of the resonant peak accounts for the natural Higgs boson width and the detector resolution.

In $Zb\bar{b}$ and $t\bar{t}$ background events, two of the muons come from b-quark decays and are usually found within a jet (i.e., non-isolated), have lower transverse momenta and often exhibit detectable displaced vertices. The isolation is defined as the amount of transverse energy in the calorimeter (calorimeter isolation), or the sum of the transverse momentum of the tracks reconstructed in the tracker (tracker isolation), inside a cone in η-ϕ space with a radius $R \equiv \sqrt{(\Delta\eta)^2 + (\Delta\phi)^2}$ around each muon. Figure 3.3 (left) shows the distribution of the calorimeter isolation variable for the least isolated muon, for two potential Higgs boson signals, $150\,GeV/c^2$ and $300\,GeV/c^2$, and for the background. Requiring a maximum isolation in all four muons drastically suppresses $t\bar{t}$ and $Zb\bar{b}$ contamination.

Further restrictions on the p_T spectrum of the 2 lowest p_T muons in the event (see Fig. 3.3 (right), for the 2nd lowest p_T muon) reduces even more the $t\bar{t}$ and $Zb\bar{b}$ contamination. In this way, the ZZ background, which presents a topology very similar to that of the signal, becomes the dominant and irreducible background. Only the four-muon mass distribution, the main discriminant, allows the resonant Higgs signal to be identified over the continuum ZZ production.

Distinction on the basis of dimuon invariant mass or displaced vertices does not increase the Higgs boson signal over the ZZ background. However, they may play an important role in eliminating other possible unaccounted for backgrounds, arising from the primary interactions, accelerator beam halo, detector mis-performance, etc.

Additional variables that may help discriminating H from the dominant ZZ background have been studied: $p_T(4\mu)$, number of jets and their E_T, etc. However, these variables are driven by the NLO production processes, while our samples were generated at the Leading

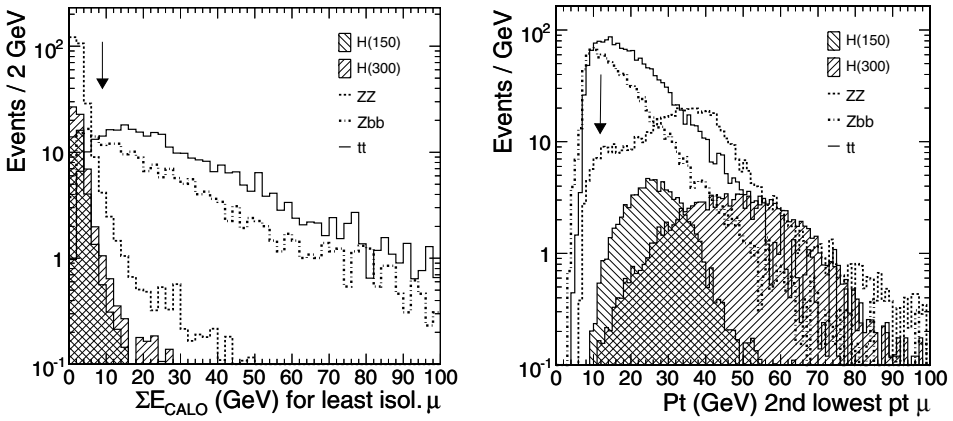

Figure 3.3. Examples of discriminating variables: (left) muon calorimeter-based isolation $\sum E_T$ for the least isolated muon and (right) transverse momentum of the 2nd lowest p_T muon. The hatched histograms represent the Higgs boson signals of masses 150 GeV/c^2 and 300 GeV/c^2, while the solid, dashed and dash-dotted lines indicate the contribution from the $t\bar{t}$, ZZ and Zb$\bar{b}$ backgrounds, respectively. The arrows indicate the positions of the cuts.

Order by PYTHIA and COMPHEP. Therefore, any conclusions that we might derive from these samples would not be reliable. Some muon angular distributions also have some differences originating from the underlying spin structures, but they are not sufficiently discriminating to be used and may be strongly affected by the NLO diagrams.

3.1.3. Higgs boson search analysis

3.1.3.1. Search using $m_{4\mu}$*-independent cuts.* Given the clear signature of the Higgs boson events, the signal extraction has been performed with a unique set of cuts, independent the Higgs boson mass, the details can be found in [60]. A Higgs mass-independent analysis is expected to minimise the dependence on the simulation of the discriminating variables in the Monte Carlo and the sensitivity to systematic errors. It is also readily applicable to real data and robust under variations of the detector conditions (calibrations, resolutions, efficiencies). Moreover, in our case, a mass-dependent selection does not significantly increase the significance of observing a signal.

A unique set of selection cuts has been designed to make the analysis robust when applied to real data. As explained below, some of the cuts (dimuon invariant mass, p_T cuts on the two hardest muons and isolation cuts on the two most isolated muons) slightly decrease the signal significance but make the selection more robust under imperfect conditions in the detector.

A loose requirement on the invariant mass of the pair of unlike-sign muons in the event which is closer to the nominal Z-boson mass, namely, $70\,\text{GeV/c}^2 < m_{\mu^+\mu^-} < 100\,\text{GeV/c}^2$, leaves more than 90% of the signal, while eliminating around 50% of the $t\bar{t}$ contamination. The loss in the signal is due to the internal bremsstrahlung and $Z \to 2\tau \to 2\mu 4\nu$ decays.

Cuts of 12 GeV/c and 8 GeV/c are set on the p_T of the two lowest-p_T muons. The p_T of the two highest-p_T muons must be larger than 15 GeV/c. The latter cut affects neither the signal nor the background, but is considered useful for eliminating unexpected background in real data. The efficiency of the p_T cuts in the signal is close to 90% while it suppresses around 50% of the remaining Zb$\bar{b}$ events, 40% of the $t\bar{t}$ events and about 20% of the ZZ background.

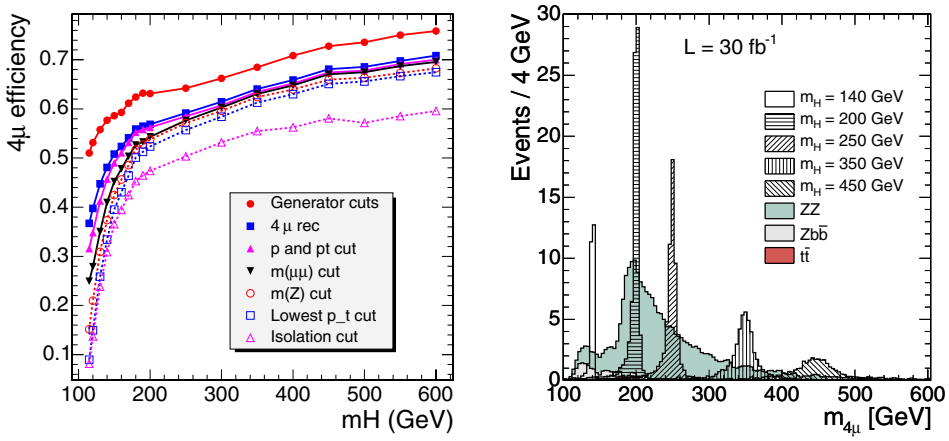

Figure 3.4. (Left) $H \to ZZ^{(*)} \to 4\,\mu$ efficiency *vs*. m_H after different cuts are applied. (Right) Reconstructed four-muon invariant mass distribution, for an integrated luminosity of 30 fb^{-1}, for background (shaded histograms) and several Higgs signals (hatched), after the selection criteria are applied.

For the purposes of the isolation cut optimisation, different cone radii and several energy and transverse momentum thresholds have been studied. Those yielding the maximum signal significance are, for calorimeter isolation, a cone radius of 0.24 and energy thresholds of 5 GeV and 9 GeV, while for tracker isolation a cone radius of 0.20 and p_T thresholds of 2.5 GeV/c and 4 GeV/c. The numbers are given for the two least isolated muons. Although a requirement on the isolation of the two most isolated muons does not increase the signal significance, following the same argument as in the case of the p_T cuts, a cut of 3.5 GeV/c and 5 GeV/c for the calorimeter isolation and 2 GeV/c and 2.5 GeV/c for the tracker isolation is set for the two most isolated muons.

After these cuts, $Zb\bar{b}$ and $t\bar{t}$ events are suppressed to a negligible level in comparison to the remaining ZZ background. The efficiencies of each selection cut over the signal, for the 18 Higgs mass points studied, are shown in Fig. 3.4 (left). The four-muon mass distributions for signal and background events that survive the selection cuts are displayed in Fig. 3.4 (right).

In order to estimate the statistical significance of the signal, the log-likelihood ratio (LLR) statistical method [61,62] is used. The distribution to discriminate signal and background is the four-muon invariant mass (Fig. 3.4 (right)). This distribution, for each Higgs boson mass hypothesis and for the background, is used to calculate the log likelihood ratio, $-2\ln Q$, which is then used to evaluate the compatibility of the data with either the *signal plus background* or the *background-only* hypothesis [60]. The $-2\ln Q$ estimator is sensitive both to the normalisation and the shape of the discriminant. Each event in the sum has a weight $\ln(1+s/b)$ which depends on the signal-to-background ratio, s/b, in the bin where it is found, which in turn depends on the m_H hypothesis. The whole spectrum of the discriminant variable enters the LLR calculation. This avoids any ambiguity in the definition of a signal region for determining the signal significance, present in counting methods.

Figure 3.5 (left) shows the statistical significance, $S_L \equiv \sqrt{<2\ln\,Q>}$, for an integrated luminosity 30 fb^{-1} at different $m_{4\mu}$ invariant masses, should the Higgs boson exist at one of these masses. Based on this distribution, the plot on the right depicts the integrated luminosity required to reach a statistical significance of the signal of 3σ and 5σ, as function of m_H. The expected integrated luminosity required to exclude the signal at the 95% confidence level

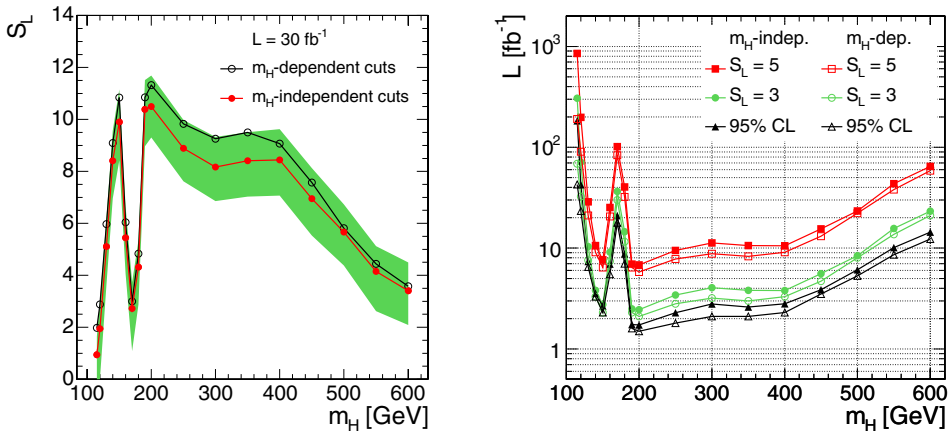

Figure 3.5. (Left) Statistical significance of the signal, S_L, as function of the Higgs boson mass for an integrated luminosity of 30 fb^{-1}, for mass-independent cuts (filled circles) and mass-dependent cuts (empty circles). The shaded band represents the statistical uncertainty on S_L. (Right) Integrated luminosity, for mass-independent (lines with filled squares, circles, and triangles) and mass-dependent cuts (lines with empty pointers), required to achieve a statistical significance of three (middle pair of curves) and five (upper pair of curves) standard deviations, as a function of the Higgs mass. The integrated luminosity required for excluding a Higgs boson signal at the 95% C.L. in a background-only experiment is also displayed (lower pair of curves).

in a background-only experiment is also shown as function of m_{H}. The effect of including systematic uncertainties (subsection 3.1.3.3) in the calculation of S_L is at the level of 15%-20% of the statistical accuracy of the expected significance, supporting that this analysis is not dominated by systematic uncertainties.

In order to more accurately quantify the degree of compatibility of the observed data with any of the two hypotheses, the confidence levels CL_b and CL_s are defined using the $-2\ln Q$ probability density functions, pdf, for both the background-only and the signal-plus-background hypotheses (details can be found in Refs. [60, 61]).

The presence of a signal can be inferred from the behaviour of $1-\mathrm{CL}_b$ for the background-only hypothesis, which is the probability of observing in a sample of simulated background-only experiments a more signal-like value of $-2\ln Q$. The observation of the value $1-\mathrm{CL}_b = 2.85\times10^{-7}$ indicates a 5σ excess in the data with respect to the background expectation. While CL_b quantifies the lack of compatibility of an excess of observed events with the background-only hypothesis, CL_s gives information about how compatible it is with an actual signal (Fig. 3.6).

3.1.3.2. Search using $\mathrm{m}_{4\mu}$*-dependent cuts.* One can take advantage of the fact that the Higgs boson resonance $\mathrm{H}\to\mathrm{ZZ}^{(*)}\to 4\,\mu$ is relatively narrow and use $\mathrm{m}_{4\mu}$-dependent cuts for its search. All details of such search strategy can be found in [51]. The analysis steps in this case would be as follows:

- First, events with 4 muons ($2\mu^+2\mu^-$) satisfying p_{T}, p, and $m_{\mu^+\mu^-}$ quality cuts as described in Section 3.1.2.1 are selected. This ensures that muons are reliably reconstructed and removes a "contamination" originating from heavy quarkonia decays.
- Second, after reconstructing a four-muon invariant mass, the $\mathrm{m}_{4\mu}$-dependent cuts are applied. The cuts, being smooth functions of $\mathrm{m}_{4\mu}$, are optimised in such a way that they maximise the significance of the Higgs signal excess *at all Higgs boson mass points*.

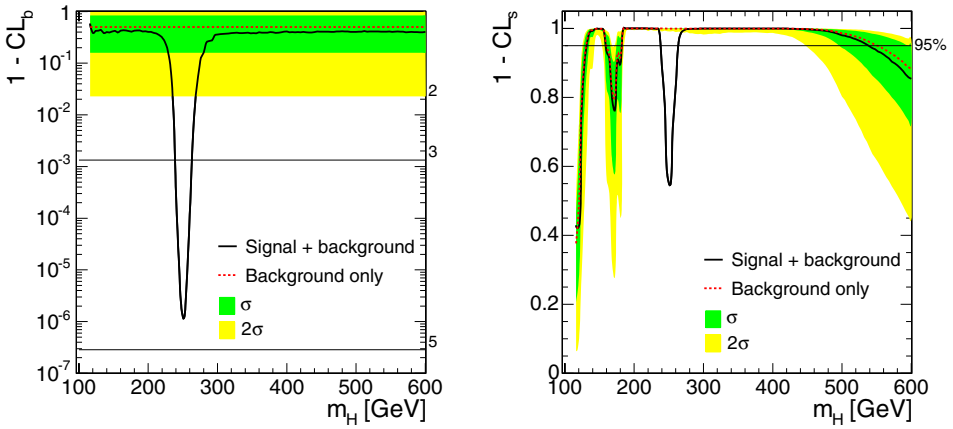

Figure 3.6. Mean values for $1-\mathrm{CL}_b$ (left) and $1-\mathrm{CL}_s$ (right) as a function of the Higgs boson mass hypothesis, assuming existence of Higgs boson at $250\,\mathrm{GeV/c^2}$ mass and for an integrated luminosity of $10\,\mathrm{fb}^{-1}$. The observation of the Higgs is just a little bit shy of the 5σ discovery (left). The mass points for which the curve $1-\mathrm{CL}_s$ is above 0.95 are excluded at 95% CL (right). The 1σ and 2σ bands on $1-\mathrm{CL}_b$ and $1-\mathrm{CL}_s$, originating from the Poisson statistical fluctuations of the number of background events in each bin of the discriminant distribution, are also shown.

- And finally, the resulting $\mathrm{m}_{4\mu}$ distribution is analysed for the presence of a Higgs boson resonance. The search can be done using either the LLR significance S_L estimator built for the whole spectrum or the LLR S_{cL} estimator built for a single-bin, or signal window (counting experiment). The direct comparison of the results can be found in [51].

To perform the desired $\mathrm{m}_{4\mu}$-dependent cut optimisation, we used a recently developed program GARCON [63]. The counting experiment significance estimator S_{cL} is the natural tool for such optimisation. The first half of the available Monte Carlo statistics was used for the cut optimisation. The results for the 18 Higgs mass points were then fit to obtain smooth $\mathrm{m}_{4\mu}$-dependent cuts. It was found that, given the level of the expected dominant backgrounds ($t\bar{t}$, $\mathrm{Zb\bar{b}}$, ZZ), there are only three critical discriminating cuts (details are given in Ref. [51]):

- The muon isolation cut, both tracker- and calorimeter-based, on the worst isolated muon, or equivalently one common cut on all four muons. This cut strongly suppresses $t\bar{t}$ and $\mathrm{Zb\bar{b}}$ backgrounds. The cuts gets tighter and tighter as $\mathrm{m}_{4\mu}$ gets smaller since $\mathrm{Zb\bar{b}}$ and $t\bar{t}$ increase (Fig. 3.2).
- The p_{T} on the second lowest p_{T} muon, or equivalently one common cut on the three highest p_{T} muons. This cut helps to further suppress $\mathrm{Zb\bar{b}}$ background to the level well below ZZ and reduces the ZZ background at high four-muon invariant masses. This cut becomes more stringent with increasing $\mathrm{m}_{4\mu}$.
- The $\mathrm{m}_{4\mu}$ window being used for scanning over the background. It roughly corresponds to the $\pm 2\sigma$ width, where σ is the Higgs boson peak width that includes the detector resolution and the Standard Model Higgs boson width.

The final results are obtained by applying these cuts to the second half of the available Monte Carlo statistics. The observed stability of the results ensures that the cut optimisation did not pick peculiar phase space corners corresponding to statistical flukes. After applying the cuts, the $t\bar{t}$ and $\mathrm{Zb\bar{b}}$ backgrounds are now suppressed well below the irreducible ZZ background.

Figure 3.5 shows, for different Higgs boson masses, the expected significance S_L at $\mathcal{L} = 30\,\mathrm{fb}^{-1}$ (left) and the average integrated luminosities at which a "5σ-discovery", "3σ-evidence", and exclusion at 95%CL are expected (right). The gain in significance with respect to the flat, $\mathrm{m}_{4\mu}$-independent, cuts can be easily translated into probabilistic terms. For example, the Higgs boson with $m_{\mathrm{H}} = 130\,\mathrm{GeV/c^2}$ is right at the "5σ-discovery" threshold for an integrated luminosity $\mathcal{L} = 30\,\mathrm{fb}^{-1}$. The difference in the average expected significance, 5.1 and 6.0, means in this case that the chances of observing significance in excess of 5 for $m_{\mathrm{H}} = 130\,\mathrm{GeV/c^2}$ at $\mathcal{L} = 30\,\mathrm{fb}^{-1}$ are 55% for the flat cuts and 80% for the $\mathrm{m}_{4\mu}$-dependent cuts.

3.1.3.3. Systematic errors. The analysis of the systematic errors can be sub-divided into two distinct stages. First, one needs to understand the level of uncertainties in predicting the level of background in the vicinity of a particular $\mathrm{m}_{4\mu}$ point being investigated for a possible event excess. Second, these uncertainties in the background need to be included in the evaluation of the significance of an excess of events, should it be observed.

Uncertainties in the signal are not very important for establishing an excess of events over the background. It is the uncertainties in the background that are of main concern. After applying the analysis cuts as described earlier, the ZZ production is the dominant irreducible background with all other processes giving much smaller contributions. This reduces the analysis of systematic errors to those of the $\mathrm{ZZ} \to 4\mu$ process.

One can try to evaluate the theoretical and detector performance related uncertainties starting from the first principles. However, especially during the earlier stages of the detector operation when the changes in the system are frequent and hard to monitor and timely incorporate into the detector Monte Carlo simulation, these estimations have limited predictability. Therefore, we developed methods evaluating various corrections, such as muon reconstruction efficiency, muon isolation cut efficiency, directly from data in order to minimise reliance on the Monte Carlo simulation, and, thus, significantly reducing the associated systematic errors. Also, throughout this analysis, we estimate the background around a particular $\mathrm{m}_{4\mu}$ with reference to a *measured* control sample. Note that this completely eliminates uncertainties associated with measuring the luminosity and reduces the sensitivity to PDF and QCD-scales. For the control sample, we use either the inclusive $\mathrm{Z} \to 2\mu$ process or sidebands of the $\mathrm{m}_{4\mu}$ spectrum itself.

The main uncertainties can be grouped as follows:

1. Uncertainties associated with the background production rates, *i.e.* not directly related to CMS Detector performance itself:
   - ZZ: PDF and QCD scale uncertainties described in details in Ref. [47].
   - ZZ: NLO and NNLO contributions vs LO described in details in Ref. [58] plus some related issues are discussed in Ref. [42]. These possible uncertainties are not taken into account in the results shown below, for details see Ref. [51].
   - LHC luminosity: when we estimate the ZZ background events in the signal region via the measured number of events in the control samples, the luminosity uncertainties largely cancel out.
2. Uncertainties associated with the CMS detector performance (hardware/software) and our analysis-specific cuts:
   - ZZ: Trigger efficiency, being very close to 100% due to presence of four muons, does not have substantial systematic errors.

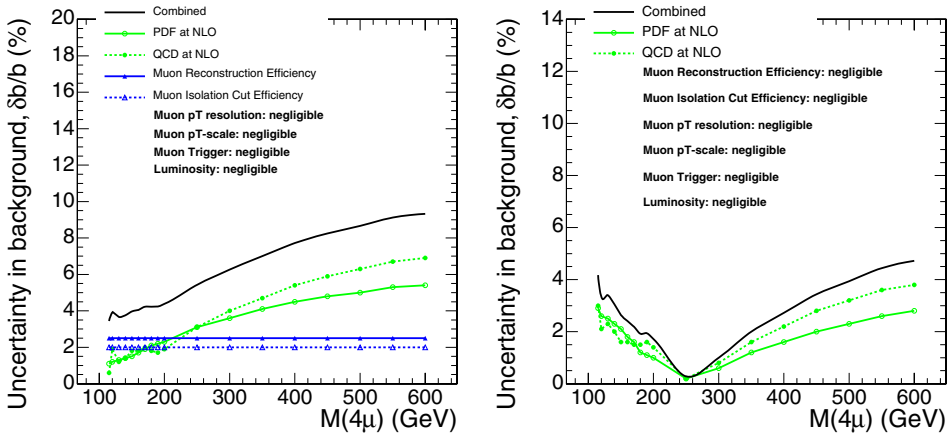

Figure 3.7. Uncertainties in the count of the $ZZ \to 4\mu$ background events in the signal region window at different $m_{4\mu}$. The window size is $\pm 2\sigma$ of the expected experimental Higgs resonance width. (Left) The background event count in the signal region is derived from the measured number of $Z \to 2\mu$ events. (Right) The background event count in the signal region, b, is calculated from the number of $ZZ \to 4\mu$ events B in the range 100 GeV/c^2–700 GeV/c^2 (excluding the signal region window), i.e. $b = \rho \cdot B$.

- ZZ: The muon reconstruction efficiency is determined directly from data [59]. The associated systematic error is less than 1% per muon. Using normalisation to the measured $Z \to 2\mu$ process, this leaves us with 2% uncertainty per event for the $ZZ \to 4\mu$ background production.
- ZZ: The muon isolation cut efficiency is also determined directly from data [64] with about 2% uncertainty per event.
- Higgs: $m_{4\mu}$ resolution is affected by muon p_T resolution. This almost does not affect the background distribution. In [51], we show that even making a mistake in the $m_{4\mu}$ distribution width by as much as 25% has only a tiny effect on evaluating a significance of an excess of events. The muon p_T resolution is fairly easy to measure from data using the measured J/ψ and Z peak widths with the precision much better than needed.
- ZZ: $m_{4\mu}$ scale. The effect of these uncertainties on the number of background events in a signal window appears only on steep slopes of the $m_{4\mu}$ distribution. For the steepest part of the $m_{4\mu}$ distribution in the 180 GeV/c^2–200 GeV/c^2 range, we obtain $\delta b/b \sim 0.1 \delta m_{4\mu}$, where $m_{4\mu}$ is in GeV/c^2 and b is the number of background events. This implies that to be able to neglect this effect, one needs to know the momentum scale with precision of 0.1 GeV at $p_T \sim 50$ GeV/c. This can be easily achieved with just a few hundreds of $Z \to 2\mu$ events.

Fig. 3.7 summaries all systematic errors on the expected number of events in the $Z \to 4\mu$ background for the two methods: via referencing to the total measured $Z \to 2\mu$ cross section and via referencing to the event count in the sidebands of the $m_{4\mu}$ spectrum itself.

Significance with the background uncertainties included

For the Gaussian-like signal over relatively flat background, the S_L and S_{cL} estimators are strongly correlated, with the typical difference of 5%–10% [51]. This stems from the fact that the signal peak is very localised and the background is relatively flat. This allows us to study

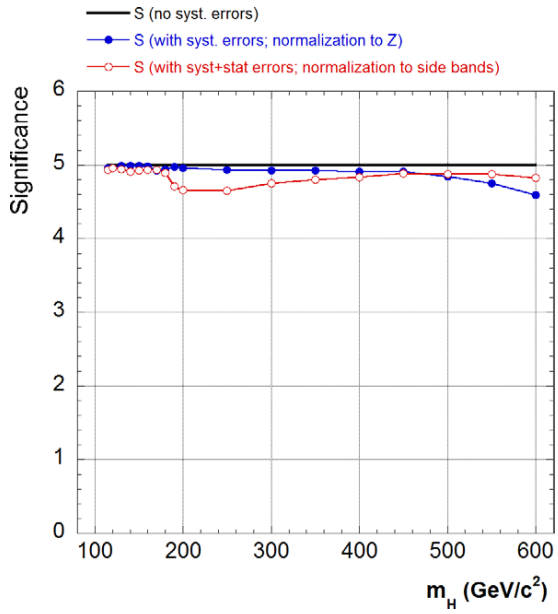

Figure 3.8. Effect of including systematic errors into evaluation of significance at the time of measurements. The reference luminosities, dependent on the Higgs boson mass, are chosen to correspond to an observation of significance $S = 5$ without systematic errors. Solid circles show degrading of significance for the case of systematic errors when the background is evaluated from the measured $Z \to 2\mu$ cross section. Open circles show the effect for the case when the background in signal region is normalised to the sidebands.

the effect of systematic errors on the evaluation of significance at the time of measurements using the counting experiment approach, for which everything can be done analytically. All details on the method we use can be found in Ref. [51]. The method allows to account for the theoretical and instrumental systematic errors as well as for statistical errors when a control sample with a limited event count is used.

The final result of these studies is presented in Fig. 3.8. Starting from an integrated luminosity at which the statistical significance of a Higgs boson observation would be equal to 5 (if the level of background without any errors was known), the figure shows how this significance must be de-rated due to the systematic errors at the time of the measurements as described in the previous sub-section. The effect of systematic errors at low or high luminosities is not as important: at lower luminosity the significance is not sufficient to make serious claims, anyway; while after surpassing the significance of 5, the existence of the Higgs boson can be considered established and the focus must be switched to measuring its parameters.

The two curves with full and open circles show the difference of the two methods for evaluating the background in the signal region: via normalisation to the measured $Z \to 2\mu$ cross section, and via normalisation to the event count in sidebands ($100\,\mathrm{GeV/c^2}$ to $700\,\mathrm{GeV/c^2}$, excluding the signal region). The effect of systematic errors at lower luminosities becomes smaller for the former method and quickly diverges for the latter. As the luminosity increases, the trends obviously reverse. Around the threshold of $S = 5$, the difference between the two methods is not very dramatic; the true benefit of using two approaches to estimating background from data is in their complementarity.

Local significance and overall statistical fluctuation probability

In a search for a relatively narrow 4μ invariant mass peak over a broad background spectrum, one must take into account that the probability of observing a background fluctuation giving an excess of events consistent with a Higgs hypothesis of *some particular mass* might be considerably higher that the local significance calculated for a given mass might imply. This over-estimation of significance strongly depends on how the analysis is set and what constraints/priors on the "phase space" of parameters are used. For example, in a search specifically tailored for the Standard Model Higgs, the only free parameter is the Higgs boson mass; its width, production cross section, and decay branching ratios are dependent on the mass. To make the search even more constrained, one can use a prior on the Higgs mass as it comes out from the precision electroweak measurements. A specific case study showing the potential scope of the effect, which may be comparable or even larger than the effect of the systematic errors discussed above, is given in Appendix A.

3.1.4. Measurement of the Higgs boson properties at $\mathcal{L} = 30\,\mathrm{fb}^{-1}$

The capabilities of the CMS detector to measure the mass, cross section and width of the Higgs boson are determined for an integrated luminosity of $30\,\mathrm{fb}^{-1}$ [65]. These parameters are measured using a binned maximum likelihood fit to the reconstructed four-muon invariant mass, which includes the signal and background contributions after all the selection cuts have been applied (Fig. 3.4 (right)). The 'observed' distribution, f_{sb}, is expressed in terms of the signal, p_s, and background, p_b, probability density functions (pdf) as:

$$f_{sb}(\mathrm{m}_{4\mu}; m_{fit}, \Gamma, N_s, N_b) = N_s \cdot p_s(\mathrm{m}_{4\mu}; m_{fit}, \Gamma) + N_b \cdot p_b(\mathrm{m}_{4\mu})$$

N_s is the number of signal events, N_b the number of background events, m_{fit} the position of the mass peak and Γ the intrinsic width of the Higgs boson. The signal pdf is the sum of two contributions: a convolution of a Breit–Wigner signal shape with a Gaussian distribution that accounts for detector resolution, p_{core}, and a function that reproduces the radiative tail due to internal bremsstrahlung, p_{tail}:

$$p_s = \beta \cdot p_{core}(\mathrm{m}_{4\mu}; m_{fit}, \Gamma, \sigma) + (1-\beta) \cdot p_{tail}(\mathrm{m}_{4\mu}; m_{fit}, \tau)$$

where $1-\beta$ is the fraction of signal events in the radiative tail. The tail shape is parameterised *ad hoc* as

$$p_{tail} = \frac{(\mathrm{m}_{4\mu} - m_{fit})^2}{2\tau^3} \exp\left(\frac{\mathrm{m}_{4\mu} - m_{fit}}{\tau}\right)$$

if $\mathrm{m}_{4\mu} < m_{fit}$ and is zero otherwise [66]. Figure 3.9 (left) illustrates the different contributions to f_{sb}. The p_s function is fitted to the signal-only distributions to obtain the parameters of the radiative tail, which remain fixed in the fit to the signal plus background spectra.

For Higgs boson masses below $190\,\mathrm{GeV/c^2}$, the intrinsic width is negligibly small compared to the mass spread introduced by the experimental resolution and the signal is thus approximated by a Gaussian shape. For masses above $400\,\mathrm{GeV/c^2}$, the natural width of the Higgs is much larger than the experimental resolution, hence the description using a pure Breit–Wigner function yields similar parameters as those obtained from the convolution.

The detector resolution is extracted from the $\mathrm{m}_{4\mu}$ distribution of ZZ events with a four-muon mass above $2m_Z$, for which the kinematics is similar to that of the signal. For masses below $2m_Z$, the intrinsic Higgs boson width is negligible, therefore the resolution is measured directly from the width of the $\mathrm{m}_{4\mu}$ distribution. This width has been found to be consistent with the extrapolation of the resolution determined using ZZ events.

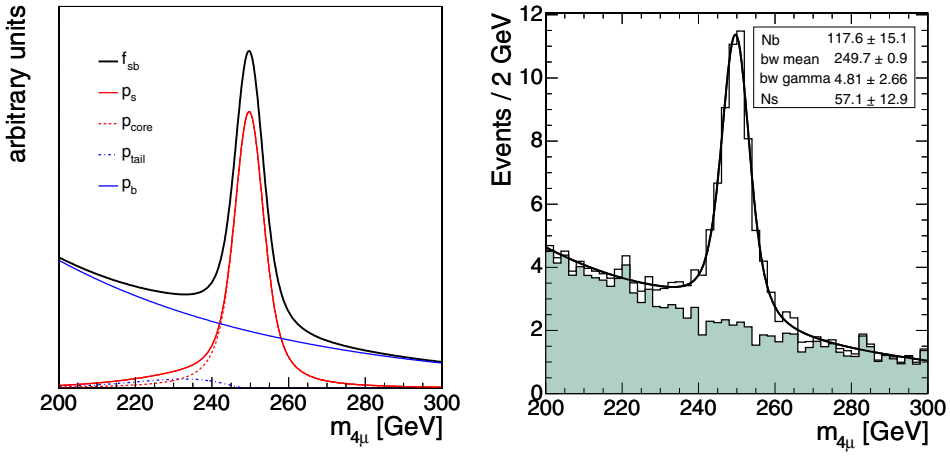

Figure 3.9. (Left) Example of the shapes of the different contributions to f_{sb}. (Right) Data-like distribution expected for a Higgs boson signals of $m_{\mathrm{H}} = 250\,\mathrm{GeV/c^2}$, for an integrated luminosity of $30\,\mathrm{fb}^{-1}$, together with the result of the fit (solid line) and the expected background (shaded area). This pseudo-experiment is selected randomly.

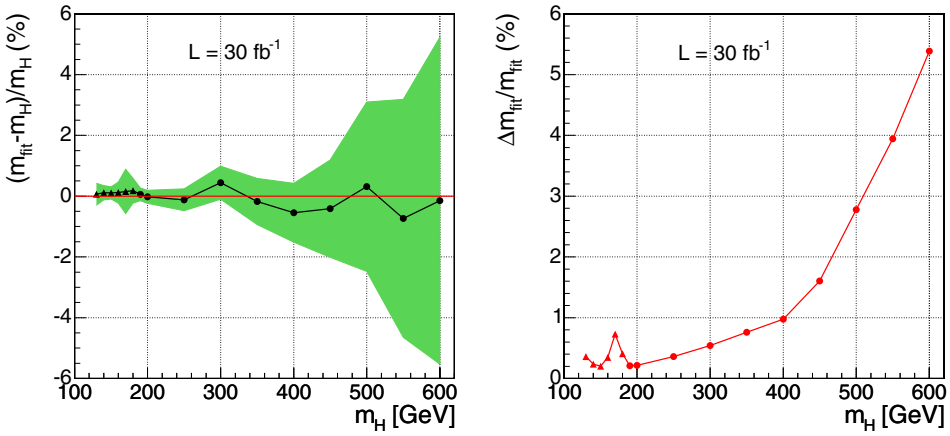

Figure 3.10. (Left) Relative shift of the fitted value of the Higgs boson mass with respect to the input m_{H} value, as function of m_{H}. The shaded area is the error in the determination of the peak value from the fit, also shown as function of the Higgs boson mass (right). The dots correspond to the result of the convolution and the triangles to the Gaussian approximation.

The background pdf, p_b, is approximated by either a polynomial or an exponential function, depending on the mass region under study. The parameters are determined performing a binned maximum likelihood fit to the background sample. The parameters defining the shape of the background are fixed in the global fit to signal plus background, but not its normalisation.

The values of the parameters, together with their errors, are obtained directly from the fit. The result of the fit to the signal plus background distribution is shown in Fig. 3.9 (right) for a Higgs boson signal of $m_{\mathrm{H}} = 250\,\mathrm{GeV/c^2}$. Figure 3.10 (left) depicts the relative shift of the fitted Higgs boson mass with respect to the true mass, together with its statistical error. These values are compatible with zero in the full range of masses, which means that the true mass

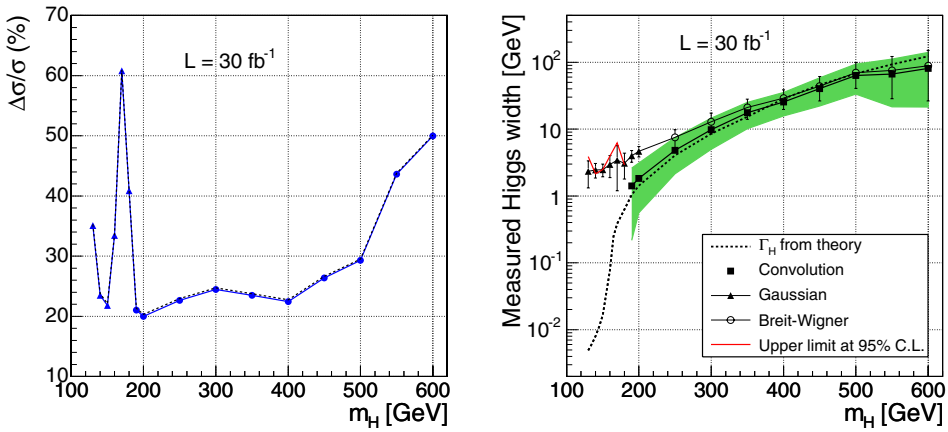

Figure 3.11. (Left) Relative error in the cross-section measurement, $\Delta N_s/N_s$, as a function of the m_{H}. ΔN_s is the statistical error of N_s obtained from the fit. The dots correspond to the result of the convolution and the triangles to the Gaussian approximation. The dashed line indicates the impact of the systematic uncertainties. (Right) Measured Higgs boson width (squares), its statistical error (green band) and the theoretical calculation of Γ_{H} (dashed line). Upper limits to the width at 95% C. L. are shown (red line) for $m_{\mathrm{H}} < 190\,\mathrm{GeV/c^2}$. The result of Gaussian (triangles) and Breit–Wigner (dots) fits are also shown for comparison.

is accurately recovered after applying the fitting method to the reconstructed sample. The evolution of the relative error as a function of the true mass is displayed in Fig. 3.10 (right), showing that the mass can be measured with precisions from 0.1% to 5.4%. The increase in this error around $170\,\mathrm{GeV/c^2}$ is due to the smaller signal statistics caused by the suppression of the $\mathrm{H} \to \mathrm{ZZ}^{(*)}$ decay at this mass. The increasing uncertainty at higher masses is due to the smaller production cross sections, the larger intrinsic width of the Higgs boson and, to a lesser extent, the worse resolution for high p_{T} muons.

The number of signal and background events is obtained from the fit. The relative error in the cross-section measurement is determined from the number of signal events (N_s) and its statistical uncertainty (ΔN_s) as $\Delta N_s/N_s$, shown in Fig. 3.11 (left) as function of the Higgs boson mass. The contribution of the background is properly taken into account, as its normalisation is a free parameter in the fit. The cross section can be determined with a precision between 20% and 45%, except for masses below $130\,\mathrm{GeV/c^2}$, where the statistics is low.

The measured width, together with its statistical error, is presented in Fig. 3.11 (right) as function of the true mass. The width can be determined with an error between 35% and 45% above $190\,\mathrm{GeV/c^2}$. Below this mass there is no sensitivity to the Higgs boson width and upper limits at 95% confidence level (C.L.) are set. For the sake of comparison, the width obtained by fitting only a Gaussian for masses below $200\,\mathrm{GeV/c^2}$ and only a Breit–Wigner for masses above $200\,\mathrm{GeV/c^2}$ is also shown, together with the statistical uncertainty. The Breit–Wigner-only fits do not take into account the detector resolution, and therefore the intrinsic theoretical values are not recovered.

The measurement of the parameters is affected by systematic uncertainties in the muon momentum resolution (determined from data), in the muon reconstruction efficiency (around 2%) and those associated to the selection cuts (close to 1%) [60]. These systematic uncertainties are mostly uncorrelated. The impact in the measured mass and width is small. The cross-section measurement is also affected by the uncertainty in the luminosity determination, which is around 3% (Fig. 3.11 (left)).

The results obtained for Higgs boson masses around 170 GeV/c^2 and above 500 GeV/c^2, for which the expected number of events is somewhat low for $\mathcal{L} = 30\,\text{fb}^{-1}$, have to be taken as representative results for the typical expected distributions. The higher errors of the parameters for those m_{H} values are consistent with statistics. For extending the measurement of the Higgs boson parameters to smaller masses or to lower luminosities, it should be more appropriate to extract the parameters from a large set of randomly chosen four-muon mass distributions with the correct statistics.

3.1.5. Conclusions

Discovery of the Standard Model Higgs boson and measurement of its mass, production cross section and width in the "golden" decay mode $\text{H} \to \text{ZZ}^{(*)} \to 4\,\mu$ were analysed with the CMS Detector. The explored range of Higgs boson masses was 115 GeV/c^2–600 GeV/c^2. The Monte Carlo samples were normalised to represent the NLO cross sections, including $\text{m}_{4\mu}$-dependent K-factors. To simulate the detector response and reconstruct physics objects, the full CMS Detector simulation and reconstruction software was used. The Higgs boson discovery potential was explored for different analysis variations, including the use of $\text{m}_{4\mu}$-dependent and flat cuts, log-likelihood ratio based on the full $\text{m}_{4\mu}$ spectrum and a straightforward counting experiment approach. A full treatment of the most important theoretical and instrumental systematic errors and their effect on evaluation of significance of the Higgs boson observation as well as measuring its parameters were presented. To minimise systematic errors, a number of methods of reconstructing the necessary corrections directly from data were developed.

It was shown that at $\sim 2\,\text{fb}^{-1}$ of integrated luminosity, CMS would be able to start excluding the Standard Model Higgs boson at 95% CL for m_{H} in vicinity of 200 GeV/c^2. By the time CMS reaches $\sim 30\,\text{fb}^{-1}$, it would exclude the Standard Model Higgs boson in its four-muon decay mode in the mass range $m_{\text{H}} = 120$ GeV/c^2–600 GeV/c^2, if indeed it does not exist.

The discoveries at the level of "5σ" local significance could be already possible at $\sim 10\,\text{fb}^{-1}$ for m_{H} in the range 140 GeV/c^2–150 GeV/c^2 and 190 GeV/c^2–400 GeV/c^2. By the time $\sim 30\,\text{fb}^{-1}$ are collected, the discovery range would open up to 130 GeV/c^2–160 GeV/c^2 and 180 GeV/c^2–500 GeV/c^2. An observation of the Higgs boson with the mass $m_{\text{H}} \sim$ 170 GeV/c^2 or $\sim$ 600 GeV/c^2 in the $\text{H} \to \text{ZZ}^{(*)} \to 4\,\mu$ decay channel would require an integrated luminosity of the order of $100\,\text{fb}^{-1}$.

At the integrated luminosity of $\sim 30\,\text{fb}^{-1}$, the Higgs boson mass could be measured with a precision between 0.1 % and 5.4 %, depending on its mass. The intrinsic width could be measured only for the Higgs boson heavier than 190 GeV/c^2, with a precision $\sim$ 35%. For lower masses, the Higgs boson width becomes much smaller than the detector resolution and only upper limits of the order of a few GeV could be set. The production cross section would be determined with a precision $\sim$30%.

3.2. Benchmark Channel: H → WW(*) → 2 muons

3.2.1. Introduction

Previous studies [67,68] demonstrated the relevance of the $\text{H} \to \text{ZZ}^{(*)} \to 2/2\nu$ channel for the Higgs discovery with an integrated luminosity of less than $5\,\text{fb}^{-1}$. The physics study was performed on the data produced at the end of the full simulation, trigger and off-line detector

reconstruction chain, including realistic assumptions for the sub-detectors misalignments. The goal of this study is to provide the discovery potential as a function of the Higgs mass using detailed simulation reconstruction code, considering all the relevant background contributions and providing an as much as possible complete estimation of the systematic errors. The muon reconstruction has an average efficiency in the detector geometrical acceptance ($\eta < 2.4$) of 95–99% for the transverse momentum ranging from 5 GeV/c up to $P_T = 1$ TeV/c, as extensively discussed in [7], while the fraction of mis-assigned charge for muons with $P_T = 100$ GeV/c is less than 0.1%.

3.2.2. Physics processes

3.2.2.1. Signal processes. The signal was studied in the range between 130 to 180 GeV using 7 samples of datasets (Table 3.1). The generation was done using the PYTHIA program [69], considering the most relevant signal sources:

$$gg \to H \to WW^{(*)} \to 2\mu 2\nu \tag{3.1}$$

$$q\bar{q} \to VVq'\bar{q}' \to Hq'\bar{q}'\,;\; H \to WW^{(*)} \to 2\mu 2\nu \tag{3.2}$$

In the simulation, digitisation and reconstruction the effect of the event pile up expected at the machine luminosity $2 \times 10^{33}\mathrm{cm}^{-1}\mathrm{s}^{-2}$ was included. An example of a pp $\to$ H + X event with H $\to$ WW $\to \mu\nu\mu\nu$ is shown in colour plate CP4.

3.2.2.2. Background processes. The dominant background giving the largest contribution at the end of the complete selection chain, is the irreducible one from the continuum production of W pairs decaying into muons and neutrinos. Other significant or critical sources of backgrounds are the production of top quarks and the Drell–Yan muon pairs. The most important backgrounds are thus the processes:

$$q\bar{q} \to W^+W^- \to 2\mu 2\nu \tag{3.3}$$

$$gg \to t\bar{t} \to 2\mu 2\nu \tag{3.4}$$

$$q\bar{q} \to \gamma^*, Z \to 2\mu \tag{3.5}$$

Further contributions from $b\bar{b}$, $ggWW$, WZ, ZZ, and Wt production processes were also considered. A part from Wt and $gg \to WW$, all the processes have been generated with PYTHIA. For the former process, the TOPREX Monte Carlo [44] has been used which correctly takes into account the top mass and the spin correlations throughout the decay chain. The latter dataset has been simulated starting from a Monte Carlo sample produced by N. Kauer et al. [70]. The full list of dataset samples used for the background study is given in Table 3.2.

3.2.2.3. Cross sections at NLO. All the processes considered in this study have been simulated with LO accuracy. In order to approximate the NLO predictions for the signal and the W-pair background, phase space depended reweighting K-factors has been applied [71]. These factors have been obtained by matching respectively the p_T distribution of the Higgs and of the W^+W^- system provided by PYTHIA to the one predicted by MC@NLO [72][38]. The K(p_T) factors used for each p_T intervals are given in Appendix of [73]. The absolute cross sections for Higgs production through gluon-gluon fusion and vector boson fusion have been calculated [20] and are listed in Table 3.1.

[38] For the signal, only the Higgs production through the gluon–gluon mechanism has been reweighted with K(p_T) factors accordingly to NLO description.

Table 3.1. The cross section at the next-to-leading order for Higgs production through gluon fusion and vector boson fusion (VFB) processes and the number of generated events are reported.

Higgs mass (GeV/c^2)	$\sigma^{NLO} \times BR(2l)$ Gluon Fusion (pb)	$\sigma^{NLO} \times BR(2l)$ VBF (pb)	$\sigma^{NLO} \times BR(2l)$ num. of events
130	0.94	0.12	20000
140	1.39	0.19	20000
150	1.73	0.25	17000
160	2.03	0.31	44000
165	2.04	0.32	49000
170	1.95	0.31	40000
180	1.71	0.28	20000

Table 3.2. The cross section at the next-to-leading order for the background processes. The $gg \to WW$ process is generated using a matrix element program linked to PYTHIA for the showering [70]. This process is only known at LO. (*) For $b\bar{b} \to 2\mu$ the pre-selection $p_T > 20, 10\,GeV/c$ was applied.

Channel	$\sigma^{NLO} \times BR(pb)$	num. of ev.
$qq \to WW \to 2l$	11.7	164000
$t\bar{t}$	840	548000
$gg \to WW \to 2l$	0.54 (LO)	50000
γ^*, Z	145000	2700000
$b\bar{b} \to 2\mu$	710 (LO)(*)	640000
$ZW \to 3l$	1.63	72000
$tWb \to 2l$ (TOPREX)	3.4	191000
$ZZ \to 2l$	1.52	99000

No reweighting has been applied to the other processes, whose total cross sections have been simply rescaled accordingly the NLO calculation performed sing the MCFM Monte Carlo program [55, 74, 75]. These cross sections are reported in Table 3.2.

3.2.3. Event selection

The signal selection requires the identification of two high p_T isolated muons. The background reduction is obtained applying suitable kinematic cuts to the reconstructed muons, a veto on the presence of central jets and a high missing E_T (MET) in the event. As discussed in the following sections, separate optimisations were performed independently on the muon isolation variables, jet and missing energy thresholds and on the muons kinematical variables.

3.2.4. The trigger selection

Events passing the global Level-1 trigger must be reduced with a more restricted trigger requirement to limit the recorded event rate. Two trigger streams were considered in this analysis:

1. the HLT double muon stream;
2. the OR of the HLT single muon and double muon stream.

Before any selection the single or double muon HLT trigger efficiency is 92%, while the double muon HLT trigger efficiency is 80% [76]. After the off-line cuts for the Higgs selection, which will be described in detail in the following section, the overall efficiency of the first stream relative to the second one is found to be $(97 \pm 1)\%$, for $m_H = 165\,\mathrm{GeV/c^2}$. In the following, the trigger selection used was the HLT double muon stream, for which the trigger rate is predicted to be a factor $\sim$7 smaller than the single muon one [76].

3.2.4.1. The muon identification and isolation. A first event selection based on the identification of two prompt muons required:

- Level-1 and HLT dimuon trigger bits found;
- two oppositely charged muons reconstructed by the Global Muon reconstructor algorithm developed in ORCA, as described in [7].

The first requirement assures the events to be found in the CMS dimuon data stream, which currently foresees a symmetric threshold of $7\,\mathrm{GeV/c}$ on the p_T of both muons as reconstructed by the High Level Trigger algorithm, for operations at a machine luminosity of $2 \times 10^{33}\mathrm{cm^{-2}\,s^{-1}}$; in addition, at least one of the muons must fulfill the HLT isolation criteria [76]. As discussed in Ref. [76], the trigger rate for this datastream is predicted to be about 4 Hz.

At the off-line reconstruction and selection stage, two cones were considered for the isolation around each reconstructed muon tracks. The $\sum P_\mathrm{T}$ summed over all the charged track candidates found in the Tracker detector was accounted inside the first cone. The $\sum Et$ over the energy deposits in the ECAL and HCAL towers was accounted in the second cone. The size of a cone around a muon track is defined as $\Delta R = \sqrt{\Delta\eta^2 + \Delta\phi^2}$. A muon is considered to be isolated if the $\sum Pt$ ($\sum Et$) inside the considered cones of size $\Delta R_{Tracker}$ (ΔR_{Calo}) is below the threshold P_T (max) (E_T (max)). An optimisation study was performed to find the four parameters:

$$(1)\ \Delta R_{Tracker} \quad (2)\ P_\mathrm{T}(\mathrm{max}) \quad (3)\ \Delta R_{Calo} \quad (4)\ E_\mathrm{T}(\mathrm{max})$$

searching for the highest signal over background ratio. The optimisation was performed using the signal dataset with $m_H = 165\,\mathrm{GeV/c^2}$ and the $b\bar{b}$ background dataset, which is the most sensitive to the isolation cut. At this first stage of the selection, the background reduction was not requested to be very large, thus keeping the signal reduction relatively small; for each combination of the cones:

$$\Delta R_{Tracker} = 0.25, 0.3, 0.35, 0.4 \quad \Delta R_{Calo} = 0.25, 0.3, 0.35, 0.4 \tag{3.6}$$

the cut efficiency of 85% for the signal was requested. With two free parameters, E_T (max) and P_T (max), several solutions are possible. A reasonable choice is to give the same weight to the Tracker and Calorimeter isolation cuts. The mean and the r.m.s. values of the p_T and energy deposition for the signal dataset within different cones are reported in [77]. For each set of isolation cones ($\Delta R_{Tracker}$,ΔR_{Calo}) the E_T and P_T thresholds were chosen as follows:

$$E_\mathrm{T}^{thresh} = < E_\mathrm{T} > + x \cdot \sigma(E_\mathrm{T}) \tag{3.7}$$

$$P_\mathrm{T}^{thresh} = < P_\mathrm{T} > + x \cdot \sigma(P_\mathrm{T}) \tag{3.8}$$

where the parameter x was set to the value giving the required 85% efficiency for the signal. Figure 3.12 shows the resulting background selection efficiency.

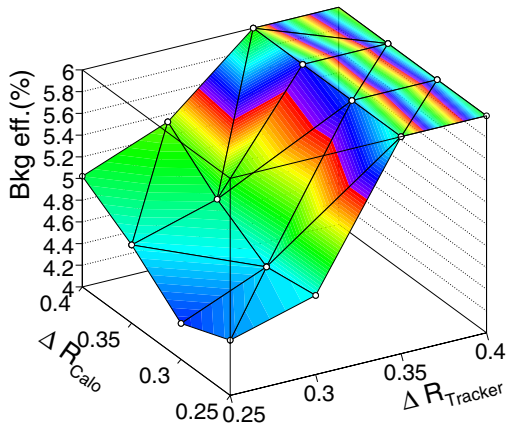

Figure 3.12. $b\bar{b}$ background efficiencies for the 16 combinations of cones considered for the muon isolation selection cut.

The best selection is obtained with:

$$\Delta R_{Tracker} = 0.25 \quad P_{\mathrm{T}} < 2.0\,\mathrm{GeV/c} \quad \Delta R_{Calo} = 0.3 \quad E_{\mathrm{T}} < 4.7\,\mathrm{GeV} \qquad (3.9)$$

corresponding to $x = 1.8$ for the energy deposition and P_{T} cut. The isolation cuts used in the analysis were:

$$\Delta R_{Tracker} = 0.25 \quad P_{\mathrm{T}} < 2.0\,\mathrm{GeV/c} \quad \Delta R_{Calo} = 0.3 \quad E_{\mathrm{T}} < 5.0\,\mathrm{GeV}. \qquad (3.10)$$

3.2.5. Jet reconstruction and the jet veto

The reconstruction of jets is needed to obtain a strong $t\bar{t}$ background reduction by applying a jet veto. The jet reconstruction algorithms can use the raw energy sum of the ECAL and HCAL towers, either with a fixed energy threshold or with η-dependent thresholds. The η-dependent threshold does not improve the $t\bar{t}$ background rejection with respect to a fixed combined E_{T} and E thresholds [73]. The jets reconstructed from raw energies with fixed E_{T} and E thresholds were finally chosen to be used for the JET veto. A strong E_{T} cut helps in the background reduction. However, below $E_{\mathrm{T}} = 25\,\mathrm{GeV}$ the fraction of jets matching with a generated jet starts to decrease, because of ghost jet candidates mainly due to pileup events. The matching was defined within a cone around the reconstructed jet candidate $\Delta R_{rec-genjet} < 0.3$. In order to reduce the number of fake jets, a quality parameter was introduced:

$$\alpha = \sum_{selected\ tracks} P_{\mathrm{T}}/E_{\mathrm{T}}(jet) \qquad (3.11)$$

where the selected tracks are those inside the jet ($\Delta R_{trk-jet} < 0.5$) with more than 5 associated hits, pointing to the primary interaction vertex ($|z_{trk} - z_{vtx}| < 0.4\,\mathrm{cm}$). The mean value of α is 0.66 (two third of the jet energy on average is due to charged particles). A reconstructed jet candidate with E_{T} in the low energy region ($< 20\,\mathrm{GeV}$) was considered only if $\alpha > 0.2$. It has been shown [73] that this selection significantly reduces the number of fake jets (the fraction of matched jets being greater than 90% for $E_{\mathrm{T}} > 15\,\mathrm{GeV}$) with negligible loss of reconstruction efficiency for true jets. Different jet reconstruction algorithms were tested. The best signal ($m_H = 165\,\mathrm{GeV/c^2}$) / background ($t\bar{t}$) ratio was obtained using an iterative

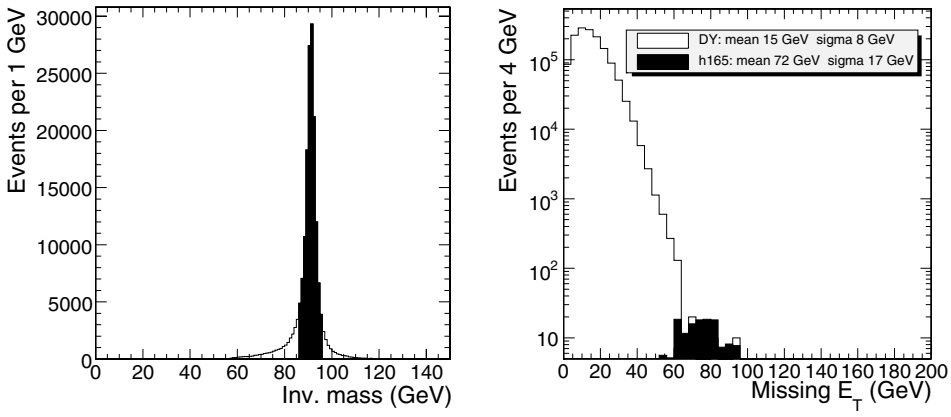

Figure 3.13. Reconstructed dimuon invariant mass for Drell–Yan events selected inside the Z mass region (left, black area); MET distributions for the selected Drell–Yan events and for signal events scaled at the integrated luminosity $\mathcal{L} = 10\,\text{fb}^{-1}$ (right).

cone algorithm [78] with a cone size R = 0.5 and calorimeter towers having raw energies $E_{\text{T}}^{tower} > 0.5\,\text{GeV}$ and $E^{tower} > 0.8$. To summarise, the jet veto is applied if:

$$E_{\text{T}} > 15\,\text{GeV} \quad |\eta_{jet}| < 2.5 \tag{3.12}$$

and the α cut is required in the jet energy range $15\,\text{GeV} < E_{\text{T}} < 20\,\text{GeV}$.

3.2.6. Missing energy reconstruction and the MET cut

The transverse missing energy is reconstructed with the sum of the ECAL and HCAL tower raw energies, corrected for the muons energy contribution. The most sensitive background to the MET cut is the dimuon production from Drell–Yan (DY) process. The right plot in Fig. 3.13 shows the MET distributions for DY events having a reconstructed dimuon invariant mass inside the Z mass region (shown by the black area in the left plot), and for signal events with $m_H = 165\,\text{GeV/c}^2$. The signal and background distribution were normalised to an integrated luminosity $\mathcal{L} = 10\,\text{fb}^{-1}$.

A MET threshold of 47 GeV is 4σ over the mean value for the background and 1.5σ under the mean value for the signal. Drell–Yan events are thus strongly suppressed by applying a MET threshold. The cut used in this analysis was MET > 50 GeV.

3.2.6.1. The kinematic cuts. The kinematic of the two muons is different for signal and background:

- signal events from gluon-gluon scattering are more central than the W^+W^- background from $q\bar{q}$ scattering, thus resulting in a slightly more central rapidity distribution for the decay muons;
- due to the scalar nature of the Higgs boson and of the V-A structure of the weak interaction, for Higgs masses close to $2M_W$, the W^+W^- spin correlation plays in favour of small opening angles between the two muons;
- signal events have a lepton P_{T} spectra peak close to $M_W/2$;
- DY background has a two muons invariant mass peak at M_Z.

In addition, the muons from b quarks (as in the case of the $b\bar{b}$ background and eventually from $t\bar{t}$) have large impact parameters. The following cuts were applied before the optimisation of the kinematical cuts:

1. $|(\mu_1))|, |(\mu_2)| < 2.0$ (pseudorapidity of the two muons);
2. $IP(\mu_1), IP(\mu_2) < 3\sigma$ (impact parameter of the two muons);
3. $P_{\mathrm{T}}(\mu_{max}) < 55\,\mathrm{GeV/c}$ (transverse momentum of the two muons);
4. $m_{\mu_1\mu_2} > 12\,\mathrm{GeV/c_2}$ (invariant mass of the two muons);
5. $\Delta\phi_{\mu_1\mu_2} < 0.8$ (opening angle between the two muons).

Cut 1 is useful for the WW background reduction, as well as cuts 3 and 5. Cut 2 reduces the $b\bar{b}$ events, while cut 4 rejects potential background from b-resonances. After the requirement of the muon isolation described before, the overall signal efficiency for cuts 1 to 4 is about 90%. The distribution of the variable $\Delta\phi\mu 1\mu_2$ will be used to search for the Higgs signal.

The optimisation study was performed by varying the following cuts:

$$P_{\mathrm{T}}(\mu_{max}) > 25, 30, 35, 40\,\mathrm{GeV/c} \quad P_{\mathrm{T}}(\mu_{min}) > 15, 20, 25, 30\,\mathrm{GeV/c^2} \tag{3.13}$$

$$m_{\mu_1\mu_2} < 35, 40, 45, 50, 55, 60\,\mathrm{GeV/c^2} \tag{3.14}$$

to find the set of cuts giving the best significance. The estimator S_{cP} was used, which gives the significance using the Poisson distribution [79]. The input of the estimator are the number of signal and background events, the statistical uncertainties and the theoretical systematics in the background. The optimisation was performed using as before the signal dataset with $M_H = 165\,\mathrm{GeV/c^2}$, and using all the background contributions, properly normalised considering their production cross sections.

The optimisation result could depend on the statistics of the event data samples and on the estimated systematic errors. We searched for the maximum significance in four different conditions:

$$\mathcal{L} = 1\mathrm{fb}^{-1} \quad \mathcal{L} = 2\,\mathrm{fb}^{-1} \quad \text{syst. err.} = 10\% \quad \text{syst. err.} = 15\% \tag{3.15}$$

Figure 3.14 shows, as an example, the significance expected as a function of $p_{\mathrm{T}}(\mu_{max})$ and $p_{\mathrm{T}}(\mu_{min})$ cuts for two different values of the dimuon invariant mass cut, for the case of an integrated luminosity $L = 1\mathrm{fb}^{-1}$ and an overall 10% systematic error.

The following cuts:

$$P_{\mathrm{T}}(\mu_{max}) > 35\,\mathrm{GeV/c} \quad P_{\mathrm{T}}(\mu_{min}) > 25\,\mathrm{GeV/c} \quad m_{\mu_1\mu_2} < 50\,\mathrm{GeV/c^2} \tag{3.16}$$

give the maximum significance (about 3.0 for $\mathcal{L} = 1\,\mathrm{fb}^{-1}$ and an assumed syst. err. = 10%) in all the four conditions.

3.2.7. The selection results

The optimised selection cuts discussed above were applied to the background and signal samples. The list of cuts is described in Table 3.3. The expected number of events for a luminosity of 1 fb^{-1} are given in Table 3.4 for the signals and the backgrounds.

Figure 3.15 shows the distributions of the MET, $P_{\mathrm{T}}(\mu_{max})$, $P_{\mathrm{T}}(\mu_{min})$ and $m_{\mu 1\mu 2}$ variables for the signal and the three most important backgrounds after the jet-veto and the following selection cuts applied in the order reported in the Table 3.3.

Figure 3.16 shows the final distribution obtained for the azimuth angle difference between the muons, expected for an integrated luminosity $\mathcal{L} = 10\,\mathrm{fb}^{-1}$ and for the Higgs signal of mass $m_H = 165\,\mathrm{GeV/c^2}$.

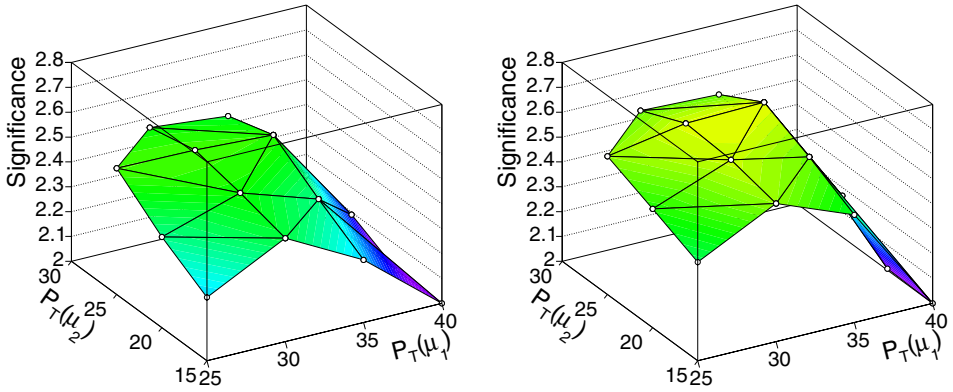

Figure 3.14. Significance as a function of P_{T} cuts for $m_{\mu_1\mu_2} < 40\,\mathrm{GeV/c^2}$ (left) and for $m_{\mu_1\mu_2} < 50\,\mathrm{GeV/c^2}$ (right) with $\mathcal{L} = 1\,\mathrm{fb}^{-1}$ and syst. err. = 10%

Table 3.3. The list of cuts applied to the signal and background samples.

1	L1+HLT dimuon	6	MET > 50 GeV
2	2 μ opposite charge	7	$35\,\mathrm{GeV/c} < P_{\mathrm{T}}(\mu_{max}) < 55\,\mathrm{GeV/c}$
3	Isolation	8	$25\,\mathrm{GeV/c} < P_{\mathrm{T}}(\mu_{min})$
4	$\eta < 2.0$ $IP < 3\sigma$	9	$m_{\mu_1\mu_2} < 50\,\mathrm{GeV/c^2}$
5	Jet Veto	10	$\Delta\phi_{\mu_1\mu_2} < 0.8$

Table 3.4. The expected number of events for a luminosity of $1\mathrm{fb}^{-1}$ for the signal with Higgs masses between 130 and 180 $\mathrm{GeV/c^2}$ and for the backgrounds.

	L1+HLT dimuon	All cuts	ε_{tot}
$m_H = 130\,\mathrm{GeV/c^2}$	112	0.68 ± 0.19	$(0.07 \pm 0.02)\%$
$m_H = 140\,\mathrm{GeV/c^2}$	162	1.7 ± 0.4	$(0.12 \pm 0.03)\%$
$m_H = 150\,\mathrm{GeV/c^2}$	228	5.3 ± 0.8	$(0.26 \pm 0.04)\%$
$m_H = 160\,\mathrm{GeV/c^2}$	256	12.6 ± 0.7	$(0.58 \pm 0.04)\%$
$m_H = 165\,\mathrm{GeV/c^2}$	264	14.3 ± 0.8	$(0.64 \pm 0.04)\%$
$m_H = 170\,\mathrm{GeV/c^2}$	259	11.0 ± 0.7	$(0.53 \pm 0.03)\%$
$m_H = 180\,\mathrm{GeV/c^2}$	233	5.9 ± 0.8	$(0.30 \pm 0.04)\%$
$qq \to WW$	1040	4.1 ± 0.5	$(0.036 \pm 0.005)\%$
$t\bar{t} \to 2\mu 2\nu$	17007	2.6 ± 0.3	$(0.012 \pm 0.001)\%$
$gg \to WW$	58	1.0 ± 0.1	$(0.18 \pm 0.02)\%$
$\gamma^*, Z \to 2\mu$	720653	0.3 ± 0.3	$(4 \pm 4)10^{-5}\%$
$b\bar{b} \to 2\mu 2\nu$	69374	0	0%
Wt	615	0.57 ± 0.10	$(0.017 \pm 0.003)\%$
ZZ	218	0.18 ± 0.05	$(0.012 \pm 0.003)\%$
ZW	384	0.13 ± 0.05	$(0.008 \pm 0.003)\%$

As stated above, all the numbers at the various selection steps refer to the analysis applied to the HLT dimuon stream. For comparison, the event numbers after all the selection cuts were also studied for the case in which the analysis were performed on the data including the single muon trigger data stream. The inclusion of this datastream, which is foreseen to have a rate about 7 times larger than the dimuon stream [76], would result in a $(3 \pm 1)\%$ increase of

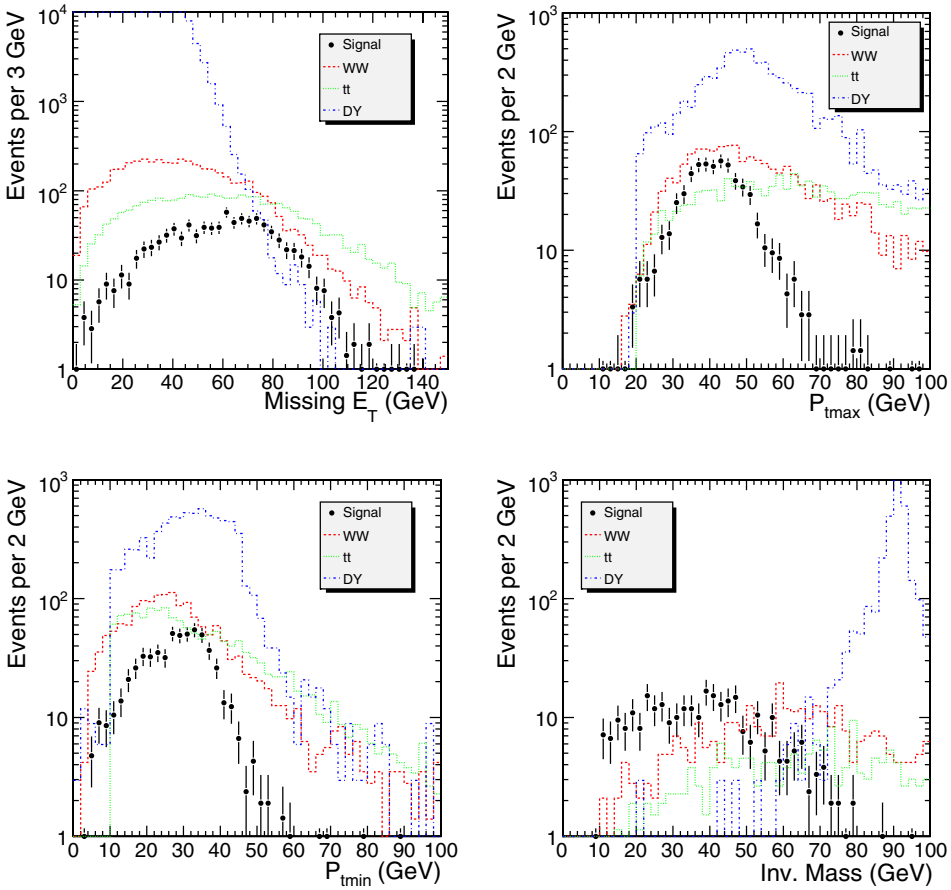

Figure 3.15. Distributions of the missing energy, transverse momentum and invariant mass for a luminosity of 10 fb^{-1} following the cut list order.

the overall signal selection efficiency. The Higgs search with mass appreciably different than 165 GeV/c^2 can take advantage from a dedicated cut optimisation, such as the one reported in [77].

3.2.8. Background estimation and systematics

The precise understanding of the backgrounds is the most critical issue concerning this Higgs discovery channel. The direct use of the Monte Carlo predictions, i.e. $N_{bkg,MC} = \sigma_{bkg,MC} \cdot \varepsilon_{ff}$, leads to high systematic uncertainties due either to theoretical calculation and to experimental systematics. The most reliable approach to address this problem is to measure the different sources of background directly from the data. The commonly used method to extrapolate the background contribution directly from the data consists of selecting a signal-free phase space region (control region) where a given background process is enhanced. The normalisation from data for the two most relevant background, i.e. $t\bar{t}$ and WW has been addressed. For both backgrounds, a dedicated control region was defined. The number of background events in

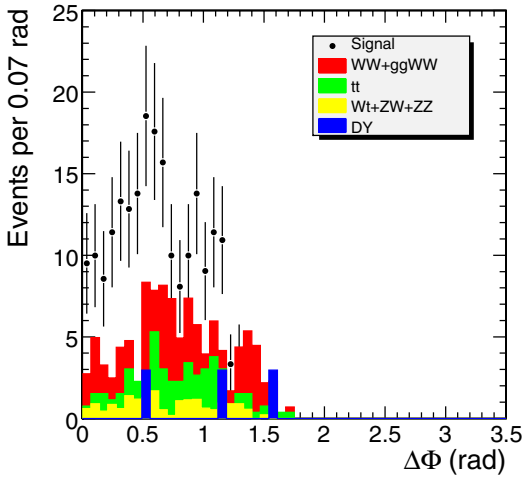

Figure 3.16. Distribution of the angle between the two muons for a luminosity of 10 fb^{-1} at the end of the selection.

the signal region can then be estimated through:

$$N_{signal\_reg} = \frac{N^{MonteCarlo}_{signal\_reg}}{N^{MonteCarlo}_{control\_reg}} N_{control\_reg} \tag{3.17}$$

where $N^{MonteCarlo}_{signal\_reg}$ and $N^{MonteCarlo}_{control\_reg}$ are the numbers of events predicted by the Monte Carlo simulation in the signal and control region. The error on the ratio $N^{MonteCarlo}_{signal\_reg}/N^{MonteCarlo}_{control\_reg}$ accounts for a theoretical contribution (scale variation, PDF uncertainty) and detector systematics effects. The precision with which the number of N_{signal_reg} can be predicted depends also on the statistical error on $N_{control\_reg}$.

3.2.9. $t\bar{t}$ background normalisation

Since the presence of two b-tagged jets is a striking evidence for $t\bar{t}$ events, the most natural control region for this process is then defined by applying the same selection cuts as for the signal region but the jet veto, with the additional request of two b-tagged jets in the detector acceptance[39]. The $t\bar{t}$ evaluation from the data for the $H \to WW^{(*)}$ channel has been studied in Ref. [80] to which we refer for further details. In this study, a jet is tagged as a b-jet if its measured E_{T} is greater then 20 GeV and if there are at least two tracks belonging to the jet (i.e. within a cone of 0.5 around the jet axis) whose σ_{IP} is higher than 2. With such settings the double b-tagging efficiency for $t\bar{t}$ events is $\mathcal{O}(30\%;)$. The mis-tagging rate has been calculated from the ratio between the number of b-tagged jets and the total number of jet with $E_{\mathrm{T}} > 20$ GeV in the fully simulated DY sample and it resulted to be $\mathcal{O}(3\%;)$.

In the following, we consider the background processes in the $t\bar{t}$ control region. For 1fb^{-1} the number of $t\bar{t}$ events in the control region just defined is foreseen to be 17, whereas the contribution from the signal and Wt is completely negligible (in both cases smaller than 0.1 events).

[39] In Ref. [80] an additional control region for $t\bar{t}$ events defined by requiring two high E_{T} jets instead of two b-tagged jets has been proposed. However, it has been shown there, that due to the high contamination from Drell–Yan events, this control region is less indicate for same flavour lepton final states.

Table 3.5. Sources of uncertainty for the $t\bar{t}$ background normalisation procedure. Results are shown for 1, 5 and 10 fb^{-1}.

Luminosity (fb^{-1})	Theoretical error	Detector systematics			Statistical error	Total error
		JES	α criterion	b-tagging		
1	10%	10%	4%	11%	24%	30%
5	10%	6%	4%	9%	11%	19%
10	10%	6%	4%	7%	8%	16%

Not all the processes with $2\mu + 2b + E_t^{\text{miss}}$ as final state have been fully simulated for this analysis, nevertheless general considerations and fast Monte Carlo generator level cross checks lead to exclude other sources of backgrounds, as briefly outlined in the following.

The more natural concurrent process is the non-resonant $W^+W^- \to 2\mu + b\bar{b}$ which is suppressed with respect to $t\bar{t}$. Its cross section is indeed expected to be smaller than $0.3\,pb$. Assuming the same efficiency for the kinematic selections as for the $W^+W^- \to 2\mu$ ($\sim 0.07\%$) and including the double-b tagging efficiency, less than 0.1 events are expected for 1fb^{-1} in the control region.

In the fully simulated Drell–Yan sample used in this analysis, the eventual additional $b\bar{b}$ pair comes only from a gluon splitting; the main mechanism of $\gamma^*/Z^* + 2b$ is not included. For an estimation of the contamination of the $t\bar{t}$ control region due to this process we thus used a parton level sample generated with a matrix element Monte Carlo (MadGraph [81]). Applying the signal kinematic selections, but the E_{T} cut on the latter sample, ~ 10 events are expected for 1fb^{-1}. The rejection due to E_{T} cut has been calculated from the fully simulated sample where actually two b-quarks were present in the final state and it turned to be smaller than 1%. Considering also the efficiency for the double b-tagging, we can safely exclude this as a dangerous background.

In the following the various contribution of uncertainty in the $t\bar{t}$ normalization procedure are listed and described. The results are summarised in Table 3.5 for 1, 5 and 10 fb^{-1}.

- **Theoretical uncertainty.** The theoretical uncertainty of the $t\bar{t}$ cross section ratio $\sigma_{signal\_reg}/\sigma_{control\_reg}$ has been studied in [82] at parton level with LO precision by varying the reorganisation and factorisation scale. The error has been estimated to range between 3% to 10% mostly due to the choice of PDF. Some studies were done also at NLO: E_{T} spectra and multiplicity of jets are not affected by higher order contributions but the estimate of the theoretical error at NLO is not available. In the following we will, assume the theoretical uncertainty on the $t\bar{t}$ normalisation procedure to be 10%.

- **Jet Energy Scale (JES) uncertainty.** In the background normalisation procedures we proposed, the JES uncertainty is particularly important since it affects in an opposite sense the signal region, defined by vetoing the jets, and the control region where the presence of two jets is required. To take into account this sort of anti-correlation of $\epsilon_{\text{signal\_reg}}$ and $\epsilon_{\text{control\_reg}}$, we estimate the effect of the JES uncertainty directly on their ratio by rescaling the measured jet four momentum by a fractional uncertainty (i.e. $\text{P}^{\mu}_{\text{jet}} = (1+\lambda)P^{\mu}_{\text{jet}}$). The relative variation of $\frac{N^{MonteCarlo}_{signal\_reg}}{N^{MonteCarlo}_{control\_reg}}$ for various values of λ is reported in [77]. The JES uncertainty foreseen at CMS is $\mathcal{O}(5\%)$ for 1fb^{-1} and it is expected to decrease down to $\sim 3\%$ for 5 fb^{-1} (thanks to the calibration on the W mass) [7]. The effect of the JES uncertainty is 10% for 1fb^{-1} and 6% for 5fb^{-1}.

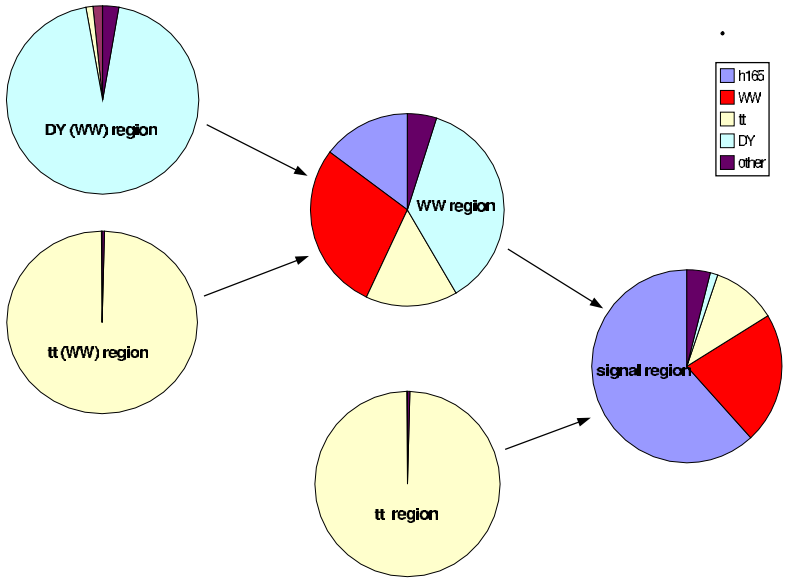

Figure 3.17. Scheme for background normalisation from the data in different phase space regions: the signal region, the $t\bar{t}$ region, the WW region, the DY (WW) region, and the $t\bar{t}$ (WW) region. The arrows indicate the extrapolation of the number of events determined in the corresponding "control region" into the corresponding "target region". Each region is represented by a pie chart that shows the fractions of certain types of events: `h165` is the Higgs signal with $m_h = 165\,\mathrm{GeV/c^2}$, `WW` is the sum of WW backgrounds, $t\bar{t}$ is the $t\bar{t}$ background, `DY` is the Drell–Yan background, and `other` is the sum of the Wt, ZW and ZZ backgrounds. The number of expected events in each region is reported in Table 3.6.

- **α criterion uncertainty.** To estimate the systematic uncertainty due to α criterion, the value of the cut has been varied from 0.15 to 0.25. Moreover, different values of the minimum p_{T} for a track to be included in the sum have been tried, from 2 to 3 GeV/c. The consequent variation of the jet veto efficiency (affecting only $N_{signal\_reg}^{MonteCarlo}$) is relatively small, i.e. of the order of 4%.
- **b-Tagging uncertainty.** The uncertainty on the b-tagging efficiency will be estimated exploiting $t\bar{t}$ events as calibration samples. The precision with which the b-tagging efficiency will be known is expected to be $\pm$ 11% for 1 fb^{-1} integrated luminosity and it is foreseen to improve to $\pm$ 7% with 10 fb^{-1} [83].
- **Uncertainties on the composition of the control region.** As it has been shown in the previous section, $t\bar{t}$ is the dominant process in the chosen control region, other processes contributing less than 1%. It is then safe to simply neglect this source of systematic error.
- **Statistical uncertainty on $N_{control\_reg}$.** Assuming a Poissonian behaviour, the statistical uncertainty scales with the integrated luminosity as the square root of the number of $t\bar{t}$ events in the control region.

3.2.10. WW background normalisation

In contrast to the $t\bar{t}$ background normalisation, which can be performed using an almost completely pure $t\bar{t}$ control sample, it is impossible to isolate the WW background in a

clean way, which means that contributions of other processes have to be subtracted and their systematic uncertainties have to be taken into account during the normalisation procedure of the WW background, including $gg \to W^+W^-$ events. In Fig. 3.17 the overall background normalisation strategy is illustrated. There are four phase space regions involved in the WW background normalisation. Each region is defined with a certain set of cuts:

- signal region: the selection of events in the signal region as described above.
- WW region: same as in the signal region, but $\Delta\phi_{\mu_1\mu_2} = 2 > 0.8$ and $50\,\text{GeV/c}^2 < m_{\mu_1\mu_2} < 80\,\text{GeV/c}^2$.
- DY (WW) region: same as in the WW region, but $80\,\text{GeV/c}^2 < m_{\mu_1\mu_2} < 100\,\text{GeV/c}^2$.
- $t\bar{t}$ (WW) region: same as in the WW region, but the jet veto is replaced with the requirement of two b-tagged jets ($E_t > 20\,\text{GeV}$ and two tracks with $\sigma_{IP} > 2$).

In all cases, the selection is independent of the Higgs mass hypothesis. The total number of events in each region is given in Table 3.6, and the contributions of individual processes are represented in form of pie charts in Fig. 3.17. The main contamination of the WW region is due to Drell–Yan, $t\bar{t}$ and the Higgs signal. The number of Drell–Yan and $t\bar{t}$ is determined by extrapolating the corresponding numbers from relatively clean control regions and are subtracted from the WW region. Additional small contributions from other backgrounds in the WW region are determined from Monte Carlos and then subtracted. So far, no concrete method has been established to subtract Higgs events from the WW control region. Therefore, we choose the conservative approach to treat these Higgs events as an additional background in the WW region.

- **Theoretical uncertainties.** The theoretical uncertainties of W pair production with subsequent decay to leptons have been studied in detail in Ref. [84], and the main sources of potential uncertainties of the shapes of kinematic variables turn out to be spin correlations, underlying event, and scale dependence. The effect of spin correlations can be taken into account properly with the correct choice of an event generator, and the underlying event is expected to be measured from the data with sufficient precision. The shape dependence on the choice of the reorganisation and factorisation scales is sizable in case of the contribution from the $gg \to W^+W^-$ subprocess, because the higher order corrections are unknown in this case. For the cuts, described below, this uncertainty is about 9% and is taken into account in the following.
- **Statistical error and uncertainties on the composition of the control region.** All background normalisation uncertainties are calculated in the following way:

$$\delta_{\text{extrapolation}} = \sum_i \sqrt{n_{\text{total}} + (n_i \times \delta_i)^2} \times \varepsilon_{\text{control}\to\text{target}} \tag{3.18}$$

  where n_{total} is the total number of events[40] in the corresponding control region, $n_i \times \delta_i$ is the product of the number of events and the systematic uncertainty of an individual process in the control region, and $\varepsilon_{\text{control}\to\text{target}}$ is the extrapolation efficiency from the control region to the target region, e.g. the signal region.

The WW background normalisation requires three extrapolations from control regions to target regions:

- DY (WW) region $\Rightarrow$ WW region: with an extrapolation uncertainty of 5% [85] the extrapolated number of events and the uncertainty from Eq. 3.18 is 15.86 ± 1.23 events (79.29 ± 4.49 events) for $1\,\text{fb}^{-1}$ ($5\,\text{fb}^{-1}$) of integrated luminosity.

[40] This term takes into account the statistical fluctuations of the control sample.

Table 3.6. Number of expected events in all the regions with an integrated luminosity of 1 fb^{-1}. The signal region numbers are referred to $m_H = 165\,GeV/c^2$.

Channel	Signal region	$t\bar{t}$ region	WW region	$t\bar{t}$ (WW) region	DY (WW) region
Signal	**14.3**	0.0	6.0	0.0	0.1
$t\bar{t}$	2.6	**17.0**	6.2	24.7	3.2
WW	5.1	0.0	**11.5**	0.0	4.4
DY	0.3	0.0	15.0	0.0	267
Wt,ZZ,WZ	0.8	0.1	1.9	0.1	7.3
all	23.1	17.1	40.6	24.8	282

- $t\bar{t}$ (WW) region $\Rightarrow$ WW region: with an extrapolation uncertainty of 20% (15%) [80] the extrapolated number of events and the uncertainty from Eq. 3.18 is 6.19 ± 1.75 events (30.93 ± 5.41 events) for 1 fb^{-1} (5 fb^{-1}) of integrated luminosity.
- WW region $\Rightarrow$ signal region: as illustrated in Fig. 3.17, the first two items are inputs to this extrapolation, which means that the obtained numbers of Drell–Yan and $t\bar{t}$ events are subtracted in the WW region and the corresponding uncertainties are propagated. The extrapolation uncertainty of WW events, which is mainly due to the unknown higher order correction of the $gg \rightarrow W^+W^-$ contribution [84], amounts to 9% for the cuts used in this analysis. In addition, the remaining backgrounds are estimated and subtracted with the following uncertainties: δ_{Wt} =40%, δ_{ZW} =20% and δ_{ZZ} =20%. According to Eq. 3.18 we obtain 7.35 ± 3.04 events (36.77 ± 7.85 events) for 1 fb^{-1} (5 fb^{-1}) of integrated luminosity.

The results of the last item are used for the calculation of the Higgs discovery potential with m_h =165 GeV/c^2, and an integrated luminosity of either 1 fb^{-1} or 5 fb^{-1}.

Furthermore, it should be pointed out that the entire background normalisation procedure is performed using only the dimuon data set and therefore no additional data sets are needed. In this way, potential uncertainties due to different trigger efficiencies and different integrated luminosities of other data sets do not play a role.

3.2.11. Other backgrounds normalisation

The Drell–Yan background has been normalised to estimate the contamination in the WW region. The same results can be achieved in the signal region. Figure 3.15 demonstrates that the invariant mass cut 80 GeV/c^2 to 100 GeV/c^2 defines a clean control region. ZW background can be normalised by requiring one additional lepton in the final state and removing the $\Delta\phi$ and the invariant mass cuts. ZZ background can be normalised by requiring two additional leptons in the final state and removing the $\Delta\phi$ and the invariant mass cuts. They are expected to contribute to the total background by only 3% (DY), 1% (ZW) and 1% (ZZ). For the Wt background, it is not easy to define a normalisation region. As this process is expected not to represent a sizable fraction of the total background ($\sim$ 6%), the Monte Carlo prediction will be then directly used, the cross section theoretical uncertainty is estimated to be about 30% at LO and 10% at NLO [75].

3.2.12. Detector misalignment systematics

A study for the misalignment impact on the track reconstruction has been done [86]. In the fist data scenario (100 pb^{-1} – 1fb^{-1}) the muon chamber position uncertainty is expected to be 1 mm and the orientation uncertainty about 0.2 mrad. The tracker position uncertainty is expected to be about 5 μm for TPE, 10 μm for TPB, 50 μm for TEC and TOB, 100 μm

Table 3.7. Total background and error for integrated luminosity of 1 and 5 fb^{-1}. The two options for the signal contamination in the WW control region were considered.

Option	Luminosity	Total background	Total error
1.	$1\,\mathrm{fb}^{-1}$	8.8	3.2 (36%)
	$5\,\mathrm{fb}^{-1}$	44.0	8.3 (19%)
2.	$1\,\mathrm{fb}^{-1}$	11.0	3.2 (29%)
	$5\,\mathrm{fb}^{-1}$	55.3	8.3 (15%)

for TIB and 400 μm for TID. The results from simulation show the muon reconstruction efficiency will be unaffected, while the momentum resolution (for 100 GeV/c tracks) will be reduced from 1–2 % to 4–5%. Under these circumstances, the systematic contribution to the signal and background selection is expected to be negligible with respect to the background normalisation systematics.

3.2.13. Signal significance

The signal significance can be obtained using counting or Likelihood methods. Here, the counting S_{cP} method (See Appendix A) was used. S_{cP} is the probability, converted in equivalent number of sigmas, to observe at least $N_s + N_b$ events from Poisson distribution with mean N_b. The presence of systematic errors influences the significance calculations. The hypothesis is to find the same number of signal and background events predicted by the Monte Carlo. The systematic errors due to the $t\bar{t}$ and WW background normalisation methods were included. Two options were considered:

1. the signal contamination in the WW control region can be subtracted;
2. the signal contamination in the WW control region must be considered as additional background.

The option 1 was considered to have a comparison with the $H \to WW \to 2l2\nu$ analysis [73]. Table 3.7 summaries the total backgrounds and errors for different integrated luminosities. The systematics and statistical errors due to the limited Monte Carlo statistics are included.

The signal to background ratio as a function of different Higgs masses and the signal significance are shown in Fig. 3.18.

3.2.14. Conclusions

The possibility to discover the Higgs boson particle through its decay channel into ($WW^{(*)} \to 2\mu 2\nu$ was studied in detail. Particular attention was given to the event selection optimisation, in the determination of the number of background events from the data and the evaluation of the experimental and theoretical systematical uncertainties. Taking all these effects into account, it was shown that in the Higgs mass range 155–175 $\mathrm{GeV/c^2}$ a signal significance bigger than 3 standard deviations can be achieved with 5 fb^{-1} integrated luminosity. On the other hand, with 1 fb^{-1} luminosity only a 2 sigma significance can be achieved even in the most favourable case $m_H \sim 2m_W$, when this final state topology alone is used for the Higgs search.

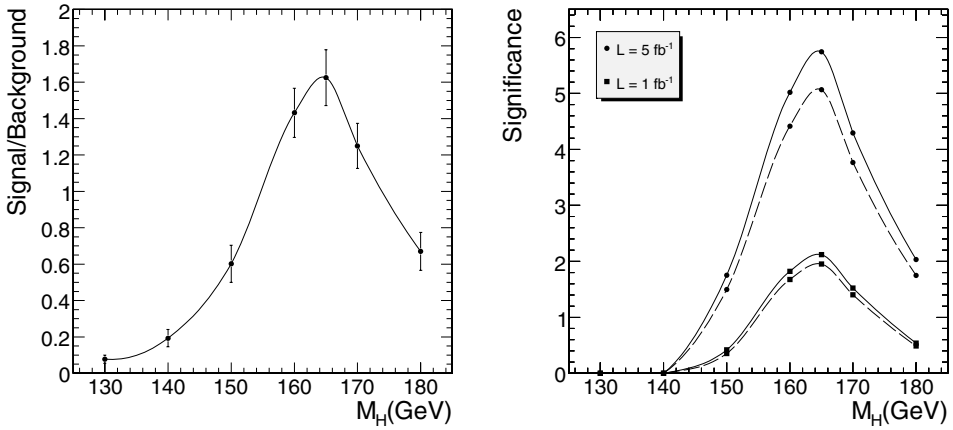

Figure 3.18. Signal to background ratio for the option 1 as a function of different Higgs masses. Error bars are the statistical contribution due to the limited Monte Carlo statistics (left). Significance as a function of different Higgs masses with a luminosity of 1 and 5 fb^{-1}, solid line for the option 1, dashed line for the option 2 (right).

3.3. Benchmark Channel: $Z' \to \mu\mu$

3.3.1. Introduction

Additional heavy neutral gauge bosons (Z′) are predicted in many superstring-inspired [87, 88] and grand unified theories (GUTs) [89], as well as in dynamical symmetry breaking [90] and "little Higgs" [91] models. There are no reliable theoretical predictions, however, of the Z′ mass scale. Current lower limits on the Z′ mass are (depending on the model) of the order of 600–900 GeV/c^2 [54]. The mass region up to about 1TeV/c^2 is expected to be explored at Run II at the Tevatron [92, 93]. The LHC offers the opportunity to search for Z′ bosons in a mass range significantly larger than 1TeV/c^2.

Observability of the $Z' \to \mu^+\mu^-$ channel in CMS is discussed in Sections 3.3.2–3.3.4. Since narrow graviton resonances such as those in Randall–Sundrum models [94] can also decay to lepton pairs (Section 14.3.1), much of the discussion in these sections is also applicable to them. If a new resonance is discovered, the characterisation of its spin and couplings will proceed via the traditional methods of measuring production and decay probabilities and distributions. For example, the two-photon decay should be observable for a graviton and not for a Z′, as discussed in Section 14.6. The measurement of forward-backward asymmetries of leptonic decay products, both at the resonance peak and off the peak, yields information on parity-violating couplings and hence can help distinguish among different Z′ models (Section 3.3.5). Angular distributions of the decay products can also be used for spin discrimination (Section 3.3.6). A simulated event of a dimuon decay of 3 TeV/c^2 Z′ is shown in colour plate CP5.

3.3.2. Signal and background processes

3.3.2.1. Signal $Z' \to \mu^+\mu^-$. Signal and background samples were generated with PYTHIA [69] version 6.227 (with photon emission off incoming or outgoing quarks and leptons switched on) and the CTEQ6L set of parton distribution functions [12] from LHAPDF [95] version 4.1.1.

Table 3.8. Summary of expected properties of Z′ bosons for six studied models. For each model, the first column shows the ratio of the total Z′ decay width Γ to its mass M, the second column shows the dimuon branching ratio Br. The three middle columns, labelled $\sigma^{\mathrm{LO}} \cdot \mathrm{Br}$, give the product of the pure-Z′ leading-order production cross section and the branching ratio for three studied Z′ masses; the last three columns give $\sigma^{\mathrm{LO}} \cdot \mathrm{Br}$ obtained when the full $\gamma^*/\mathrm{Z}^0/\mathrm{Z}'$ interference structure is included. The numbers quoted are for the mass intervals above 400 GeV/c^2 for $M = 1$ TeV/c^2, above 1.5 TeV/c^2 for $M = 3$ TeV/c^2, and above 3 TeV/c^2 for $M = 5$ TeV/c^2. The values of $\sigma \cdot \mathrm{Br}$ in the three middle columns correspond to Z′-only samples not used in our study; the values in the last three columns refer to the full-interference samples that we did use.

Model	Γ/M%	$\mathrm{Z}' \to \mu^+\mu^-$ BR in %	$\sigma^{\mathrm{LO}} \cdot \mathrm{Br}$, fb (PYTHIA)			$\sigma^{\mathrm{LO}} \cdot \mathrm{Br}$, full interference, fb (PYTHIA)		
			1 TeV/c^2	3 TeV/c^2	5 TeV/c^2	1 TeV/c^2	3 TeV/c^2	5 TeV/c^2
$\mathrm{Z}_{\mathrm{SSM}}$	3.1	3.0	480	1.9	0.034	610	2.8	0.050
Z_{ψ}	0.6	4.0	130	0.5	0.009	340	1.7	0.032
Z_{η}	0.7	3.4	150	0.6	0.011	370	1.8	0.035
Z_{χ}	1.3	5.7	280	1.0	0.014	500	2.2	0.038
$\mathrm{Z}_{\mathrm{LRM}}$	2.2	2.3	310	1.2	0.020	500	2.3	0.040
$\mathrm{Z}_{\mathrm{ALRM}}$	1.6	8.6	580	2.6	0.051	740	3.7	0.077

From a large variety of Z′ bosons described in the literature, we consider six which are frequently discussed, and whose properties are representative of a broad class of extra gauge bosons:

- $\mathrm{Z}_{\mathrm{SSM}}$ within the Sequential Standard Model (SSM), which has the same couplings as the Standard Model Z^0; it is available in PYTHIA [24].
- Z_{ψ}, Z_{η} and Z_{χ}, arising in E_6 and SO(10) GUT groups. Couplings to quarks and leptons were obtained from Refs. [96, 97].
- $\mathrm{Z}_{\mathrm{LRM}}$ and $\mathrm{Z}_{\mathrm{ALRM}}$, arising in the framework of the so-called "left–right" [98] and "alternative left–right" [92, 93] models. Their couplings were obtained from Ref. [92, 93], with the choice of $g_R = g_L$.

The generation of signal events with PYTHIA includes the full $\gamma^*/\mathrm{Z}^0/\mathrm{Z}'$ interference structure. We assume that Z′ bosons decay only to three ordinary families of quarks and leptons and that no exotic decay channels are open. Properties for these models are in Table 3.8. The cross sections are shown at leading order (LO), as predicted by PYTHIA. We scale them by a constant K factor of 1.35, see Appendix C, in order to take into account the next-to-next-to-leading order (NNLO) QCD corrections. Electroweak higher-order corrections are not yet accounted for (see discussion in Section 3.3.4.4.1).

3.3.2.2. Background from Drell–Yan production and other processes. The dominant (and irreducible) background to $\mathrm{pp} \to \mathrm{Z}' \to \mu^+\mu^-$ is the Drell–Yan production of muon pairs, $\mathrm{pp} \to \gamma/Z^{\,0} \to \mu^+\mu^-$. The Drell–Yan cross section in PYTHIA was scaled by the same K factor of 1.35, see Appendix C, to get an agreement with the NNLO QCD calculations.

The overall contribution from ZZ, ZW, WW, and $t\bar{t}$ was found to be at the level of only a few percent of the Drell–Yan background and can be further suppressed by signal-selection criteria with almost no reduction in signal efficiency; we neglect this contribution. A few other potential background sources (like cosmics, jet-jet, W-jet, $b\bar{b}$, hadron punchthroughs, and poorly measured $\mathrm{Z}^0 \to \mu^+\mu^-$ events) have not been studied yet, but their contribution is expected to be small.

3.3.2.3. Simulation and reconstruction. The detector response was simulated with the detailed CMS detector simulation and reconstruction software, including pile-up events. Misalignments of the tracker and of the muon system expected at the initial and at the well-advanced stages of the data taking have been taken into account by using two misalignment scenarios developed in the framework of the CMS reconstruction, referred to as the "first data" and the "long term" scenarios [86]:

- The "first data" scenario gives an estimate of the alignment achieved with an integrated luminosity of about 0.1 fb^{-1} and corresponds to the situation when the pixel detector is aligned with tracks and the first information from the Laser Alignment System (LAS) is available for the muon detectors.
- The "long term" scenario describes the expected residual alignment uncertainties. Once the performance of the LAS reaches its design level and the alignment with tracks is done in all tracking detectors. The current estimate is that, this can be achieved with an integrated luminosity of about 1 fb^{-1}.

As a result, for each of the Z′ models above, several sets of simulated samples corresponding to different possible combinations of luminosities and misalignment scenarios were produced at each of three mass values of 1, 3, and 5 TeV/c^2. Since the Drell–Yan cross section falls rapidly with the mass of the muon pair, Drell–Yan background was generated in six mass intervals (with lower mass bounds of 0.2, 0.4, 1, 1.5, 2, and 3 TeV/c^2), again for different combinations of luminosities and misalignment scenarios.

3.3.3. Event selection

For $\mu^+\mu^-$ invariant mass between 1 TeV/c^2 and 5 TeV/c^2, the fraction of Drell–Yan events with both muons within the full geometrical acceptance of the muon system ($|\eta| < 2.4$) increases from about 80% at 1 TeV/c^2 to almost 95% at very high masses. The acceptance of $Z' \to \mu^+\mu^-$ events is very similar.

We require that the event pass the logical OR of single-muon and dimuon triggers, both Level-1 and HLT. We use the default ORCA implementations of low-luminosity and high-luminosity muon trigger algorithms described in Refs. [7, 76], with the exception of the HLT calorimeter isolation criterion requiring that the weighted sum of energy deposits in ECAL and HCAL in a cone around the muon direction be below a pre-defined threshold. Its current implementation leads to significant efficiency losses for *isolated* high-p_T muons (since they are often accompanied by electromagnetic showers); we do not apply HLT calorimeter isolation in this study (tracker isolation is applied). An increase in the trigger rate in the absence of calorimeter isolation should be mitigated by higher p_T thresholds; we have checked that raising the p_T thresholds of the single-muon HLT by 10–20 GeV with respect to their nominal values changes trigger efficiency for our signals by a negligible amount. For the Z′ models that we study (as well as for the Drell–Yan background), the combined Level-1/HLT trigger efficiency is about 98% at 1 TeV/c^2 and decreases with the Z′ mass down to about 95% at 5 TeV/c^2. At high luminosity, the trigger efficiency is 95% at 1 TeV/c^2 and 93% at 5 TeV/c^2. These efficiencies are relative to having at least one muon inside the geometrical acceptance of the muon trigger ($|\eta| < 2.1$) and both muons from the Z′ decay inside the full acceptance of the muon system. No dependence of trigger efficiency on tracker and muon misalignment has been observed, in agreement with the results reported in Ref. [99].

We require that at least two muons of opposite sign charge be reconstructed offline. Detailed description of offline muon reconstruction can be found in Ref. [7]. For each muon candidate, we examine the results of fits to two subsets of hits associated to this

candidate: (1) excluding all muon hits except for those in the innermost muon station, and (2) excluding hits in muon chambers appearing to contain electromagnetic showers. Optimal performance for high-p_T muons is achieved by choosing the best fit on a track-by-track basis using goodness-of-fit variables. The fraction of Z′ events with an opposite-sign dimuon reconstructed offline is about 97% at 1 TeV/c^2 for both the "first data" and the "long term" misalignment scenarios, and decreases slightly with the Z′ mass, to about 95% at 5 TeV/c^2 for the "long term" misalignment scenario. The efficiencies quoted are calculated relative to the number of events accepted by the trigger and with both muons from the Z′ decay within the full geometrical acceptance of the muon system.

The overall efficiency – including acceptance, trigger and offline reconstruction – for $Z' \to \mu^+\mu^-$ events with a mass between 1 and 5 TeV/c^2 lies in the range of 77–85% at low luminosity, and of 75–83% at high luminosity.

3.3.4. Signal observability

The search for a new resonance is performed with an unbinned maximum likelihood fit to the $\mu^+\mu^-$ invariant mass spectrum over a range which includes Drell–Yan continuum as well as a possible peak. The fit takes as input the presumed signal and background shapes, and determines the best-fit background normalisation. More details are given in Refs. [100, 101].

3.3.4.1. Mass spectra and fitting procedure. Prior to the calculation of the invariant mass of an opposite-sign muon pair, $\sqrt{s}$, a search for photon candidates in a cone with a radius of $\Delta R = \sqrt{(\Delta\phi)^2 + (\Delta\eta)^2} < 0.1$ around the trajectory of each muon is performed, and the 4-momentum of the photon candidate with the smallest ΔR in the cone is added to the 4-momentum of the muon. This procedure recovers some of the energy lost by the muon via final state radiation and radiative processes in the detector, thus improving the invariant mass resolution.

The resolution for $\sqrt{s}$ depends strongly on the misalignment scenario, and weakly on the amount of pile-up. If the "long term" misalignment scenario for the tracker and the muon chambers is considered, the sigma of the Gaussian fit to the mass resolution curves varies from 4.2% at 1 TeV/c^2 to 9.0% at 5 TeV/c^2; the RMS truncated at ±30% is ∼ 6% at 1 TeV/c^2 and ∼ 10% at 5 TeV/c^2. The corresponding numbers for the "first data" misalignment scenario at 1 TeV/c^2 are σ=12.5% and RMS ∼ 12%. The bias in the mass resolution does not exceed 1% for the "long term" scenario at all masses considered and for the "first data" scenario at 1 TeV/c^2.

An example of the $\sqrt{s}$ spectra showing 1 TeV/c^2 Z_η signal and Drell–Yan background is in Fig. 3.19. The left-hand plot shows generated mass spectra (100% efficiency with no detector- and reconstruction-related effects); it can be compared to the right-hand plot for fully-recon structed events using the "first data" misalignment scenario. Signal peak is clearly visible in spite of the poor mass resolution.

The mass spectra in Fig. 3.19 are obtained by re-scaling the simulated spectra with large statistics down to a modest number of events characteristic for the regime close to the discovery limit; the statistical fluctuations are thus not to scale. In what follows, we use ensembles of Monte Carlo pseudo-experiments selected from available large-statistics samples. The number of events in each experiment, N_{evt}, fluctuates according to a Poisson distribution with a mean of $\sigma \cdot \mathrm{Br} \cdot \int \mathcal{L}dt \cdot \varepsilon$, where $\int \mathcal{L}dt$ is the integrated luminosity and ε is the combined trigger and reconstruction efficiency.

In order to test for the existence of a resonance and to measure its parameters if it is found to exist, an unbinned maximum likelihood fit of the $\sqrt{s}$ values in each MC experiment

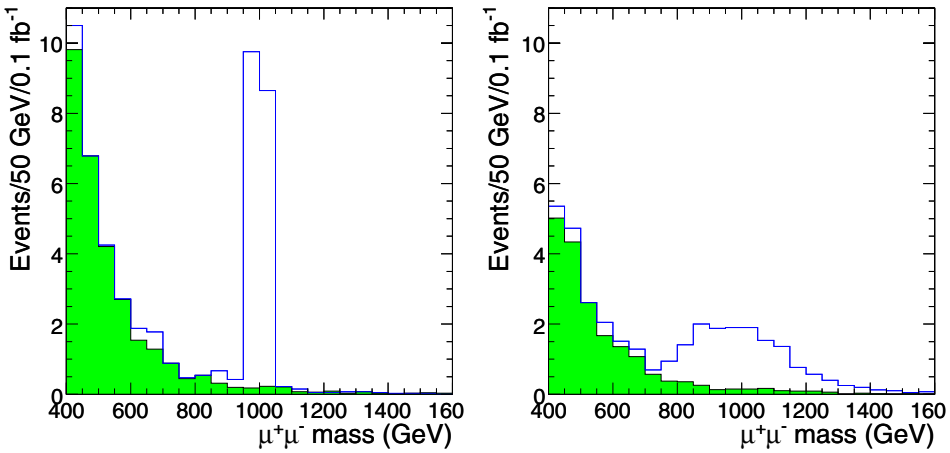

Figure 3.19. Histograms of the $\mu^+\mu^-$ invariant mass for 1 TeV/c^2 Z_η plus background (open histogram) and for background only (shaded histogram), at the event-generator level (left) and for events selected by the Level-1/HLT triggers and reconstructed assuming the "first data" misalignment scenario (right). The number of events per bin is normalised to an integrated luminosity of 0.1 fb^{-1}.

is appropriate. One can imagine that, in the initial data analysis, one is confident about the background shape but not the absolute normalisation. In this case, data can be fit with a sum of signal and background shapes, presumed known, with the signal fraction as a free parameter. In the presence of a signal, one can fix or let vary the mass and the width as well. Thus, as a model of the probability density function (pdf), p, of the parent population of the observed mass spectra, we use

$$p\,(\sqrt{s};\, f_s, m_0, \Gamma) = f_s \cdot p_s\,(\sqrt{s};\, m_0, \Gamma) + (1 - f_s) \cdot p_b\,(\sqrt{s}). \tag{3.19}$$

Here:

- p_s, the pdf of the signal, is a convolution of a Breit–Wigner signal shape with a Gaussian accounting for mass resolution smearing. The convolution includes the dependence of the mass resolution on $\sqrt{s}$, but the radiative tail of the signal is not yet accounted for.
- p_b, the pdf of the background, is modelled as an exponential, $\exp(-k\cdot\sqrt{s}^{0.3})$, with the parameter k determined from fits to Drell–Yan events. This pdf, with the value of k of 2.0, gives a good description of the background shape in the whole mass region between 400 and 5000 GeV/c^2.

There are three free parameters in the fit: the signal fraction $f_s = N_s/(N_s + N_b)$, the position of the mass peak m_0, and the full width at half maximum (FWHM), Γ, of the signal. The shape of the background distribution is fixed, while its level is determined by the fit: f_s is a free parameter. Therefore, the fit explores the difference *in shape* between the signal and the background, and is not sensitive to uncertainties in the expected signal and background levels.

The background shape is currently determined from fits to large-statistics background-only simulated distributions in the full mass region of interest, including the region under the signal peak. In the real experiment, the shape will likely have to be extracted from the data in signal-free regions. The accuracy of predicting the background shape is an important contribution to the systematic uncertainty of the analysis and is discussed in Section 3.3.4.4.3.

Table 3.9. Average values of the likelihood-ratio significance estimator $S_{\mathcal{L}}$ for six different Z′ models, at three signal mass points and for a few representative values of an integrated luminosity. The uncertainties shown are statistical only.

Mass	1 TeV/c^2	3 TeV/c^2	5 TeV/c^2
$\int \mathcal{L}dt$	0.1 fb^{-1}	10 fb^{-1}	300 fb^{-1}
Z_{SSM}	12.4 ± 0.2	10.1 ± 0.2	5.8 ± 0.1
Z_{ψ}	5.1 ± 0.2	4.4 ± 0.1	2.4 ± 0.2
Z_{η}	5.5 ± 0.2	5.1 ± 0.1	2.9 ± 0.1
Z_{χ}	9.1 ± 0.2	6.7 ± 0.2	3.2 ± 0.1
Z_{LRM}	9.0 ± 0.2	7.4 ± 0.2	4.1 ± 0.1
Z_{ALRM}	13.3 ± 0.3	11.8 ± 0.2	7.7 ± 0.2

Ref. [100] contains examples of results of fits to Monte Carlo small-event samples. With even the small number of events needed to give evidence of a resonance, the mass is determined fairly well, with a precision of 4–8% depending on the resonance mass and alignment uncertainties. However, for the narrow resonances under study, typically little information can be obtained about the width.

3.3.4.2. Significance estimator. We follow closely the approach of Ref. [102], which is based on the theorem of Wilks [103]. The test statistic is the likelihood-ratio estimator $S_{\mathcal{L}}$:

$$S_{\mathcal{L}} = \sqrt{2 \ln \left(\mathcal{L}_{s+b} / \mathcal{L}_b \right)}, \tag{3.20}$$

where $\mathcal{L}_{s+b}$ is the maximum likelihood value obtained in the full signal-plus-background fit, and $\mathcal{L}_b$ is the maximum likelihood from the background-only fit. Studies show [100] that in the small-statistics low-background regime characteristic of a Z′ search, the asymptotic conditions of Wilks's theorem [103] are satisfied well enough and $S_{\mathcal{L}}$ is the number of Gaussian-equivalent standard deviations a measurement lies from the value predicted by a background-only (null) hypothesis. This requires fixing both m_0 and Γ in the fits using the pdf of Eq. (3.19).

We follow a common convention in using the (arbitrary, but useful for comparison) specification that $S > 5$ is necessary to establish a discovery. This S refers to the local excess without accounting for the degree of freedom due to the unknown mass; how one might derate S in a time-dependent way in this context as data comes in will be the subject of a future study.

3.3.4.3. Discovery potential in $Z' \to \mu^+\mu^-$ channel. Table 3.9 gives a summary of the signal significance expected for different Z′ models, masses and integrated luminosities. The numbers shown are for the "first data" misalignment scenario and low luminosity parameters for $\int \mathcal{L}dt = 0.1$ fb^{-1}, the "long term" misalignment scenario and low luminosity parameters for 10 fb^{-1}, and the "long term" misalignment scenario and high luminosity parameters for 300 fb^{-1}. $S_{\mathcal{L}}$ scales as expected with the square root of $\int \mathcal{L}dt$.

We use the same combinations of luminosities and misalignment scenarios to calculate the integrated luminosity needed to reach 5σ significance. The results for various Z′ models are shown in Fig. 3.20 as a function of Z′ mass. One can see that:

- A very low integrated luminosity, less than 0.1 fb^{-1}, and non-optimal alignment of the tracker and the muon detectors should be sufficient to discover Z′ bosons at 1 TeV/c^2, a mass value which will likely be above the Tevatron reach. One would need about 50% less data to reach the same signal significance if, the optimal alignment is achieved.

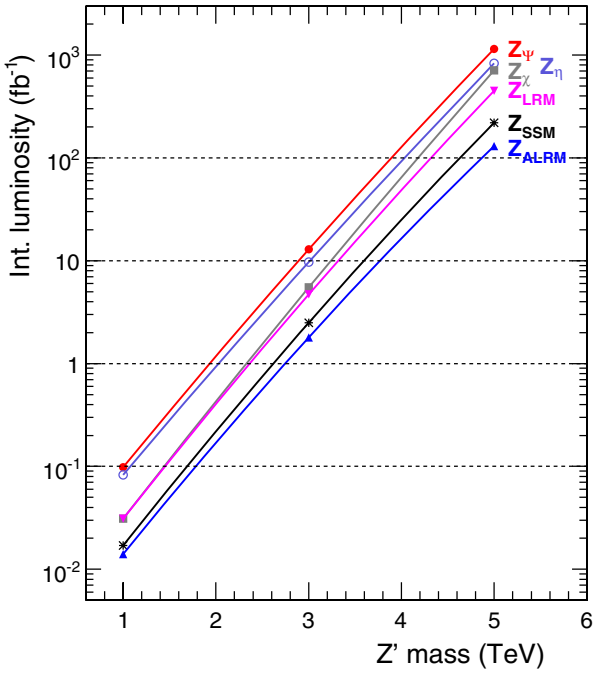

Figure 3.20. Integrated luminosity needed to reach 5σ significanc ($S_{\mathcal{L}}$=5) as a function of Z′ mass for (top to bottom) Z_ψ, Z_η, Z_χ, Z_{LRM}, Z_{SSM} and Z_{ALRM}. Symbols indicate fully-simulated mass-luminosity points, lines are the results of interpolations between the points.

- An integrated luminosity of $10\,\text{fb}^{-1}$ is sufficient to reach 5σ significance at $3\,\text{TeV/c}^2$ for most (but not all) of the Z′ models considered if the optimal alignment is available: depending on the model, the mass reach is in the range between 2.9 and $3.8\,\text{TeV/c}^2$.
- An integrated luminosity of $100\,\text{fb}^{-1}$ does not allow one to obtain 5σ significance at $5\,\text{TeV/c}^2$ with only the $Z' \to \mu^+\mu^-$ channel for any of the models considered: the corresponding mass reach lies in the region between 3.9 and $4.9\,\text{TeV/c}^2$.

These estimates of signal significance do not incorporate systematic uncertainties, which we discuss in the next section.

3.3.4.4. Systematic uncertainties. The main sources of systematic uncertainties are expected to be (a) theoretical uncertainties (parton distributions, higher-order corrections, etc.), (b) uncertainties arising from an imperfect knowledge of the detector (alignment, calibration, magnetic field), and (c) uncertainties in the fitting procedure (background shape, functional forms of pdf's, mass resolution, etc.).

3.3.4.4.1. Theoretical uncertainties. Our current estimates of the Z′ mass reach depend on the accuracy of the modelling of the Standard Model processes and of the Z′ boson production. The following sources of theoretical uncertainties have been studied.

- **Higher-order QCD corrections.** We use a constant $K_{\text{QCD}}^{\text{NNLO}}$ factor of 1.35 to rescale PYTHIA cross sections for Drell–Yan and Z′ bosons to NNLO QCD predictions. This is an approximation, since such a reweight does not take into account variations of the ratio of NNLO and LO cross sections with the invariant mass and other observables, such as rapidity and p_{T}. It is shown in Appendix C that the variations of the $K_{\text{QCD}}^{\text{NNLO}}$ factor with the mass in

the mass interval between 500 GeV/c^2 and 5 TeV/c^2 is in the range of $\Delta K_{\rm QCD} = \pm 0.05$; the dependence on other observables and the ensuing impact on acceptance, efficiency, etc. remains to be studied. Since K is expected to be nearly identical for the signal and dominant background, the effect of changes in K from the nominal value $K_0 = 1.35$ is to scale the expected significance by $\sqrt{K/K_0}$.

- **Higher-order electroweak corrections.** Only preliminary estimates of electroweak next-to-leading order corrections exist for the LHC and $\sqrt{s} > 1$TeV/c^2 [104, 105]. Currently, we use $K_{\rm EW} = 1$ for the central values of signal and background cross-sections, and assign an uncertainty of $\Delta K_{\rm EW} = \pm 0.10$ based on discussions in Refs. [104, 105].
- **Parton distribution functions (PDFs).** We use the CTEQ6.1M eigenvector PDF sets [12] and the "master" equations in Ref. [106] to evaluate the uncertainties characterising current knowledge of the parton distributions. The effect on the total cross section σ was found to be similar for the Drell–Yan background and for the studied Z′ models at any given mass, with uncertainties lying in the range of $\frac{\Delta\sigma}{\sigma} = ^{-7\%}_{+4\%}$ at $\sqrt{s} = 1$ TeV/c^2, rising to $^{-10\%}_{+12\%}$ at $\sqrt{s} = 3$ TeV/c^2, and reaching as much as $^{-20\%}_{+30\%}$ at $\sqrt{s} = 5$ TeV/c^2. The effect on other observables and on the acceptance has not been studied yet, but is expected to be small.
- **Hard process scale.** The dependence of the observables on the choice for renormalisation and factorisation Q^2 scales, μ_R and μ_F, is unphysical and is commonly taken as a rough estimate of the uncertainty due to unaccounted higher orders in QCD calculations. The study of the sensitivity of the Drell–Yan cross section to the choice for the QCD scale is described in Appendix C. Both μ_F and μ_R were varied in the range of $\sqrt{s}\ /2 < \mu < 2\ \sqrt{s}$ around the default choice of $\mu = \sqrt{s}$, and the mass-dependent variations of the cross section obtained. At NNLO, they are smaller than $\pm 1\%$ at 1 TeV/c^2, but as large as -25% (for $\mu = 2\sqrt{s}$) and +5% (for $\mu = 2\sqrt{s}$) at 5 TeV/c^2. We use the NNLO estimates given in Appendix C for both the Drell–Yan and the Z′ bosons.

Since our analysis relies only on the background shape and not on any assumptions about background normalisation, the uncertainties in signal and background cross sections described in this section will not have any direct impact on the calculation of significance once a data set is in hand. They do effect, however, estimates of the Z′ mass reach based on Monte Carlo predictions for the signal and the background. We combine them in quadrature, and use the obtained mass-dependent band as 1σ uncertainty in the expected number of signal and background events. This band is then translated into 1σ uncertainty in the prediction of the mean integrated luminosity needed to reach 5σ significance for any given Z′ model. This uncertainty, and the best estimates of the luminosity, is shown in Fig. 3.21 for the models with the smallest and the largest values of $\sigma \cdot$ Br among the models studied, Z_ψ and $Z_{\rm ALRM}$.

3.3.4.4.2. Uncertainties in the detector performance. The key element in the performance of high-$p_{\rm T}$ muon reconstruction and, therefore, for the Z′ mass reach is the alignment of the tracker and the muon system. Unlike the muons in the region of low and moderate $p_{\rm T}$ values, where the influence of the tracker alignment is predominant, both the tracker alignment and the muon system alignment play an important role for the muons at TeV scale. We take them into account by using the two realistic misalignment scenarios developed in the CMS reconstruction, the "first data" and the "long term". These scenarios, however, are only based on the current best estimates (and sometimes guesses) of expected alignment uncertainties and will be refined as better estimates from alignment studies become available. Therefore, they have intrinsic uncertainties, which at the moment cannot be evaluated. As discussed above and in Ref. [99], neither the trigger efficiency nor the offline reconstruction efficiency for high-$p_{\rm T}$ muons is affected by the misalignment even in the worst-case scenario once the alignment

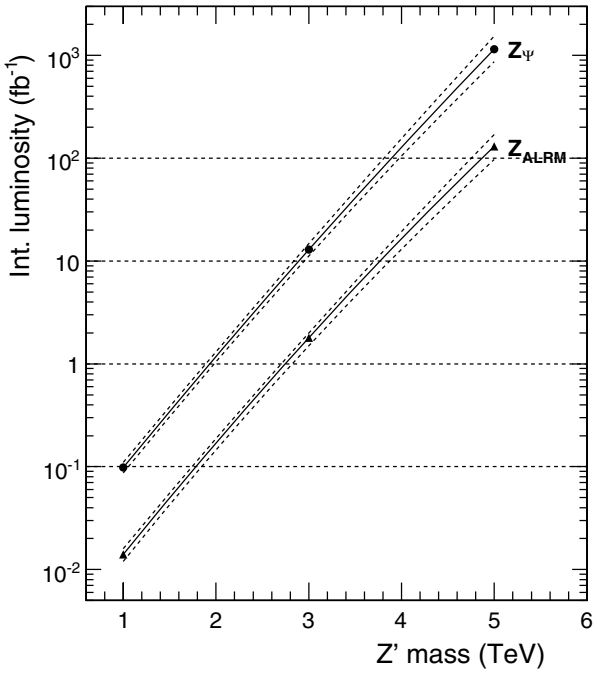

Figure 3.21. Integrated luminosity needed to reach 5σ significance ($S_{\mathcal{L}} = 5$) as a function of Z′ mass for Z_ψ and Z_{ALRM} models. Solid lines show the best estimates, dashed lines indicate boundaries of the band corresponding to the predictions with $\pm 1\sigma$ theoretical uncertainty.

position uncertainties are used in reconstruction algorithms [86]. So uncertainties in alignment translate mainly into uncertainties in the invariant mass resolution. We show below that even sizable variations in the width of the mass resolution have only a small impact on the Z′ mass reach.

Another potentially important source of systematic uncertainties is the uncertainty in the calibration precision of the muon chambers. The impact of uncertainties in the calibration of the Drift Tube chambers on the Z′ mass reach has been studied by (1) changing the t_0 offsets for all chambers by ± 2 ns, and (2) scaling drift velocity (changing time-to-distance relationship) by $\pm 3\%$. These variations represent conservative upper bounds on corresponding effects [107]. The effect of changing t_0 offset was found to be negligible for Z′ samples at all studied mass values and for both misalignment scenarios considered. The scaling of drift velocity has a negligible impact for the "first data" misalignment scenario with its rather poor mass resolution, but results in an increase of 5–10% in the width of the mass resolution for the "long term" scenario (no change in trigger and dimuon reconstruction efficiencies). This translates into a negligible effect in the Z′ mass reach. Uncertainties in the calibration of the Cathode Strip Chambers are less critical and hence are expected to have a negligible impact on the Z′ detection as well.

The effect of uncertainties in the knowledge of the magnetic field remains to be studied.

3.3.4.4.3. Uncertainties in background shape and mass resolution. Many experimental uncertainties have a negligible or small impact on the results of our studies because, the proposed analysis method is not sensitive to uncertainties in the predicted levels of signal and background processes. For example, only the mass dependence of the uncertainty in the

muon reconstruction efficiency needs to be taken into account, not the absolute uncertainty. The same is true for the trigger efficiency and for the uncertainty in the $\sqrt{s}$ scale. Among those uncertainties that do not cancel out, two seem to be particularly important: the uncertainty in the background shape, and the uncertainty in the mass resolution.

As described above, the background shape is currently determined from fits to background distributions predicted by the Monte Carlo simulation. In the analysis of real data, this MC-based shape will be compared with (and perhaps tuned to) the background shape in the region of low masses where one has high statistics of background events. The issue is then the reliability of the extrapolation from the steeply falling spectrum into the candidate signal region. This will have to be studied in detail, once the real data starts to be available. What is interesting to explore at this stage of analysis is how rapidly the significance deteriorates as the ratio of background events in the high-statistics normalisation region to background events in the candidate signal region is wrongly predicted by the MC-motivated background shape. To study this, we multiply our background pdf (p_b in Eq. (3.19)) by a function which is unity in the high-statistics background-only region and smoothly transitions to a tunable value, f, under the candidate mass peak. Values of integrated luminosity were chosen to correspond to 5σ significance for each model at $f = 1$. For $f = 2$ (assuming twice as much background in the signal region as there really is), 5σ becomes 4.2σ for $\mathrm{Z}_{\mathrm{ALRM}}$ and is about 3.7σ for Z_{ψ}. For f around 1.1 or 1.2, the change in S is of the order of a few per cent.

Sensitivity of the Z′ mass reach to uncertainties in the invariant mass resolution has been studied by applying extra Gaussian smearing to the reconstructed values of $\sqrt{s}$ of both the signal and background events and comparing the signal significance obtained with modified $\sqrt{s}$ values to that calculated with the nominal $\sqrt{s}$ values. We found that an increase of 10% in the mass resolution width, σ_M, reduces the signal significance by less than 2% at the values of $S_{\mathcal{L}}$ close to 5; 20% worse resolution gives 5% or less smaller $S_{\mathcal{L}}$. The effect is not very big, indicating that an approximate knowledge of σ_M should suffice. (This exercise does not check, however, the effect of extreme tails of the mass resolution being bigger than expected, which could lead to a background shape (and amount) different from that obtained from the simulation.) The knowledge of σ_M as a function of $\sqrt{s}$ is also used in the pdf of the signal in Eq. (3.19), where it defines the width of a Gaussian accounting for resolution smearing of the signal shape. This does not need to be very precise either: assuming resolution 20% better that it really is reduces $S_{\mathcal{L}}$ by less than 1%.

3.3.5. Distinguishing among Z′ models

The forward–backward asymmetry, A_{FB}, of the leptonic decay products provides information on parity-violating couplings, on and off resonance, as discussed for example in Refs. [96, 108].

The forward–backward asymmetry for $q\bar{q} \to \mu^+\mu^-$ interactions is defined as (e.g., Refs. [109, 110])

$$A_{\mathrm{FB}} = \frac{\sigma_F - \sigma_B}{\sigma_F + \sigma_B}, \tag{3.21}$$

where

$$\sigma_F \equiv \int_0^1 \frac{d\sigma(q\bar{q} \to \mu^+\mu^-)}{d\cos\theta^*} d\cos\theta^*, \quad \sigma_B \equiv \int_{-1}^0 \frac{d\sigma(q\bar{q} \to \mu^+\mu^-)}{d\cos\theta^*} d\cos\theta^*, \tag{3.22}$$

and where θ^* is the angle in the dimuon centre-of-mass (CM) reference frame between the negative muon and the incident quark. For spin-1 $\gamma^*/\mathrm{Z}^0/\mathrm{Z}'$ propagators, the probability density function $P(\cos\theta^*)$ is most generally of the form

$$P(\cos\theta^*;\, A_{\mathrm{FB}}, b) = \frac{3}{2(3+b)}(1 + b\cos^2\theta^*) + A_{\mathrm{FB}}\cos\,\theta^*. \tag{3.23}$$

Although $b = 1$ from general considerations, in the fits described here b is typically left as a free parameter. In Ref. [97], Rosner expresses A_{FB} for $f\overline{f} \to \gamma^*/\mathrm{Z}^0/\mathrm{Z}' \to \mu^+\mu^-$ events in terms of the left- and right-handed couplings of the photon, Z^0, and Z′ to u quarks, d quarks, and charged leptons. More details, including the couplings for the models studied, are given in Ref. [111].

For CM energies well above the Z^0 peak, the Drell–Yan background has a characteristic A_{FB} of about 0.6 [109], and provides a useful starting point.

3.3.5.1. Uncertainty in the sign of $\cos\theta^*$ *in pp collisions.* In proton-proton interactions, the quark direction is ambiguous experimentally since a quark can originate with equal probability from either proton, and the sign of $\cos\theta^*$ is not directly measurable. We follow Ref. [112] and infer the sign of $\cos\theta^*$ by assuming that the longitudinal motion of the dimuon system is in the direction of the proton contributing the annihilating quark, since a quark in a proton typically carries a larger momentum fraction x than does an anti-quark. We refer to the inference of the wrong sign of $\cos\theta^*$ as "mistagging" the sign. If not accounted for, the mistagged events, particularly at low y, reduce ("dilute") the apparent value of A_{FB}. Some authors deal with this problem by removing events below a chosen y threshold [112], or by examining A_{FB} in bins of y [113]; in Ref. [111], an approached is described which assigns the probability of a mistag on an event-by-event basis, thus using all events in a given sample. As knowledge of the mistagging probability depends on the Parton Distribution Functions, the effect of uncertainties in PDFs must be evaluated, and will be the subject of future work.

3.3.5.2. Other uncertainties. The transverse momentum p_{T} of the annihilating quark and/or anti-quark provides another source of uncertainty in the measurement of $\cos\theta^*$, since the observable quantity is the vector sum of these transverse momenta. We use the Collins–Soper reference frame [114], in which angles are measured with respect to the axis that bisects the target and beam axes in the dimuon CM frame, to minimise the effect of p_{T} on the measurement of $\cos\theta^*$, and let θ^*_{CS} denote the polar angle of the μ^- in this frame.

As described in Ref. [111], the effect of detector acceptance, combined with high mistag probability for events near $y = 0$, means that events lying near the edges of acceptance carry the largest information for the A_{FB} measurement. Hence, in addition to trying to obtain maximum acceptance, it is particularly important to understand the effect of any asymmetries in the acceptance which may arise as a result of the real detector efficiencies not being perfectly symmetric or of the beam crossing not being perfectly centred.

3.3.5.3. Likelihood function and fitting procedure. Since a Z′ can be discovered with a small number of events (Section 3.3.4), and since the search for anomalous A_{FB} in the highest mass continuum Drell–Yan events at any given luminosity will use a restricted sample of events, we consider an unbinned likelihood fit. The procedure and results with statistical errors only are described in Ref. [111]. The results of numerous fits can be summarised simply with a nominal statistical uncertainty in A_{FB} of 0.09 in a fit with 400 events for 1 TeV/c^2 Z′ samples, and of 0.08 with 400 events for 3 TeV/c^2 samples. Ref. [111] also reviews an appropriate hypothesis-testing methodology for distinguishing between Z′ models.

Table 3.10. Angular distributions for the decay products of spin-1 and spin-2 resonances, considering only even terms in $\cos\theta^*$.

Channel	d-functions	Normalised density for $\cos\theta^*$
$q\bar{q} \to G^* \to f\bar{f}$	$\lvert d^2_{1,1}\rvert^2 + \lvert d^2_{1,-1}\rvert^2$	$P_q = \frac{5}{8}(1 - 3\cos^2\theta^* + 4\cos^4\theta^*)$
$gg \to G^* \to f\bar{f}$	$\lvert d^2_{2,1}\rvert^2 + \lvert d^2_{2,-1}\rvert^2$	$P_g = \frac{5}{8}(1 - \cos^4\theta^*)$
$q\bar{q} \to \gamma^*/\mathrm{Z}^0/\mathrm{Z}' \to f\,\bar{f}$	$\lvert d^1_{1,1}\rvert^2 + \lvert d^1_{1,-1}\rvert^2$	$P_1 = \frac{3}{8}(1 + \cos^2\theta^*)$

3.3.6. Discriminating between different spin hypotheses

In order to distinguish the spins of a spin-1 Z′ bosons and a spin-2 gravitons in a dilepton decay mode, Ref. [115] considers an unbinned likelihood ratio statistic incorporating the angles of the decay products. The statistical interpretation of this statistic is discussed in detail in Ref. [116], also considering the possibility of spin 0.

To leading order, the sub-diagram for Z′ formation is quark-anti-quark ($q\bar{q}$) annihilation, while for a graviton there exist both $q\bar{q}$ annihilation and gluon-gluon (gg) fusion. One defines θ^* as the angle in the dilepton centre-of-mass reference frame between the negative lepton ℓ^- and the incident quark or gluon. In this section, we consider only the parity-conserving terms; inference from these terms can be combined with that of the parity-violating terms giving rise to A_{FB}.

For light lepton decay products, the angular probability density functions in the absence of interference are in Table 3.10. These are determined from angular momentum considerations and do not depend on the couplings. For the spin-2 graviton, only the relative fractions of $q\bar{q}$ annihilation, gluon fusion, and background (predominantly from the Drell–Yan continuum) events are needed to arrive at a parameter-free form for the expected distribution. (For spin 1, the resonance and the Drell–Yan background have the same form.)

The fractions of generated events arising from these processes are denoted by ϵ_q, ϵ_g, and ϵ_1, respectively, with $\epsilon_q + \epsilon_g + \epsilon_1 = 1$. Then the form of the probability density $P(\cos\theta^*)$ is

$$P(\cos\theta^*) = \epsilon_q P_q + \epsilon_g P_g + \epsilon_1 P_1. \tag{3.24}$$

As in the A_{FB} measurements, we let θ^*_{CS} denote the polar angle of the ℓ^- in the Collins–Soper frame. Experimentally, one will obtain a set of events with θ^*_{CS} measured along with other quantities such as dilepton transverse momentum $p_{\mathrm{T}}^{\mathrm{dil}}$ and rapidity y^{dil}. From these, one can construct the probability density $P_{\mathrm{acc}}(\cos\theta^*_{\mathrm{CS}})$ for events accepted (observed) in an experiment for each hypothesis H_i, where i labels the model such as Z′ or G*. In this study, we consider only the angular information and integrate over $p_{\mathrm{T}}^{\mathrm{dil}}$, y^{dil}, and any other relevant quantities; if one has confidence that these quantities are well described by the event generators, more variables can be added to P_{acc}. Since we do not add this information, P_{acc} for accepted events approximately factorises:

$$P_{\mathrm{acc}}(\cos\theta^*_{\mathrm{CS}}|H_i) = P(\cos\theta^*_{\mathrm{CS}}|H_i)\,\overline{\Omega}(\cos\theta^*_{\mathrm{CS}}), \tag{3.25}$$

where $P(\cos\theta^*_{\mathrm{CS}}|H_i)$ is from Eq. (3.24) with the ε_j set appropriately for the model considered (e.g. for the spin-1 hypothesis, we set $\epsilon_1 = 1$ and $\epsilon_q = \epsilon_g = 0$), and $\overline{\Omega}$ is the acceptance averaged over p_{T}, y, etc.

Eq. (3.25) has no free parameters, if the fractions ε_q, ε_g, and ε_1 are considered to be fixed. For each observed event, one evaluates $P_{\mathrm{acc}}(\cos\theta^*_{\mathrm{CS}}|H_i)$ at the observed $\cos\theta^*_{\mathrm{CS}}$ to obtain the *likelihood* $\mathcal{L}(H_i)$ of that event under the given hypothesis. The combined likelihood of the data set under a hypothesis is then the product of the events' likelihoods; henceforth in this paper,

Table 3.11. Integrated luminosity and numbers of signal and background events N_s and N_b required to discriminate spin-1 and spin-2 hypotheses with $\alpha = \beta$ corresponding to 2σ (one-tailed). The first column indicates the mass of the resonance; the second column shows the values of the RS ratio $c = k/\bar{M}_{\mathrm{Pl}}$; the third column specifies the integrated luminosity needed for 2σ discrimination; the last two columns show the corresponding numbers of signal and background events.

$\sqrt{s}$, TeV	c	$\int \mathcal{L} dt$, fb^{-1}	N_s	N_b
1.0	0.01	50	200	87
1.0	0.02	10	146	16
1.5	0.02	90	174	41
3.0	0.05	1200	154	22
3.0	0.10	290	148	6

$\mathcal{L}(H_i)$ refers to this product unless otherwise stated. As Ref. [116] discusses, the absence of free parameters means that the Neyman–Pearson hypothesis testing for *simple* hypothesis testing is applicable.

For testing a simple null hypothesis H_A of one spin against another simple alternative spin hypothesis H_B, we use the likelihood ratio $\lambda = \mathcal{L}(H_A)/\mathcal{L}(H_B)$, with critical region again chosen such that $\alpha = \beta$. For investigating and summarising which values of λ^{cut} correspond to which values of α and β, the quantity $-2\ln\lambda = 2\ln\mathcal{L}(H_B) - 2\ln\mathcal{L}(H_A)$ is particularly useful. For simple hypotheses H_A and H_B, the central limit theorem implies that $-2\ln\lambda$ tends to a Gaussian.

3.3.6.1. Testing spin 1 versus spin 2. A detailed discussion of the intermediate steps in applying the above method for discriminating spin 1 from spin 2 is in Ref. [116], using large samples of Z′ and G* events (from the Randall–Sundrum (RS) model [94]) generated with HERWIG. (Generator-level results using PYTHIA are completely compatible.) The ratio λ of the likelihoods of the hypotheses is calculated for each event, assigning spin 1 as the null hypothesis H_A and spin 2 as the alternative hypothesis H_B. In taking the ratio, the average acceptance cancels to good approximation and one essentially recovers the ratios of the angular forms. Histograms of $-2\ln\lambda$ for these events are highly asymmetric and strongly peaked at one side [116]. In view of the asymmetries in the underlying event histograms, the convergence of the sums of $-2\ln\lambda$ values for N selected events toward Gaussians is quite striking. The means and rms deviations of the sums are in excellent agreement with the means and rms deviations of the respective event histograms scaled by N and $\sqrt{N}$, respectively, as expected from the central limit theorem.

The statistical technique of Ref. [116] has been applied to fully-reconstructed Z′ and G* events [117]. Details of simulation, trigger and reconstruction are described in Sections 3.3.2, 3.3.3 and 14.3.1. From ensembles of pseudo-experiments, we determine the number N of events per experiment corresponding to various values of $\alpha = \beta$, expressed in equivalent number of Gaussian standard deviations "σ" for *one*-tailed tests, e.g., for $\alpha = 0.159$, we report $\alpha = 1\sigma$, and so on. The values of α so obtained scale as expected as $\sqrt{N}$.

Table 3.11 contains, for different studied masses and values of the Randall–Sundrum ratio $c = k/\bar{M}_{\mathrm{Pl}}$, the integrated luminosity needed for a 2σ significance, and the corresponding numbers of signal and background events. All numbers are for the "long term" misalignment scenario; the cross section for Z′ production is assumed to be equal to that of G* with the given c value. Of course, because the production cross section falls rather steeply with mass, the integrated luminosity needed for spin discrimination increases with mass. For RS gravitons, the production cross section scales as c^2; therefore, the integrated luminosity required for spin

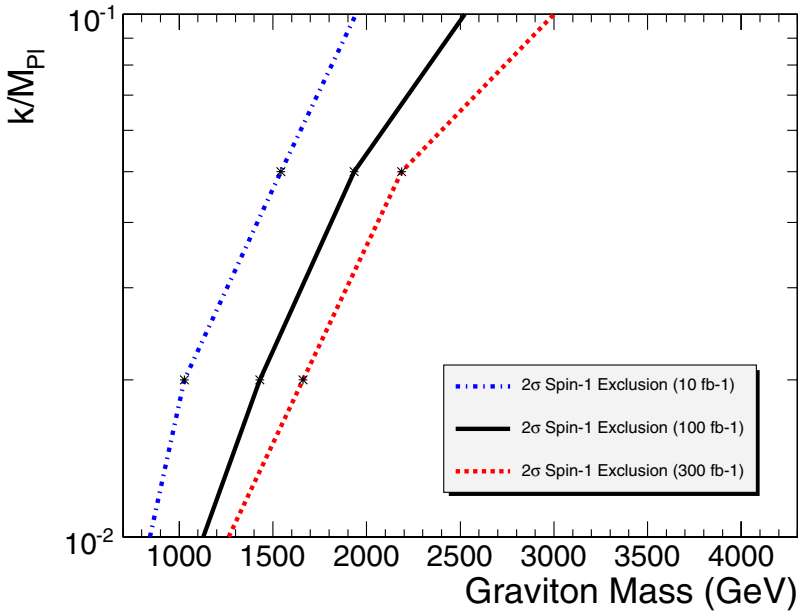

Figure 3.22. Region in the plane of M_{G^*}–c in which Randall–Sundrum G^* can be distinguished from Z' having an equal cross section with 2σ significance if one treats two spin hypotheses symmetrically, for a few representative values of the integrated luminosity. The region which can be probed lies to the left of the lines.

discrimination quickly increases as c gets smaller, and so does the number of signal events, because of a larger background contamination. The region in the plane of M_{G^*}–c in which Randall–Sundrum G^* can be distinguished from Z' with 2σ significance if one treats two spin hypotheses symmetrically is shown in Fig. 3.22 for a few representative values of the integrated luminosity.

Alternatives to the $\alpha = \beta$ criterion, in particular tests in which α is minimised for one hypothesis at the cost of increase in β, are discussed in Ref. [116].

3.3.6.2. Discrimination from spin 0. While the motivation of discriminating Z' from G^* has focused studies on discriminating spin 1 from spin 2, another possibility to be considered is spin 0 resonance (which is uniform in $\cos\theta^*$). For accepted spin-0 events, the probability density for $\cos\theta^*_{CS}$ is somewhat in between the mostly concave-upward function for spin 1 and the predominantly concave-downward function for spin 2.

As discussed in Ref. [116], discriminating either spin 1 or spin 2 from spin 0 requires significantly more events than discriminating spin 2 from spin 1.

Chapter 4. Physics Studies with Jets and $E_{\mathrm{T}}^{\mathrm{miss}}$

4.1. Benchmark Channel: new physics from dijets

Inclusive dijet production ($pp \to 2$ jets $+X$) is the dominant LHC hard scattering process. Simple to observe, and rich in potential signals of new physics, dijets are expected to be one of the earliest CMS measurements. In this section we discuss the measured distributions and their systematic uncertainties [118]. In section 14.5.2 and 15.3 we use these distributions to estimate our sensitivity to specific models of new physics.

4.1.1. Dijet analysis

We use samples generated using PYTHIA dijet processes mixed with pileup of minimum bias interactions for an assumed luminosity of $2 \times 10^{33}\,\mathrm{cm}^{-2}\,\mathrm{s}^{-1}$, simulated with OSCAR and reconstructed with ORCA. Jets are reconstructed as localised energy depositions in the CMS calorimeters arranged in a projective tower geometry. The jet energy E is defined as the scalar sum of the calorimeter tower energies inside a cone of radius $R = \sqrt{(\Delta\eta)^2 + (\Delta\phi)^2} = 0.5$, centred on the jet direction. The jet momentum $\vec{P}$ is the corresponding vector sum of energies, with the vector pointing in the tower direction. Both the jet energy and momentum are corrected back to the particles in the jet cone originating from the hard interaction excluding pileup [119]. We define the dijet system as the two jets with the highest p_{T} in an event (leading jets) and define the dijet mass $m = \sqrt{(E_1 + E_2)^2 - (\vec{P}_1 + \vec{P}_2)^2}$. We select events in which the leading jets each have $|\eta| < 1$. This cut enhances our sensitivity to new physics, produced at low $|\eta|$, compared to the predominantly t-channel processes from the QCD background. In all plots that are a function of dijet mass, we plot in bins of width equal to the Gaussian resolution measured in section 4.1.4.1.

4.1.2. Rates and efficiencies from jet triggers

We use simulated data from the single jet triggers discussed in Appendix E.4.3.2. From the three trigger tables for luminosities of $\mathcal{L} = 10^{32}$, 10^{33}, $10^{34}\,\mathrm{cm}^{-2}\,\mathrm{s}^{-1}$ we expect initial samples of size at least $100\,\mathrm{pb}^{-1}$, $1\,\mathrm{fb}^{-1}$, and $10\,\mathrm{fb}^{-1}$ respectively. This is from 10^6 seconds of collisions, equivalent to one month of continuous operation at 40% efficiency. In Fig. 4.1 we show the rate expected from these triggers as a function of dijet mass. By construction there are comparable events in each trigger, and a high statistics overlap between triggers for a given table. We see that the highest mass dijet is expected to be 5, 6 and 7 TeV for samples of size $100\,\mathrm{pb}^{-1}$, $1\,\mathrm{fb}^{-1}$, and $10\,\mathrm{fb}^{-1}$ respectively. In Fig. 4.2 we show the trigger efficiency vs. dijet mass, measured for each trigger using the neighbouring trigger with a lower p_{T} threshold, and explicitly show the mass cuts that are fully efficient. In Fig. 4.3 we show the data we will use to measure the cross section. We use each trigger where it is fully efficient and stop using the trigger where the next trigger is fully efficient. Fig. 4.3 shows there are adequate numbers of fully efficient events for analysis.

4.1.3. Dijet mass distribution from QCD

In Fig. 4.4 we combine the triggers to produce a cross section across the full mass spectrum. The prescaled triggers allow us to measure mass down to $300\,\mathrm{GeV/c}^2$, or even smaller if we can understand the efficiency of the lowest threshold trigger. The mass measured with the prescaled triggers will allow us to connect to dijet masses measured at the Tevatron.

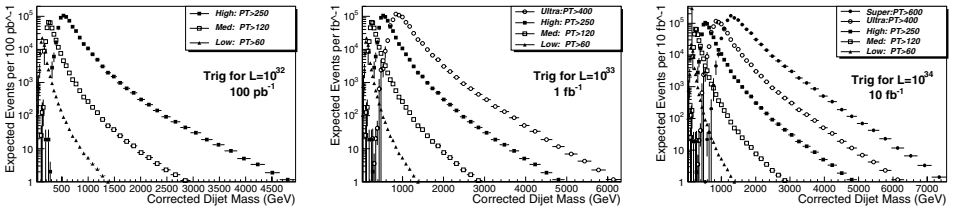

Figure 4.1. Rate of jet trigger as a function of dijet mass. The 3 plots correspond to 3 trigger tables, and each plot shows multiple triggers with various p_T thresholds and prescales.

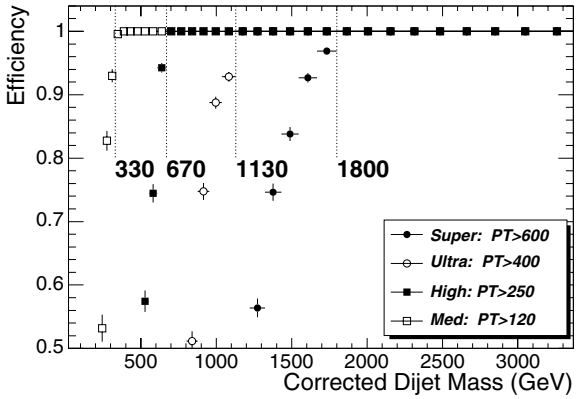

Figure 4.2. Jet trigger efficiency (points) and fully efficient dijet mass cuts (lines).

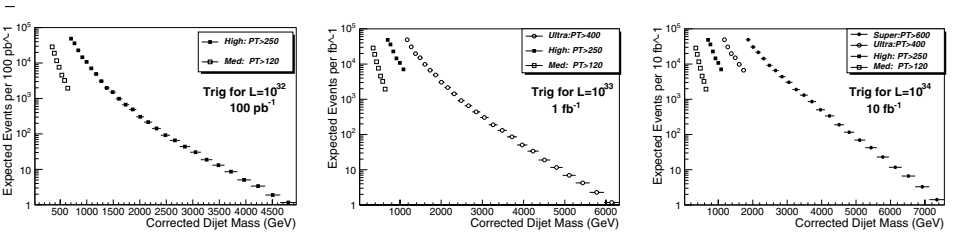

Figure 4.3. Rate of jet trigger for cross section measurement. Same triggers as Fig. 4.1.

In Fig. 4.5 we show the fractional statistical error on the cross section, the simplest measure of our sensitivity to new physics. Figure 4.5 shows that our prescaled triggers will allow a measurement of QCD with 1–3% statistical accuracy. The unprescaled triggers will have 1% error at threshold and the first unprescaled sample begins at a mass of 670 GeV/c^2, giving us full sensitivity to new physics in a region that overlaps with previous dijet mass measurements at the Tevatron.

4.1.4. Searches using dijet mass

Here we will discuss the signal and background distributions that are needed for a dijet resonance search using the mass distribution. In section 14.5.2 we use these techniques to estimate our sensitivity to seven models of narrow dijet resonances.

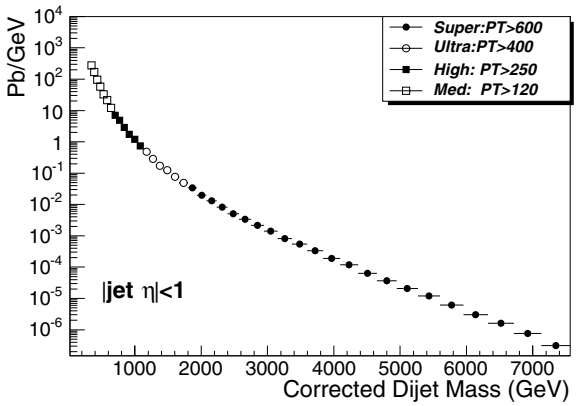

Figure 4.4. Cross section vs. dijet mass and the contributing jet triggers.

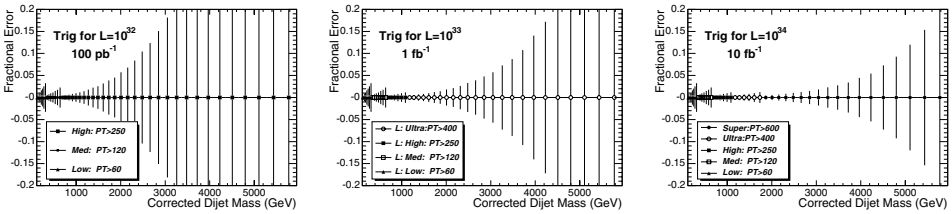

Figure 4.5. Fractional statistical error on the jet cross section for the samples in Fig. 4.5.

4.1.4.1. Narrow dijet resonance shapes. The simulated shape of a narrow dijet resonance in CMS is shown in Figure 4.6. The shape is composed of a Gaussian distribution from jet energy resolution and a long tail to low mass. The measured RMS of the Gaussian component is $\sigma/M = 0.045 + 1.3/\sqrt{M}$. The long tail to low mass comes predominately from final state QCD radiation (extra jets) which reduce the reconstructed mass. All resonances with a natural width significantly less than our resolution should look similar to this in the CMS detector. The model used in Figure 4.6 was a Z' from PYTHIA.

4.1.4.2. QCD background to dijet resonances. Figure 4.6 compares a Z' signal cross section to the QCD background found in section 4.1.3. The differential cross section for the QCD background is well fit by a simple parametrisation of the form

$$\frac{d\sigma}{dm} = \frac{p_0(1 - m/\sqrt{s})^{p_1}}{m^{p_2}} \tag{4.1}$$

where m is the dijet mass, $\sqrt{s} = 14000\,\mathrm{GeV/c^2}$ is the collision energy, and p_0, p_1, p_2 are arbitrary parameters. The resonance sensitivity estimates in section 14.5.2 use this parametrisation to smooth away background fluctuations in our simulation sample. In a search with real data, a similar parametrisation could be used to simply model the measured background, as was done by CDF [120], or a full NLO QCD calculation smeared with the jet resolution could be used to model the background, as was done by D0 [121].

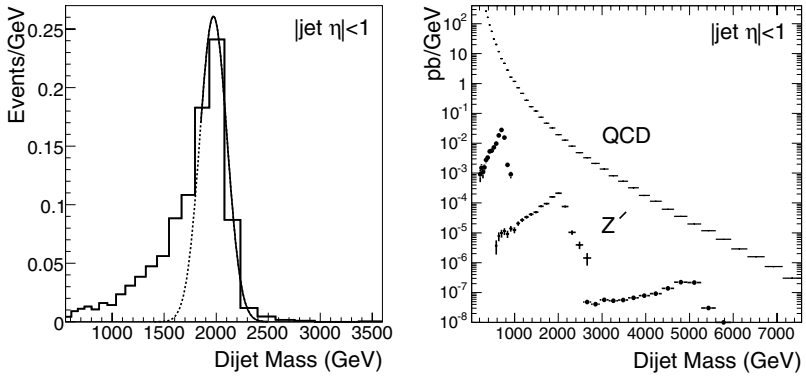

Figure 4.6. (Left) The dijet mass distribution from a 2 TeV/c^2 Z' (histogram) is fit with a Gaussian (solid curve) from the peak region to high mass and the Gaussian is extended to lower mass (dashed curve). (Right) The differential cross section as a function of dijet mass for the QCD background and three Z' signals with a mass of 0.7, 2, and 5 TeV/c^2.

4.1.5. Searches using dijet mass and angle

Here we will discuss the signal and background distributions that are used for searches for new physics in the dijet mass and angular distribution simultaneously. This technique can be used to confirm resonances observed in the dijet mass distribution, and measure their spin, or to discover other new physics that could affect the dijet angular distribution. In section 15.3 we use these techniques to estimate our sensitivity to a model of quark contact interactions.

4.1.5.1. Dijet ratio: $N(|\eta| < 0.5)/N(0.5 < |\eta| < 1.0)$. The ratio of the number of dijets in which both jets have $|\eta| < 0.5$ to the number of dijets in which both jets have $0.5 < |\eta| < 1.0$ was first introduced by D0 to search for contact interactions as a function of dijet mass [122]. It is the simplest measure of the most sensitive part of the angular distribution, providing a single number we can measure as a function of dijet mass. In Figure 4.7 we show our lowest order calculation of the dijet ratio from QCD compared with a left-handed contact interaction among quarks [123, 124] at three different values of the contact interaction scale. For this calculation we used the same code as [125] with modern parton distributions [12]. Lowest order QCD gives a fairly flat dijet ratio around 0.6 while the contact interactions produce an increase in the dijet ratio at high mass. Figure 4.7 also shows that a full CMS detector simulation of the dijet ratio from QCD, using the samples discussed in section 4.1.3, is indistinguishable from a flat ratio of 0.6 within the simulation statistical uncertainty.

4.1.6. Systematic uncertainties

In figure 4.8 we present estimates of systematic uncertainties on both the dijet cross section and the dijet ratio. The systematics discussed below have a large effect on the cross section and little effect on the dijet ratio.

4.1.6.1. Absolute jet energy scale. We have concluded that an overall uncertainty on the jet energy scale in the barrel of $\pm 5\%$ is achievable [126]. We have propagated this energy scale error to the dijet mass cross section by measuring the effect of a $\pm 5\%$ change in mass on a smooth fit to the dijet mass cross section. As shown in figure 4.8, the resulting upper uncertainty on the cross section varies from 30% at a dijet mass of 0.3 TeV/c^2 to 80% at

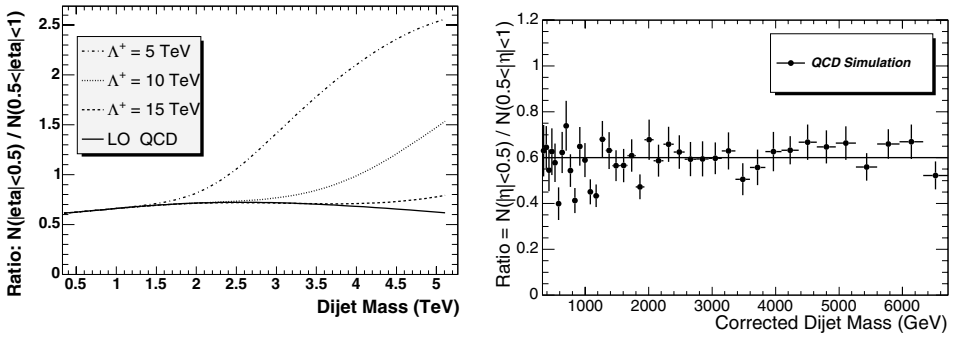

Figure 4.7. (Left) A lowest order calculation of the dijet ratio from QCD (solid curve) is compared with QCD plus a quark contact interaction at a scale Λ^+ of 15 TeV (dashed), 10 TeV (dotted) and 5 TeV (dot-dashed). (Right) The dijet ratio in the CMS simulation from QCD (points) is compared to the value 0.6 (line).

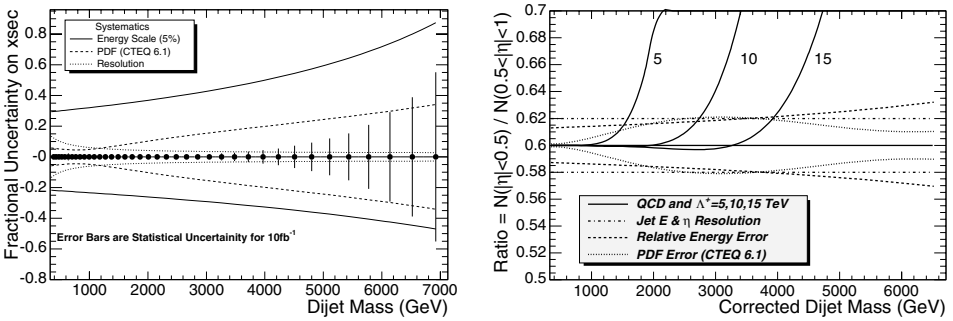

Figure 4.8. (Left) Systematic uncertainty on the dijet cross section due to jet energy scale (solid curve), parton distributions (dashed curve), and calorimeter energy and η resolution (dotted curve) are compared to the statistical uncertainties for 10 fb^{-1} (error bars). (Right) Systematic bounds on the dijet ratio from uncertainties in the relative jet energy scale (dashed curve), parton distributions (dotted curve), and calorimeter energy and η resolution (dot dash curve), are compared to the expectations of QCD and three contact interaction scales (solid line and curves).

a dijet mass of 6.5 TeV/c^2. This large systematic uncertainty, increasing with dijet mass, is the primary reason we do not use the dijet mass distribution to search for quark contact interactions. For the dijet ratio the absolute jet energy scale uncertainty has no effect, because the dijet ratio is flat versus dijet mass. The uncertainty cancels out in the ratio.

4.1.6.2. Relative jet energy scale. We have shown that by using dijet balance an uncertainty of $\pm 0.5\%$ is achievable [127] for the relative jet energy scale as a function of η within the barrel, in 0.1 steps in η. Here we assume that the relative jet energy scale, defined in this analysis as the uniformity in energy scale in the region $0.5 < |\eta| < 1.0$ compared to $|\eta| < 0.5$, can be determined to $\pm 0.5\%$. For the cross section as a function of mass this uncertainty is negligible compare to the $\pm 5\%$ error in the absolute energy scale. We have propagated this error to the dijet ratio by measuring the effect of a $\pm 0.5\%$ change in dijet mass for the measurement of $N(0.5 < |\eta| < 1)$ while keeping $N(|\eta| < 0.5)$ unchanged. As shown in figure 4.8, the resulting upper uncertainty in the ratio varies from 0.013 (2%) at a mass of 0.3 TeV/c^2 to 0.032 (5%) at a mass of 6.5 TeV/c^2.

4.1.6.3. Resolution. The effect of calorimeter resolution is the difference between the measurement with jets constructed from MC particles (Gen Jets) and the measurement with jets constructed from calorimeter depositions and corrected (Rec Jets). This difference, often called the smearing due to calorimeter resolution, is taken as a bound on the size of the systematic uncertainty due to resolution. For the cross section, the difference between Rec Jets and Gen Jets is small. This smearing varies from 15% at 0.3 TeV to 3% at 6.5 TeV, as shown in Figure 4.8. For the ratio, there is no change between Gen Jets and corrected Rec Jets within the Monte Carlo statistics presented in Fig. 4.7, and the statistical error on the simulation gives a bound on the systematic of 0.02 (3%) in the ratio, which is shown in Figure 4.8.

4.1.6.4. Parton distributions. We have used these 40 PDFs of CTEQ6.1 and the recommended procedure [12] to calculate the PDF uncertainties on both the cross section and the dijet ratio using our lowest order QCD calculation. As shown in figure 4.8, the resulting upper uncertainty in the cross section varies from 5% at a dijet mass of 0.3 $\mathrm{TeV/c^2}$ to 32% at a dijet mass of 6.5 $\mathrm{TeV/c^2}$. As shown in figure 4.8, the resulting uncertainty in the dijet ratio peaks at a value of 0.02 (3%) in the ratio at a mass of around 3.5 $\mathrm{TeV/c^2}$, and declines at both lower and higher masses.

4.1.6.5. Luminosity, efficiency and acceptance. The luminosity uncertainty on the cross section is around 10%, small compared to other uncertainties, and has no affect on the dijet ratio. For the masses we consider in this analysis there is full efficiency for finding a dijet in the event with negligible uncertainty. The acceptance for jets is defined by the cut in η, and any measured jet distributions must be compared to calculations using the same η cuts, with negligible uncertainty in the comparison of measured and calculated jet η.

4.2. Benchmark Channel: low mass supersymmetry

4.2.1. Introduction

R-parity conserving SUSY leads to characteristic signatures with missing transverse energy in the final state due to the stable lightest supersymmetric particle (LSP). In the search described below for the bosonic partners of quarks (squarks) and the fermionic partners of gluons (gluinos) it is assumed that the LSP is weakly interacting, as is the case for most of the MSSM parameter space.

This analysis focuses on gluino and squark production within the minimal supergravity model (mSUGRA). In this model the entire SUSY mass spectrum is essentially determined by only five unknown parameters: the common scalar mass at the GUT scale, M_0; the common gaugino mass at the GUT scale, $M_{1/2}$; the common trilinear coupling at the GUT scale, A_0; the sign of the Higgsino mixing parameter, $sign(\mu)$; and the ratio of the Higgs vacuum expectation values, $\tan\beta$.

We investigate whether the production and decay of gluinos and scalar quarks is observable in the rate of $\geqslant$3-jet events with large missing transverse energy. The large missing energy originates from the two LSPs in the final states of the squark and gluino decays. The three or more hadronic jets result from the hadronic decays of the squarks and/or gluinos. We use the ISAJET (7.69) Monte Carlo program interfaced with PYTHIA (6.225) which provides parton shower and an underlying event model to generate squark and gluino production with parameters $M_0 = 60\,\mathrm{GeV/c^2}$, $M_{1/2} = 250\,\mathrm{GeV/c^2}$, $A_0 = 0$, $\mu > 0$ and $\tan\beta = 10$ (LM1 test point). For this set of parameters $m(\tilde{g}) \sim 600\,\mathrm{GeV/c^2}$, $m(\tilde{q}) \sim 550\,\mathrm{GeV/c^2}$, $(m(\tilde{g}) > m(\tilde{q}))$ and production of $\tilde{g}\tilde{q}$ is 53%, $\tilde{q}\tilde{q}$ 28% and $\tilde{g}\tilde{g}$ 12%. The decay $\tilde{g} \to \tilde{q}_{L,R} + q$ is dominant.

Specifically the gluino and squark decays proceed as follows:

$$\tilde{g} \to q\bar{\tilde{q}}_{L,R}, \qquad \text{or} \qquad \tilde{g} \to \bar{q}\tilde{q}_{L,R} \tag{4.2}$$

$$\tilde{q_R} \to q\,\tilde{\chi}_1^0,\ (100\%) \tag{4.3}$$

$$\tilde{q}_L \to q + \tilde{\chi}_2^0,\ (30\%) \tag{4.4}$$

$$\tilde{q}_L \to q + \tilde{\chi}_1^+,\ (70\%) \tag{4.5}$$

while the charginos and neutralinos decay as follows:

$$\tilde{\chi}_2^0 \longrightarrow \tilde{\ell}_R\ell,\ (11.2\%) \tag{4.7}$$

$$\tilde{\chi}_2^0 \longrightarrow \tilde{\tau}_1\tau,\ (46\%) \tag{4.8}$$

$$\tilde{\chi}_1^+ \longrightarrow \tilde{\nu}_L\ell,\ (36\%). \tag{4.9}$$

The total LO production cross section for squarks and gluinos at this point of the mSUGRA parameter space is 49 pb. An example of a SUSY candidate is shown in colour plate CP6. The major Standard Model background components for a multi-jet plus large missing transverse energy search include production of Z + jets with the Z decaying invisibly, W + jets, top–anti-top pairs, dibosons, single top and QCD jets.

4.2.2. Jets and missing transverse energy at CMS

Jets are defined as localised energy depositions in the calorimeters and are reconstructed using an iterative clustering algorithm with a fixed cone of radius $\Delta R \equiv \sqrt{\Delta\eta^2 + \Delta\phi^2} = 0.5$ in $\eta - \phi$ space [7]. Jets are ordered in transverse energy, $E_{\mathrm{T}} = E\sin\theta$, where E is the scalar sum of energy deposited in the calorimeter towers within the cone, and θ is the angle formed by the beam-line, the event vertex, and the cone centre. Jets with uncorrected $E_{\mathrm{T}} > 30\,\mathrm{GeV}$ and with $|\eta| < 3$ are used throughout this analysis.

The offline missing transverse energy is defined as the negative vector sum of the transverse energy in the electromagnetic and hadronic calorimeter towers, $E_{\mathrm{T}}^{\mathrm{miss}} = -\sum_i (E_i \sin\theta_i)\hat{n}_i$, where E_i is the energy of the i-th tower, $\hat{n}_i$ is a transverse unit vector pointing to the centre of each tower, and θ_i is the polar angle of the tower; the sum extends to $|\eta| < 5$. The data sample is selected with a hardware trigger which requires $E_{\mathrm{T}}^{\mathrm{miss},L1} > 46\,\mathrm{GeV}$ ($|\eta| < 5$ coverage) and a central jet of $E_{\mathrm{T}} > 88\,\mathrm{GeV}$. A parametrisation of the Level-1 trigger efficiency as measured in a dijet sample is applied to all data analysed. For the confirmation of the High Level Trigger (HLT) the $E_{\mathrm{T}}^{\mathrm{miss}}$ is required to be above 200 GeV where the HLT trigger is fully efficient. In the following sections we detail the methodology and analysis strategies towards a search for SUSY using a dataset of events collected according to the missing transverse energy plus jet Level-1 and HLT trigger path.

4.2.3. Clean-up requirements

In anticipation of real data a pre-selection is used to reject accelerator- and detector-related backgrounds (such as beam halo and noise), and cosmic ray events. At least one primary vertex is required in the event and the pre-selection uses the event electromagnetic fraction, F_{em} (defined as the E_{T}-weighted jet electromagnetic fraction sum over the electromagnetic calorimeter acceptance, $|\eta_d| \leqslant 3.0$) and event charged fraction, F_{ch} (defined as the average over the jets ratio of the sum of the P_{T} of the associated to the jet tracks for jets within $|\eta| < 1.7$, over the calorimetric jet transverse energy) to distinguish between real and fake jet events. The pre-selection requirements and their efficiency on the signal are shown in

Table 4.1. Cleanup pre-selection efficiency.

Sample/Requirement	$F_{em} > 0.1$	$F_{ch} > 0.175$	Both (%)
LM1	99.88%	91.32%	91.24%

Table 4.2. The $E_{\mathrm{T}}^{\mathrm{miss}}$ + multi − jet SUSY search analysis path.

Requirement	Remark
Level 1	Level-1 trigger eff. parameter.
HLT, $E_{\mathrm{T}}^{\mathrm{miss}} > 200\,\mathrm{GeV}$	trigger/signal signature
primary vertex $\geqslant 1$	primary cleanup
$F_{em} \geqslant 0.175$, $F_{ch} \geqslant 0.1$	primary cleanup
$N_j \geqslant 3, \lvert\eta_d^{1,j}\rvert < 1.7$	signal signature
$\delta\phi_{min}(E_{\mathrm{T}}^{\mathrm{miss}} - jet) \geqslant 0.3$ rad, $R1$, $R2 > 0.5$ rad, $\delta\phi(E_{\mathrm{T}}^{\mathrm{miss}} - j(2)) > 20^{\circ}$	QCD rejection
$Iso^{ltrk} = 0$	ILV (I) $W/Z/t\bar{t}$ rejection
$f_{em(j(1))}$, $f_{em(j(2))} < 0.9$	ILV (II), $W/Z/t\bar{t}$ rejection
$E_{\mathrm{T},j(1)} > 180\,\mathrm{GeV}$, $E_{\mathrm{T},j(2)} > 110\,\mathrm{GeV}$	signal/background optimisation
$H_{\mathrm{T}} > 500\,\mathrm{GeV}$	signal/background optimisation
SUSY LM1 signal efficiency 13%	

Table 4.1. The values of the requirements are chosen based on the Tevatron data where similar requirements have been used to clean the high p_{T} multi-jet plus large missing transverse energy datasets from a number of spurious and instrumental backgrounds that tend to appear as spikes in the low end of the event electromagnetic and charge fraction distributions.

4.2.4. Analysis path

Events that are accepted by the pre-selection requirements, proceed through the analysis path if they have missing transverse energy $E_{\mathrm{T}}^{\mathrm{miss}} > 200\,\mathrm{GeV}$ and at least three jets with $E_{\mathrm{T}} \geqslant 30\,\mathrm{GeV}$ within $|\eta| < 3$. In addition the leading jet is required to be within the central tracker fiducial volume *i.e.* $|\eta| < 1.7$. These requirements directly define the SUSY signal signature. The rest of the analysis path is designed based on elimination of the major classes of backgrounds: the QCD production, top–anti-top pairs and the W/Z-QCD associated production. In Table 4.2 the path is shown with a remark indicating the reason and aim of each selection step.

In the following sections the motivation and details of the analysis path are discussed.

4.2.5. Missing transverse energy in QCD production

Due the very high QCD production cross section the Standard Model background to a large missing transverse energy plus jets data-sample is dominated by QCD events. The observed missing transverse energy in QCD jet production is largely a result of jet mis-measurements and detector resolution. In Figure 4.9 the missing transverse energy full spectrum is shown for QCD 3-jet events in the $\hat{p_{\mathrm{T}}}$ region between 120 GeV/c and 1.8 TeV/c.

It is to be noted that due to finite computing resources and the large production cross section it is unrealistic to fully simulate and reconstruct samples with adequate Monte Carlo statistics. It is also unrealistic due to the trigger and data acquisition bandwidth constraints and the large QCD production cross section to collect QCD datasets with low E_{T} thresholds during data-taking. However the CMS trigger table includes a large number of prescaled

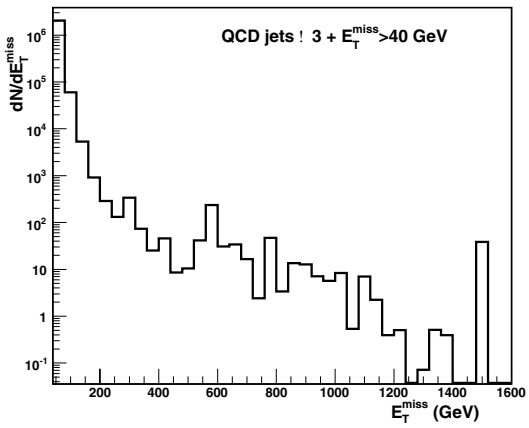

Figure 4.9. $E_{\mathrm{T}}^{\mathrm{miss}}$distribution in QCD 3-jet events.

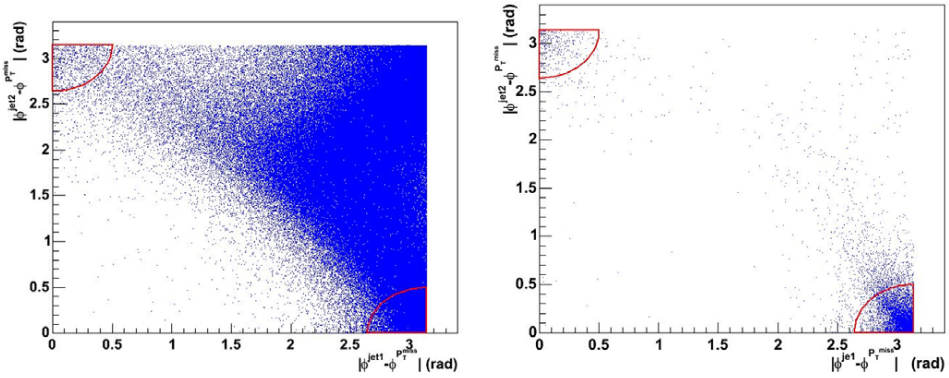

Figure 4.10. $\delta\phi_1$ versus $\delta\phi_2$ for (left) SUSY signal and (right) QCD dijet events.

QCD trigger paths that will be used to extract the shape of the missing transverse energy and the direct normalisation for the QCD background component in all-hadronic events with large missing energy. In addition, topological requirements are designed to eliminate as much as possible the QCD contribution. Well measured QCD dijet events with back-to-back in ϕ jet topology are used for obtaining jet corrections. These are well balanced events with low missing transverse energy. Large missing energy in QCD events originates from jet mis-measurements. In such events the highest E_{T} jet is typically the most accurately measured. When any jet in the event is mis-measured, usually the second or third jet, the $E_{\mathrm{T}}^{\mathrm{miss}}$ direction is pulled close in ϕ to the mis-measured jet direction. We eliminate such residual QCD component by using the correlation in the $\delta\phi_1 = |\phi_{\mathrm{j}(1)} - \phi(E_{\mathrm{T}}^{\mathrm{miss}})|$ versus $\delta\phi_2 = |\phi_{\mathrm{j}(2)} - \phi(E_{\mathrm{T}}^{\mathrm{miss}})|$ plane, as shown is Figure 4.10. Events with $R_1 > 0.5$ rad and $R_2 > 0.5$ rad, where $R_1 = \sqrt{\delta\phi_2^2 + (\pi - \delta\phi_1)^2}$ and $R_2 = \sqrt{\delta\phi_1^2 + (\pi - \delta\phi_2)^2}$, are accepted. In addition we require that no jet in the event be closer than 0.3 rad to the missing energy direction and that the second jet be further than 20° from it (Figure 4.11).

After a baseline selection of $N_j \geqslant 2$ and $E_{\mathrm{T}}^{\mathrm{miss}} > 93$ GeV the cumulative efficiency of the angular requirements is ∼90% for the SUSY signal. They reject ∼85% of all QCD events.

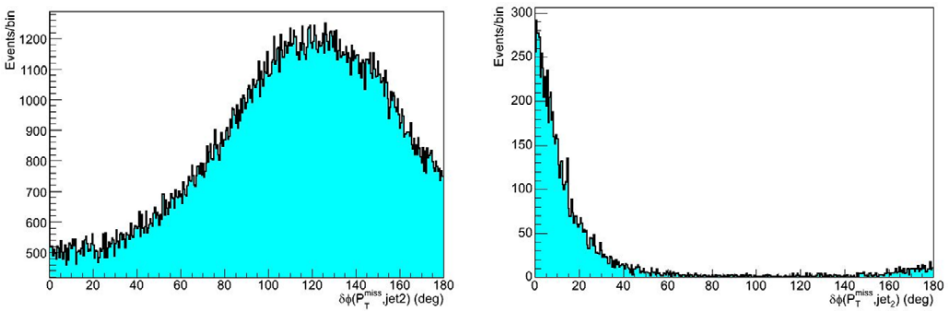

Figure 4.11. $\delta\phi_2 = |\phi_{j(2)} - \phi(E_{\mathrm{T}}^{\mathrm{miss}})|$ for (left) SUSY signal and (right) QCD dijet events.

4.2.6. Indirect Lepton Veto

W and Z + jet events with large boson P_{T} and leptonic decays of the boson are backgrounds to a large missing transverse energy plus multijet search. Similarly semileptonic $t\bar{t}$ events where the W boson decays leptonically constitute a background. In the W leptonic decays there is real missing energy due to the neutrino while in the Z decays the missing energy is mostly due to τ decays or missed leptons. Residual background when the bosons decaying hadronically (with missing energy due to jet mis-measurements) are accounted for using the real multi-jet data triggers.

In this analysis there is no explicit lepton identification. Leptons in the signal SUSY events result from cascade decays of squarks and gluinos through charginos and neutralinos. To reduce the large background contribution mainly from $W(\rightarrow \ell\nu) + jets$ and $t\bar{t}$ production and decays, an *indirect lepton veto* (ILV) scheme is designed. The aim of the indirect lepton veto is twofold: (a) to retain large signal efficiency and (b) to achieve large rejection of the W, Z, $t\bar{t}$ backgrounds (independent of the MC used, namely parton shower only versus complete matrix element in particular for the higher jet multiplicity bins).

Given that electrons are also clustered as jets, the jet electromagnetic fraction, f_{em}, which is close to 1 for electrons, is efficient in rejecting backgrounds events containing electrons while retaining good efficiency in the LM1 SUSY inclusive signal. Events are selected if the two highest E_{T} jets are not purely electromagnetic, *i.e.* $f_{em,j(1)} < 0.9$ and $f_{em,j(2)} < 0.9$. The leading and second jet electromagnetic fraction distributions for $W \rightarrow e\nu$+$\geqslant 2$ jets are shown in Figure 4.12. The corresponding distributions for the SUSY LM1 signal are shown in Figure 4.13. The signal efficiency is $\sim$87% while 90% of the $W \rightarrow e\nu + \geqslant 2$ jets are rejected. A systematic uncertainty of 5% on the background rejection efficiency is assigned due to a variation between PYTHIA and ALPGEN + PYTHIA samples.

To further reject electrons, muons and taus from W and Z decays while retaining the SUSY signal efficiency a tracking isolation strategy is employed as follows: if the leading track in the event has $p_{\mathrm{T}} \geqslant 15\,\mathrm{GeV/c}$ and the ratio of the sum of the P_{T} of all tracks around it in a cone of $\Delta R = 0.35$ over the p_{T} of the track is less than 10% the event is dropped. The requirement of accepting events with a non-isolated leading track is noted in Table 4.2 as $\mathrm{Iso}^{ltrk} = 0$.

The leading isolated track veto has $\sim$92% signal efficiency while it rejects $\sim$50% of the W/Z+jets events (in PYTHIA as well as ALPGEN generated samples). The cumulative W/Z + jets rejection efficiency when both requirements of the indirect lepton veto are applied is between 50% and 90% depending on the lepton flavour, with lower rejection as expected when the boson decay product includes a τ lepton. When applied in the full analyses path it rejects 40% of $t\bar{t}$ inclusive events. The cumulative SUSY signal efficiency is $\sim$80%.

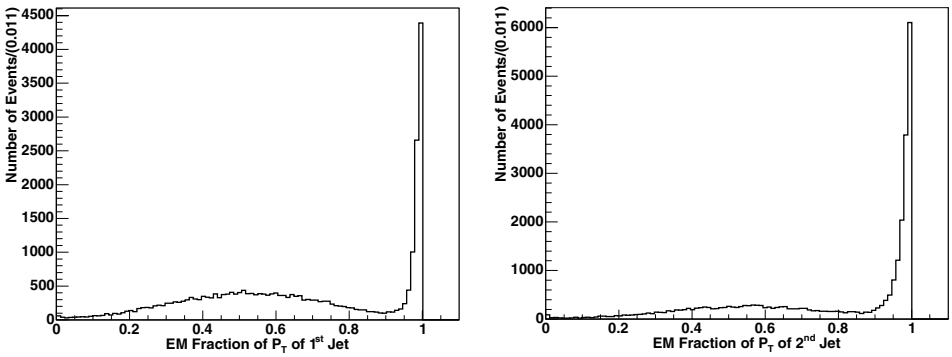

Figure 4.12. Electromagnetic fraction of (left) leading and (right) second jet in $W \to e\nu + \geqslant 2$ jets events.

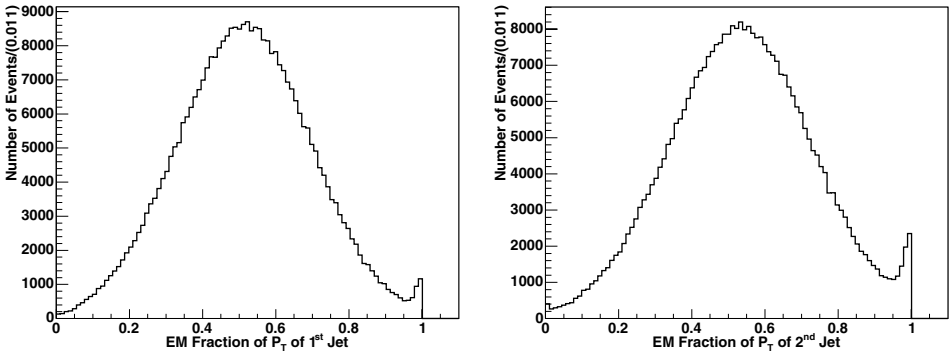

Figure 4.13. Electromagnetic fraction of (left) leading and (right) second jet in SUSY LM1 events.

4.2.7. The standard Z boson "candle" calibration

Events with large missing transverse energy and $\geqslant$3 jets in the final state are expected from $Z(\to \nu\bar{\nu}) + \geqslant 3$ jets and $W(\to \tau\nu) + \geqslant 2$ jets (the third jet originating from the hadronic τ decay) processes. Additional residual contribution is expected also from $W(\to \mu\nu), e\nu + \geqslant 3$ jets. In what follows a comprehensive normalisation program is described that relies on the Z + multi-jet data to accurately estimate the W and Z + multi-jet background contribution in a large $E_{\mathrm{T}}^{\mathrm{miss}}$ plus multi-jet search.

The $Z + N$ jets cross section is proportional to a_s^N: for each additional jet in the Z event the cross section falls by a factor proportional to a_s. The ratio of the number of events in adjacent jet multiplicity bins should remain constant and be proportional to the strong coupling constant. The multiplicity breakdown will be measured in the data and the slope returned by the exponential fit will be $R = \frac{dN_{events}}{dN_{jets}} = \frac{\mathcal{L}d\sigma}{dN_{jets}}$. This ratio measured as the two to three jet ratio in PYTHIA W + jets and Z + jets is $\sim$2.3 . An illustration of the result of the measurement that will be performed with the real data is shown in Figure 4.14 using the ALPGEN Monte Carlo cross section after parton shower matching.

The Monte Carlo predictions for events with $\geqslant 3$ jets and Z boson $P_{\mathrm{T}} > 200\,\mathrm{GeV/c}$ will be normalised to the observed $Z(\to \mu\mu) +$ 2 jets data sample (where Z boson

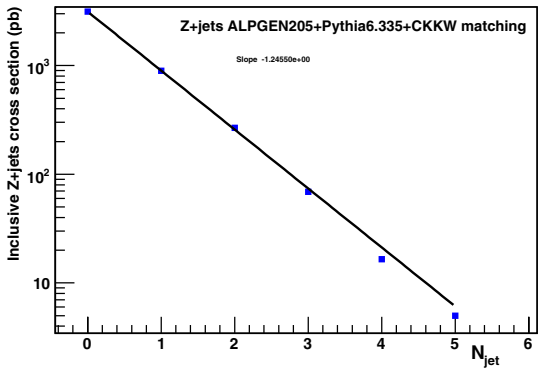

Figure 4.14. Illustration of the measurement of the $R = \frac{dN_{events}}{dN_{jets}}$ ratio in the Z + jets data. Here the ALPGEN Monte Carlo cross section is used after parton shower matching and the theoretical returned ratio is 3.8. No Z boson P_{T} requirement is used for these estimates. Slope = −1.24550

$P_{\mathrm{T}} > 200\,\mathrm{GeV/c}$) via the measured $R = \frac{dN_{events}}{dN_{jets}}$ ratio, where dN_{events} is the number of events accumulated with $\sim$1 fb^{-1} of data.

The ratio $\rho \equiv \frac{\sigma(pp \to W(\to \mu\nu) + jets)}{\sigma(pp \to Z(\to \mu^+\mu^-) + jets)}$ will be used to normalise the W+jets Monte Carlo predictions. Assuming lepton universality, the predictions for the number of events with $\geqslant 2$ jets and $\geqslant 3$ jets from W and Z production and decays to all flavours will be normalised to the $Z(\to \mu^+\mu^-)+ \geqslant 2$ jets data. By normalising the MC predictions to data large systematic effects are avoided that are due to the renormalisation scale, the choice of parton density functions, initial- and final-state radiation, and the jet energy scale. The total uncertainty ($\sim$5%) is then dominated by the uncertainty on the luminosity measurement, the uncertainty on the measured ratio $R = \frac{dN_{events}}{dN_{jets}}$ (to be measured with the data), and the uncertainty on the ratio ρ as a function of the jet multiplicity, N_{jet}.

The method will be used to absolutely normalise the Monte Carlo predictions for $Z(\to \nu\bar{\nu})+ \geqslant 3$ jets assuming that after detector simulation they will be tuned to reproduce the kinematic distributions observed in the "candle" data sample and the ratios discussed above. Note that the actual data "candle" sample can be used stand-alone to predict the rate and event kinematics of the $Z(\to \nu\bar{\nu})+ \geqslant 3$ jets process.

In this study the $Z \to \mu\mu+ \geqslant 2$ jets with $Z_{pT} > 200\,\mathrm{GeV/c}$ is the "candle" data sample. Both the muon and electron decays of the Z will be used as the standardisable candle, but for the purposes of demonstrating the method, the Z muon decays are chosen. The additional advantage of the muon channel is the efficient CMS muon detection due to the tracking and muon systems. Since the completely raw missing transverse energy is used (as is expected to be the case at the start-up of the experiment), the shape of the $E_{\mathrm{T}}^{\mathrm{miss}}$ distribution of the measured the $Z \to \mu\mu+ \geqslant 2$ jet events will be very close to the shape of the invisible $Z \to \nu\nu+ \geqslant 2$ jet events as shown in Figure 4.15. The muon decays of the Z are selected from an inclusive sample using the following requirements as baseline selection: (a) at least one primary vertex, (b) at least 2 jets with $E_{\mathrm{T}} \geqslant 30\,\mathrm{GeV}$, and $|\eta_d| \leqslant 3$, (c) $E_{\mathrm{T}}^{\mathrm{miss}} > 200\,\mathrm{GeV}$ and (d) for the Z boson identification two reconstructed muons with invariant mass closest to the measured Z boson mass (91.2 GeV/c^2) and within 20 GeV/c^2. The "Z-mass" tag requirement is 90% efficient. The selected candle sample dimuon invariant mass is shown in Figure 4.16 overlaid with the one using the Monte Carlo truth. Considering both the electron and muon decays of the Z boson, a statistically adequate (5% precision) "candle" sample to normalise the $Z \to \nu\nu + \geqslant 2$ jet predictions for $E_{\mathrm{T}}^{\mathrm{miss}} > 200\,\mathrm{GeV}$ will be obtained with $\sim$1.5 fb^{-1}.

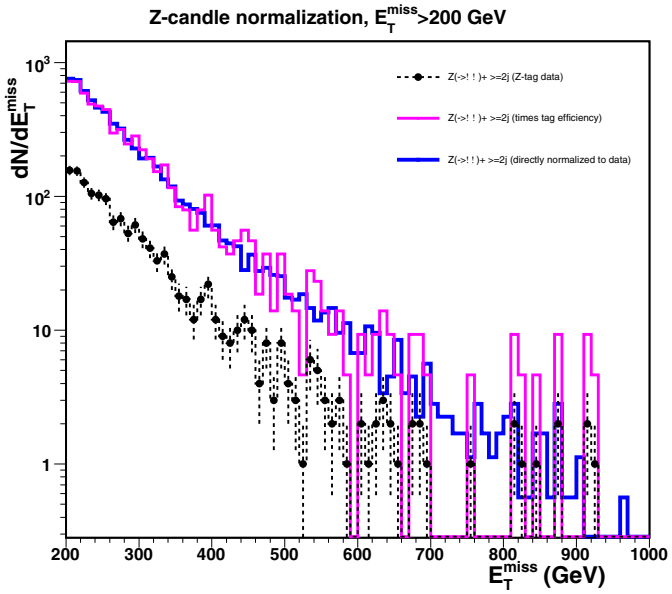

Figure 4.15. $E_{\mathrm{T}}^{\mathrm{miss}}$ in $Z \to \mu\mu + \geqslant 2$ jets candle sample and normalised $E_{\mathrm{T}}^{\mathrm{miss}}$ in $Z \to \nu\bar{\nu} + \geqslant 2$ jets sample.

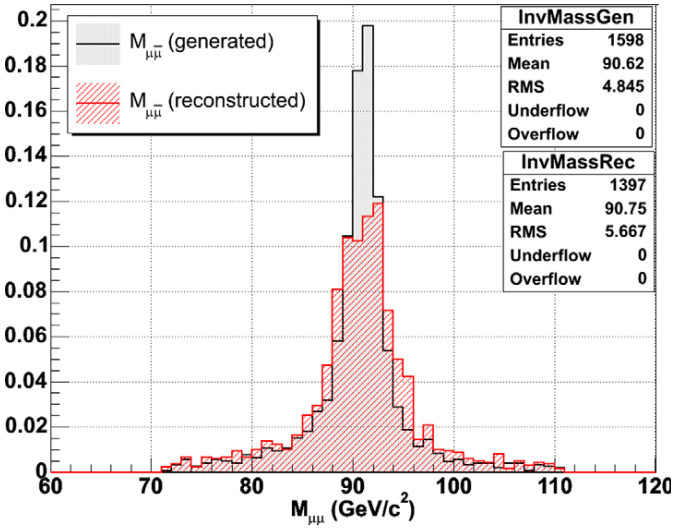

Figure 4.16. Reconstructed and generator level Z dimuon invariant mass for $Z \to \mu\mu + \geqslant 2$ jets and $E_{\mathrm{T}}^{\mathrm{miss}} > 200\,\mathrm{GeV}$.

4.2.8. Analysis results

The signal to background ratio is further enhanced in the final steps of the analysis (shown in Table 4.2) by requiring the two leading jets E_{T} be above 180 and 110 GeV respectively. Furthermore the H_{T} in the event is required to be $H_{\mathrm{T}} \equiv E_{\mathrm{T}(2)} + E_{\mathrm{T}(3)} + E_{\mathrm{T}(4)} + E_{\mathrm{T}}^{\mathrm{miss}} > 500\,\mathrm{GeV}$.

Table 4.3. Selected SUSY and Standard Model background events for 1 fb^{-1}.

Signal	$t\bar{t}$	single t	$Z(\rightarrow \nu\bar{\nu})$ + jets	$(W/Z, WW/ZZ/ZW)$ + jets	QCD
6319	53.9	2.6	48	33	107

The global signal efficiency for the analysis is 13% while the signal to background ratio is ~ 26. The results are shown in Table 4.3.

Due to the QCD Monte Carlo limited statistics to derive the QCD background component the analysis path is followed without the topological QCD clean-up requirements and ILV requirements. The estimate is conservative and is based on factorising the clean-up and ILV efficiency and assuming them uncorrelated with the rest of the analysis requirements. A parametrisation of the QCD topological clean-up requirements efficiency as a function of the $E_{\text{T}}^{\text{miss}}$ is used for $E_{\text{T}}^{\text{miss}} > 700\,\text{GeV}$.

4.2.9. Systematic uncertainties

4.2.9.1. $E_{\text{T}}^{\text{miss}}$ shape systematic uncertainty due to tails in the jet resolution. A bootstrap-like study is performed to estimate the systematic uncertainty of the $E_{\text{T}}^{\text{miss}}$ due to the non Gaussian tails in the jet resolution. The study uses the inclusive $t\bar{t}$ sample. The events are re-weighed according to a grading of the mis-measured jets, and on a jet-by-jet basis. The grading of a jet being considered mis-measured is derived from the jet resolution shape of jets in three E_{T} bins. Jets are considered mis-measured when they fall in the non-Gaussian tails of the jet resolution. The event weight is derived using each jet's weight and for three different scenarios that involve one, two or three jets being simultaneously mis-measured and positively contributing to the enhancement of the $E_{\text{T}}^{\text{miss}}$ tail. As an example when one jet is assumed to be undermeasured, 15% of the events that include the undermeasured jet (as determined by the corresponding resolution curves) are weighted up by up to 15%. A larger weight is assigned to the events with a jet lying on the downward going tail (and depending on the E_{T} of the jet) thus exaggerating the non-Gaussian jet resolution tail. The further the jet in the event is out on the tail the larger is the weight assigned to it.

The ratio of the $E_{\text{T}}^{\text{miss}}$ distribution resulting from the one, two and three under-measured jets scenarios study over the nominal $E_{\text{T}}^{\text{miss}}$ is shown in Figure 4.17 and it shows graphically the positive systematic uncertainty band as a function of the $E_{\text{T}}^{\text{miss}}$ due to jet tails in the resolution.

The positive systematic uncertainty due to one mis-measured jet in the high $E_{\text{T}}^{\text{miss}}$ tails is estimated over the bins where in the nominal distribution we have enough statistics, namely between 180 and 240 GeV (statistical uncertainty $< 5\%$). The result is 8.5%. For the scenario with the two undermeasured jets, and assuming that 50% of the times the simultaneous under-measurement results in the overestimate of the $E_{\text{T}}^{\text{miss}}$ the result is 6% and for the case of the three under-measured jets it is also 6%. We take the weighted average of these three scenarios, namely 7%, as an index of the positive systematic uncertainty due to the tails of the jet resolution in the tails of the $E_{\text{T}}^{\text{miss}}$ above 180 GeV. The result in the method presented is bound to overestimate the increase in the tails, since by design positive interference of all under-measured jets in the event is considered (in reality there is some combinatorial compensation in the $E_{\text{T}}^{\text{miss}}$ vector given the jet topology). The ultimate measurement of the shape of the high $E_{\text{T}}^{\text{miss}}$ tails and its systematic should be done using Standard Model candle physics processes in the real data such as the Z+jets and the $t\bar{t}$ data sample.

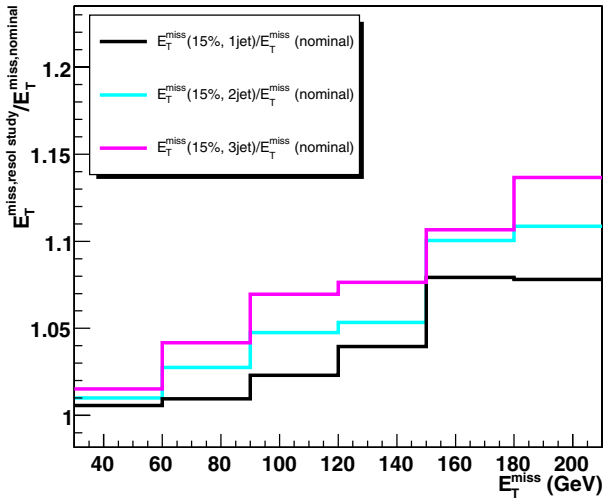

Figure 4.17. Ratio of $E_{\mathrm{T}}^{\mathrm{miss}}$ weighted distribution for one, two and three under-measured jets (described in the text) over the corresponding nominal $E_{\mathrm{T}}^{\mathrm{miss}}$ distribution.

4.2.9.2. Jet energy scale. The jet energy scale (JES) uncertainty in all hadronic analyses is playing an important role since the jet energy spectrum is steeply falling. To determine the effect of the JES uncertainty each jet four-vector is scaled with the uncertainty value α as follow:

$$\begin{aligned} p^{\mu,jet}_{scaled} &= (1 \pm \alpha) \cdot p^{\mu,jet}_{meas} \\ &= (1 \pm \alpha) \cdot (p_x, p_y, p_z, E). \end{aligned} \tag{4.10}$$

The JES uncertainty for the high E_{T} jets that enter this analysis is taken to be about 7% for 1 fb^{-1}. The resulting uncertainty in the overall analysis acceptance times efficiency in $t\bar{t}$ and QCD events is 22%.

4.2.9.3. Luminosity uncertainty. Since the W/Z + jets background is taken to be normalised with real data, the estimate carries the luminosity uncertainty on it. Hence a $\pm$5% uncertainty is taken on the background estimates due to the luminosity measurement.

4.2.9.4. ALPGEN-PYTHIA *ILV.* As discussed in section 4.2.6 a 5% positive systematic on the background estimate is taken due to the variation in efficiency of the ILV requirement between ALPGEN and PYTHIA.

4.2.9.5. Total background systematic. In summary for the major background components the uncertainties are as follows:

- $t\bar{t}$ uncertainties: 7% $E_{\mathrm{T}}^{\mathrm{miss}}$ shape, 22% JES, 13% statistical.
- $Z \to \nu\bar{\nu}$+jets, W/Z+jets: 5% Luminosity (direct candle normalisation to the data).
- QCD: $E_{\mathrm{T}}^{\mathrm{miss}}$ 7% shape, 22% JES, 10% statistical.

The number of backgrounds events per background component and their uncertainties are tabulated in Table 4.4.

Table 4.4. Standard Model background components and uncertainties for 1 fb^{-1}.

$t\bar{t}$, single top	$Z(\rightarrow \nu\bar{\nu})$+ jets	$(W/Z, WW/ZZ/ZW)$ + jets	QCD
56 ± 11(sys) ± 7.5(stat)	48 ± 3.5 (all)	33 ± 2.5 (all)	107 ± 25(sys) ± 10(stat)

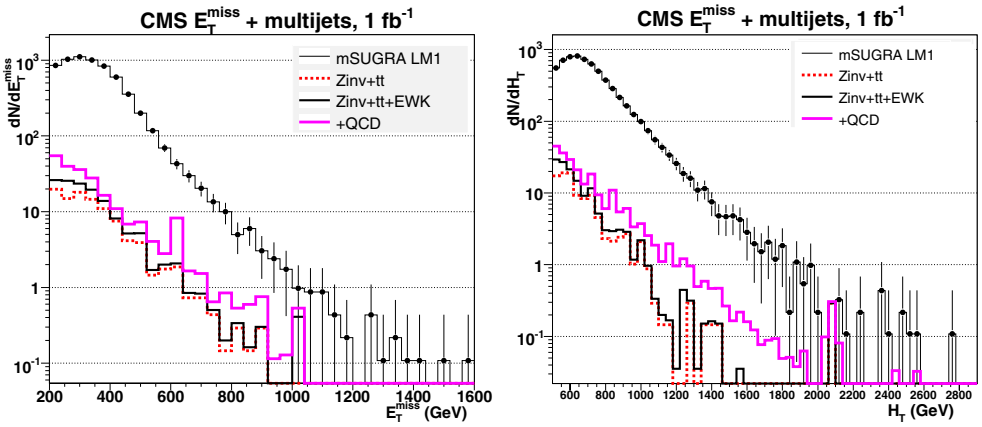

Figure 4.18. LM1 signal and Standard Model background distributions for $E_{\mathrm{T}}^{\mathrm{miss}}$ (left) and H_{T} (right).

4.2.10. Discussion

In conclusion, based on the Standard Model background estimates and their uncertainties, a 5σ observation of low mass SUSY at LM1 (gluino mass 600 GeV/c^2) is in principle achievable with ~ 6/pb in events with large missing energy plus multi-jets. It is found that with ~ 1.5 fb^{-1} the W/Z + jets background including the invisible decays of the Z boson which constitutes a large irreducible background component can be reliably normalised using the $Z \rightarrow \mu\mu$ and $Z \rightarrow ee$ + multi-jet data candle. With adequate data-based strategies of controlling and estimating the Standard Model backgrounds and their uncertainties, low mass SUSY will be discovered with 0.1–1 fb^{-1}. Furthermore the global raw $E_{\mathrm{T}}^{\mathrm{miss}}$ measurement from the calorimeter towers can be calibrated for multi-jet topologies using the tracking and muons systems and the $Z \rightarrow \mu\mu$ + multi-jet candle data sample. This analysis demonstrates that the $E_{\mathrm{T}}^{\mathrm{miss}}$ measurement from the calorimeter towers can be used as such at the startup of the experiment provided that adequate strategies are in place to discard spurious instrumental backgrounds. It is also found that an indirect lepton veto makes possible the $t\bar{t}$ and W/Z+jets background rejection, without compromising the inclusive nature of the search. In anticipation of data, there is no accurate way of accurately predicting the contribution of the QCD background tails; although the full matrix element Monte Carlo predictions (such as ALPGEN) are to date far more complete, the experiment has in place proper prescaled QCD triggers in order to estimate this background component using directly the data.

Finally the comparison of the signal, total background estimated and its components for the $E_{\mathrm{T}}^{\mathrm{miss}}$, H_{T}, N_{jet} and $M_{eff} \equiv E_{\mathrm{T}(1)} + E_{\mathrm{T}(2)} + E_{\mathrm{T}(3)} + E_{\mathrm{T}(4)} + E_{\mathrm{T}}^{\mathrm{miss}}$ are shown in Figure 4.18. It is to be underlined that the slopes of the tails of the missing energy, H_{T}, and M_{eff} distributions are very similar between the Standard Model background and the low mass SUSY signal.

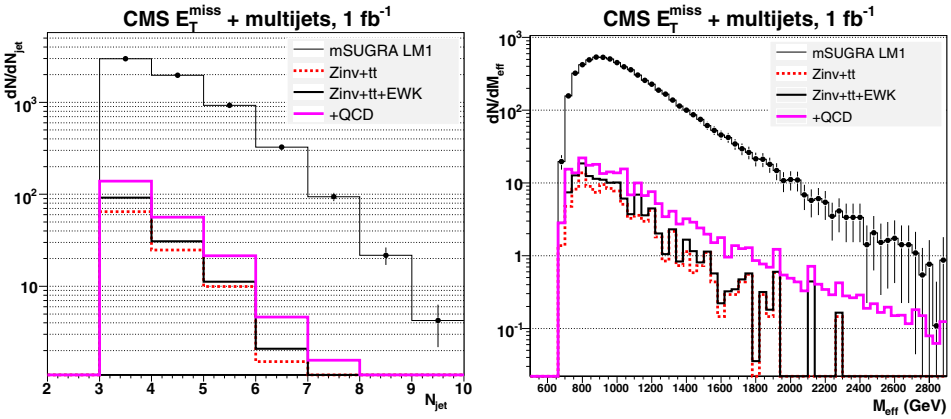

Figure 4.19. LM1 signal and Standard Model background distributions for Jet Multiplicity (left) and M_{eff} (right).

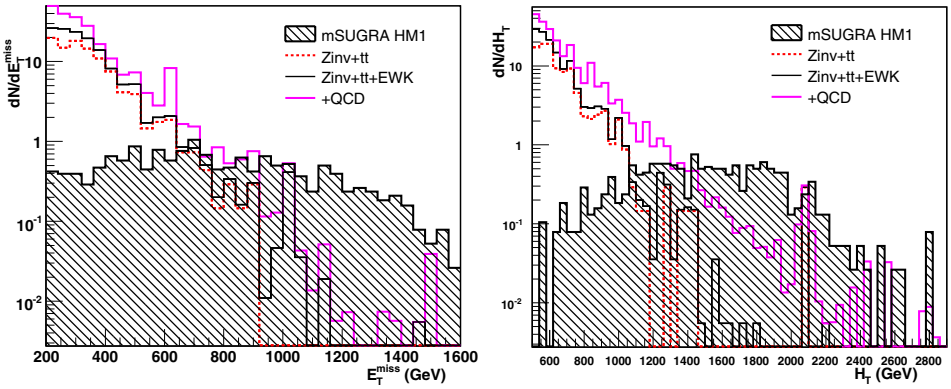

Figure 4.20. HM1 signal and Standard Model background distributions (1 fb^{-1}) for $E_{\mathrm{T}}^{\mathrm{miss}}$ (left) and H_{T} (right).

Applying the analysis in the high mass SUSY test point HM1 (with parameters $M_0 = 180\,\mathrm{GeV/c^2}$, $M_{1/2} = 850\,\mathrm{GeV/c^2}$, $A_0 = 0$, $\mu > 0$ and $\tan\beta = 10$) where $m(\tilde{g}) \sim 1890$ $\mathrm{GeV/c^2}$, $m(\tilde{q}) \sim 1700$ $\mathrm{GeV/c^2}$ the signal efficiency is 28%. The $E_{\mathrm{T}}^{\mathrm{miss}}$ and H_{T} distributions comparison between the HM1 SUSY signal and Standard Model backgrounds are shown in Figure 4.20. To perform a SUSY reach scan over the mSUGRA parameter space the optimised analysis requirements for high mass SUSY are used with $E_{\mathrm{T}}^{\mathrm{miss}} > 600\,\mathrm{GeV}$ and $H_{\mathrm{T}} > 1500\,\mathrm{GeV}$ (cf. section 13.5).

Chapter 5. Physics Studies with Tracks, B mesons, and taus

5.1. Benchmark Channels: study of the decay $B_s \to J/\psi\phi$

5.1.1. Introduction

The decay $B_s^0 \to J/\psi\phi \to \mu^+\mu^- K^+K^-$ is of particular interest, since it allows to study many properties of the B_s^0 system, such as the differences between the widths and the masses of the two weak eigenstates, B_s^H and B_s^L. Contrary to the B^0 system, the difference between the widths $\Delta\Gamma_s$ of the two weak eigenstates is expected to be large, with a relative difference $\Delta\Gamma_s/\bar{\Gamma}_s$ predicted to be in the order of 10% in the Standard Model. The first measurement from CDF ($\Delta\Gamma_s/\bar{\Gamma}_s = (65^{+25}_{-33} \pm 1)\%$ [128]) and the new preliminary result from DØ($\Delta\Gamma_s/\bar{\Gamma}_s = (15 \pm 10^{+3}_{-4})\%$ [129]) have discrepancies between the two measured values themselves and with the Standard Model prediction. It is only very recently that a first measurement of the mass difference, Δm_s, has been performed at CDF. Time-integrated measurements are not possible, as the time-integrated mixing probability χ saturates at a value of 0.5 for large mass differences, and in time-dependent measurements, the high mass difference generates very rapid oscillations. As in the B_s^0 system the ratio $\Delta m_s/\Delta\Gamma_s$ depends on the ratio $|V_{cb}V_{cs}|/|V_{tb}V_{ts}|$, which is quite well known, and on QCD corrections, a measurement of $\Delta\Gamma_s$ would therefore yield an independent measurement of Δm_s. With the measurement already performed in the B^0 system, the ratio between the mixing parameters of the B^0 and B_s^0 could provide a measurement of the ratio $|V_{ts}|/|V_{td}|$.

Furthermore, this decay provides one of the best ways to determine the height of the Unitarity Triangle, η in the Wolfenstein parametrisation. At first order of the Wolfenstein parametrisation, the CP-violating weak phase $\phi_{CKM} = [\arg(V_{cs}^* V_{cb}) - \arg(V_{ts}^* V_{tb})]$, measured in the rate asymmetry, cancels, and higher order terms have to be taken, yielding a weak phase $\phi_{CKM} = 2\lambda^2\eta$. The weak phase is therefore expected to be very small, of the order of 0.03. The measurement of a significantly larger phase would indicate contributions from non-Standard Model processes.

Because of the relative orbital angular momentum between the decay products, the $J/\psi\phi$ final state is an admixture of CP-even and CP-odd states, and the total rate asymmetry suffers from a partial cancellation. As the CP-even and CP-odd components have different angular dependences, an analysis of the angular correlation of the decay will allow to separate the two states, thereby permitting to access the different parameters.

With a total B production cross section at $\sqrt{s} = 14$ TeV expected to be as high as 500 μb, a substantial number of fully reconstructed B_s^0 candidates can be expected. Nevertheless, a high background has to be dealt with. The main sources of backgrounds identified are those containing a J/ψ decaying to two muons susceptible to satisfy the Level-1 trigger requirements.

The decay $B_s^0 \to J/\psi\phi$ is chosen as a benchmark channel since it is representative of exclusive B physics studies. It allows to study the capability of CMS to identify, select and fully reconstruct the decay of the B_s^0, which presents a significant challenge due to its relatively low momentum and high background. In addition, the measurement of the width difference $\Delta\Gamma_s$ on a sample of untagged $B_s^0 \to J/\psi\phi \to \mu^+\mu^- K^+K^-$ candidates using a maximum likelihood fit of the time dependent angular distribution can be attempted. An example of a pp $\to B_s + X$ event with $B_s \to J\psi\phi$ is shown in colour plate CP7.

5.1.2. Event generation

In addition to the signal itself, the main backgrounds identified have been simulated with low luminosity pile-up ($\mathcal{L} = 2 \times 10^{33}\,\mathrm{cm}^{-2}\,\mathrm{s}^{-1}$). Kinematic requirements were applied in

order to ensure that a significant fraction of the generated events would fulfil the Level-1 trigger requirements and that the final state particles are within the acceptance of the tracker ($|\eta| < 2.5$). The transverse momentum of the muons is thus required to be above 3 GeV/c for muons in the barrel ($|\eta| < 1.2$) and 2 GeV/c elsewhere. For the signal, the momenta of the kaons are required to be above 0.8 GeV/c.

For the samples composed of events with decays of B hadrons, $b\bar{b}$ pairs were generated with PYTHIA 6.215. The MSEL = 1 card was used in order to correctly reproduce the three different contributions to the total cross section (parton fusion, flavour excitation, and gluon splitting). The fragmentation of the b quark is performed by PYTHIA and the subsequent decay of the B hadron is performed using the SIMUB generator [130], a dedicated B physics event generator. The decay $B_s^0 \to J/\psi\phi$ has to be performed with SIMUB, since PYTHIA does not take into account the angular distributions of the final decay products.

One of the b quarks in the event is forced to hadronise to a B_s^0 or $\bar{B}_s^0$ meson and to decay through the complete decay chain. With the kinematic requirements, using the world-average branching ratios for the decays of the B_s^0, J/ψ and ϕ mesons [54], the cross section is predicted to be $\sigma(B_s^0 \to J/\psi\phi \to \mu^+\mu^- K^+K^-) = 74 \pm 27$ pb.

The inclusive decays of B hadrons to final states with a J/ψ resonance are expected to be the most important background for the measurement. These were simulated using PYTHIA, since no detailed simulation of angular distributions of the final decay products is needed. In order to increase the number of events similar to the signal events, a pair of oppositely charged particles with $p_T > 0.5$ GeV/c and $|\eta| < 2.5$ forming a fake ϕ candidate is required in a region ($|\Delta\eta| < 1.5$, $|\Delta\varphi| < 1.5$) around the J/ψ direction and with an invariant mass within 30 MeV/c^2 of the world-average ϕ mass. In addition, this fake ϕ candidate is required to form a fake B_s^0 candidate with an invariant mass within 300 MeV/c^2 of the world-average B_s^0 mass. The cross section, including the kinematic requirements and branching-fractions, is estimated to be $\sigma(b \to J/\psi X) = 3.20 \pm 0.3$ nb.

Furthermore, a sample of $B^0 \to J/\psi K^{*0} \to \mu^+\mu^- K^+\pi^-$ events were simulated, since this final state can be misidentified as a $B_s^0 \to J/\psi\phi$ decay. In addition, this decay has a similar differential decay rate [131,132] to the studied B_s^0 decay. The B^0 decay is simulated with SIMUB, where one of the b quarks in the event is forced to hadronise to a B^0 or $\bar{B}^0$ meson, and to decay through the complete decay chain. With the kinematic requirements, and using the world-average branching ratios, the cross section is predicted to be $\sigma(B^0 \to J/\psi K^{*0} \to \mu^+\mu^- K^+\pi^-) = 366 \pm 22$ pb.

The uncertainties quoted on the estimates above do not include the uncertainties on the total $b\bar{b}$ cross section at LHC energies, the b fragmentation functions, the transverse momentum distribution of b quarks, and the uncertainties introduced by using the model of $b \to J/\psi X$ decays in PYTHIA. However, since both the signal and background are proportional to the same $b\bar{b}$ cross section, the signal-to-background ratio is unaffected by the corresponding uncertainty. The parameters used in the simulation of the $B_s^0 \to J/\psi\phi$ and $B^0 \to J/\psi K^{*0}$ decays are given in Table 5.1.

The direct production of J/ψ mesons is an important background at trigger level. Measurements at the Tevatron [133] have shown that predictions of the colour-singlet model, which is presently the one implemented in the PYTHIA generator, underestimate the measurements by several orders of magnitude. Perturbative QCD is used in this model to generate $c\bar{c}$ pairs, which then hadronise to a charmonium state in a non-perturbative way.

The observed discrepancy has led to a different approach [134], which has been implemented in a modified version of PYTHIA 6.225, tuned on Tevatron data. A $c\bar{c}$ pair is first formed taking into account all perturbative QCD diagrams, regardless of the final colour

Table 5.1. Values used for the mixing parameters, decay amplitudes, strong and weak phases in the simulation of the $B_s^0 \to J/\psi\phi$ and $B^0 \to J/\psi K^{*0}$ Monte Carlo sample.

Parameter	$B_s^0 \to J/\psi\phi$	$B^0 \to J/\psi K^{*0}$
$\tau = 1/\bar{\Gamma}$	1.405×10^{-12} s	1.528×10^{-12} s
$\Delta\Gamma/\bar{\Gamma}$	-0.2	0
Δm	$17.8\,\text{ps}^{-1}$	$0.509\,\text{ps}^{-1}$
$\lvert A_0(0)\rvert^2/\Gamma$	0.570	0.570
$\lvert A_\parallel(0)\rvert^2/\Gamma$	0.217	0.217
$\lvert A_\perp(0)\rvert^2/\Gamma$	0.213	0.213
δ_1	π	π
δ_2	0	0
ϕ	-0.04	0

state. The $c\bar{c}$ state is then transformed into a colour-singlet by non-perturbative processes, such as the emission of a soft gluon.

This version of PYTHIA has been used to simulate a sample of J/ψ decaying to two muons for background studies. The J/ψ production cross section is calculated to be 141μb. Taking the $J/\psi \to \mu^+\mu^-$ branching ratio and the kinematic requirements into account, a cross section of 310 ± 5 nb is expected. Only the statistical uncertainty is quoted and used; the large uncertainties on the total cross section for J/ψ production and on the p_T distribution are not included.

5.1.3. Trigger selection

5.1.3.1. The Level-1 Trigger. The B_s^0 decay chain is selected at Level-1 by the dimuon trigger stream. At low luminosity it is foreseen [76] to use an identical threshold of 3 GeV/c on the transverse momentum of each muon, still keeping a low bandwidth occupancy of 0.9 kHz. Such a low p_T threshold ensures a very high selection efficiency on this channel, with a rate low-enough to allow the use of lower quality muon candidates in the endcap region, recovering full geometrical acceptance of the muon detector up to $|\eta| < 2.4$. For this decay, two of the identified muons are required to have opposite charge.

5.1.3.2. The High-Level Trigger. In the HLT, the signal events are identified by doing a full reconstruction of the B_s^0 decay, imposing invariant mass and vertex constraints. Indeed, at this stage, tracks can be reconstructed in the tracker in restricted (η, ϕ) regions via a partial reconstruction algorithm, where only the first 5 hits are used [7, Section 6.4.3.2]. To define the tracking regions, the primary (interaction) vertex is first identified and reconstructed using only hits in the Pixel detector, with the "Divisive Method" described in reference [135]. Since the primary vertex of $b\bar{b}$ events involves low momentum tracks, the three vertex candidates with the highest sum of the p_T^2 of the tracks, which is the default selection criterion, have to be retained in order to achieve a good efficiency.

For the muons, the tracking regions are chosen around the direction of the muons identified at Level-1. Since no link to the muon detectors can be done at this stage, all track pairs of opposite charge for which the invariant mass is within $150\,\text{MeV/c}^2$ of the world-average J/ψ mass are retained. The resolution on the invariant mass of the J/ψ meson is found to be $51\,\text{MeV/c}^2$. In addition, the p_T of each muon is required to be above 2.5 GeV/c in $|\eta| < 1.2$ or 2 GeV/c in $|\eta| \geqslant 1.2$, and the p_T of the J/ψ candidate above 4 GeV/c. To remove the prompt J/ψ background, the two muon candidates are then fitted to a common

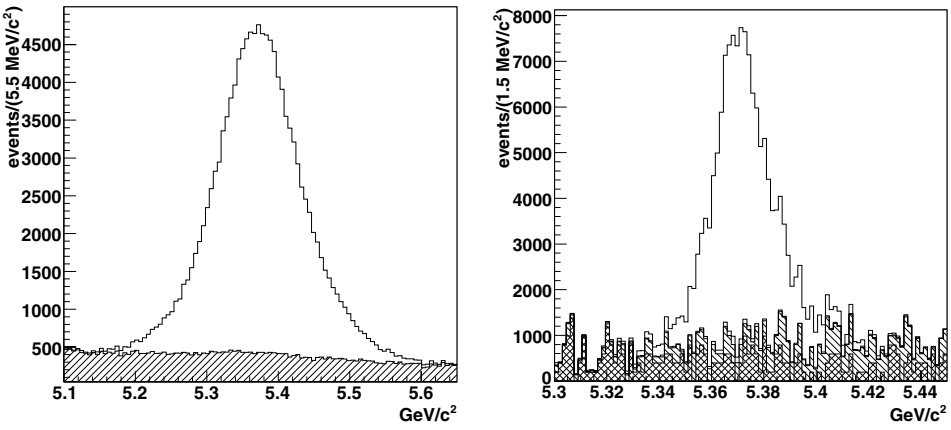

Figure 5.1. Four-track invariant mass distribution after the HLT (left) and offline (right) requirements. The right distribution includes only combinatorial background and the left distribution the expected inclusive $b \to J/\psi X$ and $B^0 \to J/\psi K^{*0}$ background.

decay vertex. The χ^2 of the fit is required to be below 10 and the significance of the transverse decay length is required to be above 3. Furthermore, the transverse momentum of the J/ψ candidate is required to be nearly parallel to its flight path in the transverse plane, since the J/ψ mesons produced in the decays of B_s^0 mesons are collimated around the direction of the B_s^0 meson by the relativistic boost. The cosine of the angle between the reconstructed momentum vector and the vector pointing from the production to the decay vertex is thus required to be larger than 0.9.

To reconstruct the kaons, a tracking region is chosen around the direction of each J/ψ candidate. Assigning the kaon mass to the reconstructed tracks, all oppositely charged track pairs for which the invariant mass is within $20\,\mathrm{MeV/c^2}$ of the world-average mass of the ϕ meson are retained, for a resolution on the invariant mass of the ϕ meson of $4.5\,\mathrm{MeV/c^2}$. The p_T of each of the kaon tracks is required to be above $0.7\,\mathrm{GeV/c}$, the p_T of the ϕ candidate above $1\,\mathrm{GeV/c}$ and the p_T of the B_s^0 candidate above $5\,\mathrm{GeV/c}$. With the two muon candidates, the four-track invariant mass is required to be within $200\,\mathrm{MeV/c^2}$ of the world-average mass of the B_s^0 meson. The resolution on the invariant mass of the B_s^0 meson is found to be $65\,\mathrm{MeV/c^2}$. Here as well, a vertex fit of the four tracks is performed, imposing similar requirements as above.

The distribution of the invariant mass of the candidates after the HLT requirements is shown in Figure 5.1 (left). The efficiencies for the different criteria, which include the respective reconstruction efficiencies, are given in Table 5.2 for the signal and the different background samples, together with the estimated rate. The total rate for this selection is well below 1 Hz, and a yield of approximately 456 000 signal events can be expected within $30\,\mathrm{fb^{-1}}$ of data.

5.1.4. Offline selection and reconstruction

The first step in the offline selection is similar to the HLT selection, with the difference that the complete information from the detector is available. Candidates are reconstructed by combining two muons of opposite charge with two further tracks of opposite charge. As CMS does not possess a particle identification system suitable for this measurement, all

Table 5.2. Trigger selection efficiencies for the signal and background (defined with respect to the number of generated events) after each requirement, and estimated HLT rate.

Requirement	Signal	Background		
	$B_s^0 \to J/\psi\phi$	Inclusive $b \to J/\psi X$	$B^0 \to J/\psi K^{*0}$	Prompt J/ψ
Level-1	45.76(6)%	38.25(13)%	46.91(13)%	36.91(12)%
HLT-J/ψ selection	28.69(7)%	21.91(11)%	30.28(12)%	0.65(2)%
HLT-ϕ selection	20.50(6)%	1.23(3)%	0.961(26)%	0.0007(7)%
HLT rate (Hz)	0.03034(8)	0.0792(18)	0.0077(2)	0.002(2)

measured tracks have to be considered as possible kaon candidates, which adds a substantial combinatorial background. At this stage, only loose requirements are applied, which are tightened after a kinematic fit.

First, all muons in the event are reconstructed using the global muon reconstruction algorithm [7, Section 9.1.3]. This algorithm is not fully efficient for low-p_T muons from J/ψ decays, being more suited to the reconstruction of high-p_T muons. Therefore, all tracks are reconstructed with the standard track reconstruction algorithm [7, Section 6.5]. Track-pairs of opposite charge for which the invariant mass is within $120\,\mathrm{MeV/c^2}$ of the world-average J/ψ mass are retained as a J/ψ candidate. The p_T of each muon is required to be above $3\,\mathrm{GeV/c}$ in $|\eta| < 1.2$ or $2\,\mathrm{GeV/c}$ in $|\eta| \geqslant 1.2$, and the p_T of the J/ψ candidate above $4\,\mathrm{GeV/c}$. The muon identification algorithm which uses information from the muon detector [7, Section 9.2.1.2], is applied to both tracks forming the J/ψ candidate. A J/ψ candidate is confirmed if both tracks share more than half of their hits in the silicon tracker with the muon tracks reconstructed by the global muon reconstructor, or if their compatibility score returned by the muon identification algorithm is greater than 0.1.

To reconstruct the ϕ meson, all tracks reconstructed with the standard track reconstruction algorithm are used. Requiring the p_T of each track to be above $0.8\,\mathrm{GeV/c}$ and assigning a kaon mass to the thus reconstructed tracks, all oppositely charged track pairs for which the invariant mass is within $20\,\mathrm{MeV/c^2}$ of the world-average mass of the ϕ meson are retained. The p_T of the ϕ candidate is required to be above $1\,\mathrm{GeV/c}$, and the p_T of the B_s^0 candidate above $5\,\mathrm{GeV/c}$.

A kinematic fit [136] is then made, where the four tracks are constrained to come from a common vertex and the invariant mass of the two muons is constrained to be equal to the mass of the J/ψ. Since the natural width of the ϕ meson is of the same order as the resolution due to the reconstruction, no mass constraint is applied to the two kaon tracks. With this fit, a resolution on the invariant mass of the B_s^0 meson of $14\,\mathrm{MeV/c^2}$ is found. The confidence level of the fit is required to be greater than 1×10^{-3} (seven degrees of freedom). The invariant mass of the two kaons is required to be within $8\,\mathrm{MeV/c^2}$ of the world-average mass of the ϕ meson. Finally, the cosine of the angle between the reconstructed momentum vector of the B_s^0 candidate and the vector pointing from the production to the decay vertex is required to be larger than 0.95. The distribution of the invariant mass of the candidates after all selection requirements is shown in Figure 5.1 (right).

The primary vertex is not used at this stage, since the efficiency of the standard primary vertex finder [7, Section 6.6.4], which uses all fully reconstructed tracks, is 92%, and drops to 83% if the vertex is required to be within $500\,\mu\mathrm{m}$ from the simulated vertex. In order to prevent this unnecessary loss of efficiency, no use is made of the primary vertex, and all quantities of interest are evaluated in the transverse plane.

Table 5.3. Offline selection efficiencies for the signal and background (defined with respect to the number of generated events) after each requirement.

Requirement	Signal	Background		
	$B_s^0 \to J/\psi\phi$	$b \to J/\psi X$	$B^0 \to J/\psi K^{*0}$	Prompt J/ψ
HLT selection	20.50(6) %	1.23(3) %	0.937(14)%	0.0007(7) %
Reconstruction + Basic p_T req.	18.15(5) %	0.63(2) %	0.675(12) %	0.0007(7) %
Muon Identification	17.89(5) %	0.585(19) %	0.636(11) %	0.0007(7) %
Kinematic fit χ^2 req.	16.58(5) %	0.282(14) %	0.503(10) %	0.0007(7) %
Pointing constraint	16.48(5) %	0.258(13) %	0.497(10) %	–
ϕ mass req.	14.65(5) %	0.113(13) %	0.202(10) %	–

Table 5.4. Expected cross sections for the signal and background, after each requirement, with number of expected events.

	Signal	Background		
	$B_s^0 \to J/\psi\phi$	Inclusive $b \to J/\psi X$	$B^0 \to J/\psi K^{*0}$	Prompt J/ψ
$\sigma \times$ BR	2.87 ± 1.07 nb	682 ± 64 nb	20.4 ± 1.7 nb	141 μb
Kin. preselection	74 ± 27 pb	3.20 ± 0.3 nb	366 ± 22 pb	176 ± 2 nb
Level-1	34 ± 12 pb	1.22 ± 0.11 nb	172 ± 10 pb	65 ± 1 nb
HLT	15.2 ± 5.5 pb	39.4 ± 3.8 pb	3.52 ± 0.21 pb	1.2 ± 1.2 pb
Offline	10.9 ± 4.0 pb	3.62 ± 0.54 pb	0.74 ± 0.06 pb	–
Events per 30 fb $^{-1}$	327 000	108 500	22 200	–

With this selection, a yield of approximately 327 000 signal events can be expected within 30 fb^{-1} of data, with a background of 108 500 events. The efficiencies for the different criteria, which include the respective reconstruction efficiencies, are given in Table 5.3 for the signal and the different background samples, and the expected cross sections are given in Table 5.4. These do not include a requirement on the four-track invariant mass of the candidates, since the sidebands will be used later in the analysis. However, only a small fraction of these events are directly under the B_s^0 peak, and even a simple cut will reduce the number of background events by a significant factor.

5.1.5. The maximum likelihood analysis

The final state of the decay of a pseudo-scalar B meson into two vector mesons $B \to V_1 V_2$ is an admixture of CP-even and CP-odd states [131,132,137]. The CP-odd states correspond to transitions in which the relative orbital momentum L between the two vector mesons is 1 and the CP-even states to transitions in which L is either 0 or 2. The amplitude of the decay can be decomposed in three independent decay amplitudes which correspond to the linear polarisation states of the two mesons. The first, A_0, describes states in which the linear polarisation vectors are longitudinal and is CP-even. The other two describe states in which the linear polarisation vectors are transverse, either parallel ($A_\parallel$ – CP-even) or perpendicular ($A_\perp$ – CP-odd) to each other.

The differential decay rate can be written as:

$$\frac{\mathrm{d}^4\Gamma(B_s(t))}{\mathrm{d}\Theta\,\mathrm{d}t} = f(\Theta,\alpha,t) = \sum_{i=1}^{6} O_i(\alpha,t)\cdot g_i(\Theta), \tag{5.1}$$

where O_i are the kinematics-independent observables and g_i the angular distributions. The set of physical parameters are represented by α and the angles which define the kinematics are

generically denoted Θ. The time evolution of the different observables is given by bilinear combinations of the polarisation amplitudes, $|A_0(t)|^2$, $|A_\parallel(t)|^2$, $|A_\perp(t)|^2$, $\Im(A_\parallel^*(t)A_\perp(t))$, $R(A_0^*(t)A_\parallel(t))$ and $\Im(A_0^*(t)A_\perp(t))$. These are functions of the widths of the two light and heavy eigenstates, Γ_L and Γ_H, the weak phase ϕ_{CKM}, the magnitudes of the amplitudes at $t=0$ ($A_0(0)$, $A_\parallel(0)$ and $A_\perp(0)$) which describe all hadronisation effects, and, for a flavour-tagged sample, the mass difference $\Delta m_s = m_H - m_L$. Since the overall phase of the polarisation states is not observable, two strong phases are defined as $\delta_1 \equiv \arg|A_\parallel{}^* A_\perp|$ and $\delta_2 \equiv \arg|A_0^* A_\perp|$. These are CP conserving, and are expected to be 0 (mod π) in the absence of final-state interactions. Assuming $SU(3)$ flavour-symmetry, the magnitudes and the two strong phases are equal for the decays $B_s^0 \to J/\psi\phi$ and $B^0 \to J/\psi K^{*0}$ in unmixed samples. The measurement of these parameters is of interest to study and improve the phenomenological models used to calculate all hadronic effects.

In such decays, the kinematics are uniquely defined by a set of three angles. The transversity base is used in this analysis, in which the set of variables is $\Theta = (\cos\theta, \phi, \cos\varphi)$. In this base, (θ, φ) are the polar and azimuthal angles of the momentum of the μ^+ in the J/ψ rest frame. This coordinate system is defined such that the ϕ moves in the positive x direction and the z axis is perpendicular to the decay plane of the decay $\phi \to K^+K^-$. The angle ψ is defined in the rest frame of the ϕ as the negative cosine of the angle between the K^+ direction and the J/ψ direction.

In order to measure the values of the different parameters, an unbinned maximum likelihood fit is performed on the observed time evolution of the angular distribution. In the absence of background and without distortion, the p.d.f. describing the data would be the original differential decay rate $f(\Theta, \alpha, t)$ (Equation (5.1)). The distortion of this distribution by the detector acceptance, trigger efficiency and the different selection criteria is taken into account by an efficiency term $\varepsilon(t, \Theta)$. In addition, a term describing the background has to be added.

It is assumed that the efficiency can be factorised in two functions, the first modelling the effects of the decay length requirements and the second the distortion of the angular distribution,

$$\epsilon(t, \Theta) = \epsilon(t) \cdot \epsilon(\Theta). \tag{5.2}$$

The angular efficiency is described by an expansion of products of spherical harmonics [138]:

$$\epsilon(\Theta) = \sum_{LRM} T^\epsilon_{LRM} \cdot \mathcal{Y}_{LRM}(\Theta), \tag{5.3}$$

$$\text{with} \quad \mathcal{Y}_{LRM}(\Theta) = \sqrt{2\pi} \cdot Y_{LM}(\theta, \varphi) \cdot Y_{RM}(\psi, 0), \tag{5.4}$$

where $\mathcal{Y}_{LRM}$ are orthonormal basis functions and Y_{LM}, Y_{RM} are spherical harmonic functions. In principle, L and R run from 0 to infinity and the sum over M from $-\min(L; R)$ to $+\min(L; R)$, but it has been found that the expansion can be limited to $L, R \leqslant 8$. These $\mathcal{Y}_{LRM}$ functions describe the partial waves involved in a scalar $\to$ vector decay [139]. The moments of the efficiency are determined from a Monte Carlo simulation with full detector simulation:

$$T^\epsilon_{LRM} = \int \epsilon(\Theta) \cdot \mathcal{Y}^*_{LRM}(\Theta) \mathrm{d}\Theta \tag{5.5}$$

$$\approx \frac{1}{N_{gen}} \sum_{i=1}^{N_{obs}} \frac{1}{f(\Theta_i)} \mathcal{Y}^*_{LRM}(\Theta_i), \tag{5.6}$$

where $f(\Theta_i)$ is the expected time-integrated angular distribution (Equation (5.1)).

The time-dependent efficiency describes mainly the effects of the requirements on the proper decay length distribution. After the initial turn-on and a stable plateau, a deficit of events can be observed. Initial studies attribute this decrease in efficiency to the restrictions imposed on the seeds by the tracking regions in the HLT, which cause an additional track reconstruction inefficiency for displaced tracks such as those originating from B decays. The tolerance on the transverse and the longitudinal direction imposed on the tracking regions in the HLT results in an implicit cut on the impact parameters. Further studies are needed to find solutions to alleviate this inefficiency. Without corrections, the main effect of this inefficiency would be to lower the estimated lifetime of the longer-lived eigenstate B_s^H.

The different features in this distribution cannot easily be described by a simple function. Two sigmoidal functions combined with a quadratic function are used to describe the efficiency:

$$\epsilon(t) = \begin{cases} c \cdot \left(1 + \tanh\left(\frac{t-t_0}{\Delta t_1}\right)\right) & t < t_0 \\ (a \cdot t^2 + b \cdot t + c) \cdot \left(1 + \tanh\left(\frac{t-t_0}{\Delta t_2}\right)\right) & t > t_0. \end{cases} \tag{5.7}$$

The parameters are found by fitting this function to the distribution obtained by the full Monte Carlo simulation.

The best way to gauge our ability to account for all effects and our capacity to correct them through this time-dependent efficiency curve is by comparing the proper time distributions foreseen by the simulation and observed in the data for the different B mesons. The first obvious choice is again the decay $B^0 \to J/\psi K^{*0}$, which is very similar to the studied B_s^0 decay, and for which the lifetime has been measured with a high precision. Any discrepancy between the efficiency determined by Monte Carlo and the data will be reflected in a mismeasurement of the B^0 lifetime. Further studies would be needed to determine the sensitivity of the efficiency on the lifetime of the selected B meson. It is dubious whether the number of B_s^0 events recovered in other trigger streams such as the dimuon stream, which has no decay length requirement, would be enough to estimate the time-dependent efficiency.

The background can be divided in two different types of distributions. The first type arises from misidentified $B^0 \to J/\psi K^{*0} \to \mu^+\mu^- K^+\pi^-$ events, which has a similar differential decay rate [131, 132] to the decay of interest. The width difference of the two eigenstates of the B^0 are assumed to be negligible, and no CP violation is present since the final state is flavour specific. To describe this background in the dataset, it is not possible to use its time dependent angular distribution, which is in principle well known, since all variables are mismeasured because of the misidentification of the π. In addition, the distortion of the distribution due to the various requirements is much more severe than in the case of the B_s^0. Indeed, due to its lower mass, the momentum of the π in the laboratory frame is lower than that of the corresponding K when the π is emitted in the direction opposite to the momentum of the K^{*0}.

The same set of functions $\mathcal{Y}_{LRM}(\Theta)$ (Equation (5.4)) is used to model the angular distribution $f_d(\Theta)$ of this background, with the moments computed in the following way:

$$T^b_{LRM} = \int b(\Theta) \cdot \mathcal{Y}^*_{LRM}(\Theta) \mathrm{d}\Theta \tag{5.8}$$

$$\approx \frac{1}{N_b} \sum_{i=1}^{N_b} \mathcal{Y}^*_{LRM}(\Theta_i) \,. \tag{5.9}$$

Here as well, the expansion is done up to $L, R \leqslant 8$. The functions are obtained by a Monte Carlo simulation and can be cross-checked by a fully reconstructed sample of well-identified $B^0 \to J/\psi K^{*0}$ decays misreconstructed as B_s^0 candidates.

The time dependence of this background is modelled as a single exponential decay, again with a time-dependent efficiency. The lifetime τ_d is left as a free parameter, since the mismeasurement of the proper decay length precludes using the well-measured lifetime of the B^0.

The other sources of background are assumed to have no angular dependence. The distribution of their proper decay time is modelled by two exponential decays, the first describing the short-lived prompt background and the second misidentified long-lived heavy-flavour hadrons.

A better separation of the signal and background is obtained by using the events in a wider invariant mass region between 5.219 and 5.559 $\mathrm{GeV/c^2}$, and including in the fit the distribution of the invariant mass of the candidates. The distribution of the B_s^0 candidates is modelled by a Gaussian $G_s(m; m_s, \sigma_s)$, where m_s is the mass of the B_s^0 meson and σ_s the variance due to the reconstruction. The distribution of the misidentified $B^0 \to J/\psi K^{*0}$ decays can reasonably well be modelled in the chosen region by a Gaussian $G_d(m; m_d, \sigma_d)$. Because of the misidentification of the pion, m_d will not correspond to the true mass of the B^0 meson, and will be left as a free parameter in the fit. The other sources of background are assumed to have a flat mass distribution and will be modelled by a linear function $L(m)$.

The total p.d.f. to be fit is thus given by

$$\begin{aligned}\mathcal{P} = {} & (1 - b_d - b_c) \cdot \epsilon(t, \Theta) \cdot f(\Theta, \alpha, t) \cdot G_s(m; m_s, \sigma_s) \\ & + b_d \cdot f_d(\Theta) \cdot \epsilon(t) \cdot \frac{1}{\tau_d} e^{-t/\tau_d} \cdot G_d(m; m_d, \sigma_d) \\ & + b_c \cdot \epsilon(t) \cdot \left(\frac{1}{\tau_{cl}} e^{-t/\tau_{cs}} + \frac{1}{\tau_{cl}} e^{-t/\tau_{cl}} \right) \cdot L(m), \end{aligned} \tag{5.10}$$

where b_d, respectively b_c, are the fraction of misidentified B^0 background, respectively combinatorial background, in the sample. These parameters are left free in the fit. The resolution of the proper decay length is taken into account by convolving the p.d.f. with a Gaussian resolution function. The standard deviation of the Gaussian is taken as the uncertainty of each candidate's proper decay length measurement multiplied by a scale factor, which is left free in the fit. Since the uncertainties of the measured angles are found to be small, these are not taken into account in the fit. A contribution is added to the systematic uncertainty to reflect this omission.

5.1.6. Result

Due to the high production cross sections of the identified backgrounds, only limited samples could be generated and analysed, which do not permit to have a final dataset with the foreseen signal-to-background ratio. Indeed, the signal sample corresponds to an integrated luminosity of 6.8 $\mathrm{fb^{-1}}$, while the inclusive background corresponds to an integrated luminosity of barely 48 $\mathrm{pb^{-1}}$. The situation is somewhat better for the decay $B^0 \to J/\psi K^{*0}$, for which the sample corresponds to an integrated luminosity of 1.3 $\mathrm{fb^{-1}}$.

First, a fit was performed on the complete set of selected and associated B_s^0 candidates only, using the efficiency functions determined in the previous section. The relative width difference $\Delta\Gamma_s/\bar{\Gamma}_s$ can be determined with an uncertainty of 0.016 (Table 5.5), but no sensitivity on the weak phase and the strong phases is obtained.

Then, a sample corresponding to an integrated luminosity of 1.3 $\mathrm{fb^{-1}}$ is considered, which allows to have a realistic ratio of $B^0 \to J/\psi K^{*0}$ and signal events. With the low number of background events which remain after all selection requirements, an accurate model through the described p.d.f. is not possible. In addition, the low number of $B^0 \to J/\psi K^{*0}$ events

Table 5.5. Results of the maximum likelihood fit for 73813 signal events.

Parameter	Input value	Result	Stat. error	Rel. error
$\|A_0(0)\|^2$	0.57	0.57398	0.00267	0.4%
$\|A_{\|\|}(0)\|^2$	0.217	0.21808	0.00473	2.1%
$\|A_\perp(0)\|^2$	0.213	0.20794	0.00396	1.9%
$\bar{\Gamma}_s$	$0.712\,\mathrm{ps}^{-1}$	$0.712358\,\mathrm{ps}^{-1}$	$0.00350643\,\mathrm{ps}^{-1}$	0.5%
$\Delta\Gamma_s$	$0.142\,\mathrm{ps}^{-1}$	$0.134645\,\mathrm{ps}^{-1}$	$0.0108247\,\mathrm{ps}^{-1}$	8.0%
$\Delta\Gamma_s/\bar{\Gamma}_s$	0.2	0.189013	0.0157993	8.4%
δ_1	π	2.94405	0.632682	
δ_2	0	−0.109493	0.639713	
ϕ_{CKM}	−0.04	−0.0297427	0.0758856	

Table 5.6. Results of the maximum likelihood fit for an integrated luminosity of $1.3\,\mathrm{fb}^{-1}$ (signal only).

Parameter	Input value	Result	Stat. error	Rel. error
$\|A_0(0)\|^2$	0.57	0.5859	0.0062	1.1%
$\|A_{\|\|}(0)\|^2$	0.217	0.2141	0.0078	3.6%
$\|A_\perp(0)\|^2$	0.213	0.2002	0.0064	3.2%
$\bar{\Gamma}_s$	$0.712\,\mathrm{ps}^{-1}$	$0.7018\,\mathrm{ps}^{-1}$	$0.0081\,\mathrm{ps}^{-1}$	1.2%
$\Delta\Gamma_s$	$0.142\,\mathrm{ps}^{-1}$	$0.1470\,\mathrm{ps}^{-1}$	$0.0256\,\mathrm{ps}^{-1}$	17.4%
$\Delta\Gamma_s/\bar{\Gamma}_s$	0.2	0.2095	0.0371	18.1%

Table 5.7. Results of the maximum likelihood fit for an integrated luminosity of $1.3\,\mathrm{fb}^{-1}$ (signal and background).

Parameter	Input value	Result	Stat. error	Rel. error
$\|A_0(0)\|^2$	0.57	0.5823	0.0061	1.1%
$\|A_{\|\|}(0)\|^2$	0.217	0.2130	0.0077	3.6%
$\|A_\perp(0)\|^2$	0.213	0.2047	0.0065	3.2%
$\bar{\Gamma}_s$	$0.712\,\mathrm{ps}^{-1}$	$0.7060\,\mathrm{ps}^{-1}$	$0.0080\,\mathrm{ps}^{-1}$	1.1%
$\Delta\Gamma_s$	$0.142\,\mathrm{ps}^{-1}$	$0.1437\,\mathrm{ps}^{-1}$	$0.0255\,\mathrm{ps}^{-1}$	17.7%
$\Delta\Gamma_s/\bar{\Gamma}_s$	0.2	0.2036	0.0374	18.4%

does not permit an accurate estimate of either the angular distribution or of its time-dependent efficiency. As such, the background events are simply added to the dataset and their expected distribution is not included in the p.d.f. used in the fit. The p.d.f. would thus simply describe the B_s^0 distribution:

$$\mathcal{P} = \epsilon(t, \Theta) \cdot f(\Theta, \alpha, t)\,.$$

With such a fit in which the invariant mass of the candidates is not taken into account, a requirement on the invariant mass of the candidates would obviously be made, choosing a window of $\pm 36\,\mathrm{MeV/c^2}$ around the world-average B_s^0 mass. This reduces the number of B^0 background events by a further 59%, while reducing the number of signal candidates by 2.9%. The results of the fit without background is given in Table 5.6 and with background in Table 5.7. With the lower number of B_s^0 candidates, the statistical uncertainty of the measurement is, as expected, markedly worse. As can be seen, the influence of the background is very small, with only a slight degradation of the width difference. The distribution of the proper decay length of the selected events with the fit projection is shown in Figure 5.2.

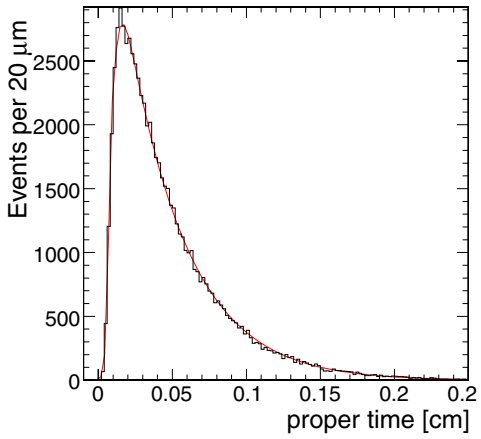

Figure 5.2. Distributions of the proper decay length of the selected signal and background events with fit projection.

Table 5.8. List of systematic uncertainties with effect on the predictions of the rates.

Source	HLT uncert.	Offline uncert.	Common uncert.
Branching ratio B_s^0			36.4 %
Branching ratio B^0			6 %
Branching ratio $b \to J/\psi X$			9 %
Tracking inefficiency	2 %	2%	
Muon reconstruction	-	1.4%	
Misalignment	17%	-	

Table 5.9. List of systematic uncertainties with effect on the measurements.

Source	$\lvert A_0(0)\rvert^2$	$\lvert A_{\lvert\lvert}(0)\rvert^2$	$\lvert A_\perp(0)\rvert^2$	$\bar{\Gamma}_s$	$\Delta\Gamma_s/\bar{\Gamma}_s$
Bckg. distrib.	0.0034	0.0011	0.0045	0.0043	0.0059
S/B ratio	0.0037	0.0001	0.0024	0.0025	0.0055
Resolution	-	-	-	0.00060	0.0045
Ang. distortion	0.0143	0.0061	0.0082	0.00083	0.0010
$c\tau$ distortion	0.0016	0.00073	0.0023	0.0221	0.0146
Alignment	0.00012	0.00042	0.00055	0.00040	0.0014
Total	0.0152	0.0063	0.0099	0.0227	0.0173

5.1.7. Systematics and detector effects

The list of systematic uncertainties which were considered are summarised in two tables. The first, Table 5.8, summarises the uncertainties which affect the HLT rate and the number of foreseen events after all selection requirements. The second, Table 5.9, summarises the uncertainties which affect the measurement of the various parameters.

- **Signal and background statistics.** Among the various uncertainties listed in Section 5.1.2, the largest single source of uncertainty in the estimate of the number of events is obviously

the poor knowledge of the $B_s^0 \to J/\psi\phi$ branching ratio. The uncertainties quoted on the estimates above do not include the uncertainties on the total $b\bar{b}$ cross section at LHC energies, the $b \to B^0$ fragmentation functions, the transverse momentum distribution of b quarks. However, since both the signal and background are proportional to the same $b\bar{b}$ cross section, the signal-to-background ratio is unaffected by the corresponding uncertainty.

- **Track reconstruction efficiency.** A 1% uncertainty per track on the track reconstruction efficiency is assumed for all tracks.
- **Muon reconstruction.** The selection relies heavily on the correct identification of muons. A 1% uncertainty per track on the combined muon identification procedure is assumed.
- **Tracker and muon detector misalignment.** The study has been conducted with a perfectly aligned detector. To gauge the sensitivity of the analysis with respect to the alignment the analysis has been repeated on a detector with the short-term alignment scenario. This scenario is expected to be representative of the relative misalignment of the detector components during the initial data taking period [86]. The effects of misalignment of the tracker on various aspects of track and vertex reconstruction have been extensively studied and reported in [140, 141]. The degradation affect both the selection, mostly through the requirement on the significance of the transverse decay length of the J/ψ in the HLT, and the analysis, through the degradation of the measurement of the proper decay length. The resolution of the latter is degraded from 24 μm for a perfectly aligned detector to 32 μm with the short-term alignment. The HLT efficiency is degraded by some 17% with respect to a perfectly aligned detector.
- **Background distributions.** To gauge the influence of the background on the fit, the variation observed between the fits performed on the reduced 1.3 fb^{-1} dataset with and without these events is added to the systematic uncertainty ("Bckg. distrib." in the table). Since the signal-to-background ratio has a significant uncertainty, the fit performed on the reduced 1.3 fb^{-1} sample is repeated varying the number of B_s^0 signal events to match the uncertainty in the signal-to-background ratio. For this estimate, a different uncertainty for the B_s^0 branching fraction has been chosen, since it is believed that it will be measured again in the current run of the Tevatron. Two main uncertainties plagued the measurement done at CDF in Run I, the low number of observed B_s^0 candidates and the uncertainty on the fragmentation. Based on recent publications, it is estimated that approximately 30 times more $B_s^0 \to J/\psi\phi$ decays than in Run 1 should already be collected in the current dataset of 1 fb^{-1}. The uncertainty of the branching fraction is therefore reduced to 20%. For the other uncertainties, the numbers listed in Table 5.8 are used. The variation observed on the fit is listed under the heading "S/B ratio." In a larger dataset, where the full p.d.f. (Eq. 5.11) is used, the influence of the uncertainty on the signal-to-background ratio should be much smaller, since the fractions of background events in the dataset are free parameters in the fit.
- **Distortion of the proper-time distribution ("$c\tau$ distortion").** Other fits were then performed where the parameters of the time dependent efficiency function are varied by one standard deviation. The mean variation of the fitted parameters was added to the systematic uncertainty. As already mentioned, the decay $B^0 \to J/\psi K^{*0}$ can be used to compare the accuracy of this model by comparing the Monte Carlo prediction with the efficiency function observed in the data.
- **Distortion of the angular distributions ("Ang. distortion").** The expansion used to model the distortion of the angular distributions (Equation (5.3)) is limited to $L, R \leqslant 8$. When

Table 5.10. Results of the maximum likelihood fit for an integrated luminosity of $1.3\,\mathrm{fb}^{-1}$ (signal and background).

Parameter	Input value	Result	Stat. error	Sys. error	Total error	Rel. error
$\|A_0(0)\|^2$	0.57	0.5823	0.0061	0.0152	0.0163	2.8%
$\|A_{\|\|}(0)\|^2$	0.217	0.2130	0.0077	0.0063	0.0099	4.6%
$\|A_\perp(0)\|^2$	0.213	0.2047	0.0065	0.0099	0.0118	5.8%
$\bar{\Gamma}_s$	$0.712\,\mathrm{ps}^{-1}$	$0.7060\,\mathrm{ps}^{-1}$	$0.0080\,\mathrm{ps}^{-1}$	$0.0227\,\mathrm{ps}^{-1}$	$0.0240\,\mathrm{ps}^{-1}$	3.4%
$\Delta\Gamma_s$	$0.142\,\mathrm{ps}^{-1}$	$0.1437\,\mathrm{ps}^{-1}$	$0.0255\,\mathrm{ps}^{-1}$	$0.0113\,\mathrm{ps}^{-1}$	$0.0279\mathrm{ps}^{-1}\mathrm{ps}^{-1}$	19%
$\Delta\Gamma_s/\bar{\Gamma}_s$	0.2	0.2036	0.0374	0.0173	0.0412	20%

limiting the expansion to $L, R \leqslant 6$ or $L, R \leqslant 10$, the result of the fit shows negligible differences. In addition, to account for the possibility that the efficiencies do not factorise and that the angular efficiency is grossly miscalculated, the fit is also repeated without the angular efficiency, i.e. without correction of the distortion. While this has little influence on the estimated lifetimes, a large variation is found for the amplitudes. This variation is used as systematic uncertainty.

- **Resolution on the angular variables ("Resolution").** In order to estimate the influence of the uncertainties of the angles and the proper decay length on the fit, a fully controlled toy Monte Carlo was used, in which only the proper time and angles were generated according to the expected p.d.f. and smeared with Gaussian resolution functions. The default standard deviations are taken to be equal to those measured in the Monte Carlo with full detector simulation. The simulation was then repeated without smearing and with a substantial smearing, where the resolution is taken to be two times larger than in the default simulation. The value of parameters found in both cases were very close to the values found with the default smearing, and the observed variation is added to the systematic uncertainty.

5.1.8. Conclusion

The present section describes a study on the selection of the $B_s^0 \to J/\psi\phi$ decay and the measurement of the width difference $\Delta\Gamma_s$ in absence of flavour tagging. An example of a trigger algorithm is presented which would be efficient for this decay and would reject a large fraction of the background. It is based on the identification of J/ψ and B_s^0 candidates with a displaced decay vertex. Nevertheless, this trigger precludes the selection of other decays of the B meson, and should certainly evolve as a true precursor to a B physics trigger. Indeed, the strategy proposed for the Level-2 would select inclusive $b \to J/\psi$ decays with high efficiency and good purity with respect to the prompt J/ψ background. Large uncertainties nevertheless plague the estimates of rates, since large uncertainties remain on the b-quark and prompt J/ψ production cross sections, on their momentum distributions, and on the $b \to B_s^0$ fragmentation function.

A first measurement of one of the main parameters of the B_s^0 system, the relative difference of the widths of the weak eigenstates could be determined with a statistical uncertainty of 0.011 in a sample corresponding to an integrated luminosity of $10\,\mathrm{fb}^{-1}$. A first measurement undertaken on approximately $1.3\,\mathrm{fb}^{-1}$ of data could already yield a measurement with an uncertainty of 20% (Table 5.10). A natural extension of this study should be a tagged analysis, for which flavour tagging algorithms need to be developed.

5.2. Associated production of MSSM heavy neutral Higgs bosons $bbH(A)$ with $H(A) \to \tau\tau$

5.2.1. Introduction

The observation of a heavy neutral scalar accompanied by b-jets and decaying into two τ leptons would be an important sign of a MSSM Higgs sector. In the MSSM the associated Higgs boson production $gg \to b\bar{b}H(A)$ is dominant at large values of $\tan\beta$. The cross section of the $gg \to b\bar{b}H(A)$, $H(A) \to \tau\tau$ process is proportional to $\tan^2\beta_{\text{eff}}$ and will be used in a global fit together with other relevant measurements to determine the SUSY parameters simultaneously. An example of a $pp \to H + X$ event with $H \to \tau\nu\tau\nu$ is shown in colour plate CP8.

This channel is an excellent benchmark for the b- and τ-tagging, jet and missing E_T reconstruction. The final state with two τ-jets requires τ tagging both at Level-1 and High Level Trigger. Along with reconstruction and tagging issues, a large number of various Standard Model backgrounds including QCD multi-jet production must be well understood from the real data to be able to establish a discovery.

5.2.2. Event generation

The signal events were generated by PYTHIA using processes the 181 ($gg \to b\bar{b}H$) and 152 ($gg \to H$) for three values of the Higgs boson mass: 200, 500 and 800 GeV/c^2. The backgrounds considered were QCD multi-jet events (for $\tau\tau \to jj$ mode), $t\bar{t}$, $b\bar{b}$, Drell–Yan production of Z/γ^*, W+jet, Wt and $\tau\tau b\bar{b}$. All background processes except $\tau\tau b\bar{b}$ were generated with PYTHIA. The $\tau\tau b\bar{b}$ process was generated by COMPHEP.

In order to reduce CPU time for full detector simulation and event reconstruction loose pre-selections were applied for some of the backgrounds at the generation level. The description of the pre-selections for each final state can be found in the following sections.

The cross sections for the associated Higgs boson production $gg \to b\bar{b}H(A)$ and the branching ratio $H(A) \to \tau\tau$ were calculated using FeynHiggs 2.3.2 [142–144][41] in the m_h^{max} scenario with $\mu = 200\,\text{GeV}/c^2$ (see Section 11.3.1).

The uncertainty of the measured cross section of the $b(\bar{b})A$, $A \to \tau\tau$ process will include the uncertainty of the Monte Carlo generation. The verification of the Monte Carlo generation for the Higgs boson production with the associated b-jets will be done with the real data using $b\bar{b}Z$ ($Z \to \ell\ell$) events [145].

5.2.3. Level-1 and High Level trigger selections

The $\tau\tau \to jj$ final state is triggered by Level-1 single or double tau triggers with thresholds of 93 GeV for the single and 66 GeV for the double tau trigger. It is followed by the double τ-jet tagging at High Level Trigger. Currently there are two selection strategies at HLT under consideration [146]. In the first strategy the calorimeter isolation using the electromagnetic calorimeter is applied to the first τ-jet in order to reduce the Level-1 output rate by a factor of 3. The tracker isolation is then applied on both jets using the tracks reconstructed with the pixel detector only. The second strategy performs tracker isolation right after the Level-1 trigger decision and uses the full tracker with regional track finding and a restricted number of hits to reconstruct tracks. In this analysis the first method is exploited.

The $\tau\tau \to \mu j$ final state uses the single muon trigger at Level-1 with a threshold of 14 GeV. At the High Level the combined muon-plus-τ-jet trigger is used with thresholds of 15 GeV for the muon and of 40 GeV for the τ-jet.

[41] The code can be obtained from http://www.feynhiggs.de

The $\tau\tau \to$ ej final state uses the Level-1 single electron trigger with a threshold of 23 GeV together with the combined electron-plus-τ-jet trigger with thresholds of 14 GeV for the electron and 52 GeV for the τ-jet. At High Level again the single electron trigger with a threshold of 26 GeV and the combined electron-plus-τ-jet trigger with a threshold of 16 GeV for the electron is used. No threshold is applied for the τ-jet candidate.

At High Level Trigger, for both the $\tau\tau \to \mu$j and the $\tau\tau \to$ ej final states, the ECAL and pixel track isolation is applied on the τ-jet candidate similar to what is used in the double τ-jet trigger. For the lepton (e and μ) the same selections are used as for the single electron and muon High Level triggers. The lepton and τ-jet are required to stem from the same vertex found with the pixel detector. Only the tracks from this vertex are used in the tracker isolation.

The search strategy for τ-jet candidates at High Level Trigger for the combined muon-plus-τ-jet and electron-plus-τ-jet triggers is the following: Two calorimeter jets are always reconstructed with the regional jet finder in the regions given by the two highest E_T Level-1 τ-jets. For the muon-plus-τ-jet trigger the first (highest E_T) jet is taken as τ-jet candidate. For the electron-plus-τ-jet trigger the requirement of non collinearity of the jet and the HLT electron candidate, $\Delta R(e - \text{jet}) > 0.3$, is checked for each jet, where $\Delta R(e - \text{jet})$ is the distance in η-φ space between the electron and the jet. The first non collinear jet is taken as the τ-jet candidate.

5.2.4. Off-line event selection

The first step in the off-line analysis is the τ-jet identification. The calorimeter jet is reconstructed in the η-φ region of the High Level Trigger τ-jet candidate with the iterative cone algorithm using a cone size of 0.4. A number of requirements for τ-jet identification [146] is applied in addition to the tracker isolation which is tighter off-line than at the HLT and uses the tracks reconstructed with the full tracker. The additional τ-jet identification criteria include requirements to have one or three tracks in the signal cone and opposite charge of the two τ-jets for the $\tau\tau \to$ jj mode or the lepton and the τ-jet for the $\tau\tau \to \ell$j modes and cuts on the transverse impact parameter and on the p_T of the leading track in the signal cone. Finally an electron rejection criterion was applied for the jets. The τ-jet tagging reduces the QCD multi-jet (including $b\bar{b}$) and the W+jet backgrounds.

The associated $b\bar{b}$H(A) production dominates at high values of tan β, thus it is natural to apply b-jet tagging which must suppress Drell–Yan $\tau\tau$ production and eliminate further the QCD multi-jet and the W+jet backgrounds. Since the b-jets in the signal are very soft in E_T and have flat distribution in pseudorapidity only single b tagging is applied. Furthermore, it is possible to veto events with additional jets to reduce $t\bar{t}$ background. The τ-jets found in the first step are not considered for b tagging. Non τ-jet candidates are reconstructed with the iterative cone algorithm using a cone size of 0.5.

The energy of the τ-jet is corrected with a dedicated calibration obtained from Monte-Carlo sample of single τ-jets at low luminosity. The energy of other jets in the event is corrected applying Monte Carlo calibration evaluated from the QCD multi-jet events at low luminosity.

5.2.5. Method of the Higgs boson mass reconstruction

Despite the escaping neutrinos, the Higgs boson mass can be reconstructed in the $H \to \tau\tau$ channels from the visible τ momenta (leptons or τ-jets) and the missing transverse energy (E_T^{miss}) with the collinearity approximation for the neutrinos from highly boosted τ's. The mass resolution depends on the angle $\Delta\varphi$ between the visible τ momenta as $1/\sin(\Delta\varphi)$ and is sensitive to the E_T^{miss} measurement, both in magnitude and particularly in direction. The measurement of E_T^{miss} is affected by the non-linear calorimeter response. A method to improve

the E_T^{miss} scale based on the jet energy corrections was used [147, 148]. The correction of the missing E_T scale improves the reconstruction efficiency by reducing the number of events with negative reconstructed τ lepton and neutrino energies. In particular, for the case of the $\tau\tau \to$ jj final state the efficiency is improved by factor of $\simeq 1.6$. The $\tau\tau$ mass reconstruction method will be verified with the real data using $Z \to \tau\tau \to e(\mu) + \text{jet}$ and $Z \to \tau\tau \to e + \mu$ channels [145, 149].

5.2.6. $H \to \tau\tau \to 2\text{jet}$ *analysis*

A detailed description of the analysis can be found in [150].

5.2.6.1. Event generation and pre-selections. The $t\bar{t}$, Drell–Yan production of Z/γ^*, W+jet and Wt backgrounds were generated with PYTHIA, forcing $W \to \tau\nu$ and $Z/\gamma^* \to \tau\tau$ decays. The TAUOLA package was used for τ-lepton decays into all possible decay modes.

The Z/γ^* generation was split into three bins of generated diτ-lepton mass $m_{\tau\tau}$: 80–130 GeV/c^2, 130–300 GeV/c^2 and >300 GeV/c^2. The $\tau\tau b\bar{b}$ generation was divided into two bins of generated diτ-lepton mass $m_{\tau\tau}$: 60–100 GeV/c^2 and >100 GeV/c^2. The $\tau\tau b\bar{b}$ background, generated with COMPHEP, was propagated to PYTHIA for showering, hadronisation and τ lepton decays into all possible modes.

The W + jet background was generated using PYTHIA processes 16 and 31 and with $\hat{p}_T > 65$/GeV/c. The QCD multi-jet background generation was done for four bins in $\hat{p}_T$: 50–80, 80–120, 120–170 and >170 GeV/c.

The loose pre-selections at the level of generation were applied for all backgrounds (except $\tau\tau b\bar{b}$): the event was required to have at least two "τ-like" jets. The jets were reconstructed with the PYTHIA PYCELL routine using a cone size of 0.5. A jet is selected as "τ-like" if it has $E_T^{MC} > 50$ GeV, $|\eta^{MC}| < 2.4$ and a transverse momentum of the leading stable charged particle in the jet, $p_T^{MC} > 30$ GeV/c. These cuts are looser than the ones applied at the trigger and off-line τ-jet selections. For Z/γ^* background no cut was applied on p_T^{MC}.

For the signal events the Higgs boson was forced to decay into two τ leptons and the τ lepton was decayed hadronically using TAUOLA. No pre-selections were applied for the signal events.

5.2.6.2. Event selections. The calorimeter τ-jet jet candidates are reconstructed in the η-φ regions of the High Level Trigger τ-jet candidates, thus no "volunteers" are searched for. This is motivated by the high ($\simeq 100\%$) purity of the HLT τ-jet candidates (fraction of true τ-jets matched with τ-jet candidates).

A cut on the uncalibrated transverse jet energy for each of the two τ-jet candidates was required. It was $E_T > 50$ GeV for $M_A = 200$ GeV/c^2. For higher Higgs boson masses asymmetrical cuts were used: 100, 50 GeV for $M_A = 500$ GeV/c^2 and 150, 50 GeV for $M_A = 800$ GeV/c^2. It allows more effective rejection of the QCD multi-jet background. The following τ-jet identification criteria were then used:

- tracker isolation with parameters: $R_m = 0.1, R_S = 0.04, R_i = 0.5, p_T^i = 1$ GeV/c;
- transverse momentum of the leading track > 35 GeV/c;
- one or three tracks in the signal cone N_{tr}^S for $M_A = 200$ GeV/c^2. For higher Higgs boson masses an effective background rejection is only possible by requiring only one track in the signal cone.

Finally, the two τ-jet candidates were required to have opposite charge. The charge was calculated as the sum of charges of the tracks in the signal cone.

After identification of two τ-jets the other jets in the event were considered. It was required to have only one additional jet with uncalibrated energy $E_T^{raw} > 20$ GeV and $|\eta| < 2.4$. It had to be tagged as b-jet. The b-jet identification was performed using the impact parameter

Table 5.11. The summary table of the selections for signals of $M_A = 200, 500$ and $800\,GeV/c^2$.

	$m_A = 200\,GeV/c^2$ $\tan\beta = 20$	$m_A = 500\,GeV/c^2$ $\tan\beta = 30$	$m_A = 800\,GeV/c^2$ $\tan\beta = 40$
Cross sections and branching ratios			
$\sigma(gg \to b\bar{b}(A+H))$ (fb)	45795 + 44888	2741 + 2744	677 + 677
BR($H/A \to \tau\tau$)	0.1	0.082	0.087
BR($\tau \to$ hadrons)^2		0.65×0.65	
$\sigma \times$ BR (fb)	3831	190	49.8
Experimental selection efficiencies			
Level-1 Trigger	0.506	0.854	0.896
HLT	0.289	0.319	0.314
two off-line calo τ jets	0.997	0.999	0.999
cuts on E_T τ jets	0.430	0.755	0.780
two off-line τ candidates	0.674	0.716	0.675
$p_T^{ltr} > 35\,GeV/c$	0.326	0.616	0.713
tracker isolation	0.859	0.950	0.954
N_{tracks} in signal cone	0.81	0.67	0.78
$Q_{\tau 1} \times Q_{\tau 2} = -1$	0.98	0.94	0.94
$\geqslant 1$ extra jet, $E_T^{raw} > 20\,GeV$, $\lvert\eta\rvert < 2.4$	0.21	0.27	0.31
only 1 extra jet, $E_T^{raw} > 20\,GeV$, $\lvert\eta\rvert < 2.4$	0.83	0.82	0.78
$M_{\tau\tau}$ reconstruction efficiency			
$E_{\tau 1,\tau 2} > 0$	0.93	0.93	0.92
$E_{\nu 1,\nu 2} > 0$	0.56	0.67	0.67
total mass reconstruction	0.52	0.62	0.62
b tagging of the extra jet	0.36	0.44	0.41
$M_{\tau\tau}$ mass window	150–300 GeV/c^2	400–700 GeV/c^2	600–1100 GeV/c^2
mass window efficiency	0.81	0.73	0.81
total efficiency	2.5×10^{-4}	2.4×10^{-3}	3.6×10^{-3}
σ after selections (fb)	0.96	0.46	0.19
number of events for $60\,fb^{-1}$	58.0	27.0	11.0

tagging in 3D space [151]. The jet had to have at least three tracks with an impact parameter significance >2. The purity of the b-tagged jet for the signal is very high (>95%).

The diτ-jet mass reconstruction efficiency is affected by the requirements to have a positive reconstructed energy of both neutrinos, $E_T^{\nu_1,\nu_2} > 0$. In the missing E_T corrections jets with raw energy $E_T^{raw} > 25$ were used.

5.2.6.3. Expected number of selected events. This section summarises the event selections, the corresponding cross sections and expected number of events for the signal and the background processes after the selections. The efficiency of all selections shown in the tables of this section was evaluated relative to the previous selection.

Signal. Table 5.11 summarises the expectations for a signal of $M_A = 200$, 500 and $800\,GeV/c^2$. The signal cross sections and the branching ratios were obtained for the m_h^{max} scenario with $\mu = 200\,GeV/c^2$ (see Section 11.3.1).

QCD multi-jet background. Despite the huge amount of generated events (more than one million) and generation pre-selections, the statistics of the QCD multi-jet background events is not enough to ensure a large number of Monte Carlo events passing all the selections. In order to decrease the statistical uncertainties a factorisation of the selections was applied. All

Table 5.12. The summary table of the selections for the QCD multi-jet background. The selections are factorised as explained in the text. The requirement to have opposite charge τ-jet candidates ($Q_1 \times Q_2 = -1$) is not included.

	QCD dijet background in bins of generated $\hat{p}_T$			
	>170 GeV/c	120–170 GeV/c	80–120 GeV/c	50–80 GeV/c
σ (fb)	1.33×10^8	5.03×10^8	2.94×10^9	2.08×10^{10}
$\varepsilon_{\text{kine pres.}}$	2.12×10^{-1}	4.19×10^{-2}	5.77×10^{-3}	2.44×10^{-4}
Group1 cuts: Level-1 trigger + L2 and offline calo reco + E_T cut				
Level-1 trigger	0.562	0.726	0.715	0.461
Two Level 2 calo jets with $\Delta R_{JJ} > 1.0$	0.927	0.959	0.982	0.987
two off-line calo τ jets	0.975	0.975	0.982	0.994
cuts on E_T τ jets	0.753	0.804	0.774	0.343
$\varepsilon_{\text{Group1}}$	0.383	0.547	0.534	0.155
Group2 cuts: τ-jet identification at HLT and off-line				
HLT Calo+Pxl τ trigger	7.15×10^{-4}	1.81×10^{-3}	4.44×10^{-3}	1.12×10^{-2}
Two off-line τ candidates	0.86	0.84	0.825	0.84
$p_T^{ltr} > 35$ GeV/c	0.47	0.41	0.42	0.38
Tracker isolation	0.24	0.21	0.25	0.35
Factorised inside group 2				
1 or 3 prongs in $^{1st}\tau$ *jet*	0.66	0.92	0.63	0.72
1 or 3 prongs in $^{2nd}\tau$ *jet*	0.48	0.54	0.65	0.72
$\varepsilon_{\text{Group2}}/\varepsilon_{\text{Group1}}$	2.30×10^{-5}	6.33×10^{-5}	1.63×10^{-4}	6.54×10^{-4}
Group3 cuts: extra jet reco and b tagging plus $M_{\tau\tau}$ reco and mass window				
$\geqslant 1$ extra jet, $E_T^{raw} > 20$ GeV, $\lvert\eta\rvert < 2.4$	0.463	0.235	0.127	0.090
Only 1 extra jet, $E_T^{raw} > 20$ GeV, $\lvert\eta\rvert < 2.4$	0.661	0.817	0.863	0.855
Factorised inside group 3: $M_{\tau\tau}$ and b tagging				
$E_{\tau 1,\tau 2} > 0$	0.921	0.898	0.882	0.834
$E_{\nu 1,\nu 2} > 0$	0.701	0.683	0.657	0.625
Total mass reconstruction	0.646	0.613	0.579	0.522
b tagging of the extra jet	0.098	0.050	0.033	0.016
$M_{\tau\tau}$ window: 150–300 GeV/c^2	0.142	0.295	0.433	0.430
$\varepsilon_{\text{Group3}}/\varepsilon_{\text{Group1}}$	2.77×10^{-3}	1.75×10^{-3}	9.15×10^{-4}	2.28×10^{-4}
$\varepsilon_{\text{Group1}} \times \varepsilon_{\text{Group2}} \times \varepsilon_{\text{Group3}}$	2.44×10^{-8}	6.07×10^{-8}	7.98×10^{-8}	2.84×10^{-8}
σ after selections (fb)	0.69	1.28	1.35	0.144
Number of events for 60 fb^{-1}	41.4	76.7	81.2	8.7

selections were combined in three groups as shown in Table 5.12. Group1 includes the Level-1 trigger and the calorimetric reconstruction of the τ-jets (at HLT and offline). It includes also the cut on the transverse energy of the jets. After the event passed the Group1 selections the two other selection groups (Group2 and Group3) were applied independently. Group2 is essentially the τ-jet identification part of the analysis, i.e. the tracker isolation (at HLT and off-line), the cut on the p_T of the leading track and the selection on the number of tracks inside the signal cone. Group3 describes the selections on the one extra jet in the event, the b tagging and the diτ-jet mass reconstruction. The choice of the second and third selection groups was made minimising the correlation among them. A further factorisation was done for some selections inside the groups. Table 5.12 summarises the selections and the QCD multi-jet background estimates for the signal of $M_A = 200$ GeV/c^2. The requirement to have opposite charge τ-jet candidates ($Q_1 \times Q_2 = -1$) is not included in Table 5.12. It reduces the QCD multi-jet

Table 5.13. The number of expected events with 60 fb^{-1} and efficiencies of some of the selections for the irreducible backgrounds.

process	$N_{exp.}$ at 60 fb^{-1}	$Q_{\tau 1} \times Q_{\tau 2} = -1$	only one extra jet	b tag. jet	$M_{\tau\tau}$ window
$t\bar{t}$	0.64	0.96	0.36	0.42	0.11
W+j	0.33	0.81	0.15	0.06	0.12
Wt	0.26	0.96	0.49	0.44	0.23
$Z/\gamma^* \to \tau\tau$ in bins of generated $m_{\tau\tau}$					
$130 < m_{\tau\tau} < 300\,GeV/c^2$	3.80	0.96	0.23	0.06	0.61
$m_{\tau\tau} > 300\,GeV/c^2$	0.18	0.95	0.27	0.05	0.04
$\tau\tau b\bar{b}$, $m_{\tau\tau} > 100\,GeV/c^2$	0.86	0.98	0.39	0.44	0.38

background by another factor of two, leading to 104 events of the QCD multi-jet background expected with 60 fb^{-1}. With the selections applied to search for signals of $M_A = 500\,GeV/c^2$ and $M_A = 800\,GeV/c^2$ the expected numbers of the QCD multi-jet background with 60 fb^{-1} are 25.0 and 4.0, respectively.

Irreducible background. The irreducible background which remains after all selections were applied is the small part of the total background dominated by the QCD multi-jet events. Table 5.13 summarises the expected number of events from the irreducible background with 60 fb^{-1} for the selections used to search for a signal of $M_A = 200\,GeV/c^2$. In total, 6.0 events are expected. The efficiencies of some of the selections are also shown in the table. With the selections applied to search for signals of $M_A = 500\,GeV/c^2$ and $M_A = 800\,GeV/c^2$ the expected numbers of the irreducible background with 60 fb^{-1} are 4.0 and 1.0, respectively.

5.2.6.4. Detector effects, experimental systematics and evaluation of the background from data.

E_T^{miss} and jet energy scale uncertainties. The effect of the E_T^{miss} and the jet energy scale uncertainty on the Higgs boson mass reconstruction efficiency was estimated. The E_T^{miss} is reconstructed with the Type 1 corrections in the following form:

$$E_{Tx(y)}^{miss} = -\left(E_{Tx(y)}^{raw} + \sum_{jets}\left(E_{Tx(y)}^{corr.jet} - E_{Tx(y)}^{rawjet}\right)\right) \tag{5.11}$$

where $E_{Tx(y)}^{raw}$ is the sum over the raw calorimeter tower energies from calorimeter towers and the jet sum in the equation is over jets with a reconstructed $E_T^{raw} > 25\,GeV$. The formula can be rewritten in the form:

$$E_{Tx(y)}^{miss} = -\left(\left[E_{Tx(y)}^{raw} - \sum_{jets} E_{Tx(y)}^{rawjet}\right]_{low\,E_T} + \left[\sum_{jets} E_{Tx(y)}^{corr.jet}\right]_{high\,E_T}\right) \tag{5.12}$$

representing of low and high E_T parts. For the low E_T part a scale uncertainty of 10% was applied, while for the high E_T part 3% uncertainty was used. The variation of the scale is applied independently for the two parts to obtain the maximal upper and lower deviations from the case with no uncertainty. It was found that the E_T^{miss} scale uncertainty brings the largest contribution to the uncertainty of the Higgs boson mass reconstruction efficiency. In the worst case the uncertainty reaches 3%. The mean fitted value of the $M_{\tau\tau}$ distribution for a

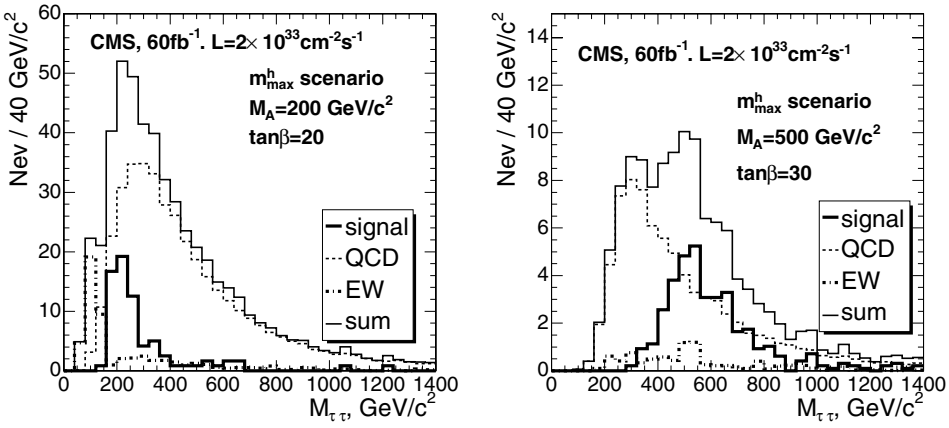

Figure 5.3. The expected $M_{\tau\tau}$ distributions for the signal of $M_A = 200\,\mathrm{GeV/c^2}$, $\tan\beta = 20$ (left plot) and $M_A = 500\,\mathrm{GeV/c^2}$, $\tan\beta = 30$ (right plot) and the background with $60\,\mathrm{fb^{-1}}$. Thick solid histogram – signal in the m_h^{max} scenario; dashed histogram – the QCD multi-jet background; thick dashed-dotted histogram – the irreducible background; normal solid histogram – signal plus background.

signal of $M_A = 500\,\mathrm{GeV/c^2}$ is varied from $-10\,\mathrm{GeV/c^2}$ to $+16\,\mathrm{GeV/c^2}$ relative to the mean value evaluated without the scale uncertainty taken into account.

Tracker misalignment. The effect of the tracker misalignment on the rate of fake τ-jets from the QCD multi-jet background was studied for the first data taking scenario (Scenario 1) and the long term data taking scenario (Scenario 2). The tracker isolation efficiency and the efficiency of the track counting in the signal cone (one or three tracks requirement) was compared with the performance of the perfect tracker alignment (Scenario 0).

It was found that in the Scenario 2 the QCD multi-jet background can be increased by $\simeq$11% due to the change of the tracker isolation efficiency. The efficiency of the requirement to have one track in the signal cone is increased by $\simeq$10% in the Scenario 2 relative to the perfect alignment.

The measurement of the QCD multi-jet background from the data. Figure 5.3 (left plot) shows the expected $M_{\tau\tau}$ distribution for two signal samples and the background. The QCD multi-jet background is the biggest background in this analysis. The following way to evaluate this background from the data is proposed: A control sample must be used where all signal selections are applied except the mass window and the requirement to have an opposite charge of the two τ-jet candidates. It is proposed to select, instead, the sample with the same charge of the two τ-jet candidates (SS sample). The contamination of the signal events and irreducible background is negligible in the SS sample, thus giving the possibility to predict from the data the QCD multi-jet background in a given mass window from the number of event and the measured shape of the diτ-jet mass in SS sample. The expected number of QCD multi-jet SS events after all selections, but the mass window, used for the signal of $M_A = 200\,\mathrm{GeV/c^2}$ is 380 with $60\,\mathrm{fb^{-1}}$. Neglecting the uncertainty of the measured shape of the diτ-jet mass leads to 5% statistical uncertainty of the QCD multi-jet background estimates under the signal mass window. For the $M_A = 500$ (800) $\mathrm{GeV/c^2}$ selections about 80 (28) SS QCD multi-jet events are expected, thus giving $\simeq$10 (20) % statistical uncertainty.

Table 5.14. The lower limit of tan β where a 5σ discovery is possible with 60fb^{-1}.

Low tanβ limit for 5σ discovery	Higgs boson mass $m_A = 200\,\text{GeV/c}^2$	$m_A = 500\,\text{GeV/c}^2$	$m_A = 800\,\text{GeV/c}^2$
no systematics	20	32	46
with systematics	21	34	49

5.2.6.5. Discovery reach in the $M_A - \tan\beta$ *plane.* Table 5.14 shows the lowest value of $\tan\beta$ for the three Higgs boson masses considered in the analysis, where the 5σ discovery is possible with $60\,\text{fb}^{-1}$. It is shown with and without QCD multi-jet background systematic uncertainty taken into account. The significance of the discovery is calculated with the S_{cP} method.

The extension of the discovery reach to lower values of $\tan\beta$ would be possible with a lower threshold on the energy of the additional jet in the event, provided that the fake jets will be then suppressed with the jet-tracks matching criteria. Another improvement is expected from the increase of the Higgs boson mass reconstruction efficiency using the improved missing E_T measurement from energy-flow like algorithms. Finally, improved b-jet tagging performance is expected to extend the discovery reach to lower values of $\tan\beta$.

5.2.7. $H \to \tau\tau \to \mu + \text{jet}$ *analysis*

A detailed description of the analysis can be found in [152].

5.2.7.1. Event generation and pre-selections. For the irreducible Drell–Yan (DY) $\tau\tau$ background the $\tau_{1(2)} \to \mu\nu\nu$, $\tau_{2(1)} \to \text{hadrons} + \nu$ decays were forced in PYTHIA. The events containing b quarks were rejected to avoid the double counting with the $\tau\tau b\bar{b}$ background. For the other background processes, $t\bar{t}$, Wt, W+jet and $b\bar{b}$ no specific decay mode was forced.

The DY $\tau\tau$ background was produced in two ranges of the $\tau\tau$ invariant mass: $40 < m_{\tau\tau} < 120\,\text{GeV/c}^2$ and $m_{\tau\tau} > 120\,\text{GeV/c}^2$. For $\tau\tau b\bar{b}$ the following mass bins were used: $60 < m_{\tau\tau} < 100\,\text{GeV/c}^2$ and $m_{\tau\tau} > 100\,\text{GeV/c}^2$. The W+jet background was generated with $\hat{P}_T > 20\,\text{GeV/c}^2$.

The SUSY background has been estimated using the events for the LM2 mSUGRA test point (see Section 13.3.2) with the total NLO SUSY cross section of 9.4 pb. For this point $\tan\beta = 35$, which makes the stau and tau production rate potentially dangerous. The number of events after all selection has been estimated to be less than one, therefore the SUSY background has been considered negligible, and was not studied in detail.

For the signal generation the Higgs boson was forced to decay into a τ pair. The τ leptons were decayed using TAUOLA and events with $\tau_{1(2)} \to \mu\nu\nu$, $\tau_{2(1)} \to \text{hadrons} + \nu$ decays were selected.

The pre-selections at generation level were chosen in a way that selected events are likely to pass the trigger selection. The requirements were: The isolation of the muon was defined as absence of charged particles with $p_T > 1\,\text{GeV/c}$ within a cone of radius 0.2 in the $\eta - \varphi$ space around the muon momentum direction. Isolation for the τ-like jet allowed for at most one charged particle with $p_T > 1\,\text{GeV/c}$ in the ring with an inner radius of 0.1 and an outer radius of 0.4 around the highest p_T charged particle in the jet. The leading track was required to have $p_T > 3\,\text{GeV/c}$. The $\tau\tau b\bar{b}$ events were generated without the pre-selection requirements.

Details on $b\bar{b}$ generation are explained in [153].

5.2.7.2. Event selection. The off-line τ-jet identification uses the parameters of the pixel HLT τ isolation, but with fully reconstructed tracks instead of pixel tracks. Additionally one or three tracks are required in the signal cone. For the τ-jet direction, the sum of the momenta of the signal tracks was used, improving the direction resolution. The leading τ-jet track is required to have $p_T > 10\,GeV/c$ in case of one track in the signal cone, and $p_T > 20\,GeV/c$ for three tracks, in order to suppress the $b\bar{b}$ and DY $\tau\tau$ backgrounds.

To select events with associated $b\bar{b}H(A)$ production, one b-tagged jet with calibrated $E_T > 20\,GeV$ was required. For the b tagging, the track counting method was used [151]: the jet is b tagged if it has at least two tracks with a 2D transverse impact parameter significance greater than two. The b tagging efficiency, including the jet finding, for the signal is 17% for $M_A = 200\,GeV/c^2$ and 27% for $M_A = 500\,GeV/c^2$. For the backgrounds with a real b-jet it is 67% for $t\bar{t}$ and 46% for Wt processes. For the backgrounds without a real b-jet the mistagging efficiency is 1% for the W+jet and 3% for the DY $\tau\tau$ processes. The b tagging purity for the signal and the $t\bar{t}$ background is 95%; it is 90% for the Wb and the $\tau\tau b\bar{b}$ processes.

Events containing W bosons decaying into $\mu + \nu_\mu$ are suppressed using a cut on the transverse mass of the muon and the missing transverse energy: $m_T = \sqrt{2 \cdot p_T^\mu \cdot \not{E}_T\,(1 - \cos(\vec{p}_T^{\,\mu}, \vec{\not{E}}_T))}$, where $\vec{\not{E}}_T$ is the missing transverse energy. The distribution of m_T has a Jacobian peak near the W mass. Rejecting events with $m_T > 60\,GeV$ largely reduces the $t\bar{t}$, Wt and W+jet backgrounds while retaining a good fraction of the signal events.

The additional selection against the $t\bar{t}$ background is the central jet veto. All events containing an additional jet (to the τ jet and the b-tagged jet) in the central region, $|\eta| < 2.5$, and with a calibrated $E_T > 20\,GeV$ were rejected.

The electrons from the W boson decays in the $t\bar{t}$ and Wt backgrounds can be misidentified as τ-jets. For the electron rejection a cut on the ratio of the τ-jet energy measured in the HCAL (E^{HCAL}) to the leading track momentum (p^{ltr}), $f = E^{HCAL}/p^{ltr}$, was used for the events with one track in the signal cone. The cut $f > 0.2$ retains 90% of the signal events, while it rejects 95% of the events with the real electrons. The cut on the upper value of the ratio is efficient against jets with a large fraction of neutral hadrons. The requirement $f < 1.1$ rejects 50% of W+j and $b\bar{b}$ events and only 20% of signal events. Figure 5.4 shows the integrated distribution of the parameter f for the signal and the background events selected by the High Level trigger. The labels on the right part of the figure are ordered by decreasing selection efficiency in the acceptance region of $0.2 < f < 1.1$, marked by the arrows.

The Higgs boson mass reconstruction requires the rejection of events with a μ and a τ jet in a back-to-back topology, therefore the cut $\cos(\Delta\varphi(\vec{p}_T, \vec{E}_T^{\,jet})) > -0.9962$ was used. In addition, an upper cut on $\cos(\Delta\varphi(\vec{p}_T, \vec{E}_T^{\,jet})) < -0.5$ was used, retaining most of the signal events, while visibly reducing a fraction of the background events. Finally, the events with a negative reconstructed neutrino energy were rejected.

5.2.7.3. Expected number of selected events. Table 5.15 presents the production cross sections in fb and the individual selection efficiencies for signals of $M_A = 200$ and $500\,GeV/c^2$. The signal cross sections and the branching ratios were obtained for the m_h^{max} scenario with $\mu = 200\,GeV$ (see Section 11.3.1). Tables 5.16–5.18 summarise the cross sections and the individual selection efficiencies for the background processes. The total efficiency of all selections and the cross sections after all selections are also presented at the end of the tables. The events were counted in the $M_{\tau\tau}$ mass windows with the width taken to be $\pm\sigma$, where σ is given by the standard deviation of a Gaussian fit of the signal $M_{\tau\tau}$ distributions. The value of σ is $41\,GeV/c^2$ for $M_A = 200\,GeV/c^2$, whereas it is $83\,GeV/c^2$ for $m_A = 500\,GeV/c^2$. With an integrated luminosity of $20\,fb^{-1}$ the expected number of signal (background) events is

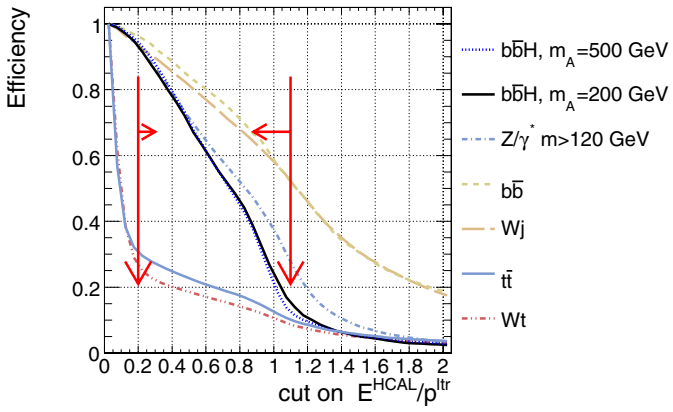

Figure 5.4. The integrated distribution of the parameter $f = E^{HCAL}/p_T^{ltr}$. The acceptance region of $0.2 < f < 1.1$ is marked by the arrows.

Table 5.15. The production cross sections, in fb, and the individual selection efficiencies for the signal.

	$gg \to b\bar{b}(A+H)$, $A, H \to \tau\tau$	
	$M_A = 200\,GeV/c^2$ $\tan(\beta) = 20$	$M_A = 500\,GeV/c^2$ $\tan(\beta) = 30$
$\sigma \times$ BR [fb]	$9.12 \cdot 10^3$	$4.51 \cdot 10^2$
kine pre-selection	$9.47 \cdot 10^{-2}$	$1.65 \cdot 10^{-1}$
Level-1 trigger	$8.99 \cdot 10^{-1}$	$9.09 \cdot 10^{-1}$
HLT	$4.17 \cdot 10^{-1}$	$4.99 \cdot 10^{-1}$
offline τ-jet isolation	$9.54 \cdot 10^{-1}$	$9.60 \cdot 10^{-1}$
1 or 3 tk. in τ-jet signal cone	$9.12 \cdot 10^{-1}$	$9.19 \cdot 10^{-1}$
$p_T^{ltr} > 10\,GeV/c$	$9.05 \cdot 10^{-1}$	$9.55 \cdot 10^{-1}$
$Q_\mu \cdot Q_{jet} = -1$	$9.61 \cdot 10^{-1}$	$9.60 \cdot 10^{-1}$
single b tagging	$1.73 \cdot 10^{-1}$	$2.56 \cdot 10^{-1}$
no jet with $E_T > 20$, $\lvert\eta\rvert < 2.5$	$8.53 \cdot 10^{-1}$	$7.72 \cdot 10^{-1}$
$m_T(l, MET) < 60\,GeV$	$8.33 \cdot 10^{-1}$	$7.01 \cdot 10^{-1}$
$-0.996 < \cos(\Delta\varphi) < -0.5$	$8.05 \cdot 10^{-1}$	$7.51 \cdot 10^{-1}$
electron veto: $0.2 < f < 1.1$	$8.22 \cdot 10^{-1}$	$8.54 \cdot 10^{-1}$
$E_{v1} > 0$, $E_{v2} > 0$	$6.84 \cdot 10^{-1}$	$7.68 \cdot 10^{-1}$
total efficiency:	$1.66 \cdot 10^{-3}$	$4.53 \cdot 10^{-3}$
σ after selections [fb]:	$1.52 \cdot 10^1$	2.05

146 (127) for $m_A = 200\,GeV/c^2$, $\tan\beta = 20$, and 21 (61) for $m_A = 500\,GeV/c^2$, $\tan\beta = 30$. Figure 5.5 shows the expected $\tau\tau$ mass distribution for the total background and for the signal plus background for $M_A = 200\,GeV/c^2$, $\tan\beta = 20$ and $M_A = 500\,GeV/c^2$, $\tan\beta = 30$.

5.2.7.4. Background estimates and uncertainty. After all off-line selections the main background is represented by the $\tau\tau b\bar{b}$, DY $\tau\tau$ and the $t\bar{t}$ production processes. The contribution of the non Z/γ^* background, mainly the $t\bar{t}$ events, can be estimated applying the inversion of the electron veto: $f < 0.1$ instead of $0.2 < f < 1.1$. All other cuts must be the same, including the $M_{\tau\tau}$ mass window. A relatively pure sample of $t\bar{t}$ can be selected, since

Table 5.16. The production cross sections, in fb, and the individual selection efficiencies for the reducible background processes.

	$t\bar{t}$	$W + jet$	Wt	$b\bar{b}$
σ [fb]	$8.40 \cdot 10^{5}$	$4.15 \cdot 10^{7}$	$6.20 \cdot 10^{4}$	$2.29 \cdot 10^{10}$
kine preselection	$9.01 \cdot 10^{-2}$	$1.44 \cdot 10^{-2}$	$6.58 \cdot 10^{-2}$	$7.56 \cdot 10^{-4}$
Level-1 trigger	$9.06 \cdot 10^{-1}$	$8.40 \cdot 10^{-1}$	$8.91 \cdot 10^{-1}$	$2.26 \cdot 10^{-2}$
H LT	$9.61 \cdot 10^{-2}$	$4.16 \cdot 10^{-2}$	$1.05 \cdot 10^{-1}$	$2.36 \cdot 10^{-4}$
offline τ-jet isolation	$8.51 \cdot 10^{-1}$	$6.70 \cdot 10^{-1}$	$8.79 \cdot 10^{-1}$	$8.69 \cdot 10^{-1}$
1 or 3 tk. in τ-jet signal cone	$8.92 \cdot 10^{-1}$	$6.30 \cdot 10^{-1}$	$9.07 \cdot 10^{-1}$	$7.19 \cdot 10^{-1}$
$p_T^{ltr} > 10$GeV/c	$9.42 \cdot 10^{-1}$	$8.58 \cdot 10^{-1}$	$9.37 \cdot 10^{-1}$	$7.17 \cdot 10^{-1}$
$Q_\mu \cdot Q_{jet} = -1$	$9.18 \cdot 10^{-1}$	$7.31 \cdot 10^{-1}$	$9.52 \cdot 10^{-1}$	$5.45 \cdot 10^{-1}$
Single b tagging	$6.73 \cdot 10^{-1}$	$1.09 \cdot 10^{-2}$	$4.56 \cdot 10^{-1}$	$9.42 \cdot 10^{-2}$
no jet with $E_T > 20, \|\eta\| < 2.5$	$3.43 \cdot 10^{-1}$	$8.17 \cdot 10^{-1}$	$8.60 \cdot 10^{-1}$	$4.30 \cdot 10^{-1}$
$m_T(l, MET) < 60\,\mathrm{GeV/c^2}$	$3.53 \cdot 10^{-1}$	$3.76 \cdot 10^{-1}$	$3.62 \cdot 10^{-1}$	1.00
$-0.996 < \cos(\Delta\varphi) < -0.5$	$4.95 \cdot 10^{-1}$	$6.56 \cdot 10^{-1}$	$4.51 \cdot 10^{-1}$	$4.16 \cdot 10^{-1}$
electron veto: $< 0.2 < f < 1.1$	$1.65 \cdot 10^{-1}$	$4.76 \cdot 10^{-1}$	$1.27 \cdot 10^{-1}$	$2.98 \cdot 10^{-1}$
$E_{\nu 1} > 0, E_{\nu 2} > 0$	$4.08 \cdot 10^{-1}$	$2.00 \cdot 10^{-1}$	$4.15 \cdot 10^{-1}$	$3.60 \cdot 10^{-1}$
total efficiency:	$1.54 \cdot 10^{-5}$	$3.31 \cdot 10^{-8}$	$1.66 \cdot 10^{-5}$	$7.86 \cdot 10^{-11}$
σ after selections [fb]:	$1.30 \cdot 10^{1}$	1.37	1.03	1.80

Table 5.17. The production cross sections, in fb, and the individual selection efficiencies for the irreducible background processes.

	$Z/\gamma^* \to \tau\tau \to \mu +$jet	
	$40 < m_{\tau\tau} < 120\,\mathrm{GeV/c^2}$	$m_{\tau\tau} > 120\,\mathrm{GeV/c^2}$
$\sigma \times$ BR [fb]	$4.63 \cdot 10^{5}$	$4.88 \cdot 10^{3}$
kine preselection	$6.56 \cdot 10^{-2}$	$2.14 \cdot 10^{-1}$
Level-1 trigger	$8.00 \cdot 10^{-1}$	$8.28 \cdot 10^{-1}$
HLT	$1.03 \cdot 10^{-1}$	$2.77 \cdot 10^{-1}$
offline τ-jet isolation	$9.12 \cdot 10^{-1}$	$9.40 \cdot 10^{-1}$
1 or 3 tk. in τ-jet signal cone	$9.03 \cdot 10^{-1}$	$8.93 \cdot 10^{-1}$
$p_T^{ltr} > 10$GeV/c	$8.12 \cdot 10^{-1}$	$9.00 \cdot 10^{-1}$
$Q_\mu \cdot Q_{jet} = -1$	$9.47 \cdot 10^{-1}$	$9.33 \cdot 10^{-1}$
single b tagging	$2.68 \cdot 10^{-2}$	$2.51 \cdot 10^{-2}$
no jet with $E_T > 20, \|\eta\| < 2.5$	$7.77 \cdot 10^{-1}$	$6.98 \cdot 10^{-1}$
$m_T(l, MET) < 60\,\mathrm{GeV/c^2}$	$9.41 \cdot 10^{-1}$	$7.74 \cdot 10^{-1}$
$-0.996 < \cos(\Delta\varphi) < -0.5$	$3.75 \cdot 10^{-1}$	$6.57 \cdot 10^{-1}$
electron veto: $0.2 < f < 1.1$	$6.46 \cdot 10^{-1}$	$7.29 \cdot 10^{-1}$
$E_{\nu 1} > 0, E_{\nu 2} > 0$	$6.45 \cdot 10^{-1}$	$6.46 \cdot 10^{-1}$
total efficiency:	$1.31 \cdot 10^{-5}$	$1.75 \cdot 10^{-4}$
σ after selections [fb]:	6.08	$8.53 \cdot 10^{-1}$

the requirement $f < 0.1$ rejects more than 95% of all processes except the $t\bar{t}$ and Wt as shown in Figure 5.4. The number of the non Z/γ^* background events in the signal region can be then predicted using the ratio of the $t\bar{t}$ events in the signal region of $0.2 < f < 1.1$ and in the region of $f < 0.1$. This ratio can be obtained from Monte-Carlo simulation or from real $t\bar{t}$ data. The systematic uncertainty on the number of the non Z/γ^* background events predicted using this method has two contributions:

- The uncertainty of the HCAL energy scale, since the variable $f = E^{HCAL}/p^{ltr}$ includes the HCAL part of the τ-jet candidate energy measured by the calorimeter. It is taken as 3%.

Table 5.18. The production cross sections, in fb, and the individual selection efficiencies for the irreducible background processes.

	$bb(Z \to \tau\tau)$	
	$60 < m_{\tau\tau} < 100\,\mathrm{GeV/c^2}$	$m_{\tau\tau} > 100\,\mathrm{GeV/c^2}$
$\sigma \times$ BR [fb]	$2.61 \cdot 10^{4}$	$1.05 \cdot 10^{3}$
kine preselection	1.00	1.00
Level-1 trigger	$1.41 \cdot 10^{-1}$	$1.64 \cdot 10^{-1}$
HLT	$4.10 \cdot 10^{-3}$	$1.21 \cdot 10^{-2}$
offline τ-jet isolation	$9.05 \cdot 10^{-1}$	$9.34 \cdot 10^{-1}$
1 or 3 tk. in τ-jet signal cone	$9.12 \cdot 10^{-1}$	$9.17 \cdot 10^{-1}$
$p_T^{ltr} > 10\,\mathrm{GeV/c}$	$8.60 \cdot 10^{-1}$	$8.98 \cdot 10^{-1}$
$Q_\mu \cdot Q_{jet} = -1$	$9.41 \cdot 10^{-1}$	$9.48 \cdot 10^{-1}$
single b tagging	$2.73 \cdot 10^{-1}$	$2.75 \cdot 10^{-1}$
no jet with $E_T > 20$, $\lvert\eta\rvert < 2.5$	$7.20 \cdot 10^{-1}$	$7.72 \cdot 10^{-1}$
$m_T(l, MET) < 60\,\mathrm{GeV}$	$9.68 \cdot 10^{-1}$	$8.80 \cdot 10^{-1}$
$-0.996 < \cos(\Delta\varphi) < -0.5$	$4.23 \cdot 10^{-1}$	$5.84 \cdot 10^{-1}$
electron veto: $0.2 < f < 1.1$	$6.98 \cdot 10^{-1}$	$5.11 \cdot 10^{-1}$
$E_{v1} > 0$, $E_{v2} > 0$	$4.32 \cdot 10^{-1}$	$5.62 \cdot 10^{-1}$
total efficiency:	$6.64 \cdot 10^{-5}$	$2.76 \cdot 10^{-4}$
σ after selections [fb]:	1.74	$2.89 \cdot 10^{-1}$

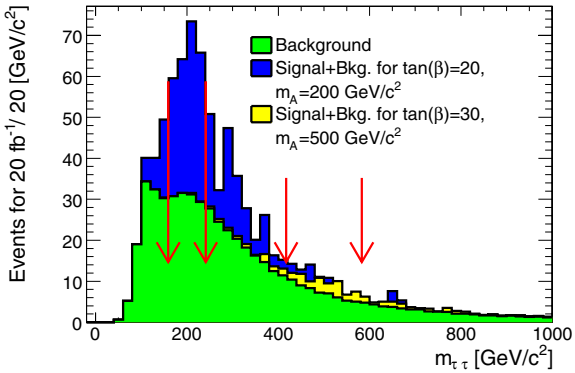

Figure 5.5. The reconstructed $\tau\tau$ mass distribution. The signal and the background contributions are shown with $20\,\mathrm{fb}^{-1}$. The mass windows in which the events are counted for the significance calculations are shown.

- The uncertainty of the shape of the distribution of f. The shape is obtained from $\bar{\mathrm{t}}\mathrm{t}$ events only, however a small fraction of events from the other processes is present in the "normalisation" region of $f < 0.1$. It leads to an uncertainty of $\simeq$12 %.

The contribution from the other systematic uncertainties, e.g. b tagging is expected to be small, due to the cancellation in the efficiency ratio. The total uncertainty on the number of the non Z/γ^* background events is thus 12.4 %.

The Z/γ^* background consists of two parts: the $\tau\tau\mathrm{b}\bar{\mathrm{b}}$ process and the DY $\tau\tau$ process without genuine b quarks in the event. The DY $\tau\tau$ background can be predicted using the DY $\ell\ell(\ell = \mathrm{e}, \mu)$ cross section, to be measured with high precision at LHC, and the selection

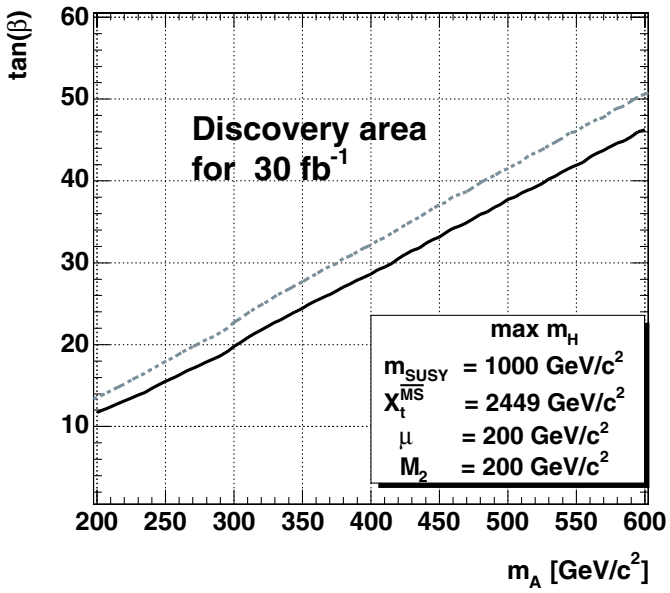

Figure 5.6. The 5σ discovery region in the $M_A - \tan\beta$ plane with 30 fb^{-1} of the integrated luminosity for the m_h^{max} MSSM scenario. The regions are shown without (lower curve) and with (upper curve) the uncertainty on the background taken into account.

efficiency obtained from the Monte-Carlo. The systematic uncertainty on the number of DY $\tau\tau$ events has two main contributions due to:

- The jet scale uncertainty. The number of the events in the $M_{\tau\tau}$ signal window varies by $\pm 6\%$ for jet scale variations of $\pm 3\%$ and missing transverse energy scale variations of $\pm 5\%$.
- The b-mistagging uncertainty. A conservative estimate of 5% is taken.

The total uncertainty on the number of the DY $\tau\tau$ events with the jet mistagged as a b-jet is therefore 8%.

For the $\tau\tau b\bar{b}$ background estimates the systematic uncertainty has the following main contributions:

- The uncertainty of the $\mu\mu b\bar{b}$ cross section measurement (without the luminosity uncertainty) is 14% [145].
- The jet scale uncertainty. It is assumed to be the same as for the DY $\tau\tau$ events.

The total uncertainty on the number of the $\tau\tau b\bar{b}$ events is 15%.

5.2.7.5. Discovery reach in the $M_A - \tan\beta$ *plane.* The CMS discovery reach in the $M_A - \tan\beta$ plane with 30 fb^{-1} in the m_h^{max} scenario is shown in Figure 5.6. The 5σ discovery curves are shown without (lower curve) and with (upper curve) the uncertainty on the background taken into account.

5.2.8. $H \to \tau\tau \to e +$ jet *analysis*

A detailed description of the analysis can be found in [154].

5.2.8.1. Event generation. The signal process $gg \to bbH/A, H/A \to \tau\tau, \tau_1 \to e\nu_e\nu_\tau, \tau_2 \to \tau$ jet $+\nu_\tau$ leads to a final state of one isolated electron, an isolated τ jet and one or two detectable b jets. The background with genuine τ's is due to two types of events, Z/γ^* events decaying into $\tau\tau$, and the $t\bar{t}$ events, where the $e+\tau$ jet final state can come from direct W decays to an electron and a τ or through $W \to \tau\nu_\tau \to e\nu_e\nu_\tau\nu_\tau$ decays:

- $Z/\gamma^* \to \tau\tau \to e + \tau$ jet $+ X$
- $b\bar{b}Z/\gamma^*, Z/\gamma^* \to \tau\tau \to e + \tau$jet $+ X$
- $t\bar{t}$ with $W_1 \to \tau\nu_\tau(\tau \to$ jet$)$, $W_2 \to e\nu_e$ or $W_2 \to \tau\nu_\tau \to e\nu_e\nu_\tau\nu_\tau$
- Wt, with $W_1 \to \tau\nu_\tau(\tau \to$ jet$)$, $W_2 \to e\nu_e$ or $W_2 \to \tau\nu_\tau \to e\nu_e\nu_\tau\nu_\tau$.

Background can arise also from the processes where a hadronic jet or an electron leads to a fake τ:

- W+jet, with $W \to e\nu_e$
- $Z/\gamma^* \to e^+e^-$
- $b\bar{b}Z/\gamma^*, Z/\gamma^* \to e^+e^-$
- $t\bar{t}$ with $W \to jj$ or $W \to e\nu_e$.

The QCD multi-jet production is a large potential background through hadronic jets faking both the electron and the τ jet.

For the inclusive Z/γ^* production the events containing b quarks in the final state were removed to avoid double counting with the $\tau\tau b\bar{b}$ background. The single top (Wt) events were generated with TopReX [44]. The τ decays in the signal were performed with the TAUOLA package [155].

5.2.8.2. Event selection. In the offline reconstruction an isolated electron from the decay of one of the τ's was first searched for. On the average $\sim$1.3 reconstructed electron candidates were found in the signal events. The reconstructed electrons were first required to be isolated in the tracker demanding that no track with $p_T > 1\,\text{GeV/c}$ was found in a cone of $\Delta R = 0.4$ around the electron candidate direction. The further electron identification was performed following the algorithm of Ref. [156]. The largest contribution to the identification efficiency and purity was obtained from the ratio of hadronic cluster energy to the electromagnetic energy of the cluster ($E^{\text{hadronic}}/E^{\text{elm}} < 0.2$) and from the ratio of the supercluster energy to the track momentum ($E^{\text{super cluster}}/p^{\text{track}} > 0.8$). The identification efficiency, including the tracker isolation, was found to be 64.2%. A good purity of 97.5% was obtained for the selected electrons.

The off-line τ-jet identification was applied to the jets with $E_T^{\text{jet}} > 40\,\text{GeV}$ reconstructed in the calorimeter with the cone of 0.4. The leading track with $p_T^{\text{ltr}} > 10\,\text{GeV/c}$ was searched for in a cone of $R_m = 0.1$ around the τ-jet direction. For an efficient isolation against the hadronic jets in the W+jet and QCD multi-jet backgrounds, a small signal cone, $R_S = 0.04$, around the leading track was used. About 83% of the $\tau^\pm \to \text{hadron}^\pm + n\pi^0 + \nu_\tau$ decays were found to be reconstructed as one prong τ's. Due to the small signal cone selected, 50% of the $\tau^\pm \to 3$ hadrons$^\pm + n\pi^0 + \nu_\tau$ decays were reconstructed as one or two prong τ-jets. The cut $p_T^{\text{ltr}} > 20\,\text{GeV/c}$ was found to be optimal for the suppression of the hadronic jets, in the presence of the QCD multi-jet background. The isolation was performed counting tracks with $p_T^i > 1\,\text{GeV/c}$ in the area between the signal cone and the isolation cone, which was taken to be then same as the jet reconstruction cone, $R_i = 0.4$. Following the method described in [146], at least eight hits were required in the full silicon tracker and an upper bound of 0.3 mm on the transverse impact parameter was set on the leading track in order to suppress the background from the fake tracks.

Table 5.19. Production cross sections times branching fraction, efficiencies (%) for the selection cuts and numbers of events for 30 fb^{-1} for the signal with $\tan\beta = 20$ and for $M_A = 130, 200, 300$ and 500 GeV/c^2.

$M_A(GeV/c^2)$	130	200	300	500
$\sigma \times BR$ (pb)	18.2	4.15	0.85	0.071
Level-1 and HLT	1.53 (8.4)	0.64 (15.4)	0.18 (21.6)	2.0×10^{-2} (28.7)
primary vertex	1.44 (94.1)	0.60 (94.2)	0.18 (97.2)	1.9×10^{-2} (93.6)
electron identification	1.11 (77.8)	0.48 (80.8)	0.14 (73.7)	1.4×10^{-2} (73.8)
one identified τ jet	0.127 (11.4)	0.11 (23.4)	4.5×10^{-2} (32.9)	5.9×10^{-3} (41.7)
$Q^{\tau\ jet} \times Q^e = -1$	0.127 (100.0)	0.11 (99.1)	4.5×10^{-2} (99.3)	5.8×10^{-3} (99.0)
$m_T < 40\,GeV/c^2$	9.9×10^{-2} (77.6)	3.8×10^{-2} (73.7)	3.1×10^{-2} (69.3)	3.9×10^{-3} (66.7)
$\geqslant$1 jet, $E_T > 20\,GeV$	4.5×10^{-2} (45.9)	3.8×10^{-2} (46.6)	1.5×10^{-2} (48.6)	2.1×10^{-3} (53.5)
b tagging	1.3×10^{-2} (29.7)	1.2×10^{-2} (32.2)	5.0×10^{-3} (32.9)	7.6×10^{-4} (36.5)
jet veto	8.1×10^{-3} (60.2)	7.2×10^{-2} (62.5)	3.1×10^{-3} (63.2)	4.6×10^{-4} (61.0)
$\Delta\varphi(\tau_1, \tau_2) < 175^\circ$	7.6×10^{-3} (94.8)	6.8×10^{-3} (93.9)	2.7×10^{-3} (85.7)	3.4×10^{-4} (74.5)
$E_{\nu_1,\nu_2} > 0$	4.1×10^{-3} (54.1)	4.2×10^{-3} (61.7)	1.7×10^{-3} (64.3)	2.4×10^{-4} (70.6)
N_{ev} at 30 fb^{-1}	123.9	126.0	51.9	7.3

The $Z/\gamma^* \to e^+e^-$ and $b\bar{b}Z/\gamma^*, Z/\gamma^* \to e^+e^-$ backgrounds contain an isolated genuine electron to pass the electron cuts and are not significantly suppressed with the τ-selection cuts. These electronic τ candidates were suppressed requiring a large energy deposition in the hadron calorimeter. A cut in the E_T of the most energetic HCAL cell in the τ jet, $E_T(\text{max HCAL cell}) > 2\,GeV$, was found to suppress the electrons with a factor of ~ 7. A further reduction was obtained comparing the HCAL energy and the leading track momentum of the τ jet. The cut $E^{HCAL}/p^{ltr} > 0.35$, applied on the one-prong τ candidates only, was found to suppress further the electronic τ candidates by a factor of $\sim$1.8. The W + jet events show a tail at large values of E^{HCAL}/p^{ltr} due to the neutral hadron component of the hadronic jets and were suppressed with the cut $E^{HCAL}/p^{ltr} < 1.5$.

Efficiencies of the τ-jet selections are shown in Tables 5.19, 5.20 and 5.21. The purity of $\sim 97\%$ is obtained for the signal events. A rejection factor of ~ 400 was obtained for the QCD multi-jet events generated with $50 < \hat{p}_T < 80\,GeV/c$ when the τ-jet selections described above were applied.

Finally, the charges of the electron and τ jet were required to be opposite. The charge of the τ jet was calculated as the sum of charges of the tracks in the signal cone.

The missing transverse energy measurement can be exploited to suppress the $t\bar{t}$ background with an upper bound on the transverse mass $m_T(e, E_T^{miss})$ reconstructed from the electron and the missing transverse energy. Figure 5.7 shows the $m_T(e, E_T^{miss})$ distribution for the signal events with $M_A = 200\,GeV/c^2$ and for the $t\bar{t}$ and $Z/\gamma^* \to e^+e^-$ backgrounds with the electron and τ-jet selections. The selected upper bound $m_T(e, E_T^{miss}) < 40\,GeV/c^2$ reduces the $t\bar{t}$ background with a factor of $\sim$4.

The events were further selected when at least one jet (in addition to the τ jet) with calibrated $E_T^{jet} > 20\,GeV$ and $|\eta| < 2.5$ was found and tagged as the b jet. A probabilistic secondary vertex algorithm with a discriminator cut from Ref. [157] was used for b tagging. The cut in the discriminator was set to 0.8, which suppresses efficiently the Z/γ^*, W+jet and the potential multi-jet background. The efficiency to tag at least one jet, including the jet finding efficiency, was found to be between 13 and 19% for the signal, below 1% for the Z/γ^* backgrounds and 1.3% for the W+jet background. For the signal events the purity of the b-tagged jets is very high (99%).

Table 5.20. Background production cross sections times branching fraction, cross sections and efficiencies (%) for the selection cuts and number of events for 30fb^{-1}.

	$Z/\gamma^* \to \tau\tau$	$b\bar{b}Z/\gamma^* \to \tau\tau$	$Z/\gamma^* \to e^+e^-$	$b\bar{b}Z/\gamma^* e^+e^-$
$\sigma \times$ BR (pb)	331.8	27.0	1890	26.3
pre-selection	173.5 (41.4)		811.2 (42.9)	
Level-1 and HLT	17.3 (10.0)	0.818 (3.1)	617.4 (76.1)	18.2 (67.2)
primary vertex	16.5 (95.4)	0.796 (97.3)	591.9 (95.9)	17.7 (97.3)
no b's in DY Z/γ^*	15.6 (94.6)		561.8 (94.9)	
electron identification	11.6 (74.4)	0.585 (80.2)	278.1 (50.1)	9.31 (52.6)
one identified τ jet	0.13 (1.2)	1.0×10^{-2} (1.8)	3.40 (1.2)	9.0×10^{-2} (1.0)
$Q^{\tau\ \text{jet}} \times Q^e = -1$	0.13 (96.3)	1.0×10^{-2} (100)	3.31 (97.4)	8.8×10^{-2} (97.8)
$m_T < 40\,\text{GeV}/c^2$	9.8×10^{-2} (76.3)	8.0×10^{-3} (80.0)	2.26 (68.3)	5.5×10^{-2} (62.5)
$\geqslant$1 jet, $E_T > 20\,\text{GeV}$	4.0×10^{-2} (40.6)	5.6×10^{-3} (70.0)	0.85 (37.6)	3.0×10^{-2} (54.2)
b tagging	8.0×10^{-4} (2.0)	2.6×10^{-3} (46.4)	1.5×10^{-2} (1.8)	9.6×10^{-3} (32.2)
jet veto	5.2×10^{-4} (65.0)	1.5×10^{-3} (57.7)	6.0×10^{-3} (41.4)	5.9×10^{-3} (67.4)
$\Delta\varphi(\tau_1, \tau_2) < 175^\circ$	4.9×10^{-4} (94.2)	1.4×10^{-3} (90.7)	4.8×10^{-3} (80.0)	5.1×10^{-3} (85.7)
$E_{\nu_1,\nu_2} > 0$	2.0×10^{-4} (40.2)	7.6×10^{-4} (55.9)	1.7×10^{-3} (35.4)	1.9×10^{-3} (50.0)
N_{ev} at $30\,\text{fb}^{-1}$	5.9	22.8	51.3	57.9

Table 5.21. Background production cross sections times branching fraction (pb), cross sections and efficiencies (%) for the selection cuts and number of events for 30fb^{-1}.

	$t\bar{t}$	Wt	W + jet
$\sigma \times$ BR (pb)	840	6.16	673.2
pre-selection			315.0 (46.8)
Level-1 and HLT	94.4 (11.3)	2.00 (32.5)	145.6 (46.2)
primary vertex	93.9 (99.5)	1.97 (98.5)	143.9 (98.8)
electron identification	66.7 (71.0)	1.43 (72.6)	114.2 (79.4)
one id. τ jet	0.66 (0.95)	4.10×10^{-2} (2.87)	0.57 (0.5)
$Q^{\tau\ \text{jet}} \times Q^e = -1$	0.57 (89.8)	4.00×10^{-2} (97.6)	0.47 (82.7)
$m_T(e, E_T^{\text{miss}}) < 40\,\text{GeV}/c^2$	0.14 (24.3)	8.0×10^{-3} (20.0)	0.12 (25.2)
$\geqslant$1 jet, $E_T > 20\,\text{GeV}$	0.14 (98.6)	6.9×10^{-3} (86.3)	5.5×10^{-2} (46.2)
b tagging	9.4×10^{-2}(68.6)	4.1×10^{-3} (59.4)	1.6×10^{-3} (2.9)
jet veto	5.1×10^{-3} (5.4)	2.38×10^{-3} (58.1)	6.6×10^{-4} (41.9)
$\Delta\varphi(\tau_1, \tau_2) < 175^\circ$	4.9×10^{-3} (96.4)	2.33×10^{-3} (98.0)	5.6×10^{-4} (83.9)
$E_{\nu_1,\nu} > 0$	2.0×10^{-3} (40.9)	9.60×10^{-4} (41.2)	2.1×10^{-4} (38.5)
N_{ev} at $30\,\text{fb}^{-1}$	60.3	28.8	6.4

The $t\bar{t}$ background, with a genuine electron, τ and b jets, cannot be significantly suppressed with the cuts described above. This background, however, was suppressed applying the jet veto: the event must contain only the b-tagged jet with calibrated $E_T^{\text{jet}} > 20$ GeV and $|\eta^{\text{jet}}| < 2.5$. The fake jets, which generally do not contain tracks from the signal vertex, were suppressed with a cut in the fraction of the track p_T sum to the jet E_T, $\alpha = \Sigma p_T^{\text{t track}}/E_T^{\text{jet}}$. The cut $\alpha > 0.1$ was found to improve the veto efficiency for the signal by about 10%. The jet veto efficiency is around 60% for the signal and ∼5% for the $t\bar{t}$ background.

For the reconstruction of the $\tau\tau$ mass the events with back-to-back configurations between the electron and the τ jet were removed with an upper bound on the angle between the τ jet and the electron in the transverse plane ($\Delta\varphi$(e, τ jet)). The reconstructed neutrino energies were required to be positive ($E_{\nu_1} > 0$ and $E_{\nu_2} > 0$), which leads to a reduction

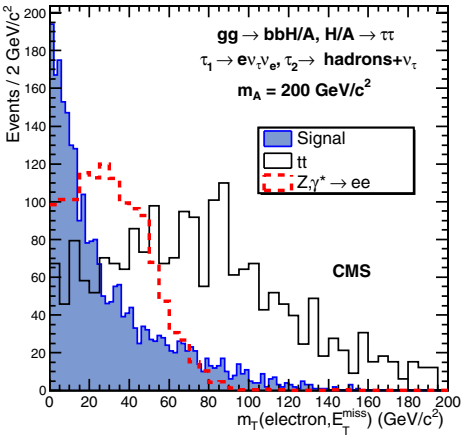

Figure 5.7. Distribution of transverse mass reconstructed from the electron and the missing transverse energy for the signal of $M_A = 200\,GeV/c^2$ and $\tan\beta = 20$ (filled histogram), for the $t\bar{t}$ (solid line) and for the $Z/\gamma^* \to e^+e^-$ (dashed line) background. Histogram normalisation is arbitrary.

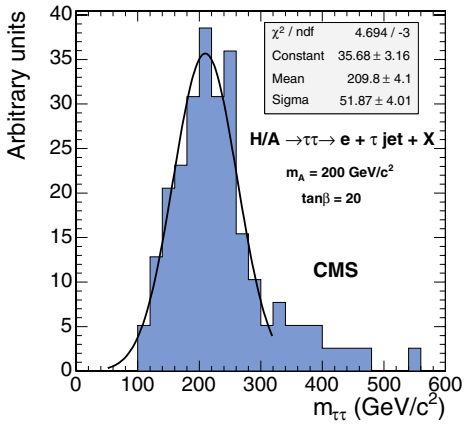

Figure 5.8. Reconstructed Higgs boson mass for $M_A = 200\,GeV/c^2$ and $\tan\beta = 20$.

of $\simeq$40% of the signal events, but rejects $\simeq$ 60% of the $t\bar{t}$, tW and W+jet backgrounds. Figure 5.8 shows the reconstructed Higgs boson mass for the signal events with $M_A = 200\,GeV/c^2$. The Gaussian fit yields a mass resolution of 25%.

Table 5.19 shows the numbers of signal events with $M_A = 130$–$500\,GeV/c^2$ and $\tan\beta = 20$ for $30\,fb^{-1}$ and the efficiency for all the event selection cuts described above. For $M_A = 130$ and $140\,GeV/c^2$, the mass of the lighter scalar Higgs boson h is only 4.4 and $11.2\,GeV/c^2$ smaller than M_A. With the mass resolution, which can be reached in the $H \to \tau\tau$ decay channels, the lighter scalar contributes to the signal and is added in the cross sections for $M_A = 130$ and $140\,GeV/c^2$. The contribution is 31 and 11% of the total production rate, respectively. Table 5.20 shows the number of events and efficiencies for the backgrounds originating from $Z/\gamma^* \to \tau\tau$ and $Z/\gamma^* \to e^+e^-$ decays in the inclusive and in the associated $b\bar{b}Z/\gamma^*$ production. The efficiency of removing the $b\bar{b}Z/\gamma^*$ component from the inclusive Z/γ^* samples is also shown. Table 5.21 shows the same for the backgrounds involving W's from $t\bar{t}$, Wt and W + jet events. The cross section times branching fraction, trigger efficiency and the efficiency of the primary vertex reconstruction are also shown in the tables. The QCD multi-jet background after all selections was estimated to be 8.4 events for $30\,fb^{-1}$ in the mass window around $M_A = 200\,GeV/c^2$, which is $\simeq$ 10% of all other backgrounds.

Figures 5.9 and 5.10 show the reconstructed Higgs boson mass distributions of the $H/A \to \tau^+\tau^- \to$ electron + jet + X signal and the total background for $30\,fb^{-1}$ for $M_A = 200\,GeV/c^2$, $\tan\beta = 20$ and for $M_A = 300\,GeV/c^2$, $\tan\beta = 25$. The sum of the $Z/\gamma^* \to e^+e^-$ and $b\bar{b}Z/\gamma^* \to e^+e^-$ backgrounds is shown separately in the figures.

5.2.8.3. Systematic uncertainties for the background determination. The background uncertainty was evaluated using the cross-section uncertainties (measured or predicted from the theory) and the experimental uncertainties for the event selections.

The uncertainty of the event selection efficiency is related to the uncertainty of the electron and τ identification, the absolute calorimeter scale and the b-tagging efficiency.

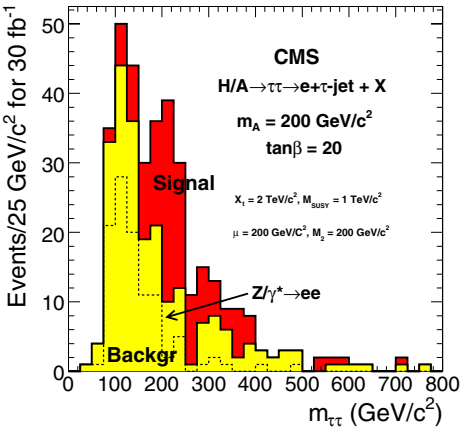

Figure 5.9. Reconstructed Higgs boson mass for the signal of $M_A = 200\,GeV/c^2$, $\tan\beta = 20$ and for the total background for an integrated luminosity of $30\,fb^{-1}$. The dashed line shows the sum of the $Z/\gamma^* \to e^+e^-$ and $b\bar{b}Z/\gamma^*e^+e^-$ backgrounds.

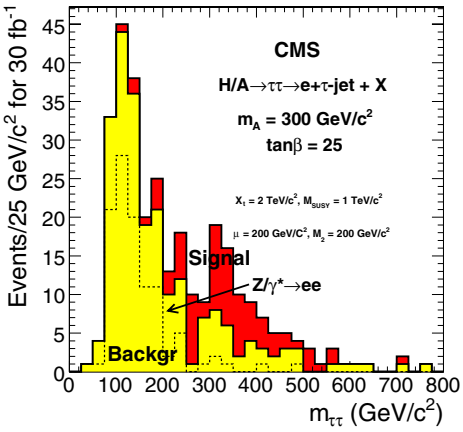

Figure 5.10. Reconstructed Higgs boson mass for the signal with $M_A = 300\,GeV/c^2$, $\tan\beta = 25$ and for the total background for an integrated luminosity of $30\,fb^{-1}$. The dashed line shows the sum of the $Z/\gamma^* \to e^+e^-$ and $b\bar{b}Z/\gamma^*e^+e^-$ backgrounds.

The systematic uncertainty due to the energy scale was estimated varying the jet energy and the E_T^{miss} values with the expected energy scale uncertainties yielding an average 5.1% uncertainty on the number of Z/γ^* events, 3.8% uncertainty on the number of $b\bar{b}Z/\gamma^*$ events, 7.3% uncertainty on the number of $t\bar{t}$ events, 11.3% uncertainty on the number of tW events and 11.8% uncertainty on the number of W+jet events passing the event selection cuts. A 5% uncertainty on the b tagging and mistagging efficiencies and a 2% uncertainty on the electron reconstruction and identification were used.

The uncertainty of the Z/γ^* cross section at the LHC is of the order of 1% [158]. For the $t\bar{t}$ background the theoretical NLO cross section uncertainty derives from the scale uncertainty, taken to be 5% according to Ref. [159], and the PDF uncertainty, about 2.5 %, yielding 5.6% for the total uncertainty. The same uncertainty is used for the cross sections of the Wt and W+jet processes. The uncertainty of the $b\bar{b}Z/\gamma^*$ cross section measurement is estimated to be 14.2% in [145]. With these estimates, the total systematic uncertainty, including the luminosity uncertainty of 3% [7], was found to be 8.1%, 15.9%, 11.1%, 14.0% and 14.5% for the Z/γ^*, $b\bar{b}Z/\gamma^*$, $t\bar{t}$, Wt and W+jet backgrounds, respectively.

5.2.8.4. Discovery reach in the M_A–tan(β) *plane.* Table 5.22 shows the number of signal plus background events and the number of background events for $30\,fb^{-1}$ in the selected mass windows and the signal significance calculated according to Poisson statistics, with and without the background systematics taken into account. The mass windows were selected to optimise the significance. The m_h^{max} scenario was used.

Figure 5.11 shows the 5σ discovery region in the M_A–tan β plane for $30\,fb^{-1}$ in the m_h^{max} scenario, evaluated with and without background systematics.

5.3. Benchmark Channels: $t\bar{t}H, H \to b\bar{b}$

5.3.1. Introduction

The Higgs boson decay to $b\bar{b}$ is the dominant mode for the Higgs mass range up to $m_H \sim 135\,GeV/c^2$. Direct Higgs production is almost impossible to detect via this decay

Table 5.22. Number of signal-plus-background events and the number of background events in the selected mass windows for 30 fb^{-1} and the signal significance without ($S_{no\ syst.}$) and with ($S_{syst.}$) the background systematics taken into account.

	$\Delta m_{\tau^+\tau^-}$	N_S+N_B	N_B	$S_{no\ syst.}$	$S_{syst.}$
$M_A = 130\,GeV/c^2$, $\tan\beta = 20$	120–200 GeV/c^2	176	83	8.9	6.4
$M_A = 140\,GeV/c^2$, $\tan\beta = 15$	130–220 GeV/c^2	136	76	9.1	6.7
$M_A = 200\,GeV/c^2$, $\tan\beta = 20$	140–280 GeV/c^2	175	83	8.8	6.3
$M_A = 300\,GeV/c^2$, $\tan\beta = 20$	240–480 GeV/c^2	78	39	5.4	4.3
$M_A = 500\,GeV/c^2$, $\tan\beta = 50$	360–780 GeV/c^2	57	22	6.2	5.3

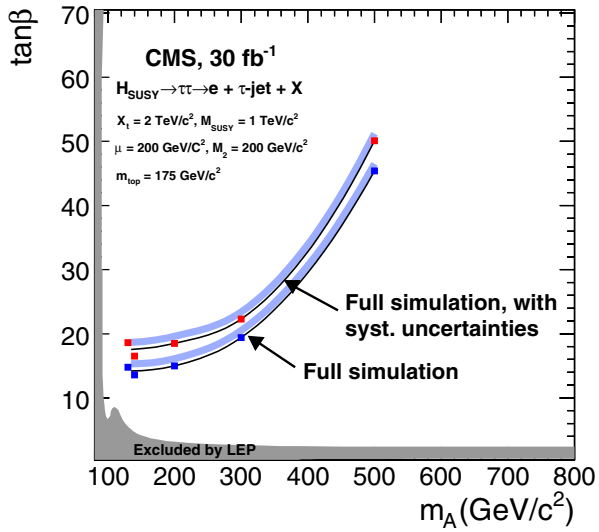

Figure 5.11. The 5σ discovery region in the $M_A - \tan(\beta)$ plane for an integrated luminosity of 30 fb^{-1} in the m_h^{max} scenario. The lower (upper) curve was evaluated without (with) the effect of background systematics taken into account.

as a result of the combination of an overwhelming QCD cross section for $b\bar{b}$ production and the inability to reconstruct the Higgs mass very precisely. While the latter is still true in the case of Higgs production in association with a $t\bar{t}$ or $b\bar{b}$ pair, these channels hold promise because they entail substantially lower backgrounds. The separation of these events into 3 salient topologies follows as a result of the ways in which the two W bosons in the event decay. Thus, in addition to the four b jets, roughly 49% of these events also contain four hadronic jets (the all-hadron channel), while some 28% have two hadronic jets together with an isolated electron or muon and missing E_t (the semi-leptonic channel), with a further 5% of events containing two oppositely-charged leptons (either of which can be an electron or muon) and missing E_t (the dilepton channel). The remaining 14% of events correspond to those cases where one or both of the W bosons decay to a tau lepton and neutrino and are not easily distinguishable as such, as a result of the rich decay repertoire of the tau meson. In fact, these events do make a small contribution to the three other classes of events in the actual analyses. Additional hadronic jets can appear in these events and originate from initial and final state QCD radiation (IFSR).

Table 5.23. NLO signal cross-sections and $H \to b\bar{b}$ branching ratios for different Higgs mass hypotheses

m_H	115 GeV/c^2	120 GeV/c^2	130 GeV/c^2
σ_{NLO} (pb)	0.747	0.664	0.532
$BR(H \to b\bar{b})$	0.731	0.677	0.525

A detailed description of the $t\bar{t}H$ analysis strategies and the results can be found in Reference [160]. All the results presented here are for an integrated luminosity of 60 fb^{-1}.

5.3.2. Event generation and simulation

As the identification of the signal relies upon the presence of top quark decay products, it comes as no surprise that the most significant backgrounds are those associated with $t\bar{t}$ events themselves. The main backgrounds are: $t\bar{t}jj$, $t\bar{t}b\bar{b}$ and $t\bar{t}Z$ with $Z \to b\bar{b}$.

These processes are studied in detail and are presented here. Secondary background sources include pure QCD multi-jet events in the case of the all-hadron channel, and W/Z plus jets or dibosons plus jets events in the case of the semi-leptonic and dilepton channels. With the exception of QCD multi-jets, the latter have substantially lower production cross-sections than $t\bar{t}$ events but very similar topologies. They are therefore not studied in detail.

Details about the primary Monte Carlo data samples used in this analysis are available in Reference [160]. The semi-leptonic and all-hadron $t\bar{t}H$ signal samples were generated using COMPHEP (version 41.10) and PYTHIA (version 6.215), while the dilepton samples used PYTHIA only. Though a leading order Monte Carlo, PYTHIA is known to do a very good job of reproducing IFSR as well as parton shower effects. This is adequate for the signal samples. For the $t\bar{t}$ plus jets backgrounds, greater care must be exercised. In particular, PYTHIA alone cannot be expected to do a realistic job since the relevant processes are not leading order. On the other hand, there is not currently a full next-to-leading order (NLO) MC for $t\bar{t}$ plus jets production. As a result, higher order matrix elements are used including additional radiated partons in conjunction with the parton showering of PYTHIA to produce the appropriate event topologies.

ALPGEN and PYTHIA are used for the matrix elements and parton showering, respectively, for the $t\bar{t}$ plus n jets background samples. The matching of the two generators is done in ALPGEN as discussed in Ref. [161]. In particular, all of the matrix elements for $t\bar{t}$ plus n additional hard partons are included and properly combined at each order taking into account the interference between amplitudes.

QCD events were generated with PYTHIA (version 6.215) in the $\hat{p}_t$ ranges from 120 to 170 GeV/c and greater than 170 GeV/c.

For the simulation of the interaction with the detector, the CMS tools, providing GEANT3 and GEANT4 based simulation of the CMS detector have been used.

The NLO signal cross-sections for different Higgs mass hypotheses are given in Table 5.23 together with the branching ratios for $H \to b\bar{b}$ [162].

The leading order COMPHEP cross-sections for the different background processes together with the effective cross-sections after the application of the generator filters are listed in Table 5.24. The ALPGEN cross sections for the different jet multiplicity processes are listed in Table 5.25. A detailed comparison of ALPGEN versus COMPHEP for the $t\bar{t}jj$ background is available in [160]. All the results that are presented here for the $t\bar{t}Nj$ backgrounds are based on the ALPGEN samples, where available.

Table 5.24. LO COMPHEP cross-sections and effective cross-sections after the generator filters of the considered background processes.

	QCD $\hat{p}_t = 120$–$170\,\mathrm{GeV/c}$	QCD $\hat{p}_t > 170\,\mathrm{GeV/c}$	$\mathrm{t\bar{t}b\bar{b}}$	$\mathrm{t\bar{t}Z}$
σ_{LO} (pb)	$3.82 \cdot 10^5$	$1.05 \cdot 10^5$	3.28	0.65
$\sigma_{LO} \times \varepsilon$ (pb)	76.4	336.0	2.82	0.565

Table 5.25. LO ALPGEN cross-sections for the different jet multiplicity samples.

	exclusive $\mathrm{t\bar{t}}$+1j	exclusive $\mathrm{t\bar{t}}$+2j	exclusive $\mathrm{t\bar{t}}$+3j	inclusive $\mathrm{t\bar{t}}$+4j
σ_{LO} (pb)	170	100	40	61

Table 5.26. Signal and background efficiencies of the Level 1 and High Level Triggers.

	Single μ	Single e	Single e OR μ OR τ	Jets
$\mathrm{H} \to \mathrm{b\bar{b}}$ (%) with $m_H = 120\,\mathrm{GeV/c^2}$	63.5	52.4	76.7	24.9
$\mathrm{t\bar{t}b\bar{b}}$ (%)	19.0	16.1	83.6	18.3
$\mathrm{t\bar{t}}$1j (%)	13.9	11.3	53.0	2.9
$\mathrm{t\bar{t}}$2j (%)	14.0	11.1	59.8	6.2
$\mathrm{t\bar{t}}$3j (%)	14.0	11.1	68.5	11.4
$\mathrm{t\bar{t}}$4j (%)	13.4	11.1	78.6	31.4
$\mathrm{t\bar{t}Z}$ (%)	20.4	18.8	84.4	25.3
QCD 120–170 GeV/c (%)	0.08	0.8	4.3	1.7
QCD > 170 GeV/c (%)	0.07	2.1	4.4	10.3

5.3.3. Level-1 and high level trigger selections

A dedicated $\mathrm{t\bar{t}H}$ trigger was not available and therefore was not implemented in the analysis. As a result, it is assumed in what follows that the signal is recorded by the CMS Level 1 (L1) and High Level Triggers (HLT) as described in [76]. Wherever possible, the cleaner signature of at least one isolated lepton in the final state is exploited. The semi-leptonic channels thus use the single muon (stream #43) or single electron (stream #2) triggers.

A logical "OR" of the single muon, single electron and single tau streams is used for the dilepton channel. The same trigger setups as for streams #43 and #2 were used, except that the p_{T} threshold was lowered to 15 GeV/c to permit selection of 20 GeV/c leptons later in the analysis. The tau trigger is the official stream (bit #91). Jet triggers are used to select all-hadron events. In particular, the single-jet, 3-jet and 4-jet triggers with low luminosity thresholds [76][163] are combined (stream #120 or #122 or #123).

Efficiencies for the various HLT and Level-1 triggers that were used are presented in Table 5.26. The efficiencies quoted are determined by counting the numbers of accepted events relative to the total numbers of events in each sample. In order to streamline the various studies that were performed, the analyses used different MC samples, produced with different final state constraints. Thus, efficiencies for single muon, single electron and fully hadronic final states were defined with respect to exclusive signal samples and inclusive background samples, as described in the preceding section. The dilepton channel efficiency on the other hand, was defined with respect to samples containing at least one leptonic top decay for the signal and inclusive samples for the backgrounds.

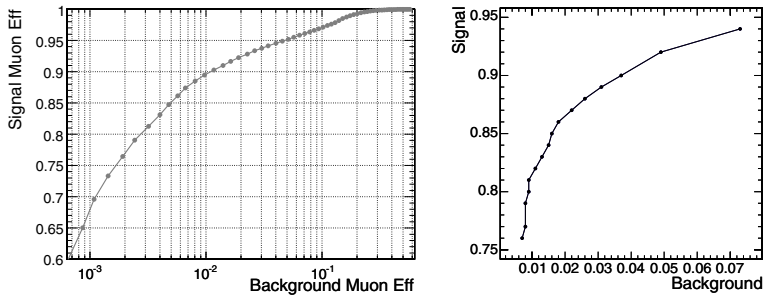

Figure 5.12. (Left) Performance of the muon likelihood discriminator for the semi-leptonic muon $t\bar{t}H$ channel. (Right) *Signal* versus *background* electron efficiencies for likelihood values ranging from 0.006 (the upper point) with a step size of 0.006, (i.e. approximately in the range $1.0 < -\log(L_e) < 2.0$).

5.3.4. Reconstruction

5.3.4.1. Muon reconstruction. The process of muon reconstruction begins in the Muon Chambers and is then extended to the tracking system, as described in Ref. [164]. For the studies presented here it is important to identify muons coming from W decays. To this end, additional selection criteria are applied to distinguish these muons, which will be referred to as *signal* muons, from the muons coming from other sources such as b decays. The latter will be referred to as *background* muons, even though they arise in signal events as well as background events. The desired discrimination between *signal* and *background* muons is achieved by constructing a discriminator that is based upon probability density functions (PDF) for the following observables associated with muon candidates:

- Transverse momentum, p_t.
- Track isolation, $IsoTk$.
- Calorimeter isolation, $IsoCalo$.
- Significance of track impact parameter, $S_{ip} = d/\sigma_d$.

The PDF's associated with these variables for *signal* and *background* muons are obtained by matching to generator-level muons.

The PDF's are combined into the following likelihood ratio:

$$L = \Pi_i \frac{P_i^{sig}(x_i)}{P_i^{sig}(x_i) + P_i^{bkg}(x_i)} \tag{5.13}$$

where P_i^{sig} and P_i^{bkg} are the PDF's of an observable x_i for *signal* and *background* muons, respectively.

The performance for *signal* and *background* muon discrimination are shown in Figure 5.12. For a *signal* muon efficiency of 90%, only 1% of background muons are selected. The PDF's are constructed using a sample of $t\bar{t}H$ events with $m_H = 120\,GeV/c^2$ in which one and only one of the W bosons decays to a muon and neutrino, while the other one decays hadronically.

If the likelihood selection is used after the HLT, a dramatic improvement in QCD ($\hat{p}_t > 170\,GeV/c$) rejection is possible with little or no loss in signal efficiency. For example, a small drop in signal efficiency from 63% to 60% reduces the QCD efficiency by more than a factor of 3 (*i.e.* from 0.07% to 0.02%).

5.3.4.2. Electron reconstruction. A full description of the electron reconstruction in CMS can be found in Ref. [46]. Electrons coming from W boson decays are typically characterised by isolated high transverse energy clusters. These electrons are thus efficiently identified by means of an isolation requirement applied to the electron candidate with respect to other reconstructed tracks in the event.

In analogy to the muon reconstruction and equation 5.13, a likelihood method is used to identify the signal electrons, making use of the following observables:

- the p_t sum of tracks inside an *isolation cone* of radius $\Delta R = 0.3$ around the candidate electron direction.
- the ΔR distance between the electron candidate and the closest track.
- the transverse momentum of the electron candidate, p_t.
- the ratio between the cluster energy and the track momentum, E/p.
- the ratio between the hadronic and electromagnetic energies of the cluster, H/E.

An appropriate choice of likelihood cut value has been studied by comparing *signal* versus *background* electron efficiencies as shown in Figure 5.12.

For a $-\log(L_e)$ cut value of 1.27, *signal* electrons are selected with an efficiency of 84% and *background* electrons with an efficiency of 1.5%. This value was chosen for the analyses described in subsequent sections.

Concerning the efficiency of the likelihood cut with respect to background rejection in $\mathrm{t\bar{t}jj}$ events in which there were no isolated electrons coming from W decays, only 6% of these events were accepted for a likelihood cut of 1.27.

As in the case of the muon selection, the likelihood approach can be used to augment the HLT selection efficiency. Maintaining a roughly constant signal efficiency, the likelihood cut in combination with the HLT trigger yields an order of magnitude reduction in the QCD background selection efficiency.

5.3.4.3. Jet and missing E_{T} reconstruction. Jets are reconstructed using the iterative cone algorithm. A cone with $\Delta R = 0.5$ is used when at least one W boson decays into leptons, while a smaller cone size was found to be more suitable for the more dense jet environments associated with the all-hadron channel (see below).

A calorimetric-tower energy threshold of 0.8 GeV and a transverse-energy threshold of 0.5 GeV are used. Calorimeter towers that exceed 1 GeV are considered as jet seeds. For the leptonic channels, the jet energy is calibrated using MC calibrations [165] provided by the JetMET group for the corresponding set of reconstruction parameters.

The single lepton analyses, as described in more detail below, make use of an event likelihood to help select and properly reconstruct events and decay chains. This is facilitated, in part, by making use of the various invariant mass constraints associated with the top quark decays. The corresponding likelihoods thus rely upon the resolutions that are obtained for the invariant masses of the hadronically decaying W boson and the two top quarks. The "best-case" invariant mass distribution for the hadronically decaying top quark is reconstructed by matching to generator-level parton information and shown in Figure 5.13. The distributions for the leptonically decaying top quark and the hadronically decaying W boson (Ref. [160]) have similar shapes but different RMS (25.7 GeV/c^2 and 15.7 GeV/c^2, respectively) since the longitudinal momentum of the leptonically decaying top quark has to be calculated from missing E_t. A reconstructed jet is considered as matched to the corresponding parton if their separation, ΔR_{j-p}, is less than 0.3.

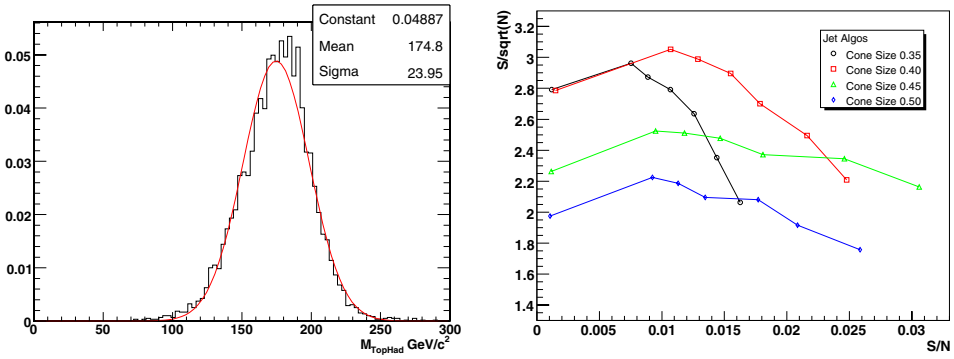

Figure 5.13. (Left) Invariant mass of the hadronically decaying Top quark using jet-parton matching with $\Delta R_{j-p} < 0.3$. (Right) Change in significance and S/N resulting from variations in the b-tagging discriminator for the various cone sizes indicated in the legend.

The missing transverse energy of the event $E_{\mathrm{t}}^{\mathrm{miss}}$ is computed as

$$E_{\mathrm{t}}^{\mathrm{miss}} = \sum_i E_{\mathrm{t}}^{\mathrm{tower}} - \left(\sum_j E_{\mathrm{t}}^{\mathrm{RawJet}} - \sum_k E_{\mathrm{t}}^{\mathrm{CaliJet}} \right) + \sum_m E_{\mathrm{t}}^{\mathrm{Muon}} \tag{5.14}$$

where the sum with index i runs over calorimeter towers, that with index j runs over raw jets, k runs over calibrated jets, and m runs over the reconstructed muons of the event. Equation 5.14 thus takes into account the corrections due to jet calibration and the contributions of muons that are not measured in the calorimeter.

The choice of the jet reconstruction algorithm is an important step in the event selection optimisation for the all-hadron $\mathrm{t\bar{t}H}$ channel, where at least 8 jets are expected in the final state. For this reason, an optimisation is obtained by means of a simple "proto" analysis as described in Reference [160].

A dedicated $\mathrm{t\bar{t}}$ H calibration [166] is applied to help recover the original transverse energy of the associated parton. Reconstructed jets with a b-tagging discriminator value higher than 0.4 are calibrated using a separate b-jet calibration procedure.

Figure 5.13 shows the significance with respect to the S/N ratio for a range of b-tag discriminator values for each of the several cone sizes indicated. Lower discriminator values yield higher significance but only at the cost of low S/N while, on the contrary, higher discriminator values give lower significance but higher S/N. A good compromise is in the middle range of each of the curves where neither S/N nor significance are unreasonably low. With this in mind, the best choice for the jet cone is seen to be $\Delta R = 0.40$.

5.3.4.4. b-Tagging. The identification of jets from b-quarks is done with the *Combined Secondary Vertex* algorithm. This algorithm exploits secondary vertex and track properties to calculate a discriminator value which separates b-jets from non b-jets. A detailed description is published in Ref. [157] which also presents results of detailed studies of the performance of the b-tagging algorithm as applied to Monte Carlo $\mathrm{t\bar{t}}$ and QCD samples.

In the $\mathrm{t\bar{t}H}$ analyses, a fixed cut value for the b-tagging discriminator is applied, and four jets are required to pass this cut in the semi-leptonic and all-hadron channels, while only 3 jets are required to be tagged in the dilepton analysis. The misidentification rate of charm and light flavour jets as a function of the b-tagging efficiency is shown in Fig. 5.14 for the $\mathrm{t\bar{t}H}$ and the $\mathrm{t\bar{t}jj}$ samples, respectively. It can be seen that the efficiencies are similar in these samples.

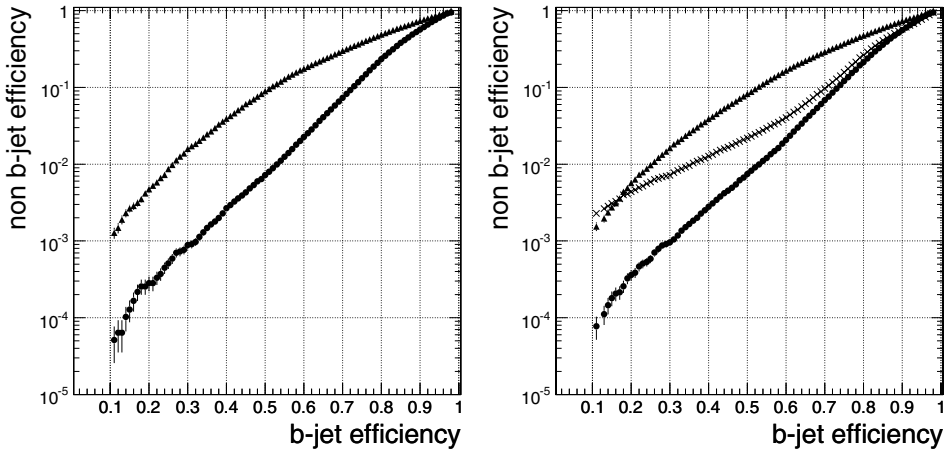

Figure 5.14. On the left: Non-b jet mistagging efficiency versus b-jet tagging efficiency for c-jets (triangles), and uds-jets (stars) for the $t\bar{t}H$ sample with $m_H = 120$ GeV/c^2 and jets with a minimum transverse momentum of 20 GeV/c. For this plot the "physics definition" of the original jet flavour has been used. In this definition there are no original gluon jets in the $t\bar{t}H$ sample. On the right: The corresponding plot for the $t\bar{t}jj$ sample, where gluon jets are represented by crosses.

This fixed-cut b-tagging approach gives reasonable results, but is not necessarily optimal. Some potential improvements are possible such as the combination with a soft lepton tag or a discriminator cut which depends on p_t and η of the jets. Studies have shown that they have the potential to improve the results at the order of some percent. These improvements were not used in the current analyses.

5.3.5. Event selection

In this section the event selection for the different channels under consideration is described. In order to be able to combine the results from all the $t\bar{t}H$ search channels, the different channels use mutually exclusive event samples. This is most easily facilitated by coordinating how high p_t electrons and muons from the W decays (previously referred to as *signal* leptons) are either selected or vetoed by the different analyses.

For the analyses reported here, the different data samples used were separated using selection and/or veto criteria based on the lepton likelihood value, as described in Ref. [160].

5.3.5.1. Semi-leptonic Channel: $t\bar{t}H \to b\bar{b}b\bar{b}qq'\mu\nu_\mu$ *and* $b\bar{b}b\bar{b}qq'e\nu_e$. The strategy for selecting $t\bar{t}H$ events with one isolated muon or electron in the final state can be summarised in the following three steps: pre-selection, choice of jet pairing and finally, selection. The pre-selection requires the HLT stream for a single muon or a single electron, one isolated lepton using the likelihood information as described in section 5.3.4.1 and 5.3.4.2, and 6 or 7 jets in the pseudorapidity region $|\eta| < 3.0$ with a calibrated transverse energy larger than 20 GeV. In order to recover some efficiency, jets with 10 GeV $< E_t <$ 20 GeV are also accepted if they have at least two associated tracks pointing to the signal primary vertex[42] within a distance along the beam (z) axis of ($|z_{PV} - z_{track}| < 1$ mm). The latter condition is required to reject low transverse energy fake jets, (i.e. jets that are not associated with any of the signature

[42] The signal interaction is generally the one which allows the event to be triggered.

partons in the signal event). For the single electron channel, the misidentification of the jet with the isolated electron has been excluded by imposing a veto on the jet if the electron lies inside a jet cone radius of 0.1.

At least 4 jets are required to be tagged as b-jets with a minimal discriminator value corresponding to a b-efficiency of about 70%.

To decrease the contamination from the dilepton channel, a double muon, double electron and muon-electron veto is applied, in which events with the second lowest $-\log(L_\mu) < 1.4$ and events with $-\log(L_e) < 1.2$ are rejected from the analysis. In the case of the semi-leptonic electron channel the previous cuts are applied respectively to the first muon likelihood candidate and to the second electron likelihood candidate. The application of these vetoes results in a lowering of the signal efficiency by about 2%, while the total background rejection is increased by 13%.

In order to perform a complete reconstruction of the event, the longitudinal momentum of the neutrino has to be computed from four-momentum conservation for the W boson: $m_W^2 = (E^\mu + E^\nu)^2 - (\vec{p}^\mu + \vec{p}^\nu)^2$. This equation gives 2 real solutions for p_z^ν in 66% of the cases, while in the remaining 34%, the neutrino is assumed to be collinear with the lepton: $p_z^\nu = p_z^l$. This leads to a small degradation in the longitudinal momentum resolution, but the reconstruction efficiency of the leptonic W boson decay is increased to 100%.

In order to choose the jet combination that does the best job of reconstructing the two top quarks, a likelihood, L_{Event}, is defined using masses, b-tagging and kinematic information from the whole event:

$$L_{Event} = L_{Mass} \times L_{bTag} \times L_{Kine}. \tag{5.15}$$

The mass information considered in the likelihood L_{Mass} is the probability returned by the kinematic fit with invariant mass constraints (top quarks and hadronic W) that is described in Reference [167].

The b-tagging function L_{bTag} is defined as the product of the b-tag discriminators: $L_{bTag} = D_{Top_{Had}} \times D_{Top_{Lep}} \times D_{H_1} \times D_{H_1} \times (1 - D_{W1}) \times (1 - D_{W2})$; where Top_{Had} and Top_{Lep} are expected to be the two b jets from the hadronic and leptonic top, respectively, while H_1 and H_2 are expected to be the two b jets coming from Higgs and W_1 and W_2 are the two jets from the hadronically-decaying W boson.

The kinematic function takes into account the observation that the b-jets coming from top quarks tend to be slightly more energetic than b-jets coming from the Higgs boson (see [160] for a definition).

Among all possible combinations of jet-parton assignments, the one with the highest value of L_{Event} is chosen for use in the final reconstruction of the top quarks and the two remaining jets with highest b-tagging discriminator values are used to reconstruct the Higgs mass.

After the jet assignment is complete, additional criteria are applied to improve background rejection. In particular, a stronger b-tag requirement is applied on the event variable $L_{bSele} = D_{Top_{Had}} \times D_{Top_{Lep}} \times D_{H_1} \times D_{H_1}$.

The signal significance as a function of the selection cut L_{bSele} is shown in Figure 5.15.

The distributions of reconstructed Higgs mass for the final selected events are shown in Figure 5.16 for signal only (left) and for the combination of the different backgrounds (right) for the muon channel only (similar results for the electron channel can be found in [160]). The fraction of signal events where the two b-jets are correctly assigned to the Higgs boson (i.e. the pairing efficiency) is roughly 31% in the muon channel and about 29% for the electron channel.

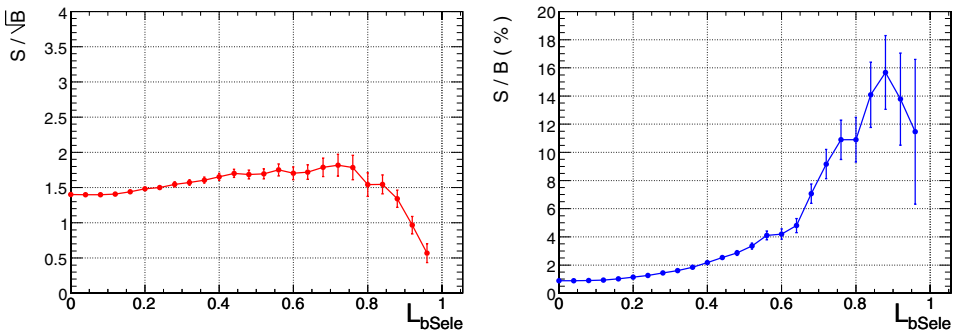

Figure 5.15. $\mathrm{t\bar{t}H}$ ($W \to qq'$, $W \to \mu\nu$): Signal Significance (left) and Signal to Background ratio (right) as function of the cut on L_{bSele}.

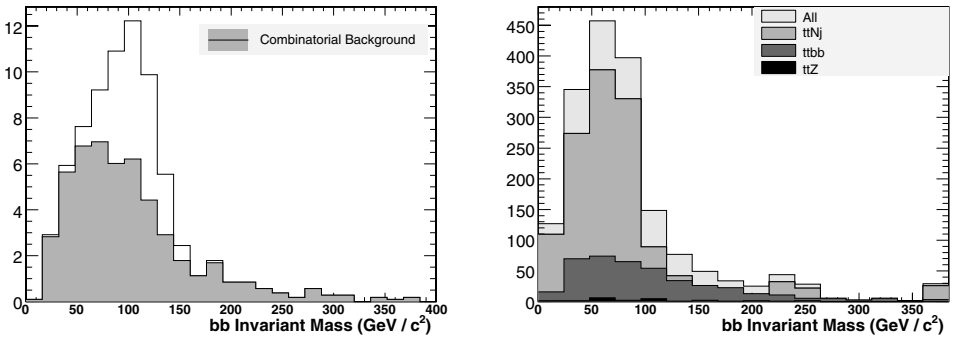

Figure 5.16. $\mathrm{t\bar{t}H}$($W \to qq'$, $W \to \mu\nu$). (Left) Invariant $b\bar{b}$ mass for signal only (combinatorial background is shaded grey). (Right) The sum of the reconstructed $m_{b\bar{b}}$ spectra for backgrounds with a value of $L_{bSele} > 0.55$. The distributions are normalised to an integrated luminosity of 60 fb^{-1}.

5.3.5.2. Results. The selection efficiencies with the corresponding numbers of expected events and signal significances are reported in Table 5.27 for the channels with a muon or an electron in the final state. The number of expected events is computed for an integrated luminosity of 60 fb^{-1} in the Standard Model Higgs mass range from 115 to 130 $\mathrm{GeV/c^2}$.

5.3.5.3. Dilepton channel: $\mathrm{t\bar{t}H} \to \mathrm{b\bar{b}b\bar{b}}\ell'\nu'\ell\nu$. Dilepton ttH events are selected by requiring two reconstructed leptons (e, μ) accompanied by significant missing transverse energy and at least four but no more than seven jets, at least three of which have been b-tagged according to the *Combined Secondary Vertex* b-tagging algorithm.

Lepton identification is performed using the electron and muon likelihoods described in Section 5.3.4. In the semi-leptonic analyses, events with more than one identified lepton are vetoed, but in the dilepton analysis those events are retained. The likelihood acceptance cuts used for leptons in the dilepton channel are therefore chosen to be the same as the second-lepton veto cuts for both semi-leptonic channels. In this way, the sample of events for the dilepton $\mathrm{t\bar{t}H}$ analysis is by construction strictly complementary to those used in the semi-leptonic channels.

Table 5.27. Selection efficiency for $L_{bSele} > 0.55$ (ε_{loose}) and for $L_{bSele} > 0.75$ (ε_{tight}), number of expected events and signal significance in 60 fb^{-1} for the muon and electron $t\bar{t}H$ channel. The numbers refer to the complete Higgs mass range.

	Analysed Ev.	$\varepsilon_{\text{loose}}$ (%)	N^{ev}_{loose} 60 fb^{-1}	$\varepsilon_{\text{tight}}$ (%)	N^{ev}_{tight} 60 fb^{-1}
muon channel					
$t\bar{t}H$ (115)	27768	2.00 ± 0.08	96 ± 4	0.80 ± 0.05	38 ± 3
$t\bar{t}H$ (120)	41929	1.90 ± 0.07	75 ± 3	0.74 ± 0.04	29 ± 2
$t\bar{t}H$ (130)	19466	2.23 ± 0.11	55 ± 3	0.84 ± 0.07	21 ± 2
$t\bar{t}b\bar{b}$	372737	0.247 ± 0.008	419 ± 14	0.0877 ± 0.0048	148 ± 8
$t\bar{t}1j$	393000	0.0051 ± 0.0011	520 ± 120	0.00076 ± 0.00044	78 ± 45
$t\bar{t}2j$	568999	0.0105 ± 0.0014	633 ± 82	0.00070 ± 0.00035	42 ± 21
$t\bar{t}3j$	101000	0.0050 ± 0.0022	119 ± 53	0	$<27(68\%C.L)$
$t\bar{t}4j$	86697	0.0035 ± 0.0020	126 ± 73	0	$<48(68\%C.L.)$
$Zt\bar{t}$	50000	0.068 ± 0.012	23 ± 4	0.026 ± 0.007	9 ± 2
Total Background			1840		< 352
$S/\sqrt{B}$ (115)			2.2		2.0
S/B (115)			5.1%		10.8%
$S/\sqrt{B}$ (120)			1.8		1.6
S/B (120)			4.1%		8.2%
$S/\sqrt{B}$ (130)			1.3		1.1
S/B (130)			3.0%		6.0%
electron channel					
$t\bar{t}H$ (115)	27692	1.39 ± 0.07	66 ± 3	0.52 ± 0.04	25 ± 2
$t\bar{t}H$ (120)	42228	1.42 ± 0.06	56 ± 2	0.53 ± 0.04	21 ± 1
$t\bar{t}H$ (130)	19127	1.57 ± 0.09	39 ± 2	0.61 ± 0.06	15 ± 1
$t\bar{t}b\bar{b}$	372737	0.176 ± 0.007	297 ± 12	0.0641 ± 0.0041	109 ± 7
$t\bar{t}1j$	393000	0.0038 ± 0.0010	390 ± 100	0.00025 ± 0.00025	26 ± 26
$t\bar{t}2j$	568999	0.0067 ± 0.0011	401 ± 65	0.00123 ± 0.00046	74 ± 28
$t\bar{t}3j$	101000	0.0040 ± 0.0020	95 ± 48	0	$< 27(68\%C.L)$
$t\bar{t}4j$	86697	0.0023 ± 0.0016	84 ± 60	0	$< 48(68\%C.L.)$
$Zt\bar{t}$	50000	0.064 ± 0.011	22 ± 4	0.022 ± 0.007	7 ± 2
Total Background			1289		< 291
$S/\sqrt{B}$ (115)			1.8		1.5
S/B (115)			5.1%		8.6%
$S/\sqrt{B}$ (120)			1.6		1.2
S/B (120)			4.4%		7.2%
$S/\sqrt{B}$ (130)			1.1		0.9
S/B (130)			3.0%		5.2%

The details of the dilepton $t\bar{t}H$ selection are summarised below:

- 2 oppositely-charged leptons (e, μ) passing identification criteria $-\log(L_\mu) < 1.4$ for muons, $-\log(L_e) < 1.2$ for electrons).
- corrected $E_{\text{T}}^{\text{miss}} > 40\,\text{GeV}$.
- 4 to 7 jets with calibrated $E_{\text{T}} > 20\,\text{GeV}$ and $|\eta| < 2.5$.
- $\geqslant$3 selected jets b-tagged with discriminator $D > 0.7$.

The above is termed the "loose" working point because there is evidence that it is possible to increase the purity (S/B) of the selection, by way of more stringent criteria:

- 4 to 6 jets with calibrated $E_{\text{T}} > 20\,\text{GeV}$ and $|\eta| < 2.5$.
- $\geqslant$4 selected jets b-tagged with discriminator $D > 0.7$.

Table 5.28. Selection efficiency ε_{loose} (including branching fraction where applicable) and resulting number of expected events N_{loose} in 60 fb^{-1}, for the dilepton $\bar{t}tH$ channel. For a glimpse of possible improvements, the same for a tighter set of cuts is provided (ε_{tight}, N_{tight}). Also quoted are binomial errors arising from the finite sizes of processed datasets. The $\bar{t}tH$ datasets are labelled by the generated Higgs mass in GeV/c^2 (parentheses).

	# analysed	ε_{loose}(%)	N^{ev}_{loose}	ε_{tight}(%)	N^{ev}_{tight}
$\bar{t}tH$ (115)	27900	0.511 ± 0.025	168 ± 8	0.088 ± 0.010	29 ± 3
$\bar{t}tH$ (120)	26141	0.490 ± 0.025	132 ± 7	0.070 ± 0.009	19 ± 3
$\bar{t}tH$ (130)	25911	0.490 ± 0.025	82 ± 4	0.072 ± 0.010	12 ± 2
$\bar{t}tb\bar{b}$	313894	0.637 ± 0.014	1080 ± 24	0.094 ± 0.007	159 ± 12
$\bar{t}t1j$	280385	0.0125 ± 0.0021	1270 ± 220	0	< 42 (68% C.L.)
$\bar{t}t2j$	276917	0.0448 ± 0.0040	2690 ± 240	0.00144 ± 0.00072	87 ± 43
$\bar{t}t3j$	90367	0.0553 ± 0.0078	1330 ± 190	0	< 31 (68% C.L.)
$\bar{t}t4j$	12281	0.0716 ± 0.0077	2620 ± 280	0.0025 ± 0.0014	92 ± 53
$\bar{t}tZ$	110156	0.304 ± 0.017	103 ± 6	0.0363 ± 0.0057	12 ± 2
all backgrounds			9090		< 422
$S/\sqrt{B}$ (115)			1.8		1.4
S/B (115)			1.8 (%)		6.9 (%)
$S/\sqrt{B}$ (120)			1.4		0.9
S/B (120)			1.5 (%)		4.5 (%)
$S/\sqrt{B}$ (130)			0.9		0.6
S/B (130)			0.9 (%)		2.9 (%)

The generated W^- was forced to decay leptonically (e, μ, τ), but the W^+ was allowed to decay freely. This "non-exclusive" dataset incurs a branching ratio of 1/3, which has been factored into the selection efficiencies reported in Table 5.28. This choice allows us to obtain a good estimate of the overlap of the contribution to the dilepton sample arising from semi-leptonic top decays which are mis-reconstructed as dilepton events; the same applies to tau decays which are mis-reconstructed as e, μ.

The background events have small efficiency to pass the selection criteria, so very large samples must be analysed. To make these samples more manageable, a loose pre-selection requiring at least 3 b-tags with discriminator $D > 0.7$ is applied before analysis.

5.3.5.4. Results. The selection efficiencies for the two working points, with the corresponding number of expected events and the signal significance, are reported in Table 5.28. The number of expected events is computed for an integrated luminosity of fb^{-1}.

Since the event selection is quite simple for the dilepton channel, it is possible to formulate simple equations predicting the selection efficiencies. This is detailed in Ref. [160], where some back-of-the-envelope calculations to estimate these efficiencies for both signal and backgrounds are presented, including some of the backgrounds that were not taken into account in this analysis.

5.3.5.5. All-hadron channel: $\bar{t}tH \to b\bar{b}b\bar{b}qq'q''q'''$. A number of kinematic variables, together with the b-tagging discriminator, have been studied to optimise the signal selection with respect to background rejection. Moreover, in order to combine the results from the 4 different decay sub-channels, a veto on leptons has been applied using the complementary cut developed within the semi and fully leptonic decays analyses: events are discarded if $-\log(L_\mu) < 1.4$ or $-\log(L_e) < 1.2$.

The final set of variables that are used in this analysis is the following:

- Jet Transverse Energy of the 8 most energetic jets in the tracker acceptance.
- Combined b-Tag discriminator variable for each jet.
- Centrality of the event defined as $\sum_{i=0}^{8} E_{\mathrm{T}}^{i}/E^{i}$.
- Centrality of the Higgs defined similarly, with the sum restricted to the 2 jets paired to the Higgs.

The jet-to-parton matching is performed using a χ^2 method as defined in [160].

Two working points have been chosen: the first uses loose cuts on the b-tagging discriminator to get higher statistical significance (but lower S/B), while the second uses a tighter cut on the b-tagging discriminator to obtain a higher S/B (but lower significance). For the first working point an event is selected if the following conditions are satisfied:

- $E_{\mathrm{T}}^{7th} > 30\,\mathrm{GeV}$ and $E_{\mathrm{T}}^{8th} > 20\,\mathrm{GeV}$ for the E_{T} ordered jets.
- the χ^2 for each of the 2 W bosons and 2 t quarks are within 3 sigma of their expected values.
- the 3 highest combined b-tagging discriminators for the 4 jets associated to the b-partons must satisfy $D_3 > 0.80$.
- Higgs centrality higher than 0.55 and no cut on Event Centrality.

For the tight working point, the b-tagging discriminator for the third highest jet is required to satisfy $D_3 > 0.85$ and the fourth one $D_4 > 0.70$, while the event and Higgs centrality are required to exceed 0.55 and 0.80, respectively.

All the applied cuts have been optimised to obtain the highest significance while keeping the S/B ratio as high as possible. All values chosen for E_{T}^{7th}, E_{T}^{8th}, D_3, D_4, Event and Higgs centrality have been varied simultaneously, thereby mapping out the complete set of combinations within the following limits:

- $20\,\mathrm{GeV} < E_{\mathrm{T}}^{8th} < 40\,\mathrm{GeV}$.
- $E_{\mathrm{T}}^{8th} < E_{\mathrm{T}}^{7th} < E_{\mathrm{T}}^{8th} + 40\,\mathrm{GeV}$.
- $0.5 < D_3$ and $D_4 < 0.95$.
- Event and Higgs Centrality in the range [0.50–0.95].

Variation of more than one cut has also been tested and the final implemented set of cut values is that for which significance and S/B are optimal.

5.3.5.6. Results. The number of analysed events, selection efficiencies with the corresponding number of expected events and the signal significance are reported in Tables 5.29 for the all-hadron decay channel. Both working points are considered.

5.3.6. Discussion of systematic uncertainties

5.3.6.1. Estimation of "standard" CMS systematics. The uncertainties in various quantities, given the knowledge of the CMS experiment at the time of writing this note, are considered first. These differ from what they are expected to be after CMS has collected 60 fb $^{-1}$ of data.

In keeping with other CMS analyses, the following "standard" sources of systematic error are considered:

- Jet energy scale (JES) (3% to 10% depending on p_t).
- Jet resolution (10%).
- b-jet and c-jet tagging efficiencies (4%).
- uds-jet tagging efficiencies (10%).
- Luminosity (3%).

Table 5.29. Analysed events, selection efficiency, number of expected events and signal significance in 60 fb^{-1} for the all-hadron $t\bar{t}H$ channel for 2 different working points: ε_{loose} and ε_{tight}. The numbers refer to the full mass range.

	# analysed	$\varepsilon_{loose}(\%)$	N^{ev}_{loose} 60 fb^{-1}	$\varepsilon_{tight}(\%)$	N^{ev}_{tight} 60 fb^{-1}
$t\bar{t}H$ (115)	49636	2.32 ± 0.07	347 ± 10	0.294 ± 0.015	44 ± 4
$t\bar{t}H$ (120)	163494	2.55 ± 0.04	314 ± 5	0.366 ± 0.024	45 ± 2
$t\bar{t}H$ (130)	43254	2.80 ± 0.08	214 ± 6	0.358 ± 0.029	27 ± 2
$t\bar{t}b\bar{b}$	203135	0.702 ± 0.019	1190 ± 31	0.0645 ± 0.0056	109 ± 9
$t\bar{t}$1j	1031551	0.0084 ± 0.0009	860 ± 92	0.0005 ± 0.0002	49 ± 22
$t\bar{t}$2j	559111	0.0333 ± 0.0024	2000 ± 150	0.0009 ± 0.0004	54 ± 24
$t\bar{t}$3j	68015	0.079 ± 0.011	1910 ± 260	0.0015 ± 0.0015	35 ± 35
$t\bar{t}$4j	97334	0.182 ± 0.014	6660 ± 500	0.0021 ± 0.0015	75 ± 53
$Zt\bar{t}$	80226	0.358 ± 0.021	121 ± 7	0.0312 ± 0.0062	11 ± 2
qcd170	264310	0.0238 ± 0.0030	4810 ± 610	0.0004 ± 0.0004	76 ± 76
qcd120	55128	0.0018 ± 0.0018	83 ± 83	0 ± 0	$< 95(68\% C.L.)$
Total Backgr.			17600		< 505
$S/\sqrt{B}$ (115)			2.6		2.0
S/B (115)			2.0%		8.7 %
$S/\sqrt{B}$ (120)			2.4		2.0
S/B (120)			1.8%		8.9 %
$S/\sqrt{B}$ (130)			1.6		1.2
S/B (130)			1.2%		5.4 %

It is assumed that the systematics listed above are uncorrelated. Each source is varied independently which produces a change in the selection efficiency $\Delta\varepsilon$ and the corresponding change in expected event yields ΔN_X ($X =$ ttH, tt1j, ...) for the signal and background.

A very detailed breakdown of the various sources of systematic uncertainties and the methods of how they are computed for all the background and signal samples is available in Reference [160]. In Table 5.30, the systematic uncertainties are propagated to the expected signal significance for "tight" and "loose" working points.

5.3.6.2. Background rates from data. There are relatively large theoretical uncertainties in the cross-sections used to normalise the signal yields [162], and even larger theoretical uncertainties in those used for the $t\bar{t}$+jets backgrounds [168]. These have not been included as part of the systematic errors considered above, because when the CMS experiment reaches maturity, estimating the $t\bar{t}$+jets background directly from data ought to be possible. In this way, the uncertainty associated with Monte Carlo derived tagging rates are avoided entirely. For example, the number of mis-tagged $t\bar{t}$+jets which can be factorised as follows:

$$N^{mistag}_{t\bar{t}jj} = N^{no-tag}_{t\bar{t}jj} \times Pr(uds \to b;\, E_{\mathrm{T}}, \eta, ...)$$

where $N^{no-tag}_{t\bar{t}jj}$ is a high purity (e.g. fully reconstructed with a mass window) top sample that has been obtained without requiring b-tagging and $Pr(uds \to b;\, E_{\mathrm{T}}, \eta, ...)$ is a parameterised "fake matrix" that is derived from some independent dataset (e.g. dijet data) which yields the probability for a light quark jet to fake a secondary vertex. It may also be possible to derive this fake matrix from the top sample itself. If a high-purity (e.g. double-tagged and fully reconstructed) semi-leptonic top sample were selected, the jets belonging to the hadronic W would provide a source of both light quark and charm jets. From these data, a measurement of the corresponding uds-tag and c-tag rates at the relevant energy could be directly obtained.

Table 5.30. Significance before and after taking into account the uncertainty dB in the total number of background events due to systematics.

muon	S/B	$S/\sqrt{B}$	$S/\sqrt{B+dB^2}$	dilepton	S/B	$S/\sqrt{B}$	$S/\sqrt{B+dB^2}$
	$L_{bSele} > 0.55(\varepsilon_{loose})$				4-7 jets, 3-4 b-tagged (ε_{loose})		
$t\bar{t}H$ (115)	0.052	2.2	0.20	$t\bar{t}H$ (115)	0.018	1.8	0.10
$t\bar{t}H$ (120)	0.041	1.8	0.15	$t\bar{t}H$ (120)	0.015	1.4	0.08
$t\bar{t}H$ (130)	0.030	1.3	0.11	$t\bar{t}H$ (130)	0.009	0.9	0.05
	$L_{bSele} > 0.75(\varepsilon_{tight})$				4-6 jets, 4-6 b-tagged (ε_{tight})		
$t\bar{t}H$ (115)	0.108	2.0	0.44	$t\bar{t}H$ (115)	0.069	1.4	0.42
$t\bar{t}H$ (120)	0.082	1.6	0.34	$t\bar{t}H$ (120)	0.045	0.9	0.27
$t\bar{t}H$ (130)	0.060	1.1	0.24	$t\bar{t}H$ (130)	0.029	0.6	0.18
electron	S/B	$S/\sqrt{B}$	$S/\sqrt{B+dB^2}$	hadron	S/B	$S/\sqrt{B}$	$S/\sqrt{B+dB^2}$
	$L_{bSele} > 0.55(\varepsilon_{loose})$				Working Point ε_{loose}		
$t\bar{t}H$ (115)	0.051	1.8	0.20	$t\bar{t}H$ (115)	0.020	2.6	0.07
$t\bar{t}H$ (120)	0.044	1.6	0.17	$t\bar{t}H$ (120)	0.018	2.4	0.07
$t\bar{t}H$ (130)	0.030	1.1	0.12	$t\bar{t}H$ (130)	0.012	1.6	0.05
	$L_{bSele} > 0.75(\varepsilon_{tight})$				Working Point ε_{tight}		
$t\bar{t}H$ (115)	0.086	1.5	0.37	$t\bar{t}H$ (115)	0.087	2.0	0.22
$t\bar{t}H$ (120)	0.072	1.2	0.31	$t\bar{t}H$ (120)	0.089	2.0	0.22
$t\bar{t}H$ (130)	0.052	0.9	0.22	$t\bar{t}H$ (130)	0.054	1.2	0.13

5.3.7. Combined significance

Since the event samples for the channels studied in this note are strictly disjoint, the results can be combined by simply adding the individual signal yields (background yields) to obtain a summed $S(B)$.

For each of the considered systematics, the resultant error in background yields are added for all four channels, since they are by definition fully correlated. The summed errors are then added by quadratures to get a combined systematic uncertainty dB. One then calculates the significance, inclusive of systematic uncertainties in the background yield, according to the formula $S/\sqrt{B+dB^2}$.

It is of interest to see how much better the results have the potential to be at tighter working points for the various analyses. Since the systematic uncertainties are not well quantified at these "tight" working points, because of a lack in Monte Carlo Statistics, the same uncertainties as for the "loose" working points are used to reduce spurious statistical effects. This procedure can be justified by the observation that the impact of the b-tagging and uds-mistagging uncertainty is smaller at the "tight" working points and the JES uncertainty becomes dominant. Since the "tight" working points are defined by stronger b-tagging cuts, while keeping the E_{T} cuts constant, no major change in the relative systematic uncertainty is expected. A more detailed study of the systematic error at the "tight" working points for samples with enough Monte Carlo Statistics is available in Ref. [160].

It is difficult to predict at this time exactly what will be the level to which the backgrounds can be understood, because the tools required are not yet in existence and because this understanding requires real data. In view of this, it is interesting to consider how the combined significance of the measurements presented in this note would vary as a function of the fractional uncertainty in background cross-sections, i.e. as dB_{xsec}/B.

The solid central line in Figure 5.17 shows how the combined significance $S/\sqrt{B+(dB_{sys}+dB_{xsec})^2}$ degrades as a function of dB_{xsec}/B. The signal and background yields for the tightest working points (N^{ev}_{tight} in Table 5.27, Table 5.28 and Table 5.29)

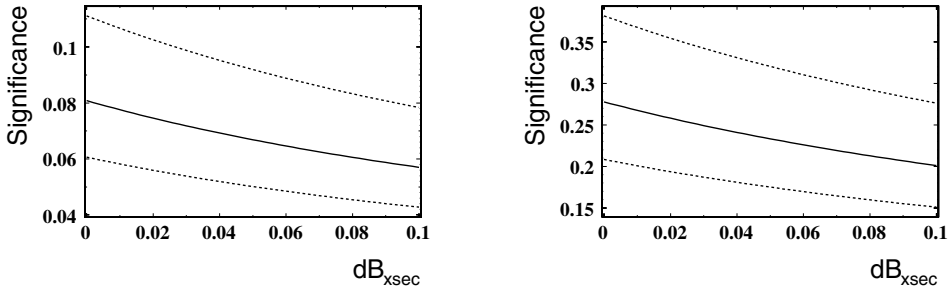

Figure 5.17. Expected range of combined significance (dilepton + semi-leptonic + all-hadron, and includes the systematic uncertainties estimated in Section 5.3.6.1) versus an additional systematic uncertainty on the background cross-section as a fraction of total background. (Left) Results for the "loose" working points. (Right) Results for the "tight" working points.

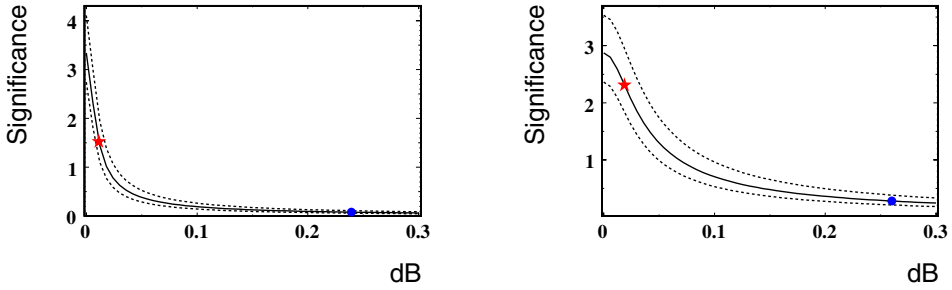

Figure 5.18. Expected range of combined significance (dilepton + semi-leptonic + all-hadron) versus the total systematic uncertainty in background as a fraction of total background. (Left) Results for the "loose" working points. (Right) Results for the "tight" working points.

are used in the right side of Figure 5.17, because these give the best results after inclusion of systematics.

Other than this "fundamental" cross-section uncertainty, there is also the "correctible" errors in the cross-sections used at the time of writing, which can be compensated for once data has been collected. The upper and lower dashed curves in Figure 5.17 show the maximum and minimum allowed excursions, should the signal and background cross-sections be off by 10% and 20% respectively. Thus the upper (lower) dashed line corresponds to the signal cross-section scaled up (down) by 10% while at the same time the background cross-section is scaled down (up) by 20%.

It is also of interest to see how much better the analyses could do if the total systematic uncertainty can be reduced (i.e. the region left of zero in Figure 5.17). Hence, Figure 5.18 shows the full range of obtainable significances, with the dot marking the currently estimated value with no cross-section uncertainty ($dB = dB_{sys}$). The star corresponds to what one would obtain for 1% and 4% uncertainties on the $t\bar{t}$Nj and $t\bar{t}b\bar{b}$ backgrounds, respectively, an arbitrarily chosen reference. It is interesting to note that it does not quite yield a substantial significance, even though background uncertainties of 1% and 4% for $t\bar{t}$Nj and $t\bar{t}b\bar{b}$ are probably substantially better than what will be accessible in reality. This highlights the challenge that is faced in observing $t\bar{t}$H.

Chapter 6. Physics Studies with Heavy Ions

6.1. Benchmark Channel: $PbPb \to Q\overline{Q} + X \to \mu^+\mu^- + X$

The measurement of the charmonium (J/ψ, ψ') and bottomonium (Υ, Υ', Υ'') resonances in PbPb collisions at $\sqrt{s_{NN}} = 5.5$ TeV provides crucial information on the many-body dynamics of high-density QCD matter. First, the step-wise suppression of heavy quarkonia production is generally agreed to be one of the most direct probes of Quark-Gluon-Plasma formation. Lattice QCD calculations of the heavy-quark potential indicate that colour screening dissolves the ground-state charmonium and bottomonium states, J/ψ and Υ, at $T_{\rm diss} \approx 2 \cdot T_{\rm crit}$ and $4 \cdot T_{\rm crit}$, respectively. While the interest of charmonia production studies in heavy-ion collisions is well established from measurements done at the SPS and at RHIC, the clarification of some important remaining questions requires equivalent studies of the Υ family, only possible at the LHC energies. Second, the production of heavy-quarks proceeds mainly via gluon-gluon fusion processes and, as such, is sensitive to saturation of the gluon density at low-x in the nucleus ("Colour Glass Condensate"). Measured departures from the expected "vacuum" (proton-proton) quarkonia cross-sections in PbPb collisions at LHC will thus provide valuable information not only on the thermodynamical state of the produced partonic medium, but also on the initial-state modifications of the nuclear parton (especially, gluon) distribution functions.

This first CMS heavy-ion physics analysis focuses on the measurement of the heavy-quarkonia cross-sections in PbPb collisions at $\sqrt{s_{NN}} = 5.5$ TeV, via their dimuon decay channel. The generation of realistic signals and backgrounds, the dimuon reconstruction algorithm and the trigger, acceptance and efficiency corrections are discussed. The obtained dimuon mass resolutions, the signal over background as well as the expected yields in one-month PbPb running are presented. An example of a $\Upsilon \to \mu^+\mu^-$ event embedded in a PbPb collision is shown in colour plate CP9.

6.1.1. Simulation of physics and background processes

The relatively low Υ production rates ($\sim 10^{-4}$ per PbPb event) and the large number of particles to track in heavy-ion collisions make it very expensive computationally to use a full nucleus-nucleus event generator (such as e.g. HIJING [169]) with detailed detector simulation and reconstruction to obtain a statistically significant sample of signal events. Instead, a combination of fast and slow simulations are used in this analysis. The input signal and backgrounds are obtained from realistic distributions: NLO pQCD for heavy-quark production processes, and HIJING for the soft background, constrained by extrapolations from lower energy heavy-ion data. A full detector and trigger simulation plus reconstruction are carried out for a few 10^7 events with single and pair particles of the different types and the corresponding response functions (acceptances, resolutions, efficiencies, etc) are parameterised in a fast MC, used to obtain the final fully corrected yields. The response functions are cross-checked by comparing the final dimuon spectra obtained with the fast MC against 5×10^5 PbPb HIJING events fully simulated and reconstructed in the detector.

The quarkonium production cross sections in PbPb are obtained from NLO pp calculations at $\sqrt{s} = 5.5$ TeV made in the colour evaporation model (CEM) [170], using MRST PDF modified with the EKS98 prescription for nuclear shadowing [171], with renormalisation and factorisation scales $\mu_R = \mu_F = m_Q$, and scaled by A^2 ($A = 208$ for Pb). The resulting (impact-parameter averaged) inclusive quarkonia production cross sections are: $B_{\mu\mu}\sigma_{Q\overline{Q}} = 49\,000, 900, 300, 80, 45\ \mu$b for J/ψ, ψ', Υ, Υ', and Υ'', respectively. The NLO

double-differential $d^2\sigma/dp_{\mathrm{T}}d\varphi$ distributions of J/ψ and Υ are also used for the other states within each quarkonium family.

The two main sources of background in the dimuon invariant mass spectrum are:

1. Uncorrelated decays of **charged pions and kaons**, which represent about 90% of the produced charged particles. This source was simulated using input pion and kaon $d^2N/dp_{\mathrm{T}}d\eta$ distributions from HIJING, absolutely normalised to give $dN_{ch}/d\eta|_{\eta=0} = 2500\ (low)$ and 5000 $(high)$ multiplicities in central PbPb. Both cases are conservative ("pessimistic"') estimates, since extrapolations from RHIC data indicate that $dN_{ch}/d\eta|_{\eta=0} \approx 2000$ at the LHC.
2. The other source of background muons are **open heavy flavour** (D, B mesons) decaying a few mm away from the interaction vertex. The probability to produce at least one muon at the end of the decay chain of charm (bottom) quarks is ∼18% (38%) according to PYTHIA 6.025. The double differential (p_{T}, η) cross-sections are obtained from pp NLO calculations (with CTEQ5M1 PDF, and $\mu_R = \mu_R = m_Q$), which give $\sigma_{c\bar{c},b\bar{b}}$ = 7.5, 0.2 mb [170], scaled by the nuclear overlap function, $\langle T_{PbPb}(b = 0\,\mathrm{fm})\rangle = 30.4\,\mathrm{mb}^{-1}$, to obtain the expected yields in central PbPb collisions.

A fast MC simulation equivalent to $5 \cdot 10^7$ PbPb events has been carried out superimposing the decay dimuon from the five quarkonium resonances on top of the background from the combinatorial decays of π, K and open heavy flavour. Each muon track (with a given momentum, pseudorapidity, charge and origin) is weighted by a factor that takes into account the corresponding detector acceptance, as well as trigger and reconstruction efficiency for the two event multiplicities considered (see next section).

6.1.2. Reconstruction and analysis

6.1.2.1. Dimuon trigger and acceptance. The response of the CMS detector to muons (as well as long-lived punch through pions and kaons reaching the muon chambers) is parameterised by 2-dimensional p, η acceptance and trigger tables. The particles are fully tracked in CMS using GEANT4 from the vertex to the chambers. Each track is accepted or rejected according to the Level-1,2 heavy-ion dimuon trigger criteria [7] and the corresponding efficiencies, $\varepsilon^{LVL1}_{trig}(p, \eta)$ and $\varepsilon^{LVL2}_{trig}(p, \eta)$, are computed. Trigger efficiencies are of the order of ∼90% for those μ reaching the muon chambers. The J/ψ and Υ acceptances are shown as a function of p_{T} in Fig. 6.1, for two η ranges: full detector and central barrel. Because of its relatively low mass, low energy J/ψ's ($p_{\mathrm{T}} \lesssim 4\,\mathrm{GeV/c}$) cannot be detected since their decay muons don't have enough energy to traverse the calorimeters and they are absorbed due to ionisation losses before reaching the muon chambers. For larger p_{T} values the J/ψ acceptance increases and flattens out at ∼15% for p_{T} 12GeV/c. The Υ acceptance starts at ∼40% at $p_{\mathrm{T}} = 0\,\mathrm{GeV/c}$ and remains constant at 15% (full CMS) or 5% (barrel) for $p_{\mathrm{T}} > 4\,\mathrm{GeV/c}$. The p_{T}-integrated acceptance is about 1.% for the J/ψ and 21% for the Υ as obtained from our input theoretical distribution.

6.1.2.2. Dimuon reconstruction efficiency, purity and mass resolution. The dimuon reconstruction algorithm used in the heavy-ion analysis is a version of the regional track finder based on the muons seeded by the muon stations and on the knowledge of the primary vertex, as described in [172, 173]. It is adapted to deal with the high hit occupancy of the silicon tracker in PbPb collisions. It uses the muon tracks found in the innermost muon stations to identify hits in the outer CMS tracker layer that can form the starting points (seeds) for the matching muon candidate tracks. The propagation in the tracker is performed from the outer

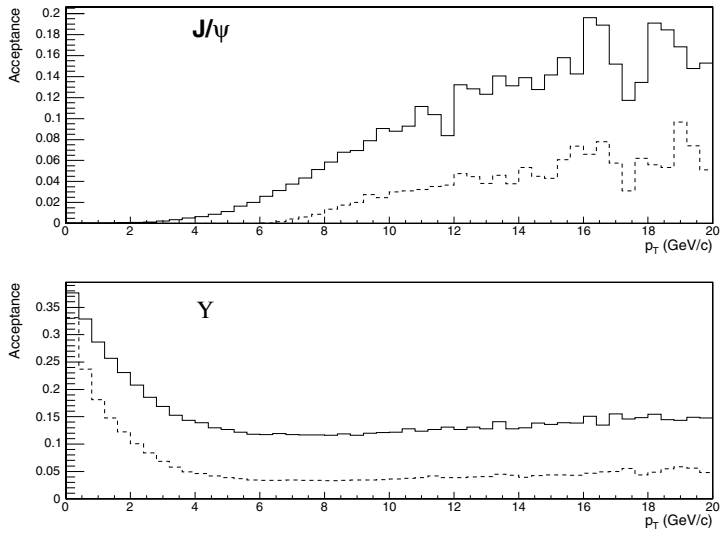

Figure 6.1. J/ψ (top) and Υ (bottom) acceptances as a function of p_{T}, in the full detector (barrel and endcap, $|\eta| < 2.4$, full line) and in the barrel alone ($|\eta| < 0.8$, dashed line).

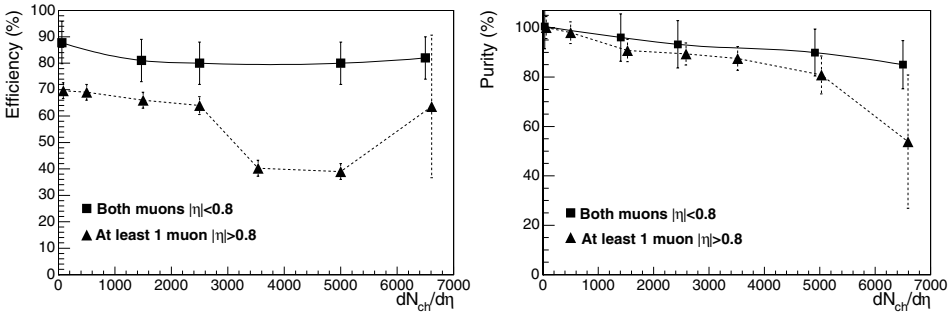

Figure 6.2. Υ reconstruction efficiency (left) and purity (right) as a function of the PbPb charged particle rapidity density, $dN_{ch}/d\eta|_{\eta=0}$.

layer towards the primary vertex, using two-dimensional parametrisation in the transverse and longitudinal planes. The final fit of trajectories is performed with a Kalman-fitter. The efficiency of a given muon pair is: $\varepsilon_{pair}(p,\eta) = \varepsilon_{track_1} \times \varepsilon_{track_2} \times \varepsilon_{vertex}$. The dependence of the Υ reconstruction efficiency on the event multiplicity was obtained from a full GEANT simulation using Υ signal dimuon embedded in HIJING PbPb events. Figure 6.2 shows the Υ efficiency and purity (where purity is defined as the ratio of true Υ reconstructed over all Υ reconstructed) as a function of charged-particle multiplicity. In the central barrel, the dimuon reconstruction efficiency is above $\sim 80\%$ for all multiplicities, whereas the purity decreases slightly with $dN_{ch}/d\eta$ but stays also above 80% even at multiplicities as high as $dN_{ch}/d\eta|_{\eta=0} = 6500$. If (at least) one of the muons is detected in the endcaps, the efficiency and purity drop due to stronger reconstruction cuts. Nonetheless, for the maximum $dN_{ch}/d\eta|_{\eta=0} \approx 2500$ multiplicities expected in central PbPb at LHC, the efficiency (purity) remains above 65% (90%) even including the endcaps.

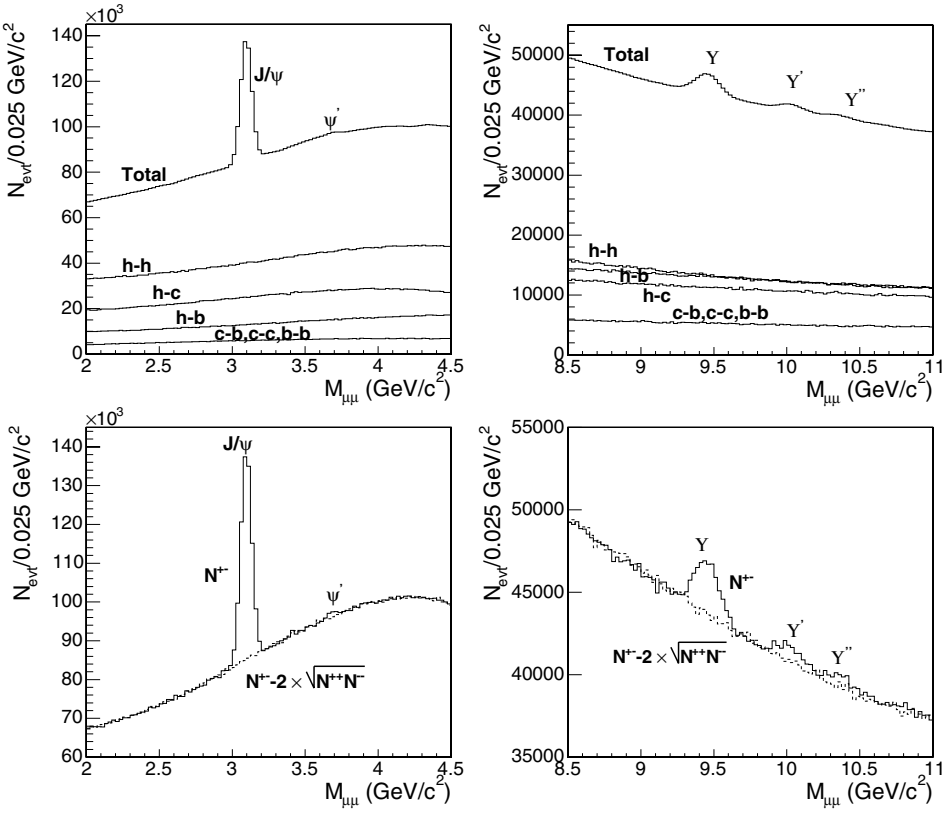

Figure 6.3. Dimuon mass distributions measured within $|\eta| < 2.4$ for PbPb events with $dN_{ch}/d\eta|_{\eta=0} = 5000$ in the J/ψ (left) and Υ (right) mass regions. The main contributions of the background are shown in the top panels (h, c, b stand for $\pi + K$, charm, bottom decay muons resp.), while the bottom panels also show the like-sign pairs (combinatorial background).

If we only consider muon pairs in the central barrel, $|\eta| < 0.8$, the dimuon mass resolution is $\sim$54 MeV/c^2 at the Υ mass, as obtained from a Gaussian fit of the reconstructed $\mu\mu\, m_{\rm inv}$ distribution (using a detailed MC simulation but without background). In the full pseudorapidity range, the dimuon mass resolution amounts to $\sim$1%: 35 MeV/c^2 at the J/ψ mass, and 86 MeV/c^2 at the Υ mass. These dimuon mass resolutions (the best among the LHC experiments) allow for a clean separation of the different quarkonia states. These values are used to smear the dimuon mass distribution in the fast MC studies.

6.1.3. Results

About 5×10^7 PbPb collisions were simulated. Muons passing the acceptance tables are combined to form pairs and each pair is weighted according to the trigger and reconstruction efficiencies (dependent on the momentum, η, purity and event multiplicity). Their invariant mass is calculated and smeared as described in the previous section. The obtained dimuon mass distributions are then scaled to 0.5 nb^{-1}, corresponding to the PbPb luminosity integrated in one month with average luminosity $L = 0.4 \cdot 10^{27}$ cm^{-2} s^{-1} and 50% machine operation efficiency. Figure 6.3 shows the resulting opposite-sign mass distributions, for

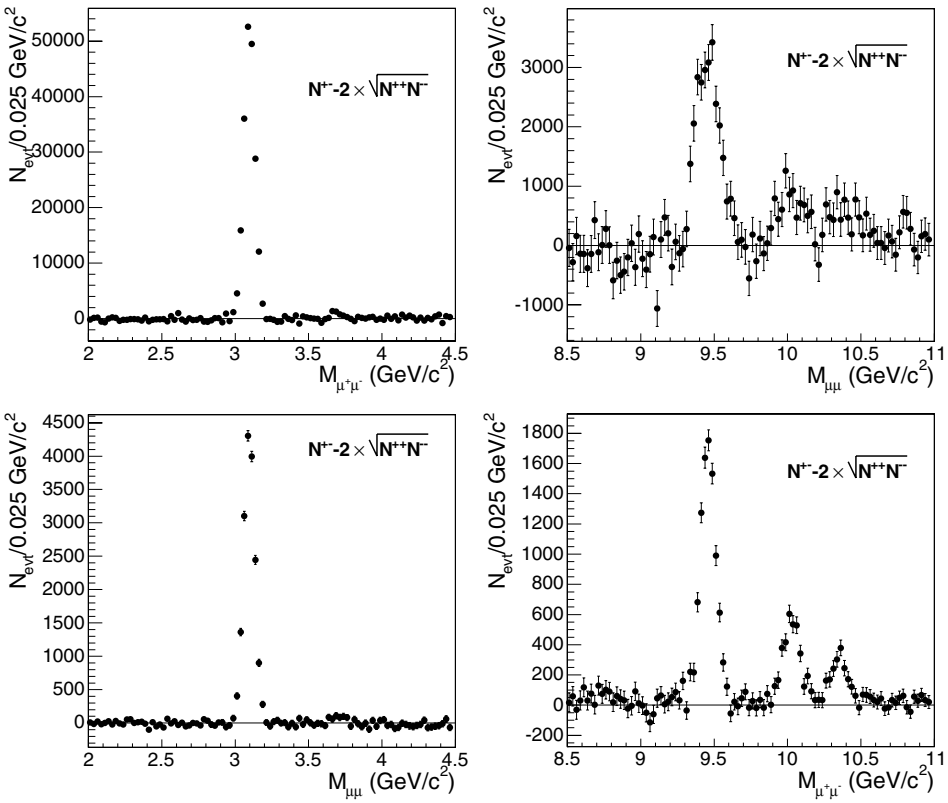

Figure 6.4. Signal dimuon mass distributions after background subtraction in the J/ψ (left) and Υ (right) mass regions expected after one month of PbPb running. Top panels for $dN_{ch}/d\eta|_{\eta=0} = 5000$ and $|\eta| < 2.4$ ("worst" case conditions); bottom panels for $dN_{ch}/d\eta|_{\eta=0} = 2500$ and $|\eta| < 0.8$ ("best" measurement conditions).

the *high* multiplicity case, $dN_{ch}/d\eta|_{\eta=0} = 5000$ and full acceptance ($\eta < 2.4$). The different quarkonia resonances appear on top of a continuum due to several combinatorial background sources, the main ones being identified in the upper plots (h, c and b stand for $\pi + K$, charm and bottom decay muons, respectively). Since the CMS trigger and acceptance conditions treat opposite-sign and like-sign muon pairs in the same way, the uncorrelated background can be subtracted using the like-sign pairs: $N^{\mathrm{Sig}} = N^{+-} - 2\sqrt{N^{++}\,N^{--}}$, shown also in the bottom panels of Fig. 6.3.

Figure 6.4 shows the *signal* dimuon mass distributions, after background subtraction, for two different scenarios: $dN_{ch}/d\eta|_{\eta=0} = 5000$, $|\eta| < 2.4$ ("worst" case conditions); and $dN_{ch}/d\eta|_{\eta=0} = 2500$, $|\eta| < 0.8$ ("best" case). Except for the ψ', all quarkonia states are clearly visible. The corresponding signal-to-background ratios and yields (counted within 1σ of the resonance peaks) are collected in the Table 6.1 for one month of PbPb running.

6.1.4. Conclusions

With its very broad muon acceptance and precise tracking, CMS will provide significant contributions to heavy ion physics at the LHC. Studies of quarkonium production in PbPb

Table 6.1. Signal-to-background ratios and expected quarkonia yields in one month of PbPb running (0.5 nb $^{-1}$ integrated luminosity) for two multiplicity scenarios and two η windows.

$dN_{ch}/d\eta\|_{\eta=0}$, $\Delta\eta$	S/B	N(J/ψ)	S/B	N(Υ)	N(Υ')	N(Υ'')
2500, $\|\eta\| < 2.4$	1.2	180 000	0.12	25 000	7300	4400
2500, $\|\eta\| < 0.8$	4.5	11 600	0.97	6400		
5000, $\|\eta\| < 2.4$	0.6	140 000	0.07	20/000	5900	3500
5000, $\|\eta\| < 0.8$	2.75	12 600	0.52	6000		

collisions at $\sqrt{s_{NN}} = 5.5$ TeV, will provide crucial information on the thermodynamical state of QCD medium formed in these collisions, through the expected step-wise "melting" pattern of the different $Q\overline{Q}$ states due to colour screening. These results will also be sensitive to modifications of the low-x nuclear parton distribution functions, as expected in case of gluon saturation.

CMS can reconstruct the charmonium and bottomonium resonances, via their dimuon decay channel, with high efficiencies (∼80%), good purity (∼90%) and a very good dimuon mass resolution (54 MeV/c^2 at the Υ mass), when both muons are detected in the central barrel ($|\eta| < 0.8$), even in the case of exceptionally high multiplicities ($dN_{ch}/d\eta|_{\eta=0} \approx 5000$). When considering the full pseudorapidity region ($|\eta| < 2.4$), the mass resolution becomes ∼86 MeV/c^2 at the Υ, and 35 MeV/c^2 at the J/ψ, with ∼ 50% dimuon reconstruction efficiencies. The Υ states can be measured all the way down to $p_T = 0$ GeV/c with acceptances as large as 40%, while the lower rest mass of the J/ψ state and the large amount of material in the calorimeters absorbs "low" energy decay muons and prevents from measuring J/ψ's below $p_T \approx 4$ GeV/c. At high p_T (above ∼12 GeV/c for the J/ψ and ∼4 GeV/c for the Υ) the dimuon acceptance flattens out at 15%.

The large aperture of the muon detectors and the precise tracking result in a very good separation between the $Q\overline{Q}$ states in the dimuon mass distributions, and in relatively high statistics and good signal to background ratios ($S/B \approx 1(5)$, $S/B \approx 0.1(1)$ for J/ψ and Υ resp. in the full (central) rapidity range). After one month of PbPb running (0.5 nb^{-1}) we should collect ∼180 000 J/ψ and ∼25 000Υ dimuon, enough to compare central and peripheral PbPb collisions, and to carry out some differential studies (dN/dy, dN/dp_T) which will surely contribute significantly to clarify the physics mechanisms behind the production (and "destruction") of quarkonia states in nucleus-nucleus collisions at the LHC.

Part II. CMS Physics Reach

Chapter 7. Physics of Strong Interactions

7.1. QCD and jet physics

7.1.1. Introduction

With the start-up of LHC, a new domain of energy will be explored and an extrapolation of our current knowledge in the form of the Standard Model may not be sufficient to describe the new measurements. Even in a first data-taking phase with a rather low luminosity, studies of jet physics in the framework of quantum chromodynamics (QCD) will allow to check our current theory against the new data.

Figure 7.1 presents the decomposition of the total jet cross section into the partonic processes for $p\bar{p}$ collisions at the Tevatron and pp collisions at the LHC in dependence of the scaling variable $x_T = 2p_T/\sqrt{s}$, and illustrates the differences in cross section contributions of the PDFs compared to measurements possible today. In Fig. 7.2 the expected statistical uncertainties on differential cross sections for all rapidities are presented for a pilot run with 0.1 fb^{-1} and for a first physics run with 10 fb^{-1}. Trigger pre-scales are taken into account. The figure demonstrates that already in the pilot run high statistics will be available up to 1.5 TeV of transverse jet energy.

On the one hand, the measured data have to be corrected for detector effects using fully simulated events. Also, an energy calibration has to be performed on the reconstructed jets which ideally is extracted from data as well, but can also be done employing Monte-Carlo methods. On the other hand, for the theory predictions, which are most precise with respect to the hard parton-parton scattering amplitudes, effects of soft physics modelled in the form of parton showers and hadronisation models with subsequent decays have to be taken into account. Once this is done, parameters of the current theory can be cross-checked or improved in precision by comparing the measured hadronic final state with the corrected theoretical predictions.

7.1.2. Jet algorithms

In order to re-establish a link between the observed particles that appear as collimated streams of hadrons in the detector and the hard process, algorithms are defined to group particles that are supposed to come from the same hard parton into jets. The required ingredients of such a jet algorithm are a distance measure to define the separation between objects, a procedure how to decide when objects are to be combined and a recombination scheme explaining how to combine objects. In addition, it has to be specified how the list of input objects has been determined.

Two principal types of algorithms are in common use: Cone type algorithms [174] that traditionally have been employed in hadron-hadron collisions where objects are clustered together that are close in angle around a high-energetic seed, and clustering algorithms where iteratively objects are combined that have the smallest distance of all pairwise combinations possible. The latter have predominantly been used in e^+e^- and $e^\pm p$ collisions, first in the form of the Jade algorithm [175, 176] and nowadays as k_T algorithm [177].

Both algorithms applied in this study use an angular distance measure based on the azimuthal angle Φ and, instead of the pseudo-rapidity η, the true rapidity $y = 0.5 \ln((E + p_z)/(E - p_z))$ which has become an established standard in recent publications

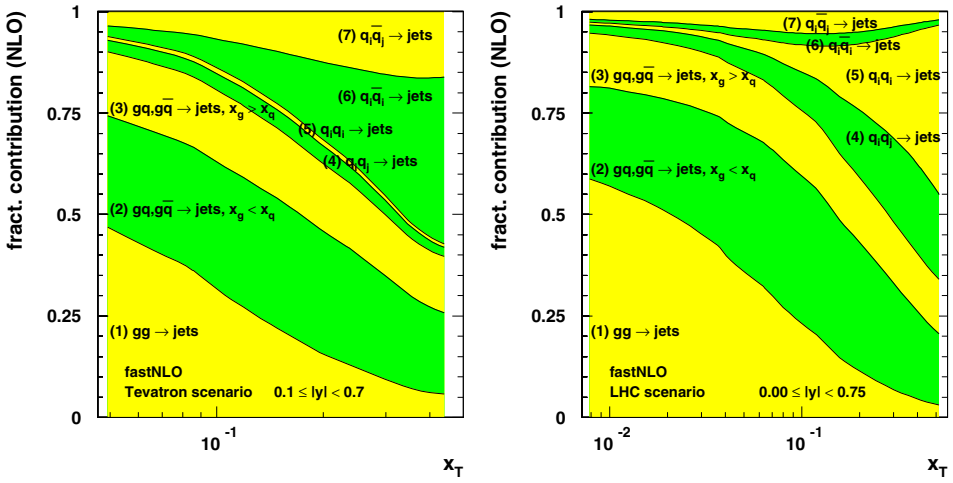

Figure 7.1. Decomposition of the total jet cross section into the partonic processes for $p\bar{p}$ collisions at the Tevatron (left) and pp collisions at the LHC (right). The fractional contributions are shown versus the scaling variable $x_T = 2p_T/\sqrt{s}$.

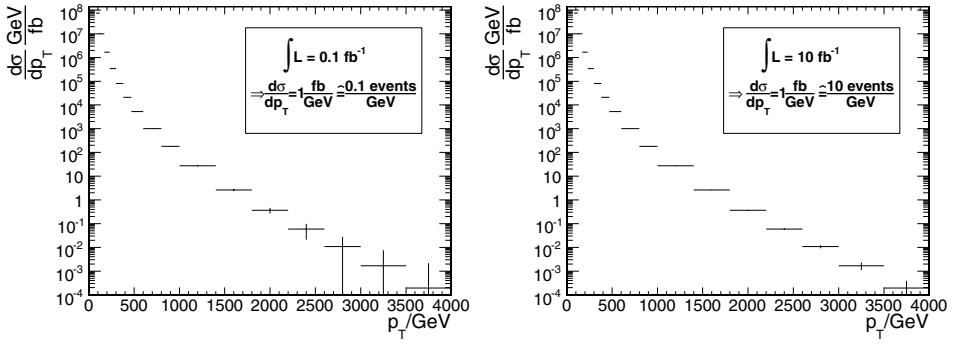

Figure 7.2. Expected statistical uncertainties on differential cross sections for all rapidities; left: for a pilot run with 0.1 fb^{-1}, and right: for a physics run with 10 fb^{-1}. The central cross section values are taken from a leading-order calculation in dependence of the transverse momenta of the hard interaction.

[178, 179]. The distance between two objects i and j hence reads

$$\Delta R_{ij} = \sqrt{(\Delta_{ij}\Phi)^2 + (\Delta_{ij}y)^2}. \tag{7.1}$$

In addition, the most frequently used recombination scheme, the E scheme, implying a simple four-momentum addition, is employed in both cases.

Two types of jet algorithms are used here. The main results have been achieved with the k_T algorithm defined below, some cross checks have been performed with the midpoint

cone algorithm:

1. Iterative clustering-type: Inclusive k_T algorithm [180] with
   - Distances are evaluated according to the ΔR scheme, i.e. $d_{ij} = \min(p_{T,i}^2, p_{T,j}^2)\frac{\Delta R_{ij}^2}{D^2}$ with R_{ij} as in Eq. 7.1
   - Jet resolution parameter $D = 1.0$
2. Cone-type: Midpoint cone algorithm [181, 182] with:
   - Cone radius $R = 0.7$, all objects within a cone have to fulfill $R_{ic} \leqslant R$ with c labelling the four-vector of the current cone.
   - Overlap threshold $f_{\text{merge}} = 0.50$, i.e. overlapping cone jets are merged when they share more than 50% of the energy in the less energetic cone
   - Search-cone radius fraction $f_{\text{search}} = 0.5$, i.e. the first step to find the stable cones (before any splitting/merging is done) is performed with a smaller radius of f_{search}^{*R}

Concerning the k_T algorithm, a jet resolution parameter of $D = 1.0$ is, from a theoretical point of view, best comparable to a cone algorithm with $R = 0.7$. In order to reduce the sensitivity to the underlying event, it is advantageous to reduce the jet resolution parameter D or the cone radius R, respectively.

Note that primarily due to the limited choice of available jet energy calibrations the definition of the midpoint algorithm above has been selected. It does not exactly correspond to the definition given in [181] but to a modified one [182] that is in use by the CDF collaboration [178]. There have been indications that this algorithm leads to an infrared sensitive behaviour [183], so it is recommended to use the original definition of the midpoint algorithm without extra search cone radius.

7.1.3. Trigger scheme, event selection and phase space

The level one (L1) and the high level triggers (HLT) required for this analysis are the single-jet triggers which are described in more detail in Section E.4.3.2. QCD jet production has, by several orders of magnitude, the largest cross section, but in contrast to most other analyses QCD jet events are the signal here. Therefore, the sole other selection requirement for this study demands all jets to have a transverse momentum larger than 50 GeV. The available phase space is then subdivided into 17 ranges in transverse momentum p_T and five ranges in rapidity y, where the focus is mostly on the central region up to 2.5 in rapidity.

7.1.4. Input data

The analysed events were generated with PYTHIA [184] and subsequently subjected to the full GEANT-4 based CMS detector simulation and reconstruction programs. Following the analysis setup presented in the Introduction 7.1.1, four classes of input objects to the jet algorithms have been considered: The initial partons of the hard interaction, partons after parton shower (partonic final state, PFS), all stable particles of the hadronic final state (HFS) other than muons or neutrinos and calorimeter towers. The calorimeter towers fulfilling the requirements $E > 0.8$ GeV and $E_T > 0.5$ GeV were subjected to the same jet algorithms as the generator particles. If necessary, a matching of generator and calorimeter jets was performed by looking for the pairs closest to each other in distance $d = \sqrt{(\Delta\Phi)^2 + (\Delta\eta)^2}$.

7.1.5. Jet energy calibration

The jet energy calibration has been performed with a MC calibration method implying calibration factors that are applied on a jet by jet basis to the calorimeter jets depending on pseudo-rapidity η and transverse momentum p_T. The alternative data based technique of gamma-jet calibration, where jet transverse energies are measured against recoiling high energetic photons could not yet be employed for this study.

7.1.6. NLO calculation

In order to compare to theoretical predictions of perturbative QCD, calculations of at least next-to-leading order (NLO) precision are required. Here, the program CLOSET++ [185] is employed for the NLO calculation. However, since precise computations in NLO are very time consuming, a more efficient set-up in the form of the fastNLO project [186] is used which allows the fast rederivation of the considered cross section for arbitrary input PDFs and α_S values. This is done by separating the PDF dependency from the hard matrix element calculation by interpolating the PDFs between fixed support points in fractional proton momentum x so that the PDF dependency can be evaluated a posteriori from one complete calculation.

Note that neither PYTHIA nor CLOSET++ contain electroweak corrections which may change high p_T cross sections from 1 TeV onwards by up to 30% [187]. Insofar this study is consistent, but before comparing to real data this has to be taken into account.

7.1.7. Experimental and theoretical uncertainties

From the experience at the Tevatron [178, 188, 189], it is known that the jet energy scale with an uncertainty of 3% represents by far the dominant source of uncertainty for high p_T jet cross sections. Similarly, PDF uncertainties lead to the dominant uncertainty of the jet cross sections from the theoretical side.

According to CMS studies the jet energy scale in this analysis has been varied by $\pm 3\%$ in order to estimate the impact on the cross section determination. Figure 7.3 presents on the left hand side the corresponding relative experimental uncertainty on the jet cross section for three regions in rapidity. Starting at about 15% at low p_T it rises up to about 50% at high p_T for central rapidity. In the two non-central rapidity regions the uncertainties are of comparable size below about 1 TeV of transverse momentum, but get considerably larger for higher p_T. In general, a similar behaviour as expected from Tevatron results is observed.

By evaluating the cross section calculation for the error set of the CTEQ6M [12] PDFs the ensuing theoretical uncertainty as shown in fig. 7.3 on the right hand side could be derived. It is of the same order of magnitude as the energy scale uncertainty and rises from about 5% for low transverse momenta with a minimum of 3% at $\approx$ 200 GeV up to $+65\%$ and -30% at the highest transverse momenta for central rapidity.

7.1.8. Summary and outlook

The dominant experimental and theoretical uncertainties on the differential inclusive cross sections of jets with high transverse momentum ranging from 80 GeV up to 4000 GeV have been investigated. A variation of $\pm 3\%$ in the jet energy scale results in an uncertainty of the derived jet cross sections of 15% at low transverse momenta, increasing up to about 50% at the highest p_T for central rapidity. The theoretical uncertainty due to the parton density functions of the proton has been found to be of the same order of magnitude and rises from

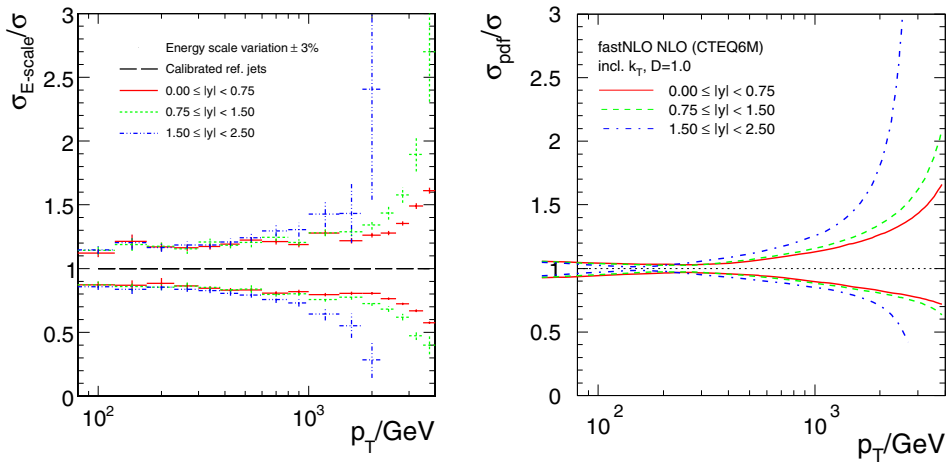

Figure 7.3. Relative systematic uncertainties of the jet cross sections for the k_{T} algorithm versus p_{T} due to a change in energy scale of $\pm 3\%$ for three bins in rapidity (left). The error bars represent the statistical uncertainty. On the right hand side, the relative uncertainties due to an evaluation of the error sets of the CTEQ6M [12] PDFs are shown for the same regions in rapidity.

about 5% for low transverse momenta with a minimum of 3% at $\approx 200\,\mathrm{GeV}$ up to $+65\%$ and -30% at the highest transverse momenta. For higher rapidities both uncertainties are considerably larger. The results shown have been derived with the k_{T} jet algorithm, similar values were obtained with the midpoint cone algorithm.

For transverse momenta below about 500 GeV further sources of uncertainties may give significant contributions to the total uncertainty, e.g. corrections due to pile-up, the underlying event and multiple interactions or hadronisation. Theoretical contributions due to scale variations are of the order of 5% (10% for transverse momenta larger than 3 GeV) for rapidities y below 1.5. Above a rapidity of 1.5 they might be larger especially at the edge of the phase space. In addition, contributions due to α_S and electroweak corrections have to be included before comparing to real data.

In the future, it will be possible to run simultaneous fits of α_S and the parton density functions, especially the gluon density at high x, to the data. To be less sensitive to the jet energy scale other jet related quantities, e.g. jet rates, will be considered. By including other processes into the fit procedure, like W/Z production as a luminosity measure or Drell–Yan reactions to fix the low x gluon density, powerful combined PDF fits to the data of one experiment will become possible.

7.2. Underlying event studies

7.2.1. Definition of the physics process and status of the art

The "Underlying Event" (UE) in a hard scattering process is everything accompanying an event but the hard scattering component of the collision. A CDF analysis [190, 191] showed that the density of particles in the UE of jet events is about a factor of two larger than the density of particles in a typical Minimum Bias (MB) collision. At the LHC the difference might be even larger.

Hard scattering collider events have a distinct topology and one can use the topological structure of the collision to define regions of the $\eta - \phi$ space that are sensitive to the UE components of the interaction. By comparing different processes such as high transverse momentum jets, "back-to-back" dijet production, or Drell–Yan, one can partially isolate the various components contributing to the UE.

Multiple parton interaction (MPI) models [192], extending the QCD perturbative picture to the soft regime, turn out to be particularly adequate to describe the physics of the UE. In the framework of these models one can regard the observed differences between the UE in a hard scattering process and a MB collision as the effect of the increased probability of partonic interactions for small impact parameter hadron-hadron collisions: one hard scattering implies a small impact parameter collision which makes it more likely that an additional parton-parton interaction will occur. Also, a hard scattering promotes initial and final state gluon radiation which inevitably contributes to the UE.

Examples of MPI models are implemented in the general purpose simulation programs PYTHIA [69], JIMMY [193], and SHERPA [194]. Other successful descriptions of UE and MB at hadron colliders are achieved by alternative approaches like PHOJET [195], which rely on both perturbative QCD and the Dual Parton Models (DPM). The purely phenomenological description available in HERWIG [196] provides a very useful reference of a model not implementing multiple interactions.

The QCD models considered in this study are different settings, called tunes, of relevant parameters in HERWIG and PYTHIA 6.2. One of the PYTHIA tunes is the ATLAS tune [197] and the other (PY Tunes DW) is a tune by R. Field which is similar to PYTHIA Tune A [198]. All these tunes use the CTEQ5L parton distribution functions. Details of the settings are given in reference [199].

Both Tune A and Tune DW fit the CDF Run 1 and Run 2 UE data [190, 191]. Tune DW also fits the CDF Run 1 Z-boson transverse momentum distribution [200]. Both Tune A and Tune DW use the same multiple parton interaction energy dependence parameter PARP(90) $= 0.25$, while the ATLAS tune uses the default value of 0.16.

The analyses summarised in this section are described in detail in reference [199].

7.2.2. Underlying event observables discussed for charged jet events

Charged jets are constructed from the charged particles using a simple clustering algorithm and then the direction of the leading charged particle jet is used to isolate regions of $\eta - \phi$ space that are sensitive to the UE. As illustrated in Fig. 7.4, the direction of the leading charged particle jet, chgjet1, is used to define correlations in the azimuthal angle, $\Delta\phi$. The angle $\Delta\phi = \phi - \phi_{\text{chgjet1}}$ is the relative azimuthal angle between a charged particle and the direction of chgjet1. The "transverse" region is almost perpendicular to the plane of the hard 2-to-2 scattering and is therefore very sensitive to the UE. We restrict ourselves to charged particles in the central region $|\eta| < 1$ and consider two p_{T} thresholds, the nominal CMS cut $p_{\mathrm{T}} > 0.9\,\mathrm{GeV/c}$ and a lower threshold with $p_{\mathrm{T}} > 0.5\,\mathrm{GeV/c}$.

Figure 7.5 shows the QCD Monte Carlo models predictions for the average density of charged particles, $dN_{chg}/d\eta d\phi$, and the average charged PT_{sum} density, $dPT_{sum}/d\eta d\phi$, respectively, in the "transverse" region for $|\eta| < 1$ with $p_{\mathrm{T}} > 0.5\,\mathrm{GeV/c}$ and $p_{\mathrm{T}} > 0.9\,\mathrm{GeV/c}$ versus the transverse momentum of the leading charged particle jet. The charged particle density is constructed by dividing the average number of charged particles per event by the area in $\eta - \phi$ space (in this case $4\pi/3$). The charged PT_{sum} density is the average *scalar* p_{T} sum of charged particles per event divided by the area in $\eta - \phi$ space.

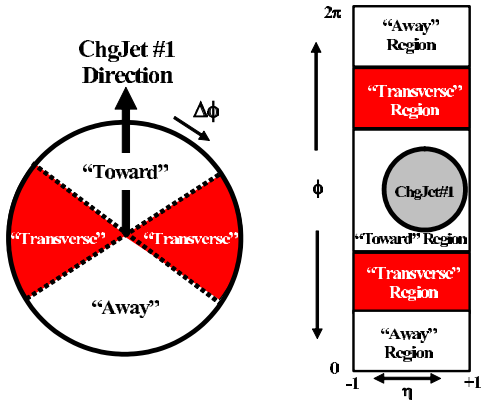

Figure 7.4. Illustration of correlations in azimuthal angle ϕ relative to the direction of the leading charged particle jet ($R = 0.7$) in the event, chgjet1. The angle $\Delta\phi = \phi - \phi_{\rm chgjet1}$ is the relative azimuthal angle between charged particles and the direction of chgjet1. The "transverse" region is defined by $60^\circ < |\Delta\phi| < 120^\circ$ and $|\eta| < 1$. We examine charged particles in the range $|\eta| < 1$ with $p_{\rm T} > 0.5\,{\rm GeV/c}$ or $p_{\rm T} > 0.9\,{\rm GeV/c}$.

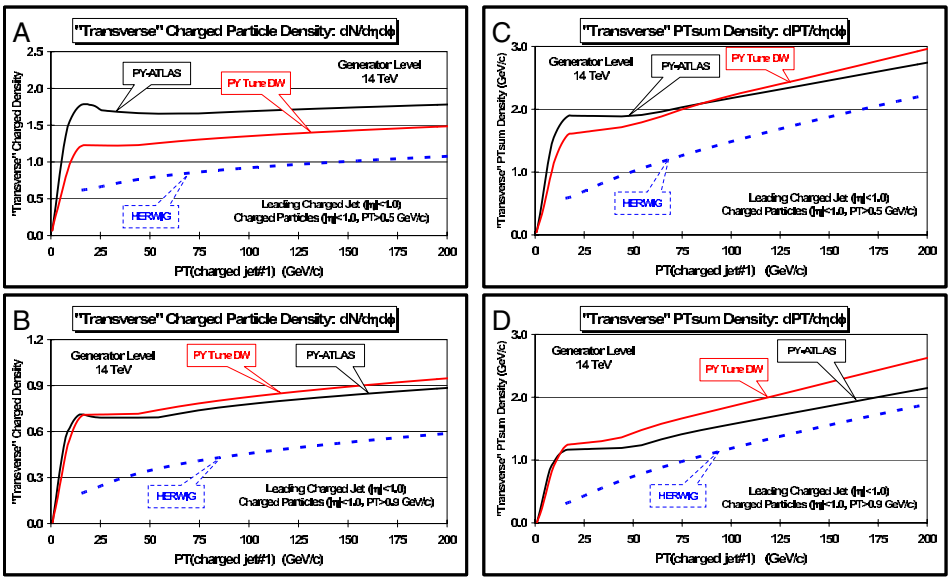

Figure 7.5. QCD Monte Carlo models predictions for charged particle jet production at 14 TeV. Left: Average density of charged particles, $dN_{chg}/d\eta d\phi$, with $|\eta| < 1$ in the "transverse" region versus the transverse momentum of the leading charged particle jet for $p_{\rm T} > 0.5\,{\rm GeV/c}$ (A) and $p_{\rm T} > 0.9\,{\rm GeV/c}$ (B). Right: Average charged PT_{sum} density, $dPT_{sum}/d\eta d\phi$, with $|\eta| < 1$ in the "transverse" region versus the transverse momentum of the leading charged particle jet for $p_{\rm T} > 0.5\,{\rm GeV/c}$ (C) and $p_{\rm T} > 0.9\,{\rm GeV/c}$ (D). The QCD models are HERWIG and two PYTHIA6.2 tunes described in the text.

Due to the multiple parton interactions the PYTHIA tunes rise rapidly and then reach an approximately flat "plateau" region. At very high P_T (chgjet1) they begin to rise again due to initial and final state radiation which increases as the Q^2 scale of the hard scattering increases. HERWIG has considerably fewer particles in the "transverse" region and predicts a steady rise resulting from initial and final state radiation. The ATLAS tune predicts a larger charged particle density than PYTHIA Tune DW for $p_T > 0.5\,\mathrm{GeV/c}$. However, the ATLAS tune and Tune DW have similar charged particle densities for $p_T > 0.9\,\mathrm{GeV/c}$. This is because the ATLAS tune has a "softer" charged particle p_T distribution than Tune DW.

7.2.3. Feasibility studies

Here we concentrate on the UE measurement that will be performed in nominal CMS conditions at low luminosity [199]. All the studies presented in this section have been obtained applying the GEANT-4 based simulation and reconstruction chain of the CMS experiment.

Events corresponding to Drell–Yan dimuon pairs and leading QCD processes with superimposed low luminosity pile-up have been generated with PYTHIA 6.2 in different $\hat{p}_T$ regions. The relevant PYTHIA 6.2 parameters adopted by CMS in simulation production are documented in [201]. The triggers used to collect Jet and Drell–Yan samples are described in reference [76].

Charged track reconstruction uses the Combinatorial Track Finder [202]. The default algorithm allows to reconstruct tracks with p_T above 0.9 GeV/c. However, the same algorithm can be used in special conditions (with reduced thresholds for the seeds) achieving reasonable performances down to 0.5 GeV/c [199]. For $\eta| < 1$, a reconstruction efficiency better than 90% and a fake rate below 1% are quoted for charged tracks with p_T above 0.7 GeV/c.

7.2.3.1. The underlying event as observed in charged jet events. The track-based measurement for the scale of the leading interaction allows to keep an acceptable resolution for jet energies below 20 GeV, where the calorimetric measurement is dominated by large systematic uncertainties.

In principle MB could be studied from any data selection, getting rid of the leading pp interaction and performing the reconstruction of all the primary vertices from all the other piled-up pp interactions. However, this methodology turns out to be challenging as the resolution on the position of the pp vertices degrades when lowering the total p_T of the associated charged tracks. In this study an MB trigger is defined requiring at least a calorimetric jet of $p_T > 20\,\mathrm{GeV/c}$. In order to combine the measurements performed at different leading charged jet scales, on top of the MB trigger, two additional triggers based on the p_T of the leading high level trigger jet are adopted: $p_T > 60\,\mathrm{GeV/c}$ and $p_T > 120\,\mathrm{GeV/c}$, which will be referred to as JET60 and JET120. Jets are reconstructed with an iterative cone algorithm of radius 0.5 in the pseudorapidity-azimuth space.

Tracks arising from the piled-up interactions are suppressed requiring the extrapolated coordinate along the beam axis to be inside 1 mm with respect to the primary vertex associated to the leading charged jet. The selection of the pp interaction with the highest p_T charged jet tends to create a small bias on the MB sample, reducing the statistics available at very low P_T (chgjet1).

The definition of the main UE observables have been introduced in Section 7.2.2. The density of charged particles, $dN_{chg}/d\eta d\phi$, and the charged PT_{sum} density, $dPT_{sum}/d\eta d\phi$, with $p_T > 0.9\,\mathrm{GeV/c}$ and $|\eta| < 1$ in the "transverse" region are reported in Fig. 7.6. Bins of $2\,\mathrm{GeV/c}$ are used up to P_T (chgjet1) $= 20\,\mathrm{GeV/c}$ and bins of $10\,\mathrm{GeV/c}$ above.

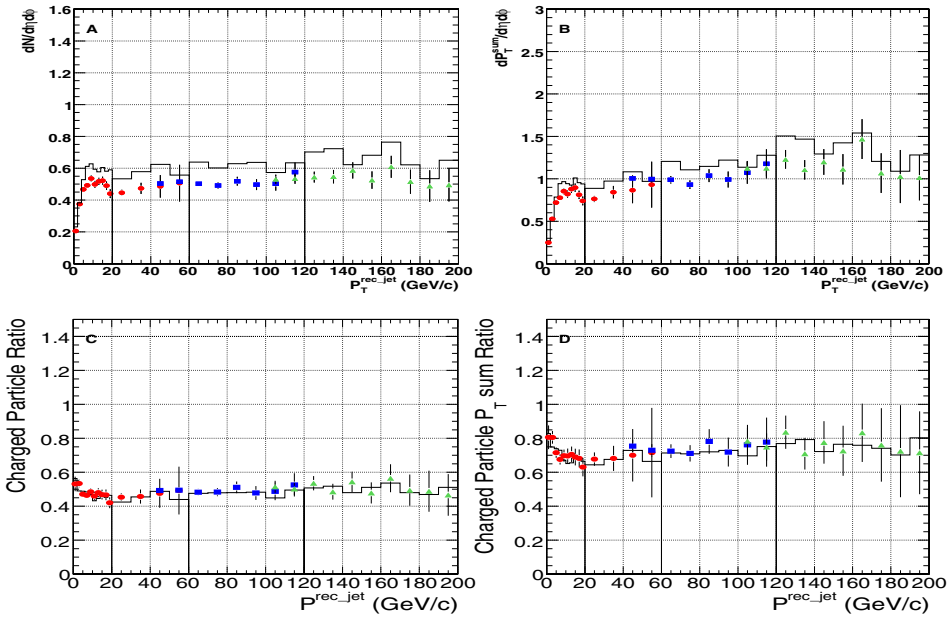

Figure 7.6. Charged jet production at 14 TeV. Charged tracks with $|\eta| < 1$ in the "transverse" region. Density of charged particles, $dN_{chg}/d\eta d\phi(A)$ and PT_{sum} density, $dPT_{sum}/d\eta d\phi(B)$, with $p_{\mathrm{T}} > 0.9\,\mathrm{GeV/c}$ versus the transverse momentum of the leading charged particle jet. Ratio between density of charged particles with $p_{\mathrm{T}} > 0.9\,\mathrm{GeV/c}$ and $p_{\mathrm{T}} > 0.5\,\mathrm{GeV/c}(C)$ and ratio between PT_{sum} density with $p_{\mathrm{T}} > 0.9\,\mathrm{GeV/c}$ and $p_{\mathrm{T}} > 0.5\,\mathrm{GeV/c}(D)$ versus the transverse momentum of the leading charged particle jet. Data from different triggers are superimposed: (circles) = MinimumBias; (squares) = JET60; (triangles) = JET120. The lines show the generator level distributions; the points with error bars correspond to the raw (uncorrected) reconstruction level distributions.

The shapes of uncorrected reconstruction level distributions basically agree with the corresponding generator level ones. The difference in absolute scale (about -20% for both $dN_{chg}/d\eta d\phi$ and $dPT_{sum}/d\eta d\phi$) turns out to be compatible with charged track inefficiencies and fake rates. Further details on these systematic effects, including the calibration and resolution of the leading charged jet have been studied in [199].

Figure 7.6 shows also the ratio between the observables for $p_{\mathrm{T}} > 0.9\,\mathrm{GeV/c}$ and $p_{\mathrm{T}} > 0.5\,\mathrm{GeV/c}$ in the "transverse" region. These ratios, which are sensitive to the differences between the models and/or to the choice of the tuning for a given model, are also nicely free from the systematic effects enumerated above, and basically do not need to be corrected when comparing to the corresponding generator level observables.

7.2.3.2. The underlying event as observed in Drell–Yan muon-pair production. Drell–Yan muon pair production provides an excellent way to study the UE. Here one studies the outgoing charged particles (excluding the $\mu^+\mu^-$ pair) as a function of the muon-pair invariant mass. After removing the muon-pair everything else is the UE. As for the charged jet production, we restrict ourselves to charged particles in the central region $|\eta| < 1$ and consider the two p_{T} thresholds $p_{\mathrm{T}} > 0.5\,\mathrm{GeV/c}$ and $p_{\mathrm{T}} > 0.9\,\mathrm{GeV/c}$.

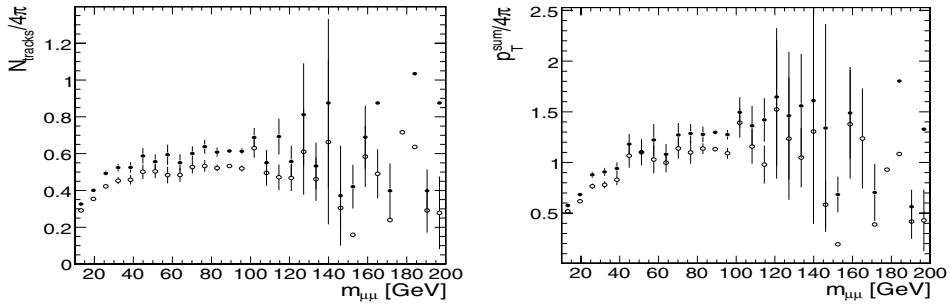

Figure 7.7. Muon-pair production at 14 TeV with two isolated muons. Density of charged particles, $dN_{chg}/d\eta d\phi(left)$, PT_{sum} density, $dPT_{sum}/d\eta d\phi(right)$, with $p_T > 0.9\,\mathrm{GeV/c}$ and $|\eta| < 1$ versus the muon-pair invariant mass. (fullcircles) correspond to the generator level distributions; (empty circles) correspond to the raw (uncorrected) reconstruction level distributions.

Single muon and muon-pair CMS triggers ensure very high efficiencies for the studied process. The relative mass shift and the corresponding resolution of the reconstructed muon-pair are studied in detail in Ref. [199]. Tracks arising from the piled-up interactions are suppressed requiring the extrapolated coordinate along the beam axis to be inside 1 mm with respect to the primary vertex associated to the leading muons.

In our study, we require "isolated muons", not to have charged tracks with $p_T > 0.9\,\mathrm{GeV/c}$ in a cone of radius $R = \sqrt{(\Delta\phi)^2 + (\Delta\eta)^2} = 0.3$ in the azimuth-pseudorapidity space centred along the direction of the muon. Selecting isolated muons turns out to be essential to reduce the QCD background to negligible levels for $p_T > 15\,\mathrm{GeV/c}$, while keeping an efficiency of 76.9% for Drell–Yan muon-pairs in the same p_T region.

The charge particle density, $dN_{chg}/d\eta d\phi$, and the charged PT_{sum} density, $dPT_{sum}/d\eta d\phi$ with $p_T > 0.9\,\mathrm{GeV/c}$ and $|\eta| < 1$ in muon-pair production with isolated muons versus the muon-pair invariant mass are shown in Fig. 7.7. Correlations between isolation and UE activity have been studied in Refs. [64, 199].

7.2.4. Conclusions

Predictions on the amount of activity in UE at the LHC based on extrapolations from the lower energy data differ greatly. In this study we have demonstrated the feasibility of reference UE measurements at CMS under nominal conditions, assessing our capability to distinguish between the predictions of different models. The UE is studied by examining charged particles in the "transverse" region in charged particle jet production and in the central region of Drell–Yan muon-pair production (after removing the muon-pair).

7.3. Physics of b-quarks and hadrons

7.3.1. Inclusive b-quark production

7.3.1.1. Introduction. At the LHC new opportunities to improve our understanding of the physics of b quarks will become available because of the high statistics data samples and the high centre-of-mass energy. A study [203] has been performed to investigate methods in CMS of identifying b jets (b "tagging") in an inclusive sample of events containing jets and at

least one muon. Here we present the capability to measure the inclusive b quark production cross section as a function of the B-hadron transverse momentum and pseudorapidity. An important result of our study is an estimate for the B-hadron p_T range reachable at LHC.

Inclusive b-quark production has been studied at other proton and electron colliders. The observed shapes of distributions and correlations are reasonably well explained by perturbative QCD. However, the observed cross-sections at the Tevatron (Run I) are larger than QCD predictions [204–211] which is confirmed by Run II data. Similar effects are observed in γp collisions at HERA [212–218] and in $\gamma\gamma$ interactions at LEP [219, 220].

The agreement between experiment and theory has improved due to more precise parton density functions and proper estimates of fragmentation effects [221–226]. But the agreement is not complete and the improvement of the phenomenological description is required using also experimental input.

7.3.1.2. Analysis. This study of the CMS capability to measure the inclusive b production is based on full detector simulation. The generated events are passed through the GEANT4 simulation of CMS. Pile-up corresponding to low-luminosity LHC running conditions ($\mathcal{L} = 2 \times 10^{33}\,\mathrm{cm}^{-2}\,\mathrm{s}^{-1}$) is also generated.

7.3.1.2.1 Event selection. About 4 million signal and background events were processed, mainly with high transverse momentum of the partons ($p_T > 50\,\mathrm{GeV/c}$). Samples of QCD jets were used. Jets in those samples cover the full geometrical acceptance in pseudorapidity of the tracking detector, $|\eta| < 2.4$. The measurement of the differential cross sections is studied for B-hadrons of $p_T > 50\,\mathrm{GeV/c}$ and within the fiducial volume of $|\eta| < 2.4$. First, the events are required to pass the Level-1 (L1) trigger selection for the single muon trigger stream which accepts events with muons having $p_T > 14\,\mathrm{GeV/c}$. The most energetic B-hadron inside the phase space defined above is selected. The trigger efficiency is flat as a function of the B-hadron pseudorapidity within the Level-1 trigger acceptance of $|\eta| < 2.1$. It increases with transverse momentum of the B-particle. The average Level-1 trigger efficiency corresponds to the expected value of the branching fractions for the semi-leptonic b quark and c quark decays, about 19% [54]. At Level-1, the single muon trigger is used. At the High Level Trigger (HLT) we require the "muon + b-jet" trigger, fired by non-isolated muons with $p_T > 19\,\mathrm{GeV/c}$ and by jets with $E_T > 50\,\mathrm{GeV/c}$, $|\eta| < 2.4$ and compatible with b tagging.

The event selection requires a b-tagged jet in the fiducial volume to be present in the event. B tagging is based on inclusive secondary vertex reconstruction in jets [157]. The tagging algorithms combine several topological and kinematic secondary vertex related variables into a single tagging variable to discriminate between jets originating from b quarks and those from light quarks and gluons.

To measure differential cross sections for inclusive B-particle production as a function of its transverse momentum p_T and pseudorapidity η, $d\sigma/dp_T$ and $d\sigma/d|\eta|$, we select as the reconstructed B-particle candidate the most energetic b tagged jet. Good correspondence between the generated B-particle and the reconstructed b-tagged jet is observed. The corresponding p_T and pseudorapidity relative resolutions are shown in Fig. 7.8 for B-particles with $p_T > 170\,\mathrm{GeV/c}$. The resolutions are 13% and 6% for p_T and pseudorapidity, respectively.

The efficiency of the b tagging by secondary vertices in jets is shown in Fig. 7.9 as function of the B-particle transverse momentum and pseudorapidity. The b tagging efficiency is defined with respect to events passing the Level-1 trigger and with a single muon of $p_T > 19\,\mathrm{GeV/c}$ selected. The efficiency decreases with increasing transverse momentum, while being rather flat as function of pseudorapidity. The slow degradation for larger

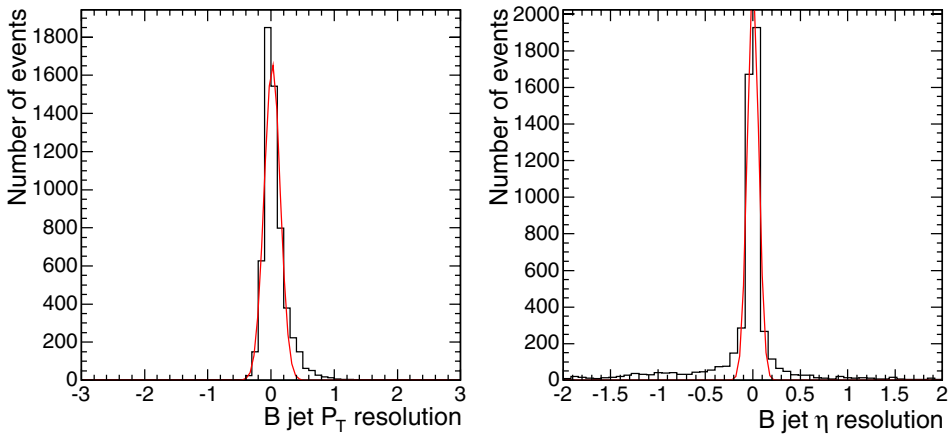

Figure 7.8. Relative resolution, (Reconstructed − True)/True, for p_T and pseudorapidity of b tagged jets in CMS.

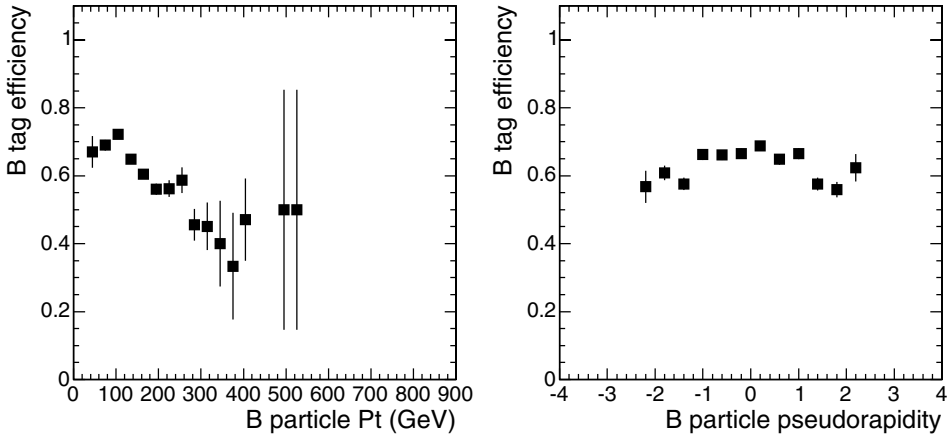

Figure 7.9. The b tagging efficiency versus p_T and pseudorapidity of the generated B-particle.

transverse momenta is caused by the worsening of the tracking resolution with increasing p_T, an increased track multiplicity from fragmentation and more difficult pattern recognition in dense jets. The average b tagging efficiency is 65% in the barrel region, while the efficiency is about 10 % less for the endcap region. The muon plus b-jet cross-channel trigger has a 4.3 Hz rate for the signal and a 6.1 Hz total event rate [203]. This trigger rate corresponds to a low-luminosity LHC run at $\mathcal{L} = 2 \times 10^{33}\,\mathrm{cm}^{-2}\,\mathrm{s}^{-1}$.

To measure the cross section one needs to know the number of selected events, the integrated luminosity, the event sample purity (signal fraction) and the signal efficiency. The signal fraction can be determined from the simulated prediction of the background contribution to the selected event sample. In order to rely less on the absolute prediction for the background one can extract the signal fraction using the prediction of the signal and background shapes for some sensitive variables. A fit to the data distribution using the

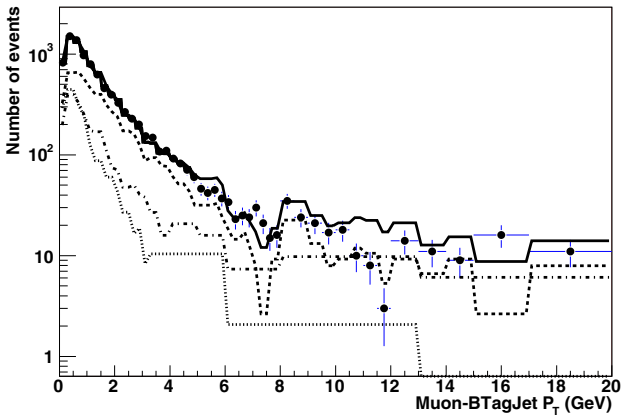

Figure 7.10. Fit of the muon p_T spectrum with respect to the closest b tagged jet. The sample of generated QCD events with "p_T-hat" parameter in the range $230 < \hat{p_T} < 300\,\mathrm{GeV/c}$ is tested. The contributions of tagged muons from b events (dashed curve), c events (dot-dashed curve) and light quark events (dotted curve) as defined by the fit are shown. The solid curve is the sum of the three contributions.

simulated shapes for the signal and background is performed. To do so we apply a lepton tag by selecting inclusive muons.

7.3.1.2.2 Muon tag. Muons are reconstructed in the muon chambers, matched to the inner tracker information and refitted using both subdetectors information. This provides the most precise muon track measurement. Each reconstructed muon is associated to the most energetic b tagged jet. The muon must be closer to this b tagged jet than to any other jet in the event. Otherwise the event is discarded.

In most cases the tagged muon is inside the b jet. The average efficiency of associating the muon with the b tagged jet is 75%.

7.3.1.2.3 Results. We calculate the transverse momentum of the muon with respect to the b-jet axis which effectively discriminates between b events and background. The slopes of the p_T spectra are very different and this is exploited in the fit of the selected events to determine the fractions of the muon sources in the sample.

Figure 7.10 shows an example of the fit of the distribution of the muon p_T with respect to the closest jet, using the expected shapes for the muons from b events, charm events and light quark events. The normalisation of the three contributions are free parameters in the fit. The events in this plot are from a sample of QCD events generated with the PYTHIA "p_T-" parameter in the range $230 < \hat{p_T} < 300\,\mathrm{GeV/c}$. In the fit, the shapes of the distributions were fixed using an independent QCD sample generated with $170 < \hat{p_T} < 230\,\mathrm{GeV/c}$. The fit results as well as the Monte Carlo input are quoted in Table 7.1. The event fractions are well reproduced within statistical errors. In the actual experiment the shapes will be verified using data at different selection stages. Also the background shape will be derived from the data itself by applying an anti-tag selection (b-suppressed event sample).

In Table 7.2 the b purity, $c\bar{c}$ and light quark event fractions for the different QCD samples are shown. The b purity decreases from about 70% down to 55% from low p_T events to the high transverse momentum events. The expected number of $b\bar{b}$ events after event selection is quoted for $10\,\mathrm{fb}^{-1}$ of integrated luminosity. For the phase space of $p_T > 50\,\mathrm{GeV/c}$ and $|\eta| < 2.4$ the event selection will allow for a b event statistics of about 16 million events. We

Table 7.1. Results of the fit to the distribution of the transverse momentum of the muon with respect to the nearest b tagged jet. The number of beauty, charm and light quark events in the Monte Carlo input are compared to the fit result.

	MC input, $230 < \hat{p_T} < 300\,\mathrm{GeV/c}$	Fit result
$N_{b\bar{b}}$	5250	5222 ± 501
$N_{c\bar{c}}$	2388	2050 ± 728
N_{uds}	1740	1778 ± 341

Table 7.2. B purity and expected number of events after final event selection. The expected number of $b\bar{b}$ events is quoted for $10\,\mathrm{fb}^{-1}$ of integrated luminosity.

$\hat{p}_T$ GeVc	$N^{QCD}_{generated}$	$b\bar{b}$ purity, %	$c\bar{c}$ fraction, %	uds fraction, %	$N^{b\bar{b}}_{expected}$
50–80	198993	66	32	2	1.4 M
80–120	294986	66	32	2	6.1 M
120–170	291982	72	26	2	5.1 M
170–230	355978	71	26	3	2.4 M
230–300	389978	73	24	3	0.9 M
300–380	283983	70	25	5	0.3 M
380–470	191989	68	27	5	88 k
470–600	190987	64	29	7	34 k
600–800	94996	60	31	9	10 k
800–1000	89999	60	30	10	2.0 k
1000–1400	89998	55	31	14	0.5 k

conclude that for B-hadrons a p_T range up to 1.5 TeV/c will be accessible with the CMS detector at the LHC.

The background contribution from $t\bar{t}$ events has been estimated from a sample of one million simulated events including all decay modes. The total number of $t\bar{t}$ events passing the selection amounts to 104 thousand events for $10\,\mathrm{fb}^{-1}$ of integrated luminosity, corresponding on average to a less than 1% background contribution. The $t\bar{t}$ background becomes more pronounced for the high p_T part of the inclusive B spectrum. In the region $p_T > 500\,\mathrm{GeV/c}$ it amounts to 2.4%.

The total event selection efficiency is about 5%. By correcting for the semi-leptonic branching ratio of b quarks and c quarks it amounts to about 25% on average. It turns out that the total efficiency is almost independent of transverse momentum and angle of the B-particle. Therefore the measurement of the differential cross section is less affected by systematic uncertainties due to bin-by-bin efficiency corrections.

7.3.1.2.4 Systematics Uncertainties. Several potential sources for systematic uncertainties are considered and their impact on the observed cross section is detailed in Table 7.3. The largest uncertainty arises from the 3% error on the jet energy scale (see Appendix B) which leads to a cross section error of 12% at $E_T > 50\,\mathrm{GeV/c}$. Other important uncertainties arise from the event-selection procedure and the Monte Carlo modelling of the detector response, including the lepton identification and the detector resolution on the energy and angular variables which identify the fiducial volume. The effect of these systematic uncertainties is estimated by varying the corresponding cuts and repeating the fits for the newly selected event samples. It results in an uncertainty of 6%. The expected b-tag systematics for $10\mathrm{fb}^{-1}$ integrated luminosity is 5% [7]. The luminosity uncertainty is also 5% [7].

Table 7.3. Sources of systematic uncertainty in % on the inclusive b production cross section measurement. The total systematic uncertainty is calculated by adding all contributions in quadrature.

Source	uncertainty, %
jet energy scale	12
event selection	6
B tagging	5
luminosity	5
trigger	3
muon Br	2.6
misalignment	2
muon efficiency	1
$t\bar{t}$ background	0.7
fragmentation	9
total	18

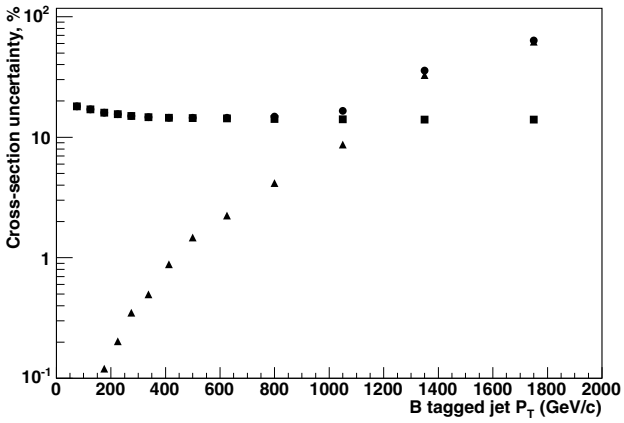

Figure 7.11. The statistical uncertainty for the cross section measurement (triangles), systematic (squares) uncertainty and total (dots) uncertainty as function of the b tagged jet transverse momentum with respect to the beam line. Total uncertainty comprises the statistical and systematic uncertainties added in quadrature.

The trigger efficiency will be determined from the data themselves. We estimate its uncertainty from Monte Carlo studies to be 3.0%. The experimental uncertainties on the semi-leptonic branching ratio of b quarks [54] is also propagated to the measurement. The impact of the detector misalignment on the CMS b tagging performance has been investigated in [157]. The effect has been found to be small (2%). The muon detection efficiency can be determined with better than 1% precision [7]. The $t\bar{t}$ background subtraction uncertainty is conservatively taken as absolute value of the expected $t\bar{t}$ contribution to the considered phase space.

A large contribution is expected from the fragmentation modelling. We estimate the magnitude of the effect from the DØ b-jet production measurement at Tevatron [211]. This uncertainty propagates to the cross section as a 9% effect independent of jet E_{T}.

The estimated statistical, systematic and total uncertainty as function of the b tagged jet transverse momentum with respect to the beam line is shown in Fig. 7.11.

7.3.1.3. Conclusion. The event selection for inclusive b production measurement at CMS will allow to study b production mechanisms on an event sample of 16 million b events for 10 fb^{-1} of integrated luminosity. The b purity of the selected events varies as function of the transverse momentum in a range from 70% to 55%. Our estimate shows that with the CMS detector we can reach 1.5 TeV/c as the highest measured transverse momentum of B hadrons.

7.3.2. Study of B_c hadrons

7.3.2.1. Introduction. The B_c meson is the ground state of the $\overline{b}c$ system, which is doubly heavy flavoured. This unique character provides a window for studying heavy-quark dynamics that is very different from the one of quarkonium. The experimental study of B_c will help us to understand heavy quark dynamics and to test the spin symmetry derived in non-relativistic quantum chromodynamics (NRQCD) [227–236]. B_c mesons have been observed at the Fermilab Tevatron collider by the CDF collaboration through the decay channel $B_c \to J/\psi\ \ell\nu$ [237]. The mass and lifetime are measured to be [238] $\text{M}(B_c) = 6.40 \pm 0.39(stat) \pm 0.13(sys)$ GeV/c^2 and $\tau(B_c) = 0.46^{+0.18}_{-0.16} \pm 0.03(sys)$ps, in agreement with the non-relativistic potential model [239–241] and other approaches [242–244].

Because of the higher colliding energy, the production cross section at the LHC is about a factor of 16 [231] larger than at the Tevatron. As also the LHC luminosity will be higher, CMS has the potential to collect much more B_c mesons than the Tevatron experiments do. We propose to study the B_c meson through $B_c \to J/\psi\ \pi$, $J/\psi \to \mu^+\mu^-$. The goal is to measure the mass and lifetime, and to compare the results with theoretical predictions which do have large uncertainties at the moment. More details on the analysis can be found in reference [245].

7.3.2.2. Monte Carlo data samples. A large amount of Monte Carlo data were produced to study the feasibility for CMS to measure the B_c mass and lifetime with the first fb^{-1}. There are two dedicated B_c generators, one is called BICEPS, developed at ITP, Beijing, by Chang *et al.* [231, 236], and the other is developed at IHEP, Protvino, by Berezhnoy *et al.* [239, 240]. Both packages are based on perturbative QCD, and have been integrated into the SIMUB package [130]. PYTHIA [246] can also generate B_c events, but it takes much more CPU time than the dedicated ones. For comparison, the p_T distribution of B_c mesons, generated by PYTHIA, BICEPS and the Protvino package (named Gouz in the plot), are shown in Fig. 7.12. One can see that the Protvino package produces higher p_T, while PYTHIA agrees with BICEPS. In order to save CPU time, BICEPS is used to generate B_c events. During generation, only events were retained which contain within $|\eta| < 2$ a B_c with $p_T > 10$ GeV/c, together with a muon of $p_T > 4$ GeV/c within $|\eta| < 2.2$. After the kinematic cuts, the cross section multiplied by the branching ratio is 1.78 pb. 52,000 B_c events were produced, corresponding to 29.2 fb^{-1} of integrated luminosity.

Important background sources are J/ψ mesons from decays of other B hadrons and prompt J/ψ mesons. Because of their large cross sections also QCD jets, in particular $b\overline{b} \to \mu^+\mu^- X$, $c\overline{c} \to \mu^+\mu^- X$, as well as W + jets and Z + jets have to be considered.

B hadrons that decay into J/ψ were generated with PYTHIA6.228 with kinematic cuts similar to B_c production, and prompt J/ψ events were generated by PYTHIA6.324, where the colour-octet contribution is included.

The full CMS detector simulation and reconstruction was applied to the generated samples. The fast simulation package FAMOS was also used to produce the B_c events, B hadrons, prompt J/ψ and $c\overline{c} \to \mu^+\mu^- X$ (Table 7.4).

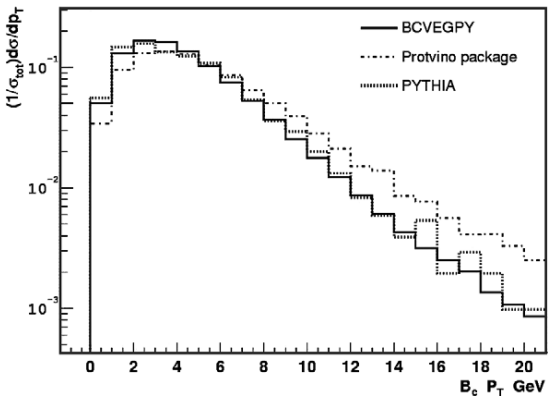

Figure 7.12. Comparison of p_T distributions of B_c mesons for the generator BICEPS, Gouz and PYTHIA.

Table 7.4. The cross section multiplied by the branching ratio after kinematic cuts and the number of events produced for B hadrons and prompt J/ψ and $c\bar{c} \to \mu^+\mu^- X$.

channel	$\sigma \cdot$ Br.(pb)	N events
B^0	70.3	740,000
B^+	70.7	740,000
B_s	14.8	190,000
Λ_b	19.4	200,000
prompt J/ψ	240.3	500,000
$c\bar{c} \to \mu^+\mu^-$ X	1690	210,000

Samples corresponding to $10\,\text{fb}^{-1}$ of B hadrons, $2\,\text{fb}^{-1}$ of prompt J/ψ and $0.12\,\text{fb}^{-1}$ of $c\bar{c} \to \mu^+\mu^-$ X events were produced for the analysis. Additional background samples of about 950,000 QCD, 880,000 W + jets, 710,000 Z + jets and 100,000 $b\bar{b} \to \mu^+\mu^- X$ events were used.

7.3.2.3. Selection. Signal events should have a b-jet, a c-jet and a B_c meson which decays into a J/ψ and a pion, with the subsequent $J/\psi \to \mu^+\mu^-$ decay. The selection starts from 2 muon tracks. The p_T of both muons should be larger than 4 GeV/c and the absolute value of η less than 2.2. The two muons should have different charge and share the same vertex. To form a J/ψ candidate the invariant mass of the muons should be in a window between 3.0 and $3.2\,\text{GeV/c}^2$. An additional track must be found at the same vertex of the J/ψ which is inconsistent with a muon or an electron. The p_T of it should be larger than 2 GeV/c and the absolute value of η less than 2.4.

The decay length L_{xy}, the proper decay length L_{xy}^{PDL} and the error of the decay length σ_{xy} are calculated from the J/ψ vertex and the primary vertex in the xy-plane. The resolution of the proper decay length is $25\,\mu$m. It is found that the resolution is almost independent of the proper decay length. In order to suppress the prompt backgrounds, the second vertex has to be displaced from the primary one. We require $L_{xy}/\sigma_{xy} > 2.5$ and $L_{xy}^{PDL} > 60\,\mu$m. In addition, the condition $\cos\theta_{sp} > 0.8$ is applied where θ_{sp} is the opening angle between the second vertex (pointing from the primary vertex) and the reconstructed B_c momentum. Finally, the reconstructed B_c candidate must be in a mass window between 6.25 and $6.55\,\text{GeV/c}^2$.

Table 7.5. Estimated number of signal and background events for 1 fb^{-1}.

B_c	B^+	B_s	B_0	prompt J/ψ	Λ_b	$c\bar{c}$	$b\bar{b}$	QCD
120 ± 11	0.7 ± 0.2	0.1	0.9 ± 0.3	0.1	0.1	0.01	0.01	0.7 ± 0.1

The number of B_c and background events for 1 fb^{-1} after the selection are listed in Table 7.5. The total number of background events was estimated to be 2.6 ± 0.4, mainly from B hadron decays into J/ψ. So far tagging of the b jet is not used in the analysis.

Because of the high cross section, the number of produced QCD Monte Carlo events is not sufficient to directly determine the QCD background which is therefore estimated in three steps [245]. At first the efficiency to select two muons is obtained directly from the QCD sample, then the efficiency to reconstruct two muons into a J/ψ candidate is calculated from the $c\bar{c} \to \mu^+\mu^- X$ sample, and finally the efficiency for the J/ψ candidate to fake a B_c meson is obtained from the prompt J/ψ sample. The probability of a QCD event to pass the selection cuts is then approximated as the product of the above three efficiencies. In this way, the total number of QCD background for 1 fb^{-1} is estimated to be 0.7 events.

This study which is aimed at the first fb^{-1} collected with the CMS detector assumes that in this initial phase the dimuon trigger threshold can be set at values such that the applied cut of $p_T > 4\,\mathrm{GeV/c}$ on both muons does not introduce a significant inefficiency at trigger level. In case the available trigger bandwidth will prohibit this, more sophisticated High Level Trigger algorithms like a J/ψ mass window could be invoked to restore the trigger efficiency. A detailed study is underway.

7.3.2.4. Mass and lifetime fitting. A kinematic fit was applied to the selected events imposing a J/ψ mass constraint and forcing the two muon tracks as well as the pion track to share the same vertex. After the kinematic fit the invariant mass of the J/ψ – pion system is shown in Fig. 7.13. A Gaussian fit provides a mean value of 6406 $\mathrm{MeV/c^2}$, close to the input of 6400 $\mathrm{MeV/c^2}$, and a mass resolution of 22 $\mathrm{MeV/c^2}$. The number of signal events in the plot for 1 fb^{-1} is 120. Backgrounds from B hadrons and prompt J/ψ are included in the plot, while other backgrounds are neglected here.

A binned likelihood fit was done on the proper decay length distribution of the selected B_c events with the likelihood defined as $L = \prod P(n_i, \mu_i)$. $P(n_i, \mu_i)$ denotes the Poisson distribution with n_i events observed and μ_i events predicted in the i-th bin:

$$\mu = N \cdot \epsilon(x) \cdot \exp(-x/c\tau) \otimes G(x, \sigma)$$

Here x represents the proper decay length, N and $c\tau$ are the parameters to be fitted and $G(x, \sigma)$ is a Gaussian smearing function with σ fixed to 25 μm which is the resolution of the proper decay length. The efficiency $\varepsilon(x)$ is obtained from the large B_c sample.

The result of the fit is $c\tau = 148.8 \pm 13.1\,\mu$m which is consistent with the used input value of 150 μm. The distribution of the proper decay length together with the fit result is shown in Fig. 7.13.

7.3.2.5. Systematic uncertainty. The influence of imperfect detector alignment which is of particular importance at the beginning of the CMS experiment on the track and vertex reconstruction has been studied in [99, 140]. It will affect the study of B_c in three ways: the momentum scale of muons and pions, the mass resolution and finally the vertex precision. Taking the scale uncertainty to be $\Delta(1/p_T) = 0.0005/\,\mathrm{GeV/c}$, the resulting uncertainties on the B_c mass is 11 $\mathrm{MeV/c^2}$ and 0.2 μm on $c\tau$.

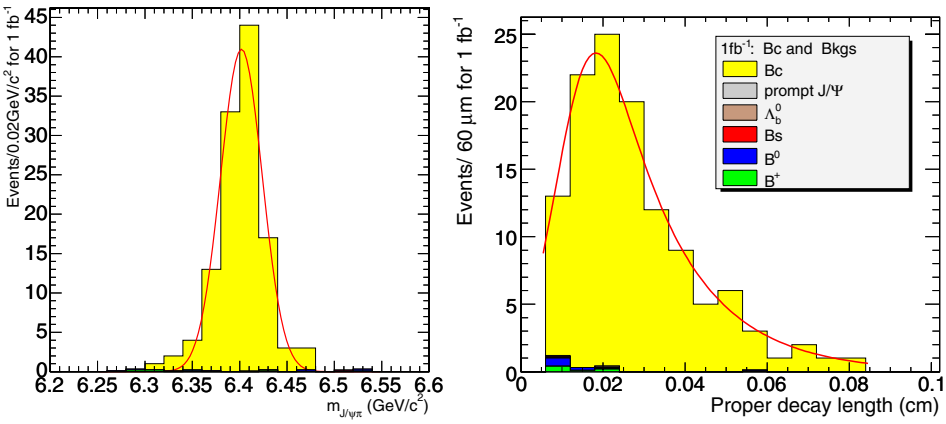

Figure 7.13. Left: The invariant mass of the J/ψ and pion candidate for the selected B_c. Right: The B_c proper decay length distribution. Both plots correspond to 1 fb^{-1}.

The effect of the muon momentum resolution was estimated following [99] and muon p_T-values of 10, 100 and 1000 GeV/c were studied for different η. The Δp_T to be smeared for a muon track from B_c was extrapolated from its p_T and η according to [99]. The resulting B_c mass uncertainty is 10 MeV/c^2, and 0.8 μm on $c\tau$. The error from the vertex uncertainty was determined according to 140 causing an uncertainty on $c\tau$ of 2.4 μm.

The uncertainty on the efficiency as function of the proper decay length origins from the limited Monte Carlo statistics. By subtracting $\sqrt{N}$ events from the sample ($N = 3600$ events), new efficiencies were calculated and the fit was repeated. The observed difference of 0.1 μm on $c\tau$ is taken as systematic uncertainty.

The theoretical uncertainty was estimated from Fig. 7.12 which shows the p_T distributions from different generator packages. The B_c events, generated by BICEPS, were reweighted to agree with the Gouz distribution and the analysis was repeated. The difference on $c\tau$ was found to be 1.5 μm which is taken as the error from this source.

To check the sensitivity on the cuts, the muon and pion p_T cuts were changed by one standard deviation of their resolution, about 1.5% depending on η. Other cuts like on $\cos\theta_{sp}$ and on the proper decay length were changed by 10%. The resulting mass uncertainty is 0.1 MeV/c^2 and 0.2 μm on $c\tau$.

In total the systematic uncertainties on the mass and on $c\tau$ are estimated to be 14.9 MeV/c^2 and 3.0 μm, respectively.

7.3.2.6. Conclusion. With the first fb^{-1} of data CMS is expected to measure the B_c mass with an uncertainty of $22.0(stat.) \pm 14.9(syst.)$ MeV/c^2 and $c\tau$ with $13.1(stat.) \pm 3.0(syst.)$ μm, corresponding to a lifetime uncertainty of $0.044(fit) \pm 0.010(syst.)$ps. About 120 $B_c^+ \to J/\psi\pi^+$, with $J/\psi \to \mu^+\mu^-$, events would be observed. At the moment, the theoretical calculation is at the leading order without the colour-octet contribution. Therefore, the uncertainties on the total cross section and the p_T distribution are large. In the real data analysis, $J/\psi+$ one track with $J/\psi \to \mu^+\mu^-$ will be selected as a control sample, $B^+ \to J/\psi K^+$ will be used to estimate the efficiency, and the side band of the J/ψ peak will be used to estimate the background to B_c.

7.4. Diffraction and forward physics

7.4.1. Introduction

This section outlines the diffractive and forward physics that CMS can do – together with the TOTEM experiment. The CMS and TOTEM detectors involved are presented in Chapter 7 of Volume 1 of the CMS Physics TDR [7].

The combined phase space coverage of the two experiments makes it possible to study many physics subjects in diffractive interactions – from QCD and the investigation of the low-x structure of the proton to the production of SM and MSSM Higgs bosons. Diffractive events are characterised by the fact that the incoming proton(s) emerge from the interaction intact, or excited into a low mass state, with only a small energy loss. Diffractive processes with proton energy losses up to a few per cent are dominated by the exchange of an object with vacuum quantum numbers, the so called Pomeron, now understood in terms of partons from the proton. For larger energy losses, mesonic exchanges – Reggeons and pions – become important. The topology of diffractive events is characterised by a gap in the rapidity distribution of final-state hadrons due to the lack of colour of the exchanged object.

Events with a fast proton in the final state can also originate from the exchange of a photon. In particular, forward tagging one leading proton allows the selection of photon-proton events with known photon energy; likewise, tagging two leading protons gives access to photon-photon interactions of well known centre-of-mass energy.

Triggering of diffractive/forward events is discussed in [247] and in Appendix E.3. More details on the work presented here can be found in [248].

7.4.2. The interest of diffractive interactions

The study of hard diffraction has been pioneered by the UA8 experiment at CERN [249]. There have been major advances in this field recently, largely driven by the study of diffraction at HERA and the Tevatron. The essential results are discussed in [250] and can be summarised as follows:

- Many aspects of hard diffractive processes are well understood in QCD: the presence of a hard scale allows the use of perturbative techniques and thus to formulate the dynamics in terms of quarks and gluons.
- A key to this success are factorisation theorems in electron-proton scattering, which render part of the dynamics accessible to calculation in perturbation theory. The remaining non-perturbative quantities are the so-called diffractive parton distribution functions (dPDFs) and generalised (or "skewed") parton distributions (GPDs). They can be extracted from measurements and contain specific information about small-x partons in the proton that can only be obtained in diffractive processes.
  Diffractive parton densities are determined from inclusive diffractive processes and can be interpreted as conditional probabilities to find a parton in the proton when the final state of the process contains a fast proton of given four-momentum. Generalised parton distributions can be accessed in exclusive diffractive processes; they quantify correlations between parton momenta in the proton. Their t-dependence is sensitive to the distribution of partons in the transverse plane.
- To describe hard diffractive hadron-hadron collisions is more challenging since factorisation is broken by rescattering between spectator partons. These soft re-interactions can produce additional final-state particles which fill the would-be rapidity gap. When such additional particles are produced, a very fast proton can no longer appear in the final state because of

energy conservation. The effect is often quantified in terms of the so called "gap survival probability". These rescattering effects are of interest in their own right because of their intimate relation with multiple scattering effects, which at LHC energies are expected to be crucial for understanding the structure of events in hard collisions.

The dynamics of rescattering and multi-gap events is still not completely understood. The available data can be described in terms of an effective, non-linear Pomeron trajectory [251]; its variation with energy would be a consequence of multi-Pomeron exchange effects [252]. Other models, also testable at the LHC have been proposed (see e.g. [253] and references therein). These topics can be pursued in more detail with the CMS-TOTEM data at the LHC.

- A fascinating link has emerged between diffraction and the physics of heavy-ion collisions through the concept of saturation, which offers a new window on QCD dynamics in the regime of high parton densities.
- Perhaps unexpectedly, the production of a SM or MSSM Higgs boson in diffractive pp collisions is drawing more and more attention as a clean channel to study the properties of a light Higgs boson or even to discover it. The central exclusive reaction, $pp \to pHp$, appears particularly promising.

7.4.3. A survey of the accessible diffractive/forward processes

The accessible physics is a function of the integrated luminosity. We assume standard LHC optics with $\beta^* = 0.5$ m unless stated otherwise. We recall that, in this case, the TOTEM Roman Pots (RP) at 220 m from the CMS interaction point have coverage for $0.02 < \xi < 0.2$, where ξ is the proton fractional momentum loss. Near-beam detectors at 420 m from the interaction point, currently also being considered [254], would cover $0.002 < \xi < 0.02$.

Low-luminosity ($\sim 10^{28}$–$10^{30}\,\mathrm{cm}^{-2}\,\mathrm{s}^{-1}$) studies could profit from running with $\beta^* > 0.5$ m, where the ξ coverage of the 220 m RPs would be wider and the t resolution would improve because of the lower transverse momentum spread of the beam.

7.4.3.1. Inclusive single diffraction and double Pomeron exchange at low luminosity. At modest instantaneous luminosities, up to $10^{32}\,\mathrm{cm}^{-2}\,\mathrm{s}^{-1}$, inclusive single diffractive (SD) events, $pp \to pX$, as well as inclusive double-Pomeron exchange (DPE) events, $pp \to pXp$, can be studied by requiring the presence of one or two rapidity gaps in the event. In the ξ range given above, the scattered proton can be detected and the kinematics of the events fully measured.

The inclusive SD and DPE cross sections, as well as their M_X dependence, even in the absence of a hard scale, are important quantities to measure at the LHC. Here M_X indicates the mass of the system X. These cross sections amount to approximately 15% and 1% of the total proton-proton cross section, respectively; their energy dependence is a fundamental parameter of (non-perturbative) QCD. In addition, since diffractive events constitute a major fraction of the pile-up events, their measurement is mandatory to be able to properly simulate and understand high-luminosity data, where, at instantaneous luminosities of $10^{34}\,\mathrm{cm}^{-2}\mathrm{s}^{-1}$, approximately 35 pile-up events are superimposed, on average, to any event.

7.4.3.2. SD and DPE production of dijets, vector bosons and heavy quarks. The study of SD and DPE events in which the diffractively excited state includes high-E_T jets, heavy quarks or vector bosons opens up the possibility of accessing dPDFs and GPDs. The comparison of the DPE and SD rates for these processes may also give information on the hard diffractive

factorisation breaking at LHC (see Section 7.4.2). A few examples of these processes are given here.

Production of dijets. The measurement of the reaction $pp \to pXjj$ (j indicates a jet) has been used for the first time by CDF to measure the diffractive structure function in antiproton-proton collisions [255]. A similar measurement is possible at LHC with wider kinematic coverage (CDF: $\xi > 0.035$) and larger minimum jet E_{T}. For $E_{\mathrm{T}} > 45\,\mathrm{GeV}$, of the order of 10^8 events per fb^{-1} can be expected.

Production of heavy quarks. Inclusive DPE production of $t\bar{t}$ pairs has been studied in the case in which the final state contains one muon and four jets (i.e. with one top quark decaying to b plus lepton and neutrino, and the other to three jets). The analysis required the detection of both final-state protons. The expected number of events is of order $1-100$ for $10\,\mathrm{fb}^{-1}$, depending on the theoretical model assumed.

SD and DPE production of B-mesons has also been looked at, with $B \to J/\psi X$ and $J/\psi \to \mu^+\mu^-$. Here the number of expected events is much larger, of the order of a few events per $10\,\mathrm{fb}^{-1}$ in the DPE case and thousands in the SD case.

Inclusive DPE production of W bosons. Inclusive DPE production of W bosons, $pp \to pXWp$, is also sensitive to the dPDFs of the proton and is a relatively abundant process that can be studied at instantaneous luminosities where pile-up is small. In these conditions, the requirement that two final state protons be measured in the 220 m RPs suppresses both the QCD background and the inclusive W production. Several thousand events with $W \to e\nu$ or $W \to \mu\nu$ are expected, after cuts, for an integrated luminosity of $1\,\mathrm{fb}^{-1}$. This process, in conjunction with SD production of W bosons, can be used to study hard diffractive factorisation breaking using the LHC data alone, as mentioned above.

7.4.3.3. SM and MSSM central exclusive Higgs production. As the delivered luminosity reaches tens of fb^{-1}, the central exclusive production process (DPE) becomes a tool to search for new physics, delivering signal to background ratios of order 0.1–1 for Standard Model (SM) Higgs production [256] and more than an order of magnitude larger for certain supersymmetric (MSSM) scenarios.

By central exclusive, we refer to the process $pp \to p\phi p$, where there are large rapidity gaps between the outgoing protons and the decay products of ϕ. There are three primary reasons why this process is attractive. Firstly, if the outgoing protons remain intact and scatter through small angles, then, under some general assumptions, the central system ϕ is produced in the $J_Z = 0$, C and P even state. Secondly, the mass of the central system can be determined very accurately from a measurement of the transverse and longitudinal momentum components of the outgoing protons alone. This means an accurate determination of the mass irrespective of the decay mode of the centrally produced particle. Thirdly, the process delivers excellent signal to background ratios, due to the combination of the $J_Z = 0$ selection rules, the mass resolution, and the simplicity of the event in the central detectors. An additional attractive property of central exclusive production is its sensitivity to CP violating effects in the couplings of the object ϕ to gluons.

The left panel of Fig. 7.14 shows the cross section times the branching ratio for central exclusive production of a Standard Model Higgs, with $H \to b\bar{b}$ and $H \to WW$, as a function of the Higgs mass for different theoretical approaches. The $b\bar{b}$ mode is particularly interesting for masses close to the current exclusion limit. The right panel of Fig. 7.14 shows the acceptance assuming various combinations of RPs at 220 m and near-beam detectors at 420 m. Both protons can be detected in the 220 m stations only for Higgs masses larger than $280\,\mathrm{GeV/c^2}$; this reflects the ξ range for which the 220 m RPs have acceptance,

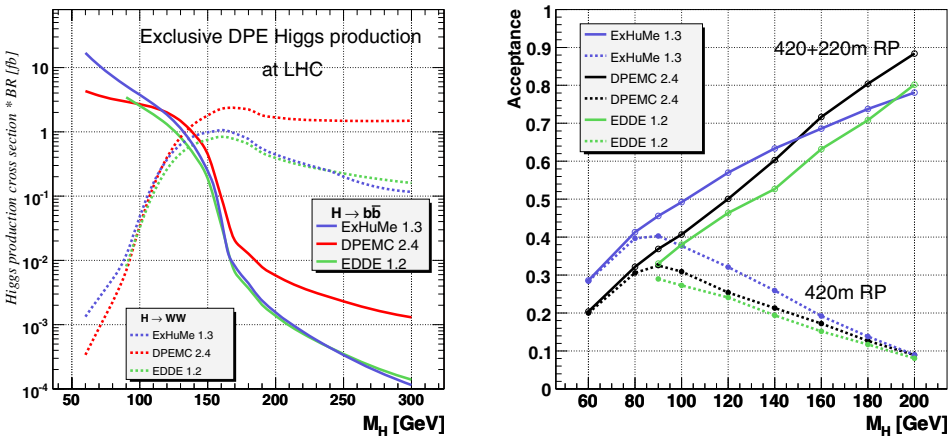

Figure 7.14. Left: The cross section for the exclusive production of the Higgs boson as a function of the Higgs boson mass for $H \to b\bar{b}$ and $H \to WW$. The different curves were obtained with the generators Exhume1.3 [259], DPEMC2.4 [260] and EDDE1.2 [261]. Right: Acceptance for the 420 m detectors alone and for the combination of the 220 m and 420 m detectors as a function of the Higgs boson mass.

$0.02 < \xi < 0.2$ (the mass of the centrally produced Higgs is related to the ξ via $M_H^2 = \xi_1 \xi_2 s$, with ξ_1, ξ_2 the fractional momentum losses of the two protons). However, asymmetric events with one proton at low ξ and another at large ξ can be detected by the combination of the 220 m and 420 m detectors ($0.002 < \xi < 0.02$).

Central exclusive production is generally an attractive way of searching for any new particles that couple strongly to glue. An example studied in [257] is the scenario in which the gluino is the lightest supersymmetric particle. In such models, there should exist a spectrum of gluino-gluino bound states which can be produced in the central exclusive channel. Likewise, central exclusive production of radions, the fields introduced in the Randall–Sundrum model of five-dimensional quantum gravity, has been studied [258].

***H* → *bb̄*.** The analysis is based on the requirement of two back-to-back central b-tagged jets in addition to the detection of both final-state protons yielding a mass of the central system consistent with that calculated from the protons alone. The event yield is very low, about 2–4 events per 30 fb^{-1} after all cuts, depending on the model. The non-resonant continuum b-jet background is largely suppressed by the $J_Z = 0$ rule. The residual background, mostly due to dijet production ($gg \to$ dijets) and diffractive $gg \to b\bar{b}$ production, is a function of the mass resolution, which is about 1.6% for the '420 + 420' combination and 5.6% for the '220 + 420' combination (for $M_H = 120\,\mathrm{GeV/c^2}$). The number of expected background events is of order 10 for 30 fb^{-1}.

***H* → *WW*.** In this case, the suppression of the background does not rely primarily on the mass resolution of the RPs. There are three main categories of WW events. Events in which at least one of the W bosons decays to an electron or a muon are the simplest, and pass the Level-1 trigger thanks to the high-p_T final-state lepton. This holds also if one of the W bosons decays into a tau, which subsequently decays leptonically. The four-jet mode occurs approximately half of the time; here, however, the RP information is necessary already at Level-1. The expected event yields range between 1 and 7 events for 30 fb^{-1}, depending on the mass. Irreducible backgrounds are small and controllable.

MSSM Higgs. Double proton tagging is especially beneficial in the MSSM case. The b-jet channel is very important in the 'intense coupling regime' of MSSM ($M_h \approx M_A \approx M_H \approx 100\,\mathrm{GeV/c^2}$) [262]: couplings of the Higgs to gg, WW^*, ZZ^* are strongly suppressed, making the discovery challenging by conventional means. Rates for central exclusive production of the two scalar (0^+) MSSM Higgs bosons (h, H) are more than a factor 10 larger than for the SM Higgs. The enhancement for $H \to b\bar{b}$ is by orders of magnitude in the M_h-max scenario for $M_H \approx 180$–$250\,\mathrm{GeV/c^2}$; likewise for $h \to b\bar{b}$ and $h \to \tau\tau$ for $M_h \approx 90$–$130\,\mathrm{GeV/c^2}$ [263]. In the small α_{eff} scenario, $h \to b\bar{b}$ and $h \to \tau\tau$ can be heavily suppressed for large $\tan\beta$ and for $M_h \approx 120\,\mathrm{GeV/c^2}$ [263], whereas $h \to WW$ may be enhanced by up to a factor 4 compared to the SM predictions. Also, the pseudo-scalar (0^-) Higgs boson (A) is practically not produced in the central exclusive channel, yielding a clean separation of the scalar and pseudo-scalar Higgs bosons, impossible in conventional channels. The good missing mass resolution allows to resolve h, H and, if enough statistics is available, measure their widths. This makes central exclusive production a possible discovery channel. Central exclusive production is also interesting in the '3-way mixing' scenario of CP-violating MSSM [264]: here the 3 neutral Higgs bosons are nearly degenerate, mix strongly and have masses close to $120\,\mathrm{GeV/c^2}$.

Central exclusive production, with its good mass resolution via the scattered protons, may allow disentangling the Higgs bosons by studying the production lineshape. Explicit CP-violation in the Higgs sector causes an asymmetry in the azimuthal distributions of tagged protons (via the interference of P-even and P-odd amplitudes) – a measurement unique at the LHC [262, 265].

7.4.3.4. High-energy photon interactions. A significant fraction of events at the LHC involves photon interactions at energies above the electroweak scale [266]. The protons radiating the photon often survive the collision intact and are scattered at angles comparable to the beam angular divergence. Detection of such events at the LHC will open up a new field of high-energy photon physics, which is briefly outlined below. By requiring the detection of one or two forward protons like in diffractive interactions, photon-photon and photon-proton interactions can be selected. The photon fluxes, and the effective luminosities of photon-photon and photon-proton collisions are well known [267, 268]. The average proton energy loss is larger and the proton scattering angle smaller in photon exchanges than for the diffractive case. This can be used to establish relative contributions of these two processes.

Two-photon exclusive production of W and Z boson pairs. The cross section for the production of W pairs via photon-photon interactions, $pp \to ppWW$, is slightly above 100 fb; in almost half of these events both forward protons are produced within the acceptance of the TOTEM RPs. About 100 events per $10\,\mathrm{fb^{-1}}$ with leptonic W decays can be detected in CMS. This allows a precise study of the gauge couplings, in particular of the $\gamma\gamma WW$ coupling. The expected sensitivity to anomalous quartic gauge couplings (QGCs) will surpass the LEP and Tevatron limits by orders of magnitude. A deviation from the Standard Model predictions would also allow a clean detection of anomalous WW production as predicted e.g. by A. White's theory of the supercritical Pomeron [269]. Two-photon production of Z pairs, $pp \to ppZZ$, is not allowed at the SM tree level, but yields similar sensitivities to the anomalous QGCs in this channel.

Two-photon exclusive production of pairs of SUSY particles. The cross sections for production of pairs of charginos, sleptons and charged Higgs bosons via photon-photon fusion at the LHC decrease rapidly with the masses of these particles [269]. This limits the

scope of SUSY searches to particle masses below 150–200 GeV/c^2. However, the very clean environment of this reaction makes it attractive compared to other production mechanisms; the final state typically consists of two opposite-sign leptons and of missing p_T. The main background is due to the exclusive production of W pairs discussed above.

Two-photon production of doubly charged Higgs bosons (appearing in GUTs) is strongly enhanced, and leads to exclusive final states with two pairs of same-sign leptons.

Two-photon lepton pair production. Exclusive production of lepton pairs – a purely QED process at low $|t|$ – may serve for calibration of the pp luminosity; it may also be used for calibration of the momentum measurement of the scattered proton. Thousands of exclusive muon pairs are expected to be reconstructed in CMS for an integrated luminosity of 1fb^{-1}. The striking signature of extremely small muon acoplanarity angles of less than about 10 mrad may be exploited already at the trigger level.

Single W and single top photoproduction. The cross section for single W photoproduction, $pp \to pWjX$, reaches almost 100 pb. This process can be therefore studied already at low luminosity. It also provides a means to study rescattering effects [268]. At higher luminosities, studies of high mass Wj states will be possible; for Wj invariant masses above 1 TeV, tens of events are expected to be detected in CMS (and tagged by TOTEM) per 10 fb^{-1}. This will allow to search for, as an example, an anomalous triple gauge coupling γWW. This process is the main background in the search for anomalous photoproduction of single top.

Associated WH and top pair photoproduction. The associated photoproduction of a SM Higgs boson and a W boson has a cross section of about 20 fb for Higgs mass below 180 GeV/c^2. About 50% of the forward protons are tagged by TOTEM, and events with leptonic W decay can be triggered efficiently in CMS. The cross section for photoproduction of top pairs is slightly above 1 pb. Top pair production is the main background for WH production, and in the photoproduction case the signal-to-background ratio for photoproduction of WH pairs is superior to the one in inclusive production.

7.4.3.5. Drell–Yan. The study of forward production of low mass Drell–Yan lepton pairs at the LHC provides a unique opportunity to directly access low-x partons in the proton. In this process, the lepton pair originates from the annihilation of a quark-anti-quark pair whose fractional momenta, x_1 and x_2, are related to the dilepton mass, M, and rapidity, y, through

$$M^2 = sx_1x_2; \qquad x_{1,2} = \frac{M}{\sqrt{s}} \exp^{\pm y}, \tag{7.2}$$

with $\sqrt{s} = 14$ TeV, the centre-of-mass energy of the colliding protons. In order to access low x, a large imbalance in fractional momenta is required, boosting the lepton pair to large rapidities.

The CASTOR calorimeter will cover the pseudorapidity range $5.3 < \eta < 6.6$, corresponding to Bjorken-x values down to 10^{-7}. With CASTOR alone, it may be possible to obtain a crude estimate of the dilepton mass. With the additional information provided by the T2 tracker, one can enhance the signal to background ratio by requiring tracks in association to the electromagnetic energy deposits. As T2 will measure both the azimuthal and polar angles of the tracks, a much more accurate measurement of the opening angle (and therefore of the dilepton mass) and a two-dimensional study in M^2 and x will become possible.

7.4.3.6. Validation of cosmic-ray generators. The correct simulation of the interaction of primary cosmic rays in the PeV energy range with the atmosphere is a key tool in the study of cosmic rays. Unfortunately, the available generators differ significantly in their predictions for the energy flow, multiplicity, hadronic energy fraction etc., in particular at high rapidities. These models can be tested at the LHC: a 100 PeV fixed-target collision in air corresponds to the centre-of-mass energy of a pp collision at the LHC. Several generators were used to simulate inelastic and diffractive collisions at CMS: QGSJET [271], SIBYLL [272], DPMJET [273], NEXUS [271]. There are significant differences in the predictions, notably in the region covered by CASTOR, T1 and T2. A measurement of these features with CASTOR, T1 and T2 may thus be used to validate/tune these generators.

7.5. Physics with heavy ions

7.5.1. High-density QCD: heavy-ion physics

Quantum Chromodynamics (QCD) is the only existing quantum field theory within the Standard Model, whose collective behaviour, phase diagram and phase transitions, are accessible to study in the laboratory. High-energy nucleus-nucleus collisions offer the only experimental means known so far to concentrate a significant amount of energy ($\mathcal{O}(10\,\text{TeV})$ at the LHC) in a "large" volume ($\mathcal{O}(100\,\text{fm}^3)$ at thermalisation times of $\tau_0 \approx 1\text{fm}/c$), allowing the study the many-body dynamics of strongly interacting matter. The programme of high-energy heavy-ion physics addresses several key open questions of the strong interaction:

- **Deconfinement and chiral symmetry restoration.** Lattice QCD calculations predict a new form of matter at energy densities above $\varepsilon \approx 1\,\text{GeV}/\text{fm}^3$ consisting of an extended volume of deconfined and bare-mass quarks and gluons: the Quark Gluon Plasma (QGP) [274]. The scrutiny of this new state of matter (equation-of-state, order of the phase transition, ...) promises to shed light on fundamental questions such as the nature of confinement, the mechanism of mass generation (chiral symmetry breaking, structure of the QCD vacuum) and hadronisation, that still evade a thorough theoretical description due to their highly non-perturbative nature.
- **Non-linear parton evolution at small-x.** At high energies, hadrons consist of a very dense system of gluons with small (Bjorken) parton fractional momenta $x = p_{parton}/p_{hadron}$. At low-$x$, the probability to emit an extra gluon is large $\sim \alpha_S \ln(1/x)$ and non-linear gluon-gluon fusion processes start to dominate the parton evolution in the hadronic wave functions. Whereas at values of $x \gtrsim 10^{-3}$, the parton evolution with Q^2 (or $\ln(1/x)$) is described by the usual DGLAP (or BFKL) equations, at lower values of x and around $Q_s^2 \sim 3\,GeV^2/c^2$, such a saturated configuration is theoretically described in terms of the "Colour Glass Condensate" (CGC) picture [275]. Since the nonlinear growth of the gluon density depends on the transverse size of the system, the effects of gluon saturation are expected to set in earlier (at higher x) for heavy nuclei than for free nucleons.

In addition, the study of heavy-ion collisions has interesting connections to other research areas such as:

- **Early Universe cosmology.** The quark-hadron phase transition took place some 10 μs after the Big-Bang and was the most important event taking place in the Universe between the electro-weak (or SUSY) transition ($\tau \sim 10^{-10}$ s) and Big Bang nucleosynthesis (BBN, at $\tau \sim 200$ s). Depending on the order of the QCD phase transition, several cosmological implications such as the formation of strangelets and cold dark-matter (WIMP) clumps or baryon fluctuations leading to inhomogeneous nucleosynthesis, have been postulated [276].

- **High-energy cosmic-ray physics.** The energy and mass of cosmic particles with energies above 10^{14} eV can only be measured via the ground-based detection of "extended air showers" (EAS) generated in upper-atmosphere interactions of cosmic rays (protons and ions up to Fe) with air (N,O nuclei). The interpretation of the EAS (and the related astro-particle phenomena) relies heavily on the accurate modelling of hadronic multi-particle production in proton-nucleus (p+N, p+O) and nucleus-nucleus (He+N, N+N, Fe+N) collisions in the TeV range. Direct measurements at LHC are needed in order to calibrate and tune the EAS models and correctly extrapolate their predictions to the highest cosmic-ray energies measured ($\sim 10^{20}$ eV).
- **Gauge/String duality.** Theoretical calculations based on the AdS/CFT correspondence permit to obtain results in strongly coupled ($g^2 N_c \gg 1$) gauge theories (QCD-like: SUSY $\mathcal{N} = 4$ Yang-Mills) in terms of a dual gravity theory. Recent applications of this formalism have allowed, for the first time, to compute finite temperature QCD transport coefficients (such as the ratio of the QGP viscosity over entropy density, η/s) experimentally accessible, from black hole thermodynamics calculations [277].

7.5.2. Hard probes of QCD matter at LHC

Nucleus-nucleus collisions at the LHC offer a unique opportunity for studying strongly interacting matter at values of energy and particle densities never reached before. The factor of 30 increase in energy between RHIC and the LHC ($\sqrt{s}_{NN} = 5.5$ TeV for PbPb) leads to copious production of hard QCD probes: high-p_{T} hadrons, jets, quarkonia, direct photons, etc., arising from parton-parton scatterings with large squared momentum transfer, Q^2. Such perturbative processes take place at time scales $\tau \approx 1/p_{\mathrm{T}} \lesssim 0.1$ fm/c, and involve primary partons with fractional momenta of order $x \sim 10^{-3}(10^{-5})$ at central (forward) rapidities. The produced hard probes are, thus, sensitive to initial-state modifications of the low-x parton distribution functions, as well as to final-state effects while propagating through the bulk matter formed in the collision.

The contribution of CMS to the heavy-ion physics programme at LHC is extremely competent based on a number of unique experimental capabilities including:

(i) Very large acceptance at midrapidity ($|\eta| < 2.5$, full ϕ) for layered detection of charged hadrons (with the best momentum resolution for charged tracks at LHC) and neutral hadrons as well as muons, electrons, and photons over a wide range of p_{T}.
(ii) The best mass resolution of any LHC detector for quarkonia (J/ψ, Υ) measurements leading to clean separation of the various states, improved signal over background, and large reconstructed yields.
(iii) Complete electromagnetic and hadronic calorimetry since day-1 for full jet triggering and reconstruction over $|\eta| < 3$ and $\Delta\phi = 2\pi$ with a large statistical significance for single jet and jet+X channels ($X =$ jet, γ, Z), and for full b- and c- jet identification, allowing detailed studies of "jet quenching" phenomena.
(iv) Unparalleled forward physics (low-x QCD) capabilities thanks to the forward hadronic calorimeter HF ($3 < |\eta| < 5$), CASTOR-TOTEM ($5.5 < |\eta| < 6.6$), and Zero-Degree-Calorimeter ($|\eta| > 8.1$ for neutrals) detector systems.
(v) A DAQ system capable of delivering almost every PbPb event to the High Level Trigger allowing maximum flexibility to select rare probes at the highest multiplicities expected at the LHC.

Among the various perturbative probes accessible to measurement, we focus on this report on the quarkonia detection via the $\mu^+\mu^-$ decay channel. Other experimental

capabilities, in the hard (notably jet reconstruction in the heavy-ion environment), soft (hadron multiplicities, elliptic flow ...), and low-x (e.g. quarkonia photoproduction in electromagnetic PbPb interactions) sectors will be discussed in detail in CMS Physics TDR addendum for Heavy Ions."

7.5.3. Gluon saturation and QGP colour screening via Quarkonia

The production of heavy-quarks at LHC proceeds mainly via gluon-gluon fusion processes and, as such, is sensitive to nuclear modifications of the gluon density at low-x. At $\sqrt{s}_{NN} = 5.5\,\text{TeV}$, the average fraction of the nucleon momentum carried by the interacting parton producing a J/ψ at mid (forward) rapidity is $\langle x \rangle \approx 3 \cdot 10^{-3} (10^{-5})$. Such a kinematical domain is well in the regime where gluon saturation effects and departures from linear Q^2 (DGLAP) and $\ln(1/x)$ (BFKL) evolutions should be observable. In addition, the final-state formation of $Q\overline{Q}$ bound states is expected to be suppressed in a deconfined medium due to colour screening of the heavy-quark potential. Recent finite-temperature lattice QCD calculations exhibit a substantial reduction of the heavy-quark internal energy $U_{Q\bar{Q}}$, with increasing temperature. The ground-state charmonium state (J/ψ) has been found to dissolve slightly below $2{\cdot}T_{crit} \approx 330\,\text{MeV}$, whereas much higher dissociation temperatures, $T_{diss} \approx 4 \cdot T_{crit}$ reachable at LHC, are needed to dissociate the Υ. Although J/ψ suppression has been indeed observed in central A+A collisions both at CERN-SPS and RHIC energies, competing mechanisms to colour deconfinement (hadronic co-movers interactions and charm quark recombination) have been proposed to explain the observed cross-sections. At variance with charmonia states, the study of the much heavier bottomonia spectroscopy accessible at LHC is free from the distorting hadronic and coalescence contributions, and is directly sensitive to the temperature conditions of the produced partonic medium.

CMS has focused on the quarkonia detection through their decays to muon pairs. The good muon momentum resolution translates in an Υ mass resolution of $\sigma = 54\,\text{MeV/c}^2$ (in the central barrel region $|\eta| < 0.8$), the best of all the LHC detectors. This good resolution provides a clean separation between the members of the Υ family with a consequent improvement in the signal to background ratio, even in head-on PbPb collisions with particle multiplicities as large as $N_{ch}/d\eta|_{\eta=0} = 5000$. The expected signal/background ratios are $S/B \approx 1(5)$, $S/B \approx 0.1(1)$ for J/ψ and Υ respectively in the full ($|\eta| < 0.8$) rapidity range. In the absence of initial- or final-state medium effects, production cross sections of $B_{\mu\mu}\sigma = 50\,\text{mb}$ and $300\,\mu\text{b}$ respectively will be measured in minimum bias PbPb collisions. The expected reconstructed yields for both charmonium and bottomonium resonances after background subtraction, in one-month data taking (with 50% overall efficiency) and nominal PbPb luminosity ($0.5\,\text{nb}^{-1}$), are $\mathcal{O}(1.5 \cdot 10^5)$, $\mathcal{O}(2 \cdot 10^4)$ respectively. These statistics will allow detailed quantitative studies of quarkonia production as a function of p_{T}, rapidity and/or centrality. Any departure from the expected "vacuum" cross-sections will provide valuable information on the initial-state modifications of the nuclear parton (especially, gluon) distribution functions, as well as on the thermodynamical state of the produced medium from the predicted "melting" pattern of different quarkonia states due to colour screening.

Chapter 8. Physics of Top Quarks

8.1. Selection of $t\bar{t}$ events and measurement of the cross sections

8.1.1. Introduction

The goal of top physics at the LHC is to characterise the properties of this heaviest fermion of the Standard Model by measuring observables in its production and decay exploiting all possible decay channels. Important examples are the production cross section and the mass and spin properties of the top quark.

Most of the top quarks at the LHC will be produced as $t\bar{t}$ pairs. The $t\bar{t}$ production cross section is estimated to be 830 pb [278] at NLO and the dominant production mechanisms are gluon-gluon fusion ($\approx 90\%$) and quark-anti-quark annihilation ($\approx 10\%$). Within the Standard Model the top quark decays almost exclusively to a W boson and a b quark. The decays of the $t\bar{t}$ system are then classified according to the decays of the W^+W^- system as dileptonic, semi-leptonic or fully hadronic. The W can decay into leptons, $e^-\bar{\nu}_e$, $\mu^-\bar{\nu}_\mu$, $\tau^-\bar{\nu}_\tau$, or into quarks, $u\bar{d}'$, $c\bar{s}'$, where the charge conjugate is implicit. Neglecting QCD corrections, branching fractions of 9/81 (11.1%) for the dileptonic, 36/81 (44.4%) for the semi-leptonic and 36/81 (44.4%) for the fully hadronic decay channel are obtained.

For our studies we use PYTHIA for the simulation of signal and background events. As it includes spin correlation in $t\bar{t}$ production also samples generated with TOPREX are used for signal events.

8.1.2. Dileptonic channel

8.1.2.1. Event selection for 1 fb^{-1}. The very clean signature of this channel combined with a high signal-to-background ratio makes it possible to select $t\bar{t}$-events with simple kinematic cuts. The selection is therefore suitable for the expected early performance of the CMS detector and will allow to establish the signal as well as to measure the top mass at an early stage of the experiment.

For an integrated luminosity of 1fb^{-1} about 54000 signal events are expected according to the leading-order estimate of PYTHIA. The main backgrounds with a final state mimicking the signal are Z, WW, WZ and ZZ production accompanied by jets. Furthermore, events from semi-leptonic and fully-hadronic top-quark pair production with misidentified leptons and leptons from b-quark jets eventually constitute the dominating background. Here, dilepton events with W bosons decaying into τ-leptons are considered signal events if the τ lepton decays leptonically. Details of the analysis can be found in Reference [279].

Events are required to pass the Level-1 and High Level Trigger, in particular the single and dilepton subtriggers. In addition to trigger criteria, events must contain at least two jets and two oppositely charged leptons. Electrons are identified using an electron likelihood method combining various electromagnetic shower variables and track-to-supercluster-matching criteria. After this pre-selection about 15000 signal events are left in a 1fb^{-1} data set with a signal over background ratio of $S/B = 1/10$. The most important background at this stage consists of Z + jets production with an accepted cross section of about 120 pb and a similar final state.

Isolation criteria reduce the contribution from misidentified leptons and leptons from b-jets. For a lepton candidate no other track or calorimeter hits amounting to 10% or more of the lepton p_T are allowed in a cone of $\Delta R < 0.2$. Two charged leptons are then chosen with a discriminant based on the likelihood ratio in case of an electron, the energy deposited in a cone of $\Delta R = 0.2$ around the lepton axis and the p_T of the lepton.

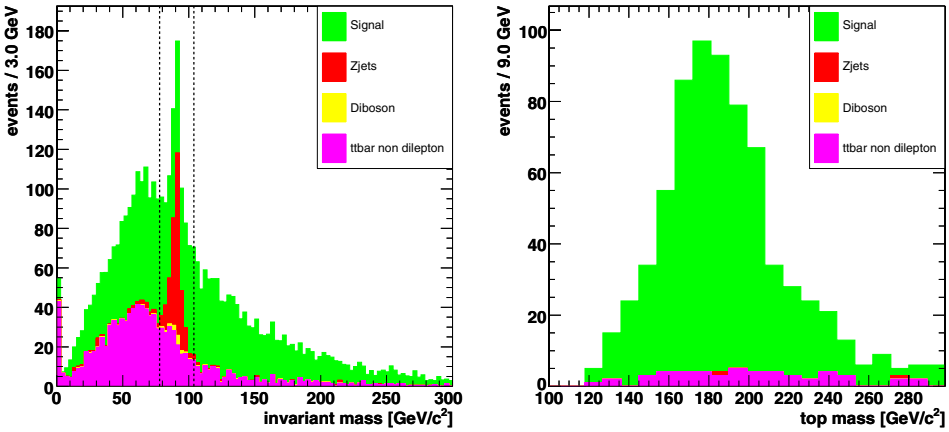

Figure 8.1. Left: Invariant mass of the two lepton candidates indicating the cut window to remove Z + jets events. Right: Most likely top mass after selection for 1fb^{-1}.

Both b-jets are selected with a discriminator based on the jet p_{T}, the invariant mass of tracks inside the jet and the output of the combined b-tagging algorithm [157]. Using this scheme the correct jets and leptons of the signal are selected for more than 90% of the events, if they could be reconstructed. It has been shown in reference [157] that, during the *first data taking phases* of the LHC, the degradation in b-tagging performance is still acceptable. This implies that the b-tagging results presented here remain essentially correct.

Figure 8.1 shows the invariant mass of the two lepton candidates. The Z mass peak of the invariant mass distribution of two same type leptons is used to remove the contamination due to Z + jets events. As a further improvement a cut on the b-tag discriminator is applied to the two selected jets.

The non-dilepton $t\bar{t}$ events usually contain more jets with a p_{T} greater than $30\,\mathrm{GeV/c}$ but do not contain two high p_{T} leptons. The second lepton candidate is considerably softer than the corresponding lepton from the signal decay channel. So a cut on the lower transverse momentum lepton is imposed with $p_{\mathrm{T}} > 20\,\mathrm{GeV/c}$. The two neutrinos in the decay of the W bosons lead to significant missing transverse energy $E_{\mathrm{T}}^{\mathrm{miss}}$ whereas the decay of Z bosons into electrons or muons does not generate $E_{\mathrm{T}}^{\mathrm{miss}}$. The cut $E_{\mathrm{T}}^{\mathrm{miss}} > 40\,\mathrm{GeV}$ further improves the signal to background ratio. At this stage about 1800 signal events are left with a signal over background ratio of $S/B = 7.3/1$.

The kinematics of the $t\bar{t}$ dilepton events yield an underconstrained equation system due to the two undetected neutrinos in the final state. However if, all other kinematic quantities have been measured it is possible to make a fit imposing m_W and assuming a top mass parameter in the range of 100 to $300\,\mathrm{GeV/c^2}$. A weight can then be assigned to the different solutions obtained [279]. Figure 8.1 shows the distribution of the most likely top mass for signal and background events in the range $100\,\mathrm{GeV/c^2} < m_t < 300\,\mathrm{GeV/c^2}$.

The event topology of most of the background events passing the previous cuts does not satisfy the dilepton kinematical constraints. Therefore considering only candidates which give a mass estimate in the range of 100 to $300\,\mathrm{GeV/c^2}$ further reduces the background and raises the signal over background ratio to about $S : B = 12 : 1$. The remaining background essentially contains only non-dilepton $t\bar{t}$ events. In a dataset equivalent to 1fb^{-1}, 657 signal events are selected with an overall efficiency of 1.2%.

We conclude that a measurement of the $t\bar{t}$ cross section and the top mass (see Section 8.2.1) in the dileptonic channel will be possible already with a modest amount of luminosity [279].

8.1.2.2. Event selection for higher luminosities. The trigger is based on the presence of one muon or electron which covers with high efficiency all the possible final states in this channel. The selection of events in this channel then requires after trigger selection the presence of just two oppositely charged leptons with $E_{\mathrm{T}} > 20\,\mathrm{GeV}$ within pseudorapidity ranges of ± 2.4 and ± 2.5 for muons and electrons respectively. Details are available in [279].

The reconstruction efficiency is good for both for muons and electrons. More than 97% of the generated muons are correctly reconstructed in the considered range, as well as 90% of the electrons, with p_{T} above $20\,\mathrm{GeV/c}$ [279]. An electron is considered isolated if the total uncorrected E_{T} of the jets within a cone $\Delta R \leqslant 0.3$, minus the lepton E_{T}, is less than 30% of the lepton E_{T}. In a similar way a muon is considered isolated, if the sum of the p_{T} of all the tracks present in a cone of $\Delta R \leqslant 0.3$ minus p_{T} of the muon is less than $2\,\mathrm{GeV/c}$. Candidate events must have $E_{\mathrm{T}}^{\mathrm{miss}} > 40\,\mathrm{GeV}$. The analysis requires at least two jets with uncorrected $E_{\mathrm{T}} > 20\,\mathrm{GeV}$ detected within $|\eta| < 2.5$, where a jet is defined as a fixed-cone cluster with a cone size of $R = 0.5$. Jets produced by electrons are discarded before applying the previous selection by removing those which have an electromagnetic supercluster within $\Delta R = 0.2$ with a ratio between the electromagnetic energy of that supercluster and the uncorrected jet energy above 0.75.

b-tagging techniques based on the explicit reconstruction of a secondary vertex in a jet [157] are used to further suppress backgrounds in which no jets from b-quarks are present. The dominant backgrounds to dilepton $t\bar{t}$ events are those which have real leptons, real $E_{\mathrm{T}}^{\mathrm{miss}}$ and jets originating from initial or final state radiation, arising mainly from dibosons (WW, WZ, and ZZ) + jets production, and also from top quark decays, either from the semi-leptonic channel or from tau decays producing leptons. This kind of backgrounds are expected to be determined using MC simulation. Instrumental backgrounds, are characterised in general by their large cross sections but not having real $E_{\mathrm{T}}^{\mathrm{miss}}$, among them are: Z + jets, Drell–Yan ($Z/\gamma^{\star} \to \ell^{+}\ell^{-}$) production, "fake" leptons in $W \to \ell\nu$ + jet events where a jet is falsely reconstructed as a lepton candidate. In principle it is harder to estimate their contribution to the final sample using MC simulation.

After this selection an efficiency close to 5% is obtained, with a very high rejection of all the backgrounds considered at the level of $10^{-3} : 1$ or better, as shown in Table 8.1. A S/B value of 5.5 is obtained, the main background being the one arising from the dilepton channel itself in which at least one of the W decays into $\tau\nu_{\tau}$ and with a subsequent leptonic tau decay.

Different sources of systematic uncertainties have been identified that affect event selection and background determination and thus the cross section measurement. Detailed studies [279] of these sources have been done based mainly on the results of the studies performed in [7] and [201]. Among the most important experimental sources are uncertainties on the jet energy scale and the b-tag efficiency. The impact of theoretical and phenomenological uncertainties such as those on hadron fragmentation and PDF have been studied using samples generated with different PYTHIA parameters and simulated and reconstructed with the CMS fast simulation and reconstruction program. The uncertainty in the cross section coming from the luminosity estimation was taken as 3% as expected for $10\,\mathrm{fb}^{-1}$ integrated luminosity. As the non-$t\bar{t}$ background is small it does not contribute significantly to the uncertainty. The results are summarised in Table 8.2 and lead to an estimated total error on the $t\bar{t}$ cross section measured in the dileptonic channel using electrons and muons of $\Delta\sigma_{t\bar{t}}/\sigma_{t\bar{t}} = 11\%\,(syst)\ \pm 0.9\%\,(stat)\ \pm 3\%\,(luminosity)$.

Table 8.1. Cumulative effect of the different selection criteria applied to the simulated $t\bar{t}$ dilepton sample (electrons and muons) and simulated backgrounds. The column denoted as τ corresponds to $t\bar{t}$ dilepton sample in which at least one W decays into a τ lepton. The numbers correspond to LO accepted cross sections in pb.

	Signal	τ	WW	WZ	ZZ	Z + jets	other $t\bar{t}$
Before selection	24.3	30.4	7.74	0.89	0.11	3912	438
Level-1 + HLT	19.4	15.1	4.4	0.37	0.07	657	92
2 jets $E_{\mathrm{T}} > 20$ GeV	11.5	9.8	0.6	0.012	0.006	23.9	73.1
$E_{\mathrm{T}}^{\mathrm{miss}} > 40$ GeV	9.6	8.1	0.5	0.01	0.003	5.8	53.6
Two opp. charged leptons	3.2	0.42	0.04	0.001	0.001	1.17	0.12
b-tag of two highest E_{T} jets	1.12	0.15	0.002	$\sim 10^{-4}$	$\sim 10^{-5}$	< 0.01	0.05

Table 8.2. Uncertainties in the $t\bar{t}$ dilepton cross section determination for 10 fb^{-1}.

Effect	$\Delta\sigma_{t\bar{t}\ dil\ e/\mu}/\sigma_{t\bar{t}\ dil\ e/\mu}$
Jet Energy Scale	3.6%
b-tag efficiency	3.8%
Lepton reconstruction	1.6%
$E_{\mathrm{T}}^{\mathrm{miss}}$	1.1%
ISR and FSR	2.5%
Pile-Up	3.6%
Underlying Event	4.1%
Heavy quark fragmentation	5.1%
PDF uncertainties	5.2%
Statistical uncertainty	0.9%
Integrated luminosity	3%

8.1.2.3. Top decays to tau leptons. In this section studies performed to select events with τ leptons in the final state are presented. We consider here dileptonic $t\bar{t}$ decays with one tau lepton decaying into hadrons in the final state $t\bar{t} \to b\bar{b}\tau\nu_\tau\ell\nu_\ell$, $(\ell = \mathrm{e}, \mu)$. The measurement of the ratio $BR(t\bar{t} \to \ell\tau + X)/BR(t\bar{t} \to \ell\ell + X)$ will allow to set new limits on the presence of non-standard physics in top decays. Furthermore, this channel is a source of background for Supersymmetry and Higgs searches, as well as for the other dileptonic top channels.

Tau candidates are selected and identified following the method of the MSSM Higgs and HLT analyses [280], adapting the different selection criteria to the momentum range in which tau candidates are expected to be produced in top decays [279]. The hadronic tau identification efficiency obtained in the dilepton samples is about 30% using this method as can be seen in Fig. 8.2.

Event selection proceeds in a similar way as in Section 8.1.2.2 but only one isolated lepton (electron or muon) is allowed. One isolated tau candidate separated from the isolated lepton has to be present, and the isolated lepton and the tau candidate must have opposite charges. The effect of these selections are described in detail for the $t\bar{t}$ sample in Table 8.3. b-tag for the two accompanying jets is also required. An efficiency close to 2% is obtained, with a very high rejection of all the backgrounds considered. A S/B value close to 1 is obtained, the main background being the one arising from the $t\bar{t}$ semi-leptonic channel. The majority of the systematic uncertainties are described in Section 8.1.2.2. There is another systematic uncertainty intrinsic to this analysis due to the τ reconstruction and identification. Based on preliminary studies, we assigned a 12% uncertainty to the τ reconstruction and identification. Statistical uncertainty in the cross section determination is about 1.3% for an

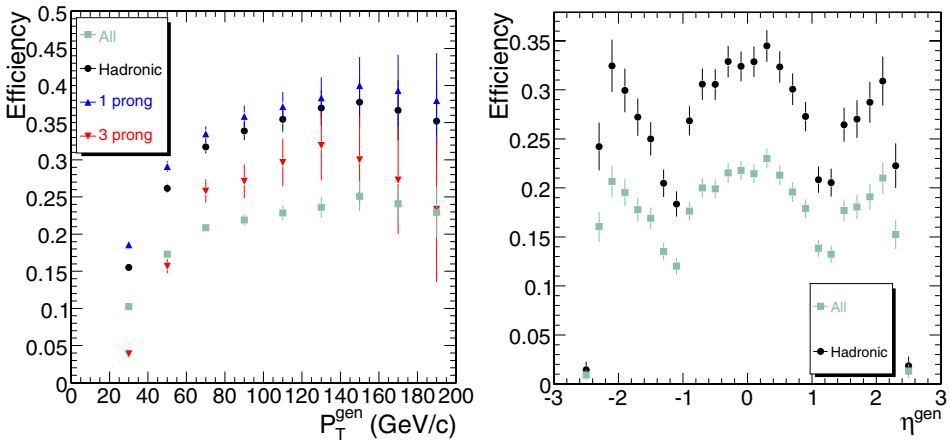

Figure 8.2. Reconstruction efficiency of tau candidates as a function of p_T and η. Errors are statistical only.

Table 8.3. Cumulative effect of the different selection criteria applied to the simulated $t\bar{t}$ sample. Numbers correspond to LO accepted cross sections.

Cut	Efficiency times cross sections (pb)			
	$t\bar{t}$ (signal)	$t\bar{t}$ (other dilepton)	$t\bar{t}$ (semi-leptonic)	$t\bar{t}$ (hadronic)
Before selection	15.62	38.94	218.88	218.88
Trigger	8.61	25.40	85.90	2.08
2 jets	6.97	18.90	80.08	2.04
$\geqslant 1$ Iso lepton	4.27	13.11	34.93	0.11
$E_T^{miss} \geqslant 40$ GeV	3.58	10.89	26.41	0.05
1 lepton	3.48	6.73	25.24	0.04
τ cand. with opp. Q	0.75	0.20	0.75	0.001
b-tagging	0.29	0.07	0.30	0.0005

integrated luminosity of $10\,\text{fb}^{-1}$. Then the relative uncertainty in the estimation of the cross section is given by $\Delta\sigma_{t\bar{t}\,dil\,\tau,e\mu}/\sigma_{t\bar{t}\,dil\,\tau,e\mu} = 16\%\ (syst)\ \pm 1.3\%\ (stat)\ \pm 3\%\ (luminosity)$.

8.1.3. Semi-leptonic channel

The semi-leptonic $t\bar{t}$ decay has a final state topology of four hadronic jets of which two originate from a b-quark, an isolated lepton and missing transverse momentum. In this section, we consider the measurement of the cross section of the semi-leptonic $t\bar{t}$ production where the lepton is a muon [281].

Both the Level-1 and the High-Level Trigger selection criteria are applied on the simulated events, resulting in the efficiencies shown in Table 8.4. The single-muon trigger stream was used. The jets are reconstructed from the combined electromagnetic and hadronic calorimeter energy deposits and clustered with the Iterative Cone algorithm using an opening angle of $\Delta R = 0.5$. A transverse energy threshold of 0.5 GeV is applied on the input objects

Table 8.4. Overview of the selection criteria applied. The expected S/B values take into account the respective Leading-Order cross-sections of the processes.

	Semi-lept. $t\bar{t}$	Other $t\bar{t}$	W + 4j	Wbb + 2j	Wbb + 3j	S/B
Before selection	365k	1962k	82.5k	109.5k	22.5k	5.9
L1 + HLTTrigger	62.2%	5.30%	24.1%	8.35%	8.29%	7.8
Four jets $E_T > 30$ GeV	25.4%	1.01%	4.1%	1.48%	3.37%	9.9
$p_T^{lepton} > 20$ GeV/c	24.8%	0.97%	3.9%	1.41%	3.14%	10.3
b-tag criteria	6.5%	0.24%	0.064%	0.52%	0.79%	25.4
Kinematic fit	6.3%	0.23%	0.059%	0.48%	0.72%	26.7
Selected cross section (pb)	5.21	1.10	0.10	0.08	0.05	26.7
Scaled $\mathcal{L} = 1\,\text{fb}^{-1}$	5211	1084	104	82	50	26.7

before clustering. Optimisation of the parameter settings of the clustering algorithms are considered in [282]. Only the jets in the vicinity of the primary vertex are considered in the analyses, rejecting in general those jets with a small transverse momentum. The energy scale of the reconstructed jets is calibrated using the methods described in [283]. Among the list of muon candidates identified flavour, the muon originating directly from the W boson decay is selected following the procedure described in [284]. The transverse momentum components of the unobserved neutrino are estimated via the missing transverse momentum which balances the vectorial sum of the energy deposits in the calorimeter above the transverse energy threshold mentioned.

The event selection consists of a series of sequential cuts on kinematic or topological variables. The event is required to have at least four jets after applying the primary vertex constraint with a calibrated transverse energy, E_T, exceeding 30 GeV and within a pseudo-rapidity in the range of the tracker, $|\eta| < 2.4$. If more than four jets match this criterion, the four leading jets are selected as those with the highest E_T. Of these four jets, two have to be b-tagged according to the method applying a combined b-tag variable described in [281, 285, 286]. The selected lepton is required to be within the tracker acceptance and to have a transverse momentum larger than 20 GeV/c.

After classifying two of the four reconstructed jets as b-quark and the other two as light quark jets, only two jet combinations remain to reconstruct the hadronically-decaying top. A kinematic fit [167] was applied on the reconstructed event for both jet combinations forcing the reconstructed W boson mass to its precisely known value. Before applying the kinematic fit the energy scale of the light quark jets is corrected for an overall bias in the reconstructed W boson mass. Following the method described in [287] after the event selection mentioned above, an inclusive jet energy scale correction of -9.7% was obtained and applied to light quark jet candidates. The event is finally selected if the fit converged for at least one of the combinations.

The selection efficiency for the signal events is estimated to be $6.28 \pm 0.04\%$. The fraction of $t\bar{t}$ signal events in the selected sample of inclusive $t\bar{t}$ decays is estimated to be $82.8 \pm 0.2\%$. The signal-to-background ratio after the event selection is 26.7, where all $t\bar{t}$ decay channels are considered as signal. Hence the systematic effect of the background contribution is minor. It is shown in [281] that after the event selection topological observables will not help much in differentiating between signal and background. The cross section is therefore estimated from counting events. The statistical uncertainty on the estimated cross section is 1.2%, 0.6% and 0.4% for integrated luminosities of $1\,\text{fb}^{-1}$, $5\,\text{fb}^{-1}$ and $10\,\text{fb}^{-1}$, respectively.

Table 8.5. Overview of the systematic uncertainties on the cross section.

	$\Delta\hat{\sigma}_{t\bar{t}(\mu)}/\hat{\sigma}_{t\bar{t}(\mu)}$		
	$1\,\text{fb}^{-1}$	$5\,\text{fb}^{-1}$	$10\,\text{fb}^{-1}$
Simulation samples (ε_{sim})		0.6%	
Simulation samples (F_{sim})		0.2%	
Pile-Up (30% On-Off)		3.2%	
Underlying Event		0.8%	
Jet Energy Scale (light quarks) (2%)		1.6%	
Jet Energy Scale (heavy quarks) (2%)		1.6%	
Radiation (Λ_{QCD}, Q_0^2)		2.6%	
Fragmentation (Lund b, σ_q)		1.0%	
b-tagging (5%)		7.0%	
Parton Density Functions		3.4%	
Background level		0.9%	
Integrated luminosity	10%	5%	3%
Statistical Uncertainty	1.2%	0.6%	0.4%
Total Systematic Uncertainty	13.6%	10.5%	9.7%
Total Uncertainty	13.7%	10.5%	9.7%

Systematic effects are introduced only on the signal events, changing the efficiency of the event selection. Similar effects on the background samples should be a second order effect on the inferred cross section. For the theoretical or phenomenological uncertainties the prescription of [201] was used as described in [281]. The list of systematic uncertainties is shown in Table 8.5. The dominant systematic effects are b-tagging, and in the early stage the uncertainty on the integrated luminosity. For an extended discussion on the studied systematic effects we refer to [281]. As a consequence of the kinematic fit, the uncertainty on both the light- and heavy-quark jet energy scale results in a limited systematic uncertainty, of about 1.6%.

The total relative systematic uncertainty on the cross section is 10.5% which can be compared to a relative statistical uncertainty of 0.6% at $5\,\text{fb}^{-1}$. The total uncertainty of 10.5% scales with the integrated luminosity as shown in Fig. 8.3. In this plot it is assumed that the uncertainty on the determination of the integrated luminosity scale as the inverse square root of the integrated luminosity. At an integrated luminosity of about $5\,\text{fb}^{-1}$ the total uncertainty is dominated by the uncertainty on the b-tagging performance. For the uncertainty on the b-tagging efficiency a conservative 5% is taken according to [286] although the Tevatron experience shows that a value of 2% can be reached [288, 289].

8.1.4. Fully hadronic channel

The fully hadronic final state, characterised by a six-jets topology $t\bar{t} \to WWb\bar{b} \to qqqqb\bar{b}$, has the largest branching fraction (46%), and kinematics that can be fully reconstructed. However, this channel is affected by a large background from QCD multi-jet production, which makes the isolation of the signal rather challenging, and internal jet-parton permutation uncertainties. Improvements in the signal-to-background ratio are possible by requiring the presence of b-quark jets and by selecting central and very high-energy kinematic configurations which are expected for jets arising from the decay of a massive object like the top quark. A specific multi-jet trigger which uses b-tagging information has been devised for this analysis and an optimised selection has been applied. The analysis is described in detail in [279].

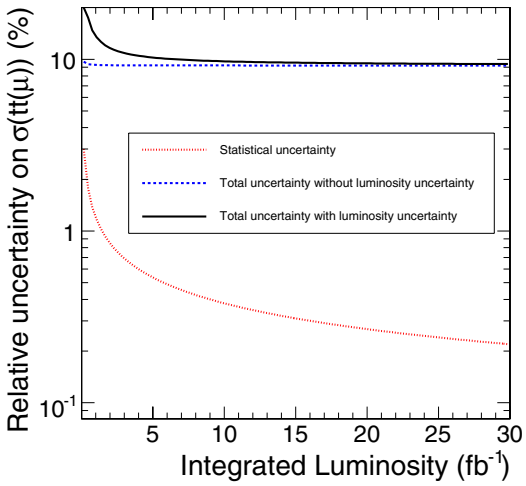

Figure 8.3. Statistical and total uncertainty on the inferred cross section of the process $pp \to t\bar{t} \to bq\bar{q}b\mu\nu_\mu$ as a function of the integrated luminosity.

The signal sample consists of 500000 inclusive $t\bar{t}$ events, from which a sub-sample of 230000 fully hadronic $t\bar{t}$ events is extracted. The background consists of 1.5 million multi-jet events (QCD) generated with $50 < \hat{p_T} < 470\,\mathrm{GeV/c}$, where the $\hat{p_T}$ symbol indicates the transverse momentum of the most energetic parton of the hard scattering before the final-state radiation processes.

8.1.4.1. Trigger pre-selection and event selection. The trigger pre-selection uses the inclusive jet trigger envisaged in [76] and a special inclusive b-jet trigger [290]. The inclusive b-jet trigger combines in the first stage the b-tagging requirement with an inclusive jet trigger which applies tuned E_T thresholds of 350 GeV for single jets, 150 GeV for 3-jet and 55 GeV for 4-jet topologies; then a b-tagging based on pixel and regional track and vertex reconstruction is performed on the two most energetic jets. The trigger requires either multiple jets in the event or a b-tagged jet among the two highest-E_T jets. After the trigger pre-selection the QCD rate is reduced to 23 Hz, the signal efficiency is 16.8% and the signal to background ratio, S/B, amounts to 1/300.

The selection is designed to optimise the statistical significance $S/\sqrt{S+B}$ for an integrated luminosity of $\mathcal{L} = 1\,\mathrm{fb}^{-1}$. The first step of the selection requires a topology of $6 \leqslant N_{jet} \leqslant 8$. For a jet to be counted, the jet pseudorapidity must satisfy $|\eta| < 2.4$ and its transverse energy must be greater than 30 GeV. Event shape variables, potentially able to separate the signal from the background are then taken into account. The useful ones are centrality, aplanarity and non-leading jet total transverse energy obtained removing the two most energetic jets ($\sum_3 E_T$) of which distributions are shown in Fig. 8.4. After the selection b-tagging is applied to the surviving samples of $t\bar{t}$ fully hadronic and QCD events. Selection criteria of at least one b-jet and two b-jets are considered.

Table 8.6 summarises the selection applied in cascade. The signal-to-background ratio amounts to 1/17 and 1/9 for the 1 and 2 b-tag samples,respectively, and resulting in signal efficiencies of 3.8% and 2.7%.

The signal efficiency relative to the total inclusive $t\bar{t}$ sample, to be used in the calculation of the total $t\bar{t}$ production cross section, becomes 2.3% (1.6%), respectively for the 1 (2) b-tag requirement. The estimated statistical uncertainty on the cross section is reported in Table 8.7.

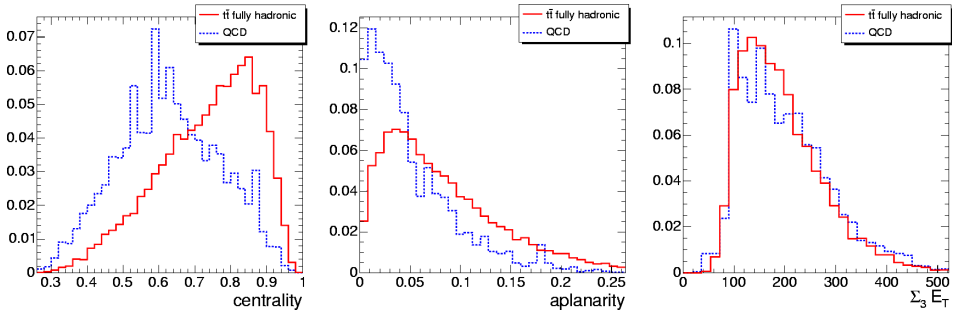

Figure 8.4. Distributions of centrality, aplanarity and $\sum_3 E_T$ for $t\bar{t}$ and QCD events (normalised to the same area).

Table 8.6. $t\bar{t}$ fully hadronic and QCD effective cross sections, signal-to-background ratio, statistical significance for 1 fb^{-1} and signal efficiency at each step of the selection.

Selection	Requirement	$\sigma\varepsilon$ [pb]	$\sigma\varepsilon_{QCD}$ [pb]	S/B	$S/\sqrt{S+B}$	ε (%)
Before Selection (PYTHIA LO)		225	25M	$1/10^5$	0.04	100
Trigger	HLT multi-jet+b-jet	38	11600	1/300	11.1	16.8
Event	$6 \leqslant N_{jet} \leqslant 8$	35	7900	1/225	12.4	15.5
	$E_T \geqslant 30$ GeV	15	930	1/60	15.4	6.6
	centrality $\geqslant 0.68$	9.9	324	1/33	17.1	4.4
	aplanarity $\geqslant 0.024$	9.0	251	1/28	17.7	4.0
	$\sum_3 E_T \geqslant 148$ GeV	9.0	229	1/25	18.4	4.0
b-tagging	1 b-tag	8.6	148	1/17	21.7	3.8
	2 b-tag	6.0	54	1/9	24.1	2.7

Table 8.7. Number of $t\bar{t}$ and QCD events, $t\bar{t}$ efficiency, absolute and relative statistical uncertainties expected on the cross section measurement for an integrated luminosity of 1fb^{-1}.

Requirement	$\mathcal{L} = 1$ fb^{-1}				
	$t\bar{t}$ events	QCD events	ε (%)	$(\Delta\sigma)_{stat}$ [pb]	$(\Delta\sigma/\sigma)_{stat}$(%)
1 b-tag	11500	148000	2.3	17	3.5
2 b-tag	8000	54000	1.6	15	3.0

Sources of systematic uncertainty are studied as described in detail in [201] and [7]. From the experience of CDF and DØ experiments at Tevatron [291], one of the dominating systematic uncertainties arises from jet energy scale. The systematic uncertainty related with the trigger selection is calculated considering contributions from b-tagging and jet energy scale. Table 8.8 summarises the contributions to the total uncertainty on the cross section, which combined lead to a relative uncertainty of $\Delta\sigma/\sigma = 3\%(stat) + 20\%(syst) + 5\%(luminosity)$.

8.1.4.2. Event selection based on neural net. A more refined selection is based on a neural net exploiting the same variables considered so far. Such approach is attempted in order to investigate the possibility of improving the S/B ratio and/or the efficiency. The previous

Table 8.8. Contributions to the systematic uncertainty on the $t\bar{t}$ cross section measurement in the fully hadronic channel (cut based approach).

	$\Delta\sigma/\sigma\,(\%)$
HLT	5.9
Pile Up	10.0
Underlying Event	4.1
Fragmentation	1.9
PDF	4.2
IS/FS Radiation	7.9
Jet Energy Scale	11.2
b-tagging	2.0
Background	5.0
Integrated Luminosity	5.0

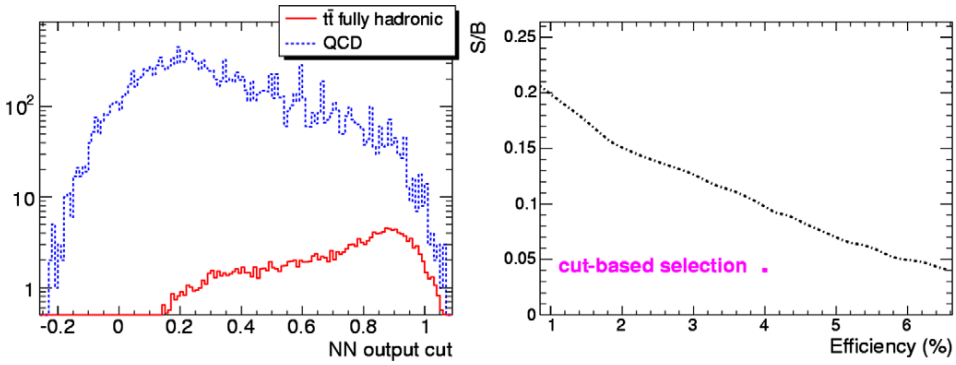

Figure 8.5. Left: distribution of the neural net output for $t\bar{t}$ and QCD. Right: signal-to-background ratio as function of the signal efficiency. For comparison the result of the cut-based selection is also shown.

selection, called “cut-based", could represent a more conservative approach for the first LHC analyses.

The most effective neural network configuration studied is applied to the $t\bar{t}$ and QCD events satisfying the topology request of $6 \leqslant N_{jet} \leqslant 8$ (jet pseudorapidity $|\eta| < 2.4$) after a cut on jet transverse energy of $E_{\mathrm{T}} > 25\,\mathrm{GeV}$ and consists of 6 input nodes: E_{T} of the first and sixth jet with the jets ordered in increasing E_{T}, centrality, aplanarity, $\sum_3 E_{\mathrm{T}}$ and sphericity. The performance of the neural net is shown in Fig. 8.5 which compares the output distributions for signal and QCD background. The S/B ratio as a function of the $t\bar{t}$ efficiency is also shown. With respect to the cut-based selection, the request for a neural net output $\geqslant 0.77$ improves the S/B ratio from 1/25 to 1/10 with same efficiency of about 4%.

As done after the cut-based selection, a b-tagging is applied to the surviving samples of $t\bar{t}$ fully hadronic and QCD events, and selection criteria of at least one b-jet and two b-jets are considered. Improved signal-to-background ratio, amounting to 1/7 (1/3) respectively for 1 (2) b-tag samples, can be achieved using the neural net keeping the same signal efficiencies of 3.8% (2.7%). This means an estimated relative statistical uncertainty on the cross section of 2.3% (2.0%), with the same expected number of $t\bar{t}$ events for an integrated luminosity of $\mathcal{L} = 1\,\mathrm{fb}^{-1}$.

8.2. Measurement of the top quark mass

8.2.1. Dileptonic events

The dilepton channel benefits of a clean signature and a large signal-to-background ratio even though the presence of two neutrinos prevents a direct reconstruction of the top-quark mass. However, the event kinematic retains a large sensitivity to the top mass which can be exploited in various ways. The method presented here is discussed in more detail in [279].

The six unmeasured kinematic quantities corresponding to the momentum components of the two neutrinos are reduced by assuming momentum balance in the transverse plane, by imposing the m_W constraint and by requiring both top-quark masses to be equal. The event kinematics can then be written as a fourth order polynomial with the top mass as a parameter. For each candidate event we step through top mass values in the range $100\,\mathrm{GeV/c^2} \leqslant m_t \leqslant 300\,\mathrm{GeV/c^2}$ in $1\,\mathrm{GeV/c^2}$ steps and weight the kinematic solutions, including their fourfold ambiguity, with the Standard Model expectations of the neutrino momentum spectrum. For each event the most likely solution, i.e. the solution with the highest weight, is retained. The mass distribution of these most likely solutions is shown in Fig. 8.1 for $1\mathrm{fb}^{-1}$. The figure shows a clear mass peak at the expected value for the fully-simulated and reconstructed events. A Gaussian fit to the signal in a range corresponding to 40% of the maximum yields $m_t = 178.5 \pm 1.5\,\mathrm{GeV/c^2}$ for an input top mass of $175\,\mathrm{GeV/c^2}$, where the uncertainty is statistical. With $10\,\mathrm{fb}^{-1}$ the statistical uncertainty will be reduced to $0.5\,\mathrm{GeV/c^2}$. The background is small and essentially flat and does not affect the mass determination significantly.

The main systematic effects are due to the assumptions used to reduce the complexity of the kinematic equation system and to detector effects. The dominating systematic effect in the first category is the uncertainty on the initial and final-state radiation which changes the amount of transverse momentum of the $t\bar{t}$-system and the kinematic constraints. This results in an uncertainty on the top mass of $\Delta m_t = 0.3\,\mathrm{GeV/c^2}$ [201]. The zero width approximation for both the W bosons and the top quarks in the equation system gives rise to another shift of about $0.1\,\mathrm{GeV/c^2}$.

The expected uncertainty on the jet energy scale for the early data amounts to 15%, independent of the jet p_T, which corresponds to an uncertainty of $\Delta m_t = 4.2\,\mathrm{GeV/c^2}$ for the first $1\,\mathrm{fb}^{-1}$ of integrated luminosity. This uncertainty is reduced to $2.9\,\mathrm{GeV/c^2}$ with an improved calibration in $1\text{–}10\,\mathrm{fb}^{-1}$ based on photons and jets, especially jets from W-boson decays in semi-leptonic and fully-hadronic $t\bar{t}$ events. Further improvement in the knowledge of the jet energy scale after $10\,\mathrm{fb}^{-1}$ are expected to reduce this uncertainty to about $1\,\mathrm{GeV/c^2}$.

In conclusion, the kinematic reconstruction of the dilepton channel will allow an early measurement of the top-quark mass. Assuming that the goal for a precise jet energy scale determination for b-quarks can be achieved the expected precision on the top mass in this channel with $10\,\mathrm{fb}^{-1}$ is $\Delta m_t = 0.5\,\mathrm{GeV/c^2}(stat) \pm 1.1\,\mathrm{GeV/c^2}(sys)$.

8.2.2. Semi-leptonic events

The semi-leptonic $t\bar{t}$ decay is traditionally called the *golden channel* for measuring the top-quark mass. A measurement based on advanced analysis tools is described in detail in [292]. The event reconstruction and initial event selection follows the one of Section 8.1.3. For the event to be selected, exactly two out of the four leading jets are b-tagged and the other two need to be anti-b-tagged. The four leading jets should not overlap in order to reduce ambiguities in the jet energy scale calibration procedure. The efficiency of each sequential cut is shown in Table 8.9.

Table 8.9. Overview of the selection criteria applied after the lepton cut $p_T^{lepton} > 20\,\mathrm{GeV/c}$ in Table 8.4.

	Signal	Other $t\bar{t}$	W + 4j	Wbb + 2j	Wbb + 3j	S/B
Before selection	365k	1962k	82.5k	109.5k	22.5k	0.032
b-tag criteria	5.5%	0.21%	0.052%	0.47%	0.70%	3.73
No jet overlap	3.0%	0.11%	0.027%	0.25%	0.44%	3.87
P_{χ^2}-cut 20%	1.4%	0.039%	0.0097	0.061	0.07	5.3
P_{sign}-cut 80%	1.2%	0.025%	0.0085	0.052	0.05	6.8
P_{comb}-cut 50%	0.7%	0.013%	0.0036	0.013	0.	8.2
Scaled $\mathcal{L} = 1\,\mathrm{fb}^{-1}$	588	64	6	2	0	8.2

The amount of events produced via a different $t\bar{t}$ decay channel in the selected event sample is reduced by a likelihood-ratio method combining three kinematic observables resulting in a variable L_{sign} which is transformed into a probability P_{sign} for the selected event to be a semi-leptonic muon $t\bar{t}$ event. An extra sequential cut is applied by requiring this probability P_{sign} to exceed 80%.

Among the four reconstructed jets, three have to be chosen to form the hadronic decaying top quark. The efficiency and purity of this selection was significantly enhanced by applying a second likelihood ratio method combining the information from several sensitive variables. The jet combination with the largest L_{comb} value is taken as the best pairing. The L_{comb} value is transformed into a probability P_{comb} for the chosen combination to be the correct one. The event probability P_{comb} is used in the event selection where events are selected if their value for P_{comb} exceeds 60%, increasing the purity of the selected jet pairings to 81.6% in the mass window of $25\,\mathrm{GeV/c^2}$ around the expected m_t of about $175\,\mathrm{GeV/c^2}$.

For each jet combination a kinematic fit was applied as described which imposes the W-boson mass for the hadronically-decaying W boson in the event [167]. Only jet combinations are considered with a probability of the kinematic fit calculated from its χ^2/ndf exceeding 20%. For some events none of the jet combinations fulfill this criterium, therefore reducing the total event selection efficiency. The fraction of fully hadronic $t\bar{t}$ events selected is negligible (less than 0.05 events expected at $1\,\mathrm{fb}^{-1}$). From this we conclude that the also influence of QCD produced jet events is minor.

When estimating m_t from the selected event sample by a simple Gaussian fit in a range of $20\,\mathrm{GeV/c^2}$ in both directions around the modal bin, a value of $176.5 \pm 0.65\,\mathrm{GeV/c^2}$ is obtained before applying the kinematic fit and $172.2 \pm 0.48\,\mathrm{GeV/c^2}$ after applying the kinematic fit, for an input value of $175\,\mathrm{GeV/c^2}$. The errors reflect the statistical precision of the available Monte Carlo signal sample. The top quark mass after the kinematic fit is shown in Fig. 8.6.

Rather than developing m_t estimators on samples of events, an event-by-event likelihood approach is used to estimate m_t from the fitted kinematics of the three jets of the hadronically decaying top quark. The uncertainty on m_t for each event is determined from the covariance matrices of the kinematic fit. This uncertainty can either be assumed Gaussian or the full m_t range can be explicitly scanned with the kinematic fit.

To obtain information about the true value of M_t we convolute the reconstructed resolution function or ideogram with the theoretical expected probability density function $P(m_t|M_t)$ in the reconstruction space

$$\mathcal{L}_i(M_t) = \int P(\{\overline{p}_j\}|m_t) \cdot P(m_t|M_t)\, dm_t \tag{8.1}$$

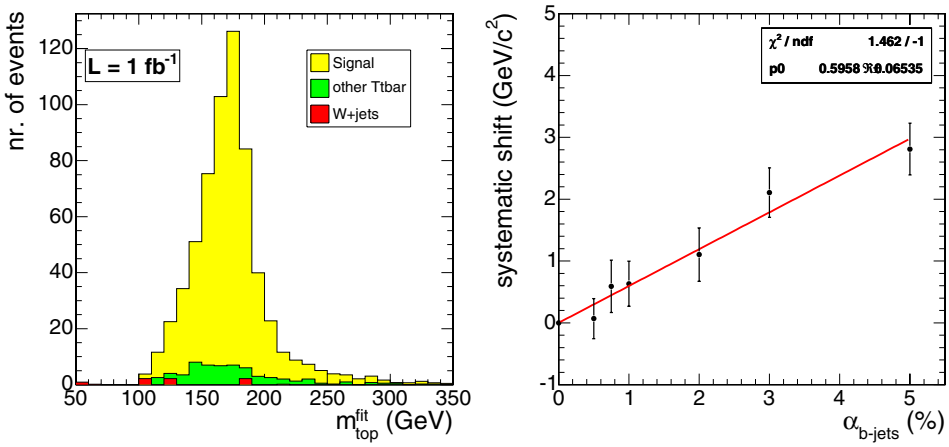

Figure 8.6. Left: Distribution of the mass of the hadronic decaying top quark for the selected events after applying the kinematic fit. Right: Estimated shift in $M_t^{FullIdeo}$ versus a relative shift α applied on the inclusive heavy quark jet energy scale.

where one integrates over the kinematic relevant range of m_t to obtain a likelihood function $\mathcal{L}_i(M_t)$ for each event i. Several contributions are added in the expected density $P(m_t|M_t)$: a Breit–Wigner shape for the correct jet combinations $S(m_t|M_t)$, a parameterised combinatorial background contribution $B_{comb}(m_t)$ and a parameterised background contribution $B_{proc}(m_t)$. This results in a function

$$P(m_t|M_t) = P_{sign} \cdot [P_{comb} \cdot S(m_t|M_t) + (1 - P_{comb}) \cdot B_{comb}(m_t)] + (1 - P_{sign}) \cdot B_{back}(m_t) \quad (8.2)$$

where each contribution is weighted according to the probabilities extracted from the observed event. After combining the likelihoods $\mathcal{L}_i(M_t)$ from all selected events, a maximum likelihood method is applied to obtain the best value for the estimator $\hat{M}_t$.

The linearity of the estimators have been checked and the slopes are found to be compatible with unity. The width of the pull distribution of the top quark mass estimators $\hat{M}_t$ are found to be 0.82 for $\hat{M}_t^{fit}$ (simple fit on reconstructed mass spectrum), 1.04 for $\hat{M}_t^{ParIdeo}$ (convolution with the parameterised ideogram) and 1.02 for $\hat{M}_t^{FullIdeo}$ (convolution with the full scanned ideogram). The resulting top quark mass for the estimator $\hat{M}_t^{fit}$ applied on the simulated events samples with a generated top quark mass of 175 GeV/c^2 is 174.16 ± 0.59 GeV/c^2, hence reflecting a bias of -0.84 GeV/c^2. For the convolution method this is 170.65 ± 0.54 GeV/c^2 and 172.42 ± 0.31 GeV/c^2 for respectively the $\hat{M}_t^{ParIdeo}$ and the $\hat{M}_t^{FullIdeo}$ estimator. Figure 8.7 illustrates the results.

Several systematic effects introduce an uncertainty on the top quark mass estimator. They originate from our understanding of the detector performance, the robustness of the reconstructed objects, for example jets, and the general description of the proton collisions in the simulation. A full description can be found in [292]. The estimation of the systematic uncertainties follows that of the cross section measurement in Section 8.1.3. We conservatively conclude that a total precision on the top quark mass of 1.9 GeV/c^2 can be reached with 10 fb^{-1} of data. The uncertainty is dominated by systematic effects like pile-up collisions and the knowledge of the jet energy scale of b-quark jets (see Fig. 8.6).

After achieving a better understanding of the accelerator settings and the detector performance, however, the total uncertainty will decrease. Our understanding of the

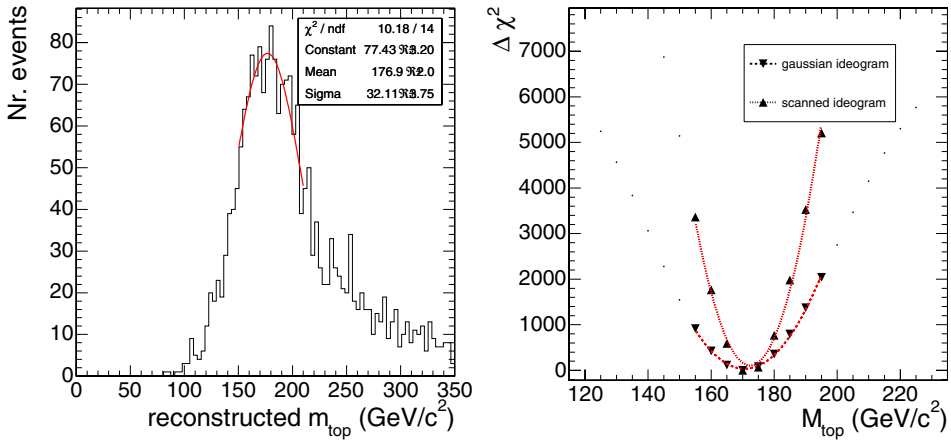

Figure 8.7. Distribution of the mass of the hadronic decaying top quark before the kinematic fit used for the $\hat{M}_t^{fit}$ estimator (left) and the combined $\Delta\chi^2(M_t)$ function over all events for both ideogram based estimators $\hat{M}_t^{ParIdeo}$ and $\hat{M}_t^{FullIdeo}$ (right).

underlying event model will improve in the future significantly when new tuning data become available. The magnitude of pile-up collisions could be monitored to the level of 10%. To take into account the overlap between the pile-up and the jet energy scale uncertainty, the systematic shift due to a 10% variation in the pile-up collisions is divided by two. The uncertainty on the energy scale of b-quark jets can be extrapolated to about 1.5% after a better understanding of the detector performance and with the application of advanced tools like energy flow algorithms or selecting jets only in well understood regions in the detector. The measurement of the b-tag efficiency [286] is dominated by systematic uncertainties of radiation effects. The experience at the Tevatron collider [288, 289] illustrates that an uncertainty of 2% could be reached.

Table 8.10 summarises and combines the extrapolated systematic uncertainties on each of the top quark mass estimators. The uncertainty on the inferred top quark mass of about $1.2\,\mathrm{GeV/c^2}$ is dominated by the uncertainty on the energy scale of the b-quark jets. This relative uncertainty is taken to be 1.5% which defines a goal for the performance of jet calibration methods.

8.2.3. Fully hadronic events

The selection described in Section 8.1.4.1, including the demand for the two b-tags, forms the basis for a selection of fully hadronic $t\bar{t}$ events suitable for a kinematic top-mass reconstruction. An additional cut on the two leading jets, $100\,\mathrm{GeV/c} < p_\mathrm{T} < 300\,\mathrm{GeV/c}$, is effective against background from mis-reconstructed events and combinatorial background.

The six partons in $pp \to t\bar{t} \to bW^+\bar{b}W^- \to bq_1\bar{q}_1'\bar{b}q_2\bar{q}_2'$ are matched to six reconstructed jets by picking the matching which minimises the sum of the angular separation between reconstructed jet and matched parton. Only jets satisfying our initial jet-definition, $p_\mathrm{T} > 30\,\mathrm{GeV/c}$ and $|\eta| < 2.4$, as employed in the selection, are taken into account in the matching process. Based on the amount of the angular separation three disjunctive classes of signal events are defined: good (36%), half-good (45%) and bad jet-parton-matching (19%). The first class being the events where all six partons are matched well by jets, the second class where only the three partons from one top are matched well by jets. The reason for the mismatch

Table 8.10. Overview of all uncertainty components on the top quark mass estimators, extrapolated to a better understanding of both the proton collisions at the LHC and the detector performance.

	Standard Selection		
	Gaussian Fit Δm_t (GeV/c^2)	Gaussian Ideogram Δm_t (GeV/c^2)	Full Scan Ideogram Δm_t (GeV/c^2)
Pile-Up (5%)	0.32	0.23	0.21
Underlying Event	0.50	0.35	0.25
Jet Energy Scale (1.5%)	2.90	1.05	0.96
Radiation (λ_{QCD}, Q_0^2)	0.80	0.27	0.22
Fragmentation (Lund b, σ_q)	0.40	0.40	0.30
b-tagging (2%)	0.80	0.20	0.18
Background	0.30	0.25	0.25
Parton Density Functions	0.12	0.10	0.08
Total Systematical uncertainty	3.21	1.27	1.13
Statistical Uncertainty (10 fb^{-1})	0.32	0.36	0.21
Total Uncertainty	3.23	1.32	1.15

Table 8.11. Distribution of the different signal event classes after jet-pairing and top-choice in the $t\bar{t}$ fully hadronic channel. The label column indicates whether the class is considered signal- or background-like.

reconstruction	pairing	[pb]	top-choice	[pb]	label
good	correct	0.62 (35%)	always correct	0.62(35%)	sig.
	wrong	0.26 (14%)	always wrong	0.26(14%)	bkg.
half-good	correct	0.46 (25%)	correct	0.33(18%)	sig.
			wrong	0.13(7%)	bkg.
	wrong	0.26(15%)	always wrong	0.26(15%)	bkg.
bad	always wrong	0.20 (11%)	always correct	0.20(11%)	bkg.

can be traced to parton-level properties, like high $|\eta|$ and low p_{T}, described in more detail in [279].

In order to perform the correct jet pairing, a likelihood variable is constructed from the following event observables: (a) average of the two W-boson masses, (b) difference of the two W-boson masses, (c) sum of the inter-jet angles of the W-boson candidates $\angle(q_1\bar{q}_1') + \angle(q_2\bar{q}_2')$, (d) difference of the two top-quark masses, (e) sum of the inter-jet angles of the top quark candidates $\angle(bq_1) + \angle(b\bar{q}_1') + \angle(q_1\bar{q}_1') + \angle(\bar{b}q_2) + \angle(\bar{b}\bar{q}_2') + \angle(q_2\bar{q}_2')$, (f) angle between the direction of the two top-quark candidates. Their distributions are shown in [279]. Taking for each event the pairing with the highest likelihood value yields pairing efficiencies of 71% for the good and 64% for the half-good jet-parton-matching.

Only one top per event is chosen for the kinematic mass determination, the choice is once again based on a likelihood variable constructed from the following event observables: (a) p_{T} of the softest of the three jets of each top-quark candidate (b) mass of the W boson as reconstructed in top decay (c) sum of the inter-jet angles of jets from top decay, $\angle(b_i q_i) + \angle(b_i\bar{q}_i') + \angle(q_i\bar{q}_i')$. Taking the top with the larger likelihood value yields a 72% efficiency, far greater than the 50% efficiency of a random choice.

The differentiation of the selected signal events into the now six classes is summarised in Table 8.11, where the six classes are being mapped onto two labels, indicating whether the events are considered signal- or background-like.

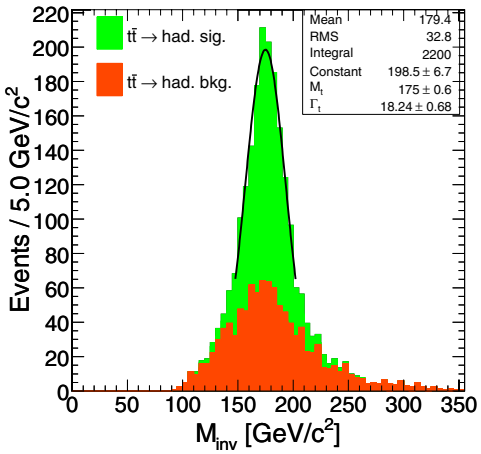

Figure 8.8. Invariant mass distribution of the reconstructed and rescaled, chosen top for both signal classes with a Gaussian fit to the peak.

Table 8.12. Summary of the systematics for the top-mass determination with fully hadronic events.

	Δm_t (GeV/c^2)
Pile Up	0.4
Underlying Event	0.6
PDF	1.4
IS/FS Radiation	2.3
Fragmentation	0.9
Jet Energy Scale	2.3
b-Tagging	0.3
Background	2.0

With all the pieces in place a kinematic reconstruction of the top quarks is straightforward and the resulting invariant mass distribution of the chosen top, with the paired non-b-jets rescaled such that they yield the W-mass, is shown in Figure 8.8.

As expected the signal-like events form a narrow peak, while the wrongly-reconstructed events have a far broader shape. Fitting a Gaussian to the peak of the invariant mass distributions with a fit range corresponding to 0.4 of the peak maximum, as shown in Fig. 8.8 serves as a simple mass estimator. The extracted top-mass is $m_t = 175.0 \pm 0.6(\text{stat.}) \pm 4.2(\text{syst.})\text{GeV/c}^2$ for an input top-mass of $175\,\text{GeV/c}^2$ and an integrated luminosity of $\mathcal{L} = 1\,\text{fb}^{-1}$.

Already with this amount of data the statistical error becomes negligible compared to the systematic uncertainties which are summarised in Table 8.12. One of the big systematic uncertainties is the QCD background. The S/B in the displayed mass window of Fig. 8.8 is about $2/3$, although not shown since the currently available number of simulated events does not allow a determination of the QCD background shape and of the uncertainty it introduces into the top-mass determination. Experience from CDF at the Tevatron [293, 294] indicates that this uncertainty can be understood at the $\sim 2\,\text{GeV/c}^2$ level, when using data for background estimation.

8.2.4. Top quark mass from J/ψ final states

8.2.4.1. Introduction. At the LHC the measurement of the top quark mass via direct reconstruction will soon be limited by systematic errors. It is expected that the most severe systematic contributions will be linked to the modelling of the hadronic environment and the knowledge of the jet energies. It would be particularly desirable, therefore, to consider methods for the extraction of m_t from the data which could reduce the contribution from these uncertainties considerably. An alternative method, which is making use of exclusive b decays in semi-leptonic top-pair events with the presence of a J/ψ decaying into an electron or muon pair was proposed in [295, 296].

The top quark mass is determined by its correlation with the invariant mass of the reconstructed J/ψ and the lepton from the W decay coming from the same top decay, $\mathrm{m}_{\mathrm{J}/\psi l}$. The correlation is present because the reconstruction of the J/ψ gives an accurate measurement of the b quark flight direction and its momentum thanks to the relatively high mass of the meson. Moreover, this measure is expected to have an excellent resolution because of the very clean experimental reconstruction of the lepton three-vectors. Details on the analysis presented here can be found in [297].

8.2.4.2. Event generation and selection. Signal events are generated using the TopReX generator [44] and consist of $t\bar{t}$ events where the presence of at least one J/ψ in the final state from the hadronisation of b-quarks is required. No distinction is made about the origin of the J/ψ; therefore the same samples also contains combinatorial background where the J/ψ is coming from a b quark produced together with a W boson decaying hadronically. Five samples corresponding to five different top masses are generated with a statistics of 200K events each. The event hadronisation and the description of the underlying event and the minimum bias is realised with PYTHIA 6.227 [24].

All the signal samples are passed through full detector simulation (ORCA) [10] with a simulation of the minimum bias corresponding to high luminosity data taking. Indeed, the statistics is expected to be so low that the use of high luminosity data must be considered. The same signal samples, and several millions more for studies on systematics, are passed through the fast simulation of the detector (FAMOS) [11]. The shape of the variables used in the selections are fully compatible in both scenarios.

The studied physics backgrounds are generated with the ALPGEN [161] generator and include W + jets, $Zb\bar{b}$ + jets, $Wb\bar{b}$ + jets. In these cases the samples are not biased by requiring an explicit J/ψ in the final state, therefore the separation from the signal is studied on the basis of cuts not involving the search for a J/ψ and the contribution of the resulting background is then rescaled taking into account the proper branching fractions. The selection, in terms of signal efficiency, is also cross-checked against $t\bar{t}$ + jets signal generated with ALPGEN, and is found to be consistent.

The main difficulty of the analysis comes from the extremely low branching ratio for a $t\bar{t}$ event to give a final state with a leptonic J/ψ. This can be written as:

$$BR(t\bar{t} \to (Wb)(Wb) \to (Xb)(\ell\nu J/\psi X)) = 2 \cdot BR(W \to \ell\nu) \cdot BR(b(\to X) \to B^{\pm,0}, B_s, B_{baryon} \to J/\psi X) \cdot BR(J/\psi \to \ell\ell) \quad (8.3)$$

where charge conjugation is implicit, ℓ indicates either an electron or a muon, and having assumed a $BR(t \to Wb)$ of 1. Replacing the branching ratios with up-to-date numbers [54] one gets for the global branching ratio the value $5.5 \cdot 10^{-4}$ that, in terms of event yield and assuming a cross section for $pp \to t\bar{t}$ of 830 pb, makes approximately 4500 events per $10\,\mathrm{fb}^{-1}$. This number does not include neither the trigger and selection efficiency, nor the efficiency for the correct pairing of the J/ψ to the correct lepton from the W decay.

Table 8.13. Selection performance on signal and expected backgrounds. The first column indicates the channel and its final state, the second the predicted cross section, where the branching ratio for producing at least a J/ψ into leptons from either a b jet or a light jet is accounted for, the third the trigger efficiency, the fourth the selection efficiency, the fifth the expected number of events in 10 fb^{-1}, the sixth the classification of the contribution as signal (S), physics background (B) or combinatorial background (C).

Channel	BR .σ (fb)	ε_{trig} (%)	ε_{sel} (%)	Events in 10 fb^{-1}	Class
$t\bar{t} \to (b \to J/\psi)\ell\nu - b\ell\nu$	107	93.9	15.7 ± 0.4	158	S+C
$t\bar{t} \to (b \to J/\psi)\ell\nu - b\tau\nu$	53	61.1	11.0 ± 0.8	36	S
$t\bar{t} \to (b \to J/\psi)\ell\nu - bqq$	320	55.3	10.9 ± 0.3	193	S
$t\bar{t} \to (b \to J/\psi)\tau\nu - b\ell\nu$	53	61.1	10.6 ± 0.8	34	C
$t\bar{t} \to (b \to J/\psi)\tau\nu - b\tau\nu$	27	14.2	2.8 ± 1.2	1	B
$t\bar{t} \to (b \to J/\psi)\tau\nu - bqq$	160	7.9	1.5 ± 0.5	2	B
$t\bar{t} \to (b \to J/\psi)qq - b\ell\nu$	320	55.3	10.7 ± 0.3	190	C
$t\bar{t} \to (b \to J/\psi)qq - b\tau\nu$	160	7.9	1.5 ± 0.5	2	B
$t\bar{t} \to (b \to J/\psi)qq - bqq$	959	0.1	0.2 ± 0.5	0	B
$W + N$ jets, $N > 1 \to J/\psi X$	394	55.3	2.1 ± 0.1	43	B
$Wb\bar{b}$ + jets $\to J/\psi X$	196	55.3	1.6 ± 0.1	16	B
$Zb\bar{b}$ + jets $\to J/\psi X$	23	93.9	9.4 ± 0.1	20	B
$b\bar{b} \to J/\psi X$	$1.3 \cdot 10^9$	$< 2 \cdot 10^{-8}$	< 1	< 2.6	B

Events are triggered using the inclusive lepton trigger with thresholds described in [76]. The efficiency for triggering signal events is reported in Table 8.13 and is included in all numbers presented here. In events passing the trigger thresholds a J/ψ is searched for by looking for same-flavour, opposite-sign leptons with invariant mass in the range [2.8,3.2] GeV/c^2 and forming an angle greater than 2 and lower than 35 degrees. No isolation requirements must be imposed on these leptons. The efficiency for reconstructing a J/ψ at this stage is (0.386 ± 0.007) and (0.114 ± 0.004) for the muon and electron channels, respectively. It is limited by the low momenta of the leptons and because they are produced inside a jet, making the reconstruction more difficult, particularly for electrons.

If a J/ψ is found in an event, the isolated lepton with the highest p_{T} and higher than 20 GeV/c is considered as the lepton candidate from the W decay. The isolation discriminant is defined as the sum of the energies in the electromagnetic and hadronic calorimeters in a cone of opening angle $\Delta R = 0.3$ around the lepton candidate. The selection requires that the isolation energy is less than 15 GeV for electrons and less than 20 GeV for muons.

We define as background all contributions from processes not resulting in the decay chain $t \to Wb \to \ell\nu J/\psi X$. We call physics background the contribution from processes other than $t\bar{t}$ (semi)leptonic and as combinatorial background the irreducible part of $t\bar{t}$ (semi)leptonic where the J/ψ is wrongly associated to the lepton not coming from the W in the same top decay. Any physics background needs to mimic a final state with the presence of a J/ψ and an isolated and energetic lepton. The obvious candidates are bosons in association with jets. It is important to distinguish between b jets and light jets, which produce J/ψ at very different rates, suppressing the contribution of processes with light jets very much. To remove these contributions the total scalar sum of the transverse jet momenta is required to be greater than 100 GeV/c. This cut is not applied if two isolated leptons are found, in order to preserve dileptonic $t\bar{t}$ events. If the flavour of the two leptons is the same, an explicit cut to remove the presence of leptonic Z is made, vetoing events where the invariant mass of the two leptons is between 85 and 97 GeV/c^2. To further reduce soft background the cut on the transverse momentum of the isolated lepton is brought to 40 GeV/c, making the analysis less sensitive

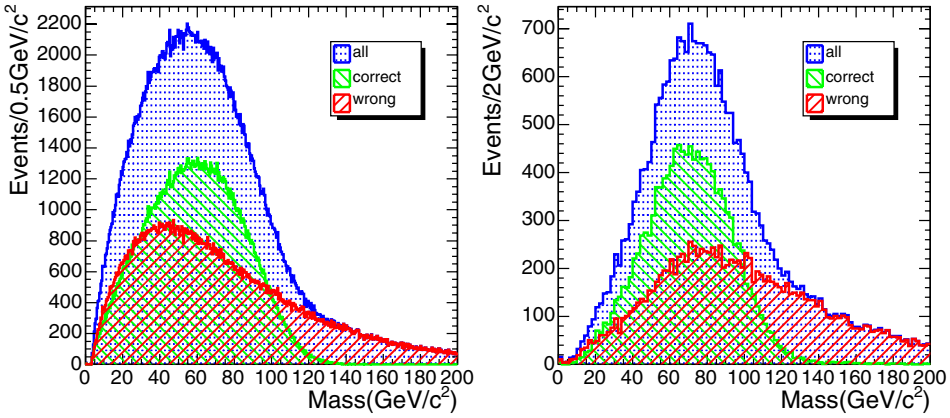

Figure 8.9. Three-lepton mass distribution for $m_t = 175\,\mathrm{GeV/c^2}$ at generator level (left) and after detector simulation and reconstruction (right). In the pictures the components coming from correct and wrong lepton pairing - from both combinatorial and physics backgrounds - are shown.

also to systematic effects involving soft QCD. Table 8.13 presents, in terms of predicted cross sections, efficiencies and events yields per $10\,\mathrm{fb}^{-1}$, the performance of the analysis.

8.2.4.3. Reconstruction of $\mathrm{m}_{J/\psi\ell}$ *and statistical performance.* In order to estimate the correct invariant mass J/ψ-lepton it would be necessary to efficiently discriminate between right pairings, where both particles are coming from the decay of the same top, and from wrong pairings where, in $t\bar{t}$ events, they come from the two different top decays. In the present analysis, in order to increase the available statistics, we propose not to attempt any separation of the combinatorial but, instead, to use the full distribution containing both signal and background.

Figure 8.9 shows the three-lepton invariant mass in $t\bar{t}$ events at generator level without selection and at full reconstruction after the selection described in the previous section. The distribution of the components of signal and background from $t\bar{t}$ are shown, where the Monte Carlo truth is used to judge when the correct pairing is made. No equivalent distribution can be done for non-$t\bar{t}$ backgrounds since no J/ψ is present in those samples. To take this into account the pure background shape is scaled up according to the extra contribution of non $t\bar{t}$ background (Table 8.13), in the hypothesis that the shape of the two samples are the same. Uncertainty in the background description will then be translated into a systematic contribution on the measurement.

The observable most sensitive to the top mass is the position of the maximum of the three-lepton mass distribution. It is determined via a fit of the full shape with a polynomial function of fourth degree. The range chosen for the fit is centred around the maximum and goes from 20 to 120 $\mathrm{GeV/c^2}$. The error on the maximum of the fitted polynomial is determined by propagating the errors on the fitted coefficients and taking into account their correlation. As a cross check, an alternative way of fitting the signal with a Gaussian was tried. In this case the background is first subtracted on a bin-by-bin basis making use of an average background distribution determined by using all the simulated samples. The results obtained are comparable.

The fitted maxima are expected to be correlated to the input value of the top mass. This correlation is proven and fitted by a line (Fig. 8.10). The two results at fast and full simulation are in impressive agreement. The correlation curves can be used to estimate the expected

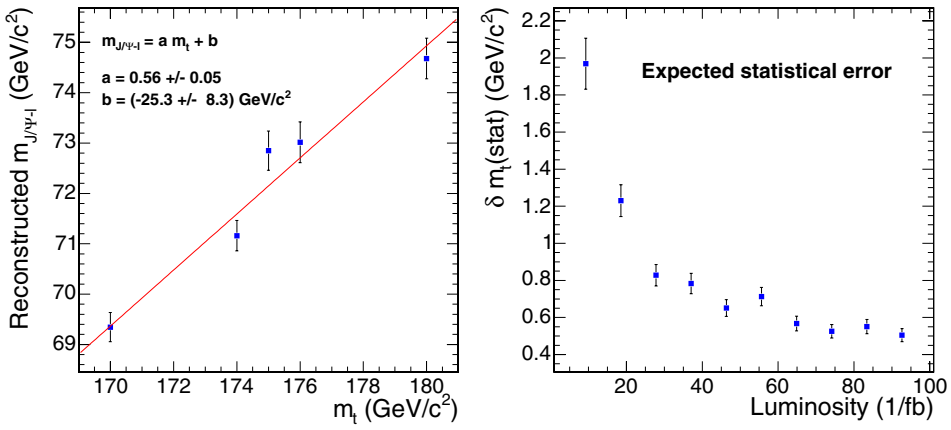

Figure 8.10. Left: correlation between the reconstructed three-lepton invariant mass and the input top mass at full simulation. Right: expected statistical error on the top quark mass as a function of the integrated luminosity.

statistical error on the top mass as a function of the available amount of data. This is done by using the number of events expected according to Table 8.13, and the result is presented in Fig. 8.10. From the figure it can be concluded that the measurement of the top quark mass with this analysis can become, on the statistical footing, competitive already with other analyses' total error after the first years of data taking. Moreover the measurement is expected to be dominated by systematic errors in the long range, as explained in the next section.

8.2.4.4. Systematic errors. The sources of systematic errors can be divided into two main categories: theoretical and experimental. The former include the description of the hard process and the modelling of radiation, fragmentation and the underlying event in the simulation, whereas the latter includes all experimental sources coming from an imperfect detector description. The sources analysed in what follows are considered as uncorrelated and the corresponding resulting errors on the top mass are summed in quadrature to form the total systematic error. To evaluate the effect of various sources the guidelines described in [201] and in Appendix B are followed.

With the exception of the PDF description, for each of the other sources of theoretical uncertainty and for each change in the simulation parameters an independent signal generation with TOPREX and PYTHIA has been performed, with statistics of a few 100K events each, and fast simulated. The variations on the resulting top masses are considered as systematics: when the mass difference with respect to the reference sample is smaller than the associated statistical error, this is conservatively quoted as the systematic error.

For all the experimental sources, smearings and shifts on the observed objects (leptons and jets) are applied after reconstruction and before selection in a consistent way. The observed difference on the top mass is taken as an estimation of the associated systematic uncertainty.

Table 8.14 presents the systematic breakdown on the top mass. The systematics error is dominated by theoretical sources, which are the ones affected by the larger statistical uncertainties, quoted here as systematics.

Putting together the systematic and the statistical error one can conclude that, with maybe exception for the first year of data taking, this measurement will be dominated by systematics,

Table 8.14. Systematic error breakdown. For each source either the maximum variation from a reference sample or the resulting statistical error on the difference is quoted as a systematic error.

Source	δm_t (GeV/c^2)
Λ_{QCD}	0.31
Q^2	0.56
Scale definition	0.71
b-quark fragmentation	0.51
Light jet fragmentation	0.46
Minimum bias/Underlying event	0.64
Proton PDF	0.28
Total theoretical	1.37
Electron E scale	0.21
Muon p scale	0.38
Electron E resolution	0.19
Muon p resolution	0.12
Jet E scale	0.05
Jet E resolution	0.05
Background knowledge	0.21
Total experimental	0.54
Total systematic	1.47

in turn dominated by our poor understanding of the theoretical sources. A total error on the top mass below 2 GeV/c^2 can be in reach from the first 20 fb^{-1} already. The present result suggests an uncertainty of 1.5 GeV/c^2 with full statistics, but this number is fully dominated by the theory systematics. A precision much better than this is not out of reach since, by the time this measurement will be made, the analysis will be hopefully repeated at (N)NLO and our understanding of the dominating systematics, for instance the minimum bias and the underlying event, will be drastically improved. More dedicated reconstruction techniques and more sophisticated analyses will considerably improve the statistical treatment of the information.

This analysis reduces to a minimum those systematics which are expected to dominate in more traditional estimations of the top mass, especially the ones from direct reconstruction, like the jet energy scale and the knowledge of the b-tagging.

8.2.5. Summary of top mass determinations

Measuring the mass of the top quark in different channels allows for a combination of the individual results [298]. As the statistical component in the total uncertainty on m_t in each channel is negligible, the correlation between the systematic uncertainties must be determined. The dominant uncertainty arises from the knowledge of the energy scale of b-quark jets, a component which is assumed to be fully correlated between decay channels. This uncertainty can however be subdivided in several components: detector understanding, clustering algorithms, related to the modelling of b- and light-quark fragmentation and decay and, finally, the statistical precision of the data-based estimates of the b-jet energy scale differentiated versus the pseudo-rapidity and the transverse momentum of the observed jet.

The measurement from the J/ψ final states is however limited by other, mainly theoretical, sources of systematic uncertainties. Therefore a reduction of the uncertainty on m_t is expected when combining the direct measurements with the measurement from the J/ψ final states. The knowledge of the top quark mass can be improved by developing alternative

methods which do not rely on the b-jet energy scale [299, 300]. Accounting for these future improvements an uncertainty of 1 GeV/c^2 on the top quark mass is feasible. The combination can be performed by applying techniques described in [301, 302].

8.3. Spin correlation in top-quark pair production

8.3.1. Introduction

Because of its large width of 1.4 GeV/c^2 the top quark decays before either hadronisation, governed by the scale Λ_{QCD}, or depolarisation, governed by the scale Λ^2_{QCD}/m_t, can take place. This unique feature is used to investigate the spin of the top quark; such investigation is not possible in the case of light quarks, where the spin information is diluted by hadronisation. Moreover, the top quark spin-flip time is much larger than its lifetime and the probability of a spin flip due to emission of one or several gluons via chromomagnetic dipole-transition is very small.

The angular distribution of a daughter particle in top quark decays can be written as [303–305]

$$\frac{1}{\Gamma}\frac{d\Gamma}{d\cos\theta_i} = \frac{1}{2}(1+\kappa_i\cos\theta_i), \tag{8.4}$$

where the decay angle θ_i is defined as the angle between the direction of motion of the daughter particle i and the chosen spin quantisation axis. As gluon fusion is the dominant production mechanism at the LHC there is no well defined spin axis in the initial state. This leads to a choice of the helicity basis along the top quark momenta in the partonic centre-of-mass frame. The spin-analyser quality κ of the top quark daughter particle is defined as the degree to which the daughter particle is correlated with the top-quark spin. The analysis presented here is based on the semi-leptonic $t\bar{t}$ decay channel with electrons or muons, which is considered to be the signal. Alternatively, the dileptonic $t\bar{t}$ decay channel can also be considered. The κ values for the daughter particles used in this analysis [306], lepton, b quark and the lower energy quark from W decay, are 1, -0.41 and 0.51, respectively.

The spin correlation in the semi-leptonic $t\bar{t}$ decay channel can be measured in terms of a double differential lepton and quark angular distribution, which, neglecting higher order QCD corrections, is given by

$$\frac{1}{N}\frac{d^2N}{d\cos\theta_l\, d\cos\theta_q} = \frac{1}{4}(1-\mathcal{A}\kappa_l\kappa_q\cos\theta_l\cos\theta_q). \tag{8.5}$$

Here, using the helicity basis the lepton and quark angles θ_l and θ_q are obtained by measuring the angle between the decay particle momentum in its parent top quark rest frame and the parent top quark momentum in the $t\bar{t}$ quark pair rest frame. The correlation coefficient

$$\mathcal{A} = \frac{N_{||}-N_X}{N_{||}+N_X} = \frac{N(t_L\bar{t}_L+t_R\bar{t}_R)-N(t_L\bar{t}_R+t_R\bar{t}_L)}{N(t_L\bar{t}_L+t_R\bar{t}_R)+N(t_L\bar{t}_R+t_R\bar{t}_L)}, \tag{8.6}$$

where $N_{||}$ and N_X give the number of events with parallel and anti-parallel top quark spins, respectively. Two angle combinations are considered: θ_l versus θ_b and θ_l versus $\theta_{q(\textit{lower energy})}$; in the following description these two combinations are denoted as $b-tl-t$ and $q-tl-t$.

8.3.2. Simulation of $t\bar{t}$ with spin correlation

A $t\bar{t}$ sample of $3.1\cdot10^6$ events containing $9.1\cdot10^5$ semi-leptonic signal events was generated with PYTHIA [24] and reconstructed using ORCA. As PYTHIA does not include spin correlations

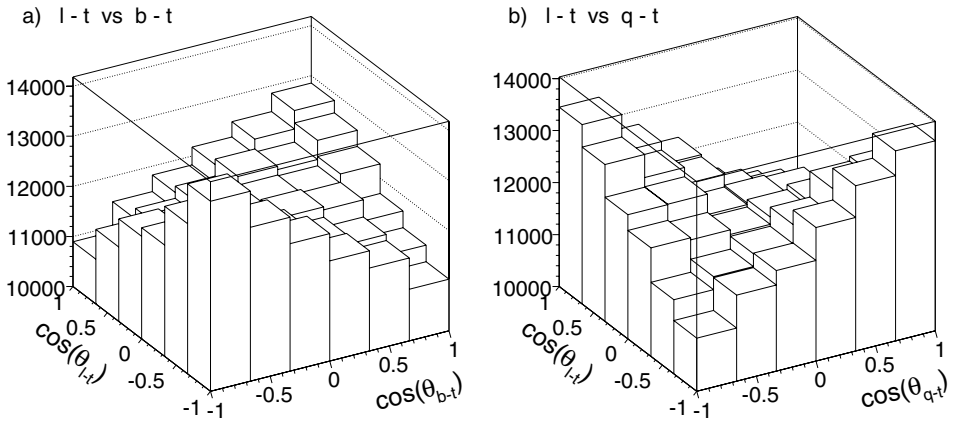

Figure 8.11. Double differential angular distributions obtained from the "analysis" sample, see text.

the events are weighted according to Equation (8.5) with $\mathcal{A} = 0.32$ [44] and appropriate values of κ. Then, this data sample is subdivided into two sub-samples: one is regarded as the "reference" sub-sample (1.61M events), used for determination of the selection efficiency and backgrounds. The other is regarded as the "analysis" sub-sample (1.50M events), used for the measurement of $\mathcal{A}$. This sample provides 436K signal events. The double differential angular distributions obtained from the "analysis" sample are presented in Figure 8.11.

The distributions in Figure 8.11 are fitted according to Equation (8.5). The results are $\mathcal{A}_{b-t\,l-t} = 0.321 \pm 0.011$ (stat.) and $\mathcal{A}_{q-t\,l-t} = 0.319 \pm 0.009$ (stat.) which are statistically compatible with the input value of $\mathcal{A} = 0.32$.

8.3.3. Online and offline event selection

The Level 1 and High Level Triggers select events with a single isolated electron or muon; the trigger efficiency is 55%.

The following requirements are applied in the offline selection: missing transverse energy $E_{\mathrm{T}}^{\mathrm{miss}} > 20\,\mathrm{GeV}$; at least one isolated lepton with $|\eta| < 2.5$, electron with $p_{\mathrm{T}} > 27\,\mathrm{GeV/c}$ or muon with $p_{\mathrm{T}} > 20\,\mathrm{GeV/c}$; at least four jets with $p_{\mathrm{T}} > 30\,\mathrm{GeV/c}$ and $|\eta| < 2.5$. Jets are reconstructed with a cone algorithm with $\Delta R = 0.5$. At least two jets must be b-jets where the tagging efficiency is 66% for b quarks in $t\bar{t}$ events. This selection results in an overall efficiency of 12%.

The reconstruction of two top quarks includes the following requirements: Two jets that are not b-tagged and have an invariant mass in the range 50–135 $\mathrm{GeV/c^2}$, consistent with the W mass, are found. A b-tag jet which combined with the above reconstructed W gives an invariant mass in the range 130–250 $\mathrm{GeV/c^2}$, consistent with the t mass. In addition to the top quark reconstructed above, another top quark is required based on the other b-tag jet plus lepton and missing energy combination. The neutrino components are determined by fitting the missing energy components, constrained with W and t quark masses. The azimuthal angle between the two top quarks is required to be greater than 2 rad. This selection results in an overall efficiency of 5% (Table 8.15).

A measure of the selection quality can be obtained by comparing the generated and reconstructed momentum directions expressed in terms of the cosine of the angles defined above. Figure 8.12 presents the differences between the generated and reconstructed cosines

Table 8.15. The physics processes considered for signal and background. The number of selected events for the non-$t\bar{t}$ processes are scaled to the same $t\bar{t}$ sample luminosity.

Process	Simulated events	σ(pb)	Efficiency	Selected events
$t\bar{t}$ (signal)	436K	246	$5.0 \cdot 10^{-2}$	21589
$t\bar{t}$ (background)	1.07M	584	$4.0 \cdot 10^{-3}$	4236
WW + jets	310K	188	$4.5 \cdot 10^{-5}$	15
W + jets($\hat{p}_{\mathrm{T}} = 20{-}400$ GeV/c)	2.06M	43K	$3.4 \cdot 10^{-6}$	260
Wbt semi-leptonic decay	328K	63.1	$1.3 \cdot 10^{-3}$	144

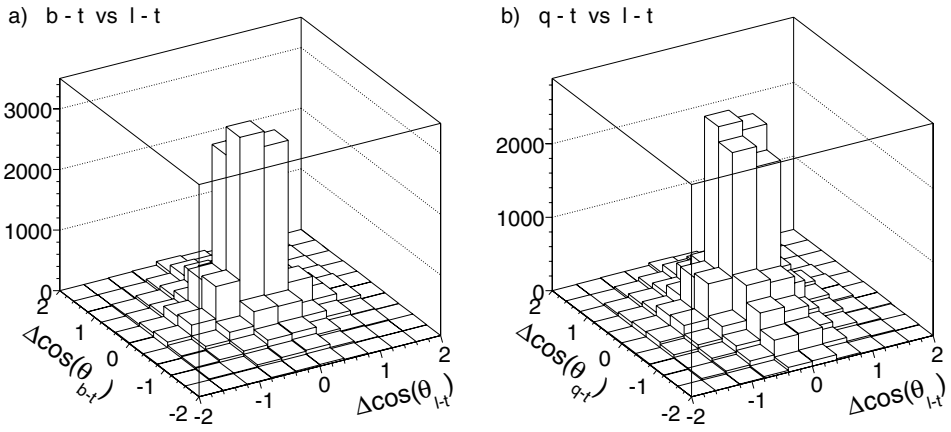

Figure 8.12. Selection quality: Difference between the generated and reconstructed cosine of the analysis angles in the $b-ll-t$ and $q-ll-t$ systems.

of the $b-ll-t$ and $q-ll-t$ systems. Quantifying this selection quality Q as the ratio of the number of events in the four central bins to all bins, one obtains: $Q_{b-tl-t} = 52\%$ and $Q_{q-tl-t} = 45\%$.

The signal-to-background ratio is 4.5. The main background, detailed in Table 8.15, is $t\bar{t}$ production with decays different from those treated as the signal. It amounts to 88% of the total background and is used to model the shape of the total background.

8.3.4. Estimation of correlation coefficient

In order to correct for the selection efficiency, an efficiency (6×6) matrix is determined by taking the ratio of the reconstructed double differential angular distribution to the generated one, using the "reference" sample. The final double differential angular distribution is obtained by subtracting, bin-by-bin, the background obtained from the "reference" sample from the total sample of signal plus background obtained from the "analysis" sample. The resulting distributions are corrected for the selection efficiency, Figure 8.13, and fitted using Equation (8.5).

The correlation coefficients obtained from the fit are:

$$\mathcal{A}_{b-t\,l-t} = 0.375 \pm 0.100(\mathrm{stat}),$$
$$\mathcal{A}_{q-t\,l-t} = 0.346 \pm 0.079(\mathrm{stat}).$$

These results agree, within statistical uncertainties, with those obtained from the generated events of Figure 8.11.

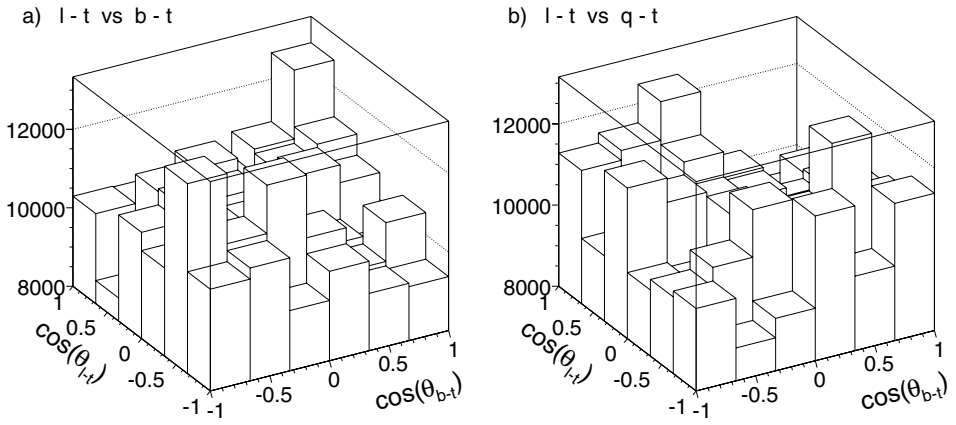

Figure 8.13. Background-subtracted and efficiency-corrected double-differential distribution of the cosine of the analysis angles in the $b-ll-t$ and $q-ll-t$ systems.

The following sources of systematic uncertainties have been evaluated. The choice of the Parton Distribution Function in modelling $t\bar{t}$ production affects the number of $t\bar{t}$ events produced via gluon fusion and that via quark-anti-quark annihilation. The relative variation in $\mathcal{A}$, determined using TopReX with different PDFs (CTEQ6M, MRST2003), is found to be 4%.

The mass of the top quark affects the result of the kinematic fit and the selection. The nominal $m_t = 175\,\mathrm{GeV/c^2}$ is varied by $\pm 5\,\mathrm{GeV/c^2}$ [54] using TopReX. The variation in $\mathcal{A}$ is found to be negligible.

The uncertainty on the $t\bar{t}$ cross section affects the shape of the final angular distribution after background subtraction; varying $\sigma(t\bar{t})$ by 10% results in 1% relative variation in correlation coefficients.

The uncertainty due to b-tagging efficiency is evaluated by varying the b-identification discriminant cut. The corresponding relative variation in $\mathcal{A}_{b-t\,l-t}$ is -20%, and in $\mathcal{A}_{q-t\,l-t}$ it is $+6.5\%/-8.3\%$.

The jet energy scale uncertainty is evaluated by varying the jet P_{T}. The relative variations in $\mathcal{A}_{b-t\,l-t}$ and $\mathcal{A}_{q-t\,l-t}$ are found to be $+7.7\%/-14\%$.

Uncertainties in the initial and final state radiation, quark fragmentation, underlying event and pile up rate could result in an underestimation of the number of non-$t\bar{t}$ jets (not originating from top decays). This possible underestimation of jet multiplicity is estimated to be 8%. To estimate the corresponding uncertainty in $\mathcal{A}$, 10% additional jets per event are generated while processing the data sample. These jets are simulated randomly according to the η and p_{T} distributions of non-$t\bar{t}$ jets, obtained from the $t\bar{t}$ Monte Carlo. The relative variations in $\mathcal{A}_{b-t\,l-t}$ and $\mathcal{A}_{q-t\,l-t}$ are found to be -6.3% and -5.3%, respectively.

Summing up the systematic uncertainties and using the statistical uncertainties estimated for $10\,\mathrm{fb}^{-1}$ of integrated luminosity, the results are:

$$\mathcal{A}_{b-t\,l-t} = 0.375 \pm 0.027(\mathrm{stat.})^{+0.055}_{-0.096}(\mathrm{syst.}),$$
$$\mathcal{A}_{q-t\,l-t} = 0.346 \pm 0.021(\mathrm{stat.})^{+0.026}_{-0.055}(\mathrm{syst.}).$$

In summary, the correlation coefficient of top quark spins in $t\bar{t}$ production is measured with a total relative uncertainty (dominated by systematic uncertainties) of 27% for $\mathcal{A}_{b-t\,l-t}$ and of 17% for $\mathcal{A}_{q-t\,l-t}$.

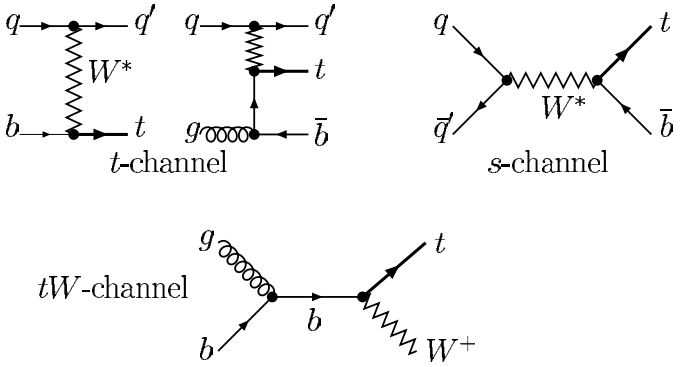

Figure 8.14. Feynman diagrams for the three channels of single top production.

8.4. Single top quark production

8.4.1. Introduction

The single top production cross section at the LHC is known at NLO level for the tree production mechanisms (see Fig. 8.14, which are classified by the virtuality of the W-boson involved as: t-channel ($q^2_W < 0$), s-channel ($q^2_W > 0$), and associated tW production ($q^2_W = M^2_W$) [307–309]. In all cases, the most dangerous background comes from $t\bar{t}$ process. Other dangerous backgrounds are multi-jet QCD and W+jets events, but such background is reduced substantially by considering only leptonic decays of the $W^{\pm}$-bosons from top-quark decays.

All results presented in this Section were done for $10/\text{fb}^{-1}$ of integrated luminosity.

8.4.1.1. Details on the signal and background simulation. Two generators, SINGLETOP [310] (based on the COMPHEP package [43]) and TOPREX [44] were used to generate events for all three single-top production processes. The background processes, namely, $Wb\bar{b}$, $Wb\bar{b}+j$, and $W+2j$ were generated with COMPHEP, TOPREX, MADGRAPH [81], and ALPGEN [161] programs as indicated in the Table 8.16. The hard process events containing all needed information were passed to PYTHIA 6.227 [24] for showering, hadronisation and decays of unstable particles. The $t\bar{t}$ and $W+$jets background events were generated with the same PYTHIA version. All simulations were done with $M_t = 175\,\text{GeV/c}^2$ and $M_b = 4.7$–$4.8\,\text{GeV/c}^2$, proper considerations of the spin correlations, and the finite W-boson and t-quark widths. The list of the signal and background process cross sections as well as generators used are given in the Table 8.16. Both the full simulation chain (OSCAR [18] and ORCA [10]) and a fast simulation (FAMOS [11]) were used.

8.4.1.2. Reconstruction algorithms and triggers. Muons are reconstructed by using the standard algorithm combining tracker and muon chamber information as described in [311]; tracker and calorimeter isolation cuts are applied as described in [312]. The electrons are reconstructed by the standard algorithm combining tracker and ECAL information, see [313]. The jets are reconstructed by the Iterative Cone algorithm with the cone size of 0.5, see [314]; for the calibration both the Monte Carlo (in the t-channel analysis) and the $\gamma+$jets (in the tW- and s-channel) methods are used, see [315]. For b-tagging a probability algorithm based on the impact parameter of the tracks is used, as described in [316].

Table 8.16. Cross section values (including branching ratio and kinematic cuts) and generators for the signal and background processes (here $\ell = e, \mu, \tau$). Different generator-level cuts are applied.

Process	$\sigma \times$ BR, pb	generator	Process	$\sigma \times$ BR, pb	generator
t-ch. ($W \to \mu\nu$)	18 (NLO)	SINGLETOP	$Wb\bar{b}$ ($W \to \ell\nu$)	100 (LO)	TOPREX
t-ch. ($W \to \ell\nu$)	81.7 (NLO)	TOPREX	$Wb\bar{b}$ + jets ($W \to \mu$)	32.4 (LO)	MADGRAPH
s-ch. ($W \to \ell\nu$)	3.3 (NLO)	TOPREX	$W + 2j$ ($W \to \mu\nu$)	987 (LO)	COMPHEP
tW ($2\ W \to \ell\nu$)	6.7 (NLO)	TOPREX	$W + 2j$ ($W \to \ell\nu$)	2500 (LO)	ALPGEN
tW ($1\ W \to \ell\nu$)	33.3 (NLO)	TOPREX	$Z/\gamma^*(\to \mu^+\mu^-)b\bar{b}$	116 (LO)	COMPHEP
$t\bar{t}$ (inclusive)	833 (NLO)	PYTHIA			

The **transverse missing energy** is reconstructed as follows:

$$\vec{E}_{\mathrm{T}}^{\mathrm{miss}} = -\left(\sum \vec{P}_{\mathrm{T}}^{\mu} + \sum \vec{E}_{\mathrm{T}}^{\mathrm{tower}} + \sum (\vec{E}_{\mathrm{T,jet}}^{\mathrm{calib}}) - \sum (\vec{E}_{\mathrm{T,jet}}^{\mathrm{raw}})\right) \tag{8.7}$$

where $E_{\mathrm{T}}^{\mathrm{tower}}$ is the sum of transverse energy of towers, $E_{\mathrm{T,jet}}^{\mathrm{calib}}$ ($E_{\mathrm{T,jet}}^{\mathrm{raw}}$) is the transverse energy of calibrated (uncalibrated) jets. For the final states with one isolated lepton the neutrino ($E_{\mathrm{T}}^{\mathrm{miss}}$) longitudinal component, $P_{z,\nu}$, is extracted from the quadratic equation:

$$M_W^2 = 2\left(E_\mu \sqrt{P_{z,\nu}^2 + (E_{\mathrm{T}}^{\mathrm{miss}})^2} - \vec{P}_{\mathrm{T},\mu} \cdot \vec{E}_{\mathrm{T}}^{\mathrm{miss}} - P_{z,\mu} P_{z,\nu}\right) \tag{8.8}$$

This equation has two solutions:

$$P_{z,\nu}^{(1,2)} = \frac{A P_{z,\mu} \pm \sqrt{\Delta}}{P_{\mathrm{T},\mu}^2}, \quad \text{where} \quad A = \frac{M_W^2}{2} + \vec{P}_{\mathrm{T},\mu} \cdot \vec{E}_{\mathrm{T}}^{\mathrm{miss}},$$
$$\Delta = E_\mu^2 (A^2 - (E_{\mathrm{T}}^{\mathrm{miss}})^2 P_{\mathrm{T},\mu}^2) \tag{8.9}$$

Among the two solutions of Equation (8.8) the minimal value of $|P_{z,\nu}|$ is used for W-boson momentum reconstruction.

About 30% of the events have negative Δ values due to the finite detector resolution and to the presence of extra missing energy. In this case for t-channel analysis the parameter M_W in Equation (8.9) is increased until Δ becomes zero. Using this value of M_W, $P_{z,\nu}$ is calculated from Equation (8.9). For the tW and s-channels analyses, only the real part of $P_{z,\nu}$ is used for further analysis.

The **transverse mass of the$W$-boson** is defined as

$$M_{\mathrm{T}}^W = \sqrt{2(P_{\mathrm{T},\mu} E_{\mathrm{T}}^{\mathrm{miss}} - \vec{P}_{\mathrm{T},\mu} \cdot \vec{E}_{\mathrm{T}}^{\mathrm{miss}})}. \tag{8.10}$$

The **sum of the transverse momentum vectors** of all reconstructed objects

$$\vec{\Sigma}_{\mathrm{T}} \equiv \vec{P}_{\mathrm{T},\ell} + \vec{E}_{\mathrm{T}}^{\mathrm{miss}} + \sum \vec{E}_{\mathrm{T},jet}, \tag{8.11}$$

is found to be very effective for signal/background separation.

The **"jet charge"** (Q_j) is defined as the sum of the charges of the tracks inside the jet cone, weighted over the projections of the track momenta along the jet axis.

The **lepton isolation** criterion used is to sum the p_{T} of all the tracks in a cone of $\Delta R < 0.2$ around the lepton track, and to reject the event if this sum is greater than 5% of the lepton p_{T}.

The present study is based on leptonic decay channels ($e\nu_e$ or $\mu\nu_\mu$) of the W-boson. The signal is triggered by the trigger on leptons. The HLT p_{T} thresholds from the CMS DAQ-TDR [76] are assumed: 19 GeV/c (29 GeV/c) for the single muon (electron); with $|\eta_\mu| \leqslant 2.1$ and $|\eta_e| \leqslant 2.4$.

8.4.1.3. The contribution from multi-jet backgrounds. A special treatment is required for QCD events with jets, due to the huge cross section. The currently available samples have very small statistics and typically no events remain after the application of pre-selection cuts. Therefore, in order to estimate the impact of the QCD-background the cuts are applied separately, assuming they are uncorrelated.

For t-channel study these cuts are: (a) one isolated muon ($p_{\mathrm{T}} > 19\,\mathrm{GeV/c}$); (b) $E_{\mathrm{T}}^{\mathrm{miss}} > 40\,\mathrm{GeV}$ and only two jets; one B-jet and one light forward jet. It was found a satisfactory suppression of the multi-jet events as compared to other background process ($N_{\mathrm{QCD}}/N_{\mathrm{bckg}} = 6924/(8.9 \times 10^4) = 0.078$ (see [317]) and the QCD-background was not considered in the analysis of the t- and s-channel single top production.

More detailed investigation of this problem was done for tW-channel [318]. The selection cuts are arranged into cut groups whose efficiencies are estimated with the Monte Carlo samples. The product of efficiencies is an indicator of the total efficiency.

Three cut groups are used in the dileptonic channel: lepton, $E_{\mathrm{T}}^{\mathrm{miss}}$, jet. The same procedure is applied on signal sample to find the ratio of total efficiency to the product of efficiencies. The ratio is used to correct the product of efficiencies found in multi-jet sample and the result is 5.6 events. Four cut groups are used in the semi-leptonic channel: jets, leptons, kinematics and finally signal region and b tagging. The b tagging requirement is taken out from jets group to have reasonable statistics for the efficiency measurement. By comparing the product of efficiencies with total efficiency of applying cut groups in series, the cut groups are found to be anti-correlated which would result in an over-estimate of the yield. The result of 508 events is kept to be conservative [318].

8.4.1.4. Systematic uncertainties. The following sources of systematic uncertainty are common for all three channels: (i) the **theoretical errors** to the total rates of the signal is $\Delta_{\mathrm{th}} \approx 4\%$, rising to 10% for tW. The uncertainties in the background events are assumed to be: 5% for $t\bar{t}$ [45], 17% for $Wb\bar{b}j$, 7% for W + jets, 5% for Wjj [319], and 5% for $Wb\bar{b}$. (ii) the **jet energy scale (JES) uncertainty:** using a calibration method based on $t\bar{t}$ events [320], the JES uncertainty after $10\,\mathrm{fb}^{-1}$ integrated luminosity is expected to be $\pm 5\%$ ($\pm 2.5\%$) for jets with $p_{\mathrm{T}} \approx 20\,\mathrm{GeV/c}$ ($p_{\mathrm{T}} > 50\,\mathrm{GeV/c}$). In the region between 20 and 50 GeV/c a linear dependence is assumed. (iii) **b-tagging identification uncertainty:** of $\pm 4\%$ on the overall selection efficiencies is expected on the b-tagging efficiencies [157]. (iv) the **luminosity uncertainty**, expected to be 5% [321].

8.4.2. Selection and cross section: t-channel

The final state in t-channel includes one isolated muon, missing energy (neutrino), one or two jets from b-quarks (B_{jet}), and one "forward" hadronic jet. A specific feature of single top events is production of a light jet in the forward/backward direction (see Figs. 8.15) providing an additional possibility for background suppression. The additional b-quark is produced with small transverse momentum, making the reconstruction of the associated low-p_{T} jet and its b-tagging very difficult. Therefore, in t-channel analysis [317] it is required to have only two hadronic jets in the final state. In this case, the most important background contribution arises from $t\bar{t}$ production and from $W^{\pm}$-boson production in association with heavy quarks ($Wb\bar{b}$ + jet) or light quark jets (W + jets).

8.4.2.1. Analysis of the fully simulated events. The selection requires the presence of only one isolated muon with $p_{\mathrm{T}} > 19\,\mathrm{GeV/c}$ and $|\eta_{\mu}| < 2.1$ (HLT selection). Then, it is required: (i) $E_{\mathrm{T}}^{\mathrm{miss}} > 40\,\mathrm{GeV}$; and (ii) at least two hadronic uncalibrated jets, with $p_{\mathrm{T}} > 20\,\mathrm{GeV/c}$. For

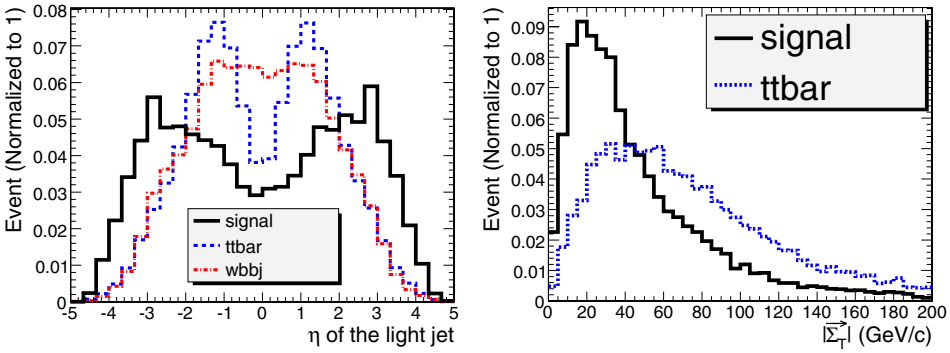

Figure 8.15. The distributions of pseudorapidity (η) of the light jet (left), and of $|\vec{\Sigma}_{\mathrm{T}}|$ (right).

Table 8.17. Number of events (t-channel) and cumulative efficiencies for each cut used in the analysis of t-channel single top production. The symbol "$p_{\mathrm{T}B} \times p_{\mathrm{T}j} \times E_{\mathrm{T}}^{\mathrm{miss}}$" means: $p_{\mathrm{T}B} > 35\,\mathrm{GeV/c}$, $p_{\mathrm{T}j} > 40\,\mathrm{GeV/c}$, $|\eta_j| > 2.5$, $E_{\mathrm{T}}^{\mathrm{miss}} > 40\,\mathrm{GeV}$.

	signal	$t\bar{t}$	$Wb\bar{b}j$	Wj	Wjj
N(events) at $10\,\mathrm{fb}^{-1}$	1.8×10^5	8.33×10^6	3.24×10^5	9.7×10^7	9.9×10^5
isolated muon	0.73	0.14	0.52	0.16	0.81
$p_{\mathrm{T}B} \times p_{\mathrm{T}j} \times E_{\mathrm{T}}^{\mathrm{miss}}$	0.036	6.4×10^{-3}	3.4×10^{-3}	9×10^{-6}	3×10^{-3}
veto on 3^{rd} jet	0.021	5.8×10^{-4}	1.6×10^{-3}	4×10^{-6}	1.1×10^{-3}
$0.0 < \Sigma_{\mathrm{T}} < 43.5\,\mathrm{GeV}$	0.018	4.1×10^{-4}	1.2×10^{-3}	4×10^{-6}	6.8×10^{-4}
$50 < M_{\mathrm{T}}^{W*} < 120$	0.015	2.2×10^{-4}	9.6×10^{-4}	1×10^{-6}	5.4×10^{-4}
$110 < M_{\mathrm{rec}}(bW)^* < 210$	0.013	1.4×10^{-4}	5.8×10^{-4}	0	4.1×10^{-4}
Number of events	2389	1188	195	0	402

*in $\mathrm{GeV/c^2}$

further analysis the following additional requirements are: at least one of the selected jets should have the b-tag: the second (light) jet should be in the forward region; only two jets (calibrated) with $p_{\mathrm{T}}^{\mathrm{calib}} \geqslant 35\,\mathrm{GeV}$ and no other hadronic jets with $p_{\mathrm{T}}^{\mathrm{calib}} \geqslant 35\,\mathrm{GeV/c}$ (jet veto). The GARCON program [63] is used for the final optimisations of the cuts. The signal-over-background ratio times significance is chosen as an optimisation criterion. Finally, the optimal cut values found are:

- muon: $p_{\mathrm{T}}(\mu) > 19.0\,\mathrm{GeV/c}$ and $|\eta(\mu)| < 2.1$ and $E_{\mathrm{T}}^{\mathrm{miss}} > 40.0\,\mathrm{GeV}$;
- b-jet: $p_{\mathrm{T}} > 35.0\,\mathrm{GeV/c}$, $|\eta| < 2.5$ and Discriminator > 2.4;
- the light forward: $p_{\mathrm{T}} > 40.0\,\mathrm{GeV/c}$ and $|\eta| > 2.5$;
- $|\vec{\Sigma}_{\mathrm{T}}|$ cut window: (0.0, 43.5) GeV; $50 < M_{\mathrm{T}}^{W} < 120\,\mathrm{GeV/c^2}$;
- the reconstructed top mass window: $110\,\mathrm{GeV/c^2} < M_{\mathrm{rec}}(bW) < 210\,\mathrm{GeV/c^2}$.

The efficiencies of these cuts and the resulting number of events are given in the Table 8.17. The resulting signal-to-background ratio and the significance are: $N_S/N_B = 1.34$ and $S_{stat} = N_S/\sqrt{N_S + N_B} = 37.0$. The final distribution of the reconstructed top mass is shown in Figure 8.16. The cuts provide a satisfactory background suppression.

The systematic uncertainties (see Section 8.4.1.4) evaluated for $10\,\mathrm{fb}^{-1}$ are given in Table 8.18. In summary, the statistical error is 2.7%, the total systematic error excluding the 5% luminosity uncertainty is 8%, resulting in a total error of 10%.

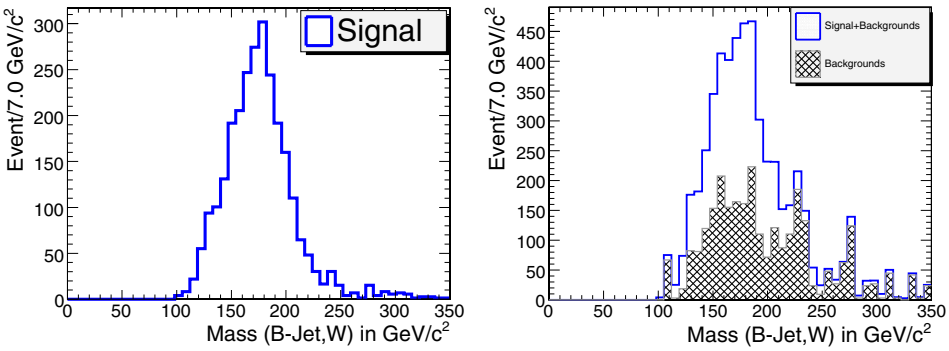

Figure 8.16. The distribution on the reconstructed top mass, for signal only (left) and with background included (right).

Table 8.18. Number of selected events (t-channel) at 10 fb^{-1} with uncertainties due to different sources. ΔN_{syst} represents the theoretical, JES and b-tagging uncertainties. ΔN_{stat} is expected statistical uncertainty.

sample	selected	ΔN_{th}	JES	$\Delta N_{\text{b-tag}}$	ΔN_{syst}	ΔN_{stat}
t-channel	2389	96	71	96	153	49
$t\bar{t}$	1188	59	73	48	105	34
$Wb\bar{b}j$	195	33	6	8	35	14
Wjj	402	20	0	16	26	20

8.4.3. Selection and cross section: tW-channel

The $pp \to tW$ process contains two W-bosons and a b-quark in the final state. In this study only leptonic decays of the W's are considered. The nominal final states are $\ell^+\ell^- E_{\text{T}}^{\text{miss}} b$ and $\ell^\pm E_{\text{T}}^{\text{miss}} b\text{jj}$ for the dileptonic and semi-leptonic modes, respectively. The dominant background arises from $t\bar{t}$ production. Other backgrounds are t- and s-channel single top production, $Wb\bar{b}$, W + jets, WW + jets, and to a lesser extent QCD multi-jet background.

8.4.3.1. Jet quality requirements and extra jet reduction. The most significant difference between tW events and $t\bar{t}$ events is the number of jets in the final state. However, most of the time there are also additional jets due to the underlying event, pile-up or calorimeter noise. These "extra jets" were identified and excluded from the counting by consideration of five jet quality variables (see [318]). It was found that the most discriminating variables are E_{T}^{max} (the maximum tower E_{T} in a cone of 0.5) and N_{track} (the number of associated tracks). A Fisher discriminant [322] (F) is constructed from the jet quality variables to separate real jets from extra jets. Each jet is classified value F into one of three categories: good ($F < -0.5$), loose ($|F| < 0.5$) and bad ($F \geqslant 0.5$) jets. This method yields 84.3% efficiency on true jets and rejects 86.9% of extra jets. Only "good" jets and "loose" jets are used in pre-selection and event reconstruction. The jet multiplicity after the extra jet reduction in semi-leptonic channels reveals that the number of good jets peaks at the 2 and 3 jet bins for signal events, and at the 3 and 4 jet bins for $t\bar{t}$ backgrounds.

8.4.3.2. Event selection and reconstruction. The kinematic cuts used for this study are presented in Table 8.19 and Table 8.20. For the semi-leptonic channel, two non-b-like jets with $m_{jj} < 115\,\text{GeV/c}^2$ are used for reconstruction of the W-boson (that decays hadronically). In

Table 8.19. Kinematic cuts used in the dileptonic channel. The final electron and muon should have the opposite charges.

Leptons	**Jets**
$\|\eta(e)\| < 2.4$, $\|\eta(\mu)\| < 2.1$	leading jet: $\|\eta\| < 2.4$, $p_T > 60\,\text{GeV/c}$, disc > 0
$p_T(e, \mu) > 20\,\text{GeV/c}$	at most one extra jet
no other lepton with $p_T > 5\,\text{GeV/c}$	No other jets with $p_T > 20\,\text{GeV/c}$
Missing E_T: $E_T^{miss} > 20\,\text{GeV}$	

Table 8.20. Kinematic cuts used in the semi-leptonic channel. The presence of a good fourth jet would veto the whole event.

Leptons
$p_T(e) > 30\,\text{GeV/c}$, $p_T(\mu) > 20\,\text{GeV/c}$, $\|\eta(e)\| < 2.4$, $\|\eta(\mu)\| < 2.1$
no other lepton $p_T > 10\,\text{GeV/c}$
Jets (after removing all bad quality jets)
b-like jet: good quality, disc >2, $\|\eta\| < 2.5$, $p_T > 35\,\text{GeV/c}$
non-b-like jet: good quality, $\|\eta\| < 3.0$, disc <0 if $\|\eta\| < 2.5$, $p_T > 35\,\text{GeV/c}$
Jet counting: one b-like jet and 2 non-b-like jets
Jet veto: no other "good" or "loose" jets with $p_T > 20\,\text{GeV/c}$ and $\|\eta\| < 3$
Missing E_T : $E_T^{miss} > 40\,\text{GeV}$

events with a 4th jet that survives jet veto cuts, it is required that the invariant mass of the 4th jet with any of the selected non-b-like jets must be outside a window of $M_W \pm 20\,\text{GeV/c}^2$. For the leptonic decays of the W-boson it is required that $M_T^W < 120\,\text{GeV/c}^2$.

To find the correct pairing of b-jet and reconstructed W-boson (coming from top decay) the following variables were used: the p_T of (b, W) systems; the separation of the b-jet with each of the W in (η, ϕ) space; the "charges" of jets (see Section 8.4.1.2) and W-bosons (see Ref. [318] for details). A Fisher discriminant based on these variables is used for discriminating leptonic top events from hadronic top events. A cut of 0.56 is optimal in separating these 2 types of events, and 72% of the events are correctly paired.

To further enhance the signal to background ratio the following "global" cuts are applied:

- p_T of the reconstructed tW system: $|\vec{\Sigma}(t + W)| < 60\,\text{GeV/c}$.
- Scalar sum of transverse energies H_T: $H_T < 850\,\text{GeV}$.
- Reconstructed top quark mass: $110\,\text{GeV/c}^2 < m(t) < 230\,\text{GeV/c}^2$.
- p_T of the reconstructed top quark: $20\,\text{GeV/c} < p_T(t) < 200\,\text{GeV/c}$.

8.4.3.3. Efficiencies and expected yields. The efficiencies estimated with Monte Carlo samples are converted to the effective cross sections by multiplying the production cross sections of each process. The effective cross sections, as well as the expected yields with $10\,\text{fb}^{-1}$ of data for all signal and background samples, are shown in Table 8.21 and 8.22. The signal to background ratio is found to be 0.37 for dileptonic channel and 0.18 for semi-leptonic channel.

8.4.3.4. The ratio method. The *ratio method* is developed to reduce systematic uncertainties related to the dominant $t\bar{t}$ background. We define a $t\bar{t}$-rich control region and use ratio of efficiencies to estimate the yield of $t\bar{t}$ in the signal region. The kinematics of tW and $t\bar{t}$ are similar so tW is present in the control region, therefore the ratio of efficiencies for tW is also

Table 8.21. Summary of cross section times branching ratio times efficiencies at each stage of the analysis for the dileptonic channel. All values are in picobarns The last row is the expected number of events for 10 fb^{-1}. Multi-jet background has been estimated separately (see Section 8.4.1.3). When only a limit on the number of events is stated, this is due to MC statistics.

	tW dil.	$t\bar{t}$ dil.	$t\bar{t}$ oth.	WW dil.	WW oth.	t ch. lept.
Production	6.667	92.222	737.778	11.111	88.889	81.667
HLT	4.865	74.090	346.151	7.674	27.259	41.409
$2\,\ell$	1.944	25.150	21.012	2.574	0.226	2.309
Lepton p_{T}	0.675	7.919	0.703	0.543	0.012	0.098
$\leqslant 1$ extra jet	0.459	6.574	0.664	0.416	0.010	0.067
Jet p_{T}, η	0.307	5.234	0.556	0.339	0.004	0.033
$\geqslant 1b$-jet	0.184	3.864	0.379	0.017	0.000	0.018
$E_{\mathrm{T}}^{\mathrm{miss}} > 20$	0.170	3.640	0.349	0.017	0.000	0.016
$\leqslant 2$ jet	0.150	2.734	0.221	0.015	0.000	0.012
Final select.	0.057	0.145	0.000	0.006	0.000	0.000
Expected events	567	1450	$\leqslant 55$	61	$\leqslant 10$	$\leqslant 20$

Table 8.22. Summary of cross section times branching ratio times efficiencies at each stage of the analysis for the semi-leptonic channel. All values are in picobarns. The last row is the expected number of events for 10 fb^{-1}.

	tW	$t\bar{t}$	t ch.	s ch.	Wbb	W2j	W3j	W4j	Multi-jet
Total cross section	60	833	245	10	300	7500	2166	522	9.73×10^9
HLT	18.9	263.9	39.5	1.52	34.0	1006	300	73	1.86×10^5
Presel. & isolation	9.05	179.4	12.0	0.54	2.15	52	35	12	1325
jet & lepton p_{T}, jet veto	1.28	18.5	1.31	0.046	0.061	0.60	4.9	1.0	4.23
b-tagging	0.669	6.13	0.476	0.013	0.016	0.10	0.99	0.26	0.85
kinematic cuts	0.223	0.999	0.047	0.002	0.003	0.017	0.101	0.008	0.105
Signal box cuts	0.170	0.771	0.035	0.001	0.001	0.013	0.054	0.008	0.051
Events in 10 fb $^{-1}$	1699	7709	351	14	10	130	539	80	508

used. The signal and background yield is determined by the following equations:

$$S = \frac{R_{t\bar{t}}(N_s - N_s^o) - (N_c - N_c^o)}{R_{t\bar{t}} - R_{tW}}, \tag{8.12}$$

$$B = \frac{(N_c - N_c^o) - R_{tW}(N_s - N_s^o)}{R_{t\bar{t}} - R_{tW}} + N_s^o. \tag{8.13}$$

Here R_x is the ratio of efficiencies $R_x = \varepsilon_x(\text{control region})/\varepsilon_x(\text{signal region})$ for $x = t\bar{t}, tW$; N_s (N_c) is total number of events in the signal (control) region; N_s^o (N_c^o) is the estimated number of non-$t\bar{t}$ background events in the signal (control) region. With S measured with 2 regions and the ratio method, the cross section can be found by $S/\epsilon\mathcal{L}$.

For the ratio method to work it is important to find a control region with similar kinematics except with one more jet. It is expected that systematic uncertainties from PDF, JES and b tagging cancel to a large extent, while the luminosity uncertainty drops out for the $t\bar{t}$ background. The lepton selection and jet quality requirements in the control region are identical to the signal region. The differences are outlined below.

Dileptonic. A second jet is required with $p_{\mathrm{T}} = 20$–$80\,\mathrm{GeV/c}$, $|\eta| < 2.4$ and b-tagged (disc > 0). No other jets with $p_{\mathrm{T}} > 20\,\mathrm{GeV/c}$ are allowed. The background region is found to be filled by 97.9% dileptonic $t\bar{t}$, 0.4% other $t\bar{t}$ decays, 1.6% dileptonic tW, and 0.1% for leptonic t channel single top while WW+jets yield is negligible.

Table 8.23. Summary of uncertainties of cross section measurement.

Source	Uncertainty	$\Delta\sigma/\sigma$(dilept.)	$\Delta\sigma/\sigma$(semi-lept.)
Statistical uncertainty	—	8.8%	7.5%
Integrated luminosity	5%	5.4%	7.8%
$t\bar{t}$ cross-section	9%	*negligible*	*negligible*
t-channel cross-section	5%	*negligible*	0.8%
W+jets cross-section	10%	*not applicable*	3.1%
WW+jets cross-section	10%	1%	*not applicable*
Jet energy scale	5%–2.5%	19.7%	9.4%
b tagging efficiency	4%–5%	8.7%	3.6%
PDF	1σ	+4%/−6.0%	1.6%
Pileup	30%	6.1 %	10.3%
MC statistics	—	9.9%	15.2%
Total uncertainty		±23.9%(syst.)	±16.8%(syst.)
		± 9.9%(MC)	±15.2%(MC)

Semi-leptonic. It requires 2 jets with $p_{\mathrm{T}} > 30$, 2 more jets with $p_{\mathrm{T}} > 20$, and no bad jets with $p_{\mathrm{T}} > 20$. It is required that one of the 2 high-p_{T} jets is b-tagged (disc > 2), and that both low-p_{T} jets be not tagged (disc < 0). The $b - W$ pairing is done in the same way, with a 72% correct pairing. It is found that the $t\bar{t}$ purity in the control region is 93.9%. The non-$t\bar{t}$ events are mainly composed of W+jets (2.8%), tW (2.0%) and t-channel single top (1.2%). The ratio of efficiencies are found to be $R_{tW} = 0.319$ and $R_{t\bar{t}} = 3.31$.

8.4.3.5. Systematic uncertainties.

- **Theoretical uncertainties.** The $t\bar{t}$ cross section does not show up in the ratio method. The effect is 0.8% for t-channel single top and 3.1% for W+jets. It is found to be negligible for other background.
- **Pileup amount.** A difference of 30% between normal pileup and no pileup is used as an estimate of the systematic uncertainty, as was done in [201] for the dileptonic $t\bar{t}$ studies.

Dileptonic mode. The analysis is found to be rather sensitive to the pileup, as the relative shift of the "measured" cross section is +20.4% for no pileup, and −16.2% for double pileup, while is the difference between the check sample and the reference sample 4.6% (which has purely statistical origin). The value of 6.1% is used as the systematic uncertainty.

Semi-leptonic mode. The extracted cross section varies by +35% for no pileup and −63% for double pile-up so a systematic uncertainty of 10.3% is obtained. The results for both channels are shown in Table 8.23.

The results from the ratio method were used in the significance calculation. In addition, the uncertainty on the background expectation, evaluated for dileptonic ($\Delta_B/B = \pm 9.6\%$) and semi-leptonic ($\Delta_B/B = +3.6\%/-4.4\%$), was taken into account. The resulting significance is 4.2 for the dileptonic channel and 5.1 for the semi-leptonic channel. Combining the two channels gives a total significance of 6.4.

8.4.4. Selection and cross section: s-channel

The present analysis of the s-channel single top production is based on leptonic channels, i.e. the top is identified and reconstructed by its semi-leptonic decays into $\ell\nu b$ final states, with $\ell = e, \mu$. For this study, a fast simulation of the CMS detector with FAMOS was used, see [317, 318] for details.

Table 8.24. Efficiencies of the pre-selection cuts, with respect to the initial number of events. For all process (except of $t\bar{t}$) the final W decays into charged lepton ($\ell = e, \mu, \tau$) and neutrino. "HLT" includes the 1μ, $1e$ and $e \times j$ triggers. N_{ev} is the number of events surviving these cuts (the uncertainties are only those due to the limited Monte Carlo statistics).

Cut	s-ch.	t-ch.	$t\bar{t}$	$Wb\bar{b}$	Wt ($1\ W \to l\nu$)
"HLT"	$37.5 \pm 0.2\%$	$42.5 \pm 0.1\%$	$30.1 \pm 0.1\%$	$29.4 \pm 0.1\%$	$46.5 \pm 0.1\%$
Isolation	$33.7 \pm 0.2\%$	$39.0 \pm 0.1\%$	$21.7 \pm 0.1\%$	$28.2 \pm 0.1\%$	$42.3 \pm 0.1\%$
$E_{\mathrm{T}}^{\mathrm{miss}}$ cut	$27.3 \pm 0.2\%$	$31.9 \pm 0.1\%$	$17.4 \pm 0.1\%$	$22.6 \pm 0.1\%$	$34.4 \pm 0.1\%$
M_{T}^{W} cut	$23.2 \pm 0.2\%$	$26.3 \pm 0.1\%$	$13.6 \pm 0.1\%$	$18.4 \pm 0.1\%$	$29.2 \pm 0.1\%$
$N_j \geqslant 2j$	$11.9 \pm 0.1\%$	$11.5 \pm 0.1\%$	$11.9 \pm 0.1\%$	$0.88 \pm 0.03\%$	$18.5 \pm 0.1\%$
$N_j = 2j$	$8.9 \pm 0.1\%$	$8.2 \pm 0.1\%$	$1.84 \pm 0.04\%$	$0.76 \pm 0.03\%$	$7.09 \pm 0.05\%$
b-tag	$3.07 \pm 0.07\%$	$0.72 \pm 0.02\%$	$0.28 \pm 0.02\%$	$0.14 \pm 0.01\%$	$0.34 \pm 0.01\%$
N_{ev}	1010 ± 10	5880 ± 70	23300 ± 200	1400 ± 35	1150 ± 40

The signal events are triggered by the single lepton triggers. Since this production mode suffers from low statistics, one could envisage the introduction of a combined trigger $e \times jet$, with threshold 19 GeV/c for the electron (in order to make the electronic sample more coherent with the muonic sample) and 45 GeV/c for the jet. This value has been chosen to be the same as the threshold for the τ-jet in the already existing $e \times \tau - jet$ trigger.

8.4.4.1. Pre-selection. The pre-selection criteria are as follows:

- The event has to fire at least one of the previously described triggers (including the proposed $e \times j$).
- The event must contain one isolated lepton (μ or e) with $p_{\mathrm{T}} \geqslant 19\,\mathrm{GeV/c}$ and $|\eta| \leqslant 2.1$ ($\leqslant 2.4$) for muons (electrons) and no other lepton above 10 GeV/c.
- Exactly two uncalibrated jets must have $p_{\mathrm{T}} \geqslant 30\,\mathrm{GeV/c}$ and $|\eta| \leqslant 2.5$ and no other jet has to be present with $p_{\mathrm{T}} \geqslant 20\,\mathrm{GeV/c}$.
- Both jets should have a positive b-tagging discriminator value.
- The event should have $E_{\mathrm{T}}^{\mathrm{miss}} > 30\,\mathrm{GeV}$.
- The transverse mass of the W-boson M_{T}^{W} should be less than $100\,\mathrm{GeV/c^2}$.

Details on the effect of the pre-selection cuts are given in Table 8.24. Note, that as in Section 8.4.2, the multi-jet QCD contribution is neglected.

8.4.4.2. Genetic algorithm analysis. The following observables have been chosen in order to further discriminate between signal and background after pre-selection: (i) the jet b-tagging discriminants; (ii) the calibrated jet transverse momenta; (iii) the mass of the reconstructed top; (iv) $|\Sigma(t, \bar{b})|$; (v) the scalar sum of the transverse momenta of all the reconstructed objects. The reconstructed top quark is formed by the reconstructed W and one of the two b-jets, chosen according to the value of the "jet charge" (Q_j, see Section 8.4.1.2). Since in top decays the W and the original b quark have opposite sign of the charge, the jet with Q_j "most opposite" to the W is used for top reconstruction, leading to a probability of 67% to identify the correct pairing.

The cuts on these variables are optimised by means of the GARCON program [63]. The surviving events after these cuts are shown in cascade in Table 8.25. With this selection, after an integrated luminosity of $10\,\mathrm{fb^{-1}}$ one gets: $N_S/N_B \approx 0.13$.

Table 8.25. Final cuts and their efficiencies, with respect to the preselected samples, for the signal and the main backgrounds. For s- and t-channel and $Wb\bar{b}$ samples the final W-boson decays into lepton (e, μ, τ) and neutrino. $t\bar{t}$ samples includes all W-boson decay modes.

Cut	s-channel	t-channel	$t\bar{t}$	$Wb\bar{b}$
b-tag(j_1)> 0.4, b-tag(j_2)> 0.1	85%	75%	78%	85%
$p_T(j_1) > 50\,\mathrm{GeV/c}$, $p_T(j_2) > 50\,\mathrm{GeV/c}$	68%	53%	70%	37%
$120 < M(lvb) < 220\,\mathrm{GeV/c^2}$	52%	34%	46%	26%
$25 < p_T(lvb) < 160\,\mathrm{GeV/c}$	48%	32%	43%	26%
$\Sigma_T < 20\,\mathrm{GeV/c}$	35%	15%	10.6%	12.5%
$H_T < 340\,\mathrm{GeV/c}$	27%	10.7%	5.4%	11.1%
number of surviving events	273 ± 4	630 ± 14	1260 ± 60	155 ± 12

Table 8.26. Number of selected events after 10 fb^{-1} and systematic uncertainties.

sample	selected	$\Delta\sigma$	JES	b-tag	M_{top}	PDF	ISR/FSR
S: s-channel	273	—	±3	±11	±1.5	±2	±1.5
B: t-channel	630	±25	±8	±25	—	—	—
B: $t\bar{t}$	1260	±63	±75	±50	—	—	—
B: $Wb\bar{b}$	155	±8	±7	±6	—	—	—

8.4.4.3. Systematic uncertainties. In addition to systematics described in Section 8.4.1.4 the following sources of systematic uncertainty are considered:

- **Top mass.** The variation of m_t within $\pm 2\,\mathrm{GeV/c^2}$ around top mass $m_t = 175\,\mathrm{GeV/c^2}$ leads to the relative systematic error on the selection efficiency $\sigma^{m_t}_{\mathrm{syst}}$ =0.5% for the s-channel single top.
- **Parton Distribution Functions.** To extract the dependence on the PDF uncertainty, two different PDF sets were used: CTEQ61and CTEQ6M [12]. The result is $\sigma^{\mathrm{PDF}}_{\mathrm{syst}}$ =0.7%.
- **Initial/Final State Radiation Modelling.** The model parameters were varied in the ranges Λ_{QCD}=0.25 ± 0.1 GeV and Q^2_{max} from 0.25 to 4 $\hat{s}$ (see [201]). The extreme values of the efficiencies are taken as systematic error: $\sigma^{\mathrm{rad}}_{\mathrm{syst}} = 0.5\%$.

8.4.4.4. Background normalisation. The $t\bar{t}$ events in Table 8.26 are, in 41% of the cases, $t\bar{t} \to l^+\nu bl^-\bar{\nu}\bar{b}$ events with a lepton missed, and in the remain cases $t\bar{t} \to l^+\nu bq\bar{q}'\bar{b}$ events with two jets missed ($t\bar{t} \to q\bar{q}'bq\bar{q}'\bar{b}$ events give a negligible contribution). These two categories of events are very differently affected by the Jet Energy Scale variation. In general, any variation going in the direction of more jets gives a better rejection of the $t\bar{t} \to l^+\nu bq\bar{q}'\bar{b}$ component with respect to the signal, while the $t\bar{t} \to l^+\nu bl^-\bar{\nu}\bar{b}$ events, having two quarks, are affected almost in the same way as the signal.

- $t\bar{t} \to \ell^\pm + X$ *enriched control sample*. In this case the difference with respect to Section 8.4.4.1 is the request of three jets instead of two and only the muon channel is used. The selection efficiency for $t\bar{t} \to \ell^\pm$ events is found to be 1.08%. The ratio R_{c1} between the efficiencies in the main sample and in this control sample is $R_{c1} = 0.0149$, whose variations under JES and b-tagging efficiency systematic shifts are $\Delta R_{c1} = \pm 0.0015(\mathrm{JES}) \pm 0.0003$ (b-tag).
- $t\bar{t} \to \ell^{+\ell^-} + X$ *enriched control sample*. This sample is obtained by the same selection as in Section 8.4.4.1, but two leptons with different flavours with the opposite sign are required. The selection efficiency for $t\bar{t} \to 2l$ events is found to be 0.822%. The ratio R_{c2} between the efficiencies in the main sample and in this control sample is $R_{c2} = 0.0681$, whose

variations under JES and b-tagging efficiency systematic shifts are $\Delta R_{c2} = \pm 0.0010$(JES) ± 0.0004 (b-tag).

8.4.4.5. Results. The number of the selected signal (N_S) and background (N_B) events and their estimated uncertainties are listed in Table 8.26. The cross section is extracted as

$$\sigma = \frac{N_{tot} - b^0 - R_{c1}(N_{c1} - b^0_{c1}) - R_{c2}(N_{c2} - b^0_{c2})}{\epsilon L}, \tag{8.14}$$

where b^0 is the sum of the non-top backgrounds in the main sample, N_{c1} and N_{c2} are the total events selected in the two control regions, and b^0_{c1} and b^0_{c2} are their contamination by non-top backgrounds, single top and other $t\bar{t}$ decays. The statistical error is evaluated to be 18%. The total systematic uncertainty is 31%, where the largest contribution arises from the effect of the JES uncertainty, on the $t\bar{t}$ single lepton background. The use of "Energy Flow" techniques, including the charged tracks information, is expected to significantly reduce this uncertainty. The total error, including also the 5% luminosity uncertainty, is 36%.

8.4.5. Conclusion

Selection strategies have been proposed for all the three single top production modes, and their effectiveness is shown, taking into account the expected statistics after 10 fb $^{-1}$. All analyses will be systematics dominated. For the s-channel and tW-associated cases, control samples have been proposed in order to constrain the dominant $t\bar{t}$ background.

The resulting signal-to-background ratio and the significance for the t-channel are: $N_S/N_B = 1.34$ and $S_{stat} = N_S/\sqrt{N_S + N_B} = 37.0$, with a statistical error of 2.7%, and a systematic error excluding the 5% luminosity uncertainty of 8%, resulting in a total error of 10%. For tW-channel we expect to reach the significance of 4.2 (5.1) for the dilepton (semi-leptonic) channel, increasing to 6.4 after combining the two channels. The total uncertainty is ± 23.9%(syst.) ± 9.9%(MC) for dilepton and ± 16.8%(syst.) ± 15.2%(MC) for semi-leptonic channels. The total systematic uncertainty for the s-channel is 31%. The total error, including also the 5% luminosity uncertainty, is 36%.

8.5. Search for flavour changing neutral currents in top decays

8.5.1. Introduction

The study of Flavour Changing Neutral Current (FCNC) interactions plays an important role in testing the Standard Model (SM) and probing new physics beyond it. The top quark is regarded to be more sensitive to new physics than other fermions, due to its mass close to the electroweak scale. Owing to the GIM mechanism of the SM, top quark FCNC interactions are absent at tree level and extremely small at loop level.

In recent years a lot of work has been done to explore the top quark FCNC couplings. On the theoretical side, various FCNC top quark decays and top-charm associated production at high energy colliders were extensively studied in the SM [323, 324], the Minimal Supersymmetric Standard Model (MSSM) [325–328] and other new physics models [329–333]. In models beyond the SM the top quark FCNC branching fractions may be significantly enhanced. Thus searching for top quark FCNC is a potentially powerful probe of new physics. The CDF and DØ collaborations have reported interesting bounds on the FCNC top quark decays [334–336]. The SM expectations for such top quark FCNC processes are far below the detectable level but the MSSM can enhance them by several orders of magnitude to make them potentially accessible at future collider experiments [337–339]. The theoretical branching ratios and the experimental limits are summarised in Table 8.27. Details of this analysis can be found in [340].

Table 8.27. Theoretical branching ratios of FCNC top quark decays in various models and experimental limits.

Decay	SM	two-Higgs	SUSY with R	Exotic Quarks	Exper. Limits (95% CL)
$t \to gq$	5×10^{-11}	$\sim 10^{-5}$	$\sim 10^{-3}$	$\sim 5 \times 10^{-4}$	< 0.29 (CDF+TH)
$t \to \gamma q$	5×10^{-13}	$\sim 10^{-7}$	$\sim 10^{-5}$	$\sim 10^{-5}$	< 0.0059 (HERA)
$t \to Zq$	$\sim 10^{-13}$	$\sim 10^{-6}$	$\sim 10^{-4}$	$\sim 10^{-2}$	< 0.14 (LEP-2)

8.5.2. Signal and background generation

Both the $t \to \gamma q$ and the $t \to Z^0 q$ decay channels are investigated. The channel $t \to gq$ is not studied because of its very high background. The $t\bar{t}$ signal is generated with TopReX [44], while PYTHIA [184] is used for modelling of quark and gluon hadronisation. The $t\bar{t}$ pair is generated through gluon-gluon and quark-anti-quark annihilation, with subsequent SM decay for one top ($t \to Wb$) and FCNC decay of the other. Only leptonic decay channels of Z and W bosons are studied, where the lepton could be either e or μ. Hadronic Z/W decays as well as decays to tau leptons are not considered because of the large QCD background. On generator level both top quarks are produced on-shell, with a mass of $m_t = 175\,\mathrm{GeV/c^2}$, including the effects of spin-state correlations on final decay products (γq, $Z^0 q$, Wb). Both ISR and FSR are simulated with CTEQ5L PDFs. The generated events are passed through the full detector simulation and digitisation, taking into account low luminosity pile-up.

Several SM processes contributing as background are studied: $t\bar{t}$ production, single top quark production (t-channel), ZW + jets, WW + jets, ZZ + jets, W + jets, Z + jets, $Zb\bar{b}$ and QCD multi-jet production.

8.5.3. Selection strategies

The $t \to \gamma q$ channel is well identified by a high-energy isolated photon accompanying the FCNC top decay. One b-tagged jet and a light jet are also used to distinguish from the standard $t\bar{t}$ decays. For the FCNC $t \to \gamma q$ channel our main selection cuts are: (a) single electron or single muon' trigger criteria at Level-1 and HLT levels; (b) one isolated $e^{\pm}$ (with $p_{\mathrm{T}} > 30\,\mathrm{GeV/c}$) or $\mu^{\pm}$ (with $p_{\mathrm{T}} > 20\,\mathrm{GeV/c}$), and missing transverse energy $E_{\mathrm{T}}^{\mathrm{miss}} > 25\,\mathrm{GeV}$, forming a transverse invariant mass $M_{\mathrm{T}}(bW) < 120\,\mathrm{GeV/c^2}$; (c) only one jet compatible with b-jet with $p_{\mathrm{T}} > 40\,\mathrm{GeV/c}$, that in combination with the W candidate gives an invariant mass in the range between $110\,\mathrm{GeV/c^2}$ and $220\,\mathrm{GeV/c^2}$; (d) one single isolated photon with $p_{\mathrm{T}} > 50\,\mathrm{GeV/c}$; (e) one light-jet (not compatible with b-jet) with $p_{\mathrm{T}} > 50\,\mathrm{GeV/c}$; (f) an invariant mass obtained from the combination of the photon and the light jet that lies in the range between $150\,\mathrm{GeV/c^2}$ and $200\,\mathrm{GeV/c^2}$; (g) the transverse momentum of the photon + light-jet system recoiling against the transverse momentum of the SM-decaying top quark satisfying $\cos\phi(t\bar{t}) < -0.95$.

The total efficiency for the signal is $\varepsilon = 0.021 \pm 0.002$. Only the SM backgrounds $t\bar{t}$ and EW single top (t-channel) contribute to the accepted background, with 54 ± 7 background events accepted for a luminosity of $10\,\mathrm{fb^{-1}}$. The uncertainties are statistical only.

Adopting a factorisation method, QCD background is proven to be not dangerous for the analysis: A set of independent cuts (hard jets, isolated hard lepton, isolated hard photon, b-tagging) is applied to both QCD and $t\bar{t}$ background and the efficiencies for single cuts are assumed to factorise. The b-tagging efficiency and the mistagging are 30% and 0.5%. The number of surviving QCD events for this pre-selection is found to be 42 for a luminosity of $10\,\mathrm{fb^{-1}}$, and the efficiency on the $t\bar{t}$ sample amounts to 2.5%. Assuming that after these

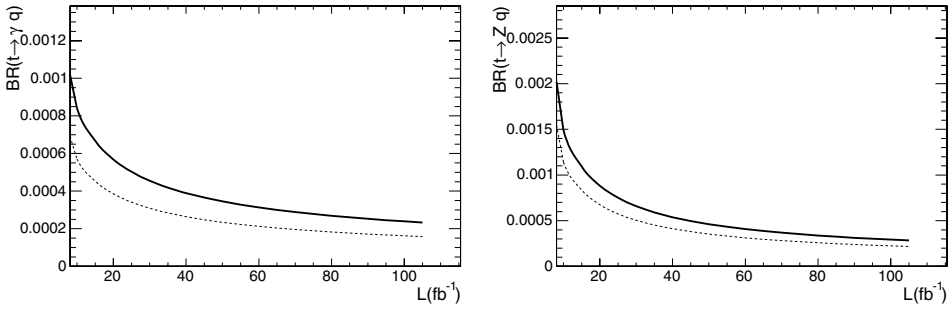

Figure 8.17. Branching Ratios of a FCNC signal detectable at the 5 sigma level as a function of the integrated luminosity, for the $q\gamma$ (left) and qZ (right) channels, shown with (solid line) and without (dashed line) systematic uncertainties.

cuts the further efficiency for the QCD backgrounds and $t\bar{t}$ is the same, leads to expect $\simeq 1$ background events.

For the FCNC $t \to Z^0 q$ channel our main selection cuts are: (a) 'double electron or double muon' trigger criteria at Level-1 and HLT levels; (b) two isolated $e^{\pm}$ (each with $p_{\mathrm{T}} > 20\,\mathrm{GeV/c}$) or $\mu^{\pm}$(each with $p_{\mathrm{T}} > 10\,\mathrm{GeV/c}$), having an invariant mass $\pm 10\,\mathrm{GeV/c^2}$ around the nominal Z^0 mass; (c) third lepton (e with $p_{\mathrm{T}} > 20\,\mathrm{GeV/c}$ or μ with $p_{\mathrm{T}} > 15\,\mathrm{GeV/c}$), which, in combination with the missing transverse energy ($E_{\mathrm{T}}^{\mathrm{miss}} > 20\,\mathrm{GeV}$) have a transverse mass less than $120\,\mathrm{GeV/c^2}$; (d) only one jet compatible with b jet with $p_{\mathrm{T}} > 40\,\mathrm{GeV/c}$; (e) invariant mass of candidate W and b jet in the range [110–220] $\mathrm{GeV/c^2}$; (f) one light-jet (not compatible with b jet) with $p_{\mathrm{T}} > 30\,\mathrm{GeV/c}$ (g) an invariant mass obtained from the combination of the Z and the light jet that lies in the range between $110\,\mathrm{GeV/c^2}$ and $220\,\mathrm{GeV/c^2}$; (h) the transverse momentum of the Z + light-jet system recoiling against the transverse momentum of the SM-decaying top quark satisfying $\cos\phi(t\bar{t}) < 0$.

The total efficiency for the signal is $\varepsilon = 0.041 \pm 0.002$. A total of 1 ± 1 background events are accepted for a luminosity of $10\,\mathrm{fb^{-1}}$. The SM background $t\bar{t} \to (\nu lb)(\nu lb)$ is the only background that gives a significant contribution. The uncertainties are statistical only.

8.5.4. Sensitivity estimation

For the FCNC sensitivity estimation, it is assumed that new physics is observed when the signal significance is 5 at least. When dealing with a small number of background (B) events with respect to signal ones (S), an appropriate definition of significance is [49]:

$$S_{12} = 2\left(\sqrt{B+S} - \sqrt{B}\right). \tag{8.15}$$

S_{12} defines the probability (in number of sigmas) that a background with expected value B fluctuates above observed number of events $S+B$ with Poisson statistics. The number of signal events for the $t \to Zq$ and $t \to \gamma q$ channel can be expressed as:

$$\begin{aligned} S(t \to Zq) &= 2 \times BR(t \to Zq) \times Br\,(W \to l\nu) \times Br\,(Z \to ll) \times \sigma(t\bar{t}) \times L \times \epsilon(t \to Zq) \\ S(t \to \gamma q) &= 2 \times BR(t \to \gamma q) \times Br\,(W \to l\nu) \times \sigma(t\bar{t}) \times L \times \epsilon(t \to \gamma q) \end{aligned} \tag{8.16}$$

where $L = 10\,\mathrm{fb^{-1}}$, $\sigma(t\bar{t}) = 833\,\mathrm{pb}$, $BR(W \to l\nu) = 0.2136$, $BR(Z \to ll) = 0.0673$ ($l = e, \mu$), ε selection efficiency for the signal. From these formulae, the FCNC branching ratios $BR(t \to Zq)$ and $BR(t \to \gamma q)$ can be calculated for a given significance level S_{12}. Without the inclusion of systematic uncertainties, the sensitivity for a significance level

Table 8.28. Effects of systematic uncertainties on the five-sigma observable FCNC branching ratios induced by different sources of systematic uncertainty. The last row indicates the smallest five-sigma observable FCNC branching ratios for 10 fb^{-1} of integrated luminosity including all sources of systematic uncertainty.

	$t \to Zq$ ($\times 10^{-4}$)	$t \to \gamma q$ ($\times 10^{-4}$)
$BR(stat)$	11.4	5.7
jet energy scale	+0.4	+0.6
b jet mistagging	+0.2	+1.8
light jet antitagging	+0.5	+0.9
lepton energy scale	+2.4	+0.5
$\sigma(t\bar{t})$	+0.1	+0.5
MC statistics in B	+2.4	+1.3
MC statistics in S	+0.7	+0.5
Luminosity	+0.1	+0.5
$BR(total)$	14.9	8.4

of $S_{12} = 5$ is $BR(t \to Zq) = 11.4 \times 10^{-4}$ and $BR(t \to \gamma q) = 5.7 \times 10^{-4}$, also shown in Figure 8.17.

The sources of systematic uncertainty are divided into two groups: those related to detector effects and those related to theoretical issues. For both kind of sources, the impact on the selection efficiency and the surviving number of background events is evaluated. Experimental effects considered here include: (a) the lepton energy scale uncertainty, accounted for with relative increase/decrease of the reconstructed photon and electron four-momenta by ± 0.005; (b) the jet energy scale uncertainty, expected to lie in the range from $\pm 5\%$ at $p_T = 20\,GeV/c$ to $\pm 2.5\%$ at $p_T > 50\,GeV/c$, and totally correlated to missing energy uncertainty (assumed to be $\pm 5\%$, [320]); (c) b-tagging uncertainty (4% after 10 fb^{-1} integrated luminosity [285]), that is studied by assuming a non-b-tagged jet is actually a b-tagged jet 4% of the time; (d) uncertainty in anti-tagging b-jet instead of non-b ones (4% after 10 fb^{-1} integrated luminosity), simulated by assuming a b-tagged jet is a non-b-tagged jet with the same probability.

The impact of the single sources of systematic uncertainty is detailed in Table 8.28. Experimental sources of systematic uncertainties, such as the control of the lepton energy scale and of the b-tagging procedure are expected to be the most significant. The statistical uncertainty on the prediction of the background level of this analysis has a large contribution to the global systematic uncertainty. Refined techniques for the background estimation will reduce this uncertainty once data will be available.

Including all systematic uncertainties, the smallest detectable FCNC branching ratios, for a five-sigma sensitivity and 10 fb^{-1} of luminosity, are $BR(t \to Zq) = 14.9 \times 10^{-4}$ and $BR(t \to \gamma q) = 8.4 \times 10^{-4}$. Under the assumption that the selection efficiency is unaffected by moderate instantaneous luminosity increases (i.e., pile-up), the decrease in the upper limit on the branching fraction with increasing luminosity can be evaluated in a straightforward way. Figure 8.17 shows the branching ratio for both channels as a function of the integrated luminosity. An improvement in the branching ratio limits by a factor of 2 is expected for a luminosity increase by a factor of 5.

Chapter 9. Electroweak Physics

9.1. Production of W and Z bosons

9.1.1. Introduction

The reactions $pp \to W + X$ and $pp \to Z + X$ with subsequent leptonic decays of the massive electroweak vector bosons, $W \to \ell\nu$ and $Z \to \ell^+\ell^-$, have a large cross section and are theoretically well understood. Cross sections above 10 nb (1 nb) are expected at the LHC for the $W \to \ell\nu$ ($Z \to \ell^+\ell^-$) channel in the fiducial region of the CMS detector. Hence these reactions are useful for many purposes, including a precise luminosity monitor, a high-statistics detector calibration tool and to demonstrate the performance of the CMS experiment. These reactions will be among the first to be measured at the LHC.

Here we discuss prospects for precise measurements of the reactions $pp \to Z + X$ and $pp \to W + X$ at the LHC using the decays of the gauge bosons into electrons and muons. Studies have been performed based on Monte Carlo samples generated with PYTHIA including realistic detector simulation and addressing the most relevant systematic effects. The potentially most dangerous background in these analyses consists of QCD events with leptons from hadron decays or tracks misidentified as leptons. However, these lepton candidates are associated to jets and can be largely suppressed using isolation algorithms.

Robust criteria are developed which allow for a low-background event selection which is rather insensitive to detector inhomogeneities. This robust selection is considered as especially useful for the CMS startup phase. The results show that a determination of the W and Z rates with an experimental precision on the percent level is feasible already in the early phase of the experiment.

9.1.2. W/Z into electrons

The process pp → ZX and pp → WX with subsequent decay of Z and W into electrons is studied using the full CMS detector simulation and analysis scheme. The aim is to define some baseline selection which is suppressing background to a very small level and detector inhomogeneities can be controlled. This selection can thus be considered as especially useful for the CMS startup phase. Details can be found in [341].

Electron (positron) candidates are selected with the following criteria [313]:

- The minimal E_{T} of the electromagnetic cluster has to be larger than 20 GeV with $|\eta_{\mathrm{cluster}}| < 1.4$ for barrel electron candidates and $1.6 < |\eta_{\mathrm{cluster}}| < 2.4$ for endcap electron candidates.
- The cluster should be consistent with the shower shape expected for electromagnetic showers. The spread of the electromagnetic shower along the η direction is rather insensitive to bremsstrahlung, thus allowing a good separation of signal and background shower shapes. Therefore it is required that the spread of the electromagnetic shower in η with respect to η of the supercluster, $\sigma_{\eta\eta}$, is smaller than 0.01.
- The energy deposit in the associated hadron calorimeter cluster should be very small. For this selection the ratio $E_{\mathrm{Had}}/E_{\mathrm{EM}}$ has to be smaller than 0.05.
- In order to be identified as an electron, a reconstructed track has to be matched with the cluster such that $\Delta R < 0.15$ (where $\Delta R = \sqrt{\Delta\phi^2 + \Delta\eta^2}$). Furthermore, it is required that the ratio of the cluster energy and the track momentum, E/P, is larger than 0.9 and that $|1/E - 1/P| < 0.02$.
- Finally, it is required that the electron candidate is isolated. The transverse momentum sum of all other tracks found within a cone radius ΔR of 0.35 divided by the electron candidate

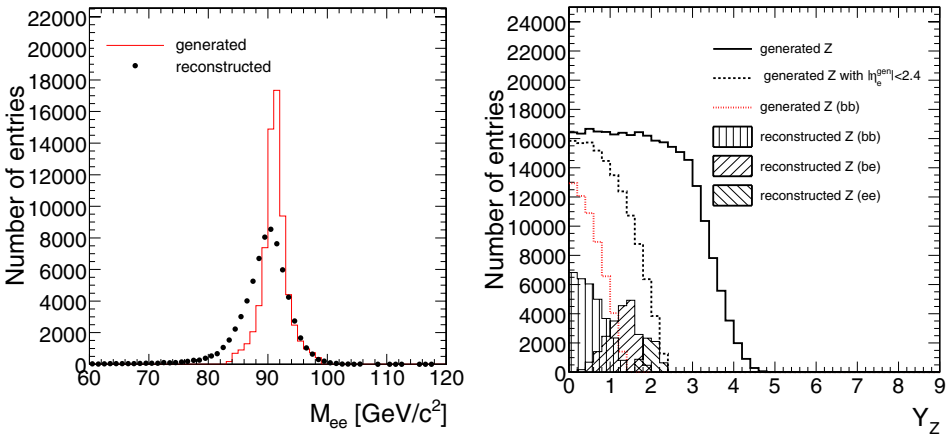

Figure 9.1. Left: Reconstructed and generated Z mass distribution with all cuts. Right: Generated rapidity distribution for all Z candidates and for those where both electrons were generated within the geometrical acceptance of the electromagnetic calorimeter. For comparison, the rapidity distribution of the finally accepted Z events is already shown here.

transverse supercluster energy has to be smaller than 0.2. Only tracks with a transverse momentum above 1.5 GeV/c and with at least four hits in the central tracker which are close to the interaction vertex are considered.

9.1.2.1. $pp \to Z \to eeX$ Selection. We analyse events where one e^+e^- pair consistent with the Z mass is found (if more than two electrons pass the selection criteria, only those two with the highest transverse momenta are considered). The generated and reconstructed mass distribution are shown in Figure 9.1 (left). For now, the "electron" clusters are not corrected for bremsstrahlung within the tracker and the reconstructed Z peak is found to be about 1 GeV lower than the generated one.

Using this selection, the rapidity distribution of the accepted Z events is shown in Fig. 9.1 (right). In addition, the rapidity distribution of the potentially accepted Z bosons, separated for the three cases where both decay electrons are within the acceptance of the barrel calorimeter (BB) $|\eta_{BB}| < 1.4$, both within the endcaps (EE) $1.6 < |\eta_{EE}| < 2.4$ or one within the barrel and the other one in the endcaps (EB) are also shown. In the case that both generated electrons are in the barrel, a Z detection efficiency of about 60% is reached.

Here the electron efficiency is defined by the ratio of reconstructed electrons from accepted Z events to the number of electrons from generated Z events, where the generated electrons fulfilled the condition $|\eta^e_{gen}| < 1.4$. Fig. 9.2 (left) shows the efficiency distribution for all supermodules folded such that the local ϕ angle for all odd supermodules goes from 0–20 degrees and for all even supermodules from 20–40 degrees.

The efficiency drop of about 10% between the supermodules is clearly visible with the available sample of Z events corresponding to roughly 0.2 fb^{-1}. Similar inefficiencies were found in the η direction at supermodule boundaries. From the analysis of the reconstruction efficiency as function of the phi angle, we get an efficiency of $27.1\% \pm 0.4\%$ (if the inter-supermodule regions are excluded) while the average over the whole phi range is $26.5 \pm 0.4\%$.

The average Z efficiency, when both electrons are generated and reconstructed in the barrel calorimeter, is found to be $57.3 \pm 0.2\%$ (where the uncertainties are from the finite number of Monte Carlo events). Half the efficiency loss is caused by the

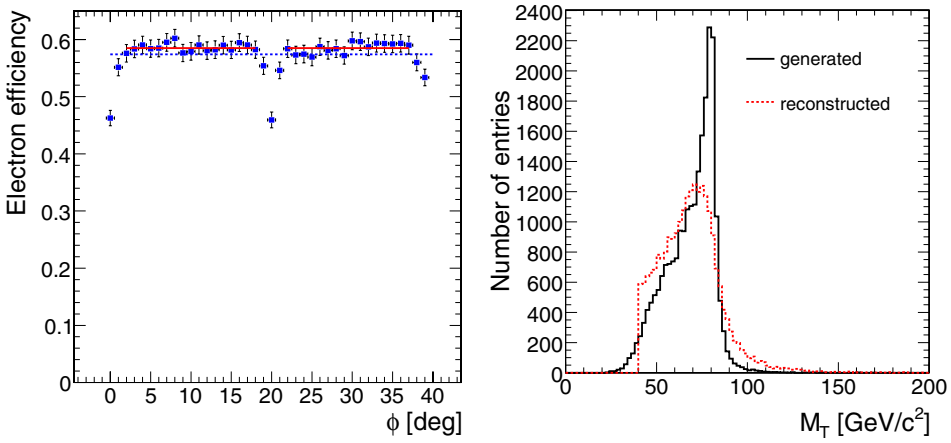

Figure 9.2. Left: The electron reconstruction efficiency in $Z \to e^+e^-$ events as a function of ϕ, all even and odd numbered supermodules are folded such that the odd (even) numbered supermodules always cover local ϕ angles from 0 to 20 degrees and from 20 to 40 degrees respectively. The dotted line corresponds to the average efficiency $57.3 \pm 0.2\%$ over the whole ϕ range and the solid lines correspond to the average efficiency $58.4 \pm 0.2\%$ with the gap regions excluded. Right: Generated (solid line) and reconstructed (dashed line) transverse W mass. The W transverse mass is reconstructed from the electron four-momentum and the missing transverse energy. In this plot, only events with no reconstructed jet above 20 GeV transverse energy are included.

shower-shape requirement, and another quarter by the energy-momentum matching requirement. If events, where at least one electron is reconstructed within the gaps, are removed, the average efficiency is found to be $58.4 \pm 0.2\%$. Assuming that the produced electrons must be homogeneous in ϕ and that the effects from geometrical gaps can be monitored with some reasonable statistics, it should be straightforward to correct for the detector gaps. Already with the available statistics used for this study, the corrections for the efficiency loss in the gaps can certainly be determined with a relative accuracy smaller than about 25%. This number is estimated from comparing the minimal efficiency in the gap and the efficiency in the non-gap regions.

We conclude that already with a few 100 000 reconstructed Z events, collected at the early stage of the experiment, an efficiency determination with a systematic accuracy of better than 1–2% should be possible. Obviously, with the much larger statistics of a few million Z events, these uncertainties can be further reduced. Once data from the CMS detector becomes available, these cuts can be applied on one electron and varied on the other electron to compare the selection efficiency in data and Monte Carlo simulation. This can be used to further improve the detector simulation and to better access systematic uncertainties.

9.1.2.2. $pp \to W \to e\nu X$ Selection. In order to pass the $W \to e\nu$ selection, events must have exactly one electron candidate in the barrel fulfilling the requirements described above, and missing transverse energy associated with the neutrino: a cut on the transverse mass of the $e\nu$ system is applied. The transverse mass m_T is defined as follows:

$$m_T = \sqrt{2 p_T^{(e)} p_T^{(\nu)} (1 - \cos \Delta\phi)} \tag{9.1}$$

where $p_T^{(e,\nu)}$ is the (reconstructed) transverse momentum of the electron and the neutrino respectively and $\Delta\phi$ is the azimuthal angle between the electron and the neutrino.

The missing transverse energy can be determined in several ways, for example:

1. From the vector sum of all clusters in the calorimeter.
2. From the vector sum of hard objects only.

In the electromagnetic calorimeter, the electron transverse energy can be measured accurately. However, the reconstructed transverse missing energy shows a significant bias.

Suspecting that low energy objects (randomly distributed across the detector) are responsible for this bias, we follow the second approach: We select reconstructed jets with a transverse energy above 20 GeV and absolute pseudorapidity less than 2.4 and reconstruct the missing transverse energy only from these jets and the electron. Here we use uncalibrated jets, i.e. whenever we refer to the jet energy we mean raw jet energy.

To study this possibility in more detail, we split our sample into events without jets (as defined in the previous paragraph) and events with one or more jets. Note that in the case of zero accepted jets, only the electron is used to calculate the neutrino transverse energy which is then very close to the electron transverse energy (pointing into opposite directions in ϕ). The transverse mass is equal to twice the electron transverse energy in this case.

No systematic bias is found with this method and the mean value is close to zero. We thus use this method to reconstruct the neutrino transverse energy. The reconstructed W transverse mass is shown in Fig. 9.2 (right). For the purpose of this analysis and the counting of resonant W events, we require the transverse mass to lie in the interval 60 to 100 GeV/c^2.

We consider two sources of systematic uncertainties here: The uncertainty due to inhomogeneities in the detector geometry and the uncertainty related to the jet veto. We expect that the uncertainty from the reconstruction efficiency as function of the electron azimuthal angle for the efficiency correction will be similar as for the Z selection.

To address the effect of the scale uncertainty of the absolute calibration on the jet definition, we investigated the changes in the selection efficiency when moving the threshold transverse energy for the jet definition. It follows that for a cut on the transverse jet energy at 20 GeV, the efficiency slope is roughly 0.1% (absolute) per GeV, corresponding to a relative uncertainty of about 0.25% per GeV.

Assuming a jet energy scale uncertainty of 15% at the LHC startup we obtain an efficiency uncertainty of 0.75% relative. For 5% uncertainty in the jet energy scale expected after the final detector calibration), this value reduces to 0.25%.

The efficiency change due to the jet veto can also be estimated directly from $\mathrm{Z} \to \mathrm{e}^+\mathrm{e}^-$ events (applying a jet veto to these events). In the future, this can be done directly from the data recorded with the CMS detector. Thus with the expected large data samples of $\mathrm{Z} \to \mathrm{e}^+\mathrm{e}^-$, remaining differences between data and Monte Carlo can be studied and corrected with very small uncertainties.

9.1.3. W/Z into muons

Simple sets of cuts can be used in CMS to select large statistics samples of $Z \to \mu\mu$ and $W \to \mu\nu$ events with high purity. They are described in detail in Ref. [342] and summarised here.

The $Z \to \mu\mu$ selection criteria have been chosen to minimise uncertainties from the muon chamber response and from the matching between the inner tracker and the muon spectrometer. The basic idea is to accept events in which one of the muons is reconstructed as an isolated track in the central tracker detector, even if no associated track in the muon spectrometer is present. This results in a more uniform efficiency as a function of the pseudo-rapidity, as observed in Fig. 9.3 (left). From the kinematics point of view only muons with

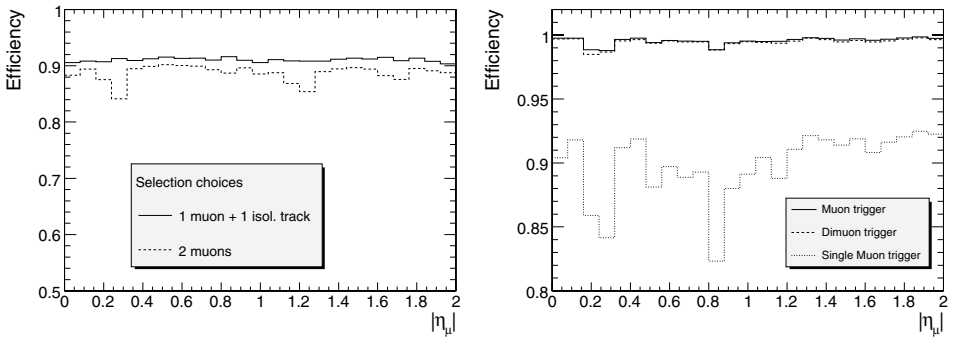

Figure 9.3. Left: Muon efficiency as a function of pseudo-rapidity in the selected $Z \to \mu\mu$ sample. Two cases are considered: a selection using only muons reconstructed in the muon chambers (dashed histogram) and the selection described in the text (solid histogram), which also accepts isolated tracks in the inner tracker. For this test, no HLT trigger criteria have been applied. Right: HLT efficiency on the selected $Z \to \mu\mu$ sample as a function of the pseudorapidity of one of the muons. All but the HLT trigger criteria have been applied. The regions at $|\eta| \approx 0.25$ and $|\eta| \approx 0.8$, with a slightly lower trigger efficiency, are visible. The fraction of events triggered by dimuon and single-muon triggers are also shown.

$p_T > 20\,\text{GeV}$ and pseudorapidity $|\eta_\mu| < 2.0$ are considered in the present analysis. A dimuon mass window of $\pm 3\Gamma_Z = 7.5\,\text{GeV}$ around the reconstructed Z mass is used. Figure 9.3 (right) shows the efficiency of the HLT criteria on the selected sample as a function of the muon pseudo-rapidity. One can clearly observe two regions with smaller efficiency, around $|\eta| \approx 0.25$ and $|\eta| \approx 0.8$, where transitions between two muon wheels take place. The efficiency is dominated by the dimuon component, which represents a unique tool to study the performance of the single-muon subtrigger, which is of relevance for other selections, like $W \to \mu\nu$.

Even if the rate of $W \to \mu\nu$ events is expected to be larger than the $Z \to \mu\mu$ rate by an order of magnitude, the experimental context is more demanding due to a lower trigger efficiency, only moderate transverse missing energy in the event, the absence of a precise mass constraint and a full dependence on tracker and muon spectrometer behaviours. This will lead to larger experimental uncertainties, which can be studied with the $Z \to \mu\mu$ data samples. The selection of $W \to \mu\nu$ events uses the same η cut but a higher p_T threshold, 25 GeV, due to the higher threshold for the single-muon trigger. Figure 9.4 shows the transverse invariant mass distribution of the muon-E_T^{miss} system in $W \to \mu\nu$ events, compared to QCD expectations.

Systematic uncertainties in the determination of $Z \to \mu\mu$ and $W \to \mu\nu$ acceptances are summarised in Tables 9.1 and 9.2. The various sources of uncertainties are discussed in detail in Ref. [342]. Most of them are evaluated for a CMS detector calibrated with $1\,\text{fb}^{-1}$. The experimental components are well under control in the case of the $Z \to \mu\mu$ selection, with the limited knowledge on the track efficiency as the dominant source. In the $W \to \mu\nu$ case, many of them contribute at a similar level, with E_T^{miss} providing the largest uncertainty. Concerning theoretical sources, the boson p_T uncertainties are the dominant contribution. They are estimated from a comparison between LO and NLO CMS simulations using MC@NLO as event generator [343], as shown in Fig. 9.5.

The results of the study can be summarised in terms of cross section measurement accuracies, for $1\,\text{fb}^{-1}$ of integrated luminosity, as follows: $\Delta\sigma/\sigma(pp \to Z + X \to \mu\mu + X) = 0.13\ (stat) \pm 2.3\ (syst.) \pm 10\ (lumi)\%$ and $\Delta\sigma/\sigma(pp \to W + X \to \mu\nu + X) = 0.04\ (stat.) \pm 3.3\ (syst.) \pm 10\ (lumi)\%$, where luminosity represents the dominant uncertainty which will eventually decrease to 5% with more integrated luminosity.

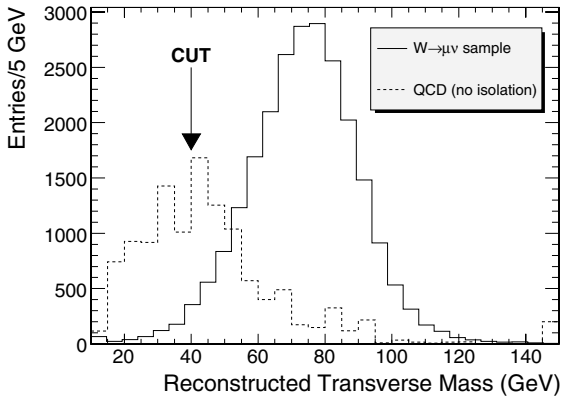

Figure 9.4. Transverse invariant mass reconstructed in $W \to \mu\nu$ events. In order to observe the shape of the QCD background with more statistics, the HLT muon isolation criteria have not been applied to obtain the plot. The position of the lower cut ($M_{\mu\mu} > 40\,\mathrm{GeV/c^2}$) is indicated with an arrow.

Table 9.1. Relative systematic uncertainties on the acceptance for the $Z \to \mu\mu$ sample.

Source	Uncertainty (%)
Tracker efficiency	1
Magnetic field knowledge	0.03
Tracker alignment	0.14
Trigger efficiency	0.2
Jet energy scale uncertainties	0.35
Pile-up effects	0.30
Underlying event	0.21
Total exp.	1.1
PDF choice (CTEQ61 sets)	0.7
ISR treatment	0.18
p_{T} effects (LO to NLO)	1.83
Total PDF/ISR/NLO	2.0
Total	2.3

QCD backgrounds seem to be under control, even if final checks with data will be necessary to determine the level of background with more precision.

Therefore, rates within the fiducial volume of the detector can be determined with high accuracy, even for the first stages of the LHC ($\approx 2.3\%$ for $Z \to \mu\mu$ and $\approx 3.3\%$ for $W \to \mu\nu$). These uncertainties will be significantly reduced with the use of the next generation of NLO Monte Carlos and final detector calibrations, and allow these reactions to be used to determine the luminosity.

9.1.4. Parton distribution functions and parton luminosities

The production of inclusive W and Z events is theoretically well understood and the couplings to quarks and leptons have been measured with accuracies of 1% or better. Thus, it follows from the previous sections that a precise counting of $W \to e\nu$, $\mu\nu$ and $Z \to ee$, $\mu\mu$ events is

Table 9.2. Relative systematic uncertainties on the acceptance for the $W \to \mu\nu$ sample.

Source	Uncertainty (%)
Tracker efficiency	0.5
Muon efficiency	1
Magnetic field knowledge	0.05
Tracker alignment	0.84
Trigger efficiency	1.0
Transverse missing energy	1.33
Pile-up effects	0.32
Underlying event	0.24
Total exp.	2.2
PDF choice (CTEQ61 sets)	0.9
ISR treatment	0.24
p_{T} effects (LO to NLO)	2.29
Total PDF/ISR/NLO	2.5
Total	3.3

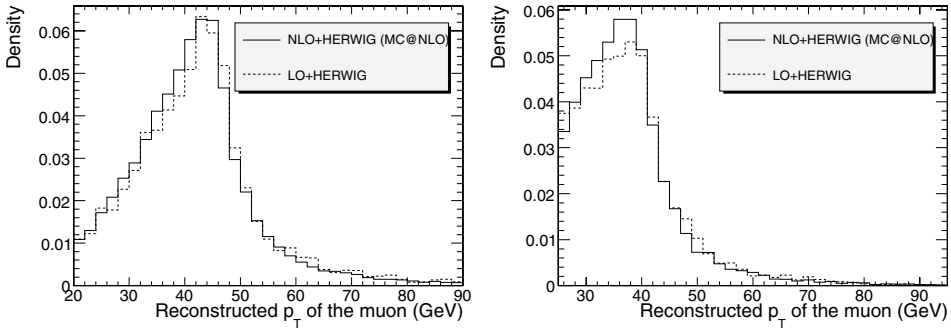

Figure 9.5. Left: Comparison between LO and NLO predictions for the muon p_{T} distribution in $Z \to \mu\mu$ selected events. Both histograms have been normalised to the total number of events generated in the fiducial volume: $|\eta_\mu| < 2.5$, $p_{\mathrm{T}\mu}^{max} > 20\,\mathrm{GeV/c}$, $p_{\mathrm{T}\mu}^{min} > 10\,\mathrm{GeV/c}$ and $M_Z - 6\Gamma_Z < M_{\mu\mu} < M_Z + 6\Gamma_Z$ Right: Comparison between LO and NLO predictions for the muon p_{T} distribution in $W \to \mu\nu$ selected events. Both histograms have been normalised to the total number of events generated in the fiducial volume: $|\eta_\mu| < 2.5$.

equivalent to a precise measurement of the quantity

$$\int_{q,\bar{q}\ partons} \mathrm{d}x_1\,\mathrm{d}x_2\,\sigma_{q\bar{q}\to W,Z} \times L_{pp} \times PDF(x_1, x_2, Q^2), \tag{9.2}$$

where L_{pp} is the LHC integrated luminosity, $\sigma_{q\bar{q}\to W,Z}$ is the cross section for inclusive W or Z production at the partonic level and $PDF(x_1, x_2, Q^2)$ denotes the probability to produce quarks and anti-quarks with proton fractions x_1 and x_2 at a scale Q^2. The prospect studies of Ref. [342], summarised in Table 9.3, show that uncertainties on the parton distribution functions (PDF) have a relatively small influence on the experimental acceptance for the rates, but a large effect on the global rate expectations.

We conclude from Table 9.3 that a comparison between theory and experiment with a 6–7% accuracy is possible. This comparison provides a measurement of the integrated luminosity L_{pp} with a similar level of precision. The small theoretical uncertainties on the experimentally measured rate (from the acceptance uncertainty) allow precise measurements of cross section ratios, such as $\sigma(pp \to ZZ + X)/\sigma(pp \to Z + X)$, in which

Table 9.3. Estimated uncertainties in the rate and in the acceptance for the $pp \to Z + X \to \mu\mu + X$ and $pp \to W + X \to \mu\nu + X$ processes. The global rate is referred to the fiducial volumes used in Ref. [342], which include a pseudorapidity cut of $|\eta_\mu| < 2.5$.

	$Z \to \mu\mu$	$W \to \mu\nu$
Global rate uncertainty (%)	$^{+5.8}_{-7.9}$	$^{+5.6}_{-7.4}$
Acceptance uncertainty (%)	$^{+0.4}_{-0.7}$	$^{+0.6}_{-0.9}$

PDF and luminosity uncertainties cancel. Current studies within theoretical and experimental communities [344] aim to a further reduction of uncertainties associated to PDFs. Finally, PDF validity tests and further reductions in the acceptance uncertainty (below the percent level) will require dedicated studies of the lepton rapidity distributions observed in data, like those suggested in Ref. [345].

9.2. Muon pairs from the Drell–Yan process

9.2.1. Introduction

In the Standard Model, the production of lepton pairs in hadron-hadron collisions, the Drell–Yan (DY) process [346], is described by s-channel exchange of photons or Z bosons. The parton cross section in the lepton-pair centre-of-mass system has the form:

$$\frac{\mathrm{d}\sigma}{\mathrm{d}\Omega} = \frac{\alpha^2}{4s}[A_0(1+\cos^2\theta) + A_1\cos\theta] \tag{9.3}$$

where $\sigma = \frac{4\pi\alpha^2}{3s}A_0$ and $A_{\mathrm{FB}} = \frac{3}{8}\frac{A_1}{A_0}$ are the total cross section and the forward-backward asymmetry, and θ is angle of lepton in the dilepton rest frame with respect to the quark direction. The terms A_0 and A_1 are fully determined by the electroweak couplings of the initial- and final-state fermions. At the Z peak the Z exchange is dominating and the interference term is vanishing. At higher energies both photon and Z exchange contribute and the large value of the forward-backward asymmetry is due to the interference between the neutral currents. Fermion-pair production above the Z pole is a rich search field for new phenomena at present and future high energy colliders. The differential cross section is sensitive to manifestation of new physics from a multi-TeV scale by adding new amplitudes or through their interference with the neutral currents of the SM. At hadron colliders the parton cross sections are folded with the parton density functions (PDF): $pp \to l_1 l_2$

$$\frac{\mathrm{d}^2\sigma}{\mathrm{d}M_{ll}\mathrm{d}y}[pp \to l_1 l_2 + X] \approx \sum_{ij}\left(f_{i/p}(x_1)f_{j/p}(x_2) + (i \leftrightarrow j)\right)\hat{\sigma} \tag{9.4}$$

where $\hat{\sigma}$ is the cross section for the partonic subprocess $ij \to l_1 l_2$, $M_{ll} = \sqrt{\tau s} = \sqrt{\hat{s}}$ the mass of the lepton-pair system, y the rapidity of the lepton pair, $x_1 = \sqrt{\tau}e^{y}$ and $x_2 = \sqrt{\tau}e^{-y}$ the parton momentum fractions, and $f_{i/p(\bar{p})}(x_i)$ the probability to find a parton i with momentum fraction x_i in the proton.

The total cross section and the forward-backward asymmetry are function of observables which are well measured experimentally for final states containing e^+e^- or $\mu^+\mu^-$: the invariant mass and the rapidity of the final-state lepton pair. This allows to reconstruct the centre-of-mass energy of the initial partons, even if their flavours are unknown. For a $(x_1 \geqslant x_2)$ pair of partons we have 4 combinations of *up*- or *down*-type quarks initiating the interaction: $u\bar{u}, \bar{u}u, d\bar{d}, \bar{d}d$. In pp collisions the anti-quarks come always from the sea and the quarks can

Table 9.4. x_1 and x_2 for different masses and rapidities.

y	0	2	4	0	2	4	0	2	4
	$M = 91.2\,GeV/c^2$			$M = 200\,GeV/c^2$			$M = 1000\,GeV/c^2$		
x_1	0.0065	0.0481	0.3557	0.0143	0.1056	0.7800	0.0714	0.5278	-
x_2	0.0065	0.0009	0.0001	0.0143	0.0019	0.0003	0.0714	0.0097	-

have valence or sea origin. The x-range probed depends on the mass and rapidity of the lepton pair as shown in Table 9.4.

The results presented here extend the studies for the LHC SM workshop (see [158] and references therein), using more data and the CMS full detector simulation and reconstruction. More details can be found in [347].

9.2.2. Cross section measurements

Simulation of Drell–Yan events in proton-proton collisions at 14 TeV centre-of-mass energy is performed with PYTHIA 6.217 using the CTEQ5L parton distribution functions. The possible contributions from higher-order terms in the dimuon production cross section are taken into account by using a K factor of 1.3 as calculated with the program PHOZPRMS [348]. Eleven samples of 10 000 events each with different cut-off values on the dimuon invariant mass are generated: $M_{inv} \geqslant 0.2, 0.5, 1, 1.5, 2, 2.5, 3, 3.5, 4, 4.5, 5\,TeV/c^2$. Only events with at least two muons in the pseudorapidity range $|\eta| \leqslant 2.5$, with transverse momentum $p_T \geqslant 7\,GeV/c$ are preselected. No cuts on isolation of muons are made at the pre-selection stage. The total efficiency for dimuon pre-selection, ε, is about 87% for a mass of $1\,TeV/c^2$ and 96% for a mass of $5\,TeV/c^2$. To simulate the detector geometry, materials and particle propagation inside the detector, the GEANT 4-based simulation of the CMS detector is used.

The trigger simulation is based on the on-line reconstruction algorithms. Events are selected by the single- and double-muon triggers. This means that at least one muon candidate is within pseudorapidity region $|\eta| \leqslant 2.1$. The total efficiency of triggering including reconstruction and trigger selection efficiency is 98% at 1 TeV. There is significant decrease in trigger efficiency after applying calorimeter isolation cuts (down by 15%). The tracker isolation practically does not affect the trigger efficiency. Thus the additional cuts on calorimeter and tracker isolation of muon tracks are not applied in this analysis.

The off-line muon reconstruction algorithm is applied only to events which have passed trigger selection. At the off-line level two muons inside the CMS acceptance $|\eta| \leqslant 2.4$ are required. The overall efficiency of the full reconstruction procedure taking into account trigger and off-line reconstruction inefficiency is between 97% and 93% for a mass range of 0.2 to $5\,TeV/c^2$, as shown in Fig. 9.6 (left). In the case of an ideal detector the mass resolution smearing for fully-reconstructed events is between 1.8% and 6% for the same mass range, Fig. 9.6 (right). The effect of misalignment on the mass resolution varies from 1.1% up to 2.3% (1.3%) for the *First Data* (*Long Term*) scenarios at the Z and from 5% up to 25% (6%) for 3 TeV/c^2.

The cross sections of Drell–Yan production for the simulated CMS runs are shown in Table 9.5. The non-reducible backgrounds considered are vector boson pair production ZZ, WZ, WW, $t\bar{t}$ production etc. The simulation and pre-selection of background events is done with the same cuts as for the signal above. In the SM the expected leading-order cross section of these events is negligible in comparison with the Drell–Yan one, see Table 9.5.

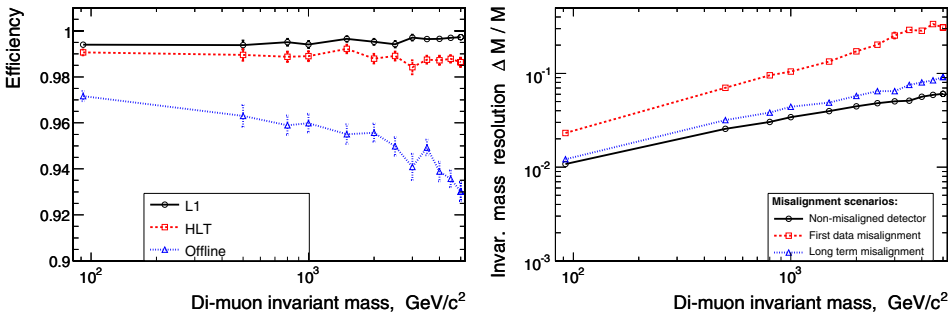

Figure 9.6. Left: dimuon reconstruction efficiency, and right: invariant mass resolution; both as function of the invariant mass cut.

Table 9.5. Leading-order cross sections of Drell–Yan, preselected Drell–Yan, dibosons (ZZ, ZW, WW) and $t\bar{t}$ events in fb. The CTEQ5L parton distributions are used.

$M_{\mu^+\mu^-}$, TeV/c^2	$\geqslant 1.0$	$\geqslant 1.5$	$\geqslant 2.0$	$\geqslant 2.5$	$\geqslant 3.0$	$\geqslant 4.0$
Drell–Yan	6.61	1.04	$2.39 \cdot 10^{-1}$	$6.53 \cdot 10^{-2}$	$1.97 \cdot 10^{-2}$	$2.09 \cdot 10^{-3}$
Pre-sel. D-Y	5.77	$9.53 \cdot 10^{-1}$	$2.24 \cdot 10^{-1}$	$6.14 \cdot 10^{-2}$	$1.87 \cdot 10^{-2}$	$2.00 \cdot 10^{-3}$
Dibosons	$2.59 \cdot 10^{-4}$	$1.51 \cdot 10^{-4}$	$5.6 \cdot 10^{-5}$	$2.26 \cdot 10^{-5}$	$9.06 \cdot 10^{-6}$	$1.66 \cdot 10^{-6}$
$t\bar{t}$	$2.88 \cdot 10^{-4}$	$2.58 \cdot 10^{-4}$	$1.55 \cdot 10^{-4}$	$7.02 \cdot 10^{-5}$	$2.93 \cdot 10^{-5}$	$3.65 \cdot 10^{-6}$

Table 9.6. Relative errors of the Drell–Yan muon pairs cross section measurements in the fiducial volume.

$M_{\mu^+\mu^-}$, TeV/c^2	Detector smearing	Statistical 1 fb^{-1}	Statistical 10 fb^{-1}	Statistical 100 fb^{-1}	Theor. Syst.
$\geqslant 0.2$	$8 \cdot 10^{-4}$	0.025	0.008	0.0026	0.058
$\geqslant 0.5$	0.0014	0.11	0.035	0.011	0.037
$\geqslant 1.0$	0.0049	0.37	0.11	0.037	0.063
$\geqslant 2.0$	0.017		0.56	0.18	0.097
$\geqslant 3.0$	0.029			0.64	0.134

The $\tau\tau$ background (from τ decaying to μ and neutrinos) is 0.8% at the Z pole and 0.7% for masses above 1 TeV/c^2. The background from Drell–Yan production of $q\bar{q}$ pairs (mostly semi-leptonic b or c decays) is 0.3% at the Z pole without applying any isolation cuts and below 0.1% for masses above 1 TeV/c^2. The other background sources are negligible. If the need arises they can be further suppressed by acoplanarity and isolation cuts in the tracker.

The main experimental systematic effects in the cross section measurement arise from the total muon inefficiency and momentum resolution. The latter is very important at high mass as smearing from lower masses from the steeply falling Drell–Yan spectrum can contaminate the high mass measurements, especially if the tails of the momentum resolution are not under control. The main sources of systematic uncertainties on the momentum resolution come from the alignment of the muon chambers and the central tracker, both at start-up and high luminosity.

The statistical errors for 1, 10 and 100 fb^{-1} runs, the systematic uncertainty due to smearing in the detector and from theory side are given in Table 9.6. The modification of the measured cross section due to uncertainty of the mass resolution does not exceed 2.9% which is reached for a mass of 3 TeV/c^2, see Table 9.6. This has been estimated by applying

an additional smearing to the dimuon mass (see [99,347]). The misalignment does not affect the efficiency of dimuon reconstruction for any masses [99]. Taking into account the trigger efficiency changes from 98.5% to 97% for masses from 0.2 to 5 TeV/c^2, very conservatively we may assign half of this change with mass, i.e., 0.75%, as a systematic uncertainty.

An important ingredient in the cross section measurement is the precise determination of the luminosity. A promising possibility is to go directly to the parton luminosity [345] by using the $W^{\pm}(Z)$ production of single (pair) leptons. New estimates show that in this way the systematic error on $\sigma_{DY}^{high\,Q^2}$ *relative* to σ_Z can be reduced to $\approx$ 5–12% [349].

On the theory side we consider several sources of systematic uncertainties. Higher order QCD corrections are often taken into account with K-factor of 1.3 as calculated with the program PHOZPRMS [348]. It is expected that the total value of additional NNLO contributions does not exceed 8% .

A full-scale analysis of experimental data (comparison data with theory, taking into account acceptance corrections for precise measurement of σ and A_{FB} at large centre-of-mass energies $\hat{s}$) requires good knowledge of the different types of genuine electroweak (EW) radiative corrections to the DY process: vertex, propagator, EW boxes. A complete one-loop parton cross section calculation has been included in [158] and confirmed in [350]. The EW corrections change the cross section by 10–20%. The calculation [105] of the weak radiative corrections to the Drell–Yan processes due to additional heavy bosons contributions shows that these corrections are about 2.9% to 9.7% for mass region between 0.2 TeV/c^2 and 5 TeV/c^2.

The phenomenological origin of PDF gives one additional systematic error. First of all, estimates of cross section obtained by using different sets of structure functions do not give exactly the same values. The results vary within $\pm$7% for $M_{ll} \geqslant 1$ TeV/c^2. The internal PDF uncertainties are estimated using the LHAPDF library [95,351]. The PDF-dependence of the acceptance efficiency is estimated by using the PDF sets CTEQ5L, CTEQ6L and MRST2001E. The changes in the acceptance efficiency are up to 0.5%. The ambiguity in the acceptance efficiency due to internal PDF uncertainties is larger, but less than 1.4% for any mass region.

The summary of the estimated systematic uncertainties as function of the dilepton mass is given in Fig. 9.7. The CMS experiment has excellent potential to measure the cross section for dimuon pairs up to the highest masses that will be accessible at the LHC, and to test the Standard Model up to very high momentum transfers in a new and unexplored energy range. Current uncertainties from theory are larger than the experimental uncertainties. The statistical errors will dominate for invariant masses larger than 2 TeV/c^2 even for 100 fb^{-1}.

9.2.3. Prospects on the measurement of the forward-backward asymmetry

To measure the forward-backward asymmetry we need the original quark and anti-quark directions of the initiating partons, but these are not known in the case of pp experiments, where the initial state is symmetric. In Ref. [96,112] it is shown that it is possible to approximate the quark direction with the boost direction of the dimuon system with respect to the beam axis. This is due to the fact that the valence quarks have on average larger momentum than the sea anti-quarks, and therefore the dimuon boost direction approximates the quark direction. The most unambiguous tagging occurs for large dimuon rapidity.

The approximation of the original quark direction for pp collisions leads to a flattening out of the original asymmetry ($\approx$ 0.61 for Drell–Yan events) by a factor of almost 2. However, using multi-dimensional fits [111] or reweighting techniques depending on the mistag and acceptance which are under development, we can measure the original asymmetry.

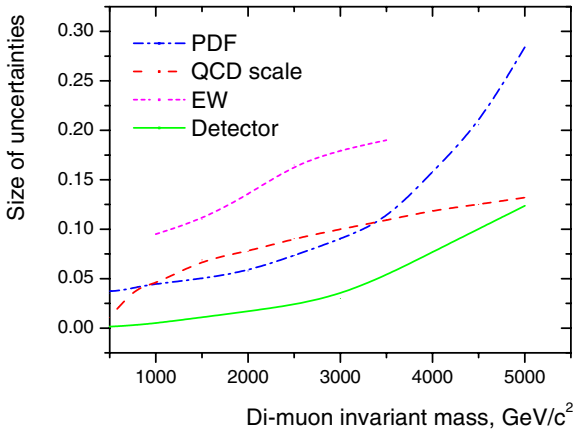

Figure 9.7. Size of the EW corrections and the cross section uncertainties from PDFs, hard process scale and detector understanding as a function of the dimuon invariant mass cut.

The accuracy of asymmetry measurements depends on:

- statistical uncertainty which grows with rising mass cut value, as the number of events for integrated luminosity of e.g. $\int \mathcal{L}\,\mathrm{d}t = 100\,\mathrm{fb}^{-1}$ decreases with mass;
- systematic uncertainty from the variation of the mistag probabilities for various PDF sets, typically below 10%.

We expect the systematic uncertainty to dominate the statistical one for integrated luminosity of $\int \mathcal{L}\,dt = 100\,\mathrm{fb}^{-1}$ and dimuon masses around $500\,\mathrm{GeV/c^2}$, while the statistical one to be more important for dimuon mass cuts above $1000\,\mathrm{GeV/c^2}$.

9.3. Determination of the W mass

9.3.1. Introduction

The precise measurement of the mass of the W boson constitutes an important consistency check of the Standard Model and, together with the top quark mass, is sensitive to supersymmetric corrections. Such a precision measurement of the W mass at the LHC becomes feasible because a huge sample of data available at the LHC will guarantee a nearly negligible statistical uncertainty and a good control of the systematic effects. Extrapolating from traditional approaches based on the reconstruction of the transverse mass $m_{\mathrm{T}} = \sqrt{2p_{\mathrm{T}}^{l}p_{\mathrm{T}}^{\nu}(1-\cos(p_{\mathrm{T}}^{l}, p_{\mathrm{T}}^{\nu}))}$ in leptonic W decays, the most relevant contributions to the systematic uncertainties come from the lepton energy or momentum scale, the lepton energy or momentum resolution, the modelling of the system recoiling against the W boson, the parton distribution functions, the W intrinsic width, from radiative decays and from backgrounds. To accomplish a competitive measurement of the W boson mass, new strategies must be considered [352]. The most promising one consists in predicting the distribution of experimental observables sensitive to the W mass, such as the transverse momentum of the charged lepton (p_{T}^{l}) and the transverse mass of the boson from the corresponding distribution measured in Z boson decays into two charged leptons. The concept of transverse mass measurement can be applied to Z boson events by regarding one of the reconstructed

leptons as missing energy. The theoretical description of both decays is very similar and the resulting distributions in transverse mass are comparable for a wide range in kinematics.

The advantage of this approach, conceptually discussed in [353], is that most of the experimental and theoretical uncertainties, being common between W and Z, cancel in the comparison, leading to a global reduction of the systematic uncertainty. The drawback is a larger statistical uncertainty due to the smaller production rate of Z bosons decaying to charged leptons. Yet a statistical precision of order $10\,\mathrm{MeV/c^2}$ and $30\,\mathrm{MeV/c^2}$ for an integrated luminosity of $10\,\mathrm{fb}^{-1}$ and $1\,\mathrm{fb}^{-1}$ respectively is anticipated. In order not to be limited by statistics, the analyses are performed using large data samples produced with the fast simulation of the CMS experiment [11]. Smaller samples of fully simulated events are used for cross checks.

Two different ways to relate Z to W boson events are considered. One is based on the comparison of the same experimental observables in W- and Z-events scaled to the boson masses. The sensitivity of this method, which can take advantage of the precision calculation of the theoretical ratio of the W and Z boson differential production cross-sections, is fully addressed in the analysis of transverse energy distribution of the electrons from $W \to e\nu$ decays. An alternative approach considered in the analysis of $W \to \mu\nu$ events consists of predicting W boson distributions from Z-events by means of kinematic transformations of measured Z events, parameterised as a function of the boson masses and widths. This more phenomenological approach is exploited in the analysis of the transverse mass distributions, and relies less on the theoretical prediction of the boson p_{T}.

9.3.2. Event selections

In order to obtain a clean signal of $W \to \mathrm{l}\nu$ decays, events that passed the High Level Trigger (HLT) for single leptons are required to satisfy the following selection cuts: one isolated muon with $p_{\mathrm{T}} > 25\,\mathrm{GeV/c}$ within the pseudo-rapidity region $|\eta| < 2.3$ or one isolated electron with $p_{\mathrm{T}} > 25\,\mathrm{GeV/c}$ and within $|\eta| < 2.4$; missing transverse energy $E_{\mathrm{T}}^{\mathrm{miss}} > 25\,\mathrm{GeV}$; no jets in the event with $p_{\mathrm{T}jet} > 30\,\mathrm{GeV/c}$; the transverse momentum of the system recoiling against W has to be lower than $20\,\mathrm{GeV/c}$, measured from the lepton p_{T} and the missing transverse energy.

The difference in minimum p_{T} of the charged lepton is determined by the single lepton trigger threshold. The last two selection cuts are intended to select W bosons produced with a small transverse momentum. The selection efficiency is about 15% for the electron channel and 25% for the muon channel, with a background at the percent level, dominated by leptonic Z decays with one lepton outside the acceptance, as shown in Fig. 9.8.

Z events used to predict the W distribution are also selected from the sample of events passing the HLT for single leptons. Z candidates contain a pair of identified charged leptons consistent with the Z mass hypothesis [352]. One of the two leptons, randomly chosen, is removed from the event to mimic a W decay. The same selections discussed above are then applied, with the cut values on the lepton quantities (minimum lepton p_{T} and event missing transverse energy) scaled by the ratio M_Z/M_W. This choice is intended to minimise kinematic and acceptance differences in Z and W events and thus the theoretical uncertainties implied by the above mentioned approaches.

9.3.3. $W \to e\nu$

The analysis strategy is based on the prediction of the experimental distribution of the electron transverse energy in W events scaled to the boson mass from the corresponding distribution

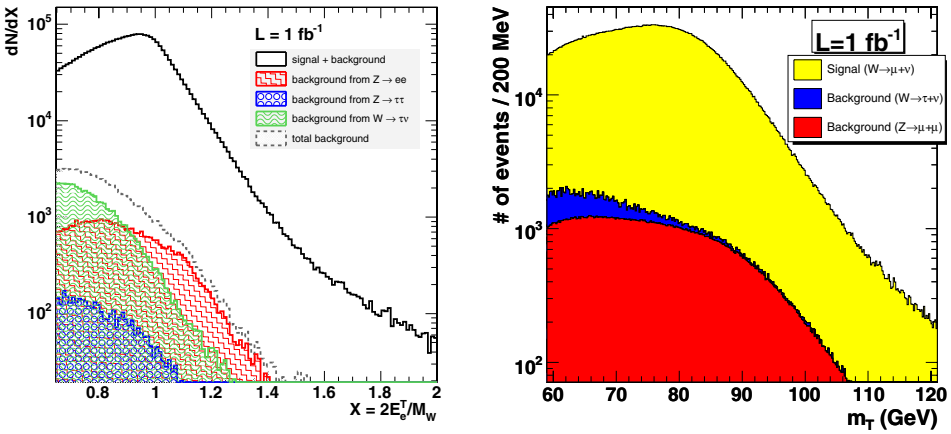

Figure 9.8. W events and main backgrounds for 1 fb^{-1}. Left: Electron scaled transverse energy distribution in $W \to e\nu$ decays and the backgrounds from $Z \to e^+e^-$, from $Z \to \tau^+\tau^-$ and from $W \to \tau\nu$ for 1fb^{-1}. Right: Transverse mass distribution in the muon channel with the fractions of $Z^0/\gamma^* \to \mu^+\mu^-$ (red/grey) $W \to \tau\nu$ (blue/dark), and W $\to \mu\nu$ (yellow/light) events.

measured for Z bosons decaying into e^+e^- pairs, along with the theoretical ratio between the W and Z cross-sections, calculated at a fixed perturbative order. Ideally, the differential cross section for the W boson can be predicted from the one measured for Z boson by scaling the lepton transverse momenta with the boson masses, $p_{\mathrm{T}}^{\mathrm{lept,Z}} = M_Z/M_W\, p_{\mathrm{T}}^{\mathrm{lept,W}}$, as:

$$\left.\frac{\mathrm{d}\sigma^{W}}{\mathrm{d}p_{\mathrm{T}}^{\mathrm{lept,W}}}\right|_{\mathrm{pred}} = \frac{M_Z}{M_W} R(X) \left.\frac{\mathrm{d}\sigma^{Z}}{\mathrm{d}p_{\mathrm{T}}^{\mathrm{lept,Z}}}\left(p_{\mathrm{T}}^{\mathrm{lept,Z}} = \frac{M_Z}{M_W} p_{\mathrm{T}}^{\mathrm{lept,W}}\right)\right|_{\mathrm{meas}}, \tag{9.5}$$

where $R(X) = \frac{\mathrm{d}\sigma^W}{\mathrm{d}X^W} / \frac{\mathrm{d}\sigma^Z}{\mathrm{d}X^Z}$ is the ratio, deduced from theoretical calculations, between the differential cross sections in terms of the scaled variable $X^V = \frac{p_{\mathrm{T}}^{\mathrm{lept},V}}{M_V}$, with $V = \mathrm{W}, \mathrm{Z}$. The parameter M_W can be extracted by fitting this prediction to the distribution for W events observed in the experiment. In practice, additional corrections to $R(X)$ are needed to account for the acceptance to Z and W events and for the experimental resolution. This calls for a detailed understanding of the detector response by means of Monte Carlo simulations compared to control samples. Clearly, the definition of $R(X)$ is the most critical aspect and must include both detector effects and theoretical predictions.

The results for 1 fb^{-1} of integrated luminosity using the technique just described are shown in Fig. 9.9. The statistical precision of the method is determined from the resulting χ^2 distribution. The evaluation of the systematic uncertainties affecting the measurement of the W mass is performed by determining the distortions implied by the different systematic effects mentioned above. The effects of instrumental origin have been studied by fixing $R(X)$ to the theoretical prediction exactly describing the samples of generated events (i.e. an exact knowledge of the theory is assumed) and by introducing distortions and biases in the detector response. The resulting shift in M_W is assumed as the systematic uncertainty associated to the effect. The detector response to electrons, the largest source of systematic uncertainty of instrumental origin with this method, can be determined with the required precision from $Z \to ee$ events.

The prediction of the lepton transverse spectrum is plagued by large radiative QCD corrections. Yet, in the method adopted, large cancellations occur and $R(X)$ can be reliably

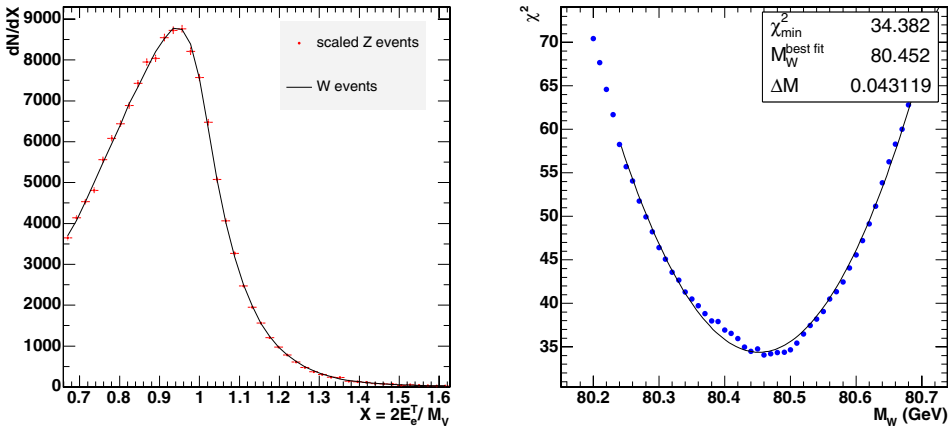

Figure 9.9. Comparison of the scaled electron E_{T} spectra for Z (dots) and W boson (line) events (left) and χ^2 dependence on M_W (right) for 1 fb^{-1} of integrated luminosity.

predicted. The uncertainty related to the missing orders in the perturbative expansion can be quantified by the dependence of the available NLO prediction on the choice of the renormalisation and factorisation scales. A conservative figure of 30 MeV/c^2 for the mass uncertainty is deduced. This will become the dominant error at 10 fb^{-1}. Yet the reduction of this error by extending the calculation one order higher in α_S is technically feasible [353].

9.3.4. $W \to \mu\nu$

As a complementary method, the transverse mass distribution of W events in the muon channel is modelled from $\mathrm{Z} \to \mu^+\mu^-$ events by a kinematic transformation. In the rest frame of the Z boson, the lepton momenta are scaled such that their invariant mass distribution represents that of the W boson [352]. After removing one randomly chosen muon to mimic a neutrino, the whole system is boosted back into the detector frame, thus obtaining a template for the expected distribution of W events, which depends on the W and Z boson masses and widths as parameters. By iterating the procedure for different W boson masses, the best agreement with the observed transverse mass distribution in W events is determined using a χ^2 criterion. In practice, weighting factors take into account unavoidable differences between the W and Z samples, such as the acceptance for the second lepton, photon radiation, and differences in η and p_{T} of W and Z bosons. Thus perfect agreement of the distributions at the nominal W mass and for the simulated detector is ensured, while systematic effects are studied by introducing distortions of experimental or theoretical origin. The resulting shifts in the extracted W mass are taken as the related systematic uncertainties.

The dominant systematic error arises from scale and resolution uncertainties in the missing energy determined from the calorimeters. These can be controlled by using the Z sample, where the boson p_{T} can be measured from the two charged leptons, as is shown in Fig. 9.10. The observed differences of 2% on the scale and 5% on the resolution are taken as the systematic uncertainties.

9.3.5. Expected precision and systematic uncertainties

The expected size of various detector effects for the early detector operation, after the analysis of an initial integrated luminosity of 1 fb^{-1}, and for a better detector understanding

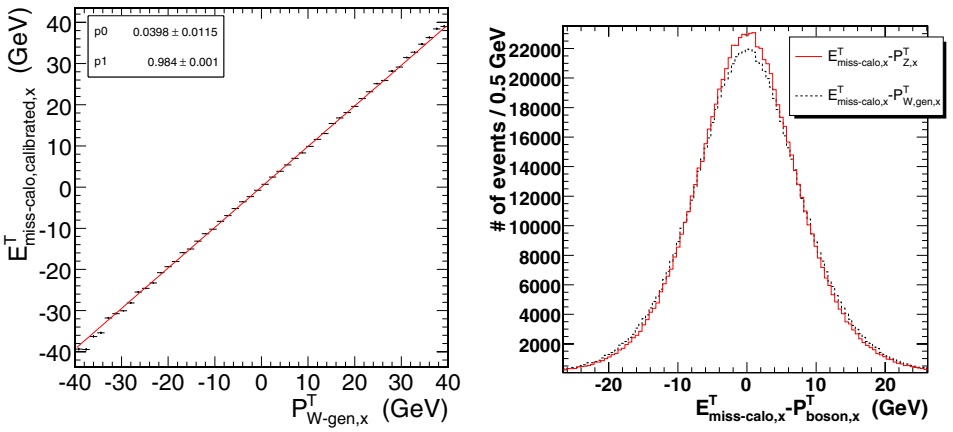

Figure 9.10. Left: x-component of the calibrated missing transverse energy in the calorimeters using the reconstructed muon p_{T} in Z events, as a function of the transverse W boson momentum at generator level. The slope of a fitted straight line is 0.98. Right: Difference between the reconstructed missing energy in the calorimeters and the measured muon p_{T} in Z events (red/grey line) or the W boson p_{T} at generator level (black dashed line). The RMS of the distribution is 8.15 GeV for Z events and 8.65 GeV for W events.

expected after employing an integrated luminosity of $10\,\mathrm{fb}^{-1}$, is shown in Table 9.7 for the scaled p_{T}-lepton method applied to the electron channel, and for the muon channel using the transformation method.

The measurements of the W mass by means of $W \to e\nu$ and $W \to \mu\nu$ decays are largely independent. Common experimental uncertainties arise from the systematics involving the missing transverse energy in the calorimeters.

Based on the estimated systematic errors, it is clear that the scaled p^T-lepton method suffers less from experimental systematic errors than the transformation method. If systematic uncertainties arising from the theoretical prediction of the transverse momenta of the Z and W bosons can be brought to a level of $\approx 10\,\mathrm{MeV/c^2}$, the scaled p^T-lepton method is clearly the first choice. Using the scaled p_{T}-lepton method in the muon channel leads to a better statistical precision of $30\,\mathrm{MeV/c^2}$ for $1\,\mathrm{fb}^{-1}$ due to the higher acceptance for muons compared to electrons. The total instrumental uncertainty of the p_{T}-lepton method applied to the muon channel is estimated from the findings in the electron channel and amounts to about $25\,\mathrm{MeV/c^2}$ for the initial measurement with an integrated luminosity of $1\,\mathrm{fb}^{-1}$. Uncertainties due to the recoil modelling are fully correlated with the electron channel. The component of the experimental error in common with the electrons amounts to about $20\,\mathrm{MeV/c^2}$. Clearly, all theoretical uncertainties are of similar size and also correlated between the electron and muon channels.

The transformation method has the advantage of providing templates for observables in W events from measured observables in Z events. In particular, the measurement of the transverse momentum of Z bosons and the cross checks on the modelling of the missing energy are of vital importance to quantify systematic uncertainties.

The combination of the electron and muon channels brings the statistical uncertainty to a final precision of better than $10\,\mathrm{MeV/c^2}$ for an integrated luminosity of $10\,\mathrm{fb}^{-1}$, and a systematic uncertainty of instrumental origin below $20\,\mathrm{MeV/c^2}$ should be within reach.

Table 9.7. Expected systematic uncertainties on M_{W} for the scaled E^T-lepton method with electrons (upper part) and for the Z transformation method applied to the muon channel (lower part). The first column lists the systematic effect considered, the second and third columns show the assumed detector uncertainty for an initial integrated luminosity of $1\,\mathrm{fb}^{-1}$ and the resulting uncertainty on M_W. The last two columns show the extrapolation to an integrated luminosity of $10\,\mathrm{fb}^{-1}$, when the detector understanding is assumed to have significantly improved.

Source of uncertainty	uncertainty	ΔM_W[MeV/c^2]	uncertainty	ΔM_W [MeV/c^2]
	with $1\,\mathrm{fb}^{-1}$		with $10\,\mathrm{fb}^{-1}$	
	scaled lepton-p_{T} method applied to $\mathrm{W} \to \mathrm{e}\nu$			
statistics		**40**		15
background	10%	10	2%	2
electron energy scale	0.25%	10	0.05%	2
scale linearity	0.00006/ GeV	30	<0.00002/ GeV	<10
energy resolution	8%	5	3%	2
MET scale	2%	15	<1.5%	<10
MET resolution	5%	9	<2.5%	< 5
recoil system	2%	15	<1.5%	<10
total instrumental		**40**		**<20**
PDF uncertainties		20		<10
Γ_W		15		<15
$p_{\mathrm{T}}^{\mathrm{W}}$		30		30 (or NNLO)
	transformation method applied to $\mathrm{W} \to \mu\nu$			
statistics		**40**		15
background	10%	4	2%	negligible
momentum scale	0.1%	14	<0.1%	<10
$1/p^T$ resolution	10%	30	<3%	<10
acceptance definition	η-resol.	19	$< \sigma_\eta$	<10
calorimeter $E_{\mathrm{T}}^{\mathrm{miss}}$, scale	2%	38	$\lesssim$1%	<20
calorimeter $E_{\mathrm{T}}^{\mathrm{miss}}$, resolution	5%	30	<3%	<18
detector alignment		12	–	negligible
total instrumental		**64**		**<30**
PDF uncertainties		≈20		<10
Γ_W		10		< 10

9.4. Multi-boson production

9.4.1. Introduction

The study of multiple gauge-boson production at the TeV scale constitutes a unique opportunity to test the Standard Model of Electroweak interactions at the highest possible energies. The production of $W^{\pm}Z^0$ and $W^{\pm}\gamma$ events at the LHC probes the triple gauge-boson couplings and therefore the non-Abelian gauge symmetry of the Standard Model. On the other hand, no neutral gauge-boson couplings exist in the Standard Model, thus anomalies in Z^0Z^0 and $Z^0\gamma$ production, hinting at large s-channel contributions, could be the first indirect manifestation of New Physics. In the following, the selections of $W^{\pm}Z^0$ and Z^0Z^0 events are described, their signal-over-background ratio discussed and the outlook for an early measurement of multiple gauge-boson production is assessed. Further details are given in Ref. [354].

The multi-lepton final states of multiple gauge-boson production are an important background in the search for New Physics, in particular Supersymmetry. A sound

understanding of their production process is therefore needed in the first phase of LHC data-taking before any discovery can be claimed. In particular, Z^0Z^0 production is an irreducible background to the most-coveted discovery at the LHC: the Standard Model Higgs boson. Its early measurement is therefore important.

The cross sections for multiple gauge-boson production at the LHC are of about 50 pb for the $W^{\pm}Z^0$ channel and 20 pb for the Z^0Z^0 channel [158]. These large cross sections and the clean signature of fully-leptonic final states make $W^{\pm}Z^0$ and Z^0Z^0 production observable in the early LHC data. Final states where the gauge bosons decay into electrons and muons are considered: $e^{\pm}e^+e^-$, $\mu^{\pm}e^+e^-$, $e^{\pm}\mu^+\mu^-$ and $\mu^{\pm}\mu^+\mu^-$ for $W^{\pm}Z^0$ production and $e^+e^-e^+e^-$ for the Z^0Z^0 channel. The competing background processes are the Standard Model production of gauge bosons and top quarks, which also yield leptonic final states.

9.4.2. Signal definition and modelling

Both the $W^{\pm}Z^0$ and Z^0Z^0 analyses focus on on-shell gauge bosons. On-shell production of the $W^{\pm}Z^0$ final state proceeds mainly through the s-channel, involving a WWZ triple gauge-boson coupling. Additional contributions from the $W^{\pm}\gamma^*$ final state through a $WW\gamma$ coupling are effectively suppressed by constraining the mass of the observed lepton pair to be compatible with a Z^0 boson. The PYTHIA Monte Carlo generator [24] is used to model $W^{\pm}Z^0$ production and subsequent decay into fully-leptonic final states. Gauge-boson decays into tau leptons are also included. These tau leptons are left free to decay into either leptons or hadrons.

Four-electron final-states can originate from Z^0Z^0 production as well as via either $Z^0\gamma^*$ or $\gamma^*\gamma^*$ production. The requirement of on-shell boson is enforced by considering only electron-positron pairs with a mass between 70 and 110 $\mathrm{GeV/c^2}$. The PYTHIA Monte Carlo is used to generate events of this process, with the additional requirement that the electrons have a rapidity $|\eta| < 2.7$ and a transverse momentum $p_{\mathrm{T}} > 5\,\mathrm{GeV/c}$. Of all generated events, 72% are classified as Z^0Z^0 signal while 26% are ascribed to the $Z^0\gamma^*$ process and 2% to the $\gamma^*\gamma^*$ process.

Taking into account the branching fraction into leptons, $\mathcal{B}$, and the kinematic requirements, ε_{KIN}, the relevant NLO cross sections using the MCFM [56] Monte Carlo are:

$$\sigma_{NLO} \times \mathcal{B} \times \epsilon_{KIN}(pp \to W^+Z^0 \to \ell^+\ell^+\ell^-) = 1034\,\mathrm{fb}$$
$$\sigma_{NLO} \times \mathcal{B} \times \epsilon_{KIN}(pp \to W^-Z^0 \to \ell^-\ell^+\ell^-) = 630\,\mathrm{fb}$$
$$\sigma_{NLO} \times \mathcal{B} \times \epsilon_{KIN}(pp \to Z^0Z^0 \to e^+e^-e^+e^-) = 18.7\,\mathrm{fb}$$

The NLO corrections correspond to k-factors of 1.9 and 1.4 for $W^{\pm}Z^0$ and Z^0Z^0 production, respectively. The NNLO box-diagram contribution to Z^0Z^0 production is not taken into account.

Three-lepton final-states from $W^{\pm}Z^0$ and Z^0Z^0 production are collected with high efficiency by the Level-1 and HLT electron and muon triggers. The Level-1 and HLT efficiencies for events retained by the selections discussed below is 100% [76].

9.4.3. Background processes

The background to the selection of $W^{\pm}Z^0$ and Z^0Z^0 events comprises other processes with multiple leptons in the final states, some of which might be due to fake signals. The most copious sources of multiple leptons at the LHC are $t\bar{t}$ and $Z^0b\bar{b}$ production. The cross section of these processes is large: 830 pb and 1492 pb, respectively, as calculated with MCFM at NLO.

These processes may have two leptons in the final states from leptonic decays of the W bosons arising from $t \to Wb$ decays or of the Z^0 boson, respectively. The other leptons can be produced in the direct or cascade decays of the b quarks. The $Z^0 b\bar{b}$ process is modelled with the COMPHEP Monte Carlo generator [43, 355] and the $t\bar{t}$ process with the TOPREX Monte Carlo program [44]. In addition, the special case in which four electrons are produced in $t\bar{t}$ events is considered in detail and modelled with PYTHIA. Contributions from Wt and $Zc\bar{c}$ to the selected samples are negligible.

Events from $Z^0 Z^0$ production also constitute a background to the $W^{\pm}Z^0$ selection. Events from the $Z^0\gamma^*$ and $\gamma^*\gamma^*$ processes are a background for both the $W^{\pm}Z^0$ and $Z^0 Z^0$ analyses.

9.4.4. $W^{\pm}Z^0$ selection

Events with three charged leptons, either electrons or muons, with $p_{\mathrm{T}} > 10\,\mathrm{GeV/c}$ and $|\eta| < 2.5$, are considered by the $W^{\pm}Z^0$ selection. All possible Z^0-boson candidates from same-flavours opposite-charge lepton pairs are formed. Events are retained if the mass of the Z^0 candidate is within $20\,\mathrm{GeV/c^2}$ of the Z^0-boson mass, m_Z. These criteria effectively suppress Z^0 decays into tau leptons. The background from $Z^0 Z^0$ final states is reduced by rejecting events with a second Z^0 candidate with a mass within $40\,\mathrm{GeV/c^2}$ of m_Z. The remaining lepton is associated to the $W^{\pm}$-boson decay; its transverse momentum must be larger than 20 GeV. This criterion results in lower efficiencies for the $W^{\pm}$ boson decays in tau leptons. The highest-p_{T}lepton associated to the Z^0 boson must satisfy $p_{\mathrm{T}} > 15\,\mathrm{GeV/c}$. If the event contains more than three leptons, the lepton with highest p_{T} is chosen as originating from the $W^{\pm}$. The signal efficiency after these cuts is 9.2% while the $t\bar{t}$, $e^+e^-b\bar{b}$ and $\mu^+\mu^-b\bar{b}$ efficiencies are 0.7%, 0.4% and 0.6%, respectively.

Leptons from the decay of b quarks in the background processes are produced in a higher-multiplicity environment and isolation criteria suppress the background contamination. Electrons associated to the W $^{\pm}$ boson must have no other charged track with $p_{\mathrm{T}} > 2\,\mathrm{GeV/c}$ within a $\Delta R = 0.3$ cone around their direction. All muon candidates must have an energy measured in the calorimeters within a $\Delta R = 0.3$ cone around their direction smaller than 5 GeV and the sum of the p_{T} of tracks within a $\Delta R = 0.25$ cone smaller than 2 GeV/c. The significance of the lepton impact parameter in the plane transverse to the beam, S_{IP}, discriminates against leptons from heavy-quark decays. This variable is defined as the ratio between the measured impact parameter and its uncertainty and is required to satisfy $S_{IP} < 3$. The signal efficiency after these cuts is 7.3% while the $t\bar{t}$, $e^+e^-b\bar{b}$ and $\mu^+\mu^-b\bar{b}$ efficiencies are 0.07%, 0.008% and 0.03%, respectively.

The $t\bar{t}$ and Z^0 $b\bar{b}$ final states are associated with one or more hard jets and their contribution is reduced by removing events containing at least a jet with $E_{\mathrm{T}} > 25\,\mathrm{GeV}$. Only jets outside cones of $\Delta R = 0.3$ around the three leptons are considered. The reconstructed mass of the Z^0 boson is required to be within $10\,\mathrm{GeV/c^2}$ of m_Z, leading to the total efficiencies presented in Table 9.8.

9.4.5. $Z^0 Z^0$ selection

The $Z^0 Z^0$ selection is based on events with four electrons, identified from superclusters in the electromagnetic calorimeter matched with a charged track. The transverse momenta of the electron candidates, ordered from the largest to the smallest, have to be above $30\,\mathrm{GeV/c}$, $20\,\mathrm{GeV/c}$, $15\,\mathrm{GeV/c}$ and $10\,\mathrm{GeV/c}$, respectively. This cut suppresses the contribution from the $Z^0\gamma^*$ and $\gamma^*\gamma^*$ final states and reduces by 30% and 60% the $t\bar{t}$ and $Z^0 b\bar{b}$ backgrounds,

Table 9.8. Yield of the $W^{\pm}Z^0$ selection for an integrated luminosity of 1fb^{-1}. Signal efficiencies include gauge-boson decays into tau leptons.

	$e^{\pm}e^+e^-$	$\mu^{\pm}e^+e^-$	$e^{\pm}\mu^+\mu^-$	$\mu^{\pm}\mu^+\mu^-$	Total	Efficiency
$W^{\pm}Z^0 \to \ell^{\pm}\ell^+\ell^-$	14.8	26.9	28.1	27.0	96.8	6.1%
Z^0Z^0	0.63	1.54	1.50	1.51	5.18	4.7%
$t\bar{t}$	0.93	1.55	–	0.31	2.79	0.02%
$\mu^+\mu^-b\bar{b}$	–	–	6.54	4.9	11.4	0.005%
$e^+e^-b\bar{b}$	1.21	1.82	–	–	3.03	0.005%

Table 9.9. Yield of the Z^0Z^0 selection for integrated luminosities of $1\,\text{fb}^{-1}$ and $10\,\text{fb}^{-1}$. The last row indicates the signal significance, which include systematic effects.

	Efficiency	$N_{\text{events}}/1\,\text{fb}^{-1}$	$N_{\text{events}}/10\,\text{fb}^{-1}$
Z^0Z^0	38%	7.1	71.1
$Z^0\gamma^*$	4.5%	0.16	1.60
$Z^0b\bar{b}$	0.07%	0.08	0.84
$t\bar{t}$	0.06%	0.12	1.22
S_L		4.8	13.1

respectively. Leptons from b quarks decays in the $t\bar{t}$ and $Z^0b\bar{b}$ background processes are produced in association with hadrons. Their contribution is reduced by requiring the electrons to be isolated: the ratio between the energy deposited in the hadronic and the electromagnetic calorimeters must be below 8%; no more than two other charged track with $p_{\text{T}} > 2\,\text{GeV/c}$ must be within a $\Delta R = 0.3$ cone around the electron; $\Sigma_i(p_{\text{T}}^i - E_{\text{T}})_i/E_{\text{T}} < 0.34$, where E_{T} is the transverse energy of the electron candidate and the sum runs on all tracks with $p_{\text{T}} > 2\,\text{GeV/c}$ within a $\Delta R = 0.3$ cone around the electron.

Electron-positron pairs are combined to form Z^0 candidates. Pairs with reconstructed masses between 50 and 120 GeV/c^2 are retained. Of the two possible Z^0Z^0 pairings, the one where the Z^0 candidate masses are closest to m_Z is chosen. This pairing is correct for almost all events with two on-shell Z^0 bosons. For 2.5% of the events, more than four electrons are present and only the Z^0Z^0 pairing which contains the highest-p_{T} electron is retained. Table 9.9 presents the signal and background selection efficiencies.

9.4.6. Systematic uncertainties

For the first $1\,\text{fb}^{-1}$ of integrated luminosity, the total systematic uncertainties on the $W^{\pm}Z^0$ and Z^0Z^0 cross section measurements are 17.4% and 12.9%, respectively. These figures include a 10% uncertainties on the determination of the integrated luminosity.

The most important sources of systematic uncertainties are lepton identification and isolation, and background subtraction. A 2% uncertainty on the efficiency of each lepton propagates to an uncertainty on the cross section between 2.6% and 7.8%, according to the channel. Background subtraction dominates the $W^{\pm}Z^0$ systematics with an uncertainty of 12%, while it accounts for a 1.3% uncertainty in the Z^0Z^0 channel. An additional uncertainties of 5% on the jet energy scale affects the $W^{\pm}Z^0$ channel, while an uncertainty of 1% on the trigger efficiency affects both channels.

The significance of the observation of the $W^{\pm}Z^0$ and Z^0Z^0 signals in the first $1\,\text{fb}^{-1}$ is not sensitive to the luminosity uncertainty. It is affected by all other sources of systematic uncertainty listed above, with a total effect of 14.8% and 14.2% on the two channels,

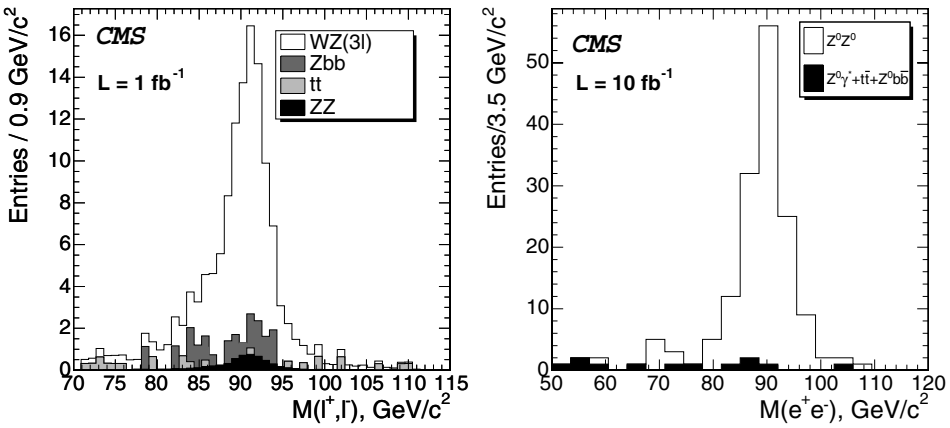

Figure 9.11. Left: Distribution of the mass of the Z^0 candidates for events retained by the $W^{\pm}Z^0$ selection, for an integrated luminosity of 1 fb^{-1}. Right: Distribution of the mass of the Z^0 candidates, two entries per event, retained by the Z^0Z^0 selection, for an integrated luminosity of 10 fb^{-1}.

respectively. These uncertainties include additional PDF and QCD uncertainties in the Monte Carlo modelling, contributing 3.7% and 6.4% for the $W^{\pm}Z^0$ and Z^0Z^0 selections, respectively.

9.4.7. Results

Figure 9.11 left presents the mass distribution of the Z^0 candidates in the $W^{\pm}Z^0$ channel for an integrated luminosity of 1fb^{-1} before the last requirement of a $\pm 10\,\mathrm{GeV/c^2}$ window is applied. A large signal-over-background ratio is observed, as shown in Table 9.8.

Figure 9.11 right shows the mass distribution of the Z^0 candidates, two entries per event, selected by the Z^0Z^0 selection for an integrated luminosity of 10 fb^{-1}. Table 9.9 lists the selection yield for 1 fb^{-1} and 10 fb^{-1}. The selection results into an almost background-free signal sample, which will constitute a valuable input to assess the background in the search for the Higgs boson.

Both the $W^{\pm}Z^0$ and Z^0Z^0 final states can be selected with high purity. A significance of 12.8 and 4.8, respectively, is expected in the first 1 fb^{-1} of integrated luminosity, including systematic uncertainties. The $W^{\pm}Z^0$ channel can be observed with a significance of 5, including systematic effects, in an integrated luminosity of 150 pb^{-1}.

This study of multiple gauge-boson production and couplings at the LHC will be extended to include the $W^{\pm}\gamma$ and $Z^0\gamma$ channels, as well as the other flavours of Z^0Z^0 fully-leptonic decays.

In conclusion, the large signal-over-background ratios achieved by the $W^{\pm}Z^0$ and Z^0Z^0 selections suggest that early observation of these channels will take place at the LHC start up. In addition, precise investigations of triple gauge-boson couplings will be possible with the first 10 fb^{-1} of LHC data.

Chapter 10. Standard Model Higgs Bosons

10.1. Introduction

The Higgs mechanism is a cornerstone of the Standard Model (SM) and its supersymmetric extensions. The introduction of the fundamental Higgs field [356–359] renders the standard electroweak theory weakly interacting up to high energy scales without violating the unitarity bounds of scattering amplitudes [360–363]. Due to spontaneous symmetry breaking in the Higgs sector the electroweak gauge bosons W, Z as well as the fermions acquire masses through the interaction with the Higgs fields. Since the gauge symmetry, though hidden, is still preserved, the theory of electroweak interactions is renormalisable [364–368]. In the Standard Model one weak isospin Higgs doublet is introduced and leads to the existence of one elementary Higgs particle after electroweak symmetry breaking. The Higgs couplings to the electroweak gauge bosons and all fermions grow with their masses. The only unknown parameter of the Higgs boson itself is the value of its mass M_H. Once this is known, all production and decay properties of the SM Higgs boson will be fixed [20, 369, 370]. The search for the Higgs boson is a crucial endeavour for establishing the standard formulation of the electroweak theory.

Although the Higgs mass cannot be predicted in the Standard Model, there are several constraints deduced from consistency conditions on the model [371–381]. Upper bounds can be derived from the requirement that the Standard Model can be extended up to a scale Λ, before perturbation theory breaks down and new non-perturbative phenomena dominate the predictions of the theory. If the SM is required to be weakly interacting up to the scale of grand unified theories (GUTs), which is of $\mathcal{O}(10^{16}\,\mathrm{GeV})$, the Higgs mass has to be less than $\sim 190\,\mathrm{GeV/c^2}$. For a minimal cut-off $\Lambda \sim 1\mathrm{TeV/c^2}$ a universal upper bound of $\sim 700\,\mathrm{GeV/c^2}$ can be obtained from renormalisation group analyses [371–378] and lattice simulations of the SM Higgs sector [379–381]. This issue can be rephrased by stating that the Higgs sector has to be trivial, if the cut-off is extended to arbitrary magnitudes. Triviality means the absence of Higgs self-interactions.

If the top quark mass is large, the Higgs self-coupling can become negative and the Higgs potential deeply negative, thus rendering the SM vacuum unstable. The negative contribution of the top quark, however, can be compensated by a positive contribution due to the Higgs self-interaction, which is proportional to the Higgs mass. For a given top mass $m_t = 175\,\mathrm{GeV/c^2}$ a lower bound of $\sim 60\,\mathrm{GeV/c^2}$ can be obtained for the Higgs mass, if the SM remains weakly interacting up to scales $\Lambda \sim 1\mathrm{TeV/c^2}$. For $\Lambda \sim M_{GUT}$ this lower bound is enhanced to $M_H \gtrsim 130\,\mathrm{GeV/c^2}$. However, the assumption that the vacuum is metastable, with a lifetime larger than the age of the Universe, decreases these lower bounds significantly for $\Lambda \sim 1\mathrm{TeV/c^2}$, but only slightly for $\Lambda \sim M_{GUT}$ [378].

The direct search in the LEP2 experiments via the process $e^+e^- \to ZH$ yields a lower bound of $114.4\,\mathrm{GeV/c^2}$ on the Higgs mass [62]. After LEP2 the search for the SM Higgs particle is continued at the Tevatron for Higgs masses up to $\sim 130\,\mathrm{GeV/c^2}$ [382] and the LHC for Higgs masses up to the theoretical upper limit [383, 384].

The Higgs decay modes can be divided into two different mass ranges. For $M_H \lesssim 135\,\mathrm{GeV/c^2}$ the Higgs boson mainly decays into $b\bar{b}$ and $\tau^+\tau^-$ pairs with branching ratios of about 85% and 8% respectively (see Fig. 10.1, right plot). The decay modes into $c\bar{c}$ and gluon pairs, with the latter mediated by top and bottom quark loops, accumulate a branching ratio of up to about 10%, but do not play a relevant role at the LHC. The QCD corrections to the Higgs decays into quarks are known up to three-loop order [385–391] and the electroweak corrections up to NLO [392–395]. The latter are also valid for leptonic decay modes. One of

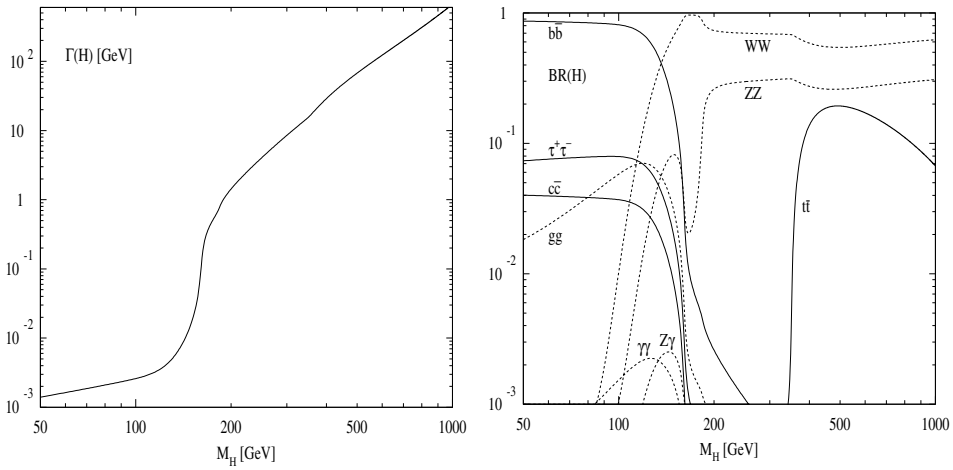

Figure 10.1. Left plot: total decay width (in GeV/c^2) of the SM Higgs boson as a function of its mass. Right plot: Branching ratios of the dominant decay modes of the SM Higgs particle. All relevant higher-order corrections are taken into account.

the most important Higgs decays in this mass range at the LHC is the decay into photon pairs, which is mediated by W, top and bottom quark loops. It reaches a branching fraction of up to 2×10^{-3}. The NLO QCD [396–402] and electroweak [403–405] corrections are known. They are small in the Higgs mass range relevant for the LHC.

For Higgs masses above 135 GeV/c^2 the main decay modes are those into WW and ZZ pairs, where one of the vector bosons is off-shell below the corresponding kinematical threshold. These decay modes dominate over the decay into $t\bar{t}$ pairs, the branching ratio of which does not exceed $\sim 20\%$ as can be inferred from Fig. 10.1 (right plot). The electroweak corrections to the WW, ZZ decays are of moderate size [392, 393, 406, 407]. The total decay width of the Higgs boson, shown in Fig. 10.1 (left plot), does not exceed about 1 GeV/c^2 below the WW threshold. For very large Higgs masses the total decay width grows up to the order of the Higgs mass itself so that the interpretation of the Higgs boson as a resonance becomes questionable. This Higgs mass range coincides with the upper bound of the Higgs mass from triviality.

The dominant Higgs production mechanism at the LHC will be the gluon-fusion process [408]

$$pp \to gg \to H\,,$$

which provides the largest production cross section for the whole Higgs mass range of interest. This process is mediated by top and bottom quark loops (Fig. 10.2a). Due to the large size of the top Yukawa couplings and the gluon densities gluon fusion comprises the dominant Higgs boson production mechanism for the whole Higgs mass range.

The QCD corrections to the top and bottom quark loops have been known a long time including the full Higgs and quark mass dependences [409–411]. They increase the total cross section by 50–100%. The limit of very heavy top quarks provides an approximation within $\sim$10% for all Higgs masses [20, 369, 370, 409–412]. In this limit the NLO QCD corrections have been calculated before [409–411, 413–416] and recently the NNLO QCD corrections [417–420] with the latter increasing the total cross section further by $\sim 20\%$. A full massive NNLO calculation is not available, so that the NNLO results can only be trusted

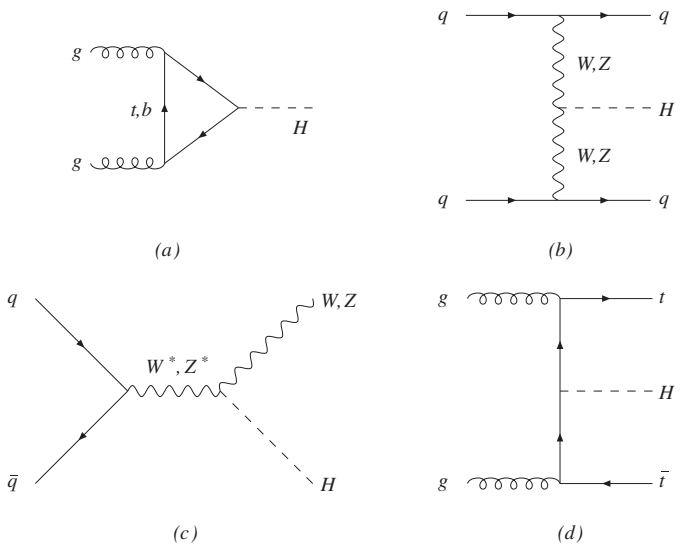

Figure 10.2. Typical diagrams for all relevant Higgs boson production mechanisms at leading order: (a) gluon fusion, (b) vector boson fusion, (c) Higgs-strahlung, (d) Higgs bremsstrahlung off top quarks.

for small and intermediate Higgs masses. The approximate NNLO results have been improved by a soft-gluon resummation at the next-to-next-to-leading log (NNLL) level, which yields another increase of the total cross section by $\sim 10\%$ [421]. Electroweak corrections have been computed, too, and turn out to be small [403, 422–425]. The theoretical uncertainties of the total cross section can be estimated as $\sim 20\%$ at NNLO due to the residual scale dependence, the uncertainties of the parton densities and due to neglected quark mass effects.

At LO the Higgs boson does not acquire any transverse momentum in the gluon fusion process, so that Higgs bosons with non-vanishing transverse momentum can only be produced in the gluon fusion process, if an additional gluon is radiated. This contribution is part of the real NLO corrections to the total gluon fusion cross section. The LO p_{T} distribution of the Higgs boson is known including the full quark mass dependence [426, 427]. The NLO corrections, however, are only known in the heavy quark limit, so that they can only be trusted for small and moderate Higgs masses and p_{T} [428–443]. In this limit a NLL soft gluon resummation has been performed [433–443], which has recently been extended to the NNLL level [444–448] thus yielding a reliable description of the small p_{T} range. It should be noted that these results are only reliable, if the top quark loops provide the dominant contribution and p_{T} is not too large. In the regions where the NLO and resummed results are valid the theoretical uncertainties have been reduced to $\mathcal{O}(20\%)$.

For large Higgs masses the W and Z boson-fusion processes [449–451] (see Fig. 10.2b)

$$pp \to qq \to qq + WW/ZZ \to qqH$$

become competitive. These processes are relevant in the intermediate Higgs mass range, too, since the additional forward jets offer the opportunity to reduce the background processes significantly. Since at NLO there is no colour exchange between the two quark lines, the NLO QCD corrections can be derived from the NLO corrections to deep inelastic lepton-nucleon scattering. They turn out to be $\mathcal{O}(10\%)$ for the total cross section [20, 369, 370, 452].

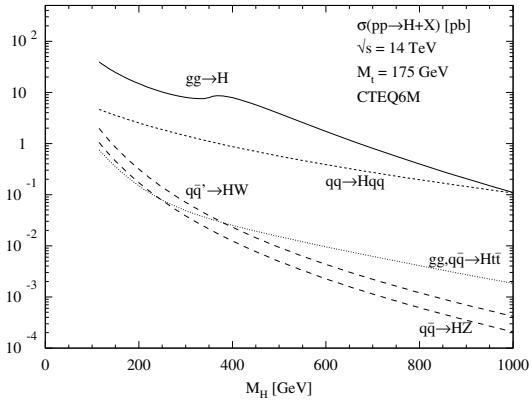

Figure 10.3. Higgs production cross sections at the LHC for the various production mechanisms as a function of the Higgs mass. The full QCD-corrected results for the gluon fusion $gg \to H$, vector-boson fusion $qq \to VVqq \to Hqq$, vector-boson bremsstrahlung $q\bar{q} \to V^* \to HV$ and associated production $gg, q\bar{q} \to Ht\bar{t}$ are shown.

Quite recently the NLO corrections to the differential cross sections have been computed, too, resulting in modifications of the relevant distributions by up to $\sim 30\%$ [453]. The residual uncertainties are of $\mathcal{O}(5\%)$.

In the intermediate mass range $M_H \lesssim 2M_Z$ Higgs-strahlung off W, Z gauge bosons [454,455] (see Fig. 10.2c)

$$pp \to q\bar{q} \to Z^*/W^* \to H + Z/W$$

provides alternative signatures for the Higgs boson search. Since only the initial state quarks are strongly interacting at LO, the NLO QCD corrections can be inferred from the Drell–Yan process. They increase the total cross section by $\mathcal{O}(30\%)$ [20,369,370,456]. Recently this calculation has been extended up to NNLO [457]. The NNLO corrections are small. Moreover, the full electroweak corrections have been obtained in Ref. [458] resulting in a decrease of the total cross sections by 5–10%. The total theoretical uncertainty is of $\mathcal{O}(5\%)$.

Higgs radiation off top quarks (see Fig. 10.2d)

$$pp \to q\bar{q}/gg \to Ht\bar{t}$$

plays a significant role for smaller Higgs masses below $\sim 150\,\mathrm{GeV/c^2}$. The LO cross section has been computed a long time ago [459–463]. During the last years the full NLO QCD corrections have been calculated resulting in a moderate increase of the total cross section by $\sim 20\%$ at the LHC [162,464,465]. These results confirm former estimates based on an effective Higgs approximation [466]. The effects on the relevant parts of final state particle distribution shapes are of moderate size, i.e. $\mathcal{O}(10\%)$, too, so that former experimental analyses are not expected to alter much due to these results. All SM Higgs production cross sections including NLO QCD corrections are shown in Fig. 10.3.

In the following Standard Model Higgs boson analyses the NLO cross sections and branching ratios for the Higgs boson calculated with the programs HDECAY [41], HIGLU [40], VV2H, V2HV and HQQ [20] are used, as well as the NLO cross sections for the background processes, when available.

10.2. Higgs boson channels

10.2.1. Inclusive Higgs boson production with $H \to ZZ^{(*)} \to e + e^- \mu^+ \mu^-$

10.2.1.1. Introduction. The $H \to ZZ^{(*)} \to 4\ell$ channel has a very clean signature with relatively small backgrounds and is therefore an important discovery channel for the Higgs boson for a large range of masses. This channel is also important for the measurement of the mass and width of the Higgs boson.

A detailed description of the analysis can be found in [467].

10.2.1.2. Event generation. All Monte Carlo event samples used in the analysis were generated using the PYTHIA [69] event generator, except for the $Zb\bar{b}$ ($e^+e^-b\bar{b}$ and $\mu^+\mu^-b\bar{b}$) background samples which were generated with COMPHEP [355].

Higgs-boson production was simulated through leading order gluon-gluon scattering and vector-boson fusion. Monte Carlo samples were produced for 18 values of the Higgs boson mass m_H ranging from 115 GeV/c^2 to 200 GeV/c^2 in 10 GeV/c^2 steps, and from 200 GeV/c^2 to 600 GeV/c^2 in 50 GeV/c^2 steps.

Three background processes which yield the same signature of two electrons and two muons in the final state, with significant cross-section times branching ratio, are considered:

1. $q\bar{q}/gg \to t\bar{t} \to W^+W^-b\bar{b} \to e^+e^-\mu^+\mu^-$.
2. $q\bar{q}/gg \to Zb\bar{b} \to e^+e^-\mu^+\mu^-$.
3. $q\bar{q} \to ZZ^\star/\gamma^\star \to e^+e^-\mu^+\mu^-$.

For the $t\bar{t}$ and $Zb\bar{b}$ backgrounds, no restrictions are applied on b decays prior to the pre-selection. Only events with $|\eta_b| < 2.5$ were generated for the $Zb\bar{b}$ background. For the $Zb\bar{b}$ and $ZZ^\star/\gamma^\star$ backgrounds, $m_{\gamma^\star}$ is required to be greater 5 GeV/c^2.

For the $ZZ^\star/\gamma^\star$ background, only the t-channel production through $q\bar{q}$ fusion is simulated. In order to account for contributions from all NLO diagrams and from the NNLO gluon fusion ($gg \to ZZ^\star/\gamma^\star$), all events are re-weighted at analysis level with an $m_{4\ell}$ dependent K-factor, calculated [51][468] using MCFM.

The potential background contribution from $Zc\bar{c} \to e^+e^-\mu^+\mu^-$ was also investigated using fully simulated events and was shown to be negligible.

For all Monte Carlo samples, a pre-selection is applied at generator level with the following requirements:

1. Final state contains $e^+e^-\mu^+\mu^-$.
2. $p_T(e) > 5$ GeV/c and $|\eta(e)| < 2.5$ for both electrons.
3. $p_T(\mu) > 3$ GeV/c and $|\eta(\mu)| < 2.4$ for both muons.

The cross-section times branching ratio and the cross-section times branching ratio times pre-selection efficiency, are shown for the signal as a function of m_H in Fig. 10.4. The NLO cross-section and the cross-section times branching ratio times pre-selection efficiency are shown for each background process in Table 10.1.

10.2.1.3. Online selection. Events selected by the dimuon or the dielectron triggers are considered. This choice follows from the presence of an on-shell Z-boson in most events. The additional use of single-electron and single-muon triggers does not increase the significance of the results.

The efficiencies of the Level-1 and High Level Triggers are shown for the signal as a function of m_H in Fig. 10.5. The corresponding trigger efficiencies for background processes are shown in Table 10.2.

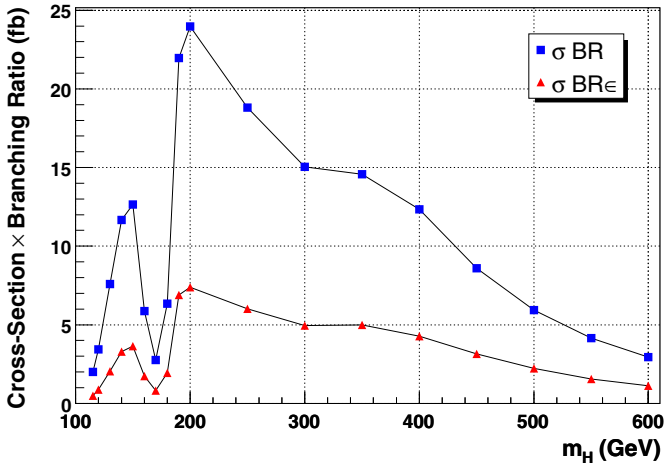

Figure 10.4. Cross-section times branching ratio, and cross-section times branching ratio times pre-selection efficiency for $H \rightarrow ZZ^{(\star)} \rightarrow 2e2\mu$.

Table 10.1. NLO cross-section and the cross-section times branching ratio times pre-selection efficiency for the three background process.

Process	σ_{NLO} (pb)	$\sigma_{NLO} \times BR \times \varepsilon$ (fb)
$t\bar{t} \rightarrow W^+W^-b\bar{b} \rightarrow e^+e^-\mu^+\mu^-$	840	744
$e^+e^-b\bar{b} \rightarrow e^+e^-\mu^+\mu^-$	276	262
$\mu^+\mu^-b\bar{b} \rightarrow e^+e^-\mu^+\mu^-$	279	128
$ZZ^\star\gamma^\star \rightarrow e^+e^-\mu^+\mu^-$	28.9	37.0

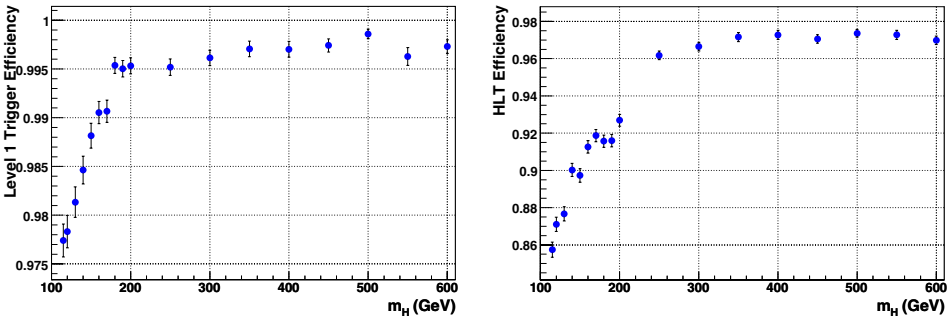

Figure 10.5. Efficiency of the Level-1 and High Level Triggers for the Higgs signal. Monte Carlo Statistical uncertainties are shown.

Table 10.2. Efficiency of the Level-1 and High Level Triggers for each of the three background processes. Monte Carlo Statistical uncertainties are shown.

	$t\bar{t}$	Zbb	ZZ^*/γ^*
Level-1 Trigger efficiency (%)	95.1 ± 0.1	92.3 ± 0.1	97.9 ± 0.2
HLT efficiency (%)	39.9 ± 0.1	65.8 ± 0.1	89.6 ± 0.4

10.2.1.4. Offline event selection. Offline reconstruction of electrons and muons is performed using standard algorithms. It is required that four leptons of type $e^+e^-\mu^+\mu^-$ are reconstructed.

The two largest backgrounds after the HLT, $t\bar{t}$ and $Zb\bar{b}$, are reducible, since unlike the Higgs signal, two of the leptons will be associated with b-jets and will therefore be displaced relative to the primary vertex and will not be isolated. These two considerations can be used to powerfully cut against these processes, whereas the $ZZ^\star/\gamma^\star$ background is irreducible by such means. Kinematic cuts are then applied, which further reduce all three backgrounds.

Vertex and Impact Parameter. Three criteria are applied:

1. The transverse distance of the $\mu^+\mu^-$ vertex from the beam line is required to be less than 0.011 cm.
2. The three-dimensional distance between the $\mu^+\mu^-$ vertex and the e^+e^- vertex is required to be less than 0.06 cm.
3. The transverse impact parameter significance of all leptons required to be less than 7.

For events passing this selection, the primary vertex is reconstructed by performing a fit to the tracks of the four reconstructed leptons. The lepton tracks are then refitted using the reconstructed vertex position as an additional point, in order to obtain a more accurate measurement of the momentum at the primary vertex.

Isolation. A cut is applied on the sum of the p_T of reconstructed tracks with $p_T > 0.9$ GeV/c and at least five hits, which satisfy the following conditions:

1. The track lies within the region defined by the sum of cones of size $\Delta R = 0.25$ around each of the four leptons and lies outside veto cones of size $\Delta R = 0.015$ around each lepton.
2. The track is consistent with originating from the reconstructed primary vertex to within $|\Delta z| < 0.2$cm, where Δz is the difference between the z position of the point of closest approach of the track to the reconstructed vertex, and the z position of the reconstructed vertex.

Kinematic Cuts. The following kinematic cuts are applied:

1. Lower thresholds on the transverse momenta of each of the four reconstructed leptons.
2. Upper and lower thresholds on the invariant masses of the reconstructed e^+e^- and $\mu^+\mu^-$ pairs.
3. Upper and lower thresholds on the invariant mass of the four reconstructed leptons.

These kinematic thresholds, together with the threshold on Σp_T for tracker isolation are optimised simultaneously using MINUIT, such that the log-likelihood ratio:

$$S_L = \sqrt{2 \ln Q}, \qquad \text{where} \qquad Q = \left(1 + \frac{N_S}{N_B}\right)^{N_S+N_B} e^{-N_S} \tag{10.1}$$

is maximised. The optimisation is performed separately for each Higgs mass.

10.2.1.5. Results. Tables 10.3 and 10.4 show the production cross-section, cross-section times branching ratio, cross-section times branching ratio times pre-selection efficiency and the cross-section times branching ratio times efficiency after each stage of the online and offline event selection, for Higgs masses of 140 GeV/c^2 and 200 GeV/c^2, respectively. Values are shown for signal and for each of the three background processes. For all values of m_H, the background after all selections is strongly dominated by ZZ^*/γ^*. For low m_H $t\bar{t}$ and $Zb\bar{b}$ each

Table 10.3. Production cross-section (NLO), cross-section times branching ratio, cross-section times branching ratio times pre-selection efficiency and cross-section times branching ratio times efficiency after each stage of the online and offline event selection, for $m_H = 140\,\mathrm{GeV/c^2}$, for signal and backgrounds. All values in fb, except for expected number of events. Uncertainties are statistical only.

	Signal	$t\bar{t}$	$Zb\bar{b}$	ZZ^*/γ^*
Production cross-section (NLO)	33.6×10^3	840×10^3	555×10^3	28.9×10^3
$\sigma \times$ BR(4 lepton final state)	11.6	-	-	367.5
Pre-selection: $\sigma \times$ BR $\times \varepsilon$	3.29 ± 0.04	743 ± 2	390 ± 1	37.0 ± 0.4
Level-1 trigger	3.24 ± 0.04	707 ± 2	360 ± 1	36.3 ± 0.4
High Level trigger	2.91 ± 0.03	282 ± 1	237 ± 1	32.5 ± 0.4
$e^+e^-\mu^+\mu^-$ reconstructed	2.23 ± 0.03	130 ± 1	141 ± 1	24.1 ± 0.3
Vertex and impact parameter cuts	2.01 ± 0.03	18.9 ± 0.3	18.4 ± 0.2	21.5 ± 0.3
Isolation cuts	1.83 ± 0.03	1.34 ± 0.07	5.8 ± 0.1	20.0 ± 0.3
Lepton p_T cuts	1.61 ± 0.03	0.40 ± 0.04	0.56 ± 0.03	17.6 ± 0.3
Z mass window cuts	1.35 ± 0.02	0.20 ± 0.03	0.23 ± 0.02	13.8 ± 0.3
Higgs mass window cuts	1.17 ± 0.02	0.02 ± 0.01	0.025 ± 0.007	0.15 ± 0.03
Expected events for $\int \mathcal{L} = 10\,\mathrm{fb}^{-1}$	11.7 ± 0.2	0.2 ± 0.1	0.25 ± 0.07	1.5 ± 0.3

Table 10.4. Production cross-section (NLO), cross-section times branching ratio, cross-section times branching ratio times pre-selection efficiency and cross-section times branching ratio times efficiency after each stage of the online and offline event selection, for $m_H = 200\,\mathrm{GeV/c^2}$, for signal and backgrounds. All values in fb, except for expected number of events. Uncertainties are statistical only.

	Signal	$t\bar{t}$	$Zb\bar{b}$	ZZ^*/γ^*
Production cross-section (NLO)	17.9×10^3	840×10^3	555×10^3	28.9×10^3
$\sigma \times$ BR(4 lepton final state)	23.8	-	-	367.5
Pre-selection: $\sigma \times$ BR $\times \varepsilon$	7.39 ± 0.09	743 ± 2	390 ± 1	37.0 ± 0.4
Level-1 trigger	7.36 ± 0.09	707 ± 2	360 ± 1	36.3 ± 0.4
High Level trigger	6.82 ± 0.08	282 ± 1	237 ± 1	32.5 ± 0.4
$e^+e^-\mu^+\mu^-$ reconstructed	5.51 ± 0.07	130 ± 1	141 ± 1	24.1 ± 0.3
Vertex and impact parameter cuts	5.03 ± 0.07	18.9 ± 0.3	18.4 ± 0.2	21.5 ± 0.3
Isolation cuts	4.92 ± 0.07	5.1 ± 0.1	12.3 ± 0.2	21.3 ± 0.3
Lepton p_T cuts	4.78 ± 0.07	1.93 ± 0.09	1.78 ± 0.06	18.7 ± 0.3
Z mass window cuts	4.45 ± 0.07	0.15 ± 0.03	0.12 ± 0.02	14.4 ± 0.3
Higgs mass window cuts	3.64 ± 0.06	0.006 ± 0.005	0.006 ± 0.003	1.61 ± 0.09
Expected events for $\int \mathcal{L} = 10\,\mathrm{fb}^{-1}$	36.4 ± 0.6	0.06 ± 0.05	0.06 ± 0.03	16.1 ± 0.9

contribute around 10-15% to the total residual background, whereas for $m_H > 200\,\mathrm{GeV/c^2}$, ZZ^*/γ^* constitutes more than 99%.

Figure 10.6 shows the invariant mass of the four reconstructed leptons before and after the application of the offline selection, for signal events for $m_H = 140\,\mathrm{GeV/c^2}$ (left) and $m_H = 200\,\mathrm{GeV/c^2}$ (right), and for the three background processes.

Figure 10.7 shows the final cross-section times branching ratio times efficiency for selected events, for signal and background, as a function of the Higgs boson mass. The number of expected events passing all selections for $10\,\mathrm{fb}^{-1}$ of integrated luminosity is shown in Table 10.5 for several values of the Higgs boson mass.

Significance. Figure 10.8 shows the S_{cP} significance after all selection cuts for integrated luminosities of $10\,\mathrm{fb}^{-1}$ and $30\,\mathrm{fb}^{-1}$, with and without the systematic uncertainty on the background estimation taken into account. The background systematic uncertainty will be

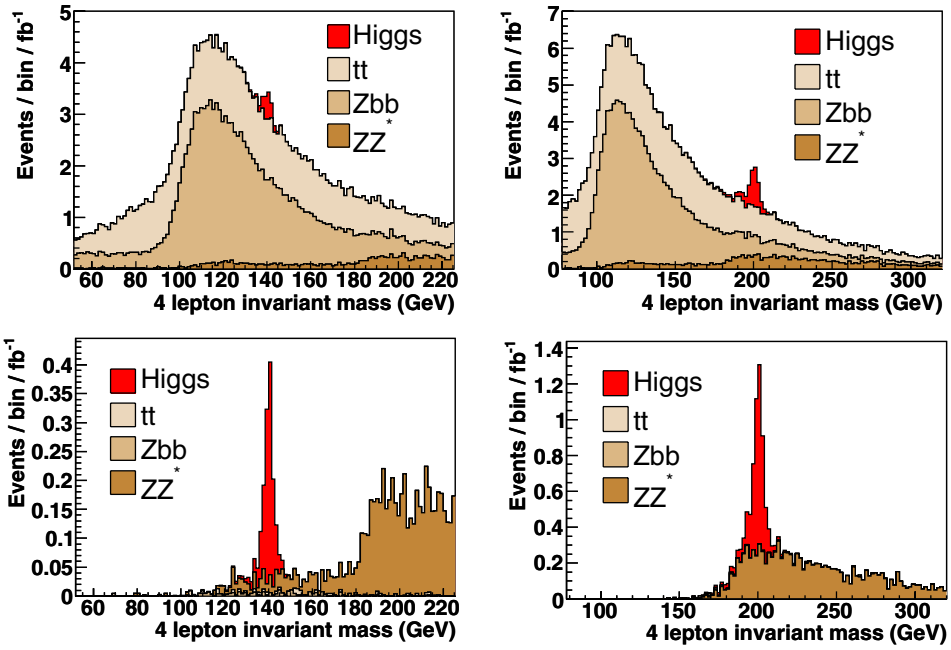

Figure 10.6. Invariant mass of the four reconstructed leptons before (top) and after (bottom) the application of the offline selection, for signal events for $m_H = 140\text{GeV/c}^2$ (left) and $m_H = 200\text{GeV/c}^2$ (right), and for the three background processes.

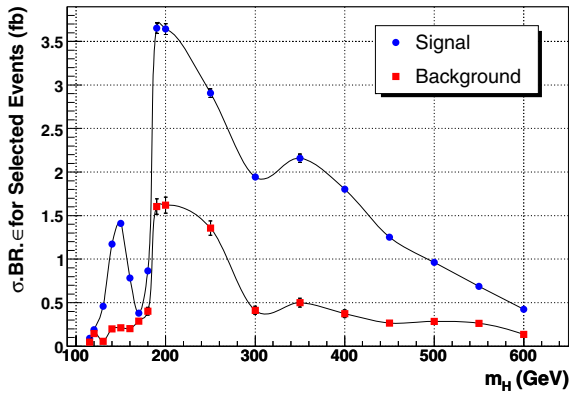

Figure 10.7. Cross-section times branching ratio times efficiency after all selections.

Table 10.5. Expected number of events from signal and background processes after all selections for an integrated luminosity of $10\,\text{fb}^{-1}$.

m_H (GeV/c^2)	120	130	140	150	160	170	180	200	250	300	400	500
N signal for $10\,\text{fb}^{-1}$	1.9	4.6	11.7	14.1	7.8	3.8	8.7	36.4	29.1	19.4	18.0	9.6
N back for $10\,\text{fb}^{-1}$	1.5	0.6	2.0	2.1	2.0	2.9	4.0	16.2	13.6	4.1	3.7	2.6

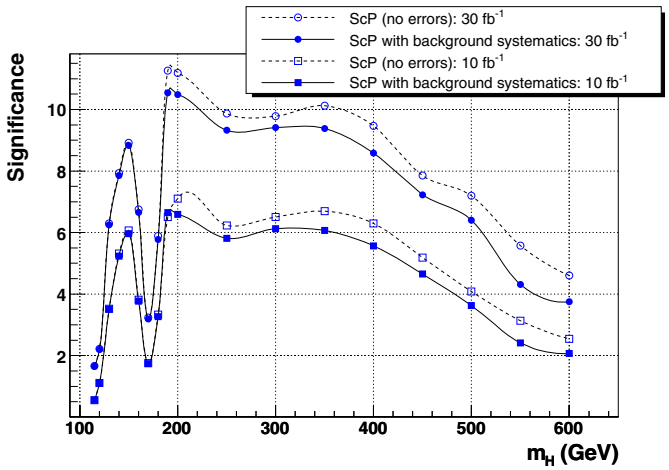

Figure 10.8. The S_{cP} significance after all selection cuts for integrated luminosities of $10\,\mathrm{fb}^{-1}$ and $30\,\mathrm{fb}^{-1}$, with and without the systematic uncertainty on the background estimation taken into account.

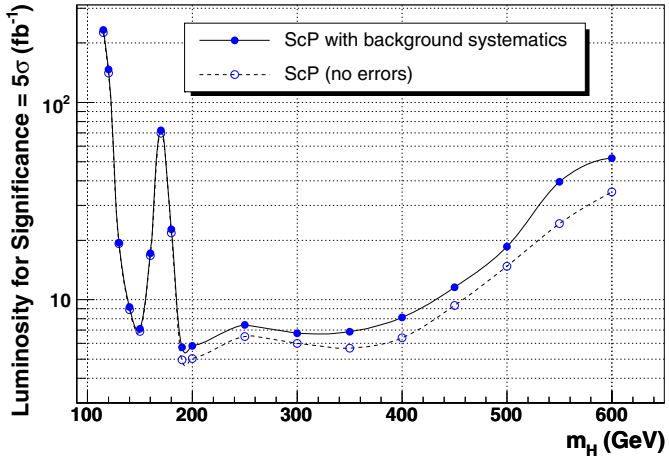

Figure 10.9. Integrated luminosity required to obtain a significance of 5σ using the $\mathrm{H} \rightarrow \mathrm{ZZ}^{(*)} \rightarrow 2\mathrm{e}2\mu$ channel, with and without the systematic uncertainty on the background estimation taken into account.

discussed in Section 10.2.1.6. Figure 10.9 shows the integrated luminosity required to obtain a significance of 5σ using the $\mathrm{H} \rightarrow \mathrm{ZZ}^{(*)} \rightarrow 2\mathrm{e}2\mu$ channel alone, with and without the background systematic uncertainty. It can be seen that a significance of 5σ can be achieved with less than $30\,\mathrm{fb}^{-1}$ of integrated luminosity for a Higgs boson with mass in the range $130 \leqslant m_H \leqslant 500\,\mathrm{GeV/c^2}$, excluding a gap of about $15\,\mathrm{GeV/c^2}$ close to $m_H/170\,\mathrm{GeV/c^2}$ for which close to $100\,\mathrm{fb}^{-1}$ is required. If the Higgs boson mass lies in the range $190 \leqslant m_H \leqslant 400\,\mathrm{GeV/c^2}$, 5σ significance can be attained with less than $8\,\mathrm{fb}^{-1}$ of integrated luminosity.

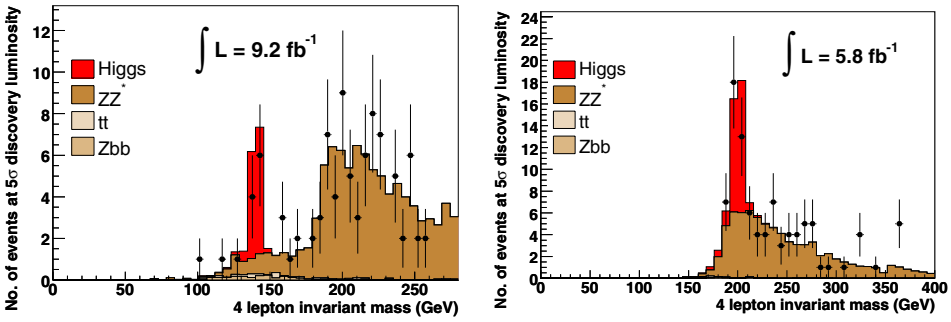

Figure 10.10. Number of expected events for signal and background for an integrated luminosity corresponding to a discovery significance of 5σ, for Higgs boson masses of 140 and 200 GeV/c^2. The results of a simulated experiment are also shown to illustrate the statistical power of the analysis and the determination of the background normalisation from data.

10.2.1.6. Evaluation of background from data. The background normalisation can be estimated from data by using the sidebands in the reconstructed four-lepton invariant mass distribution. Figure 10.10 shows the number of expected events from the signal and background Monte Carlo simulations for an integrated luminosity corresponding to a discovery significance of 5σ, for Higgs boson masses of 140 and 200 GeV/c^2: 9.2 and 5.8 fb^{-1}, respectively. Figure 10.10 also shows the results of a simulated experiments with these luminosities.

The number of background events measured from the data within the signal region, N^{IN}_{Data}, is calculated as:

$$N^{IN}_{Data} = \alpha_{MC} N^{OUT}_{Data}, \qquad \text{where} \qquad \alpha_{MC} = \frac{N^{IN}_{MC}}{N^{OUT}_{MC}}. \tag{10.2}$$

N^{OUT}_{Data} is the number observed events lying outside the signal region and α_{MC} is the ratio of the number of background events inside the signal region (N^{IN}_{MC}) to outside the signal region (N^{OUT}_{MC}), as determined from the background Monte Carlos.

The uncertainty on the number of background events in the signal region measured using this method is given by:

$$\Delta B = \Delta B_{Stat} \oplus \Delta B_{Theory}, \qquad \text{where} \qquad \Delta B_{Stat} = \alpha\sqrt{N^{OUT}_{Data}}.$$

ΔB_{Stat} provides the dominant contribution to the uncertainty. Taking N^{OUT}_{Data} as the expected number of events outside the signal region for an integrated luminosity corresponding to 5σ significance, the value ΔB_{Stat} varies between 2% and 13% for m_H <200 GeV/c^2 and increases to around 30% for high m_H where the statistics in the sidebands are low.

ΔB_{Theory} is the theoretical uncertainty on the shape of the $m_{4\ell}$ distribution for the ZZ^*/γ^* background. The value is taken from [51], which takes into account PDF and QCD scale uncertainties in the ZZ^*/γ^* production cross-section at NLO, and varies between 0.5 and 4.5% for the range Higgs boson masses considered.

10.2.1.7. Measurement of the properties of the Higgs boson. The $H \to ZZ^{(*)} \to 4\ell$ channel can be used to evaluate the mass, width and production cross-section of the Higgs boson.

Mass Measurement. The statistical uncertainty on the Higgs boson mass measurement is given by $\Delta stat = \sigma_{Gauss}/\sqrt{N_S}$, where σ_{Gauss} is the measured Gaussian width of the four

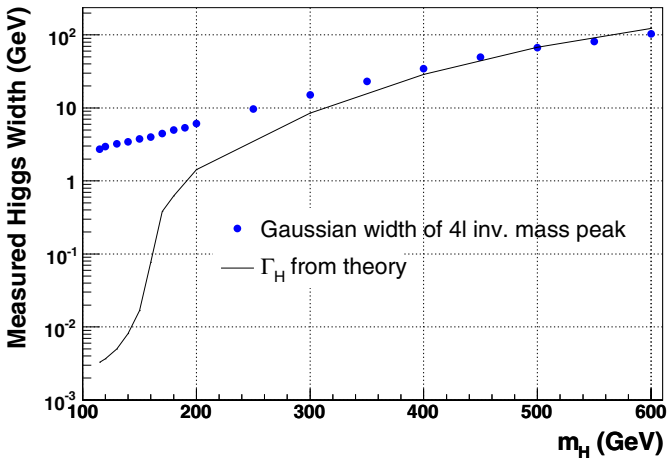

Figure 10.11. Measured width of the Higgs boson mass peak, obtained from a Gaussian fit to the peak, as a function of the true Higgs mass. The true width from theory is also shown.

Table 10.6. Statistical uncertainty on the measurement of the mass, width and production cross-section of the Higgs boson.

m_H (GeV/c^2)	115	120	130	140	150	160	170	180	190
$\Delta_{Stat}(m_H)(\%)$	0.722	0.512	0.335	0.206	0.193	0.256	0.388	0.27	0.134
$\Delta_{Stat}(\Gamma_H)(\%)$	-	-	-	-	-	-	-	54.8	17.6
$\Delta_{Stat}(\sigma_H)(\%)$	75	55.6	28.6	18.2	16.5	23.1	39.2	23.7	11.5
m_H (GeV/c^2)	200	250	300	350	400	450	500	550	600
$\Delta_{Stat}(m_H)(\%)$	0.145	0.207	0.328	0.408	0.588	0.896	1.25	1.62	2.43
$\Delta_{Stat}(\Gamma_H)(\%)$	14.4	7.38	8.2	5.43	5.8	5.91	6.52	6.61	8.36
$\Delta_{Stat}(\sigma_H)(\%)$	11.5	13	14.4	13.8	14.9	18	21.2	25.9	32.3

lepton invariant mass peak from the signal Monte Carlo and N_S is the expected number of signal events passing all selections. The value, as a fraction of the true mass, is shown in Table 10.6, for an integrated luminosity and 30 fb^{-1}, as a function of m_H.

Width Measurement. Figure 10.11 shows the measured width of the Higgs boson mass peak, obtained from the Gaussian fit, as a function of m_H. The true width from theory Γ_H is also shown. The measured width is a convolution of the natural width and the experimental resolution. It can be seen that for m_H less than around 200 GeV/c^2, the measured width is completely dominated by the experimental resolution. The statistical uncertainty on the width measurement is given by $\Delta stat = \sigma_{Gauss}/\sqrt{2N_S}$, where σ_{Gauss} is the measured Gaussian width of the peak and N_S is the expected number of signal events passing all selections. The value, as a fraction of the true width, is shown in Table 10.6, for an integrated luminosity and 30 fb^{-1}, as a function of m_H. The direct measurement the Higgs boson width is possible with $\Delta stat < 30\%$ for $m_H \geqslant 200$ GeV/c^2.

Production Cross-Section Measurement. The Higgs boson production cross-section can be determined from the number of observed events N_{obs} after all selections, given the efficiency ε of the event selection and the integrated luminosity $\mathcal{L}$:

$$\sigma = \frac{N_{obs}}{\mathcal{L}\epsilon}.$$

The total uncertainty on the cross-section measurement is given by:

$$\Delta\sigma^2 = \Delta stat^2 + \Delta syst^2 + \Delta\mathcal{L}^2 + \Delta B^2$$

where $\Delta stat$, $\Delta syst$, $\Delta\mathcal{L}$ and Δ B are the statistical uncertainty, the systematic uncertainty from the event selection, the uncertainty on the luminosity measurement and the background systematic uncertainty, respectively.

The statistical uncertainty $\Delta stat$ is shown in Table 10.6 for an integrated luminosity 30 fb^{-1}, as a function of m_H.

The total systematic uncertainty arising from the offline reconstruction and event selection can be summarised as:

$$\Delta syst^2 = 2\Delta\epsilon_e^2 + 2\Delta\epsilon_\mu^2 + \Delta\epsilon_{iso}^2$$

where $\Delta\varepsilon_e$ is the uncertainty in the reconstruction efficiency for electrons, estimated to be around 1% per electron [469], $\Delta\varepsilon_\mu$ is the uncertainty in the muon reconstruction efficiency, which has been shown to be measurable to be better than 1% per muon [51], and $\Delta\varepsilon_{iso}$ is the uncertainty in the efficiency of the isolation cut, estimated in the $H \to ZZ^{(*)} \to 4\mu$ analysis [51] to be around 2% per event. This gives a total uncertainly $\Delta syst = 3\%$.

The uncertainty on the measurement of the LHC luminosity $\Delta\mathcal{L}$ is expected to be around 3% at the 30 fb^{-1}. The background uncertainty ΔB is discussed in Section 10.2.1.6.

10.2.2. Inclusive Higgs boson production with $H \to WW^* \to 2\ell 2\nu$

The Higgs $H \to WW^{(*)} \to 2\ell 2\nu$ decay into two Ws and subsequently into two leptons ($H \to WW \to \ell\nu\ell\nu$) is the discovery channel for Higgs boson masses between $2m_W$ and $2m_Z$ [470]. In this mass range, the Higgs to WW branching ratio is close to one, leading to large number of events. The signature of this decay is characterised by two leptons and missing energy. However, since no narrow mass peak can be reconstructed, good understanding of the background together with a high signal to background ratio is needed. The most important backgrounds, which give similar signature as the signal (i.e. two leptons and missing energy), are the continuum WW production and the $t\bar{t}$ production. To reduce these backgrounds, one has to require a small opening angle between the leptons in the transverse plane and apply a jet veto.

A detailed description of the analysis can be found in [471].

10.2.2.1. Signal and background generation. The signal samples were generated using PYTHIA. The two major Higgs production modes for the mass range studied, gluon and vector boson fusion were generated. The $p_t(H)$ spectrum predicted by PYTHIA was reweighted to the MC@NLO prediction, defining p_t dependent k-factors, as proposed in [472].

For the backgrounds, continuum vector boson production (WW, ZZ, WZ) was generated using PYTHIA. The p_t(WW) spectrum was reweighted using the same technique than for the signal. A NLO cross section of respectively 16 pb, 50 pb and 114 pb was taken for ZZ, WZ and WW. WW production via gluon box diagram, ggWW, was generated using a parton Monte Carlo provided by N. Kauer and linked to PYTHIA for the parton shower [70]. Top production ($t\bar{t}$ and tWb) was generated using TOPREX. NLO cross sections of respectively 840 pb and 33.4 pb were used for $t\bar{t}$ and tWb [473].

10.2.2.2. Signal reconstruction. The signal signature is characterised by two leptons in the final state with opposite charge, missing energy and no jet. The leptons, either electrons or muons, are required to have $p_t > 20\,\text{GeV/c}$ and $|\eta| < 2$.

Muons candidates are asked to be isolated: The energy left in the calorimeters around the muon candidate within a $\Delta R = 0.3$ cone must be smaller than 5 GeV and the sum of the p_t of the tracks within a $\Delta R = 0.25$ cone around the muon candidate must be smaller than 2 GeV.

Electrons candidates are reconstructed combining tracks and ECAL clusters. They must fulfill in addition the following identification requirements:

- The electron must deposit small energy in the HCAL: $E_{hcal}/E_{ecal} < 0.05$?
- The electron track and cluster must be precisely matched:
  in direction: $|\eta_{track} - \eta_{SC\,corr}| < 0.005$ and $|\phi_{track\,prop} - \phi_{SC}| < 0.02$[43] in magnitude: $E/p > 0.8$ and $|1/E - 1/p| < 0.02$

The electron candidate must be also isolated by requiring, $\sum_{tracks} p_t(track)/E_t(SC) < 0.05$, where the sum runs on all the tracks (excluding electron) which have:

- $\Delta R_{SC-track} < 0.2$ (at vertex);
- $p_t^{track} > 0.9\,GeV/c$;
- $|z_{track} - z_{electron}| < 0.2$ cm.

Finally a cut on the impact parameter significance in the transverse plane is applied in order to reduce the $b\bar{b}$ background. Each lepton is required to have $\sigma_{IP} < 3$ where σ_{IP} is the impact parameter significance. The two leptons are also required to come from the same vertex by asking $|z_{lep1} - z_{lep2}| < 0.2$ cm.

With this lepton selection, the contribution of reducible backgrounds like W+jet where one jet is misidentified as a lepton or $b\bar{b}$ is expected to be less than 5 fb after all cuts applied.

Missing energy is reconstructed by summing the raw energy of all ECAL and HCAL towers, and correcting for muons. Since a jet veto is applied in the signal selection, further correction on the missing energy did not bring a significant improvement.

Jets are reconstructed using a Cone algorithm of size $\Delta R = 0.5$ and requiring its component calorimeter towers to have $E_T^{tow} > 0.5\,GeV$ and $E^{tow} > 0.8\,GeV$. Since jets are reconstructed to be vetoed, no energy calibration was applied. For the events studied, $E_T(jet) \approx (1.5 - 2) \cdot E_T(raw)$. To veto electrons and Bremsstrahlung photons, the jets are also required to be away from the leptons ($\Delta R_{jet-lepton} > 0.5$).

For jets with a raw energy between 15 and 20 GeV an additional cut on their track content was applied in order to reduce the contamination from fake jets coming from the underlying event. For this, the so-called alpha parameter is defined, as the ratio of the sum of p_t of tracks from the signal vertex inside the jet over the transverse jet energy in the calorimeter. For a perfect detector, the alpha parameter of a jet would be around 0.66, as in mean two third of a jet are charged particles. This ratio is smeared and reduced by the detector energy resolution and not 100% efficiency of the charged particle reconstruction in the tracker. In a fake jet, the sum of p_t of tracks from the signal vertex inside the fake jet is small, leading to an alpha parameter around zero.

Alpha is determined using only tracks that are 'inside' the jet, i.e. with $\Delta R_{track-jet} < 0.5$ and coming from the event vertex[44], fulfilling $|z_{trk} - z_{vtx}| < 0.4$ cm. Finally, these tracks should have more than 5 hits and $p_t > 2\,GeV/c$. Alpha is then defined as alpha $= \frac{\sum p_t(tracks)}{E_T(jet)}$. If its raw energy lies between 15 and 20 GeV a jet is then required to have $\alpha > 0.2$ to be kept.

[43] Where $\phi_{track\ prop}$ is the track angle propagated in the magnetic field up to the ECAL cluster position.
[44] The event vertex is defined as the mean z position of the two leptons.

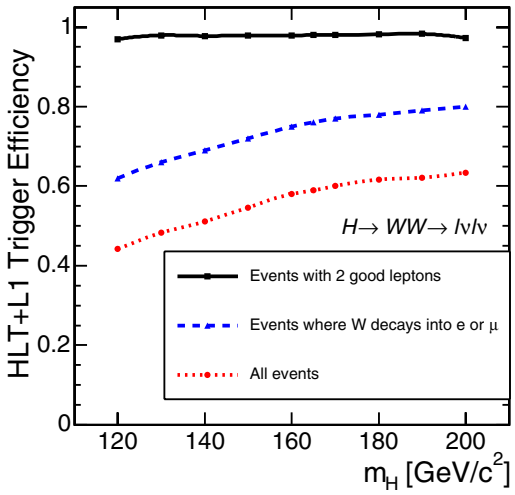

Figure 10.12. Trigger efficiencies (L1+HLT) as a function of the Higgs mass on all events (dotted line), on events where the W decays in electrons and muons (dashed line) and on events with exactly two leptons passing the lepton selection cuts (solid line).

10.2.2.3. Event selection and results. Events are first required to pass globally the Level-1 trigger and at least one of the following HLT triggers: single electron, double electron, single muon or double muon trigger.

Figure 10.12 shows the Level-1 trigger efficiency (blue dashed curve) and the combined L1+HLT trigger efficiencies (red dotted curve) as a function of the Higgs mass. To estimate the numbers of 'useful events' rejected by the trigger it is interesting to look at the trigger efficiency on events having exactly two leptons which fulfill the lepton selection cuts defined before. This is shown by the solid black curve on Fig. 10.12. In this case, the trigger efficiency is higher than 95% on the full mass range and is around 100% for $\mu\mu$ final state, whereas for ee final state it is around 96%.

Then each event has to contain exactly two opposite charge leptons with $p_t > 20\,\mathrm{GeV/c}$ and $|\eta| < 2$ passing the cuts described before. The following kinematic selections were applied:

- $E_t^{miss} > 50\,\mathrm{GeV}$
- $\phi_{\ell\ell} < 45^\circ$ (angle between the leptons in the transverse plane)
- $12\,\mathrm{GeV/c^2} < m_{\ell\ell} < 40\,\mathrm{GeV/c^2}$ (the invariant mass of the two leptons)
- no jet with $E_t^{raw} > 15\,\mathrm{GeV}$ and $|\eta| < 2.5$
- $30\,\mathrm{GeV/c} < p_t^{\ell max} < 55\,\mathrm{GeV/c}$ (lepton with the maximal p_t)
- $p_t^{\ell min} > 25\,\mathrm{GeV/c}$ (lepton with the minimal p_t).

These cuts were optimised for a Higgs mass of $165\,\mathrm{GeV/c^2}$. The expected number of events for the signal for three different Higgs masses and the different backgrounds in fb are given in Table 10.7. The first column shows the signal times branching ratio for the different processes, the second one shows the number of events passing the trigger requirement, the third one the number of events with two opposite charge leptons passing the lepton selection cuts and the last one the number of events after all selection cuts are applied. Figure 10.13, left shows the $\phi_{\ell\ell}$ distribution for the signal plotted on the top of the sum of all background when all selection cuts are applied except the one on $\phi_{\ell\ell}$.

Table 10.7. The expected number of events for the signal for three different Higgs masses and the different backgrounds given in fb. The first column shows the number of expected events after HLT requirement, the second one after having found two opposite charge leptons and the last one the number of events after all selection cuts are applied.

Reaction $pp \to X$	$\sigma_{NLO} \times BR$	L1 + HLT	2 leptons	All cuts
$\ell = e, \mu, \tau$	pb	Expected event rate in fb		
$H \to WW \to \ell\ell$, $m_H = 160\,GeV/c^2$	2.34	1353 (58%)	359 (27%)	42 (12%)
$H \to WW \to \ell\ell$, $m_H = 165\,GeV/c^2$	2.36	1390 (59%)	393 (28%)	46 (12%)
$H \to WW \to \ell\ell$, $m_H = 170\,GeV/c^2$	2.26	1350 (60%)	376 (28%)	33 (8.8%)
$qq \to WW \to \ell\ell$	11.7	6040 (52%)	1400 (23%)	12 (0.9%)
$gg \to WW \to \ell\ell$	0.48	286 (60%)	73 (26%)	3.7 (5.1%)
$t\bar{t} \to WWbb \to \ell\ell$	86.2	57400 (67%)	15700 (27%)	9.8 (0.06%)
$tWb \to WWb(b) \to \ell\ell$	3.4	2320 (68%)	676 (29%)	1.4 (0.2%)
$ZW \to \ell\ell\ell$	1.6	1062 (66%)	247 (23%)	0.50 (0.2%)
$ZZ \to \ell\ell, \nu\nu$	1.5	485 (32%)	163 (34%)	0.35 (0.2%)
Sum backgrounds	105	67600 (64%)	18300 (27%)	28 (0.2%)

10.2.2.4. Background normalisation and systematics. The following procedure for background normalisation is proposed.

- *Top background normalisation*. Two procedures are proposed. A first possibility is to define a sample with the same lepton and missing energy cuts as for the signal selection but requiring two b-tagged jets with $E_t > 20\,GeV$. A second possibility is to apply the same kinematic cuts on the leptons and require two additional jets with respectively $E_T^{raw} > 50\,GeV$ and $E_T^{raw} > 30\,GeV$. In this case, only $e\mu$ final states are considered in order to avoid a contamination from Drell–Yan. Both methods are expected to give an error of about 16% on $t\bar{t}$ estimate for a luminosity of $5\,fb^{-1}$.
- *WW background normalisation*. A normalisation region can be defined for WW by keeping the same cuts than the signal but requiring $\phi_{\ell\ell} < 140$ and $m_{\ell\ell} > 60\,GeV/c^2$. Moreover only opposite flavour leptons are considered in order to reduce the Drell–Yan and WZ contribution. A systematic error of about 17% is expected with a luminosity of $5\,fb^{-1}$, dominated by statistical uncertainty. Figure 10.13 right shows the $\phi_{\ell\ell}$ distribution for the different process in this normalisation region.
- *WZ background normalisation*. WZ can be normalised by keeping the same signal cut and requiring an additional lepton in the final state. The cuts on $\phi_{\ell\ell}$ and $m_{\ell\ell}$ are removed. An accuracy of about 20% is expected on this background with $5\,fb^{-1}$.
- *ggWW and tWb normalisation*. The contribution of these backgrounds will be estimated using Monte Carlo prediction, since they represent only a small fraction of signal events. The error on ggWW is about 30% whereas the one on tWb is about 22%, both largely dominated by theoretical errors.

Taking into account the sum of the different backgrounds, an overall error of 13% is found on the total background. These results are calculated for a luminosity of $5\,fb^{-1}$. For luminosities of 1,2 and $10\,fb^{-1}$, the total systematic errors scale to 19%, 16% and 11% respectively. Table 10.8 show the signal to background ratio for the different Higgs masses together with the luminosity needed for a 5σ discovery, with and without the inclusion of background uncertainties. For Higgs masses of 120–140 GeV/c^2 and 190–200 GeV/c^2, the background errors are too high to get a significant signal.

Figure 10.14 shows the signal to background ratio (left) and the luminosity needed for a 5σ discovery (right) as a function of the Higgs mass. A signal of more than 5σ significance

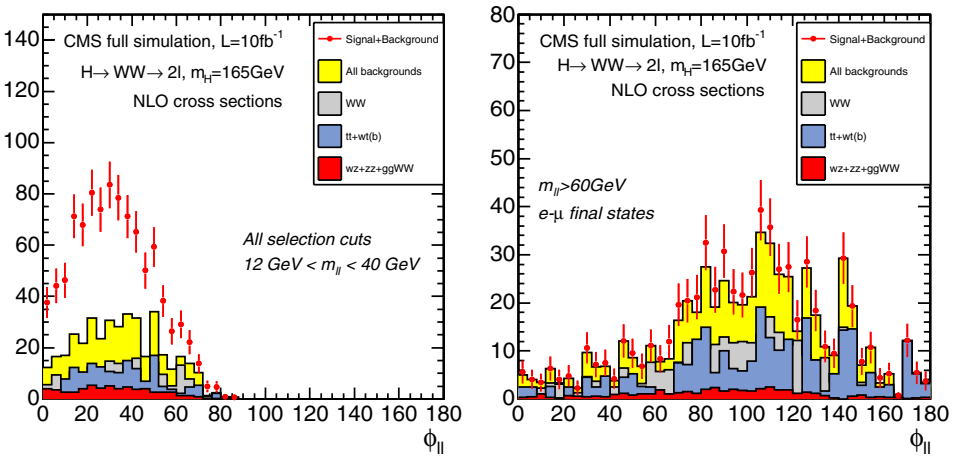

Figure 10.13. The angle between the leptons in the transverse plane for the signal and the different background and a luminosity of $10\,\mathrm{fb}^{-1}$, (Left) For the signal cuts taking out the one on $\varphi_{\ell\ell}$. (Right) For the WW background normalisation region where all signal cuts are applied except the one on the lepton invariant mass, which was set to $m_{\ell\ell} > 60\,\mathrm{GeV/c^2}$ and only electron-muon final states are kept.

Table 10.8. The signal to background ratio for the different Higgs masses together with the luminosity needed for a 5σ discovery, with and without the inclusion of background uncertainties. Also the statistical errors due to the restricted Monte Carlo statistics are taken into account.

m_H [GeV]	S/B	Significance for $5\,\mathrm{fb}^{-1}$		$\mathcal{L}_{\mathrm{disc}}$ [fb]	$\mathcal{L}_{\mathrm{disc}}$ [fb]
		no bkg syst	with bkg syst	no bkg syst	with bkg syst
150	0.61	6.6	4.0	3.0	8.2
160	1.51	14	7.7	0.58	1.1
165	1.66	15	8.3	0.50	0.90
170	1.19	11	6.3	0.88	1.7
180	0.65	6.7	3.7	2.7	7.3

could be already observed with a luminosity of $7\,\mathrm{fb}^{-1}$ for a Higgs mass between 150 and $180\,\mathrm{GeV/c^2}$. For a Higgs mass of $165\,\mathrm{GeV/c^2}$ the luminosity needed for a 5σ discovery is expected to be less than $1\,\mathrm{fb}^{-1}$.

10.2.2.5. Selection optimisation for M_H *in the 130–150* $\mathrm{GeV/c^2}$ *mass range with* $e^+e^-\nu\nu$ *final state.* A dedicated optimisation for the $e^+e^-\nu\nu$ final state in the mass range of $130 \leqslant M_H \leqslant 150\,\mathrm{GeV/c^2}$ has been performed [474]. The largest significance is searched assuming a known M_H. The latest developments in detailed electron reconstruction are used and allow a good rejection of the W + jets background which is characterised by the misidentification of a jet as an electron. New kinematical variables have been designed to reduce the W+jets background as well as the contribution from Drell–Yan events with recoiling jets (Z+jets). For instance, in the signal, the two electrons tend to be close to each other, and the dielectron system is essentially emitted in the central region. On the contrary, in the Z + jets background, the dielectron pair is emitted uniformly in η, and the electrons candidates in the W + jets backgrounds are well separated. Other selection criteria relying on the absence of a true source of missing transverse energy in the Z + jets events have been introduced: in the events where

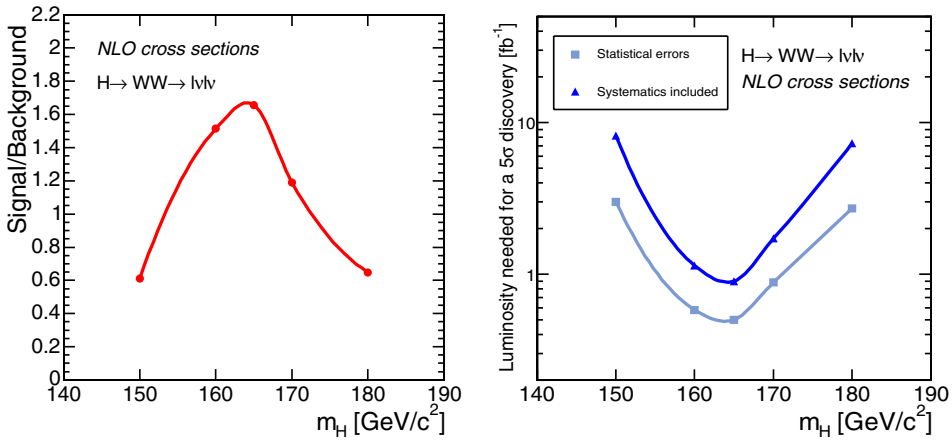

Figure 10.14. Signal to background ratio for a luminosity of $5\,\mathrm{fb}^{-1}$ (left) and the luminosity needed for a 5σ discovery (right) as a function of different Higgs masses for the $\mathrm{H} \to \mathrm{WW}$ channel.

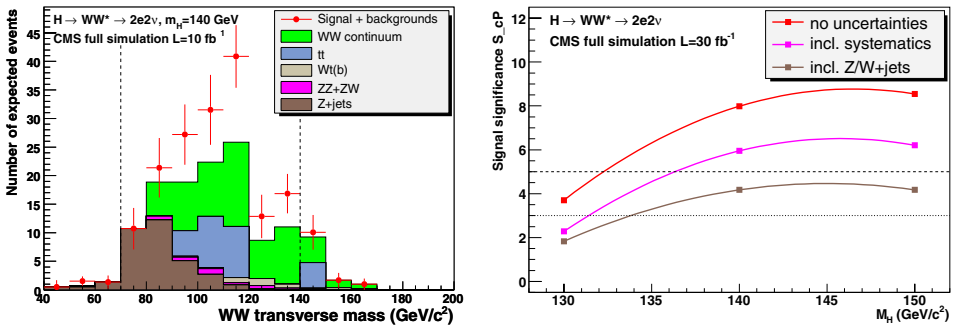

Figure 10.15. Left: the reconstructed WW transverse mass for the 140 GeV Higgs signal selection with $10\,\mathrm{fb}^{-1}$. The dashed lines show the window of events entering in the signal significance calculation. Right: the signal significance as function of the Standard Model Higgs mass for an integrated luminosity of $30\,\mathrm{fb}^{-1}$.

the missing transverse energy is mis-measured, it is usually in the same direction as the leading jet. Similarly, the imbalance of the missing energy and the dilepton system in the transverse plane is exploited.

Both W + jets and Z+jets backgrounds are thus explicitly reduced to a manageable level. Fig. 10.15 (left) shows the reconstructed WW transverse mass for the 140 GeV Higgs signal selection with $10\,\mathrm{fb}^{-1}$. Figure 10.15 (right) shows the signal significance as function of the Standard Model Higgs mass for the integrated luminosity of $30\,\mathrm{fb}^{-1}$ with and without systematics taken into account. A 3σ observation is possible for Higgs masses from 135 GeV. A 5σ discovery is reached with $60\,\mathrm{fb}^{-1}$.

10.2.3. The vector boson fusion production with $\mathrm{H} \to \tau\tau \to \ell + \tau$ jet $+ E_{\mathrm{T}}^{\mathrm{miss}}$

In the early parton level simulation studies [475, 476] and fast detector simulation studies of ATLAS and CMS [477] it was shown that the Higgs boson production in the vector boson

fusion qq → qqH (qqH or VBF) and decay into τ lepton pair could be the discovery channel with $\sim 30\,\mathrm{fb}^{-1}$. The cross section measurement of qqH, H → $\tau\tau$, WW, $\gamma\gamma$ channels will significantly extend the possibility of the Higgs boson coupling measurement [478,479] and provide the possibility of the indirect measurement of the light Higgs boson width [478]. In the MSSM the qqH(h), H(h)→ $\tau\tau$ channel could be discovered in the largest region of the $M_A - \tan\beta$ parameter plane [475,480]. The forward jet tagging and the central jet veto are the key selections of the VBF Higgs boson channels. The study of the observability of the VBF Higgs boson production and H→ $\tau\tau \to \ell$ + jet decay with the full detector simulation is presented in the following. A detailed description of the analysis can be found in [481].

10.2.3.1. Signal and background generation and pre-selections. The signal events were generated using PYTHIA for four different values of the Higgs boson mass: 115, 125, 135 and 145 $\mathrm{GeV/c^2}$. The Higgs boson was forced to decay to two τ leptons with one τ decaying to leptons and the other τ to hadrons. The TAUOLA package was used to simulate the τ polarisation.

For background events, following processes are considered:

QCD 2 τ+2/3 j
The QCD production of 2τ+2jet and +3jet events with the invariant mass of two τ leptons, $M_{\tau\tau} > 70\,\mathrm{GeV/c^2}$, was generated using ALPGEN with CTEQ5L PDF. Given the limit of the detector acceptance and requirements in the course of the event reconstruction, all jets were required to satisfy $p_{Tj} > 20\,\mathrm{GeV}$, $|\eta_j| < 5.0$ and $|\Delta R_{jj}| > 0.5$. Further pre-selections were applied on the two highest p_T jets (j1 and j2) reflecting the offline VBF selection cuts: $|\Delta\eta_{j1j2}| > 4.0$, $M_{j1j2} > 600\,\mathrm{GeV/c^2}$. Then the events 2$\tau$+2j and 2$\tau$+3j were added together with the MLM prescription in PYTHIA to avoid double counting of the jets. The TAUOLA package was used in PYTHIA to force one τ lepton to decay leptonically and the other hadronically.

Electro Weak (EW) production of 2 τ+2 j
The EW production of two τ's with $M_{\tau\tau} > 70\,\mathrm{GeV/c^2}$ and two jets in the final state was generated using MADGRAPH with CTEQ5L PDF. Soft pre-selections were applied during generation with MADGRAPH on the kinematics of the jets: $p_{Tj} > 20\,\mathrm{GeV/c}$ and $M_{jj} > 500\,\mathrm{GeV/c^2}$. Further pre-selection cuts were applied on jets and τ's given the limit of the detector acceptance and requirements of the event reconstruction: $|\eta_j| < 5.2$, $|\Delta R_{jj}| > 0.5$, $|\Delta R_{\tau\tau}| > 0.4$. The showering and hadronisation of the MADGRAPH parton level events were carried out using PYTHIA where all decay modes of the τ lepton were open.

W + jets
The W + 3j and W + 4j events with W → $\mu\nu$ decays were generated using ALPGEN with CTEQ5M PDF. In addition to the kinematical cuts on jets used for the QCD Z + jets production described above, further pre-selections were made based on the lepton properties with $|\eta_\ell| < 3$ and $p_{T\ell} > 10\,\mathrm{GeV/c}$. The MLM prescription was applied in PYTHIA.

$t\bar{t} \to WbWb$
The $t\bar{t}$ background was generated using PYTHIA, TOPREX, ALPGEN, COMPHEP and MADGRAPH. All leptonic W decays were included and no kinematical pre-selection was applied.

10.2.3.2. Event reconstruction and selection. Events are triggered at Level 1 by the single isolated e, single μ and combined e-τ triggers. At the High Level the following triggers are used: the single isolated e, single μ, combined e-τ and combined μ-τ triggers.

In the off-line analysis the electron and muon candidates were selected and for the electron candidates three additional requirements are applied: $E/p > 0.9$, tracker isolation, $(\sum_{0.01<\Delta R<0.2}^{trk} p)/E < 0.05$, and E_T of the hottest HCAL tower, $E_T^{Htow} < 2\,GeV$. The highest p_T off-line lepton candidate with $p_T > 15\,GeV/c$ is then selected. The lepton track is used to identify tracks originating from the signal vertex. The tracks are used for the electron isolation, τ tagging and in central jet veto. A track is associated to the signal vertex if its z impact parameter lies within $|\Delta z| < 0.2\,cm$ from that of the lepton track.

The τ-jet identification is seeded from the L1/HLT τ candidates. A jet is formed around each candidate which does not coincide with the identified electron, and the jet is passed through a series of τ-tagging criteria. The τ tagging used in HLT (Ref. [76]) has been adapted to offline use with parameters $R_m = 0.1$, $R_s = 0.07$, $R_i = 0.45$, $p_T^{ltr} = 6\,GeV/c$ and $p_T^{i} = 1\,GeV/c$. The charge of the τ-jet is required to be opposite of the lepton charge, and $E_T^{Htow} > 2\,GeV$ is required if the jet coincides with any of the electron candidates. A further cut is applied on the transverse energy of the τ-jet, $E_T > 30\,GeV$.

The jets from the VBF process are identified as the two highest E_T calorimeter jets with $E_{Tj} > 40\,GeV$, excluding the electron and the τ-jet. The jets are required to satisfy: $|\eta_j| < 4.5$, $\eta_{j1} \times \eta_{j2} < 0$, $\Delta\eta_{j1j2} > 4.5$, $\Delta_{\phi j1j2} < 2.2$, and the invariant mass, $M_{j1j2} > 1\,TeV$. The jets after these selections will be referred to as tagging jets.

A cut is applied on the transverse mass of the lepton-E_T^{miss} system, $M_T(lep, E_T^{miss}) < 40\,GeV$, in order to reject backgrounds with $W \to \ell\nu$ decays.

The central jet veto was applied. An event is vetoed if there is an additional jet (j3) with $E_{Tj3}^{raw} > 10\,GeV$ in the rapidity gap between the two tagging jets, satisfying the following:

- $(\eta_{min} + 0.5) < \eta_{j3} < (\eta_{max} - 0.5)$
  where η_{min} and η_{max} correspond to the tagging jets which has smaller and larger value of η respectively.
- $\alpha_{j3} = \sum p_{Ttrk}/E_{Tj3}^{raw} > 0.1$
  where p_{Ttrk} is the p_T of the track originating from the signal vertex, which lie within the 0.5 cone around the jet axis, and E_{Tj3}^{raw} is the raw E_T of the jet measured in the calorimeter.

α_{j3} is defined for each additional jet, and the one which satisfies the first criteria and has the highest α_{j3} is considered for the veto.

The invariant mass of the two reconstructed τ's is calculated as described in the MSSM H(A)$\to \tau\tau$ analysis (Section 5.2) using the collinear approximation of the visible part of τ's and neutrinos. The E_T^{miss} is reconstructed by summing the E_T of the calorimeter towers and the muon candidates, and applying the jet energy corrections (Type 1 E_T^{miss}). The events were accepted if $E_{\nu 1,\nu 2} > 0$.

10.2.3.3. Expected number of events. The efficiency of each reconstruction and selection step and the cumulative cross section expected at the LHC are given in Table 10.9. The total selection efficiencies are, 0.32%, 0.34%, 0.42%, 0.39%, for the signal events with the Higgs boson masses, M_H = 115, 125, 135 and 145 GeV/c^2 respectively.

For the W+3/4j background, the efficiencies of some selection cuts have been obtained from factorisation of cuts. The trigger and the lepton identification are carried out as other samples, and the remaining steps are carried out in two uncorrelated parallel streams – A: VBF and $M_T(lep, E_T^{miss})$ cuts, B: central jet veto, τ tagging and mass calculation – after pre-selections of forward jets and τ-jet candidates.

10.2.3.4. Reconstructed mass and fit. The distribution of the invariant mass of two reconstructed τ's for different samples is shown in Fig. 10.16, where the signal sample with

Table 10.9. Cumulative cross sections in fb after successive selection cuts. The efficiency (%) of each cut is listed inside the brackets. The entry, "valid mass", corresponds to the fraction remained after the calculation of the diτ mass when some events are lost due to the negative reconstructed neutrino energies. For the W + 3/4j samples, efficiencies are obtained from factorisation of cuts and the τ-jet ID efficiency includes the p_T cut, and the number of events at 30 fb^{-1} (indicated by*) is calculated for all leptonic decay modes of W.

	cross section, σ [fb] (% from previous cut)				
	signal	background			
Selection	$M_H = 135$	EW2τ+2j	QCD$\tau\tau$+2/3j	W + 3/4j	$t\bar{t} \rightarrow$ WbWb
Starting σ	82.38	299.	1615.	14.45×10^3	86×10^3
Level-1	46.50 (56.5)	179.8 (60.1)	543.8 (33.7)	9186. (63.6)	71.39×10^3 (83.0)
L1+HLT	24.60 (52.9)	58.81 (32.7)	201.3 (37.0)	6610. (71.9)	55.42×10^3 (77.6)
lepton ID	23.34 (94.9)	50.67 (86.2)	187.4 (93.1)	6549. (99.1)	54.08×10^3 (97.6)
lepton p_T	23.16 (99.3)	49.13 (97.0)	185.6 (99.0)	6543. (99.9)	53.54×10^3 (99.0)
τ-jet ID	8.276 (35.7)	10.49 (21.3)	39.64 (21.4)	(0.21)	5.056×10^3 (9.4)
τ-jet p_T	6.422 (77.6)	7.360 (70.2)	24.25 (61.2)	-	3.215×10^3 (63.6)
Valid mass	4.461 (69.5)	4.232 (57.5)	14.49 (59.8)	(17.4)	848.6 (26.4)
VBF cuts	0.545 (12.2)	0.391 (9.2)	1.666 (11.5)	(11.0)	2.738 (0.3)
M_T(lep,E_T^{miss})	0.423 (77.6)	0.322 (82.4)	1.382 (83.0)	(30.5)	0.942 (34.4)
Central Jet Veto	0.344 (81.3)	0.230 (71.4)	0.555 (39.7)	(28.9)	0.224 (23.8)
N events at 30 fb^{-1}	10.3	6.9	16.6	1.5*	6.7

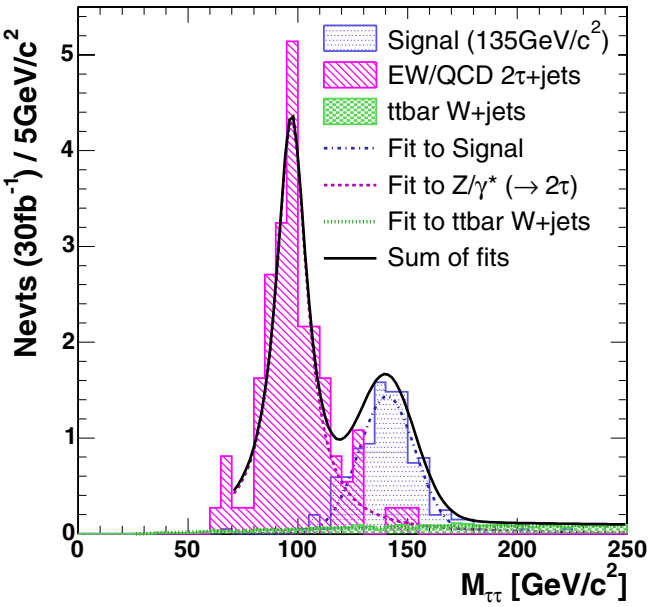

Figure 10.16. The invariant mass of two reconstructed τ's. The number of entries in each histogram is normalised to the expected number of events at an integrated luminosity of 30 fb^{-1}.

the Higgs boson mass, $M_H = 135\,\mathrm{GeV/c^2}$ is used. A Gaussian function is used to fit the signal distribution, a Breit–Wigner function for the 2τ+jets background from EW and QCD processes, and a second order polynomial for the reducible background from W+jets and $t\bar{t}$ events. The Higgs boson mass resolution is 9.1%.

Table 10.10. The production cross section and significance of the expected number of signal events within the optimum mass window for each of the four different simulated masses of the Higgs boson.

M_H [GeV]	115	125	135	145
Production σ [fb]	4.65×10^{3}	4.30×10^{3}	3.98×10^{3}	3.70×10^{3}
$\sigma\times$ BR($H\to\tau\tau\to lj$) [fb]	157.3	112.9	82.38	45.37
N_S at 30 fb^{-1}	10.5	7.8	7.9	3.6
N_B at 30 fb^{-1}	3.7	2.2	1.8	1.4
Significance at 30 fb^{-1} ($\sigma_B = 7.8\%$)	3.97	3.67	3.94	2.18
Significance at 60 fb^{-1} ($\sigma_B = 5.9\%$)	5.67	5.26	5.64	3.19

10.2.3.5. Signal significance. The significance is calculated using a window with a fixed width of 40 GeV/c^2, which slides in 5 GeV/c^2 steps. An optimum window position which maximises the significance is chosen for each of the four different masses of Higgs boson. The numbers of signal and background events within the window, N_S and N_B, are estimated from the fits to individual samples. The method S_{cP} (Ref. [79]) is used for calculating the significance, including the systematic uncertainty of 7.8% for 30 fb^{-1} and 5.9% for 60 fb^{-1}. The results are summarised in Table 10.10.

It is envisaged that the shapes of the two background distributions will be extracted experimentally from the LHC data in a region unaffected by the signal contribution, using some relaxation of selection cuts. Since the number of background events in the signal region will be estimated using real data, the fitting procedure is the only contribution to the uncertainty in the significance estimate. The fit uncertainty has been evaluated by performing MC trials, randomly generating a mass distribution from the original fit functions and re-fitting the distribution at each trial. With the data, the Higgs boson mass will be estimated by repeating the fitting procedure for different mass hypotheses and finding the value where the χ^2 of the fit is minimised.

10.2.4. Searching for standard model Higgs via vector boson fusion in $H\to W^+W^-\to \ell^\pm\nu jj$ with m_H from 120 to 250 GeV/c^2

The signal topology of Higgs boson with $H\to W^+W^-\to \ell\nu jj$ via vector boson fusion has been shown as a good potential discovery channel for the medium-high mass range ($m_H > 300$ GeV/c^2). The final state is characterised as two forward jets, two central jets from W hadronic decay, and one high p_T lepton and missing transverse energy (E_T^{miss}) from the W leptonic decay. Extending the use of this channel to the low mass range ($m_H < 300$ GeV/c^2) makes valuable physics analysis possible and is complementary to the Higgs boson search using $H\to W^+W^-\to \ell\nu\ell\nu$, especially for $160 < m_H < 180$ GeV/c^2, where $H\to ZZ^*$ branching ratio is highly suppressed due to the opening of $H\to W^+W^-$ decay with two on-shell W bosons.

The result of this section shows that in the Higgs boson mass range between 140 and 200 GeV/c^2, a significance of $\sim 5\ \sigma$ can be achieved with integrated luminosity of 30 fb^{-1}. Major backgrounds include $t\bar{t}$ + jets, W + $t\bar{b}(\bar{t}b)$, W + jets, Z+jets, WW/WZ/ZZ + jets, and QCD events. For WW + jets, the QCD and Electroweak (EW) processes are generated separately. A detailed description of the analysis can be found in [482].

10.2.4.1. Event selection strategy. Major difficulties concerning the low mass Higgs analysis using $\ell\nu$jj final state include: many background processes of very large cross section have one

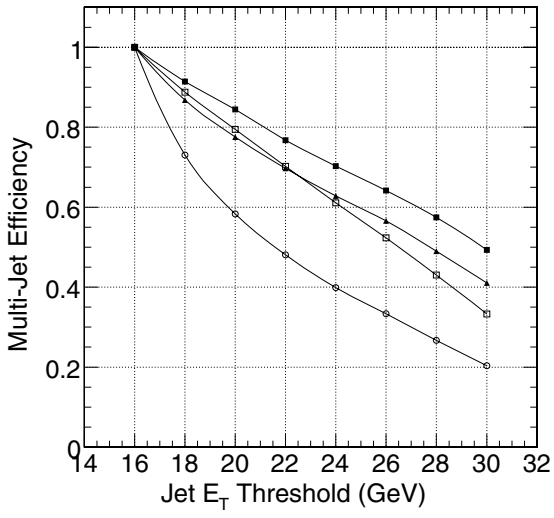

Figure 10.17. Multiple jet selection efficiency (requiring at least 4 jets in an event) as a function of jet E_T threshold. The efficiency is normalised to the rate with jet E_T threshold of 16 GeV for each sample. The physics channels include: $t\bar{t}$ + jets (solid square), W + 3jets (open circle), W + 4jets (solid triangle), and VBF Higgs with $m_H = 170\,GeV/c^2$ (open square).

lepton and multiple jets in the final states; simulating the requisite huge number of background events is both a computing and analysis challenge; hard selection cuts and heavy exploitation of physics signal characteristics are necessary to suppress backgrounds and enhance the statistical significance of the signal, which can lead to large systematic uncertainties; the relatively low Higgs boson mass domain limits the application of high jet E_T thresholds that would normally be used to suppress backgrounds, in contrast to the situation at high mass; low E_T^{miss} and low E_T jets affect the resolution of Higgs mass. To meet these challenges, a robust reconstruction and selection strategy is developed.

Low p_T objects are ignored (e.g. leptons with $p_T < 10\,GeV/c$ and jets with $E_T < 25\,GeV$). The jet E_T threshold is chosen around 25 GeV where there is a stable signal to background ratio (S/B), so that the systematic uncertainty of jet energy scale is minimised (Fig. 10.17). Due to a number of soft jets in the central detector region, the hadronic W reconstruction looks for a dijet mass with the smallest deviation from the true W boson mass. The extra jet veto after forward jet tagging and hadronic W reconstruction is applied. Two schemes are studied: full extra jet veto ($N_{extra} < 1$) and loose extra jet veto ($N_{extra} < 2$). The full extra jet veto is very powerful in reducing the $t\bar{t}$ + jets and W + jets background.

The selection chain is divided into two major steps: basic selection (Table 10.11) and optimised selection. This strategy helps optimise the selection cuts and factorise the selection efficiency to evaluate the systematic uncertainty and QCD background efficiency.

The optimised selection for $m_H \geqslant 160\,GeV/c^2$ ($m_H < 160\,GeV/c^2$) includes 3 steps:

- $E_T^{FH} > 45\,(40)\,GeV$, $E_T^{FL} > 35\,(30)\,GeV$, $\Delta\eta > 4.2$, and $m_{jj} > 1000\,GeV/c^2$. $E_T^{FH}(E_T^{FL})$ is the high (low) jet E_T threshold for forward jets.
- $E_T^{CH} > 30\,GeV, E_T^{CL} > 25\,GeV, \Delta m_W < 20\,GeV/c^2$ ($30 < m_W < 90\,GeV/c^2$), and $N_{extra} < 1$. E_T^{CH} (E_T^{CL}) is the high (low) jet E_T threshold for central jets that are used for hadronic-W reconstruction.

Table 10.11. Summary of basic event selection cuts.

Selection	Configuration
Lepton selection	calorimeter-based e/μ isolation
	$30 < p_T < 120\,GeV/c$
	$\Delta R_{\ell,j} > 0.5$
Jet selection	$N_{jet} \geqslant 4$ jets with $E_T > 25\,GeV$
	$E_T^{miss} > 30\,GeV$
Forward jet tagging	$E_T > 30\,GeV$
	$\eta_1 \cdot \eta_2 < 0$
	$\lvert\eta_1 - \eta_2\rvert > 3.8$
	$m_{jj} > 800\,GeV/c^2$
Hadronic-W	$\Delta m_W < 25\,GeV/c^2$ ($m_H \geqslant 160\,GeV/c^2$)
	$30 < m_W < 90\,GeV/c^2$ ($m_H < 160\,GeV/c^2$)
	select dijet with the least Δm_W
Leptonic-W	using lepton and E_T^{miss}
	select Leptonic-W candidates of
	smaller ΔR(Leptonic − W, Hadronic − W)

Table 10.12. Cross section (fb) of the signal and background in optimised selection with $m_H \geqslant 160\,GeV/c^2$ for full extra jet veto.

Channels	Basic Selection	Step 1	Step 2	Step 3
VBF Higgs ($m_H = 160$)	16.15	9.531	4.580	2.989
VBF Higgs ($m_H = 170$)	15.99	9.814	4.828	3.006
VBF Higgs ($m_H = 180$)	16.28	9.916	4.711	2.738
VBF Higgs ($m_H = 190$)	14.16	9.363	4.294	2.340
VBF Higgs ($m_H = 200$)	13.78	8.626	4.341	1.983
VBF Higgs ($m_H = 210$)	13.43	8.211	4.080	1.571
VBF Higgs ($m_H = 220$)	13.35	8.227	4.128	1.259
VBF Higgs ($m_H = 250$)	10.71	6.900	3.426	0.810
$t\bar{t}$ + jets	1494.2	626.5	16.751	1.232
WW + jets (QCD)	9.27	1.265	0.422	< 0.008
WW + jets (EW)	7.88	9.683	4.454	< 0.0277
ZZ + jets	1.00	0.269	0.0245	< 0.001
ZW + jets	7.23	2.335	0.223	< 0.001
$W + t\bar{b}(\bar{t}b)$	92.8	35.21	4.427	< 0.05787
W + 4j ($W \to e/\mu/\tau + \nu$)	1110.8	583.0	72.066	0.323
Z + 4j ($Z \to ee/\mu\mu$)	82.3	3.713	0.141	0.0104
Z + 3j ($Z \to ee/\mu\mu$)	72.4	2.313	0.233	< 0.0067
Sum of Background	3579.7	1492.5	167.38	1.565

- E_T^{miss}(qqWW) < 40 GeV, ΔR(lepton,Hadronic-W) < 2.0, and ΔR(Leptonic-W, Hadronic-W) < 1.0. E_T^{miss}(qqWW) is the E_T^{miss} of qqWW system that includes reconstructed Higgs boson and two forward jets.

The efficiency of basic selection and three steps of optimised selection is summarised in Table 10.12 and 10.13 for $m_H \geqslant 160\,GeV/c^2$ and $m_H < 160\,GeV/c^2$ respectively. Loose extra jet veto with tightening cuts: $m_{jj} > 1200\,GeV/c^2$ and ΔR(lepton,Hadronic-W) <1.6, gives a conservative result.

The reconstructed Higgs boson mass distributions for signal plus background and background are shown in Fig. 10.18 for $M_H = 160\,GeV/c^2$ (left) and $M_H = 170\,GeV/c^2$ (right) for 60 fb^{-1}.

Table 10.13. Cross section (fb) of signal and background in optimised selection with $m_H < 160\,GeV/c^2$ for full extra jet veto.

Channels	Basic Selection	Step 1	Step 2	Step 3
VBF Higgs ($m_H = 120$)	1.28	0.951	0.363	0.231
VBF Higgs ($m_H = 130$)	4.03	3.004	1.125	0.664
VBF Higgs ($m_H = 140$)	7.12	5.520	2.369	1.656
VBF Higgs ($m_H = 150$)	11.01	8.345	3.505	2.317
$t\bar{t}$ + jets	1483.0	859.5	20.94	0.493
WW + jets (QCD)	9.70	4.215	0.422	< 0.004
WW + jets (EW)	7.94	11.21	5.395	< 0.0277
ZZ + jets	0.96	0.465	0.0979	< 0.001
ZW + jets	7.45	3.781	0.334	< 0.01
$W + t\bar{b}(\bar{t}b)$	101.5	54.37	6.799	< 0.0289
W + 4j ($W \to e/\mu/\tau + \nu$)	1110.7	778.5	118.9	0.667
Z + 4j ($Z \to ee/\mu\mu$)	81.3	4.700	0.152	0.00522
Z + 3j ($Z \to ee/\mu\mu$)	70.0	3.160	0.353	< 0.01333
Sum of Background	3630.6	2066.5	267.2	1.164

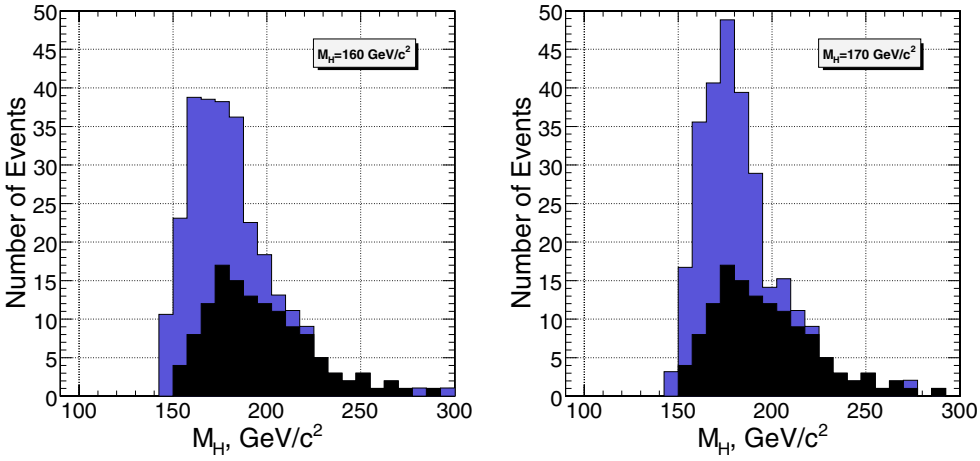

Figure 10.18. The Higgs boson mass reconstruction of signal plus background (blue/grey) and background (black) for $M_H = 160\,GeV/c^2$ (left) and $M_H = 170\,GeV/c^2$ (right).

The overall QCD multi-jet contamination is estimated with the factorisation of the selections as 2-5 events for an upper limit with $60\,fb^{-1}$, which causes possible 2-4% increase of background, which has almost no change in the significance.

10.2.4.2. Detector systematic uncertainties and control. Several calorimeter level systematic uncertainties have significant impact on this channel including: jet energy scale and resolution, E_T^{miss} scale and resolution, and calorimeter-based lepton isolation cut. Their impacts on the rate of signal (S), background (B) and S/B are summarised in Table. 10.14. The total detector level systematic uncertainty is about 16% in the absolute rate of background in the final result.

Table 10.14. Systematic Uncertainties due to Jet and E_T^{miss}.

Source	S	B	S/B
Jet energy scale	10.6%	14.5%	5.2%
Jet energy resolution	0.1%	2.0%	2.0%
E_T^{miss}	2.5%	1.2%	1.7%
Lepton isolation	1.4%	1.3%	0.5%

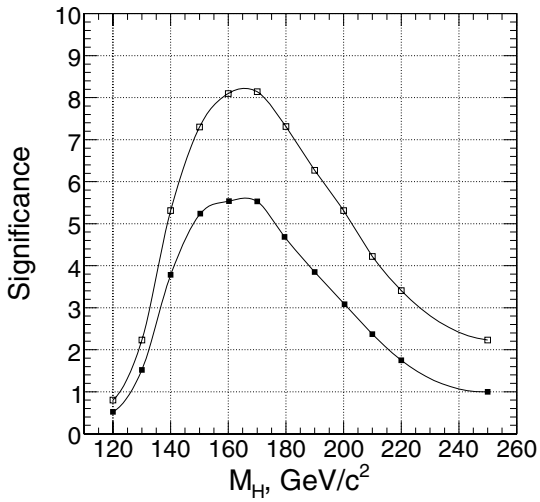

Figure 10.19. The signal significance for 30 fb^{-1}. The high (low) curves correspond to full (loose) extra jet veto.

The data driven technique is able to significantly reduce the detector level systematic uncertainties. For example, the largest uncertainty comes from the selection efficiency with respect to lowest jet E_T threshold. The event rate of the background near this threshold can be measured from data and used to tune the MC prediction, which leaves much less uncertainty due to the systematic bias of jet energy scale. Ignoring the uncertainty in the rate for from lowest jet E_T threshold, the uncertainty of jet energy scale only causes about 5.5% error in the rest of the selection chain which immediately reduces the total detector level systematic uncertainty down to 10% level.

10.2.4.3. Discovery potential. The signal significance for 30 fb^{-1} after optimised selection cuts is shown in Fig. 10.19 for the Higgs boson masses between 120 and 250 GeV/c^2. The background systematic uncertainty of 16% as discussed in the previous section is included.

10.2.5. Vector boson fusion production with $H \to \gamma\gamma$

A detailed description of the analysis can be found in [483].

10.2.5.1. Signal and background generation and simulation. The Higgs boson production from the vector boson fusion $qq \to qqH$ and $H \to \gamma\gamma$ decay was generated by PYTHIA for the Higgs boson masses, $M_H = 115, 120, 130, 140$ and 150 GeV/c^2.

Table 10.15. Cross sections of different types of background.

Background process	Cross section (pb)
QCD hadronic jets	$2.8^{*}10^{7}$
Gluon fusion	83
Drell–Yan	4.1×10^{3}
$\gamma\gamma + 2$jets, QCD	47.24
$\gamma\gamma + 2$jets, EW	0.33
$\gamma + 3$jets, QCD	5970
$\gamma + 3$jets, EW	5.15

The backgrounds considered are:

- QCD multi-jet production, where an electromagnetic energy deposit results from the decay of neutral hadrons (especially isolated π^0s) in a jet. It was generated by PYTHIA with $\hat{p_T} > 50\,\mathrm{GeV/c}$.
- Drell–Yan e^-e^+ production (generated with PYTHIA) which could mimic photons when correspondent electron tracks will not be assigned to the clusters in the ECAL during the reconstruction.
- Diphoton production from the gluon fusion (box diagram) when two additional jets from the initial state radiation are presented in the event. It was generated by PYTHIA with $\hat{p_T} > 20\,\mathrm{GeV/c}$.
- QCD and Electro Weak (EW) $pp \rightarrow \gamma\gamma + 2$ jets process generated with COMPHEP.
- QCD and EW $pp \rightarrow \gamma + 3$ jets generated with COMPHEP.

Table 10.15 shows the cross sections of different types of backgrounds.

Generator level pre-selections for QCD multi-jet background. Selection based on the generated particles was devised, aimed at selecting events which could produce in the detector two electromagnetic showers consistent with isolated photons. In order to apply cuts on the invariant mass of the two candidates an attempt to estimate lower and upper limits to the energy of the candidates that will be reconstructed after the simulation was done.

The idea of this pre-selection, is to pick up events that will give rise to energy depositions in ECAL large enough and isolated enough to be important for this analysis. Pre-selection algorithm is getting all particles which might deposit electromagnetic energy in ECAL, and looking around each particle in a narrow cone, to find another, may be less energetic particles which will make deposits in ECAL as well, and will potentially be reconstructed as one cluster. In addition to that, a very loose tracker isolation was applied: three charged particles were required in a cone $\Delta R = 0.2$ around the "cluster candidate", described above, per one "cluster candidate", and no more than 6 per two first most energetic candidates.

After that some other cuts were applied for the "cluster candidates" as well, $p_T > 37.5\,\mathrm{GeV/c}$ for most energetic one and $p_T > 22.5\,\mathrm{GeV/c}$ for the second most energetic one. The invariant mass of the first most energetic and second most energetic "cluster candidates" should be more than $90\,\mathrm{GeV/c^2}$ for the purpose of this analysis.

Generator level pre-selections for $\gamma + 3jets$ and $\gamma\gamma + 2jets$ backgrounds. At COMPHEP partonic level event generation the following cuts were applied:

- $p_T^{\gamma} > 20\,\mathrm{GeV/c}$
- $p_T^{j} > 20\,\mathrm{GeV/c}$
- $\Delta R_{ij} > 0.4$
- at least one pair of jets must exist with the jets in the opposite hemispheres with the rapidity gap greater than 3.5.

Table 10.16. Number of generated and simulated events for different types of background.

Background process	Number of generated events	Rejection with pre-selections	Number of simulated events	L_{intg} (fb^{-1})
QCD multi-jets	31.2×10^9	6048	4.5M	~ 1
Gluon fusion	2.25×10^6	2	1M	~ 52
Drell–Yan $e^+ e^-$	1.0×10^6	1	1M	0.25
$\gamma\gamma$ + 2jets, QCD	0.5×10^6	2.56	200k	6
$\gamma\gamma$ + 2jets, EW	41×10^3	1	41k	120
γ + 3jets, QCD	0.3×10^6	7.8	40k	0.05

The CTEQ5L PDF set was used; the factorisation and renormalisation scales were set to 50 GeV. Hadronisation was done by PYTHIA and the same pre-selections were applied as it was described above for QCD multi-jet background. Rejection factors of PYTHIA pre-selections are 2.5 for $\gamma\gamma$ + 2jets dataset and 7.8 for γ + 3jets dataset.

The signal and background events passed the full detector simulation and digitisation with pile-up for luminosity $2 \times 10^{33}\,cm^{-2}\,s^{-1}$. The numbers of generated and fully simulated events are shown in Table 10.16 for different types of background. In the last column the corresponding equivalent integrated luminosity is shown.

10.2.5.2. Event reconstruction and selection. The events were triggered by the double-isolated electron trigger at Level 1 and HLT.

Photons are reconstructed with the hybrid algorithm in the ECAL barrel and with the island algorithm in the ECAL endcap. Both photon candidates had to match Level 1 trigger photon candidates, such that, the distance R ($R = \sqrt{\delta\eta^2 + \delta\phi^2}$) between the photon candidate and trigger object be less than 0.5. The transverse energies of the two photon candidates were required to be greater than 40 GeV and 25 GeV respectively. The fiducial volume in rapidity was restricted to $|\eta| < 1.4442$ in the barrel and $1.566 < |\eta| < 2.5$ in the endcap for both photon candidates.

Three different algorithms were studied for the Higgs boson vertex reconstruction:

- **P_T balance.** The P_T balance for charged particle tracks along the reconstructed Higgs boson direction is defined as $P_T^B = -\Sigma P_{Ti} \cos\theta_i$, where θ_i is the angle between the Higgs boson and track i direction in the transverse plane
- **Maximal P_T.** The primary vertex is selected as the vertex with the track of highest P_T
- **Number of charged particle tracks** above P_T cutoff in pixel vertex. The primary vertex is selected as the vertex with a largest number of tracks.

To compare different vertex reconstruction algorithms, the number of events reconstructed in a $5\,GeV/c^2$ mass window are determined. The P_T balance and Maximal P_T algorithms give exactly the same number of events, while track counting algorithm gives a few percent less efficiency. The Higgs boson efficiency in $5\,GeV/c^2$ mass window is improved by 15%.

The photon candidates were required to be isolated in the tracker and calorimeter. The tracker isolation criteria are based on the number of charged particle tracks with p_T greater than a p_T threshold, p_T^{thresh}, calculated in a cone R ($R = \sqrt{\delta\eta^2 + \delta\phi^2}$) around the photon

candidate. The algorithm contains three parameters:

- The size of the cone R around the photon candidate, wherein the number of charged tracks is counted.
- The p_T threshold, p_T^{thresh}. Only charged particle tracks with p_T greater than p_T^{thresh} are considered in isolation calculations.
- The 'number of tracks' threshold N^{thresh}. If the number of charged particle tracks in cone R with p_T greater than the chosen p_T^{thresh} is greater than N^{thresh}, then the photon candidate is considered non-isolated, otherwise isolated.

The jet rejection factor is very sensitive to the 'number of tracks' threshold, N^{thresh}. By increasing N^{thresh} from 0 to 1, the Higgs boson signal efficiency is improved by 6–10%, but the jet rejection factor drops by a factor of ~ 2. Therefore, the parameter N^{thresh} was fixed to zero. The cone size $R = 0.30$ and $p_T^{thresh} = 1.5\,GeV/c$ were used in this study.

The isolation of the photon candidates in the electromagnetic calorimeter is also required. The isolation criteria is based on the sum of transverse energies deposited in basic clusters in some cone R ($R=\sqrt{\delta\eta^2+\delta\phi^2}$) around the photon candidate. The basic clusters that belong to the photon candidate's supercluster are not counted as part of the sum. The algorithm contains four parameters:

- The size of the cone R around the photon candidate wherein the transverse energies deposited in the basic clusters are summed.
- The transverse energy sum threshold E_T^{thresh}. If the sum of transverse energies is below this threshold, the photon candidate is considered isolated, otherwise non-isolated.
- The ratio, r, of the transverse energy sum in all surrounded basic clusters to the transverse energy of the most energetic super cluster.
- The ratio (H/E) of the energy deposited in the HCAL behind the super-cluster to the energy of the super-cluster.

There is no strong dependence of the jet rejection factor on the cone size R, though slightly better rejection factors are empirically obtained for a cone size $R = 0.30$–0.35. The cone size $R = 0.30$ is used in this study. The transverse energy sum thresholds, E_T^{thresh}, were chosen to be 1.2 GeV in the barrel and 1.6 GeV in the endcap. Finally, the photon candidate must pass the cuts: $r < 0.01$ and H/E <0.1.

Jet tagging was done based on the jets reconstructed with the iterative cone algorithm using cone size 0.7. The two highest E_T jets were chosen and initial selection cuts were applied:

- $E_T^{jet} > 20\,GeV$, $|\eta_{jet}| \leqslant 4.5$, $\Delta R_{\gamma jet} \geqslant 0.5$
- $\Delta\eta_{jets} = |\eta_{jet1} - \eta_{jet2}| \geqslant 4.0$, $\eta_{jet1} \times \eta_{jet2} < 0$

Two additional cuts were applied to the already selected two forward jets in order to reduce the background even more than it was done with forward jet tagging procedure:

- $E_T^{jet1} > 50\,GeV$, where E_T^{jet1} is the transverse momentum of the first most energetic forward jet, selected by forward jet tagging procedure, described above.
- $E_T^{jet2} > 35\,GeV$, where p_t^{jet2} is the transverse momentum of the second most energetic forward jet, selected by forward jet tagging procedure, described above.
- $m_{j1j2} > 500\,GeV/c^2$, where m_{j1j2} is the invariant mass of the two most energetic forward jets, selected by forward jet tagging procedure, described above.
- Two photons must in the η region between the two forward jets: $\min(\eta_{jet1}, \eta_{jet2}) + 0.7 < \eta_{\gamma 1,2} < \max(\eta_{jet1}, \eta_{jet2}) - 0.7$.

Table 10.17. The number of signal and background events and signal significance after all selections within the $5\,\mathrm{GeV/c^2}$ mass window around the considered Higgs boson masses for $60\,\mathrm{fb^{-1}}$. The ΔN_b is the background uncertainty estimated from the side bands.

	$m_H = 115$ GeV/c^2	$m_H = 120$ GeV/c^2	$m_H = 130$ GeV/c^2	$m_H = 140$ GeV/c^2	$m_H = 150$ GeV/c^2
N_s	20.2	21.1	19.1	15.7	11.2
γ+3jets (QCD)	2.7	4.7	3.5	2.0	5.8
γ+3jets (EW)	2.5	2.5	2.5	2.5	2.5
$\gamma\gamma$ + 2jets (QCD)	11.2	13.2	9.85	8.9	4.6
$\gamma\gamma$ + 2jets (EW)	10	7.0	7.0	11.0	2.0
Drell–Yan	0	0	0	0	0
N_b	26.0	26.2	21.4	28.2	14.9
ΔN_b	2.8	3.2	2.4	3.0	1.8
S	3.07	3.15	3.21	2.32	2.30

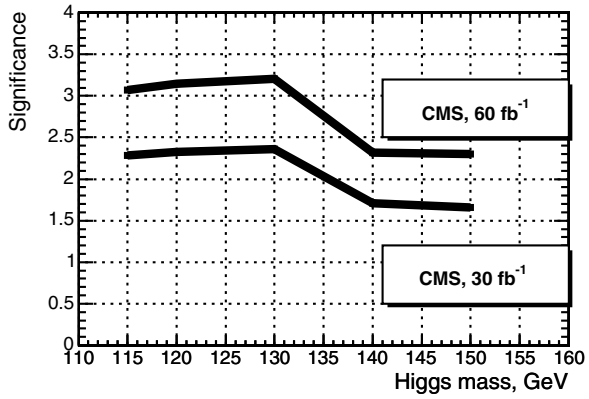

Figure 10.20. Signal significance for 30 and $60\,\mathrm{fb^{-1}}$.

10.2.5.3. Results. After all selections the contribution of the QCD multi-jet events and diphoton events from gluon fusion was found to be negligible. Due to the lack of Monte Carlo statistics only upper limits were estimated conservatively for the contribution from QCD and EW γ+3 jets backgrounds. Table 10.17 shows the number of signal and background events after all selections within $5\,\mathrm{GeV/c^2}$ mass window around the considered Higgs boson masses for $60\,\mathrm{fb^{-1}}$. The ΔN_b shown in the Table is the background uncertainty estimated from the side bands around the Higgs boson mass peak.

The signal significance with the background uncertainty taken into account is shown in Fig. 10.20 for 30 and $60\,\mathrm{fb^{-1}}$.

10.2.6. Associated WH *production with* $H \to WW^{(*)} \to 2\ell 2\nu$

The cross-section for this process exhibits a maximum near the Higgs boson mass of 160–180 GeV/c^2 due to the combined behaviour of the production cross-section and the Higgs boson branching ratio. The intermediate mass region between $120\,\mathrm{GeV/c^2}$ and $190\,\mathrm{GeV/c^2}$,

Table 10.18. Background processes considered into the present analysis. The cross-section includes the decay of W and Z bosons into leptons. The generator and the number of events processed are also shown together with the corresponding weight for a luminosity of 1 fb^{-1}.

Background	Cross-section	Generator	MC statistic	weight (1 fb^{-1})
WWW($3l^{\pm}$)	4.95 fb	COMPHEP	10000	5.19×10^{-4}
WZ($3l^{\pm}$)	1.71 pb	PYTHIA	50000	3.46×10^{-2}
ZZ($4l^{\pm}$)	0.17 pb	PYTHIA	50000	3.67×10^{-3}
$t\bar{t}(l^+l^-b\bar{b})$	90.9 pb	TOPREX	100000	0.93
$Wt(l^+l^-b)$	5.25 pb	TOPREX	50000	0.11

where the cross-section exceeds 300 fb was investigated using the events containing three leptons, electrons and muons (including leptonic tau decays), in the final state.

A detailed description of the analysis can be found in [484].

10.2.6.1. Signal and background generation. The Higgs boson with masses of 115, 125, 130, 140, 150, 160, 170, 180 and 190 GeV/c^2 has been considered. Events were generated with PYTHIA for each of the nine Higgs boson masses, without any kinematical cut. W bosons are forced to decay leptonically (e, μ, τ).

All Standard-Model processes likely to produce three leptons must be considered as background for this analysis. This includes events where three leptons are actually produced in the hard process but also events with a fake or missed lepton. One particular case is the production of leptons in the semi-leptonic decay of a B meson. In the present analysis, we considered the production of WWW, WZ, ZZ, $t\bar{t}$, and Wt. Most of the processes are simulated with PYTHIA, except for WWW, which is generated with COMPHEP, and Wt generated with TOPREX. In all cases, PYTHIA is used for the hadronisation step. Table 10.18 shows the cross-section, the generator used and the number of events produced.

10.2.6.2. Selection streams at Level-1 and HLT. The global (cumulative) trigger efficiency after Level-1 and HLT is found to reach 72% for a 140 GeV/c^2 Higgs boson using the full trigger table. Main contributions come from single and double leptonic (e and μ) triggers (65%). There is a small contribution from the missing transverse energy trigger (E_T^{miss}) and from combined (e and τ) and (μ and τ) triggers, further reduced by the event selection, which favours multi-leptonic patterns. For this analysis, events are selected by the triggers known to have the highest impact on the total efficiency: single- and double-electron and muon triggers. Figure 10.21(a) shows the efficiency for each (exclusive) trigger pattern, given the above choice of interesting bits.

Details about the efficiency for each type of event (defined from the number of muons, electrons and taus in the event) are given in Fig. 10.21(b). Events containing one or more muons are more easily retained (efficiency reaches 85% for events with three muons) while tau events are only marginally selected (efficiency: 12%). Efficiency rises slightly with the Higgs boson mass, from 58% at 115 GeV/c^2 to 74% at 190 GeV/c^2.

Table 10.19 shows the trigger efficiency for each source of background. Efficiency of the single- and double-electron and muon triggers, varies from 64% to 73%, which is the same magnitude as the trigger efficiency for signal events. It is 15% (for $t\bar{t}$) to 5% (for ZZ) less efficient than the inclusive High-Level trigger.

10.2.6.3. Off-line selection. Electrons and muons are reconstructed using default offline reconstruction algorithms. For electrons, additional quality cuts are applied: the energy

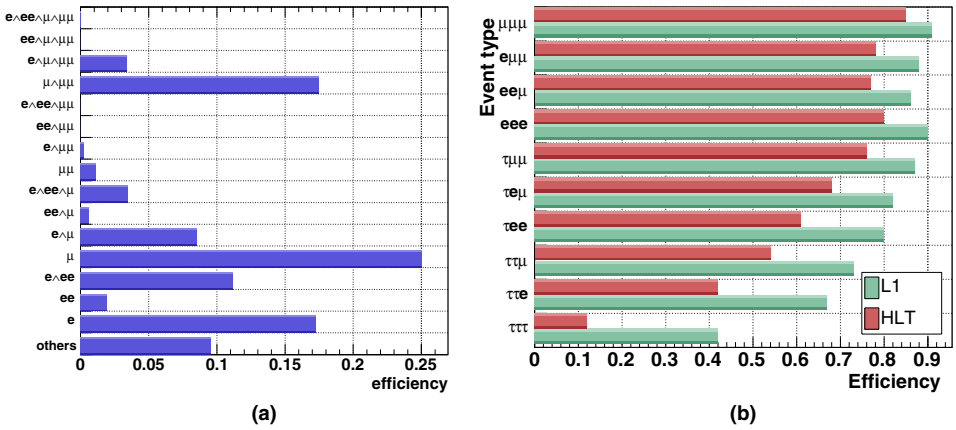

Figure 10.21. (a) Trigger efficiency by trigger pattern, for the signal. Efficiency is calculated as N_x/N_{HLT}, where x is one of the 2^4 exclusive trigger classes. "Others" stands for unconsidered trigger patterns; (b) Trigger efficiency for each class of Monte-Carlo events. Results are given after Level-1 and after HLT. Efficiency is computed as the ratio between the number of triggered events and the total number of generated events.

Table 10.19. Trigger efficiency for each source of background. Efficiency at HLT with the restricted trigger set (e, ee, μ, $\mu\mu$) used in the present analysis is also shown.

Background	Level-1 efficiency	HLT efficiency	$e, ee, \mu, \mu\mu$ HLT efficiency
WWW($3l^{\pm}$)	0.87	0.79	0.73
Wt(l^+l^-b)	0.88	0.78	0.67
WZ($3l^{\pm}$)	0.8	0.72	0.65
ZZ($4l^{\pm}$)	0.78	0.69	0.64
$t\bar{t}(l^+l^-b\bar{b})$	0.91	0.79	0.65

measured by ECAL and the momentum obtained by the tracker must agree within 50%, and the ratio of energy measured by HCAL and ECAL must be lower than 0.15. Only leptons with $p_T^{\ell} > 14\,\mathrm{GeV/c}$ are retained. A first set of selection criteria is applied to select signal-like topologies, requiring three and only three leptons, for a total charge of either +1 or −1. A cut on the distance in the z direction between the points of closest approach of lepton tracks to the beam is applied to ensure that all of the three leptons are coming from the same interaction. The two closest (in the $\eta - \phi$ plane) opposite-sign leptons are then assigned to the Higgs boson decay. The angle between leptons attributed to the Higgs boson can be used to distinguish signal and background. The acollinearity between two leptons is defined as the angle between the two leptons, in the space, and their acoplanarity is defined as the same angle projected onto the transverse plane. Both the acollinearity ($\theta_{\mathrm{aco}} < 1.75\,\mathrm{rad}$) and the acoplanarity ($0.1\,\mathrm{rad} < \phi_{\mathrm{aco}} < 0.75\,\mathrm{rad}$) between the leptons are used, as they provide complementary information. Leptons required to be isolated in the tracker, i.e. the angle between the lepton's track and the closest track with p_T above $3\,\mathrm{GeV/c}$ must be more than 0.2.

A jet veto is applied rejecting events with a jet, reconstructed with the iterative cone algorithm (using cone size of 0.7) with raw E_T above 25 GeV in the central region, $|\eta| < 2.1$. An additional B veto is applied, imposing that no single B-jet is reconstructed by the default *combined B-tag* algorithm. This removes low-energy b jets passing the jet veto.

Table 10.20. Summary of the optimised selection cuts. The cross-section for the signal and backgrounds, for each step in the selection, is given in fb. An upper limit for the *Wt* and $t\bar{t}$ cross-sections is given when no simulated event remains.

Cut		Signal (fb)	Background (fb)				
Id.	Type	140 GeV/c^2	$t\bar{t}$	Wt	ZW	ZZ	WWW
0	Level-1 and HLT	12.24	72067	4115.8	1238.4	118.438	3.91
1	$N_{lept} = 3$, $\Sigma Q_\ell = \pm 1$	3.81	16432.7	680.0	339.4	34.65	1.05
2	Lepton cuts	2.67	5629.1	245.3	245.9	23.53	0.70
3	Angular cuts	0.87	400.6	15.0	18.3	2.29	0.11
4	B veto	0.43	3.85	0.42	9.77	1.19	0.06
5	Jet veto	0.27	< 1.93	0.31	7.26	0.58	0.04
6	Z veto	0.21	< 1.93	0.21	0.40	0.08	0.03
7–9	Topological	0.13	< 1.93	< 0.11	0.06	0.01	0.02

A cut on the invariant mass of any pair of leptons compatible with the Z hypothesis (via charge flavour and invariant mass constraints, $M_Z \notin [65]\text{GeV/c}^2$) is used to reject ZZ and WZ events. Finally, kinematical cuts are used: $\not{p}_\text{T} > 50\,\text{GeV/c}$, $M_\text{T}(W_3) > 40\,\text{GeV/c}^2$ and $\sum \vec{p}_\text{T}^{\,\ell} > 40\,\text{GeV/c}$, where $\sum \vec{p}_\text{T}^{\,\ell}$ is the transverse momentum of the vector sum of momenta of all three leptons, and $M_\text{T}(W_3)$ is the reconstructed transverse mass of the associated W boson:

$$M_\text{T}(W_3) = \sqrt{2 * p_\text{T}^{l_3} \not{p}_\text{T} (1 - \cos \Delta\phi_{l_3 \not{p}_\text{T}})}, \tag{10.3}$$

with $p_\text{T}^{l_3}$ being the transverse momentum of the lepton not associated to the Higgs boson, $\not{p}_\text{T}$ the missing transverse momentum, and $\Delta\phi_{l_3 \not{p}_\text{T}}$ the polar angle between the lepton and the missing transverse momentum. Optimised cuts are summarised in Table 10.20.

The Higgs boson transverse mass is computed from the two chosen leptons and from the missing transverse momentum:

$$M_\text{T}(H) = \sqrt{M_\text{T}^{ll\,2} + 2E_\text{T}^{ll} \not{p}_\text{T} - 2P_\text{T}^{ll} \not{p}_\text{T} \cos \Delta\phi_{ll \not{p}_\text{T}}}, \tag{10.4}$$

Figure 10.22 shows the distribution of $M_\text{T}(H)$ for the signal, on top of remaining background, after all cuts for a Higgs boson mass of 140 GeV/c^2 and an integrated luminosity of 100 fb^{-1}. The cumulated efficiency (including trigger and event selection) depends on the Higgs boson mass hypothesis. Starting at 0.5% for a mass hypothesis of 115 GeV/c^2, the efficiency rises to a maximum at the "WW resonance" (1.3%). Beyond the WW production threshold, efficiency drops since W bosons start to be boosted in the Higgs boson frame, which influences the angular distribution of leptons. Efficiency in that region could certainly be improved by optimising the analysis for a Higgs boson mass of 190 GeV/c^2.

10.2.6.4. Systematic uncertainties. Systematic sources considered in this study are related to the normalisation of backgrounds, to the reconstruction, the event selection, the luminosity and the structure functions of protons.

Background will be normalised to signal-free regions of the phase-space. By looking at the acoplanarity distribution when the angular cuts are not applied, data can be fitted to a sum of signal and background shapes. For that purpose, the signal is described by a sigmoid distribution, while the background remains constant. The Monte Carlo distribution for signal and background are first fitted independently, and the shapes obtained that way are used to fit data from pseudo-experiments (Figure 10.23). The uncertainty on the background normalisation is then related to the uncertainty on the background level in that fit. The

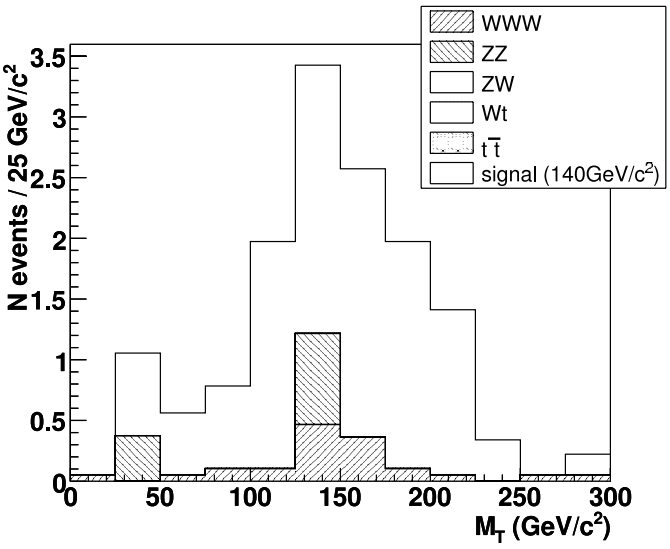

Figure 10.22. Reconstructed transverse mass from Equation (10.4) for a 140 GeV/c^2 Higgs boson and an integrated luminosity of 100 fb^{-1}.

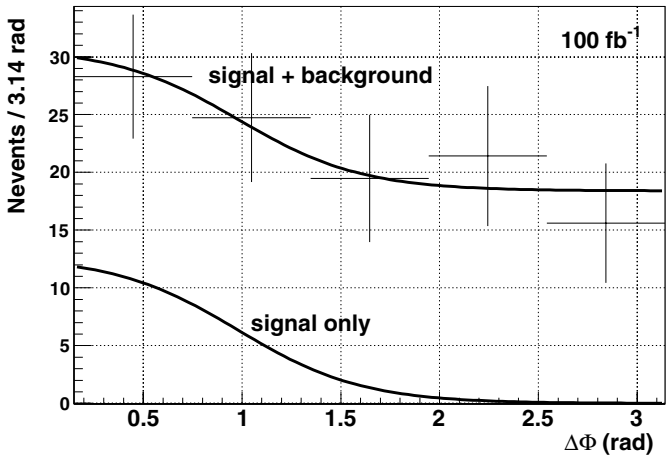

Figure 10.23. Distribution of the acoplanarity for pseudo-experiments, fitted by a signal + background shape, as described in the text.

uncertainty on the background level is found to be 15% for an integrated luminosity of 100 fb^{-1}, and rises up to 20% for 30 fb^{-1}. That value will be used in the following.

Reconstruction and selection uncertainties arise from the jet veto, the b veto and lepton reconstruction. Experience from Tevatron tells that a typical 2% uncertainty on lepton reconstruction efficiency has to be considered, while 5% uncertainty comes from lepton isolation [485] Since three leptons are present in our analysis, a 12% uncertainty from lepton reconstruction and selection has been taken. The additional uncertainties from the jet veto and the b veto will be assumed to be 5% each.

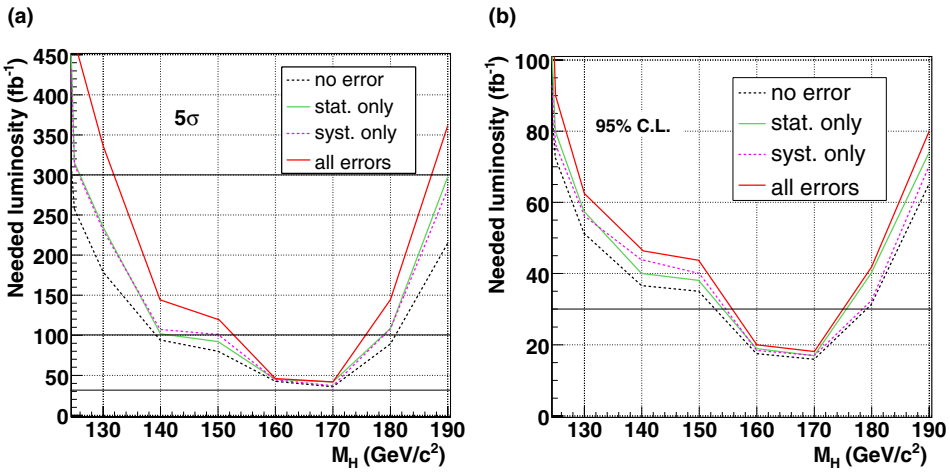

Figure 10.24. (a) Luminosity needed to obtain a 5σ significance using the likelihood-ratio method, with systematics only, Monte-Carlo statistical uncertainties only, or with both effects considered; (b) luminosity needed to exclude a Higgs boson at 95%C.L. if no excess is observed, using the same method.

To take into account other uncertainties related to the event selection, cuts are varied within the resolution of the associated quantity. The signal efficiency and background rejection are found to be stable with respect to such variations. A conservative value of 3% for the associated uncertainty is considered in the following.

The last uncertainty considered comes from the product of the luminosity and the proton structure functions, known as the parton luminosity. Considering these two quantities separately, a 5% uncertainty on the luminosity is assumed, while the uncertainty from the proton parton distribution function (PDF) is taken to be 4% [486]. This latter uncertainty is reduced for the process considered, for which the mid-x region (where uncertainties are small) dominates.

The additional source of systematic uncertainties arising from the limited Monte Carlo statistics is also considered in the following result. With the likelihood ratio method used in the analysis, this is done bin per bin in the distributions of signal and background, so that a single value cannot be quoted. For the time being, this has a large impact on the results, but this effect will easily be reduced in the future, as more events become available.

10.2.6.5. Signal significance. In order to integrate the effect of systematic uncertainties and to exploit the discriminative power from the transverse mass distribution, the likelihood-ratio method (S_{CL}) is used. Figure 10.24(a) shows the luminosity needed to obtain a 5σ significance using this method, with systematics only, with Monte Carlo statistical uncertainties, or with both effects considered. Figure 10.24(b) shows the luminosity needed to exclude a Higgs boson at 95%C.L. if no excess is observed, using the same method. Less than 50 fb^{-1} are required in most of the mass range, while only 20 fb^{-1} are needed at 170 GeV/c^2.

One important motivation for studying this channel is also that it is one of the only allowed signatures for a fermiophobic Higgs boson model. If the Higgs boson does not couple to fermions, the usual gluon-fusion diagrams are indeed forbidden, as well as $b\bar{b}$ decays. A fermiophobic Higgs boson will present a large cross-section at low mass, as the branching ratio does not drop down as in the Standard Model. Figure. 10.25(a) shows the luminosity

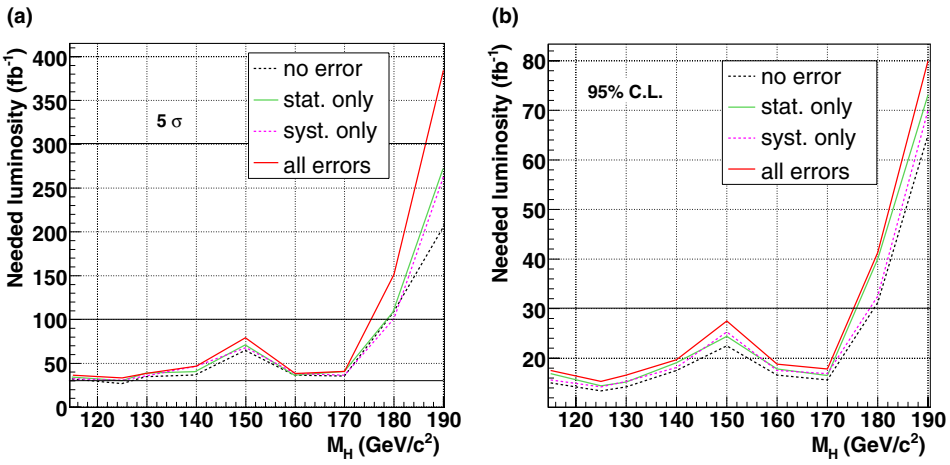

Figure 10.25. Results obtained using the benchmark fermiophobic model; (a) Luminosity needed to obtain a 5σ significance using the likelihood-ratio method, with systematics only, Monte-Carlo statistical uncertainties only, or with both effects considered; (b) luminosity needed to exclude a Higgs boson at 95%C.L. if no excess is observed, using the same method.

needed to obtain a 5σ significance for a fermiophobic Higgs boson. Compared to Fig. 10.24, the needed luminosity is found to be similar in the most favourable mass region for the Standard Model (around $170\,\mathrm{GeV/c^2}$) and above, but far better results are obtained in the low mass region. After $100\,\mathrm{fb^{-1}}$, all masses between the LEP limit and $175\,\mathrm{GeV/c^2}$ will be covered by this analysis alone. Figure 10.25(b) shows the luminosity needed to exclude a fermiophobic Higgs boson at 95%C.L. if no excess is observed. In the absence of signal, less than $30\,\mathrm{fb^{-1}}$ are required to reject any fermiophobic Higgs boson up to $175\,\mathrm{GeV/c^2}$.

10.2.7. Associated $\mathrm{t\bar{t}H}$ *production with* $\mathrm{H} \to \gamma\gamma$

10.2.7.1. Introduction. A Higgs boson produced in association with a $\mathrm{t\bar{t}}$ pair, with an $\mathrm{H} \to \gamma\gamma$ decay would share a fully reconstructible mass peak with the inclusive $\mathrm{H} \to \gamma\gamma$ signature. But like the WH and ZH channels [487], the signature could contain an isolated high-transverse- momentum charged lepton which can be used both to discriminate against QCD background and reconstruct the primary vertex; the associated production channels could hence be less dependent on photon energy resolution. In particular, the presence of two top quarks would tend to produce high-multiplicity events, which could offer additional discriminating power against light jet QCD background. In the case of the two-Higgs-doublet MSSM, the gluon fusion Higgs boson production channel could in fact be subject to suppression with respect to the associated production channels in the case of top-stop degeneracy ("maximal mixing") [488]. Prior generator-level studies for the detection of the SM [489] and MSSM [490] Higgs bosons in CMS via this channel have indicated a signal-to-background ratio of approximately 1. A full simulation study in the ATLAS Physics Technical Design Report [491] has predicted a signal significance of $\mathrm{S}/\sqrt{B} = 4.3 - 2.8$ for $\mathrm{m}_H = 100$–$140\,\mathrm{GeV/c^2}$ with a signal efficiency of ~30%. A more recent, related ATLAS study involving a 2-photon signature accompanied by missing energy [492] has indicated, for $100\,\mathrm{fb^{-1}}$, a signal-to-background ratio of ~ 2 for $\mathrm{m}_H = 120\,\mathrm{GeV/c^2}$.

Table 10.21. Estimated number of signal events for $t\bar{t}H$, $H \to \gamma\gamma$, assuming NLO production cross sections [162], Higgs boson branching ratios to two photons [21], and one electron or muon from top decay (including from tau lepton decays).

Higgs Boson Mass (GeV/c^2)	After 30 fb^{-1}	After 100 fb^{-1}
115	20.80	69.33
120	19.61	65.36
130	15.96	53.20
140	11.20	37.33

10.2.7.2. Signal production cross-sections, event rates and event generation. Production cross-sections for $t\bar{t}H$ have been calculated at next-to-leading order [162,464,465]. Taking the branching ratio for $H \to \gamma\gamma$ from HDECAY [21] and assuming in addition that the decay of exactly one of the top quarks yields a lepton (electron or muon) from $W^{\pm} \to l + \nu_l$ (including the possibility of tau lepton decays to muons or electrons), we estimate for several Higgs boson masses the number of signal events for 30 and 100 fb^{-1} (Table 10.21).

Signal events were generated with both the MADGRAPH [81,493,494] and ALPGEN [161,495, 496] LO exact matrix element generators, for each of the Higgs boson masses shown in Table 10.21. Events from both generators were found to yield comparable LO cross-section and kinematical distributions. The LO cross-sections were also found to agree with those from the program HQQ [20] at the percent level. The samples analysed were those generated with ALPGEN. For the current study all signal events have been generated such that exactly one of the two W bosons from the two top quarks decays leptonically.

10.2.7.3. Background processes considered and event generation. Standard Model processes resulting in both irreducible and reducible backgrounds have been identified. A background is called irreducible if it is capable of giving rise to the same signature on the particle level as that searched for in a signal event, that is to say, a lepton and two photons ($l\gamma\gamma$). Special care has been taken to properly treat the irreducible $t\bar{t}\gamma\gamma$ background. Feynman diagrams of three possible types of $t\bar{t}\gamma\gamma$ processes considered are shown in Fig. 10.26. In the first case, called "Type 1", both photons are radiated from either outgoing top quarks or incoming partons. In the third case, called "Type 3", both are radiated from top quark decay products. The second case, "Type 2" combines one photon radiated according to "Type 1" with the second radiated according to "Type 3". (A fourth process arises from both photons being radiated from different decay products of the *same* top quark; for the relevant event selection (see pertinent section below) with $m_{\gamma\gamma} > 70\,GeV/c^2$ we have verified that this contribution is completely negligible). The Types 2 and 3 processes, as well as the process $W\gamma\gamma$+ 4 jets, previously unavailable in any matrix element generator, have been specifically added to ALPGEN for this and future studies. Where applicable in the ALPGEN samples, top quarks and W bosons are decayed within ALPGEN which assures preservation of spin correlation information which could impact kinematical distributions.

Table 10.22 lists the considered irreducible background processes, the generators used to either generate or cross-check event samples, the LO cross-section with statistical errors, the number of events expected for 30 (100)fb^{-1} of integrated luminosity, the number of events generated, simulated, reconstructed and analysed as well as the equivalent integrated luminosity, which ranges from 400 to over 6000 fb^{-1}. The cross-sections reflect pre-selection criteria imposed at generator-level which are described in the next section. In the processes involving real top quarks as well as in the $W\gamma\gamma$+ 4j process, one top quark/the W boson was forced to decay leptonically, and the stated cross-section therefore implicitly includes

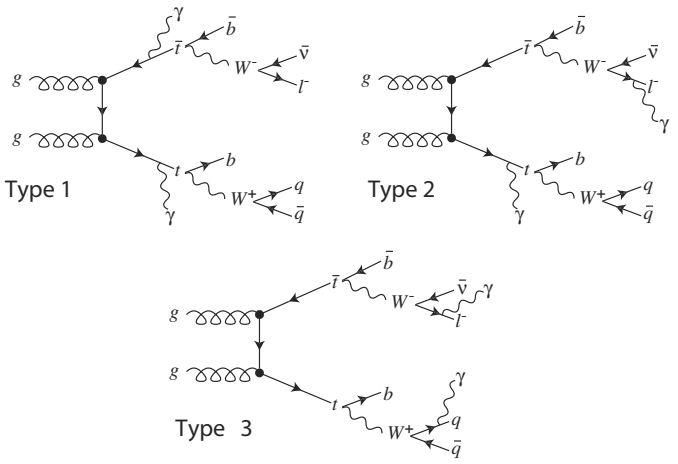

Figure 10.26. A sub-sample of the relative Feynman graphs illustrating the three types of $t\bar{t}\gamma\gamma$ processes.

Table 10.22. Cross-sections at leading order (statistical errors in parentheses), number of events generated, simulated and reconstructed, and equivalent integrated luminosity for the irreducible backgrounds considered.

Process	$\sigma \times$ BR [fb] (1 W $\to l\nu$)	Ngen	N 30 fb^{-1}	N 100 fb^{-1}	Generator	N simul./ reconstr.	N Anal.	Anal. Eq. Int. Lumi. [fb^{-1}]
tt$\gamma\gamma$ 1	1.6 ($\leqslant$ 1/mil)	52202	48	160	AL,MG	10000	4695	6250
tt$\gamma\gamma$ 2	6.1 ($\leqslant$ 1%)	6238	183	610	AL	6000	5109	1000
tt$\gamma\gamma$ 3	4.9 ($\leqslant$ 1%)	2967	147	490	AL	2500	2250	510
W $\gamma\gamma$ 4j	11.5 (1.2%)	4587	345	1150	AL	4500	3957	400

the relevant branching ratio. The effect of the inclusion of background Types 2 and 3 is to augment the total initial contribution (before selection) from $t\bar{t}\gamma\gamma$ by approximately one order of magnitude.

A background is called reducible if at least one element of the final-state signature is mistakenly identified due to incomplete detector coverage or other instrumental effects. This could arise if one or more electrons or jets are misidentified as photons, or a jet as an electron or a muon. It has been heretofore possible to evaluate only the irreducible backgrounds discussed above with acceptable statistics, so only these will be presented here. Low-statistics tests on most of the reducible background processes have been performed, and strong requirements have been implemented in the following selection in order to veto them.

10.2.7.4. Event simulation and reconstruction. All generated signal and background events were fragmented and hadronised with PYTHIA [69, 246] version 6.227, using the CTEQ5L [12] PDFs. They were then simulated, digitised and reconstructed using the standard CMS tools. All samples were digitised with high-luminosity (10^{34}cm^{-2}s^{-1}) pile-up.

10.2.7.5. Description of generator-level pre-selections. No generator-level pre-selections were made on signal events. For the irreducible background events, the following

pre-selection was made:

- $m_{\gamma\gamma} \geqslant 80\,\mathrm{GeV/c^2}$ for all four processes;
- $p_{T\gamma} \geqslant 20\,\mathrm{GeV/c}$, $|\eta_\gamma| \leqslant 2.5$ (MADGRAPH) or $p_{T\gamma} \geqslant 15\,\mathrm{GeV/c}$, $|\eta_\gamma| \leqslant 2.7$ (ALPGEN) for all four processes;
- $p_{Tl} \geqslant 15\,\mathrm{GeV/c}$ for all processes except $tt\gamma\gamma$ 1;
- $p_{Tj} \geqslant 15\,\mathrm{GeV/c}$, $|\eta_{j,l}| \leqslant 2.7$, Δ R(l, j or j, j or γ ,j or γ, γ) $\geqslant 0.3$ for the process $W\gamma\gamma$ 4j, where 'j' refers to one of the four additional light quark jets;

where p_T refers to the transverse momentum of the particle, η its pseudorapidity and $\Delta R = \sqrt{(\Delta\eta^2 + \Delta\phi^2)}$ where ϕ is the azimuthal angle.

The intersection (most restrictive set) of the above generator-level criteria except that pertaining to the additional light quark jets was then imposed on all signal and background event samples at the particle level.

10.2.7.6. Event selections. The events are selected by the single and diphoton triggers at Level-1 and High Level Triggers (HLT) configured for high luminosity ($10^{34}\,\mathrm{cm^{-2}s^{-1}}$).

A prior study of this channel at particle-level [497] found that reliance on p_T alone to identify the two Higgs boson photon candidates results in considerable sidebands (at approximately the 10% level) in the two-photon invariant mass distribution in signal events. It is the choice of the second (lower in p_T) photon which is overwhelmingly contaminated by these combinatorial photons, which originate approximately 80% from π^0s, 10% from ηs, a few percent from ωs, and the remainder from other particles. Fully 80% of these fake Higgs photon 'mother' particles appear to come from parton showers whose origin is one of the two final-state top quarks, and as such are peculiar to the $t\bar{t}H$ process. The other 20% come from showering from the initial-state partons and hence are common to all the associated production channels. For reconstructed signal events, the misidentification percentage grows to $\sim 30\%$ (see the pertinent curve in Fig. 10.28(left)).

To improve the Higgs photon selection procedure, we have evaluated the performance of the photon isolation variables investigated and used by the $H \to \gamma\gamma$ inclusive analysis [7]. We obtain the best results by considering linear combinations of the variables 'ECALIso' (the sum of E_T of ECAL basic clusters within a cone after removing the E_T of those basic clusters constructed with the Island algorithm included in the supercluster matched ($\Delta R < 0.2$) with the offline photon itself) and 'HCALIso' (the sum of E_T of HCAL calorimeter towers within a cone centred on the photon candidate), as illustrated in Fig. 10.27(right).

For this study, the two highest-p_T Offline Photons satisfying the following requirement on the isolation energy Iso = HCALIso + (2.*ECALIso) were retained as Higgs photon candidates:

- For photons in the barrel: Iso $< 25\,\mathrm{GeV}$,
- For photons in the endcap: Iso $< 22\,\mathrm{GeV}$,

with $\Delta R < 0.25$ for ECALIso and $\Delta R < 0.3$ for HCALIso (see comparison of performance with different isolation cone radii in Fig. 10.27 (left). These values yield approximately 95% efficiency for true Higgs photons[45] and less than 40% for combinatorial photons. This strategy successfully restores approximately one-half of the true Higgs photon pairs previously lost to misidentification when selection based on only photon p_T is used, as is demonstrated by Fig. 10.28.

[45] "True Higgs photons" are considered to be those Offline Photons lying within a cone of radius $\Delta R < 0.1$ of one of the two particle-level photons coming from the Higgs boson decay.

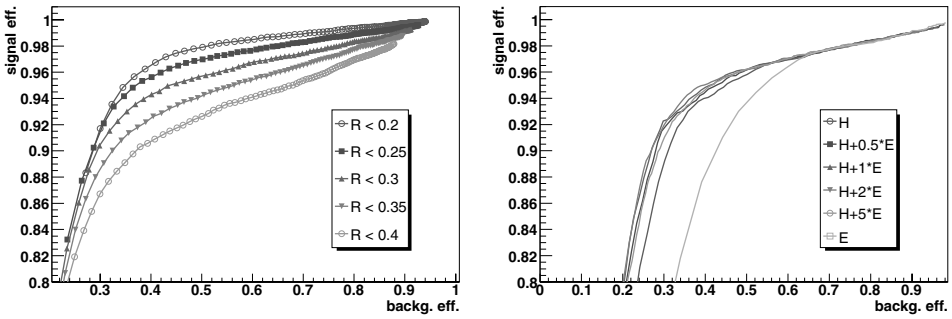

Figure 10.27. Left: Efficiency for true Higgs photons vs. that for combinatorial photons in the ECAL barrel for the ECAL isolation variable, for different isolation cone sizes. Right: Efficiency for true Higgs photons vs. that for combinatorial photons in the ECAL endcap, for several linear combinations of isolation variables.

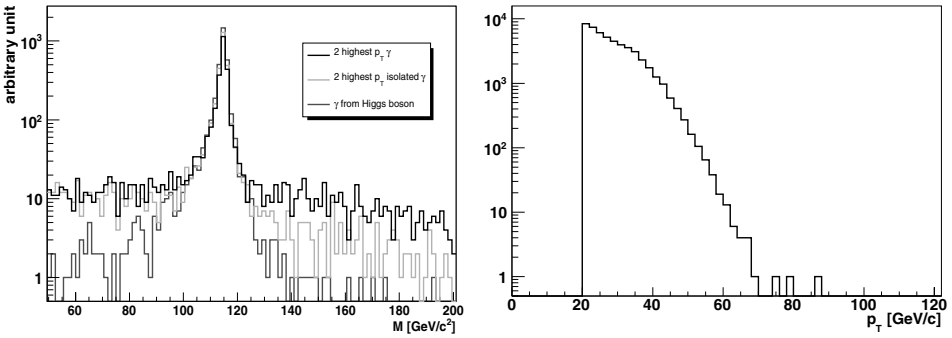

Figure 10.28. Left: Invariant mass of the two Higgs photon candidates selected according to p_T alone (dark grey curve), p_T and isolation (light grey curve), and where both candidates are geometrically matched to particle-level Higgs photons (medium grey curve). Right: Distribution of the p_T of jets from pile-up events. Jets not matched to generated particle jets from the signal are considered to be pile-up jets.

A similar technique is employed for the selection of candidate leptons from top quark decays (via a W boson). We obtain the best performance in selecting 'true' W leptons[46] with the previously-defined ECALIso variable for Offline Electrons and with transverse momentum of tracks in a cone of radius $\Delta R < 0.25$ ('IsoByTkPt025') for GlobalMuons. We retain as the W-decay (top) lepton candidate the highest-E_T OfflineElectron or highest-p_T GlobalMuon satisfying the following requirement:

- For electrons, ECALIso < 5 GeV,
- For muons, IsoByTkPt02 < 9 GeV.

These values yield ∼92% efficiency for 'true' W leptons and approximately 35% for combinatorial leptons. In the selection criteria involving photons described below, as well as those involving leptons described thereafter, the pertinent distributions are constructed using

[46] As for Higgs photons, considered to be those OfflineElectrons or GlobalMuons lying within a cone of radius ΔR <0.1 of a particle-level electron or muon from a W boson which itself is a decay product of one of the final-state top quarks.

the Higgs photon and W lepton candidates selected according to the procedure combining p_T and isolation described above.

After selection of the two Higgs photon and one W lepton candidates, the remainder of the selection aims for a signal efficiency of between 85 and 95% per selection criterion. Five variables involving the Higgs photon candidates have demonstrated effective performance: the p_T of each of the two OfflinePhoton candidates ($p_{T\gamma 1}$, $p_{T\gamma 2}$), the sum of their p_T ($p_{T\gamma 1} + p_{T\gamma 2}$), the angular distance between them ($\Delta R_{\gamma_1,\gamma_2}$), and $\cos\theta^*$, where $\tan\theta^* = \frac{|\vec{p}_i|\sin\theta_i}{\gamma(|\vec{p}_i|\cos\theta_i - \beta E_i)}$, and $\vec{p}_i$ and θ_i refer respectively to the momentum of and the 3-space angle between either of the two Higgs photon candidate directions and the direction of their joint 4-vector, in the laboratory frame (the scalar nature of the Higgs boson should assure a flat distribution of this variable for signal events, and one peaked in the forward and backward directions for background events). We have established the following eventwise selection involving the two Higgs photon candidates:

- $p_{T\gamma 1,\gamma 2} \geqslant 50, 18\,\mathrm{GeV/c}$
- $p_{T\gamma 1} + p_{T\gamma 2} \geqslant 85\,\mathrm{GeV/c}$
- $\Delta R_{\gamma_1,\gamma_2} \leqslant 3.2$
- $\cos\theta^* \leqslant 0.85$.

Three variables involving the W lepton candidates have demonstrated effective performance: the E_T (OfflineElectron) or p_T (OfflineMuon) of the candidate, and the angular distances between the candidate and each of the two Higgs photon candidates ($\Delta R_{\gamma_1,lepton}$, $\Delta R_{\gamma_2,lepton}$). We have established the following eventwise selection involving the W lepton candidate:

- $p_{Tlepton} \geqslant 15\,\mathrm{GeV/c}$
- $\Delta R_{\gamma_1,lepton}$, $\Delta R_{\gamma_2,lepton} \geqslant 0.3, 1.0$.

In order to remove part of the irreducible backgrounds studied here and also eventually to remove backgrounds from QCD processes, we take advantage of the high jet multiplicity of our signal events as well as the presence of two real top quarks yielding b-quark jets as decay products. Jets including those possibly corresponding to b-quarks are constructed with the iterative cone algorithm [7] with a cone radius of $\Delta R = 0.5$. A discriminant (BtagDisc) is then calculated for each candidate b-quark jet with the Combined BTag [7] b-quark-tagging algorithm. We require the presence of a minimum number of jets having a value of p_T greater than $60\,\mathrm{GeV/c}$, which permits the removal of jets from pile-up from consideration (we consider a reconstructed jet to be from pile-up if it is not geometrically matched with a particle-level jet, which has been constructed using the same algorithm and parameters as the reconstruction-level jets). Figure 10.28 (right) shows the p_T distribution of the jets thus attributed to pile-up in a signal sample with $m_H = 115\,\mathrm{GeV/c^2}$. We require $\geqslant 4$ jets with $p_T > 60\,\mathrm{GeV}$.

To specifically target the $W + 2\gamma$ + jets background (and eventually other non-b-quark reducible backgrounds), we make limited use of tagging of b-quark jets. We require that at least one candidate jet having $p_T > 60\,\mathrm{GeV}$ have BtagDisc > 0.8.

10.2.7.7. Performance of off-line selection. Tables 10.23 and 10.24 show the progression of the signal ($m_H = 115\,\mathrm{GeV/c^2}$) and background samples through the selection. Prior to checking for the Level-1 and HLT decision, we apply the pre-selection at particle-level described in Section 10.2.7.5 to all signal and background samples. The number of surviving events is expressed as an effective cross-section in fb. The final results are also expressed as numbers of surviving signal and total background events with statistical errors, for both 30 and $100\,\mathrm{fb^{-1}}$.

Table 10.23. Progression of the signal ($m_H = 115\,GeV/c^2$) and background samples through the trigger portion of the selection, expressed as an effective cross-section in fb. Efficiencies with respect to the previous sequential requirement are expressed as percentages.

Requirement	$M_H = 115\,GeV/c^2$	$tt\gamma\gamma 1$	$tt\gamma\gamma 2$	$tt\gamma\gamma 3$	$W2\gamma 4j$
Before selection	0.693 (100.0)	1.59 (100.0)	6.12 (100.0)	4.95 (100.0)	11.4 (100.0)
Pre-selection	0.533 (76.8)	1.4 (87.9)	5.05 (82.5)	3.94 (79.6)	11.3 (98.9)
L1 + HLTAccept	0.517 (97.0)	1.34 (95.4)	4.71 (93.4)	3.36 (85.7)	10.5 (93.0)
HLT $\gamma\gamma$, γ accept	0.508 (98.3)	1.30 (96.9)	4.57 (96.9)	3.25 (96.6)	10.0 (96.0)

Table 10.24. Progression of the signal ($m_H = 115\,GeV/c^2$) and background samples through the offline portion of the selection, expressed as an effective cross-section in fb. Efficiencies with respect to the previous sequential requirement are expressed as percentages.

Requirement	Criterion	$M_H = 115\,GeV/c^2$	$tt\gamma\gamma 1$	$tt\gamma\gamma 2$	$tt\gamma\gamma 3$	$W2\gamma 4j$
Number of γ's	$\geqslant 2$	0.506 (100.0)	1.29 (100.0)	4.56 (100.0)	3.24 (100.0)	10.0 (100.0)
Number isolated γ's	$\geqslant 2$	0.482 (95.2)	1.22 (94.0)	3.96 (86.8)	2.53 (78.2)	9.58 (95.7)
$pT\gamma_1$ (GeV/c)	>50	0.432 (90.0)	1.04 (85.3)	3.14 (79.4)	1.48 (58.5)	7.90 (82.5)
$pT\gamma_2$ (GeV/c)	>18	0.386 (89.2)	0.88 (84.7)	2.25 (71.6)	1.03 (69.7)	6.72 (85.0)
$pT\gamma_1 + pT\gamma_2$ (GeV/c)	>85	0.379 (98.2)	0.847 (96.3)	2.17 (96.5)	0.926 (89.8)	6.40 (95.3)
$\Delta R(\gamma_1\gamma_2)$ (GeV/c)	<3.2	0.364 (96.4)	0.738 (87.2)	1.86 (85.9)	0.719 (77.7)	5.30 (82.8)
$\cos\theta^*$	<0.85	0.332 (91.4)	0.589 (79.8)	1.48 (79.5)	0.583 (81.0)	4.36 (82.3)
pT_{lep} isolated (GeV)	>15	0.238 (72.2)	0.443 (75.2)	0.984 (66.4)	0.387(66.4)	3.15 (72.3)
$\Delta R(\gamma_1 l)$	>0.3	0.236 (99.0)	0.441 (99.5)	0.925 (94.0)	0.321 (83.0)	3.14 (99.6)
$\Delta R(\gamma_2 l)$	>1.0	0.208 (87.4)	0.389 (88.2)	0.607 (65.7)	0.163 (50.7)	2.34 (74.6)
N jets $p_T > 60\,GeV$	$\geqslant 4$	0.179 (86.2)	0.338 (87.0)	0.455 (74.9)	0.110 (67.6)	1.79 (76.6)
Btag Disc for $\geqslant 1$ jet	>0.8	0.110 (61.6)	0.217 (64.0)	0.276 (60.7)	0.051 (46.0)	0.294 (16.4)
$M_H +/- 1.5\,GeV/c^2$		0.074 (67.1)	0.005 (2.51)	0.011 (3.86)	<0.002 (3.92)	<0.003 (1.02)
N_{evts} at $30\,fb^{-1}$		$2.22 +/- 0.10$		$0.483 +/- 0.158$		
N_{evts} at $100\,fb^{-1}$		$7.42 +/- 0.334$		$1.61 +/- 0.53$		

10.2.7.8. Uncertainties, systematic errors, and strategy for background measurement from data. To estimate the systematic error on the surviving signal cross-section, the following global source of error is applied directly to the estimated number of signal events:

- Luminosity <3%.

The error due to the inclusion/non-inclusion of initial and final-state photon radiation at the fragmentation/hadronisation level as well as that due to the matrix element generator used (ALPGEN or MADGRAPH) was found to be insignificant.

We have also considered the following sources of uncertainty relevant to the detector:

- Electron/Photon/Muon identification: 1% per identified object.
- Efficiency to tag jets containing b quarks: 5% per identified b-quark jet.
- Uncertainty on the jet energy scale: 3%.

Only the effect of the uncertainty on the jet energy scale is evaluated by propagation through the selection, and yields a net uncertainty of $+1.6/-3.9\%$ for a Higgs boson mass of $115\,GeV/c^2$. All the above contributions are summed in quadrature and a systematic error of $+6.3/-7.2\%$ is obtained for the number of signal events for a Higgs boson mass of $115\,GeV/c^2$. The uncertainty on the number of surviving background events, calculated below and amounting to an average of $\pm 15\%$, is finally added to the above quadratic sum yielding an error of $+16.3/-16.6\%$ on the number of events in a peak containing both signal and background events, corresponding to the case of a signal cross-section measurement.

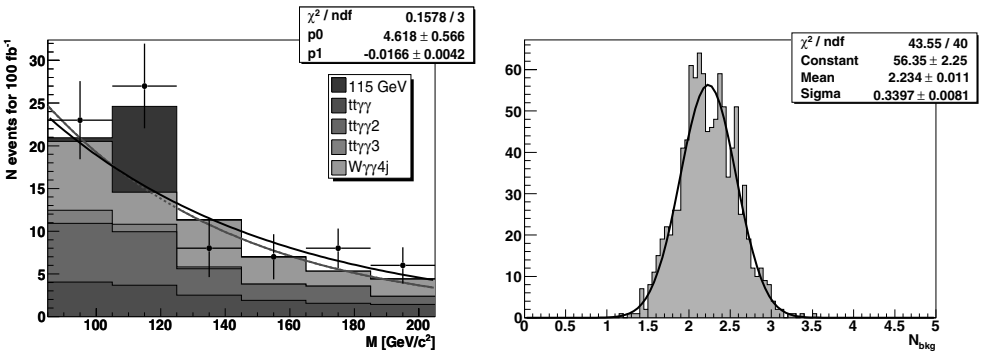

Figure 10.29. Left: Background estimation from the fit of the sidebands: Example of a gedanken experiment giving a possible set of real data points consistent with the Poisson distribution of the simulated number of surviving background events. The fit through these points is superimposed on the original fit. Right: Distribution of the estimated number of background events from the fit of the gedanken experiments.

Table 10.25. The signal selection efficiency, the total number of surviving signal and background events at 100 fb^{-1} with statistical errors (from the number of generated events), the number of background events estimated from the fit with the fit error, and the signal significance calculated using the ScP estimator without and with the background uncertainty evaluated from the fit.

Higgs Boson Mass (GeV)	115	120	130	140
Sig. Selection Eff. (%)	10.7	11.2	11.3	11.3
Number Signal	7.42 ± 0.33	7.33± 0.33	5.96 ± 0.27	4.21 ± 0.19
Total Number Bcgkd	1.61 ± 0.53	2.79 ± 0.62	1.98 ± 0.66	1.10± 0.51
Total Number Bcgkd from fit w. syst.	2.23 ± 0.34	1.94 ± 0.32	1.60 ± 0.22	1.39 ± 0.22
Signal Significance (ScP)	3.541	3.662	3.257	2.510
Signal Significance (ScP) w. syst.	3.414	3.523	3.184	2.453

The background spectrum can be obtained from the sidebands surrounding the positions of the putative Higgs boson masses and fit to a decreasing exponential function (shown by the grey curve in Fig. 10.29 (left)). The bin width has been chosen to be large enough (20 GeV/c^2) to have a sufficient number of events for an integrated luminosity of 100 fb^{-1} (The bin centred around the generated Higgs boson mass is not used for the fitting procedure). The number of background events and its error are estimated by fitting test distributions obtained with the average of the bin contents according to a Poisson distribution (gedanken experiments corresponding to possible future real data sets). One such fit is shown in the black curve in Fig. 10.29 (left). The mean and width of the gaussian fit of the distribution thus obtained (Fig. 10.29 (right)) yield respectively estimates of the number of background events and its systematic error, which are used to compute the signal significance.

10.2.7.9. Results. Table 10.25 shows, for each of the four Standard Model Higgs boson mass values considered, the signal selection efficiency, the total number of surviving signal and background events at 100 fb^{-1} with statistical errors (from the number of generated events), the number of background events estimated from the fit with the fit error, and the signal significance calculated using the ScP estimator [498] with and without the background uncertainty evaluated from the fit.

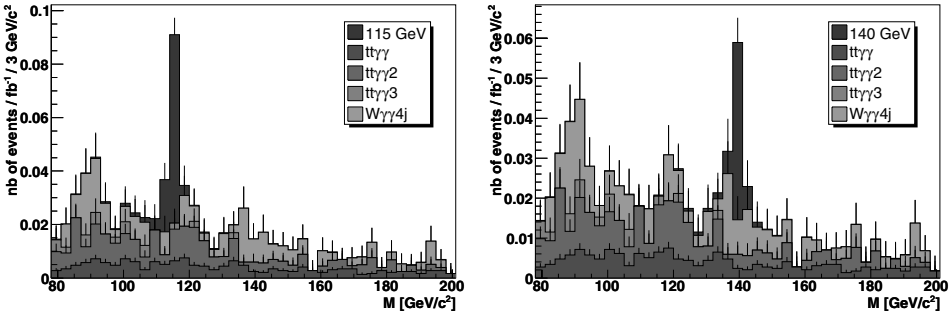

Figure 10.30. The diphoton mass after all selections for signal of $m_H = 115\,\mathrm{GeV/c^2}$ (left) and $140\,\mathrm{GeV/c^2}$ (right) added to the surviving backgrounds.

Figure 10.30 shows the diphoton mass distribution of the signal added to the background after all selections for Higgs boson masses $115\,\mathrm{GeV/c^2}$ (left) and $140\,\mathrm{GeV/c^2}$ (right).

10.2.7.10. Conclusion. A full-reconstruction-level sequential study has been performed for the channel $t\bar{t}H$, with $H \to \gamma\gamma$, taking into account irreducible backgrounds not previously studied. The ratio of signal to background events is approximately 4:1 representing a factor of 2 improvement over prior CMS and ATLAS studies. Signal observability in excess of 3σ is indicated for masses up to $130\,\mathrm{GeV/c^2}$ with full simulation and reconstruction and with estimated systematic errors taken into account for $100\,\mathrm{fb^{-1}}$ of integrated luminosity.

10.2.8. Associated WH, ZH production with $H \to \gamma\gamma$

Compared to the gluon-gluon fusion channel $gg \to H \to \gamma\gamma$, the associated production channels WH/ZH [499, 500] suffer from a much lower production cross section. Several advantages, however, make these channels attractive when the decay of the gauge boson results in a charged lepton: requiring an additional relatively high transverse-momentum lepton greatly reduces the significant QCD background in the $\gamma\gamma$ topology and improves the primary vertex reconstruction [501]. In the context of supersymmetric models, maximal mixing in the stop sector could result in a strong suppression of the $gg \to h$ signal, which the associated production channels would not be subject to [502]. The searched-for final state is therefore comprised of 2 isolated photons and at least one isolated electron or muon. Prior generator-level or fast simulation studies [489, 490, 503, 504] conclude to the possibility of a discovery at the LHC in this channel.

A detailed description of the analysis can be found in [505].

10.2.8.1. Event generation and reconstruction. All the process considered in this study have been simulated at the leading order. Signal events were generated by the matrix element generator COMPHEP [43] for Higgs boson masses ranging from 90 to $150\,\mathrm{GeV/c^2}$, in steps of $5\,\mathrm{GeV/c^2}$. Total cross-sections have been rescaled accordingly to the NLO calculation [20]. K-factors from 1.15 to 1.16 are obtained on the whole mass range. Branching ratios for $H \to \gamma\gamma$ were taken from HDECAY program [21]. The irreducible backgrounds from the processes $W\gamma\gamma$ et $Z\gamma\gamma$ were also generated with COMPHEP, with the same K-factors applied as those pertinent to the signal. Fragmentation and hadronisation was performed by PYTHIA [246].

The reducible background processes $\gamma\gamma$, γ-jet, Wγ, $b\bar{b}$, and $t\bar{t}$, retained due to their capacity to mimic the $l\gamma\gamma$ signal, have been generated with PYTHIA and leading order cross-sections were considered, except for the $t\bar{t}$ production where a NLO cross section of 840 pb is used [278].

To ensure an efficient generation and preserve sufficient statistics of the most signal like events, a pre-selection is applied at generator level. Three electromagnetic candidates or two electromagnetic candidates and one muon candidate with $E_T > 20\,\text{GeV}$ and $|\eta| < 2.7$ are required. An electromagnetic candidate is obtained by clustering electrons and photons in a $\Delta\eta = 0.09$, $\Delta\phi = 0.09$ window. Muon candidates are either μ, τ, π, or K particles.

The generated events were passed through the GEANT3 simulation of CMS [25]. The events were then digitised and reconstructed with the standard CMS software [506] with the addition of pile-up event corresponding to the high luminosity phase ($\mathcal{L} = 10^{34}\,\text{cm}^{-2}\text{s}^{-1}$).

10.2.8.2. Trigger selection. Events are required to pass the global Level 1 trigger [506] and the double photon High Level Trigger (HLT) [76] configured for the high luminosity phase. The trigger efficiencies for the preselected signal events are higher than 95% on the whole Higgs boson mass range (90–150 GeV/c^2) as shown in Table 10.26 and 10.27.

10.2.8.3. Offline event selection. To suppress the reducible backgrounds, four discriminant combined variables are first constructed using a likelihood ratio method to estimate the isolation of the photons, the quality of the lepton reconstruction, the isolation of the lepton and the QCD/multi-jets nature of the event. The reference histograms for the four likelihoods are all produced on independent simulated event samples after a very loose pre-selection requiring two offline photons and one electron or muon reconstructed by the standard algorithms. Photon candidates with a matching seed in the pixel detector are rejected. The two photons with the highest transverse energy are assigned to the Higgs boson decay. Several isolation variables [507] were tested in the likelihood and the best performance is obtained with the sum of the transverse energy of the basic clusters within a cone $\Delta R < 0.3$ around the photon, excluding the basic clusters belonging to the photon supercluster and the sum of the transverse energy of the HCAL towers within a cone $\Delta R < 0.3$ around the photon.

Then the offline lepton with the highest E_T is selected. The reconstruction quality of the electron is carefully checked. The four variables yielding the most significant discriminating power are the ratio E/p between the electron energy as measured in the calorimeter and its momentum measured by the tracker, the hadronic energy fraction E_{had}/E, the distance $\Delta\eta$ between the track and the associated supercluster and the ratio R_9 between the sum of the energies of 9 crystals (3×3 matrix centred on the maximum-energy crystal) and the energy of the corresponding supercluster. In the case of muons the purity obtained by the standard CMS reconstruction algorithms has already proven sufficient; therefore, no additional criteria are applied.

For the lepton isolation, similar calorimeter variables as for photons are used. In addition, the number of pixel lines within a cone $\Delta R < 0.3$ around the lepton improves the discriminative power of the likelihood.

Finally a global discriminant variable against multi-jet background is constructed. The rejection of π^0 faking signal photons, effective against QCD backgrounds, has been accomplished by a neural network procedure exploiting the information on the lateral profile of the electromagnetic shower. Variables involving the multiplicity of reconstructed objects in the electromagnetic calorimeter improve the discriminating power.

The results of the selection applied on the four combined variables are presented in Tables 10.26 and 10.27. The multi-jet backgrounds are entirely suppressed. To obtain a more

Table 10.26. Expected rates (in fb) after each stage of the event selection for signals ($m_H = 120\,GeV/c^2$) and irreducible backgrounds. Errors are statistical only.

	WH	ZH	W$\gamma\gamma$	Z$\gamma\gamma$
σ.BR	0.810	0.137	-	-
Pre-selection: σ.BR.ε	0.460	0.0440	13.58	18.92
Double photons HLT	0.439 ± 0.005	0.0423 ± 0.0004	8.80 ± 0.04	12.13 ± 0.07
2 isolated photons	0.387 ± 0.005	0.0370 ± 0.0004	7.14 ± 0.04	6.51 ± 0.04
1 good quality lepton	0.331 ± 0.004	0.0350 ± 0.0003	5.56 ± 0.04	4.58 ± 0.03
Lepton isolation	0.299 ± 0.004	0.0318 ± 0.0003	4.83 ± 0.04	4.11 ± 0.03
QCD rejection	0.281 ± 0.004	0.0273 ± 0.0003	4.50 ± 0.04	3.53 ± 0.03
$80 < m_{\gamma\gamma} < 160$	0.271 ± 0.004	0.0259 ± 0.0003	2.04 ± 0.02	1.42 ± 0.02

Table 10.27. Expected rates (in fb) after each stage of the event selection for reducible backgrounds. Contributions of the different p_T bins are summed. Errors are statistical only.

	$\gamma\gamma$	Wγ	b$\bar{b}$	t$\bar{t}$	γ-jet (jet)
σ.BR	1.1×10^5	5.79×10^3	1.78×10^9	86.2×10^3	1.21×10^8
Pre-selection: σ.BR.ε	270.1	26.5	2.96×10^5	6.00×10^3	7.16×10^4
Double photons HLT	197.7 ± 1.0	16.8 ± 0.1	77120 ± 764	1948 ± 17	35045 ± 256
2 isolated photons	161.6 ± 0.8	9.97 ± 0.07	682 ± 72	31.2 ± 2.2	7235 ± 115
1 good quality lepton	27.3 ± 0.3	7.98 ± 0.07	311 ± 49	23.5 ± 1.9	2552 ± 68
Lepton isolation	9.8 ± 0.2	6.59 ± 0.06	(0.87)	14.2 ± 1.5	209 ± 20
QCD rejection	7.6 ± 0.2	5.74 ± 0.06	(0.003)	(0.35)	(6.6)
$80 < m_{\gamma\gamma} < 160$	3.2 ± 0.1	2.40 ± 0.04	(0.001)	(0.26)	(3.7)

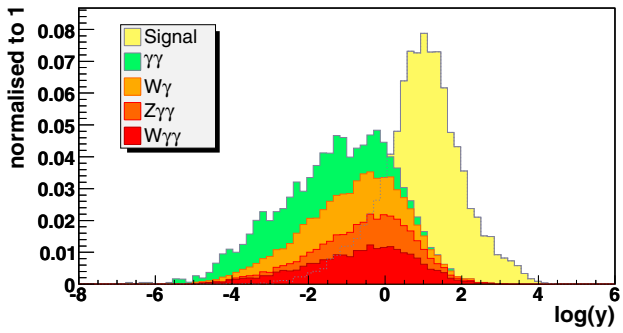

Figure 10.31. Distribution of the final combined variable for the signal ($m_H = 120\,GeV/c^2$) and for the background. The optimal working point is obtained with a cut $\log(y) > 0.35$.

precise estimation of these backgrounds, the cut factorisation method has been applied and the result is given between parentheses in Table 10.27. After rejecting events outside the 80–160 GeV/c^2 diphoton mass window, the expected rate of events is 0.297 ± 0.003 fb for signal and 13.1 ± 2.6 fb for background. Some simple kinematical variables are then used to form a final likelihood. The best discrimination was obtained with the transverse energy of the photons and of the lepton, the ΔR distances between lepton and each photon, the missing transverse energy, and the $\Delta\Phi$ angle between the directions of the missing transverse energy and of the highest E_T photon. The distribution of the resulting combined variable y is shown in Fig. 10.31 for a Higgs boson mass of 120 GeV/c^2.

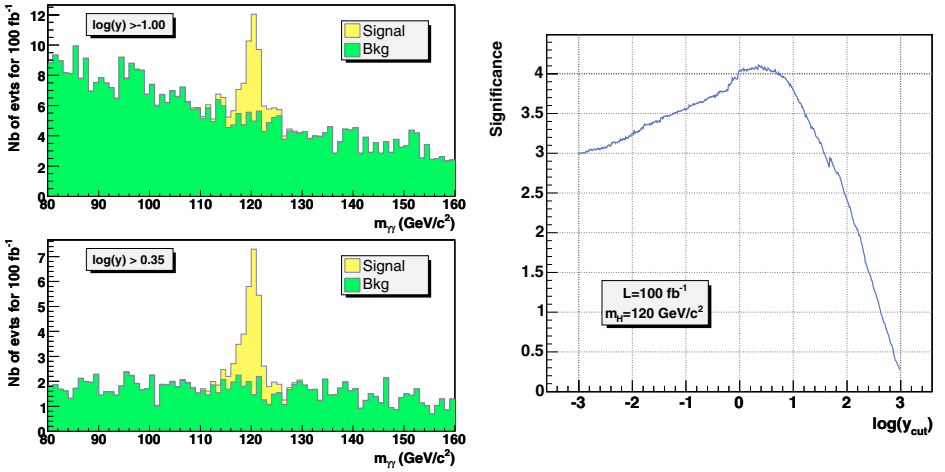

Figure 10.32. Left: Reconstructed $\gamma\gamma$ mass for different selection values on the final combined variable y for an integrated luminosity of 100 fb^{-1}. Right: Statistical significance as a function of the cut on the combined variable $\log(y)$, for $m_{\mathrm{H}} = 120\mathrm{GeV/c^2}$ and an integrated luminosity of 100 fb^{-1}. The highest significance is obtained with a cut $\log(y) > 0.35$.

Table 10.28. Optimal working points for different Higgs boson mass hypotheses. The significance and the expected number of signal and background events are given for an integrated luminosity of 100 fb^{-1}.

m_{H} ($\mathrm{GeV/c^2}$)	working point $\log(y) >$	significance	WH	ZH	W$\gamma\gamma$	Z$\gamma\gamma$	Wγ	$\gamma\gamma$	γ-jet	$\mathrm{t\bar{t}}$	$\mathrm{b\bar{b}}$
115	0.41	4.30 σ	22.1	1.8	49.3	30.9	33.0	10.2	1.7	0.16	10×10^{-5}
120	0.35	4.09 σ	20.7	1.6	51.2	36.2	34.5	12.4	1.9	0.15	10×10^{-5}
130	0.68	3.64 σ	14.6	1.3	30.7	16.9	18.7	6.0	1.4	0.10	4×10^{-5}
140	0.99	3.35 σ	11.4	1.0	18.9	10.3	10.6	3.7	1.0	0.04	1×10^{-5}
150	0.83	2.87 σ	10.4	0.9	20.2	11.7	12.3	5.4	1.1	0.03	3×10^{-5}

10.2.8.4. Statistical method and optimisation. The statistical methods developed by the LEP Higgs working group [508, 509] are used in this analysis to optimise the selection criteria and determine the statistical significance of the final results. To form the test-statistic, the three obvious variables to be used are the counting rates, the $\gamma\gamma$ invariant mass and the kinematic likelihood variable y. The limited statistics of the MC events prohibit however the use of a two-dimensional method for the determination of the Higgs boson discovery potential. So, only the counting rates and shape of the reconstructed $\gamma\gamma$ mass distribution will be used along with a cut on the combined likelihood variable y. The optimal working point is the y cut value which maximises the discovery potential as shown in Fig. 10.32.

The list of the optimal working points obtained for the different Higgs boson mass hypotheses is given in Table 10.28. The significance and the expected number of signal and background events are given for a luminosity of 100 fb^{-1}. For the γ-jet, $\mathrm{t\bar{t}}$ and $\mathrm{b\bar{b}}$ backgrounds, the rates are estimated by the method of cut factorisation.

10.2.8.5. Use of real data in sidebands: systematic uncertainties. The signal is characterised by a strongly peaked diphoton mass and the $m_{\gamma\gamma}$ distribution of the background is quite

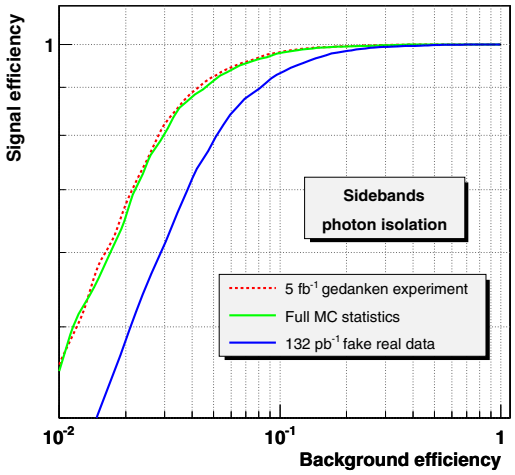

Figure 10.33. Comparison of the performance obtained when optimising the photon isolation likelihood with a sample of $132\,\text{fb}^{-1}$ of "fake real data" taken in the $20 < m_{\gamma\gamma} < 80\,\text{GeV/c}^2$ sideband (dash-dotted line) with the performance obtained by the standard analysis using the full MC statistics (solid line). To increase the available statistics in the sideband, gedanken experiments were generated for an equivalent luminosity of $5\,\text{fb}^{-1}$. The results of the optimisation on these sideband events is represented by the dotted line.

smooth at the considered working points. Therefore, when real data will be available, the data taken in $m_{\gamma\gamma}$ sidebands will be used to optimise the likelihood analysis and to estimate the background.

Likelihood optimisation with sideband events. No kinematic observables were used to construct the four primary likelihoods aimed at rejecting multi-jet events to avoid correlations with the diphoton mass. If the shapes of the distributions of the variables used in the likelihoods are sufficiently similar for different diphoton mass regions, then data taken outside the signal region can be used to optimise the likelihoods. To test the feasibility of the method, a sample of "fake real data" (the number of MC events for each background is equal to the expected number of events for a given luminosity) taken in the $20 < m_{\gamma\gamma} < 80\,\text{GeV/c}^2$ sideband is used to produce the reference S/B histograms of the likelihoods. The equivalent luminosity of the sample is limited to $132\,\text{pb}^{-1}$ by the available statistics and is composed of 4682 $\text{b}\bar{\text{b}}$, 465 γ-jet, 222 $\text{t}\bar{\text{t}}$, 2 $\gamma\gamma$, 1 Wγ and 1 Z$\gamma\gamma$ events. The performance obtained with the likelihood on the events in the 80–160 GeV/c^2 band is compared to the results obtained by the standard analysis optimised with the full MC statistics available. For the four global discriminant variables, up to 20% loss of efficiency is observed for the same rejection power. The degradation of the performance is mainly due to the insufficient statistics of γ-jet and $\text{t}\bar{\text{t}}$ events in $132\,\text{pb}^{-1}$ of data. To increase the size of the "fake data sample", gedanken experiments were generated using the fitted shapes of the variables used in the likelihoods (correlations between the variables are neglected). The results are presented in Fig. 10.33 for the photon isolation likelihood. An integrated luminosity of $5\,\text{fb}^{-1}$ will be sufficient to optimise the four primary likelihoods with the real data taken in the $m_{\gamma\gamma}$ sideband and to reproduce the results obtained when using the full MC statistics.

Background measurement from data. The $m_{\gamma\gamma}$ distribution of the background is smooth enough to be easily fit in the sideband to estimate the background in the signal region.

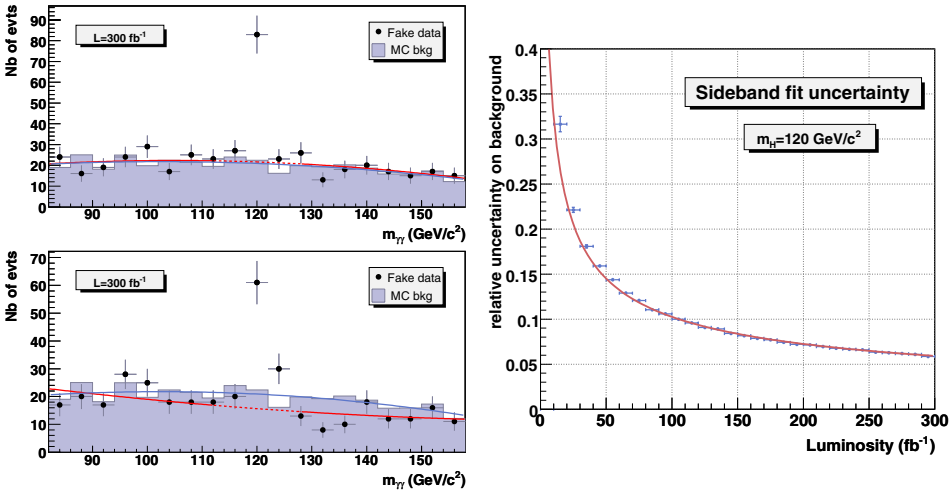

Figure 10.34. Left: Background measurement in the signal region with a fit on the $m_{\gamma\gamma}$ sideband. The fit of the full MC statistics is represented by the solid light gray line. The fit of the fake data (dark grey) is performed on the sidebands (i.e. after the exclusion of the signal window represented by the dotted line). Two gedanken experiments are represented for an integrated luminosity of 300 fb^{-1} and a 120 $\mathrm{GeV/c^2}$ Higgs boson mass hypothesis. Right: Relative uncertainty on the background estimation by the sideband fit method as a function of the integrated luminosity with LHC running at high luminosity for a Higgs boson mass of 120 $\mathrm{GeV/c^2}$.

To optimise the method (size and position of the window, bin width, choice of the fit function) and to estimate the uncertainty on background, 10000 signal + background pseudo-experiments were generated for each Higgs boson mass and luminosity hypothesis, as illustrated in Fig. 10.34. For a luminosity of 100 fb^{-1} and a Higgs boson mass of 120 $\mathrm{GeV/c^2}$, the background is measured with a precision of 11%, and with a precision of 6.6% for 300 fb^{-1}.

Systematic uncertainties for signal and cross-section measurement. The theoretical cross-section error due to the scale variation are estimated to ±3% for WH and ZH production for all considered Higgs boson masses [20]. The uncertainty on the parton density function of the CTEQ collaboration [12] is almost constant for the associated production $q\bar{q} \rightarrow VH$ at the LHC and of the order of 4% over a Higgs boson mass range between 100 and 200 $\mathrm{GeV/c^2}$ [510]. The error on the measured luminosity is expected to be 3% for luminosity above 30 fb^{-1}. The error on the lepton or photon reconstruction and identification has been estimated to 1% for each photon and lepton. An error of 5% on the missing transverse energy, see Appendix B, propagated in the final likelihood gives a −1.08% +0.49% variation of the final signal rate for $m_{\mathrm{H}} = 120\,\mathrm{GeV/c^2}$. The quadratic sum of all these errors gives a 6% total error on the expected signal rate.

In the case of a Higgs boson discovery, this channel will be used to measure the cross-section times the branching ratio:

$$\sigma_s \times BR = \frac{N_s}{\epsilon_{sel}\,\mathcal{L}} = \frac{N - N_b^{fit}}{\epsilon_{sel}\,\mathcal{L}}$$

where N_s is the number of signal events given by the difference between the total number N of observed events and the number N_b^{fit} of background events measured by the sideband fit.

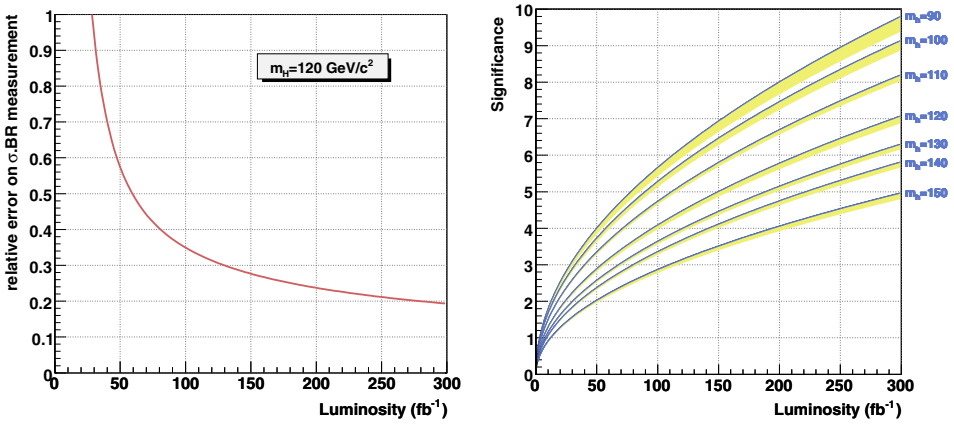

Figure 10.35. Left: Precision on the measurement of the product of cross-section and branching ratio as a function of the integrated luminosity with LHC running at high luminosity for a 120 GeV/c^2 Higgs boson. Right: Statistical significance for different Higgs boson mass hypotheses as a function of the integrated luminosity with LHC running at high luminosity. The 1σ systematic uncertainty is represented by the grey (yellow online) band.

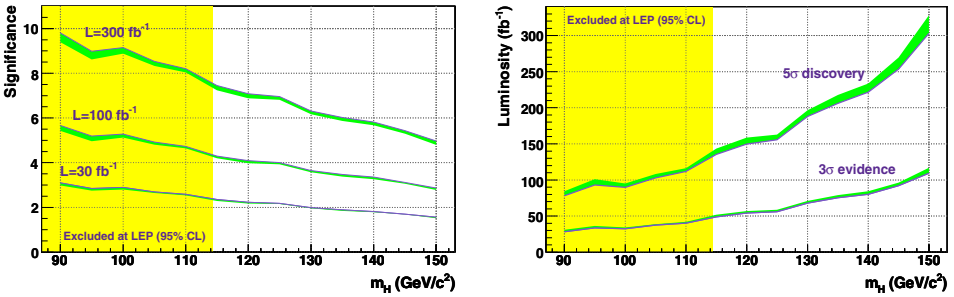

Figure 10.36. Statistical significance (left) and luminosity needed for a 5σ or 3σ observation (right) as a function of m_{H}. The 1σ systematic uncertainty is represented by the grey (yellow online) bands.

The total uncertainty on the measure is given by:

$$\left(\frac{\Delta(\sigma_s \times BR)}{\sigma_s \times BR}\right)^2 = \left(\frac{\Delta N}{N - N_b^{fit}}\right)^2 + \left(\frac{\Delta N_b^{fit}}{N - N_b^{fit}}\right)^2 + \left(\frac{\Delta \mathcal{L}}{\mathcal{L}}\right)^2 + \left(\frac{\Delta \epsilon_{sel}}{\epsilon_{sel}}\right)^2$$

The expected precision on the $\sigma \times BR$ measurement is represented as a function of the integrated luminosity in Fig. 10.35. For a 120 GeV/c^2 Higgs boson, the product of the cross-section and branching ratio will be measured with a precision of 35% after one year of LHC running at high luminosity, and with a precision of 19% after three years of high luminosity running.

10.2.8.6. Results for the Standard Model Higgs boson. The statistical significance is represented as a function of the luminosity in Fig. 10.35 for different m_{H} hypothesis. The statistical significance and the luminosity needed for a 5σ or 3σ observation are represented as a function of m_{H} in Fig. 10.36. One year of high luminosity running allows the observation

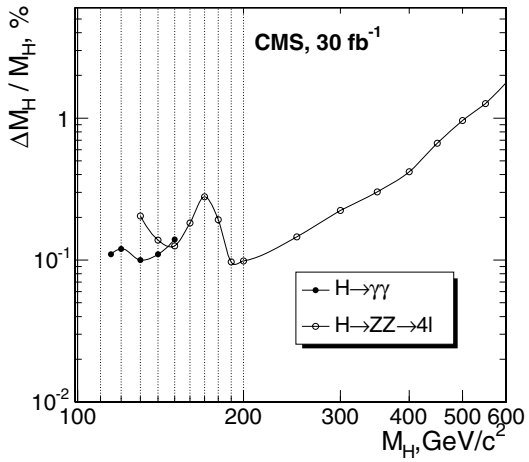

Figure 10.37. The statistical precision of the Higgs boson mass measurement for the $30\,\mathrm{fb}^{-1}$ using inclusive Higgs boson production $\mathrm{pp} \to \mathrm{H} + \mathrm{X}$ and the $\mathrm{H} \to \gamma\gamma$ and $\mathrm{H} \to \mathrm{ZZ} \to 4\ell$ decay modes.

at 3σ of the SM Higgs boson up to $m_{\mathrm{H}} = 150\,\mathrm{GeV/c^2}$, and three years of running at high luminosity are required to reach a 5σ discovery.

10.3. Discovery reach

10.3.1. Accuracy of the Higgs boson mass measurement

Figure 10.37 shows the statistical precision of the Higgs boson mass measurement for the $30\,\mathrm{fb}^{-1}$ using inclusive Higgs boson production $\mathrm{pp} \to \mathrm{H} + \mathrm{X}$ and the $\mathrm{H} \to \gamma\gamma$ and $\mathrm{H} \to \mathrm{ZZ} \to 4\ell$ decay modes.

10.3.2. Discovery reach for the Standard Model Higgs boson

This section summarises the discovery reach for the Standard Model Higgs boson. The NLO cross sections and branching ratios for the Higgs boson calculated with the programs HDECAY [41], HIGLU [40], VV2H, V2HV and HQQ [20] are used, as well as the NLO cross sections for the background processes, when available.

Figure 10.38 shows the integrated luminosity needed for the 5σ discovery of the inclusive Higgs boson production $\mathrm{pp} \to \mathrm{H} + \mathrm{X}$ with the Higgs boson decay modes $\mathrm{H} \to \gamma\gamma$, $\mathrm{H} \to \mathrm{ZZ} \to 4\ell$, and $\mathrm{H} \to \mathrm{WW} \to 2\ell 2\nu$.

Figure 10.39 shows the signal significance as a function of the Higgs boson mass for $30\,\mathrm{fb}^{-1}$ of the integrated luminosity for the different Higgs boson production and decay channels.

10.3.3. Study of CP properties of the Higgs boson using angle correlation in the $\Phi \to ZZ \to \mathrm{e}^+\mathrm{e}^-\mu^+\mu^-$ process

The most general ΦVV coupling ($V = W^{\pm}, Z^0$) for spin-0 Higgs boson Φ (Φ means the Higgs particle with unspecified CP-parity, while H (h) and A mean the scalar and

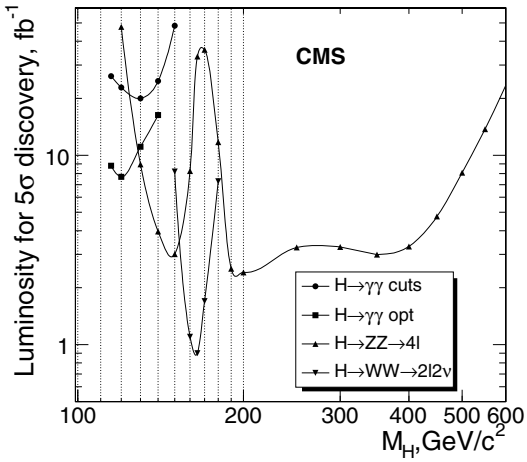

Figure 10.38. The integrated luminosity needed for the 5σ discovery of the inclusive Higgs boson production $pp \to H + X$ with the Higgs boson decay modes $H \to \gamma\gamma$, $H \to ZZ \to 4\ell$, and $H \to WW \to 2\ell 2\nu$.

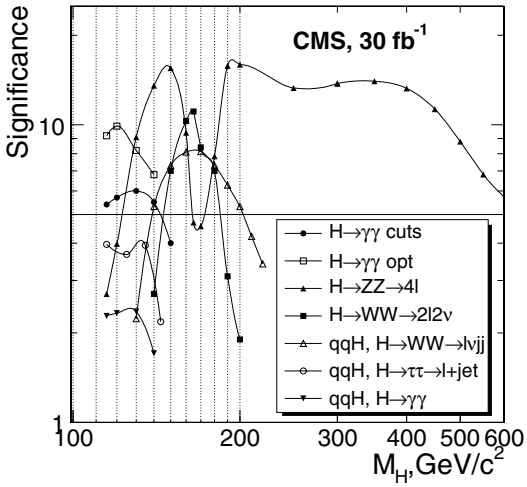

Figure 10.39. The signal significance as a function of the Higgs boson mass for 30 fb $^{-1}$ of the integrated luminosity for the different Higgs boson production and decay channels.

pseudoscalar Higgs particles, respectively) looks as follows [511–514]:

$$\mathcal{C}^{J=0}_{\Phi VV} = \kappa \cdot g^{\mu\nu} + \frac{\zeta}{m_V^2} \cdot p^\mu p^\nu + \frac{\eta}{m_V^2} \cdot \epsilon^{\mu\nu\rho\sigma} k_{1\rho} k_{2\sigma}, \tag{10.5}$$

where k_1, k_2 are four-momenta of vector bosons V and $p \equiv k_1 + k_2$ is four-momentum of the Higgs boson. In the present analysis a simplified version of above ΦVV coupling (Eq. 10.5) is studied with a Standard-Model-like scalar and a pseudoscalar contributions (i.e. $\kappa, \eta \neq 0$ and $\zeta = 0$). To study deviations from the Standard Model ΦZZ coupling we take $\kappa = 1$[47].

[47] The ΦVV coupling with $\kappa = 1$ and arbitrary η is implemented in the PYTHIA generator.

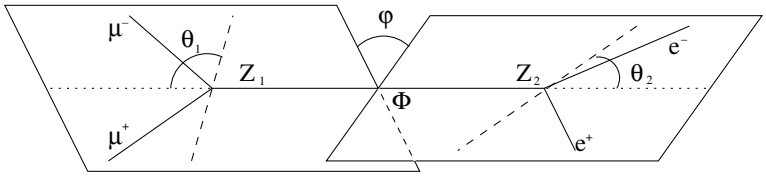

Figure 10.40. Definitions of the angles in the $\Phi \to ZZ \to e^+e^-\mu^+\mu^-$ process.

The decay width for the $\Phi \to ZZ \to (\ell_1\bar{\ell}_1)(\ell_2\bar{\ell}_2)$ process consists now of three terms: a scalar one (denoted by H), a pseudoscalar one $\sim \eta^2$ (denoted by A) and the interference term violating CP $\sim \eta$ (denoted by I):

$$d\Gamma(\eta) \sim H + \eta\, I + \eta^2 A. \tag{10.6}$$

This way the Standard Model scalar ($\eta = 0$) and the pseudoscalar (in the limit $|\eta| \to \infty$) contributions could be recovered. It is convenient to introduce a new parameter ξ, defined by $\tan\xi \equiv \eta$, which is finite and has values between $-\pi/2$ and $\pi/2$. Expressions for H, A and I can be found in article [512].

In study of the CP-parity of the Higgs boson two angular distributions were used. The first one is a distribution of the angle φ (called plane or azimuthal angle) between the planes of two decaying Zs in the Higgs boson rest frame. The negatively charged leptons were used to fix plane orientations. The second one is a distribution of the polar angle θ, in the Z rest frame, between momentum of negatively charged lepton and the direction of motion of Z boson in the Higgs boson rest frame (Figure 10.40).

The analysis was performed for scalar, pseudoscalar and CP-violating Higgs boson states, the latter for $\tan\xi = \pm 0.1, \pm 0.4, \pm 1$ and ± 4.

A detailed description of the analysis can be found in [515].

10.3.3.1. Generation and event selections. The production and decay of the scalar, pseudoscalar and CP-violating Higgs boson states were generated using PYTHIA [69] for three masses of the Higgs boson, $M_\Phi = 200$, 300 and 400 GeV/c^2. Backgrounds and event selections are the same as in the analysis of the Standard Model Higgs boson $H \to ZZ \to e^+e^-\mu^+\mu^-$ described in Section 10.2.1. The reconstructed angular distributions after all selections for the signal with mass $M_\Phi = 300$ GeV/c^2 for various values of the parameter ξ, and for the background are shown in Fig. 10.41 at 60 fb^{-1}. The Standard-Model signal cross-section and branching ratio were used for the signal normalisation in Fig. 10.41.

10.3.3.2. Determination of the parameter ξ. The parameter ξ was determined by maximisation of the likelihood function $\mathcal{L}(\xi, R)$, which was constructed from angular distributions and invariant mass distribution of four leptons, for the signal and the background. The function depends on two parameters: ξ describing CP property of the signal, and R describing fraction of the signal in the data sample. The function has the following form:

$$\mathcal{L}(\xi, R) \equiv 2 \sum_{x_i \in data} \log \mathcal{Q}(\xi, R; x_i), \tag{10.7}$$

where $\mathcal{Q}(\xi, R; x_i) \equiv R \cdot \mathcal{PDF}_S(\xi; x_i) + (1 - R) \cdot \mathcal{PDF}_B(x_i)$.

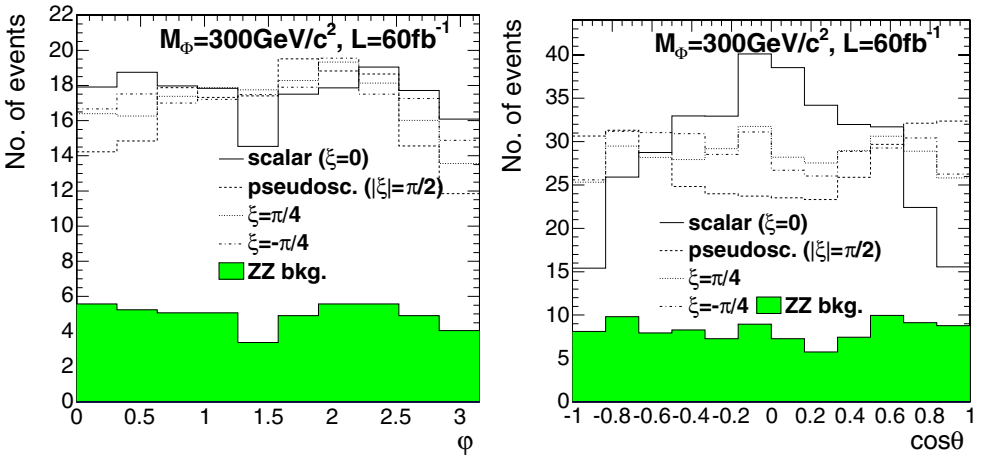

Figure 10.41. The φ-distributions (left) and the θ-distributions (right) for various values of the parameter ξ after final selections at 60 fb^{-1}. Empty histograms - the signal for $M_\Phi = 300\,\mathrm{GeV/c^2}$ and $\xi = 0$ (scalar), $\xi = -\pi/4$, $\xi = +\pi/4$ and $|\xi| = \pi/2$ (pseudoscalar). The filled histogram - the ZZ background. The Standard-Model signal cross-section and branching ratio were used for the signal normalisation.

$\mathcal{PDF}_B(x_i)$ and $\mathcal{PDF}_S(\xi; x_i)$ are probability density functions for background and signal respectively; $\{x_i\}$ are values of the measured quantities (angles and invariant mass) in the event i. $\mathcal{PDF}$s are products of probability densities $\mathcal{P}^M$, $\mathcal{P}^\varphi$, $\mathcal{P}^{\cos\theta_{1,2}}$ of four leptons invariant mass and angles φ and $\cos\theta_{1,2}$: $\mathcal{PDF} \equiv \mathcal{P}^M \cdot \mathcal{P}^\varphi \cdot \mathcal{P}^{\cos\theta_1} \cdot \mathcal{P}^{\cos\theta_2}$. The $\mathcal{P}^M$, $\mathcal{P}^\varphi$, $\mathcal{P}^{\cos\theta_{1,2}}$ are obtained by the Monte Carlo technique, using normalised histograms of given quantities after the final selection.

A part of the function $\mathcal{Q}$ which describes angular distributions of signal depends on the parameter ξ, namely from Eq. (10.6) we obtain:

$$\mathcal{P}(\xi) \equiv \mathcal{P}_S^\varphi(\xi) \cdot \mathcal{P}_S^{\cos\theta_1}(\xi) \cdot \mathcal{P}_S^{\cos\theta_2}(\xi) \equiv$$
$$(\mathcal{H} + \tan\xi \cdot \mathcal{I} + \tan^2\xi \cdot a^2\mathcal{A})/(1 + a^2\tan^2\xi), \tag{10.8}$$

where $\mathcal{H} \equiv \mathcal{P}_H^\varphi \cdot \mathcal{P}_H^{\cos\theta_1} \cdot \mathcal{P}_H^{\cos\theta_2}$ and $\mathcal{A} \equiv \mathcal{P}_A^\varphi \cdot \mathcal{P}_A^{\cos\theta_1} \cdot \mathcal{P}_A^{\cos\theta_2}$ are probability densities obtained by the Monte Carlo technique for the scalar (H) and the pseudoscalar (A) Higgs boson, respectively. The parameter a^2 is a (mass dependent) relative strength of the pseudoscalar and scalar couplings. For example $a^2 = 0.51,\ 1.65,\ 1.79$ for $M_\Phi = 200,\ 300,\ 400\,\mathrm{GeV/c^2}$, respectively. The $\mathcal{I}$ is a normalised product of angular distributions for the CP-violating term. The $\mathcal{I}$ is not always positive, and its integral is equal to zero, so it is not possible to simulate it separately. The $\mathcal{I}$ contribution can be obtained indirectly from the combined probability density for the signal with non-zero value of the parameter ξ. For example by introducing $\mathcal{P}_+ \equiv \mathcal{P}(\pi/4) = (\mathcal{H} + \mathcal{I} + a^2\mathcal{A})/(1 + a^2)$ and $\mathcal{P}_- \equiv \mathcal{P}(-\pi/4) = (\mathcal{H} - \mathcal{I} + a^2\mathcal{A})/(1 + a^2)$ we have $\mathcal{I} = (1 + a^2)/2 \cdot (\mathcal{P}_+ - \mathcal{P}_-)$. Finally we obtain:

$$\mathcal{P}(\xi) \equiv \left[\mathcal{H} + \tan\xi \cdot \frac{1 + a^2}{2} \cdot (\mathcal{P}_+ - \mathcal{P}_-) + \tan^2\xi \cdot a^2\mathcal{A}\right]/(1 + a^2\tan^2\xi). \tag{10.9}$$

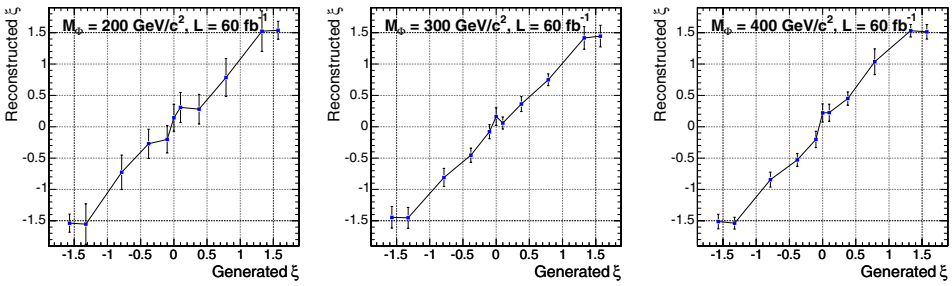

Figure 10.42. Reconstructed value of the parameter ξ as function of the generated value of the parameter ξ for $\mathcal{L}$=60 fb^{-1} and Higgs boson masses $M_\Phi = 200, 300, 400\,\mathrm{GeV/c^2}$. Uncertainties correspond to one standard deviation. The Standard-Model signal cross-section and branching ratio were used.

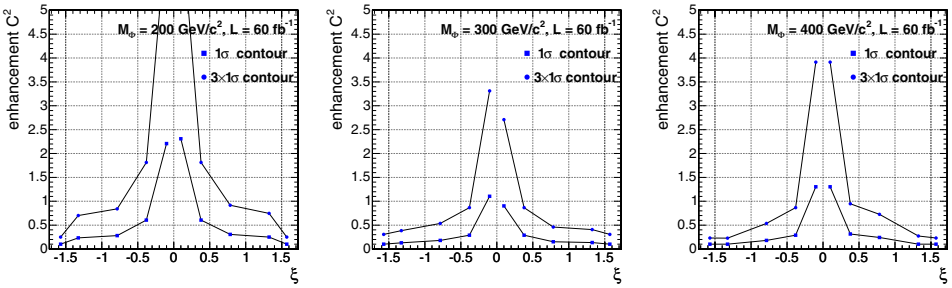

Figure 10.43. The minimal value of the factor C^2 needed to exclude the Standard Model, scalar Higgs boson at Nσ level (N = 1, 3) as a function of the parameter ξ for the Higgs boson masses $M_\Phi = 200, 300$ and $400\,\mathrm{GeV/c^2}$ (from left to right) at 60 fb^{-1}.

10.3.3.3. Results. After selection all background contributions, but $ZZ \to e^+e^-\mu^+\mu^-$, are negligible, therefore only these events were used to construct probability density function for the background. Signal probability density functions were constructed using samples of scalar Higgs boson (H), pseudoscalar (A) and $\mathcal{P}_+, \mathcal{P}_-$ samples ($\xi = \pm\pi/4$).

For each value of the parameter ξ and for each Higgs-boson mass we made 200 pseudo-experiments for the integrated luminosity $\mathcal{L} = 60\,\mathrm{fb}^{-1}$. For each pseudo-experiment we randomly selected events from the signal and background samples to form a test sample. The number of selected events was given by a Poisson probability distribution with mean defined by the process cross-section, selection efficiency and the examined luminosity. Then we performed a maximisation of the likelihood function $\mathcal{L}(\xi, R)$ for the test sample to obtain a value of the parameter ξ. The generated and reconstructed values of the parameter ξ with its uncertainty, obtained for three masses of the Higgs boson are shown in Fig. 10.42. The Standard-Model signal cross-section and branching ratio were used to normalise signal for each value of the parameter ξ.

An influence of enhancement (or suppression) factor C^2 of the Higgs boson production cross section times branching ratio, in respect to the Standard Model

$$C^2 = (\sigma \times Br)/(\sigma_{SM} \times Br_{SM}) \tag{10.10}$$

on the accuracy of the ξ measurement and thus, on possibility to exclude the Standard Model, scalar Higgs boson was studied. It was found that the precision of ξ measurement

is approximately proportional to $1/C$ (i.e. it depends on square-root of number of events, as one can expect):

$$\Delta\xi(\xi, C^2) \equiv \frac{\Delta\xi_{SM}(\xi)}{\sqrt{C^2}}. \tag{10.11}$$

A value of $\Delta\xi_{\mathrm{SM}}(\xi)$ corresponds to the precision of the parameter ξ measurement assuming the Standard Model Higgs boson production cross section times branching ratio. It is shown as the error bars in Fig. 10.42. Figure 10.43 shows the minimal value of the factor C^2 needed to exclude the SM Higgs boson at Nσ level (N $= 1, 3$), where N $= \xi/\Delta\xi$, as a function of the parameter ξ.